

Distribution Agreement

In presenting this thesis or dissertation as a partial fulfillment of the requirements for an advanced degree from Emory University, I hereby grant to Emory University and its agents the non-exclusive license to archive, make accessible, and display my thesis or dissertation in whole or in part in all forms of media, now or hereafter known, including display on the world wide web. I understand that I may select some access restrictions as part of the online submission of this thesis or dissertation. I retain all ownership rights to the copyright of the thesis or dissertation. I also retain the right to use in future works (such as articles or books) all or part of this thesis or dissertation.

Signature:

Qiuyang Li

Date

**Physical Properties and Dynamics of Excitons in Two-Dimensional
Semiconductor Nanoplatelets for Lasing and Solar-to-Fuel Conversion**

By
Qiuyang Li
Doctor of Philosophy

Chemistry

Dr. Tianquan Lian
Advisor

Dr. Michael Heaven
Committee Member

Dr. James Kindt
Committee Member

Accepted:

Lisa A. Tedesco, Ph.D.
Dean of the James T. Laney School of Graduate Studies

Date

**Physical Properties and Dynamics of Excitons in Two-Dimensional
Semiconductor Nanoplatelets for Lasing and Solar-to-Fuel Conversion**

By

Qiuyang Li

B.S., University of Science and Technology of China, P.R. China, 2013

Advisor: Tianquan Lian, Ph. D.

An abstract of

A dissertation submitted to the Faculty of the
James T. Laney School of Graduate Studies of Emory University
in partial fulfillment of the requirements for the degree of

Doctor of Philosophy

in Chemistry

2019

Abstract

Physical Properties and Dynamics of Excitons in Two-Dimensional Semiconductor Nanoplatelets for Lasing and Solar-to-Fuel Conversion

By Qiuyang Li

2D semiconductor nanoplatelets (NPLs) exhibit many unique properties, such as uniform quantum confinement, large exciton binding energy, and giant oscillator strength transition effect, long Auger lifetime, and high emission quantum yield, and have been intensively investigated for lasing and solar-to-fuel conversion applications. The optoelectronic and photocatalytic performances of 2D NPLs depend on the physical properties of band-edge excitons, including the exciton size, exciton in-plane transport, multi-exciton annihilation, and exciton dissociation. In this dissertation, we focus on the physical properties and dynamics of 2D excitons and how these properties affect the optical gain (gain mechanism, gain threshold) and light-driven H₂ generation performance in cadmium chalcogenide (CdX, X=Se, S, Te) and CsPbBr₃ Perovskite NPLs.

We first discuss the 2D exciton in-plane transport using CdSe/CdS type I and CdSe/CdTe type II core/crown (CC) NPLs as model systems, respectively. Both hot and cold excitons transport diffusively in 2D NPLs with a diffusion constant close to their bulk counterparts. This is followed by an investigation of multi-exciton Auger recombination of NPLs, emphasizing the difference of Auger mechanisms in 2D NPLs, 0D QDs, and 1D NRs, and the deviation from the “universal volume scaling” law. We established a new Auger recombination model for 2D NPLs that accounts for both a lateral area dependent exciton collision frequency and thickness dependent Auger probability per collision. The Auger recombination rate depends on the product of the exciton collision frequency and Auger probability, which provides a general scheme for Auger recombination in 1D and 2D nanocrystals.

Next, we discuss optical gain (OG) mechanisms and models of CdSe NPLs and show that OG thresholds are independent on the NPL lateral size but increase with the optical density of NPLs at the excitation wavelength. We also show that the extension of exciton coherent area at low temperature (<4K) and the resulting giant oscillator strength transition effect reduces the OG threshold by ~4-fold compared to the value at room temperature (298K), providing a new strategy for the rational design of NC-based low-threshold lasing materials. We also discuss exciton gain mechanism in CdSe/CdTe type II CC NPLs, where the OG is achieved in a tri-exciton state with two charge-transfer excitons at the core/crown interface and one CdTe exciton localized in CdTe crown.

Finally, we summarize our study of exciton dissociation in 2D NPLs and show that the light-to-H₂ conversion quantum efficiency can be significantly improved using 2D CdS NPLs. Detailed transient absorption study and modeling indicate that the improvement comes from slowing down charge recombination by the 2D morphology. We also show efficient exciton dissociation in CsPbBr₃ perovskite 2D NPLs by selectively transferring electron and hole to different acceptors and an over 100-fold longer-lived charge-separated state in CsPbBr₃ NPL-hole acceptor complexes compared to that in QD-hole acceptor complexes. These results indicate great potentials of 2D NPLs as in absorbers in solar-to-fuel conversion.

**Physical Properties and Dynamics of Excitons in Two-Dimensional
Semiconductor Nanoplatelets for Lasing and Solar-to-Fuel Conversion**

By

Qiuyang Li

B.S., University of Science and Technology of China, P.R. China, 2013

Advisor: Tianquan Lian, Ph. D.

A dissertation submitted to the Faculty of the
James T. Laney School of Graduate Studies of Emory University
in partial fulfillment of the requirements for the degree of
Doctor of Philosophy
in Chemistry
2019

Acknowledgment

First, I would like to express my deepest gratitude to my advisor, Prof. Tianquan Lian, for his guidance and support in the past 6 years at Emory University. He led me to this fantastic world of physical chemistry and taught me to think deep and thoroughly like a real scientist. He always provides invaluable insights into scientific problems, and his encouragement and support give me the confidence to communicate and collaborate with scientists in and outside the department. He is and will always be the model in my future academic career. I also wish to express my sincere thanks to my graduate committee professors, Prof. Michael Heaven and Prof. James Kindt, for their insightful comments and valuable support.

Second, I acknowledge my colleagues and friends that I interacted with during my PhD period. Dr. Kaifeng Wu, Dr. Haiming Zhu, and Dr. Ye Yang showed me the fundamentals of nanocrystals and ultrafast spectroscopy and helped me integrate into American life in my first year. Mr. Zihao Xu, Dr. Zheyuan Chen, and Dr. Jinquan Chen oversee the laser system in the lab, and their excellent job guarantees my productivity. Dr. Shaoxiong Wu and Dr. Bing Wang taught me skills and knowledge of NMR that benefits my research. Dr. Chen Qu from Prof. Bowman's group provided me helps on simulation and modeling in my research. Dr. Xinlin Song from University of Michigan shared valuable experience and knowledge about low temperature experiments with me. I also thank Dr. Aimin Ge, Dr. Laura Kiefer, Dr. Wenxing Yang, Dr. Chenyang Li, Dr. Yanyan Jia, Dr. Weiwei Guo, Dr. Yao Jing, Dr. Dongmei Xiang, Dr. Xinru Huang, Arshad Karumbamkandathil, Qiongyi Shang, Li Yu, Jia Song, Boyang Zhou, Yawei Liu, Tao Jin, Qiliang Liu, Jinhui Meng, Sara Gebre, Fengyi Zhao, Sheng He, Tianyuan Zhang, Qu Yu, Hanquan Su, Yixuan Han, Fengjiao Zhao, Yawei Yang, Xu Guo, Tony Xu, Xinhe Shan, and Yulei Cao for the happiness they brought.

Finally, I would like to thank my parents for their support and encouragement over the years. Special thanks to my dear wife, Huichang Xu, whose understanding and accompaniment in the last 13 years has encouraged me at every step on my way to PhD.

Table of Content

Chapter 1. Introduction	1
1.1. Backgrounds of Semiconductor 2D Nanoplatelets	1
1.2. Physical Properties of 2D Excitons of Nanoplatelets for Optoelectrical and Photocatalytic Applications.....	4
1.2.1. COM coherent delocalization of band-edge excitons.....	5
1.2.2. Exciton in-plane transport	6
1.2.3. Multi-exciton annihilation	8
1.2.4. Exciton dissociation.....	10
1.3. Summary	11
Chapter 2. Experimental Methods	14
2.1. Sample Preparation	14
2.1.1. Synthesis of cadmium chalcogenide nanoplatelets	14
2.1.2. Synthesis of core/crown nanoplatelet heterostructures	16
2.1.3. Synthesis of CdS nanorods	17
2.1.4. Synthesis of nanocrystal-Pt heterostructures	17
2.1.5. Synthesis of CsPbBr ₃ perovskite nanoplatelets	19
2.1.6. Sample preparation for low temperature measurement	20
2.1.7. Procedures of ligand exchange	20
2.2. Spectroscopy Setup	21
2.2.1. Femtosecond transient absorption spectroscopy setup.....	21

2.2.2. Nanosecond transient absorption spectroscopy setup	22
2.2.3. Static-photoluminescence measurement setup	22
2.2.4. Time-resolved photoluminescence measurement setup	22
2.2.5. Amplified spontaneous emission measurement setup	23
2.3. Light-Driven H ₂ generation.....	24
2.4. Electrochemical method for the estimation of Nanocrystal band-edge position	25
Chapter 3. Size-Independent Exciton Localization Efficiency in CdSe/CdS Type-I Core/Crown Nanoplatelet Heterostructures	29
3.1. Introduction	29
3.2. Results and Discussion.....	31
3.2.1. Sample Preparation and Characterizations	31
3.2.2. Type I Band alignment in CdSe/CdS core/crown heterostructure	33
3.2.3. Size independent crown-to-core exciton localization (XL) efficiency.....	37
3.2.4. Size dependent crown-to-core exciton localization dynamics	40
3.2.5. Mechanisms of exciton transport and trapping.....	45
3.3. Conclusion.....	50
Appendix 3.1	52
Appendix 3.2.	54
Appendix 3.3.	55
Appendix 3.4.....	59
Appendix 3.5	60
Appendix 3.6.....	63
Chapter 4. Efficient Diffusive Transport of Hot and Cold Excitons in CdSe/CdS Type-II Core/Crown Nanoplatelet Heterostructures	72

4.1. Introduction	72
4.2. Results and Discussion.....	75
4.2.1. Sample characterization.....	75
4.2.2. Unity CT exciton formation efficiency.	77
4.2.3. Size dependent exciton in-plane transport.....	78
4.2.4. 2D exciton diffusion model.	82
4.2.5. Hot exciton transport.	85
4.3. Conclusion.....	90
Appendix 4.1	92
Appendix 4.2	94
Appendix 4.3	95
Appendix 4.4	96
Appendix 4.5	101
Chapter 5. Area- and Thickness-Dependent Biexciton Auger Recombination in CdSe Nanoplatelets	112
5.1. Introduction	112
5.2. Results and Discussion.....	113
5.2.1. Sample characterization.....	113
5.2.2. Transient absorption spectroscopy on colloidal CdSe NPLs.....	115
5.2.3. Lateral size and thickness dependent Auger recombination	117
5.3. Conclusion.....	124
Appendix 5.1	126
Appendix 5.2	128
Appendix 5.3	129

Appendix 5.4	132
Appendix 5.5	135
Chapter 6. A Model for Optical Gain in CdSe Nanoplatelets.....	137
6.1. Introduction	137
6.2. Results and Discussion.....	139
6.2.1. Sample characterization.....	139
6.2.2. Lateral area independent optical gain threshold	140
6.2.3. Optical density dependent OG threshold.....	143
6.2.4. Amplified spontaneous emission measurements	144
6.2.5. Model of optical gain threshold.....	146
6.3. Conclusions	151
Appendix 6.1	152
Appendix 6.2	153
Appendix 6.3	154
Chapter 7. Reducing Optical Gain Threshold in Two-Dimensional CdSe Nanoplatelets by Giant Oscillator Strength Transition Effect.....	160
7.1. Introduction	160
7.2. Results and Discussion.....	163
7.2.1. Sample characterization.....	163
7.2.2. Temperature-dependent OG threshold by GOST effect.....	164
7.2.3. Measurement of exciton coherent area	167
7.2.4. Temperature-dependent S_x	171
7.2.5. Temperature-dependence of gain threshold in 0D, 1D, 2D, and bulk materials ..	174

7.3. Conclusion.....	175
Appendix 7.1	176
Appendix 7.2	178
Appendix 7.3	179
Appendix 7.4	181
Appendix 7.5	189
Appendix 7.6.....	199
Chapter 8. Low Threshold Multi-Exciton Optical Gain in CdSe/CdTe Core/Crown Type-II Nanoplatelets Heterostructures	201
8.1. Introduction	201
8.2. Results and Discussion.....	202
8.2.1. Sample characterization.....	202
8.2.2. Charge transfer exciton state	205
8.2.3. Long-lived excitons in the CdTe crown	208
8.2.4. Higher energy excitons in the CdSe core	212
8.2.5. Spatial distribution and energetics of exciton states.....	215
8.2.6. Pump wavelength dependent optical gain threshold	216
8.3. Conclusion.....	218
Appendix 8.1	220
Appendix 8.2	221
Appendix 8.3	225
Appendix 8.4	232
Chapter 9. Two-Dimensional Morphology Enhances Light-Driven H₂ Generation Efficiency in CdS Nanoplatelet-Pt Heterostructures.....	236

9.1. Introduction	236
9.2. Results and Discussion.....	238
9.2.1. Sample characterization.....	238
9.2.2. Enhanced H ₂ generation internal quantum efficiency	240
9.2.3. Ultrafast charge separation.	243
9.2.4. Ultrafast and pH dependent hole removal	247
9.2.5. pH and morphology dependent charge recombination in NPL-MV ²⁺ complexes	249
9.2.6. A Model for pH dependent H ₂ generation IQE	252
9.2.7. A Model for Enhanced H ₂ IQE in 2D NPL-Pt Heterostructures	253
9.3. Conclusion.....	256
Appendix 9.1	258
Appendix 9.2	263
Appendix 9.3	266
Appendix 9.4	271
Appendix 9.5	283
Appendix 9.6	285
Chapter 10. Efficient Charge Separation in Two-Dimensional CsPbBr₃ Perovskite Nanoplatelets	291
10.1. Introduction	291
10.2. Results and Discussion.....	292
10.2.1. Sample characterization.....	292
10.2.2. Spectroscopy of CsPbBr ₃ NPLs	294
10.2.3. Charge separation in CsPbBr ₃ NPLs	296

10.3. Conclusion.....	301
Appendix 10.1	302
Appendix 10.2	304
Appendix 10.3	307
Appendix 10.4	311
Chapter 11. Conclusion and Outlooks	314
References.....	318

List of Figures

Figure 1.1. Scheme of 0D quantum dots, 1D nanorods, and 2D nanoplatelets.	1
Figure 1.2. Scheme (upper panel) and TEM image (lower panel) of 4 monolayer (ML) CdSe NPLs.	2
Figure 1.3. Scheme of exciton internal motion and center-of-mass (COM) motion. The former determines the exciton binding energy and the latter determines the exciton COM coherent delocalization.	4
Figure 1.4. (a) The absorption (solid lines) and emission (dashed lines) spectra of 3-5 ML CdSe NPLs. (b) Scheme of energy diagram and band-edge excitonic transitions in CdSe NPLs.	5
Figure 1.5. Scheme (left) and energy diagram with band-edge transitions (right) of CdSe/CdS type I core/crown (CC) NPLs (upper panel) and CdSe/CdTe type II CC NPLs (lower panel). 7	
Figure 1.6. Schemes of Auger recombination process in NPLs (upper panel), the multi-carrier radiative recombination in NPL-based light emitting diodes (LED) (left in lower panel), biexciton emission in NPLs (middle in power panel), and MEG process in NPLs (right in lower panel).....	8
Figure 1.7. (a) Scheme of solution-processed artificial solar-to-H ₂ conversion system based on nanocrystal absorber with electron and hole acceptors. HT and ET represent hole transfer and electron transfer, respectively. (b) Exciton dissociation in cadmium chalcogenide nanoplatelet-metal heterostructures for light-driven H ₂ generation.	10
Figure 2.1. The pH dependent CV curves for (a) CdS NPLs and (b) CdS NRs. Dashed lines mark the reduction peaks. The pH dependent reduction potential of (c) CdS NPLs and (d) CdS NRs.	26

Figure 2.2. Reduction potentials of CdS NPLs and NRs. The electrochemical potentials of H^+ or water reduction (orange solid line) and hydroxyl anion oxidation (red solid line) as a function of pH. Purple spots represent the measured CB position of CdS NPLs. Blue solid line (green dashed line) represent the CB and VB position of CdS NPLs (NRs) as a function of pH.28

Figure 3.1. Optical and morphological properties of CdSe/CdS CC NSs. (a) Representative HAADF TEM image of CC3. (b) EDX image of a selected area in (b) showing the spatial distribution of Cd(red), Se(green), and S(blue). (c) The absorbance (solid lines) and photoluminescence (dashed lines) of CC NSs with different crown sizes: CC1 (black), CC2 (red), CC3 (green), CC4 (orange), CC5 (blue), and CdSe NS core (gray). Inset: expanded view of the spectra from 510 to 520 nm.31

Figure 3.2. Band alignment and exciton decay dynamics in CdSe core. (a) Schematic type I band alignment between CdSe core and CdS crown. HH is heavy hole band, LH is light hole band. T1, T2, T3 are the lowest exciton transitions as in Figure 3.1c. HTr are the hole trapping states. Dashed yellow line indicates an exciton generated by direct excitation at 485 nm (T2 transition) (b) Transient spectra of CdSe/CdS at indicated delay time after 485 nm excitation (of the core). (c) Comparison of exciton bleach recovery of CC5 (black solid line) and the PL decay (red dashed line) in CdSe/CdS after 485 nm excitation. The fit of T1 bleach is showed as green solid line.....36

Figure 3.3. PLE spectra and crown-to-core exciton localization efficiencies (a) Absorptance (black solid lines) and PLE spectra (red dashed lines) of CC5. All spectra have been scaled to the same height at 515 nm. (b) The average exciton localization efficiency (η_{ave}) of CC1 to CC5. (c) Crown-to-core exciton localization efficiency (η_{CdS} , circles) and the normalized absorption spectra (solid lines) of CdS crowns in CC1 to CC5. The latter was obtained by normalizing the absorption spectra of CdSe/CdS to the same CdSe peak amplitude at 512 nm and subtracting the contribution of CdSe.....38

Figure 3.4. TA study of crown-to-core exciton localization dynamics (a) TA spectra of CC5 at indicated delay times after 400 nm excitation. (b) Normalized T3 bleach kinetics of CC1 to CC5 measured at 400 nm excitation. Inset showed the fit of T3 kinetics of CC5 (c) Subtracted T1 (T1S) bleach kinetics of CdSe of CC1 (black solid line), CC2 (red solid line), CC3 (green solid line), CC4 (orange solid line), CC5 (blue solid line) resulted from the excitation of CdS domain. These kinetics were obtained by subtracting the contribution of direct CdSe excitation from the total T1 bleach signal measured at 400 nm excitation (where both CdSe and CdS domains absorbed), following the procedure discussed in the text. Also shown for comparison is the fit to the T1 (purple dashed line) of CC5 measured at 485 nm excitation along with the fits of the CC1-CC5 T1S decay process (gray solid line). The inset showed the same comparison in early time range (within 1 ps).42

Figure 3.5. Model for exciton transport, interfacial transfer and trapping. (a) Scheme of crown size independent interfacial branching of exciton transfer (XL) and trapping (XI) parthways. (b) Energy levels of initially generated excitons in CdS (red dashed line), excitons transported to CdSe (XL, yellow dashed line) and excitons trapped interface (XI, blue dashed line).44

Figure 3.6. T1S kinetics at 400 nm excitation of CC1 to CC5 and the fit using $N_L(t)$ convoluted with IRF47

Figure 3.7. (a) Exciton localization dynamics for CC1 to CC5 at different excitation wavelength. Localization efficiency and rate increases at large excitation energy. (b) The T1 bleach formation kinetics of free CdSe NSs at 400 nm (black dots), 485 nm (red dots), and 510 nm (green dots) excitation. Solid lines are fits with parameters listed in Table 3.6 in Appendix 3.6.....48

Figure 3.8. The HAADF scanning TEM images and EDX images in the green selected area of (a) CC1, (b) CC2, (c) CC3, (d) CC4, (e) CC5.52

Figure 3.9. TEM images of (a) CdSe core, (b) CC1, (c) CC2, (d) CC3, (e) CC4, (f) CC5.53

Figure 3.10. Carrier decay pathways in CC NSs at 485 nm excitation: (A) single particle (electron and hole) representation, (B) state representation. See the text for the notations of various states and carrier trapping and decay process. (C) Morphology and coordinate system of CdSe NS core. The surrounding CdS crown is not depicted because there is not net carrier transport from CdSe core to CdS crown at 485 nm excitation.	55
Figure 3.11. (a-e) Absorptance (black solid lines) and PLE spectra (red dashed lines) of CdSe NSs and CC1 to CC5. All spectra have been scaled to the same height at 515 nm. (f-k) Extinction and (estimated) scattering spectra of CdSe NS and CC1 to CC5.....	59
Figure 3.12. The T3 (a-e) and T1S (f-j) bleach kinetics and fittings of (a, f) CC1, (b, g) CC2, (c, h) CC3, (d, i) CC4, (e, j) CC5 within 20 ps.	62
Figure 3.13. The schematic exciton in-plane diffusion model for CC NSs.....	63
Figure 3.14. Schematic of CdSe/CdS CC core/crown structures used for solving the diffusion equations. Key carrier/exciton processes at different spatial region along x are indicated. Top half: exciton diffusion, interfacial transfer and trapping process. Bottom half: trapped exciton ionization, electron diffusion, and recapture processes.	64
Figure 3.15. Schematic of solving hot exciton diffusion equations for CdSe/CdS CC structure.	67
Figure 4.1. (a) Type II CdSe/CdTe core/crown NPL heterostructures with CdTe crown extending laterally on CdSe core. (b) Absorption (solid lines) and photoluminescence (dashed lines) of CdSe core (black), CC1 (red), CC2 (green), CC3 (orange), and CC4 (blue). Inset: HAADF-STEM and EDX images of CC2 with Cd in red, Se in green, and Te in blue. (c) Band alignment and exciton transitions (see main text for further details).....	74
Figure 4.2. CT exciton formation efficiency in CdSe/CdTe core/crown NPLs. (a) Comparison of normalized absorptance and PLE spectrum of CC2. (b) CT exciton formation efficiency of CC1 to CC4.....	77

Figure 4.3. TA spectra and kinetics of CdSe/CdTe CC NPLs at 530 nm excitation. Inset: TA spectrum from 530 to 680 nm at 800-1000 ps. (a) The TA spectra of CC2 at different delay time. (b) Comparison of the T1S bleach decay kinetics of CC1 to CC4. Insets in b): expanded view of the kinetics (dots) with their multi-exponential fit (black lines) at early delay times (<3ps). (c) Comparison of the CT bleach formation kinetics of CC1 to CC4. Insets in (c): expanded view of the kinetics (dots) with their 2D diffusion model fit (black lines) at early delay times (<3ps)..... 79

Figure 4.4. Normalized T1 and CT kinetics of (a) CC1, (b) CC2, (c) CC3, (d) CC4 at 530 nm pump. 81

Figure 4.5. 2D diffusional model for exciton transport. Schematic of CdSe/CdTe core/crown quantum well heterostructures used for solving the 2D exciton diffusion equations. The black arrows represent exciton transport with rate constant k_x and the red arrows represent exciton interfacial dissociation with rate constant k_{XD} 82

Figure 4.6. Hot exciton transport. (a) Normalized T1S kinetics of CC1 at indicated excitation wavelength. The dashed lines are initial T1S bleach amplitude at 530 nm (blue), 510 nm (red), 490 nm (green), and 400 nm (orange) excitation, obtained after de-convolution of the IRF, representing the number of cold excitons at band edge. (b) Comparison of normalized CT kinetics of CC1 at different pump wavelength. (c) The percentage of hot exciton transport in CC1 to CC4 as a function of crown sizes at 510 nm (blue circles), 490 nm (red squares), and 400 nm (green triangles) pump. The dashed lines represented the estimated percentage of hot exciton transport according to 2D hot exciton diffusion model. (d) The effective hot exciton diffusion constant as a function of pump wavelength. The red dashed line represented the value of cold exciton diffusion constant..... 85

Figure 4.7. (a) The TEM images of CdSe core. The HAADF-STEM images with EDX mapping of (b) CC1, (c) CC2, (d) CC3, (e) CC4. In core/crown samples, CdTe crown and CdSe core were shown in purple and green, respectively.	92
Figure 4.8. The comparison of normalized absorptance and PLE spectra of (a) CdSe core, (b) CC1, (c) CC3, and (d) CC4.....	95
Figure 4.9. T1S kinetics (red dots) and their fits (black lines) of (a) CC1, (b) CC2, (c) CC3, (d) CC4; and CT kinetics (orange dots) and their fits with (black lines) of (e) CC1, (f) CC2, (g) CC3, (h) CC4. All kinetics were measured at 530 nm excitation. Also shown are fit functions (dashed line) without convolution with instrument response.	98
Figure 4.10. (a-c) The comparison of normalized T1S kinetics of (a) CC2, (b) CC3, (c) CC4 at different pump wavelength. Horizontal dashed lines are the initial amplitude of T1S bleach at different pump wavelength. (d-f) The comparison of normalized CT kinetics of (d) CC2, (e) CC3, (f) CC4 at different pump wavelength.....	99
Figure 4.11. Schematic of CdSe/CdTe core/crown NPL heterostructures used for solving the 2D cold exciton diffusion equations numerically.	101
Figure 4.12. The CT kinetics at 530 nm pump of (a) CC1, (b) CC2, (c) CC3, (d) CC4 and the fit using 2D diffusion model.	105
Figure 4.13. Schematic of CdSe/CdTe core/crown NPL heterostructures used for solving the 2D hot exciton diffusion equations numerically.	106
Figure 4.14. The simulated hot exciton transport kinetics of CC1 to CC4 at (a) 510 nm, (b) 490 nm, and (c) 400 nm excitation.	110
Figure 5.1. TEM images of (a) 3MLb, (b) 4MLc, and (c) 5MLb CdSe NPL samples. (d) Absorption spectra of CdSe NPLs. (e) Schematic energy levels of CdSe NPLs.....	113
Figure 5.2. Transient absorption (TA) spectra and kinetics of 5MLb NPLs. TA spectra at (a) early delay time (2-4 ps) and (b) long delay time (800-1000 ps) at indicated pump fluences. (c)	

A exciton bleach kinetics at indicated pump fluences. (d) Normalized A exciton bleach amplitude at early (2-4 ps, blue circles) and long (800-1000 ps, red circles) delay times. The solid line shows a fit to the probability of excited NPLs at long delay time (800-1000 ps) according to a Poisson distribution model (see Appendix 5.3). The dashed line represents the initial average number of excitons per NPL as a function of pump fluence. (e) Comparison of normalized A exciton kinetics at low pump fluences ($<20 \mu\text{J}/\text{cm}^2$). These kinetics have been scaled to the same amplitude at long delay time (800-1000ps). (f) Biexciton decay kinetics (circles) and fit (solid line)..... 115

Figure 5.3. Size and thickness dependence of biexciton lifetimes in NPLs. (a) Biexciton lifetime (symbols) as a function of NPL lateral area (A_{NPL}) and their linear fits for 3, 4 and 5 ML NPLs. (b) Biexciton lifetime of different NPL samples as a function of NPL volume (V_{NPL}). (c) Biexciton lifetime of different NPL samples as a function of the product of NPL lateral area (A_{NPL}) and the reciprocal of electron quantization energy ($E_{k(e)}$) to the 7/2 order. The black solid line is the best linear fit according to Eq. 5.3. (d) Schematic of bi-exciton annihilation process in colloidal CdSe NPLs, showing both the collision and Auger recombination processes (e) Relevant energy levels and band diagrams in exciton Auger recombination process in NPLs. 118

Figure 5.4. TEM images of NPL samples. (a) 3MLa, (b) 3MLb, (c) 4MLa, (d) 4MLb, (e) 4MLc, (f) 4MLd, (g) 5MLa, and (h) 5MLb..... 126

Figure 5.5. The normalized TA spectra at long delay time (800-1000 ps) at different pump fluences of (a) 3MLa, (b) 3MLb, (c) 4MLa, (d) 4MLb, (e) 4MLc, (f) 4MLd, and (g) 5MLa. 129

Figure 5.6. Normalized A exciton bleach amplitude (ΔS) at early (2-4 ps, blue circles) and long (800-1000 ps, red circles) delay times. (a) 3MLa, (b) 3MLb, (c) 4MLa, (d) 4MLb, (e) 4MLc, (f) 4MLd, and (g) 5MLa. The black solid lines are fit of ΔS at long delay time as a function of

fluence to Eq. 5.8. Orange dashed lines are the average exciton number per NPL as a function of pump fluence obtained from the fit and Eq. 5.7. 131

Figure 5.7. Normalized A exciton bleach kinetics at different pump fluences of (a) 3MLa, (b) 3MLb, (c) 4MLa, (d) 4MLb, (e) 4MLc, (f) 4MLd, and (g) 5MLa. 133

Figure 5.8. Subtracted A exciton bleach kinetics (red circles) and their single-exponential fits (black lines) of (a) 3MLa, (b) 3MLb, (c) 4MLa, (d) 4MLb, (e) 4MLc, (f) 4MLd, and (g) 5MLa. 133

Figure 5.9. Scheme of 2D exciton collision theory..... 135

Figure 5.10. Biexciton lifetime of NPLs as a function of $A_{NPL}d^7$, where A_{NPL} and d are lateral area and thickness of NPLs, respectively. Black line is the linear fit. 136

Figure 6.1. (a) TEM image of NPLd. (b) Absorption spectra of all CdSe samples of different sizes (NPLa-d) in hexane (solid lines). The blue dashed line is the static photoluminescence spectrum of NPLb. (c) Comparison of static PL spectra of all CdSe NPL samples..... 140

Figure 6.2. TA spectra of NPLc at indicated delay times after 400 nm pump measured at a pump fluence of (a) $3 \mu\text{J}/\text{cm}^2$ and (b) $629 \mu\text{J}/\text{cm}^2$. (c) Gain spectra, $-(\Delta A(\lambda,t)+A_0(\lambda))$, of NPLc at 3-4 ps at indicated fluences of 400 nm excitation. (d) OG kinetics (probed at 528 nm) of NPLc at different pump fluences. (e) Saturation OG amplitudes (at 3-4 ps) of different NPL samples as a function of lateral area. (f) Normalized OG amplitude (at 3-4 ps) of all NPL samples as a function of pump fluences. Inset shows the OG amplitude at low pump fluence ($20\text{-}100 \mu\text{J}/\text{cm}^2$), where the intercept on x-axis gives OG threshold. 142

Figure 6.3. Optical density dependent optical gain threshold. (a) Absorption spectra of NPLc samples with different concentrations (and optical density at 400 nm). (b) OG amplitudes as a function of pump fluence for NPLc samples with different concentrations. (c) OG thresholds as a function of NPLc optical density at pump wavelength (400 nm). The blue solid line is the

fit according to the OG threshold model described in the main text. (d) Saturation OG amplitude as a function of NPLc optical density at 400 nm. Black line is a linear fit..... 144

Figure 6.4. (a) Absorption spectra of different NPLc films. ASE spectra of NPLc (b) Film1, (c) Film2, and (d) Film3 at different pump fluences. (e) ASE peak intensity (circles) as a function of pump fluence for NPLc films. The solid lines are linear fits. (f) ASE thresholds as a function of NPLc film absorbance at pump wavelength (400 nm). The blue solid line is a fit according to the OG threshold model described in the main text..... 145

Figure 6.5. A model for biexciton optical gain in colloidal CdSe NPLs. Relevant states and transitions in (a) single particle (electron or hole) and (b) exciton state representations, respectively. N_0 (0), N_1 (X) and N_2 (XX) are population probabilities (and label) of NPL states with 0, 1 and 2 excitons, respectively. Color of arrows indicates transition energy of stimulated absorptions (upward arrow, A_i) and emissions (downward arrow, A_i^*) from state i ; Figure 4a shows an example NPLs that can contain up to 4 conduction band edge excitons ($N_s=4$)... 146

Figure 6.6. TEM images of (a) NPLa, (b) NPLb, and (c) NPLc. The length and width of all samples are determined by the solid lines marked in lower panels of (a) for NPLa, right panel of (b) for NPLb, and lower panel of (c) for NPLc. 152

Figure 6.7. Optical gain kinetics at ~528 nm at different pump fluences of (a) NPLa, (b) NPLb, (c) NPLd, (d) NPLc1, (e) NPLc2, and (f) NPLc4..... 153

Figure 6.8. The average number of photons encountered with NPLs at OG threshold (m_{th}) as a function of N_s (red dots) and the linear fit (blue line). 155

Figure 6.9. OG as a function of excitation fluence. (a) Simulated OG amplitude as a function of average number of excitons per NPL (m). (b) OG amplitude (at 3-4 ps) as a function of pump fluence of NPLa to NPLd. (c-f) Normalized A exciton bleach amplitude at long delay time (800-1000 ps) as a function of pump fluence (open circles) and their fits (lines) for (c) NPLa, (d) NPLb, (e) NPLc, and (f) NPLd. (g) Photon encountering cross-section (C) of NPLs as a

function of lateral area. Blue line is the linear fit. (h) Normalized OG amplitude of NPLa (red circles), NPLb (gray squares), NPLc (green triangles), and NPLd (blue rhombus) as a function of m . Solid lines are their fits according to Eq. 6.7: red line for $N_S=3$, green line for $N_S=4$, and blue line for $N_S=5$ 158

Figure 7.1. (a) Scheme of different exciton states in NPLs at room temperature with the saturation number of the band-edge exciton (N_S) as 4. (b) Scheme of different exciton states in NPLs at low temperature ($<4K$). The exciton COM coherence delocalized throughout the whole NPL due to GOST effect, giving $N_S=2$. Sample characterization of CdSe NPLs. (c) TEM image of NPL1. (d) Selected absorption spectra of NPL1 in hexane (at 298K) and PMAO at indicated temperatures. (e) The scheme of band structure and band-edge transitions of NPL1 at 298K. HH and LH represent heavy hole and light hole, respectively. 162

Figure 7.2. Temperature-dependent optical gain (OG) thresholds of CdSe NPLs. (a) Gain spectra, $-\Delta Abs(E,t)-Abs(E)$ (gain-loss), of NPL1 in hexane at 2-3 ps at indicated pump fluences of 3.1 eV excitation. The inset is the same spectra at OG region. (b) OG kinetics (probed at ~ 2.34 eV) of NPL1 in hexane at different pump fluences. (c) Normalized OG amplitude (at ~ 2.34 eV, 2-3 ps) at different temperatures as a function of pump fluences, where the intercept on the x-axis (black dashed line) gives OG threshold. (d) The OG threshold and the average exciton number per NPL at the OG threshold (m_{th}) of NPL1 in hexane as a function of temperature. 165

Figure 7.3. (a) TA spectra of early delay time ($t_E=2-3$ ps) and (b) normalized TA spectra at long delay time ($t_L=800-1000$ ps) of NPL1 at indicated pump fluences (circles). Solid lines are the fits of TA spectra at the highest pump fluence ($1592 \mu J/cm^2$). (c) Schematic depiction of decay from the initial multi-exciton state with a saturated number of band-edge excitons to final single exciton state. The saturation number of the initial band-edge exciton is determined by the exciton spatial area (S_X) and lateral size of NPLs (S_{NPL}) determined by TEM. (d, e) The

fits of the absorption spectra of the excited region in NPL1 NPLs before pump (Abs, solid black lines) and after pump (Abs*, blue dashed lines) at (d) early delay time ($t_E=2-3$ ps) and (e) long delay time ($t_L=800-1000$ ps) at the highest pump fluence ($1592 \mu\text{J}/\text{cm}^2$). Red circles are the normalized static absorption spectra of NPL1. Green shaded regions represent the A exciton absorbance in NPL1 NPLs before pump..... 168

Figure 7.4. Temperature- and size-dependent S_X of CdSe NPLs. (a) Comparison of experimental S_X of NPL1 (blue spheres) and NPL2 (orange circles) and estimated S_X (Est., gray squares) as a function of temperature. The y-axis of the right side represents the percentage of the lateral area of NPL1. (d) Scheme of S_X of CdSe NPLs at room temperature (RT, 298K) and low temperature (low T, <4K). (c) The average exciton number per NPL at gain threshold (m_{th}) as a function of the saturation number of band-edge exciton of NPLs (N_s)..... 171

Figure 7.5. (a) Photoluminescence spectra of NPL2 in PMMA at different temperatures. (b) The S_X of CdSe NPLs with different thicknesses as a function of NPL lateral area. The dashed lines represent the average S_X for 3 (green), 4 (orange), and 5ML (red) CdSe NPLs..... 173

Figure 7.6. The TEM images of (a) 3MLa, (b) 3MLb, (c) 4MLa, (d) 4MLb, (e) NPL2, (f) 4MLc, (g) 5MLa, and (h) 5MLb..... 176

Figure 7.7. The gain spectra at early delay time (2-3 ps) of NPL1 in PMAO at (a) 298K, (b) 100K, (c) 50K, (d) 20K, (e) 10K, and (f) 4K. The insets are the same spectra at the optical gain (OG) region, where the shaded areas represent the OG from s-state (red) and p-state (gray) of A exciton, respectively. The gain kinetics at the s-state OG peak energy (marked by the red shaded area in (a)-(f)) of NPL1 in PMAO at (g) 298K, (h) 100K, (i) 50K, (j) 20K, (k) 10K, and (l) 4K..... 178

Figure 7.8. (a) The A exciton kinetics of NPL1 in hexane at selected pump fluences. (b) Normalized A exciton bleach amplitude at long delay time (800-1000 ps) as a function of pump

fluence (open circles) and their fits (solid black line) for NPL1 in hexane. Blue dashed line is the average exciton number per NPL (m) as a function of pump fluence. 180

Figure 7.9. (a) Absorption spectra of NPL1 in hexane and PMAO at different temperatures for optical gain studies. (b) Absorption spectra of the same spot on NPL1 PMAO film at different temperatures. Absorption spectra and fits of NPL1 in PMAO at (c) 298K, (d) 100K, (e) 50K, (f) 20K, (g) 10K, and (h) 4K. 183

Figure 7.10. (a) The absorption spectra of NPL2 in PMMA at different temperatures. (b) Comparison of TA spectra of NPL2 in PMMA (solid lines) and hexane (dashed lines) at room temperature (298K). The comparison of absorption spectra of NPL2 in PMMA (solid gray lines) and NPL2 solid films (red circles) at (c) 298K, (d) 100K, (e) 20K, and (f) 2.6K. Black solid lines and dashed lines are the fits of absorption spectra of NPL2 solid films. 184

Figure 7.11. (a) Scaled absorption spectra of 3MLa&b (circles) and the fit. (b) Scaled absorption spectra of NPL1&2 and 4MLa-c (circles) and the fit. (c) Scaled absorption spectra of NPL2 in hexane, toluene, and chloroform (circles) and the fit. (d) Scaled absorption spectra of 5MLa&b (circles) and the fit. 185

Figure 7.12. The absorption spectra (a) before pump, (b) after pump, and (c) the TA spectra of NPL1 in hexane at early delay time (t_E , 2-3 ps). The absorption spectra (d) before pump, (e) after pump, and (f) the TA spectra of NPL1 in hexane at long delay time (t_L , 800-1000 ps). 193

Figure 7.13. The TA spectra at early delay time (circles) and the fits (solid lines) of NPL1 in PMAO at (a) 298K, (b) 100K, (c) 50K, (d) 20K, (e) 10K, and (f) 4K. The TA spectra at long delay time (circles) and the fits (solid lines) of NPL1 in PMAO at (g) 298K, (h) 100K, (i) 50K, (j) 20K, (k) 10K, and (l) 4K. 193

Figure 7.14. The TA spectra at early delay time (circles) and the fits (solid lines) of NPL2 in (a) hexane, (b) toluene, (c) chloroform, (d) PMMA at 298K, (e) PMMA at 100K, (f) PMMA

at 20K, and (g) PMMA at 2.6K. The TA spectra at long delay time (circles) and the fits (solid lines) of NPL2 in (h) hexane, (i) toluene, (j) chloroform, (k) PMMA at 298K, (l) PMMA at 100K, (m) PMMA at 20K, and (n) PMMA at 2.6K. 194

Figure 7.15. The TA spectra at early delay time (circles) and the fits (solid lines) of (a) 3MLa, (b) 3MLb, (c) 4MLa, (d) 4MLb, (e) 4MLc, (f) 5MLa, and (g) 5MLb. The TA spectra at long delay time (circles) and the fits (solid lines) of (h) 3MLa, (i) 3MLb, (j) 4MLa, (k) 4MLb, (l) 4MLc, (m) 5MLa, and (n) 5MLb..... 195

Figure 7.16. Exciton coherent spatial area of 4MLc as a function of solvent dielectric constant. 199

Figure 8.1. TEM images, absorption spectra and band alignment. (a) HAADF-STEM images and (b,c) EDX images of elemental distribution of Cd (red), Se (green), and Te (blue) of CdSe/CdTe CC NPLs. (d) Absorptance spectra of CdSe core (black solid line) and CdSe/CdTe CC (blue solid line), photoluminescence spectra (right vertical axis) of CdSe core (green solid lines) and CdSe/CdTe CC (red solid lines), and PLE spectrum of CC NPLs (orange dashed line). (e) Relevant energy levels, type-II band alignment and exciton transitions in CdSe/CdTe CC NPLs. 203

Figure 8.2. The CT exciton formation efficiency of CdSe/CdTe CC NPLs according to the ratio of the normalized PLE to absorptance spectra in Figure 8.1c. 204

Figure 8.3. Transient absorption spectra and kinetics of CdSe/CdTe CC NPLs measured at 620 nm excitation. The TA spectra at indicated delay times measured at a pump fluence of (a) 364 $\mu\text{J}/\text{cm}^2$ and (b) 14867 $\mu\text{J}/\text{cm}^2$. (c) Normalized T4 kinetics at selected pump fluences (circles) and their fits (solid lines). (d) Average electron number per NPL in CdSe core at 1-2 ps (blue circles) and 800-1000 ps (red circles), their fits (solid line, see the main text and the Appendix 8.3 for details), and average total initial exciton number per CC NPL (orange dashed line). 205

Figure 8.4. Transient absorption spectra and kinetics of CdSe/CdTe CC NPLs measured at 550 nm excitation. (a) TA spectra at indicated delay times measured at a pump fluence of 80 $\mu\text{J}/\text{cm}^2$. (b) Normalized optical gain (OG) kinetics at selected pump fluences (circles) and their fits (solid lines), where ΔS represents normalized TA signal. (c) Normalized T4 kinetics at selected pump fluences (circles) and their fits (solid lines), where ΔS represents normalized TA signal. (d) Average electron number in CdSe core per CC NPL as a function of pump fluence at 1-2 ps (blue circles) and 800-1000 ps (red circles), average number of long-lived electrons in CdTe crown at 1-2 ps, and fits (solid lines) to these data according to a Poisson distribution model (see Supporting Information). Dashed orange line represents the average total initial exciton number per CC NPL as a function of pump fluence.208

Figure 8.5. Transient absorption spectra and kinetics of CdSe/CdTe CC NPLs measured at 520 nm excitation (a) The TA spectra indicated delay times measured at a high pump fluence (11096 $\mu\text{J}/\text{cm}^2$). (b) Comparison of OG kinetics measured at 400, 525 and 550 nm excitation at saturation fluences, where ΔS represents normalized TA signal. (c) Comparison of T4 bleach kinetics measured at 400, 525, 550 and 620 nm excitation at saturation fluences, where ΔS represents normalized TA signal. (d) Average electron number in CdSe core per CC NPL as a function of 525 nm pump fluence at 1-2 ps (blue circles) and 800-1000 ps (red circles), average number of additional CdTe crown excitons per CC NPL at 1-2 ps (Green circles), fits to these data (solid lines) according to Poisson distribution model (see Supporting information), and is the total average exciton number per CC NPL as a function of pump fluence (dashed line) obtained from the fit.....212

Figure 8.6. Three exciton states in CC NPL. (a) Scheme of the three energetically separated exciton states in CdSe/CdTe CC NPLs. (b, c) Three spatially separated exciton states in CdSe/CdTe CC NPLs.215

Figure 8.7. OG in CC NPLs. (a) The gain/loss ratio spectra at early delay time of different 550 nm pump fluences. (b) The gain/loss ratio at ~607 nm (1-2 ps) as a function of pump fluence at different pump wavelengths. The point of intersection of the black dashed line and the shaded areas represent the OG thresholds. (c) The gain/loss ratio kinetics at ~607 nm at the highest pump fluence with different pump wavelengths. (d) The optical gain threshold as a function of pump wavelength (blue circles) and their fit (red dots). The black line represents the reciprocal of relative absorptance of CC NPLs.217

Figure 8.8. The TEM images of (a) CdSe core and (b) CdSe/CdTe CC NPLs.220

Figure 8.9. The normalized TA spectra of CdSe/CdTe CC NPLs at long delay time (800-1000 ps) at different pump fluences with (a) 400 nm, (b) 525 nm, (c) 550 nm, and (d) 620 nm excitation, where ΔS represents normalized TA signal.....221

Figure 8.10. The comparison of T3, T4, and CT kinetics at $364 \mu\text{J}/\text{cm}^2$ with 620 nm excitation.225

Figure 8.11. (a) The TA spectra at $2 \mu\text{J}/\text{cm}^2$ with 550 nm excitation. (b) The comparison of T3, T4, CT and T1 kinetics after normalized them at 100-1000 ps time region. (c) The normalized T1S (squares), T4, T3, and CT kinetics (dots) with their fits (solid lines), where ΔS represents normalized TA signal.225

Figure 8.12. Transient kinetics of CdSe/CdTe NPLs measured at 525 nm excitation. (a) Normalized OG kinetics at indicated pump fluences (circles) and their fits (solid lines), where ΔS represents normalized TA signal. (b) Normalized T4 kinetics measured at indicated pump fluences (circles) and their fits, where ΔS represents normalized TA signal. (c) The comparison of OG (dots) and T1 (solid lines) kinetics at different pump fluences.227

Figure 8.13. The pump fluence dependent TA results of CdSe/CdTe CC NPLs at 400 nm excitation. (a) The TA spectra of CdSe/CdTe CC NPLs at different delay times with 400 nm excitation and pump fluence of $1164 \mu\text{J}/\text{cm}^2$. (b) The comparison of T1 (solid lines) and OG

(circles) kinetics of CdSe/CdTe CC NPLs at selected pump fluence with 400 nm excitation. (c) The normalized OG kinetics of CdSe/CdTe CC NPLs at different pump fluences with 400 nm excitation, where ΔS represents normalized TA signal. (d) The T4 kinetics of different 400 nm pump fluences. (e) The average electron number in CdSe core per CC NPL as a function of pump fluence at 1-2 ps (blue circles) and 800-1000 ps (red circles) with 400 nm excitation. Green circles are the average number of additional CdTe crown excitons per CC NPL at 1-2 ps with 400 nm excitation. Solid lines are the fits according to Poisson distribution. Dashed line is the total average exciton number per CC NPL as a function of pump fluence at 400 nm excitation.....231

Figure 8.14. The gain/loss ratio spectra at 1-2 ps at different (a) 400 nm and (b) 525 nm pump fluences.232

Figure 8.15. The schematic of the optical gain mechanisms in CdSe/CdTe CC NPLs. The left and right panel shows the exciton states in single particle (electron and hole) representation and state representation, respectively.233

Figure 9.1. Absorption (Abs) and static-photoluminescence (PL) spectra of CdS NPLs, CdS NPL-Pt heterostructures dispersed in (a) hexane and (b) water (pH=10). TEM images of CdS NPL-Pt heterostructures in (c) hexane and (d) water. Insets in (c) and (d): TEM images showing preferential deposition of Pt at the CdS NPL edge. (e) Normalized H₂ production amount as a function of illumination time of CdS NPL-Pt heterostructures at different pH values. Inset: H₂ generation kinetics of CdS NPL-Pt at pH 8.8 up to 30 h. The black line is the linear fit for data between 5-30 h. (f) The pH dependent light-driven H₂ generation IQE of CdS NPL-Pt (green column) and CdSe NPL-Pt (red column). The black dots with dashed line is the fit of pH dependent IQE of CdS NPL-Pt.....240

Figure 9.2. Mechanism of efficient light-driven H₂ generation in CdS NPL-Pt heterostructures. (a) Schematic depiction of key forward processes. (b) Simplified energy level diagram and

charge separation and recombination processes. All band-edge positions and redox potentials correspond to aqueous solution at pH = 14.7.....244

Figure 9.3. Average TA spectra at indicated delay time windows of (a) free CdS NPLs and (b) CdS NPL-Pt heterostructures in hexane. Inset in (a) and (b): expanded view of the TA spectra at long delay times (0.1-0.2, 0.8-1 and 4-5 μ s). The dashed lines mark the wavelength of 412 nm (green) and 416 nm (red). (c) Comparison of exciton bleach (XB) kinetics at 416 nm of CdS NPLs (blue circles) and CdS NPL-Pt heterostructures (red squares), and the scaled charge separated state (CS) kinetics (green triangles). Their fits according to the model in the Appendix 9.3 are shown in solid lines.245

Figure 9.4. pH dependent hole removal. (a) The static-PL spectra of CdS NPLs dispersed in hexane and aqueous solution with different pH. Inset shows the location of two types of hole traps (Tr1 and Tr2). (b) The quantum yield (QY) of band-edge (X) and trap state (Tr1, Tr2) emissions of CdS NPLs in hexane (shaded area) and aqueous solution at pH 10 to 14.7. (c) The PL decay kinetics (circles) and fits (solid lines) of the emission of the band-edge excitons and the 1st type of trapped excitons (Tr1+X, upper panel) and 2nd type of trapped excitons (Tr2, lower panel) in CdS NPLs dispersed in hexane and aqueous solution. (d) The HT rate ($1/\tau_{HT}$, 2) of 2nd type of trapped excitons (Tr2) in CdS NPLs dispersed in aqueous solution as a function of pH. The black dashed line is a fit to a model that described in Appendix 9.4.247

Figure 9.5. pH and morphology dependent charge recombination kinetics in CdS-methyl viologen (MV^{2+}) complexes. (a) TA spectra of CdS NPL- MV^{2+} complexes in aqueous pH=9 solution at indicated delay times after 400 nm excitatoin. Inset: expanded view of the TA spectrum at 1.4-1.6 ns. (b) Comparison of normalized $MV^{+\bullet}$ radical kinetics of CdS NPL- MV^{2+} complexes at different pH. (c) The half-life of $MV^{+\bullet}$ radicals of CdS NPL- MV^{2+} complexes as a function of pH. (d) Comparison of $MV^{+\bullet}$ radical kinetics of CdS NR- MV^{2+} (red line) and NPL- MV^{2+} complexes (black line) at pH 9.250

Figure 9.6. Scheme of charge recombination processes in 2D NPL-Pt and 1D NR-Pt heterostructures in aqueous solution at pH <13.....	253
Figure 9.7. The TEM images of free CdS NPLs in (a) hexane and (b) aqueous solution with pH of 10. The TEM images of CdS NPL-Pt heterostructures in (c) hexane and (d) aqueous solution with pH of 10.	258
Figure 9.8. (a) The absorption spectra of CdS NPL-Pt heterostructures in hexane (blue solid line), which can be considered as the sum of the absorption spectrum of Pt particles (green solid line) and the CdS NPLs (red dashed line). The latter is consistent with the absorption spectrum of free CdS NPLs (black solid line). The absorption spectra of CdS NPL-Pt heterostructures in aqueous solution with pH of (b) 8.8, (c) 11.4, (d) 13.2, and (e) 14.7 for H ₂ generation. The red lines are the normalized Pt absorption. (f) The comparison of subtracted CdS NPL absorption (dashed lines) obtained from (b-e) and the free CdS NPL absorption at pH of 10 (purple circles).....	259
Figure 9.9. (a) The comparison of CdS NPL-Pt absorption spectra at aqueous solution with pH of 8.8 before and after 5, 19, 25, and 30 h's illumination. The inset shows the same spectra near exciton peak region. (b) The CdS NPL-Pt absorption spectra (red circles) with fit (lines) at aqueous solution with pH of 8.8 before and after 5, 19, 25, and 30 h's illumination. The Pt absorption are in gray solid lines, exciton peak and continuous band are in green solid lines, and the total absorption fits are in black dashed lines. The TEM image of CdS NPL-Pt at aqueous solution with pH of 8.8 (c) before and (d) after 30 h's illumination.	261
Figure 9.10. The absorption spectra of CdS NR-Pt heterostructures in aqueous solution with different pH (dashed lines) and the absorption of Pt particles in water (gray solid line).	263
Figure 9.11. The TA spectra of CdS NR-Pt heterostructures in aqueous solution with (a) pH=7, (b) pH=10, (c) pH=11, (d) pH=12, (e) pH=13, (f) pH=14, and (g) pH=14.7.	264

Figure 9.12. The comparison of XB kinetics of CdS NR-Pt heterostructures in aqueous solution with different pH.....	265
Figure 9.13. The comparison of normalized XB kinetics at different wavelength (412 and 416 nm) of (a) free CdS NPLs and (b) CdS NPL-Pt heterostructures. Carrier decay pathways in free CdS NPLs in (c) single particle (electron and hole) representation and (d) state representation at 400 nm excitation. Carrier decay pathways in CdS NPL-Pt heterostructures in (e) single particle (electron and hole) representation and (f) state representation at 400 nm excitation.	266
Figure 9.14. The static PL spectra and the fits of CdS NPLs in (a) hexane and aqueous solution with pH of (b) 10, (c) 11.1, (d) 13.2, and (e) 14.7. (f) The comparison of band edge emission (solid lines), Tr1 emission (dashed lines), and Tr2 emission (dots) in aqueous solution with pH of 10 (black), 11.1 (red), 13.2 (green), and 14.7 (orange).	271
Figure 9.15. (a) The TEM image of CdS NRs in hexane. (b) The absorption spectra of CdS NRs in chloroform and aqueous solution with different pH. (c) The static PL spectra of CdS NRs in chloroform and KOH aqueous solution with different pH. (d) The pH dependent static-PL spectra of CdS NR in KOH aqueous solution. (e) The TR-PL decay kinetics (solid lines) with IRF (dashed line) of CdS NRs in chloroform and KOH aqueous solution with different pH. (f) The TR-PL decay kinetics (solid lines) with IRF (dashed line) of CdS NPLs in hexane and KOH aqueous solution with different pH.	273
Figure 9.16. Carrier decay pathways in (a) single particle (electron and hole) representation and (b) state representation of CdS NPLs in aqueous solution at 400 nm excitation.....	274
Figure 9.17. (a) The comparison of exciton bleach (XB) kinetics of free CdS NPLs in hexane and aqueous solution with different pH. The comparison of XB kinetics and TR-PL decay kinetics (400 to 550 nm) of free CdS NPLs in (b) hexane and aqueous solution with pH of (c)	

10.0, (d) 11.0, (e) 13.2, and (f) 14.7. X and Tr1 represent the band-edge exciton and the first trap state, respectively.....280

Figure 9.18. The average number of OH⁻ (mOH) and L-cysteine (mC) per NPL as a function of pH.282

Figure 9.19. (a) Absorption of CdS NPL- MV²⁺ complexes aqueous solution with different pH. The TA spectra of CdS NPL- MV²⁺ complexes aqueous solution with (b) pH=11, (c) pH=13, and (d) pH=14 at indicated delay times. The insets show the same spectra at 1.4-1.6 ns.283

Figure 9.20. (a) TEM image of CdS NRs used for charge recombination study. (b) Absorption spectra of free CdS NRs and CdS NR-MV²⁺ complexes in aqueous solution with pH of 9. (c) TA spectra of CdS NR-MV²⁺ complexes in aqueous solution with pH of 9 at indicated delay times. Inset shows the same spectra at 1.4-1.6 ns.284

Figure 9.21. Scheme of charge recombination process in (a) CdS NPL-Pt and (b) CdS NR-Pt heterostructures with presence of hole acceptors on NPL and NR surfaces.....285

Figure 9.22. The survival probability of electron on Pt tip of 2D NPL-Pt (solid lines) and 1D NR-Pt (dashed lines) heterostructures under fast ($k_h/k_x \gg 1$, black) and slow ($k_h/k_x \ll 1$, red) trapped hole diffusion conditions.....290

Figure 10.1. CsPbBr₃ NPLs. (a) The TEM image of CsPbBr₃ NPLs. (b) The photoluminescence (solid blue line) and absorption (blue dots) spectra of CsPbBr₃ NPLs Black solid line is the fit of the absorption spectrum. (c) The scheme of energy levels of CsPbBr₃ NPLs, the oxidation potential (HOMO) of PTZ, the reduction potential (LUMO) of BQ, and the interfacial ET and HT pathways from NPL to molecular acceptors (BQ or PTZ).294

Figure 10.2. TA spectra and kinetics of free CsPbBr₃ NPLs. (a) TA spectra at indicated delay times (dots) and their fits (solid black lines). Inset: the expanded view of the TA spectra at low energy range (480-680 nm). (b) Fits of absorption spectra before pump (Abs, solid lines) and

after pump (Abs*, dashed lines) that contribute to TA spectra. The arrows show the state-filling (red) and BGR (green) effects on absorption after pump. (c) The comparison of XB, PA, and PL decay kinetics. The solid line is the fit.295

Figure 10.3. Electron and hole transfer from NPLs. (a) TA spectra of NPL-PTZ complexes at indicated delay times. Inset: a comparison of TA spectra of NPL-PTZ and free NPL at long delay time (0.2-1 μ s). (b) Comparison of kinetics of subtracted exciton bleach of NPL-PTZ (SXB, red circles), exciton bleach of free NPLs (free XB, gray dashed line) and subtracted oxidized PTZ signals (SPTZ, green squares). The black lines are the fits of SXB and SPTZ kinetics of NPL-PTZ. (c) TA spectra of NPL-BQ complexes at indicated delay times. (d) Comparison of kinetics of subtracted exciton bleach of NPL-BQ (SXB, red circles) and exciton bleach of free NPLs (free XB, gray dashed line). The black lines are the fits of SXB kinetics of NPL-BQ.....297

Figure 10.4. The normalized TA spectra of NPLs at different delay times.....305

Figure 10.5. The comparison of (a) XB and PA kinetics of NPL-PTZ complexes and XB kinetics free NPLs, (b) total kinetics at \sim 525 nm, PA kinetics (600-650 nm), and XB kinetics of NPL-PTZ complexes, and (c) XB and PA kinetics of NPL-BQ complexes and XB kinetics of free NPLs.....307

Figure 10.6. Carrier decay pathways in (1) free CsPbBr₃ NPLs and (b) NPL-BQ (or NPL-PTZ) complexes in state representation.308

Figure 10.7. The XB kinetics of (a) NPL-BQ and (b) NPL-PTZ at different BQ and PTZ concentrations, respectively. The dashed lines represent the half bleach amplitude. (c) The apparent decay rate ($1/\tau_{1/2}$) of XB kinetics of NPL-BQ (black dots) and NPL-PTZ (red dots) as a function of acceptor concentration. Solid lines are the fits according to the model. (d) The average number of BQ or PTZ per NPL as a function of acceptor concentration.....313

List of Tables

Table 2.1. pH dependent reduction potential and the fits of CdS NPLs and NRs	26
Table 3.1. The length, width, and crown length with errors of CdSe core and CC NSs.....	53
Table 3.2. The fitting parameters and errors for T1 kinetics (485 nm excitation)	58
Table 3.3. Fitting parameters and errors for bleach kinetics	61
Table 3.4. The fitting parameters for T1S kinetics (400 nm excitation).....	66
Table 3.5. The fitting parameters for hot exciton transport simulation at different excitation wavelength	69
Table 3.6. Fitting parameters and errors for free CdSe T1 bleach kinetics.....	70
Table 4.1. The length, width, and area with errors of CdSe core and CC NPLs	92
Table 4.2. The fitting parameters and errors of bleach kinetics at 530 nm pump.....	97
Table 4.3. The formation time constants and errors of T1S kinetics at different pump	99
Table 4.4. The percentage of hot exciton transport (ϕ_{HET}) at different pump	100
Table 4.5. The fitting parameters and errors with the estimated ϕ_{HET} /%	111
Table 5.1. Averages and standard deviations (error bar) of length, width and area distributions of CdSe colloidal NPLs	127
Table 5.2. Fitting parameter C of all NPL samples.....	130
Table 5.3. Biexciton lifetime and errors of all NPL samples.....	134
Table 6.1. The length, width, and area with errors of CdSe colloidal NPLs	152
Table 6.2. The average number of photons encountered with NPLs at OG threshold.....	155
Table 7.1. Exciton and gain parameters of NPL1 as a function of temperature. These parameters include the temperature-dependent OG threshold (I_{th}), optical density (OD) at 3.1 eV, NPL extinction coefficient per unit NPL volume (ϵ) at 3.1 eV, average exciton number per	

NPL at the OG threshold (m_{th}), band-edge exciton coherent area (S_X), and saturation number of band-edge excitons per NPL (N_S).....	166
Table 7.2. The average length, width, area (S_{NPL}), saturation number of the band-edge exciton (N_S), and band-edge exciton coherent area (S_X) with errors of CdSe NPLs in hexane	177
Table 7.3. Fitting parameters and errors for absorption spectra of NPL1 in PMAO at different temperatures	186
Table 7.4. Fitting parameters and errors for absorption spectra of NPL2 solid films at different temperatures	187
Table 7.5. Fitting parameters and errors for absorption spectra of 3ML, 4ML and 5 ML NPLs in solution.....	188
Table 7.6. Fitting parameters and errors of TA spectra of NPL1 at different temperatures .	196
Table 7.7. Fitting parameters and errors of TA spectra NPL2 at different temperatures.....	197
Table 7.8. Fitting parameters and errors of TA spectra of 3MLa&b, 4MLa-c, and 5MLa&b in hexane	198
Table 7.9. Temperature- and solvent-dependent band-edge exciton coherent area (S_X) and the saturation number of band-edge excitons per NPL (N_S) of NPL2.....	200
Table 8.1. The length and width with errors of CdSe core and CC NPLs	220
Table 8.2. Fitting parameters and errors of T1S and T4 kinetics at 550 nm excitation	226
Table 8.3. Fitting parameters and errors of normalized T4 kinetics at 620 nm pump	227
Table 8.4. Fitting parameters and errors of normalized T4 kinetics at 550 nm pump	228
Table 8.5. Fitting parameters and errors of normalized T4 kinetics at 525 nm pump	229
Table 8.6. Fitting parameters and errors of normalized OG kinetics at 550 nm pump.....	229
Table 8.7. Fitting parameters and errors of normalized OG kinetics at 525 nm pump.....	230
Table 9.1. Comparison of the initial H_2 generation efficiency of CdS Nanorods (NRs) or NPL based heterostructures at $pH < 12$	242

Table 9.2. Fitting parameters with errors of CdS NPL-Pt absorption spectra before and after photocatalysis.....	261
Table 9.3. TA exciton bleach kinetics fitting parameters with errors	270
Table 9.4. Static PL spectra fitting parameters and errors	272
Table 9.5. The half-life of TR-PL decay of CdS NRs and NPLs.....	274
Table 9.6. TR-PL decay kinetics fitting parameters and errors	278
Table 9.7. The simulation parameters and half-life of $N_e(t)$ for 2D and 1D morphologies ..	290
Table 10.1. The fitting parameters and errors of static and TA spectra	306
Table 10.2. Fitting parameters and errors of TA kinetics	309
Table 10.3. Acceptor concentration-dependent XB decay half-life and m with errors	313

Chapter 1. Introduction

Reproduced in part with permission from *Nano Research* **2018**, *11*, 3031. Copyright 2018 Springer Nature.

1.1. Backgrounds of 2D Semiconductor Nanoplatelets

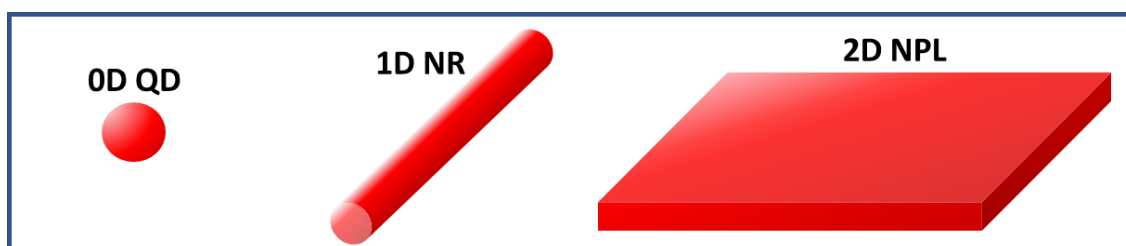


Figure 1.1. Scheme of 0D quantum dots, 1D nanorods, and 2D nanoplatelets.

Quantum-confined semiconductor nanocrystals (NCs) have their carrier and exciton motion confined in three, two or one dimension, and can be classified as 0D quantum dots (QDs), 1D nanorods (NRs) or nanowires, and 2D nanoplatelets (NPLs), respectively (Figure 1.1).¹ Quantum confinement occurs when the dimension is smaller than the size of their exciton Bohr radius, which is usually in the scale of a few to 10s of nanometers.²⁻³ This effect gives rise to quantized and size-dependent energy levels near the band-edge.^{2, 4-5} Compared with bulk materials, semiconductor NCs show size-tunable band-gap over a wide range of energy (e.g., 1.8 to 3.0 eV for CdSe QDs⁶). Compared with molecules, semiconductor NCs have a much larger absorption coefficient and cross-section for solar energy harvesting, typically on the

order of $10^7 \text{ cm}^{-1} \text{ M}^{-1}$.⁷⁻¹¹ Moreover, the carrier wavefunction in NCs can be engineered by forming NC heterostructures to enable novel charge separation properties.¹² With those advantages mentioned above, NCs have been widely used in optoelectrical devices¹³⁻¹⁶ and as sensitizers in photocatalytic systems.¹⁷⁻¹⁸

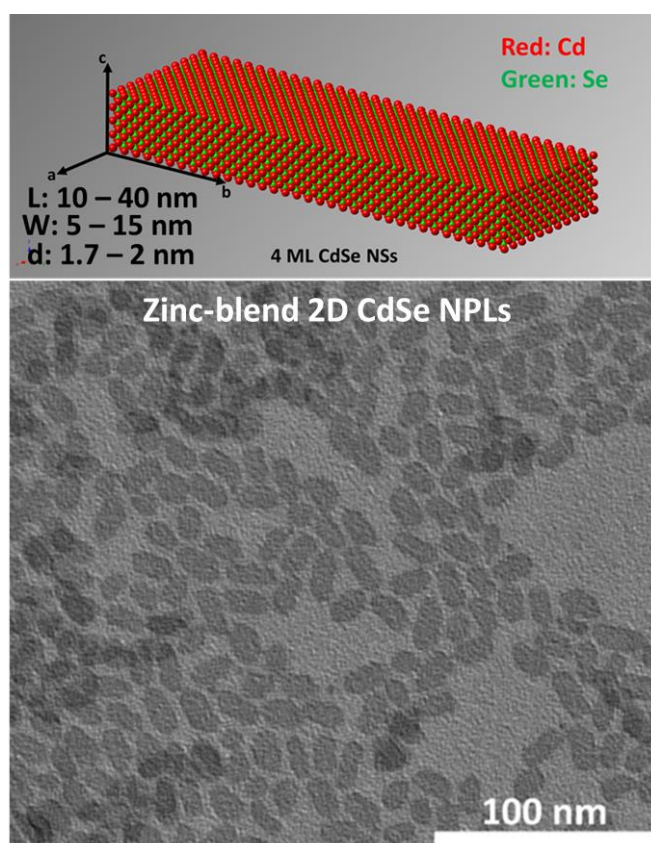


Figure 1.2. Scheme (upper panel) and TEM image (lower panel) of 4 monolayer (ML) CdSe NPLs.

Among the low-dimensional semiconductor NCs, colloidal 2D NPLs is a new class of quantum-confined NCs.¹⁹⁻²² Taking zinc-blend cadmium chalcogenide (CdX , $\text{X}=\text{Se}, \text{S}, \text{Te}$) NPLs as an example (Figure 1.2), these NPLs have a 2D morphology with the length and width

about 10s of nm and the thickness < 2 nm. Compared to 0D QDs and 1D NRs, 2D morphology has introduced several unique advantages to NPLs. The extended lateral dimension of 2D NPLs increases both absorption cross-section and intrinsic absorption coefficient.¹⁰⁻¹¹ 2D CdX NPLs also possess uniform quantum confinement along their thickness direction and a tunable thickness in the atomic precision.²¹ The thickness distribution in their ensembles is narrow so that the emission line-width of NPL ensemble is almost the same as that of a single NPL (~ 42 meV),²³ which is sharper than the best-reported core/shell QDs (~ 67 meV).²⁴ The basal plane of 2D NPLs is well passivated by ligands,²⁵ which effectively suppresses the trapping process and results in a photoluminescence (PL) quantum yield (QY) over 50% without any shell coating.^{21, 25} Moreover, the multi-exciton lifetime of cadmium chalcogenide NPLs (hundreds of ps)²⁶⁻²⁸ is longer than that of similar QDs (10s of ps).²⁹ These advantages have made CdX NPLs promising materials for optoelectrical applications, such as lasing with a large gain coefficient and low threshold,^{28, 30-41} and photocatalysis, such as solar-to-H₂ conversion.⁴²⁻⁴⁴

Besides cadmium chalcogenide NPLs, other 2D NPLs also attract people's attention recently. Highly efficient multiple exciton generation (MEG) in PbS 2D NPLs has been reported with a higher MEG efficiency than PbS 0D QDs with the same pump-energy/band-gap ratio.⁴⁵ Single-layered Ag₂S nanoplatelets are expected to possess an enhanced Coulombic interaction compared to Ag₂S 0D QDs due to the 2D morphology and are expected to be a new class of MEG materials due to their high photostability and low toxicity.⁴⁶ These 2D NPLs are great candidates for enhancing solar energy conversion efficiency over unity through MEG process.⁴⁷ Moreover, HgSe and HgTe 2D NPLs have been reported recently as promising near-infrared emitters.⁴⁸⁻⁴⁹ Perovskite 2D NPLs are also reported recently with tunable band-gap

from ultraviolet to the near-infrared region and great performances in emitting devices.⁵⁰⁻⁵⁵ Many of the promising performances and properties of 2D NPLs are determined by the nature of the 2D excitons within NPLs. Herein, this dissertation focuses on the physical properties of excitons in cadmium chalcogenide and CsPbBr₃ perovskite 2D NPLs and their performances in optoelectrical (e.g., lasing) and photocatalytic (e.g., solar-to-fuel conversion) applications.

1.2. Physical Properties of 2D Excitons of Nanoplatelets for Optoelectrical and Photocatalytic Applications

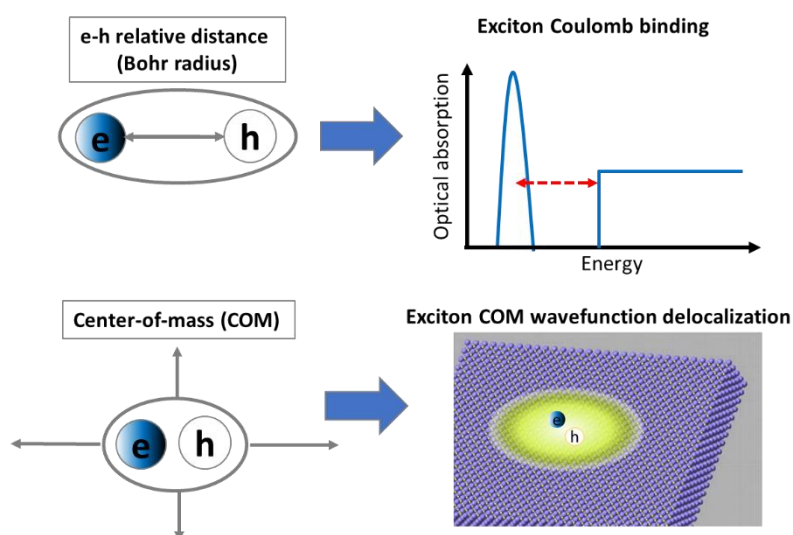


Figure 1.3. Scheme of exciton internal motion and center-of-mass (COM) motion. The former determines the exciton binding energy and the latter determines the exciton COM coherent delocalization.

The optoelectronic and photocatalytic performances of colloidal NPLs depend on the physical properties of band-edge excitons, which are bound pairs of conduction band (CB)

electrons and valence band (VB) holes.⁵⁶ They are characterized by both the internal relative motion of the electron and hole and the motion of the exciton center-of-mass (COM). As shown in Figure 1.3, the relative distance between the electron-hole pair is called the exciton Bohr radius (or exciton size), which determines how strong the exciton Coulomb binding is. The exciton COM motion describes how exciton moves as a quasi-particle, and the exciton COM wavefunction extension determines the oscillator strength and the radiative decay lifetime of the corresponding excitonic transition. In 2D NPLs, excitons are quantum-confined along the thickness direction and can only move two-dimensionally along the basal plane. The physical properties of 2D excitons in NPLs contain the exciton COM coherent delocalization, exciton in-plane transport, multi-exciton annihilation, and exciton dissociation.

1.2.1. COM coherent delocalization of band-edge excitons

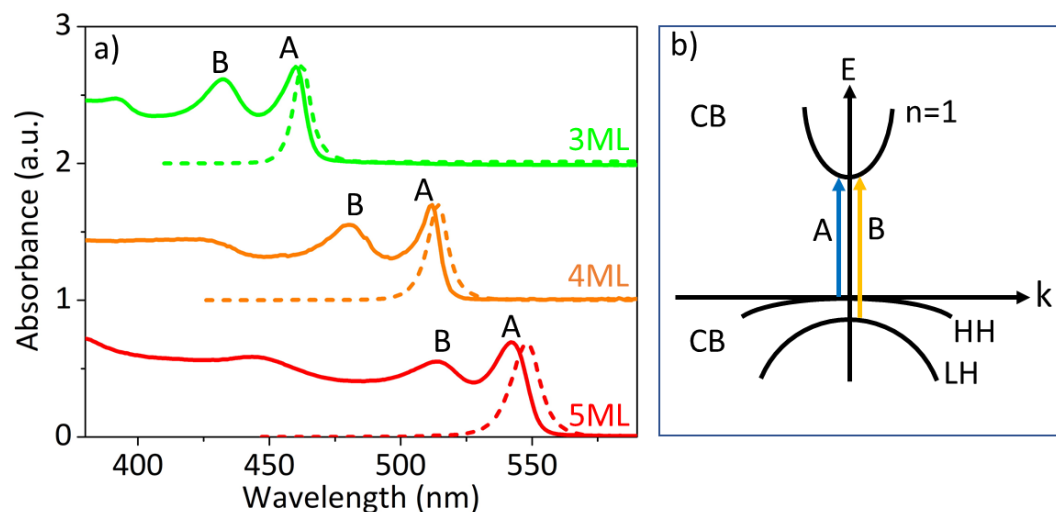


Figure 1.4. (a) The absorption (solid lines) and emission (dashed lines) spectra of 3-5 ML CdSe NPLs. (b) Scheme of energy diagram and band-edge excitonic transitions in CdSe NPLs.

Figure 1.4a shows the absorption (solid lines) and emission (dashed lines) spectra of CdSe NPLs with 3-5 CdSe monolayers (ML). The two sharp absorption peaks represent the electron-heavy hole (A exciton) and electron-light hole (B exciton) transition, respectively, and the emission results from the radiative recombination of the band-edge A exciton.²¹ Both the absorption and emission properties of NPLs are determined by the exciton COM coherent delocalization of NPLs, in particular, the excitonic transition oscillator strength and the radiative recombination lifetime are both proportional to the exciton COM coherent area.^{21, 57} With uniform quantum confinement along the thickness direction, it has been speculated that the exciton COM coherent area can extend over the entire 2D NPL at low temperature, giving rise to the giant oscillator strength transition (GOST) effect.^{21, 58-60} We show in this dissertation that this exciton coherent area extension due to GOST effect reduces the degree of the degeneracy of the band-edge excitons of CdSe NPLs, which reduces the optical gain threshold by ~4-fold. This provides a new strategy for rational design and improvement of NC-based low-threshold lasing materials.

1.2.2. Exciton in-plane transport

In 0D QDs, both electrons and holes are completely confined within the particle. However, in 2D NPLs, the electron and hole are bound together as an exciton due to the large exciton binding energy at room temperature,^{21, 61} and can move along the nonquantum-confined lateral dimension. The mechanism by which the excitons are transported is important to the understanding and improvement of their properties in applications from photocatalysis to light emitting. For example, the exciton transport process reflects the energy transport process in

NPLs. It competes with charge separation process with charge carriers (electron and hole) transferred to different places for different chemical reactions,⁶² which is one of the key processes in NC-based photocatalysis systems,^{12, 18, 42-44, 63} and affects the multi-exciton annihilation rate in NPLs.²⁶⁻²⁷ Excitons in 2D NPLs could transport ballistically and diffusively. The former dominates when the exciton COM wavefunction extends throughout the whole NC.^{26, 64-67} The latter occurs when the exciton COM is smaller than the dimension of NC and exciton COM transports can be described with a diffusion constant.⁶⁸⁻⁷⁰

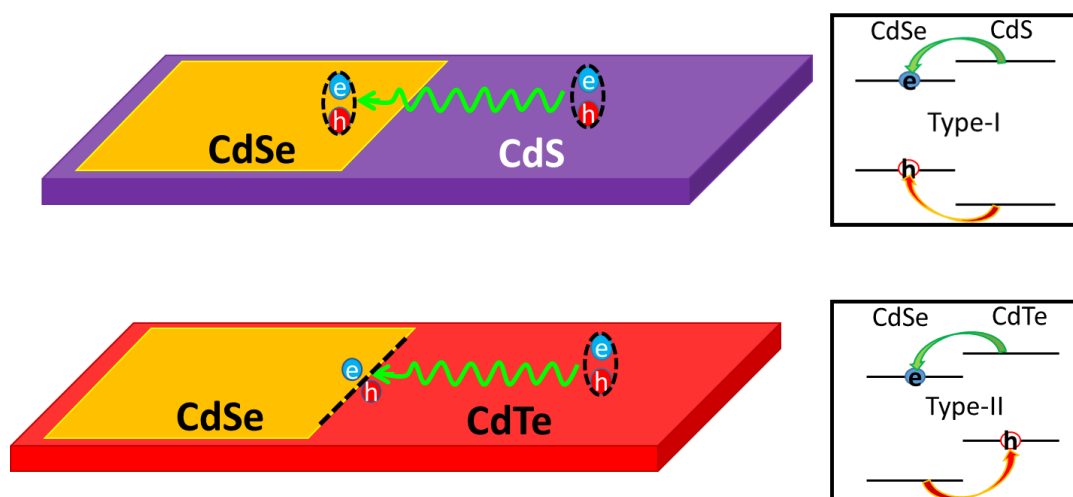


Figure 1.5. Scheme (left) and energy diagram with band-edge transitions (right) of CdSe/CdS type I core/crown (CC) NPLs (upper panel) and CdSe/CdTe type II CC NPLs (lower panel).

Core/crown (CC) NPL heterostructures with one NPL extends laterally around another without changing their thickness provide an ideal model for exciton in-plane transport study. As shown in Figure 1.5, the excitons in the crown are driven to the core (core/crown interface) according to type-I (type-II) band alignment, and this crown-to-core (or interface) transport

process can be captured and quantified by transient absorption spectroscopy. We show that the exciton transports diffusively in both CdS⁶⁹ and CdTe NPLs⁶⁸ with a diffusion constant close to their bulk counterparts. This result also benefits the Auger recombination mechanism in 2D NPLs.²⁷

1.2.3. Multi-exciton annihilation

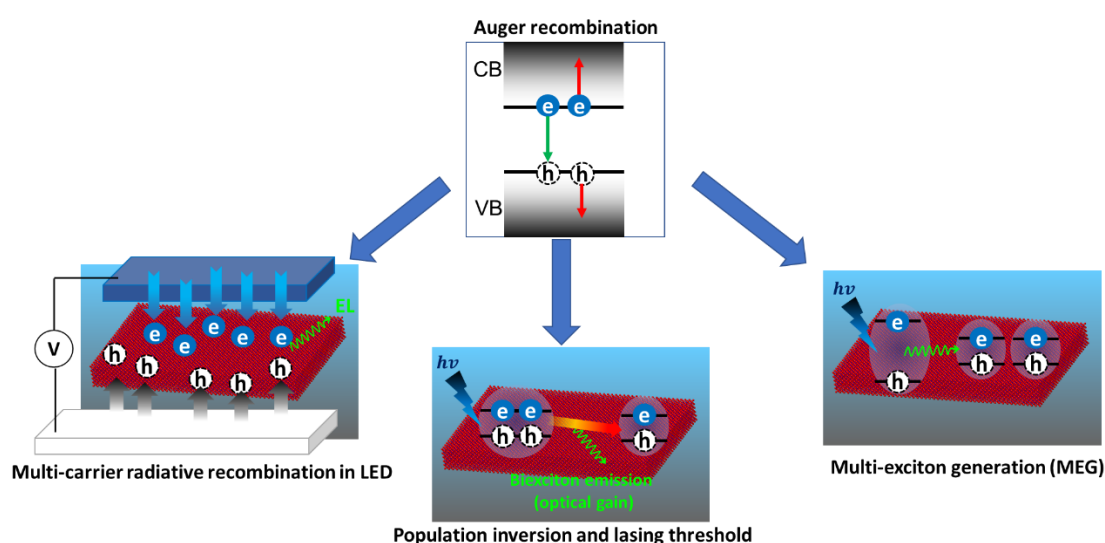


Figure 1.6. Schemes of Auger recombination process in NPLs (upper panel), the multi-carrier radiative recombination in NPL-based light emitting diodes (LED) (left in lower panel), biexciton emission in NPLs (middle in power panel), and MEG process in NPLs (right in lower panel).

As shown in Figure 1.6, the detrimental multi-exciton annihilation process is involved and affects many optoelectrical applications of NCs, such as light-emitting diodes (LED),^{55, 71-75} lasing,^{14, 31, 40} and MEG process.⁷⁶⁻⁷⁹ The nonradiative Auger recombination, in which the recombination energy of one electron-hole pair excites another carrier to its higher energy

level, dominates the multi-exciton annihilation process and is enhanced in NCs as the quantum confinement effect relaxes the requirement of momentum conservation during Auger process.^{26-27, 29, 80-95} Previous studies on 0D QDs have shown the bi-exciton Auger recombination lifetime scales linearly with the QD volume, regardless of the indirect- or direct-gap semiconductors, providing a “universal volume scaling law.”^{29, 96-100} Later, the bi-exciton lifetime of PbSe NRs is also reported to scale linearly with NR volume,⁹⁰ indicating Auger lifetime have the same dependence on the quantum-confined (diameter direction) and nonquantum-confined dimensions (rod length axis) in NRs. To test the “universal volume scaling law” and unveil the dependence of Auger recombination in 2D NPLs, we studied the Auger recombination in CdSe NPLs with different lateral areas and thicknesses *via* pump fluence dependent TA spectroscopy.²⁷ We established a new model that accounts both the lateral area and thickness dependent bi-exciton Auger lifetime of CdSe NPLs: their nonquantum-confined dimension determines the exciton collision frequency, while their quantum-confined dimension determines the Auger probability per collision, and the Auger recombination rate is the product of exciton collision frequency and Auger probability per collision.

1.2.4. Exciton dissociation

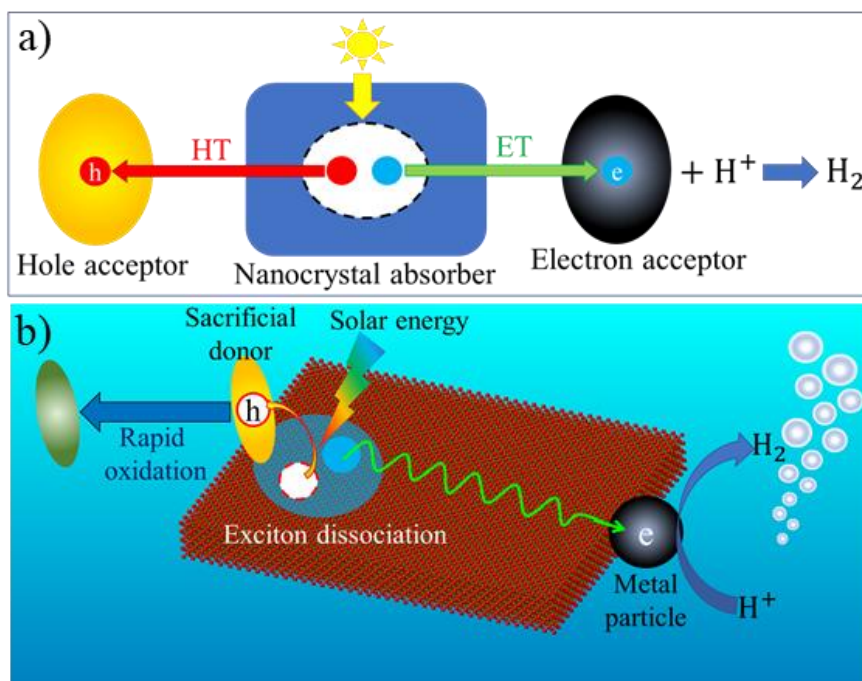


Figure 1.7. (a) Scheme of solution-processed artificial solar-to- H_2 conversion system based on nanocrystal absorber with electron and hole acceptors. HT and ET represent hole transfer and electron transfer, respectively. (b) Exciton dissociation in cadmium chalcogenide nanoplatelet-metal heterostructures for light-driven H_2 generation.

In a typical photosynthetic system for solar-to- H_2 conversion by water splitting (shown in Figure 1.7a), semiconductors are used as a solar energy absorber, which generates excitons after photon absorption. The excitons then dissociate with electrons and hole transferred to catalysts, where holes oxidize water and electrons reduce H^+ (or water at high pH) to form H_2 .¹⁰¹ Because the catalytic reactions are often slow, their efficiencies are reduced due to the competition with the recombination of electrons and holes. An efficient photosynthetic system requires semiconductor absorbers that have both large absorption cross sections and can

undergo efficient charge separation. For typical cadmium chalcogenide NC-Pt heterostructures, although the exciton dissociation process is fast and efficient, the efficiency of solar-to-H₂ conversion is still often limited by recombination of the electrons and holes due to the relatively slow catalytic reactions.^{63, 102-104}

As shown in Figure 1.7b, the 2D morphology, with a precise thickness of a few monolayers and lateral dimensions of 10s-100s nm, provides several key potential advantages of 2D NPLs for enhanced solar-to-H₂ conversion. The large lateral area leads to large absorption cross-section of NPLs.¹¹ The strong quantum confinement in the thickness direction enhances interfacial charge transfer, while the uniform quantum confinement across the whole NPL enables ultrafast carrier in-plane transport.^{62, 68-69} We show that the 2D morphology extends the charge-separated state in both CdS NPLs⁴³ and CsPbBr₃ perovskite NPLs¹⁰⁵ decorated with electron or hole acceptors. The light-driven H₂ generation performance of the 2D CdS NPL-Pt heterostructures are also tested and compared with the 1D CdS NR-Pt heterostructures.⁴³

1.3. Summary

In this dissertation, we have systematically studied the physical properties of 2D excitons (i.e., exciton coherent area, in-plane transport, Auger recombination, and dissociation) in cadmium chalcogenide NPLs, CC NPL heterostructure, NPL-Pt heterostructures, and CsPbBr₃ perovskite NPLs and how these exciton properties affect their optoelectrical and photocatalytic performances. Our work reveals two directions for utilizing 2D NPLs. (1) Exciton COM delocalization, the large lateral dimension for suppressed Auger recombination, and large

absorption strength and sharp emission in 2D NPLs for low-threshold lasing. (2) Efficient exciton dissociation and extended charge-separated state in NPL-acceptor heterostructures for enhanced solar-to-fuel conversion.

The rest of the dissertation is organized as follows. In Chapter 2, we summarize the experimental methods, including the sample preparation and the spectroscopy setups. In Chapter 3&4, we study the 2D exciton diffusive in-plane transport in CdSe/CdS type I and CdSe/CdTe type II CC NPLs, respectively, and the comparison of exciton transport in 2D NPLs, 1D NRs, and bulk materials. In Chapter 5, we show the lateral area and thickness dependent Auger recombination of NPLs, emphasizing the difference of Auger mechanisms in 2D NPLs, QDs, and NRs, and the deviation from the “universal volume scaling” law. We then discuss optical gain mechanisms and model of CdSe NPLs: how is optical gain threshold affected by NPL lateral size, optical density in Chapter 6. In Chapter 7, we focus on the direct measurement of exciton coherent area of 2D CdSe NPLs with its dependence on NPL thickness, lateral area, dielectric environment, and temperature, and how it relates the GOST effect and affects the optical gain threshold in 2D NPLs. In Chapter 8, we unveil the optical gain mechanisms in CdSe/CdTe type II CC hetero-NPLs. In Chapter 9, we show that the light-to-H₂ conversion quantum efficiency can be significantly improved using 2D cadmium chalcogenide NPLs and 2D morphology enhances H₂ generation by slowing down charge recombination through detailed transient absorption study and modeling. In Chapter 10, we show the efficient exciton dissociation in CsPbBr₃ perovskite 2D NPLs by selective charge transfer to electron or hole acceptors and an over ~100-fold longer-lived charge-separated state in CsPbBr₃ NPL-hole acceptor complexes compared to that in QD-hole acceptor complexes.

In the last Chapter, we summarize the main results and outlook the challenges remained in this field.

Chapter 2. Experimental Methods

Reproduced in part with permission from *ACS Nano* **2016**, *10*, 3843. Copyright 2016 American Chemical Society; *ACS Energy Lett.* **2017**, *2*, 174. Copyright 2017 American Chemical Society; *Nano Lett.* **2017**, *17*, 3152. Copyright 2017 American Chemical Society; *Chem. Sci.* **2018**, *9*, 728. Copyright 2018 Royal Society of Chemistry; *J. Am. Chem. Soc.* **2018**, *140*, 11726. Copyright 2018 American Chemical Society; *J. Phys. Chem. Lett.* **2019**, *10*, 566. Copyright 2019 American Chemical Society. *J. Phys. Chem. Lett.* **2019**, *10*, 1624. Copyright 2019 American Chemical Society.

2.1. Sample Preparation

2.1.1. Synthesis of cadmium chalcogenide nanoplatelets

3 monolayer (ML) CdSe nanoplatelets (NPLs): The CdSe colloidal NPLs were synthesized following the reported procedures with slight modifications.²¹ Typically, 170 mg cadmium acetate dihydrate ($\text{Cd}(\text{Ac})_2 \cdot 2\text{H}_2\text{O}$) and 14 mL of 1-octadecene (ODE) were introduced to a 25 mL three-neck flask. After degassed under vacuum at 100 °C for 1 hour, 12 mg selenium powder in 1 mL ODE were injected, then the mixture was heated to 180 °C under argon flow. The reaction continued for 5 min and 10 min at 180 °C for 3 ML CdSe NPLs with increasing lateral area, respectively, before it stopped by quenching the flask in a water bath.

4 ML CdSe NPLs: 170 mg cadmium myristate ($\text{Cd}(\text{myr})_2$) and 14 mL of 1-Octadecene (ODE) were introduced to a 25 mL three-neck flask. After degassed under vacuum at 100 °C

for 1 hour, 12 mg selenium powder in 1 mL ODE were injected, then the mixture (Solution 1) was heated under argon flow. 40 mg cadmium acetate dihydrate ($\text{Cd}(\text{Ac})_2 \cdot 2\text{H}_2\text{O}$) was introduced into the Solution 1 when its temperature reached 205 °C. The smallest 4ML CdSe NPL sample was obtained by stopping the reaction (with a water bath) when the temperature reached 230 °C. Larger samples were obtained by stopping the reaction at 1, 5, and 15 mins, respectively, for increasing lateral area after the reaction temperature had reached 240 °C.

5 ML CdSe NPLs: 170 mg cadmium myristate ($\text{Cd}(\text{myr})_2$) and 14 mL of 1-Octadecene (ODE) were introduced to a 25 mL three-neck flask. After degassed under vacuum at 100 °C for 1 hour, 12 mg selenium powder in 1 mL ODE were injected, then the mixture (Solution 1) was heated under argon flow. 12 mg Selenium powder in 1 mL ODE was injected into Solution 1 when its temperature reached 250 °C. After 60 seconds, 120 mg cadmium acetate dihydrate ($\text{Cd}(\text{Ac})_2 \cdot 2\text{H}_2\text{O}$) was introduced into the solution. The reaction continued for 5 min and 10 min at 250 °C for 5ML CdSe NPLs with increasing lateral area, respectively, after which it was stopped by quenching the solution in a water bath.

4 ML CdS NPLs: The CdS NPLs were synthesized following the reported procedures with slight modifications.¹⁰⁶ Typically, 210 mg cadmium acetate dihydrate ($\text{Cd}(\text{Ac})_2 \cdot 2\text{H}_2\text{O}$), 0.25 mL OA, 10 mL 1-Octadecene (ODE), and 1 mL of 0.2 M sulfur-ODE solution were introduced to a three-neck flask. After bubbling with argon at room temperature for 30 min, the mixture was heated to 260 °C and was kept there for 4 min under argon flow, then stopped by water bath.

For all samples, after the reaction solution reached room temperature, 1 mL of oleic acid (OA) was injected. The product was a mixture of NPLs and quantum dots (QDs) and the NPLs

were separated from QDs by washing with ethanol: hexane/ODE mixture with ratio of 1: 3 and centrifuged at 5000 rpm for 3 min. The final NPL samples were dispersed in hexane.

2.1.2. Synthesis of core/crown nanoplatelet heterostructures

CdSe/CdS type I core/crown (CC) NPLs: The CdSe/CdS CC NPLs were synthesized according to the procedures in reported literatures with slight modifications.¹⁰⁷⁻¹⁰⁸ A total of 480 mg of $\text{Cd}(\text{Ac})_2 \cdot 2\text{H}_2\text{O}$ and 340 μL of OA was dissolved in 2 mL of ODE and heated up at 150 °C during 15 min under sustained stirring. 3 mL of 0.1 M of S dissolved in ODE was added into the solution and kept stirred as CdS growth mixture. The entire product of CdSe NPLs with 5 mL of ODE was added in a three-neck flask. The CdS growth mixture was injected continuously in the NPLs solution at 5 mL/h at 220 °C under argon flow. Different samples were withdrawn from the solution at different time for different sized CC NPLs in Chapter 3. Then CdSe/CdS CC NPLs were precipitated with ethanol and dispersed in hexane.

CdSe/CdTe type II CC NPL heterostructures: The CdSe/CdTe CC NPLs were synthesized following the procedures reported in the literature with slight modifications.¹⁰⁹ 3 mL CdSe NPLs (with optical density of 1 at 512 nm in 1 mm cuvette), 80 mg of $\text{Cd}(\text{Ac})_2 \cdot 2\text{H}_2\text{O}$, and 50 μL of OA was dissolved in 10 mL of ODE and degassed under vacuum at 100 °C for 30 min, then heated to 190 °C under argon flow. 25 mg Te powder was dissolved in 800 μL trioctylphosphine (TOP) and 9.2 ml ODE as Te precursor. The Te precursor was then slowly injected using a syringe pump at a rate of 1mL/hour. Different samples were withdrawn from the solution at different time after the injection using a syringe, in particular, 50, 70, 90, and 105 mins for CC1 to CC4 in Chapter 4, respectively. All the products were washed with ethanol

and hexane mixture and centrifuged at 5000 rpm for 3 min. The final CC NPL samples were dispersed in hexane.

2.1.3. Synthesis of CdS nanorods

The CdS nanorods (NRs) were synthesized following the reported procedures with slight modifications.¹¹⁰⁻¹¹¹ Typically, 0.06 g Cadmium Oxide (CdO), 3 g trioctylphosphine oxide (TOPO), 0.29 g octadecylphosphonic acid (ODPA), and 0.08 g hexylphosphonic acid (HPA) are degassed under vacuum for 1 hour at 150 °C. After heating to 350 °C under argon for 30 min, the mixture turns into clear solution, indicating the dissolution of CdO. At this point, 1.8 mL trioctylphosphine (TOP) is injected to the solution. In a separated container, sulfur injection solution (0.12g S in 1.8 mL TOP) is mixed with CdS QD seeds. When the temperature of the CdO-containing solution is stabilized at 350 °C, the seed-containing sulfur injection solution is quickly injected. The temperature drops down upon the injection and recovers to 350 °C in ~1 min. The solution is kept for 3-8 min. Reactions are stopped by removing the heating mantle. Products are precipitated out of the reaction crudes by addition of ethanol. The precipitation processes are repeated for several times. Final products are dispersed in chloroform.

2.1.4. Synthesis of nanocrystal-Pt heterostructures

CdS NPL-Pt heterostructures and free Pt particles: The thermal deposition of Pt particles on CdS NPLs followed the reported procedures for CdSe NPL-Pt heterostructures with slight modifications.⁶² Typically, a mixture of 0.2 mL OA, 0.4 mL oleylamine (OLAm), 40 mg 1,2-hexadecanediol (HDT) and 10 mL diphenyl ether (DPE) was degassed under

vacuum for 1 hour at 100 °C. Then, the temperature of the solution was raised to 195 °C under argon flow. 3 mL as-prepared CdS NPLs with optical density of 1 at 408 nm in a 1 mm cuvette was dried and dispersed with 15 mg Pt acetylacetonate in 1 mL dichlorobenzene solution and sonicated for 5 minutes to dissolve the Pt precursor. This solution was swiftly injected into the DPE solution at 195 °C. The reaction was kept for 4 min before quenched by water bath. The product was washed by precipitation with ethanol followed by centrifugation, and finally dispersed in hexane. Free Pt nanoparticles were also synthesized under similar conditions without the addition of CdS NPLs. The growth time was longer, typically 15 minutes because the homogeneous nucleation of Pt nanoparticles was slower than the heterogeneous nucleation on the edges of CdS NPLs.

CdS NR-Pt heterostructures: The CdS NR-Pt heterostructures were synthesized following the reported procedures for with slight modifications.¹¹⁰ Typically, 0.2 mL oleic acid (OA), 0.2 mL oleylamine (OLAm), 43 mg 1,2-hexadecanediol (HDT) and 10 mL diphenyl ether (DPE) were mixed in a 3-neck flask and degassed under vacuum for 1 hour at 90 °C. Then, the temperature of the solution was raised to 190 °C under argon flow. 2 mL CdS NRs with optical density of 1 at the first exciton peak in a 1 mm cuvette were dried and redispersed in 1 mL dichlorobenzene with 10 mg Pt acetylacetonate and sonicated for 5 minutes. This solution was then swiftly injected into the DPE solution at 190 °C. The reaction was kept for 9 min before quenched by water bath. The product was washed by precipitation with ethanol followed by centrifugation, and finally dispersed in chloroform.

CdSe NPL-Pt heterostructures: The CdSe NPL-Pt heterostructures were synthesized following the reported procedures for with slight modifications.⁶² Typically, a mixture of 0.2

mL oleic acid (OA), 0.4 mL oleylamine (OLAm), 40 mg 1,2-hexadecanediol (HDT) and 10 mL diphenyl ether (DPE) was degassed under vacuum for 1 hour at 100 °C. Then, the temperature of the solution was raised to 195 °C under argon flow. 3 mL as-prepared CdSe NPLs with optical density of 1 at 512 nm in a 1 mm cuvette was dried and dispersed with 15 mg Pt acetylacetonate in 1 mL dichlorobenzene solution and sonicated for 5 minutes to dissolve the Pt precursor. This solution was swiftly injected into the DPE solution at 195 °C. The reaction was kept for 4 min before quenched by water bath. The product was washed by precipitation with ethanol followed by centrifugation, and finally dispersed in hexane.

2.1.5. Synthesis of CsPbBr₃ perovskite nanoplatelets

In Chapter 10, the CsPbBr₃ NPLs were synthesized using reported procedures with slight modifications.⁵² Typically, Cs-oleate was first prepared by mixing 0.35g Cs₂CO₃ and 1.25 mL oleic acid (OA) in 20 mL 1-octadecene (ODE) and the mixture was kept at 150 °C for 15 min under vacuum. 0.125 mL OA, 0.125 mL oleylamine (OL), 0.1 mL Cs-oleate, and 1.25 mL ODE were mixed in a glass vial followed by sonication of 20 sec and denoted as Cs-precursor solution. Then the Cs-precursor solution was injected into 0.2 mL of PbBr₂ solution (0.4 M, PbBr₂ in N, N-dimethylformamide). After 10 sec sonication, 5 mL of acetone was injected into the solution and kept sonicating for another 10 sec. Then, the CsPbBr₃ NPLs along with their assemblies were precipitated by centrifuging with 3500 rpm for 5 mins and dispersed in toluene. After 20 hours, the dispersed CsPbBr₃ solution was centrifuged again at 3500 rpm for 5 mins to precipitate the NPL assemblies, and the supernatant was kept as the final CsPbBr₃ NPL product.

2.1.6. Sample preparation for low temperature measurement

In Chapter 7, for low temperature TA measurements, the as-prepared CdSe NPLs were dried and re-dispersed in saturated poly (maleic anhydride-*alt*-1-octadecene) (PMAO) or poly(methyl methacrylate) (PMMA) chloroform solution and were put on a sapphire substrate *via* drop-casting method and mounted into the Janis STVP-100 cryostat. For NPL solid film samples, the as-prepared colloidal NPLs were dried and re-dispersed in hexane/ethyl cyclohexane mixture. The re-dispersed NPLs were put on a sapphire substrate *via* drop-casting method and mounted into the cryostat.

2.1.7. Procedures of ligand exchange

In Chapter 9, the original ligands on CdS NPLs (oleic acid) were replaced by L-cysteine following the reported procedures with slight modifications.¹¹²⁻¹¹³ Typically, 1.5 mL NPLs solution (in hexane), with the optical density of 2 at their first exciton peak in 1 mm cuvette, was diluted to 5 mL solution. 28 mg L-cysteine was then added to the solution. 5 mL 1 mol/L KOH aqueous solution was then mixed with NPL solution and the mixture was stirred vigorously for 4 hours under dark condition. After NPLs were all in aqueous phase, the organic phase was discarded and the NPLs were deposited by the addition of ethanol followed by centrifuge. The NPLs after ligand exchange were finally dispersed in water or KOH aqueous solution for measurements.

2.2. Spectroscopy Setup

2.2.1. Femtosecond transient absorption spectroscopy setup

Femtoseconds (transient absorption) TA measurements were conducted using a Helios spectrometer (Ultrafast Systems LLC) with pump and probe beams generated by a regenerative amplified Ti: sapphire laser system (Coherent Legend, 800 nm, 150 fs, 2.4 mJ/pulse, and 1 kHz repetition rate). The 400 nm pump beam was generated from a frequency-doubled 800 output pulse. We use neutral-density filter wheels to adjust the power the pump beam. The pump beam was focused at the sample with a beam waist of about 600 μm . A white light continuum (WLC) from 360 to 800 nm was generated by attenuating and focusing the 800 nm pulse into a CaF_2 window. The WLC was split into a probe and reference beam. The probe beam was focused by an Al parabolic reflector onto the sample (with a beam waist of $\sim 150 \mu\text{m}$ and intensity per pulse as $\sim 450 \mu\text{J}/\text{cm}^2$ at the sample). The reference and probe beams were focused into a fiber-coupled multichannel spectrometer with complementary metal-oxide-semiconductor (CMOS) sensors and detected at a frequency of 1 kHz. The intensities of the pump and probe beams were controlled to correct for pulse-to-pulse fluctuation of the WLC. The delay between the pump and probe pulses was controlled by a motorized delay stage. The pump beam was chopped by a synchronized chopper to 500 Hz. The change in absorbance for the pumped and un-pumped samples was calculated. 1 mm cuvettes were used for all solution sample measurements. The instrument response function (IRF) of this system was measured to be ~ 160 fs by measuring solvent responses under the same experimental conditions (except for a higher excitation power).

2.2.2. Nanosecond transient absorption spectroscopy setup

Nanosecond TA was performed with the EOS spectrometer (Ultrafast Systems LLC). The pump beam at 400 nm was generated in the same way as femtosecond TA experiments. The WLC (380-1700 nm, 0.5 ns pulse width, 20 kHz repetition rate) was generated by focusing a Nd: YAG laser into a photonic crystal fiber. The delay time between the pump and probe beam was controlled by a digital delay generator (CNT-90, Pendulum Instruments). The probe and reference beams were detected with the same multichannel spectrometers used in femtosecond TA experiments. The IRF of this system was measured to be ~ 280 ps. 1 mm cuvettes were used for all solution sample measurements. The data from femtosecond and nanosecond transient spectrometers overlap at delay time windows from 0.8 to 1 ns. To connect spectra and kinetics from these spectrometers, we scale the amplitudes of the nanosecond data to match the femtosecond results in the overlapping delay time windows.

2.2.3. Static-photoluminescence measurement setup

All static photoluminescence (PL) measurements were performed with FluoroMax-3 Spectrofluorometer of HORIBA Scientific. 1 cm cuvettes were used for all solution sample measurements.

2.2.4. Time-resolved photoluminescence measurement setup

Time-correlated single photon counting (TCSPC) method was used to measure the Time-resolved (TR) PL decay of the solution samples. Samples were held in a 1 cm cuvette and measured at the right angle geometry. The output pulses centered at 780 nm (~ 100 fs, 80 MHz)

from a mode-locked Ti: sapphire laser (Tsunami oscillator pumped by a 10 W Millennia Pro, Spectra-Physics) were passed through a pulse picker (Conoptics, USA) to reduce the repetition rate by a factor of 20 and then frequency-doubled in a BBO crystal to generate pump pulses at 390 nm and used to excite samples. The emissions from samples were detected by a microchannel-plate photomultiplier tube (Hamamatsu R3809U-51), the output of which was amplified and analyzed by a TCSPC board (Becker & Hickel SPC 600). The IRF of this system was determined to be ~ 110 ps by measuring the scattered pump light.

2.2.5. Amplified spontaneous emission measurement setup

In Chapter 6, CdSe NPL films used in amplified spontaneous emission (ASE) measurement were prepared using spin-coating method following the reported procedures with slight modifications.³³ The as-prepared CdSe NPLs were precipitated by ethanol to remove additional ligands (OA) in NPL solutions. NPLs was then dispersed in 4:1 (v:v) hexane/octane mixture and deposited on a glass substrate by spin-coating in air. all ASE measurements were conducted at room temperature in air. The NPL film was pumped with the same 400 nm pulses. The pump beam was focused into a stripe along the NPL films by a cylindrical lens. The length of the stripe was determined to be the same as the beam size before focusing (2.2 mm) and the width of the stripe was determined to be $32 \mu\text{m}$ using the knife-edge technique. The emission was detected at the edge of NPL films along the stripe direction by a USB spectrometer (HR2000+, Ocean Optics).

2.3. Light-Driven H₂ generation

In Chapter 9, the H₂ generation experiments were conducted in a cylindrical cuvette (NSG, 32UV10) with a total volume of 2.5 mL and light path of 1 cm. The reaction solutions are L-cysteine covered CdS NPL-Pt heterostructures dispersed in 1:9 volume ratio of ethanol/KOH aqueous solution with different KOH concentration. The reaction was constantly stirred and illuminated by a 405 nm monochromatic LED light (5 mW with a beam area of 0.78 cm²). H₂ generated in the reaction headspace was detected using a HP5890A model gas chromatograph equipped with a thermal conductivity detector and a HP-MOLESIEVE capillary GC column (30m x 0.535 mm x 25.00 μm) packed with 5 Å molecular sieves. Argon was used as a carrier gas. Typically, the H₂ amount was quantified by withdrawing a gas sample from the headspace at certain intervals without stopping the reaction. Internal quantum efficiency (IQE) for H₂ generation is calculated using: $\text{IQE} = 2\Delta(\text{H}_2) / \Delta(\hbar\nu)$, where $\Delta(\text{H}_2)$ is the H₂ generation rates (number of generated H₂ molecules per second) extracted from the H₂ evolution slope and $\Delta(\hbar\nu)$ is the number of absorbed photons per second calculated from the excitation power and sample optical density. The number of absorbed photons by NPLs is used as $\Delta(\hbar\nu)$, which is obtained by excluding the light absorbed or scattered by the cuvette (by subtracting the absorption spectra of cuvette with water) and Pt particles (by subtracting Pt absorption tail from absorption of CdS NPL-Pt heterostructure) from the total number of absorbed photons.

2.4. Electrochemical method for the estimation of Nanocrystal band-edge position

In Chapter 9, the conduction band (CB) edge of CdS NPLs and NRs were estimated *via* electrochemical measurements. The CdS NPLs or NRs electrode were prepared following reported procedures with slight modifications.¹¹⁴ Typically, after ligand exchange, CdS NPLs or NRs were dispersed in water. 1.74 g NaCl was dissolved in 100 mL of 2 mg/mL of poly (diallyldimethylammonium chloride) (PDDA) solution. The fluorine-doped tin oxide (FTO) substrates were sonicated in acetone, ethanol, and water. They were then dried and immersed in PDDA solution for 2 hours. After rinsing with water, CdS NPL or NR water solution were deposited by drop-casting on the FTO substrates. The samples were then dried at room temperature and subsequently annealed at 300 °C in air for 1 hour.

Current-voltage (CV) curve for CdS NPLs or NRs were measured in the dark condition *via* electrochemical work station using a three-electrode experiment with CdS NPL electrode as working electrode, silver chloride electrode (SCE, 0.222 V *vs* NHE) as reference, and Pt electrode as counter electrode. Copper paint was used to provide a good electrical contact to the electrode. The scan started from 0 to -1.5 V *vs* NHE and the scan speed was 20 mV/s. pH dependent CV curves were measured by changing the pH of electrolyte. The CV curves of CdS NPLs and NRs are shown in Figure 2.1a and 2.1b, respectively. The pH dependent reduction potential of CdS NPLs and NRs were determined by reduction peak in CV curve. The reduction potential of CdS NPLs and NRs as a function of pH are plotted in Figure 2.1c and 2.1d, respectively, and the values and fitting parameters are listed in Table 2.1.

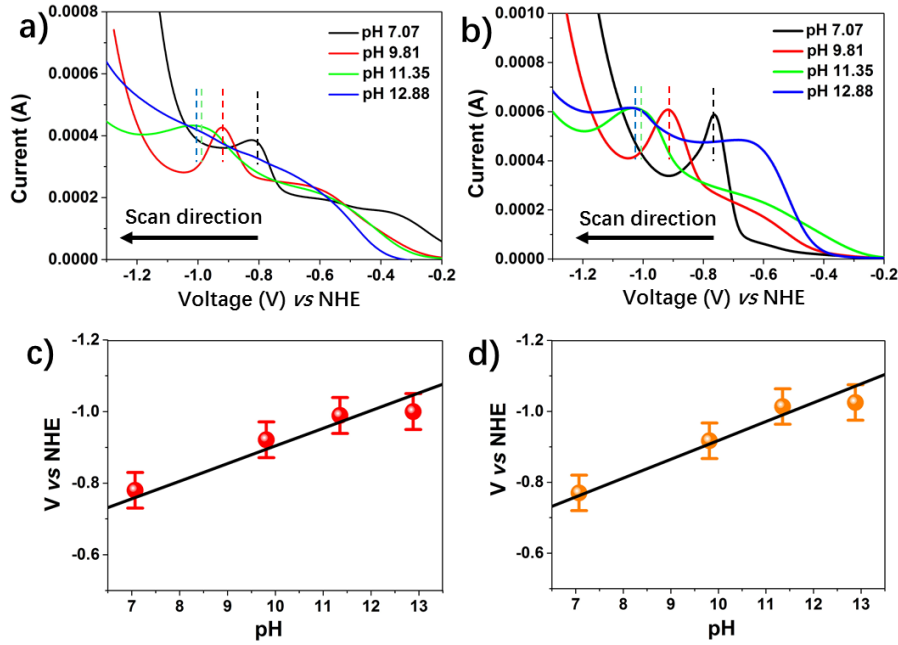


Figure 2.1. The pH dependent CV curves for (a) CdS NPLs and (b) CdS NRs. Dashed lines mark the reduction peaks. The pH dependent reduction potential of (c) CdS NPLs and (d) CdS NRs.

Table 2.1. pH dependent reduction potential and the fits of CdS NPLs and NRs

	pH 7.07	pH 9.81	pH 11.35	pH 12.88	Slope (mV/pH)
NPL CB/ V vs NHE	0.78 ± 0.05	0.92 ± 0.05	0.99 ± 0.05	1.00 ± 0.05	43.1 ± 0.8
NRs CB/ V vs NHE	0.77 ± 0.05	0.92 ± 0.05	1.01 ± 0.05	1.02 ± 0.05	46.5 ± 1.2

pH dependent reduction potential of H^+ at low pH or H_2O at high pH (E_{H^+/H_2} or E_{H_2O/H_2})

and the oxidation potential of OH^- (E_{OH^-/OH^-}) are estimated by Nernst equations:¹¹⁴

$$E_{H^+/H_2} \text{ or } E_{\frac{H_2O}{H_2}}(pH) = -0.059 \text{ pH (V vs NHE)} \quad (2.1)$$

$$E_{OH^-/OH^-}(pH) = 2.466 - 0.059 \text{ pH (V vs NHE)} \quad (2.2)$$

As shown in Figure 2.2, we determine the CB edge position (purple dots) of CdS NPLs as a function of pH *via* this electrochemical method. We approximate the CB edge using the reduction potential peak (Figure 2.1).¹¹⁴⁻¹¹⁵ The linear fit (blue solid lines) of the pH dependent CB edges gives the CdS NPLs CB edge as a function of pH as shown in Figure 2.2. The slope of the linear fit is -43.1 ± 0.8 mV/pH. The valence (VB) edge as a function of pH is determined by the CB edge and exciton peak (430 nm, 2.88 eV). The CdS NR electrode was prepared and analyzed the same way and the linear fit (green dashed line) gave a slope of -46.5 ± 1.2 mV/pH. We assume the electrochemical potentials of water reduction (orange solid line) and hydroxyl anion oxidation (red solid line) as a function of pH are determined by their Nernstian response to the pH with a slope of -59.2 mV/pH.¹¹⁴ Noted that the CB edge position of CdS NPLs is similar to the one of CdS NRs according to the electrochemical measurements. With larger quantum confinement, CdS NPL is predicted to have higher (more negative *vs* NHE) CB edge than NRs.¹¹⁶⁻¹¹⁸ This deviation from prediction is likely due to different bulk CB edge positions of zinc-blend and wurtzite structured CdS: bulk CB edge in wurtzite CdS is higher than it in zinc-blend CdS.¹¹⁹⁻¹²⁰ The higher bulk CB edge in wurtzite CdS NRs and the larger CB edge shifts due to larger quantum confinement in zinc-blend CdS NPLs cancels out each other, which results in the similar CB edge position of CdS zinc-blend NPLs and wurtzite NRs.

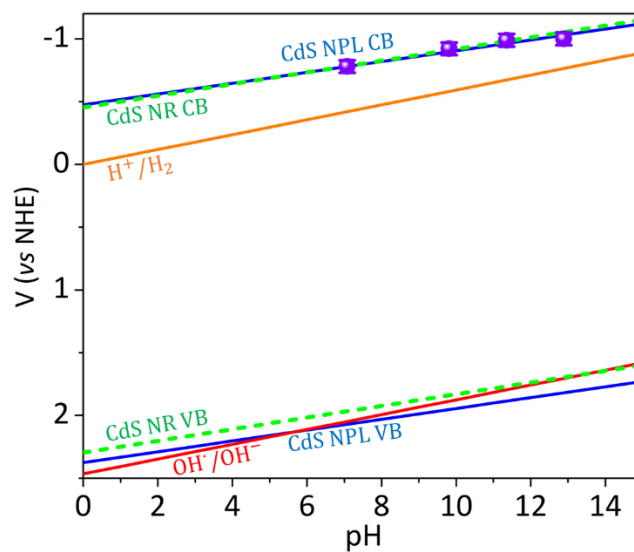


Figure 2.2. Reduction potentials of CdS NPLs and NRs. The electrochemical potentials of H^+ or water reduction (orange solid line) and hydroxyl anion oxidation (red solid line) as a function of pH. Purple spots represent the measured CB position of CdS NPLs. Blue solid line (green dashed line) represent the CB and VB position of CdS NPLs (NRs) as a function of pH.

Chapter 3. Size-Independent Exciton Localization Efficiency in CdSe/CdS Type-I Core/Crown Nanoplatelet Heterostructures

Reproduced with permission from *ACS Nano* **2016**, *10*, 3843. Copyright 2016 American Chemical Society.

3.1. Introduction

Two-dimensional (2D) cadmium chalcogenide nanoplatelets (NPLs) or nanosheets (NSs) with atomically controlled thickness have attracted broad research interests since recent reports of their colloidal synthesis.¹⁹⁻²¹ Unlike 0D quantum dots (QDs)^{5, 24, 121-125} and 1D nanorods (NRs),¹²⁶⁻¹²⁹ 2D NSs have precise quantum confinement throughout the sheet which reduces energetic disorder and, in principle, provides long distance exciton and carrier transport.³⁰⁻³¹ These properties make 2D NSs promising light harvesting and charge transport materials for solar energy conversion. Recently reported CdSe/CdS core/crown (CC) NSs,^{108,107} where CdSe NSs are extended laterally by CdS crowns with exactly the same number of monolayers, represents a new type of heterostructure with potential applications in solar concentrators.¹³⁰⁻¹³⁵ This material is believed to have a type I band alignment, in which both lowest energy conduction band (CB) electron and valence band (VB) hole states are confined in the CdSe core.¹³⁶⁻¹³⁹ In principle, the excitons generated in CdS can be localized to CdSe driven by the band offset and emit at CdSe band-edge. This provides an efficient separation between the absorption at the crown and the emission at the core. Recent investigations of CdSe/CdS core-

shell QDs,¹³⁰⁻¹³¹ doped QDs,¹³²⁻¹³³ and 1D dot-in-rods (DIR)¹³³⁻¹³⁵ as active materials for luminescent solar concentrators have reported promising performance. However, ultrafast trapping of excitons on CdS rods reduce the efficiency of exciton localization to the CdSe.¹⁴⁰⁻¹⁴² The hole trapping states are likely related to unpassivated sulfur atoms on wurtzite CdS rod.^{63, 103, 140} In comparison, 2D CdSe/CdS core/crown NSs have two potential advantages: first, the basal planes of zinc blend NSs are terminated by cadmium atoms which might eliminate hole trapping states; and second, due to absence of energetic disorder, it may be more efficient to transport excitons over a large distance. It has been proposed that the exciton center-of mass wave function in these materials can delocalize over the entire NS.²⁶ Despite these potential advantages, the mechanism of exciton transport in these material remains not well understood.

In this chapter, we report a study of exciton dynamics of CdSe/CdS CC NSs in room temperature by steady state photoluminescence excitation (PLE) spectroscopy and ultrafast transient absorption (TA) spectroscopy. The PLE study reveals that the exciton localization (XL) efficiency in CdSe/CdS CC NSs is independent of crown size but increases with excitation energy. TA studies (at 400 nm excitation) show that ~70% of excitons can localize into CdSe core with exciton localization times increase with the NS size, while the remaining 30% has hole trapped at the interface and electron transferred to the CdSe core. We discuss how the competition of exciton localization and hole trapping gives rise to the observed size dependent exciton localization dynamics and size independent exciton localization efficiency.

3.2. Results and Discussion

3.2.1. Sample Preparation and Characterizations

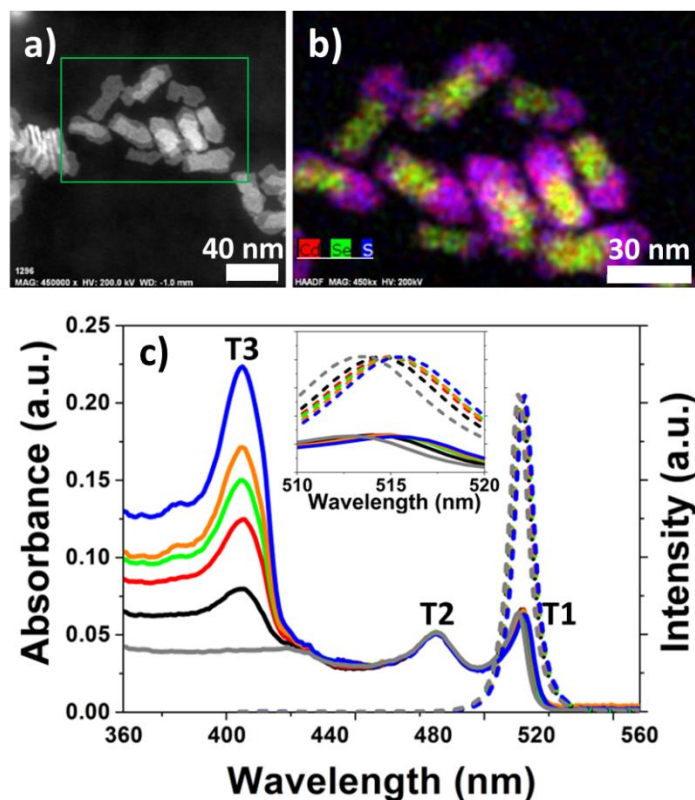


Figure 3.1. Optical and morphological properties of CdSe/CdS CC NSs. (a) Representative HAADF TEM image of CC3. (b) EDX image of a selected area in (a) showing the spatial distribution of Cd (red), Se (green), and S (blue). (c) The absorbance (solid lines) and photoluminescence (dashed lines) of CC NSs with different crown sizes: CC1 (black), CC2 (red), CC3 (green), CC4 (orange), CC5 (blue), and CdSe NS core (gray). Inset: expanded view of the spectra from 510 to 520 nm.

CdSe/CdS CC heterostructures were synthesized following literature procedures with slight modifications.¹⁰⁷ Zinc-blend CdSe NS cores with a thickness of 4 CdSe monolayer (ML)

(~1.8 nm) were first synthesized.¹⁹⁻²¹ The 4 ML CdSe NSs contain 5 crystal plane of Cd and 4 crystal plane of Se as reported.^{32, 107, 143} Zinc-blend CdS crowns with the same number of layers were then grown laterally on the CdSe core by slowly injecting Cd(Ac)₂ and Sulfur powder mixtures into CdSe NS-octadecene (ODE) solution. Five CdSe/CdS CC NSs, from CC1 to CC5 in the order of increasing crown sizes, were prepared from the same CdSe core and the crown sizes were controlled by the growth time. Detailed synthesis procedures are described in Chapter 2.1. High-angle annular dark-field (HAADF) scanning TEM image of CC3 sample (Figure 3.1a) showed typical rectangular shape of the CC NSs. Energy-dispersive X-ray (EDX) image of the selected areas (Figure 3.1b) showed that Se was in the middle of CC NSs, S was only found at the crown, and while Cd was spread over the whole sheet. These images confirm the CdSe core/CdS crown morphology although the crown growth is not isotropic, with preferential growth along one of the four directions to give rise to the rectangular shape. The TEM, HAADF-STEM images and EDX maps for other samples are shown in Appendix 3.1, from which the dimension of core and crown were determined (Table 3.1 in Appendix 3.1). These CCs had a rectangular core (11.1 ± 2.2 nm width and 21.2 ± 2.1 nm length) and the total length was extended from 33.9 ± 1.4 nm in CC1 to 42.0 ± 3.2 nm in CC5 while the width remained constant. Thickness of the CC NSs is estimated to be ~1.8 nm or 4 layers of CdS according the peaks in the absorption spectra (see below).^{19, 21}

UV-vis absorbance spectra and photoluminescence spectra of CdSe core and CC1- CC5 NS samples are shown in Figure 3.1c. Two sharp absorption peaks located at 512 nm (T1) and 483 nm (T2) are the lowest energy electron-heavy hole and electron-light hole exciton peaks of CdSe NSs, respectively, while the broader peak at 410 nm (T3) can be assigned to the

overlapping lowest energy electron-heavy hole and electron-light hole exciton peaks of CdS crowns (Figure 3.2a).^{21, 107-108} From CC1 to CC5, the relative absorption strengths of CdS crowns increases compared to the CdSe core, while the peak positions only shows a small red shift (~ 2 nm, see Figure 3.1c inset), indicating an increase in the crown area and negligible change in their thickness. The small peak shift is likely due to the slight change of the dielectric environment and/or weak lateral quantum confinement after crown growth.¹⁰⁸ Photoluminescence (PL) spectra of all samples (excited at 400 nm) show a sharp peak centered at ~ 515 nm (Figure 3.1c) similar to that of CdSe NS (prior to the growth of the crown). Note that the PL peaks red shift slightly from CC1 (514 nm) to CC5 (516 nm) consistent with the shift in the absorption spectra. PL spectra of these samples show neither band edge emission (415 nm) nor trap-state emission (broad peak centered at ~ 630 nm) of CdS NSs, indicating negligible amounts of free CdS NSs in CC NSs solution,²¹ and all emissions in these CC heterostructures are due to CdSe NS band-edge emission, independent of the crown size.

3.2.2. Type I Band alignment in CdSe/CdS core/crown heterostructure

The excitation wavelength independent PL spectra (Figure 3.1c) imply that CdSe/CdS NSs have type I band alignment between the core and crown (Figure 3.2a) and excitons generated in the CdS crown are transported to the CdSe core, where they emit. The type I band alignment of CC NSs can be estimated from CdSe and CdS bulk band edge positions and shifts due to quantum confinement, dielectric confinement, and exciton binding energy.^{21, 61, 144-145} The binding energy and self-image energy resulted from dielectric confinement for CdSe and CdS NSs in organic solvents with low dielectric constants are ~ 100 meV.^{61, 146} Although these

values may change for the CdSe/CdS core/crown structure due to the change in dielectric environment, we have assumed that they remain similar for CdS and CdSe and only consider the quantum confinement effects here. The ratio of quantum confinement energies in CB and VB are $1/m_e^*$ to $1/m_h^*$, where $m_e^*(m_h^*)$ is the electron (hole) effective mass. Using m_e^* (m_h^*) values of $0.13m_0$ ($0.45m_0$) and $0.21m_0$ ($0.8m_0$) (m_0 is the free electron mass) for CdSe and CdS, respectively,^{62, 116-117} the calculated CB (VB) edge positions are roughly -3.4 eV (-5.8 eV) for CdSe and -3.3 eV (-6.3 eV) for CdS. Therefore, these CdSe/CdS CC NSs are expected to have type I band alignment (Figure 3.2a) with CB and VB band offset of 100 and 500 meV, respectively. The details of the calculation can be found in the Appendix 3.2.

TA studies were carried out to verify the expected type I band alignment in these materials. Our recent TA studies show that the exciton bleach signals in CdSe and CdTe NSs can be attributed to the state-filling of the CB electron level with negligible contribution of VB holes,^{62, 147} similar to cadmium chalcogenide QDs and NRs.^{78, 110, 148-149} Thus TA spectroscopy provides a convenient probe of CB electron dynamics and relative alignment of CB band edge positions between CdSe and CdS. All TA measurements to be discussed below were carried out at low excitation flux ($5 \mu\text{J}/\text{cm}^2$), so that the TA signal was dominated by single exciton excitation in the core/crown structure with negligible multiple exciton contributions. The TA spectra measured with 485 nm excitation (Figure 3.2b), where only CdSe domain absorbs, show only the bleach of the T1 and T2 bands of CdSe without bleach of CdS T3 band at ~410 nm, indicating that the electron is localized in CdSe CB. This result confirms the type-I band alignment in these CC NSs with both the CB and VB edges of CdSe sandwiched between those of CdS (Figure 3.2a).

Detailed kinetics model for accounting the exciton bleach formation and decay is derived in Appendix 3.3, which shows that in the absence of exciton transfer from CdSe to CdS, this kinetics can be fit by multiple exponential functions. Fitting of the T1 bleach kinetics (see Appendix 3.3) revealed a formation time of 0.10 ± 0.02 ps, and bi-exponential decay with a fast component time (amplitude) of 0.83 ± 0.02 ns ($83.0 \pm 1.8\%$) and slower component of 50.4 ± 4.4 ns ($17.0 \pm 1.9\%$). The T1 bleach rise time reflects a ultrafast formation of the electron at the CdSe CB edge ($n=1$) level. 485 nm excitation selectively excite CdSe, directly generating CB electrons with excess energy from 0 (resonant with T_2 transition) to 150 mV above the $n=1$ level. This result is consistent with a previously reported instrument response time limited (<5 ps) carrier cooling time in related CdSe NSs under low excitation fluence.^{23, 150} The fast (0.83 ns) component of bleach recovery agrees well with the crown size-independent PL decay (Figure 3.2c). According to the kinetic model shown in Appendix 3.3, this decay component can be attributed to decay of band edge excitons by band edge electron-hole recombination, electron trapping and hole trapping. The slower bleach recovery (~ 50.4 ns) component is not observed in the PL decay and can be attributed to the no-radiative recombination of the CB electron with trapped holes and electron trap.^{62, 151} Different exciton recombination lifetimes, ranging from ~ 200 ps to ~ 100 ns in CdSe NSs have been reported recently.^{21, 23, 145, 150-152} The origin for the difference is unclear, but it likely related to different rates of carrier trappings in these materials.

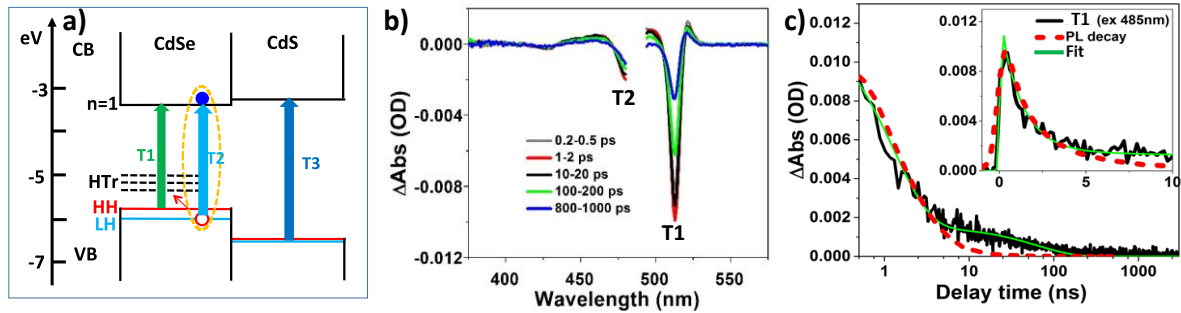


Figure 3.2. Band alignment and exciton decay dynamics in CdSe core. (a) Schematic type I band alignment between CdSe core and CdS crown. HH is heavy hole band, LH is light hole band. T1, T2, T3 are the lowest exciton transitions as in Figure 3.1c. HTr are the hole trapping states. Dashed yellow line indicates an exciton generated by direct excitation at 485 nm (T2 transition) (b) Transient spectra of CdSe/CdS at indicated delay time after 485 nm excitation (of the core). (c) Comparison of exciton bleach recovery of CC5 (black solid line) and the PL decay (red dashed line) in CdSe/CdS after 485 nm excitation. The fit of T1 bleach is showed as green solid line.

It should be noted that although the dynamics of band edge bright exciton state is probed in TA exciton bleach recovery (through CB electron state filling) and PL decay (through e-h radiative recombination), it is in thermal equilibrium with many other exciton states in CdSe core. The energy level spacing between the VB HH and LH levels is ~ 50 meV, $\sim 2k_B T$ at room temperature. Free in-plane carrier gives rise to continua of states in the CB and VB and free in-plane exciton center-of-mass motion gives rise to continua of exciton states. In addition, due to spin multiplicity, there exists a manifold of dark exciton states. At room temperature, these exciton states are in an equilibrium.¹⁵² In the model described above, we have assumed a fast

equilibrium between these exciton states and the decay constants reflect the rate limiting decay channels out of these exciton states.

3.2.3. Size independent crown-to-core exciton localization (XL) efficiency

To investigate how the crown-to-core exciton localization efficiency depends on the crown size, we measured the photoluminescence excitation spectra (PLE, monitoring emission at 514 nm) of CC1-CC5. The PLE and absorbance (percentage of absorbed photons: $1 - 10^{-\text{Absorbance}}$) spectra of CC5 NSs are compared in Figure 3.3a and the comparisons of CC1 to CC4 are showed in Appendix 3.4. The absorbance of the sample was obtained from the extinction spectra after correcting for Rayleigh Scattering of the NSs. We have approximately accounted for scattering contribution by a λ^4 dependence with a proportionality constant determined by the amplitude of the extinction spectra at >520 nm when only scattering contributes. Because scattering cross section also depends on the wavelength dependent dielectric constant, it may deviate from of λ^4 dependence assumed in our analysis. To evaluate the errors introduced by this approximation, we have also measured, using the same procedure, the exciton localization efficiency of CdSe NSs (without the crown) in which the localization efficiency is expected to be 100%, independent of the excitation wavelength. As shown in Appendix 3.4, Figure 3.12a, the PLE and absorbance of this sample agree with each other from 520 to 370 nm as expected, giving rise to an average localization efficiency of 100.5 (± 2.2)%. This result supports the validity of the approximate procedure described above and suggests an estimated error of less than 2.2%.

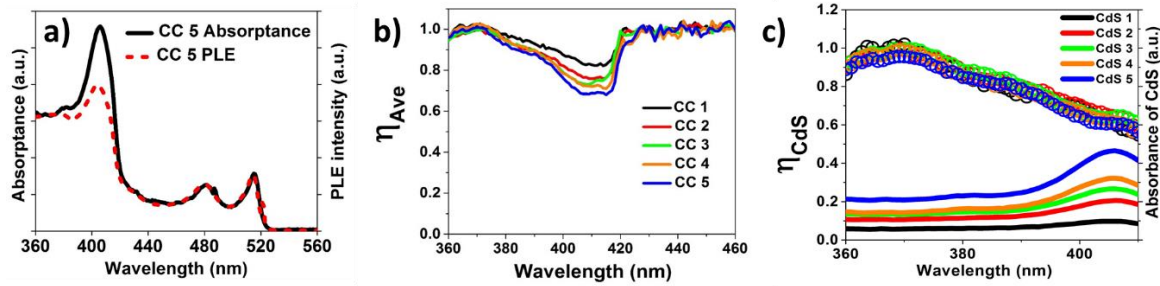


Figure 3.3. PLE spectra and crown-to-core exciton localization efficiencies (a) Absorbance (black solid lines) and PLE spectra (red dashed lines) of CC5. All spectra have been scaled to the same height at 515 nm. (b) The average exciton localization efficiency (η_{ave}) of CC1 to CC5. (c) Crown-to-core exciton localization efficiency (η_{CdS} , circles) and the normalized absorption spectra (solid lines) of CdS crowns in CC1 to CC5. The latter was obtained by normalizing the absorption spectra of CdSe/CdS to the same CdSe peak amplitude at 512 nm and subtracting the contribution of CdSe.

The ratio of the PLE and absorbance reflects the relative exciton localization efficiency as a function of wavelength. In calculating the ratio, we have also scaled the PLE spectra to the same value as the absorbance spectra at the lowest energy exciton band of the CdSe NS of all samples, which is equivalent to setting the relative localization efficiency to 1 for excitation at the band edge of CdSe (Figure 3.3b). The normalized PLE spectra, $PLE(\lambda)_{nor}$, can be represented by:

$$PLE(\lambda)_{nor} = \frac{PLE(\lambda)}{C \cdot \phi_{CdSe}(\lambda)} = A_{CdS}(\lambda) \cdot \eta_{CdS}(\lambda) + A_{CdSe}(\lambda) \cdot \eta_{CdSe}(\lambda) \quad (3.1)$$

where λ is the wavelength, $PLE(\lambda)$ the PLE intensity, ϕ_{CdSe} the PL quantum yield of CdSe core and C an instrument specific calibration factor, and η_{CdS} the CdS-to-CdSe exciton localization (XL) efficiency. We have assumed that $\eta_{CdSe}(\lambda) = 1$ as all excitons generated in

CdSe remains inside the core due to the type I band alignment. The percentage of absorbed photons (absorptance) by CdS ($A_{\text{CdS}}(\lambda)$) and CdSe ($A_{\text{CdSe}}(\lambda)$) is given by:

$$A_i(\lambda) = \frac{OD_i(\lambda)}{OD_{\text{CdS}}(\lambda) + OD_{\text{CdSe}}(\lambda)} \left(1 - 10^{-[OD_{\text{CdS}}(\lambda) + OD_{\text{CdSe}}(\lambda)]}\right) \quad (3.2)$$

where $i = \text{CdS}$ or CdSe , and OD is the optical density. The ratio of normalized PLE and absorptance is the absorptance weighted average exciton localization efficiency, η_{ave} , given by:

$$\eta_{\text{ave}}(\lambda) = \frac{\text{PLE}(\lambda)_{\text{nor}}}{A_{\text{CdS}}(\lambda) + A_{\text{CdSe}}(\lambda)} = \frac{A_{\text{CdS}}(\lambda) \cdot \eta_{\text{CdS}}(\lambda) + A_{\text{CdSe}}(\lambda) \cdot \eta_{\text{CdSe}}(\lambda)}{A_{\text{CdS}}(\lambda) + A_{\text{CdSe}}(\lambda)} \quad (3.3)$$

As shown in Figure 3.3b, at wavelength longer than 430 nm, where only CdSe contributed to the absorption (see Figure 3.3c), the measured average localization efficiency was one, consistent the assumption that all excitons generated at CdSe core remains in the core. At < 430 nm, average exciton localization efficiency decreased abruptly at the onset of CdS absorption and increased at shorter wavelength. Using the known absorptances of CdSe and CdS, the measured average exciton localization efficiency was fit to obtain η_{CdS} , which was plotted as a function of excitation wavelength in Figure 3.3c. Surprisingly, the crown-to-core localization efficiency was independent of the crown size, but increased with excitation photon energy (from 0.56 ± 0.04) at 415 nm to near unity (1.00 ± 0.02) at 370 nm. Although the localization efficiency appeared to decrease again at wavelengths shorter than 365 nm, a clear trend at shorter wavelength was not established due to limited spectral range of the measurement.

In the above analysis, we have assumed that $\eta_{\text{CdSe}}(\lambda) = 1$, i.e. all excitons generated in CdSe remain inside the core due to the type I band alignment. This assumption is supported by three experimental evidences. First as shown in Figure 3.3b, the exciton localization efficiency

is one from 520 to 430 nm (before the onset CdS absorption), independent of excitation energy. Second, as shown in Appendix 3.4, Figure 3.12a, for free CdSe NSs, the absorbance and PLE spectra agree with each other from 520 to 360 nm, suggesting that the efficiency of band edge exciton formation is independent of excitation energy in free CdSe NSs. Third, in CdSe/CdS CC NSs, at excitation energy above the CdS bandgap, some of the carriers generated in CdSe core can also move to CdS crown, in competition to relaxing to CdSe band edge, to lower $\eta_{\text{CdSe}}(\lambda)$. However, as shown in Figure 3.3b, from 420 to 370 nm, with increasing excitation photon energy, the apparent localization efficiency increases (approaching 1 at 370 nm), suggesting the above effect is negligible. This effect is likely negligibly small because only VB holes in the CdSe domain with energy above the CdS band edge can move into CdS due to the large VB offset. This represents a small fraction of carriers because most of the excess energy (above the band edge) of the initial excitation goes to the CB electron because of its ~ 3.5 smaller effective mass compared to VB hole.^{62, 116-117}

3.2.4. Size dependent crown-to-core exciton localization dynamics

To understand the origin of the crown size independent exciton localization efficiency in CdSe/CdS core/crown structures, we carried out ultrafast TA spectroscopy studies to directly follow the localization dynamics of photogenerated electrons from the CdS crown to CdSe core. Take CC5 as an example, TA spectra of CC5 at 400 nm excitation are shown in Figure 3.4a. These spectra showed time dependent bleaches of the CdSe exciton bands at ~ 513 nm (T1) and ~ 480 nm (T2) and CdS exciton band at ~ 410 nm (T3), which can be attributed to the state-filling of the lowest energy CB electron levels in CdS and CdSe domains, respectively.

T1 bleach results from both excitation of CdS (from which electron/excitons are transferred to CdSe) and direct excitation of CdSe. The contribution of the latter was subtracted from the total T1 bleach signal to obtain the kinetics of the former signal. The subtracted kinetics was further normalized by the amount of absorbed photons by CdS to yield normalized and subtracted T1 bleach kinetics (T1S) that corresponded to the same number of absorbed photons by CdS in CC1-CC5 (Figure 3.4c). The same normalization procedure was used to scale the T3 bleach kinetics (Figure 3.4b), which results only from the excitation of the CdS domain. These TA spectra and kinetics show that T3 bleach signals decay completely within 100 ps to give rise to a corresponding growth of the T1S bleach, suggesting that all CB electrons are transferred from CdS to CdSe. Because PLE measurements showed a CdS-to-CdSe XL efficiency of 0.70 ± 0.02 at 400 nm excitation, it suggests the remaining 30% of excitons also transfer electrons to CdSe with the hole located in CdS. The latter pathway may correspond to electrons ionized from trapped holes (referred to as XI in Figure 3.5b), driven by the CB offset.

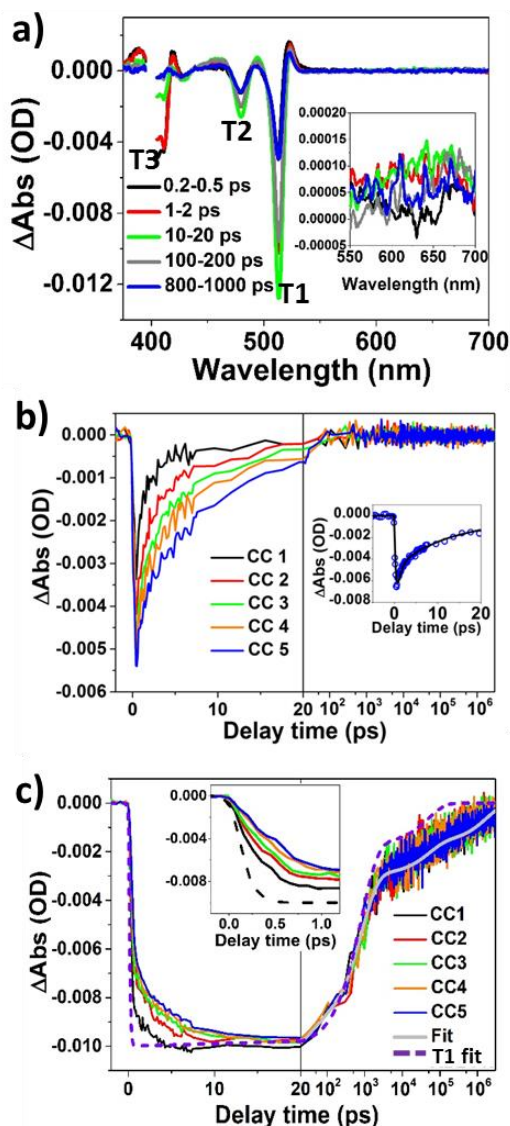


Figure 3.4. TA study of crown-to-core exciton localization dynamics (a) TA spectra of CC5 at indicated delay times after 400 nm excitation. (b) Normalized T3 bleach kinetics of CC1 to CC5 measured at 400 nm excitation. Inset showed the fit of T3 kinetics of CC5 (c) Subtracted T1 (T1S) bleach kinetics of CdSe of CC1 (black solid line), CC2 (red solid line), CC3 (green solid line), CC4 (orange solid line), CC5 (blue solid line) resulted from the excitation of CdS domain. These kinetics were obtained by subtracting the contribution of direct CdSe excitation from the total T1 bleach signal measured at 400 nm excitation (where both CdSe and CdS

domains absorbed), following the procedure discussed in the text. Also shown for comparison is the fit to the T1 (purple dashed line) of CC5 measured at 485 nm excitation along with the fits of the CC1-CC5 T1S decay process (gray solid line). The inset showed the same comparison in early time range (within 1 ps).

The T1S and T3 bleach kinetics can be fit to a model that accounts for both XL and XI pathways (Figure 3.5a&b). The total amplitudes of XL and XI are fixed at 70% and 30%, and the decay kinetics of exciton in CdSe generated by XL pathway is given by T1 kinetics measured by 485 nm excitation. The only fitting parameters are the time constants of exciton localization (τ_1) and exciton ionization and recombination. The best fits are shown in Figure 3.4b inset and Appendix 3.5, Figure 3.13 (showing individual kinetics and fits) and the fitting parameters are listed in Appendix 3.7, Table 3.3. Further details of the fitting model are described in Appendix 3.5.

The best fits of the data reveal a clear size-dependent XL process (0.31 to 0.65 ps from CC1 to CC5), which can be clearly seen in the inset of Figure 3.4c. Note that because the XL process occurs on a similar time scales as T3 bleach formation, the initial bleach amplitude decreases from CC5 to CC1 due to increasingly faster XL process (more missing amplitudes in the raw kinetics). Both the XL and XI components become slower in larger crowns, which can be clearly seen in the kinetics shown in Figure 3.4b&c. These decay kinetics can be fit with bi-exponential function. The fit also revealed an ionized electron recombination time constant of 1570 ± 240 ns that is independent of the crown size (Table 3.3 in Appendix 3.5). This time constant is considerably longer than that of e-h recombination time for excitons generated within CdSe, which is consistent with interfacial charge separation expected for this species.

3.2.5. Mechanisms of exciton transport and trapping

One of the most surprising findings of this work is that the crown-to-core XL process shows crown size-independent efficiencies and size-dependent rates. This suggests that branching between exciton transfer to the CdSe core and hole localization in the CdS crown is independent of the crown size. There are two possibilities for these branching pathways; the hole traps in CdS are located at both the core/crown interface and the CdS edges (the crown growth front), or at only the interface (see Figure 3.5a&b). In both cases, with increasing crown size, the diffusion time for excitons to reach the core/crown interface becomes longer, but the relative rates (and therefore the branching ratio) of exciton trapping at the interface and transfer to CdSe is independent to the crown size. Although the hole location wasn't directly probed spectroscopically, energetic considerations suggest that the trapped hole eventually locates at the CdSe/CdS interface. Because the estimated CB band offset and e-h binding energy are similar in magnitude (~ 100 meV),^{61, 146} the driving force for moving the electron to CdSe with the hole remaining in CdS is substantial only when the electron-hole Coulomb interaction can

be maintained in the ionized state. This is possible if the CB electron in the CdSe and trapped hole in CdS are localized at the core/crown interface (Figure 3.5b). Assuming similar densities of states and e-h Coulomb interactions for the electron in the CdSe or CdS domain (with the hole trapped at the interface), the Boltzmann distribution can be used to estimate the electron population ratio between the CB of CdSe (N_{CdSe}) and CdS (N_{CdS})

$$\frac{N_{\text{CdS}}}{N_{\text{CdSe}}} = e^{-\frac{\Delta E}{kT}} \quad (3.4)$$

where k is Boltzmann constant, T is the room temperature (300K), and ΔE is the CB band offset between CdSe and CdS (100 meV). The estimated ratio is 0.02, which indicates that most electrons are in CdSe and negligible electrons remain in CdS.

To provide further support for this model, we fit the size dependent TIS kinetics by solving the diffusion equation of excitons and carriers in CdSe/CdS core/crown structures. Because of the morphology of the nanosheets (with CdS crown extending linearly on the CdSe core mainly in one dimension), the exciton transport problem can be treated as effective one-dimensional exciton diffusion along the length direction. As shown in Figure 3.5c, we divided CdS crown into N segments ($N= 10, 11, 13, 14, 16$ for CC1 to CC5) of length of ΔL . We set the segment length to the 2D exciton radius (a_{2D}), $\Delta L= a_{2D} = a_0/4 = 1.32$ nm, where a_0 is the Bohr radius of the bulk CdS crystals.¹⁵³⁻¹⁵⁴ We assume exciton transport rate between CdS segments of k_X , interfacial exciton trapping rate of k_t , interfacial CdS to CdSe exciton transport rate of k_L . We further assume that trap excitons can be ionized thermally with rate constant of k_I and half of the ionized electrons are transferred to CdSe instantaneously. The other half of the electrons diffuse in CdS conduction band with rate constant of k_e and recaptured by the trapped hole with rate constant k_B . The ratio of the electron and exciton transport rates is constrained to the ratio of their bulk diffusion constants. With these parameters, the rate equations governing the exciton and electron kinetics can be solved numerically to yield the population kinetics of electrons in CdSe, which, with proper convolutions of the instrument response function, can

be used to fit the TIS kinetics. Further details of the calculation are provided in Appendix 3.6. As shown in Figure 3.6, this model provides an excellent fit to the data and the fitting parameters and error bars are listed in Table 3.4 in Appendix 3.6. The fit result yields an exciton diffusion constant (D_X) of 2.2 ± 0.2 cm²/s in CdS crown. This value is similar to the diffusion constant of CdS nanorods (2.3 cm²/s) and smaller than bulk CdS single crystals (3.2 cm²/s), likely due to surface scattering in these nanocrystals.^{62, 70}

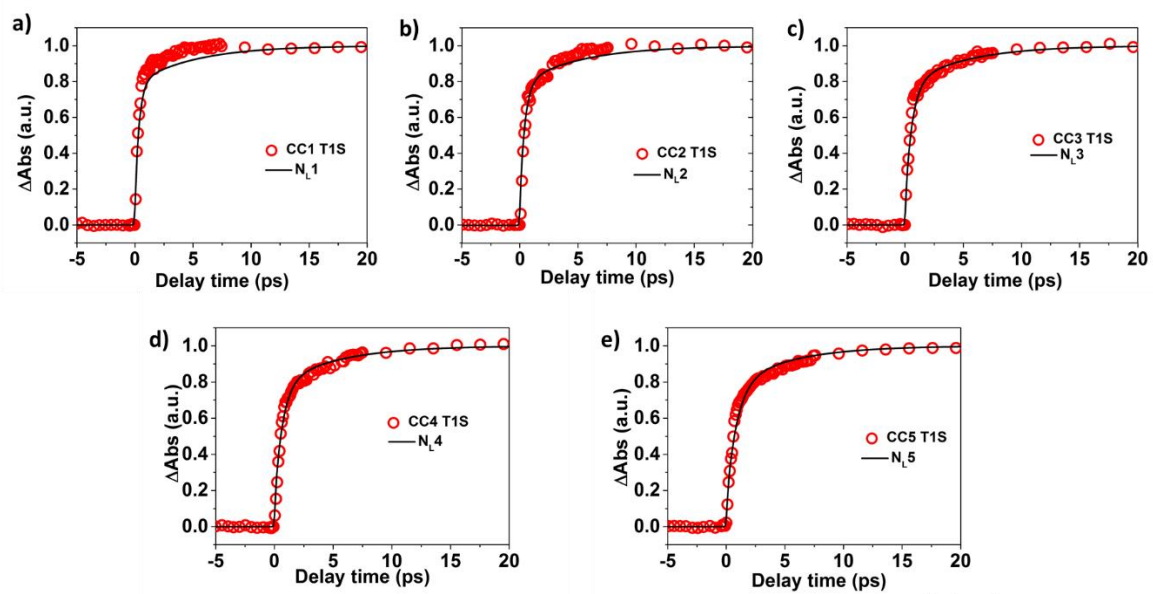


Figure 3.6. TIS kinetics at 400 nm excitation of CC1 to CC5 and the fit using $N_L(t)$ convoluted with IRF

To account for the excitation energy dependent localization efficiency shown in Figure 3.3c. we add an excitation energy dependent hot exciton channel into the diffusion model discussed above. We assume that with increasing excess energy, the hot exciton relaxes more slowly to the cold exciton state (with rate constant k_r), has a larger diffusion constant (k_h) in CdS (than the cold exciton, k_c), and has a faster localization rate constant into CdSe (k_{L1}) at the CdSe/CdS interface than the cold exciton (k_{L2}). The rate of hot exciton trapping at the interface

is assumed to be the same as cold excitons. The rates of cold exciton trapping, localization, diffusion have already been determined in the simulation above and are kept being the same. The diffusion equations of excitons can be solved with the same method described above. Further details can be found in Appendix 3.6. With these assumptions, we show that with increasing excess energy of the initially generated excitons, the exciton localization efficiency increases, and the exciton localization rate becomes faster (Figure 3.7a and Table 3.5 in Appendix 3.6). The former prediction is consistent with the results shown in Figure 3.3c. Unfortunately, the prediction of faster exciton localization rates at higher excitation energy cannot be easily verified for the current system due to limited tunability of our TA setup. The excitation energy dependence of exciton localization rate and efficiency is a direct consequence of the assumption of increased hot exciton diffusion constant and slower relaxation rate at higher excess energy. Support for the latter assumption was provided by excitation energy dependent hot exciton relaxation rates in CdSe NSs. As shown in Figure 3.7b and Table 3.6, the formation of band edge exciton becomes slower with increasing excitation energy above the band edge.

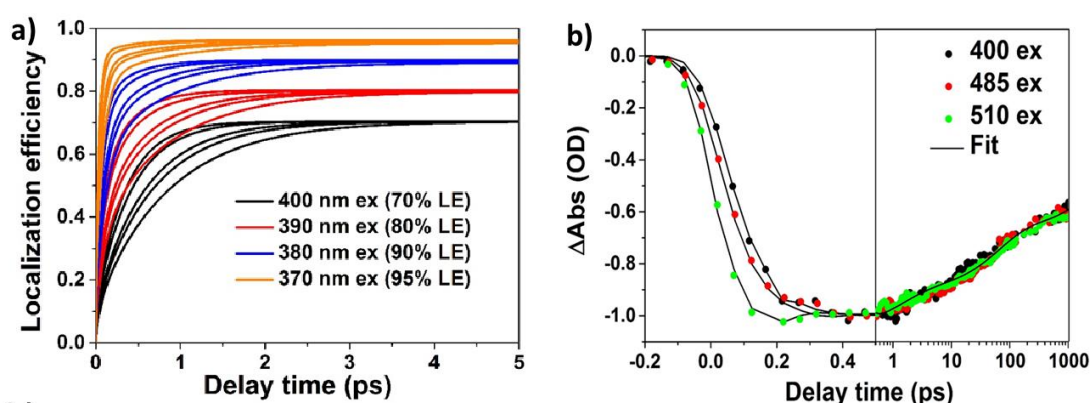


Figure 3.7. (a) Exciton localization dynamics for CC1 to CC5 at different excitation wavelength. Localization efficiency and rate increases at large excitation energy. (b) The T1 bleach formation kinetics of free CdSe NSs at 400 nm (black dots), 485 nm (red dots), and 510

nm (green dots) excitation. Solid lines are fits with parameters listed in Table 3.6 in Appendix 3.6.

This result suggests that exciton localization can be described by diffusion motion. Such diffusive behavior can be expected since the NS size is much larger than the upper limit of mean free path of electrons (4 nm) and holes (1.6 nm) in bulk CdS single crystals.⁷⁰ In a previous study of related CdSe NSs of 42.0 by 11.2 nm in size (similar to CC5 in this study),²⁶ bi-molecular Auger recombination process is shown to be not-diffusion limited. It was proposed that the exciton center-of mass wave function can delocalize over the entire NS. Our result suggests that exciton wave function does not delocalize throughout the whole sheet and their motion is diffusive. It is therefore likely that the Auger recombination rate is not limited by diffusion encounter of excitons (which occurs on the sub-picosecond time scale). Instead, it is limited by the Auger transitions within the encountered exciton pair.

It is interesting to compare the exciton localization processes in the CdSe/CdS core/crown NSs and CdSe/CdS dot-in-rod nanorods.^{70, 140-141} Our recent studies of CdSe/CdS nanorods⁷⁰ show that exciton localization efficiencies decrease with increasing rod length and there remain a long lived CB electron population in the CdS rod. CdSe/CdS nanorods have a wurtzite structure with exposed Cd and S atoms on the surface. Because these surface S atoms, likely the hole traps in CdS,^{63, 103, 140} are distributed along the rod, far away from the CdSe/CdS interface, it is energetically unfavorable to transfer the electron to the CdSe core (without moving the hole with it). CdSe/CdS NSs have zinc blend structures with only Cd atoms on both the highly exposed (001) basal plane. It is likely that the defects exist mainly at the edge of the NSs or at the core/crown interface due to the lattice mismatch.¹⁰⁸ Compared to CdSe/CdS nanorods, the core/crown structure can achieve high exciton localization efficiency with larger crown/core volume ratio, a property that is advantageous for solar concentrator applications.

^{130, 133, 135} Our study suggests that interfacial lattice mismatch is likely the origin of hole trap. Therefore, it may be possible to remove these defects in alloyed CdSe/CdS CC NSs to achieve higher XL efficiency across a broader spectral window, similar to recent demonstration of alloyed CdSe/CdTe core/crown structures.¹⁵⁵ In the previous study of single CdSe/CdS dot-in-rods at 4K, the exciton localization efficiency was shown to be independent of excitation photon energy. It was argued that there likely exists a barrier for carrier transport at the CdSe/CdS interface due to lattice mismatch and the lack of excitation energy dependence indicates that barrier crossing occurs after thermal relaxation of the carriers in those nanocrystals.¹⁵⁶ This differs from the excitation energy dependent exciton localization efficiency in our CdSe/CdS CC NSs, although the origin of the difference is not clear. Our result suggests that at room temperature, the interfacial barrier is smaller and barrier crossing process is faster, competing effectively with hot exciton relaxation.

3.3. Conclusion

Exciton dynamics in CdSe/CdS core/crown NS heterostructures has been investigated in an effort to understand exciton transport properties in these 2D quantum well materials with atomically precise thickness. PL and transient absorption studies show that these NSs have a type I band alignment between the CdSe core and CdS crown, with lowest energy excitons localized in the CdSe core. PLE measurements revealed that the crown-to-core exciton localization efficiency is independent of the CdS crown size (~70% at 400 nm excitation) but increases at higher excitation energy (approach 100% at 370 nm). TA studies suggest that 70% of the excitons generated at the CdS crown (with 400 nm excitation) undergo ultrafast (< 1ps) exciton localization to CdSe crown (driven by the type I band alignment and large valence band offset) and the remaining 30% have holes trapped at the core/crown interface and electrons transferred to CdSe (driven by the CB offset). The exciton localization time increases with

crowns size and can be described by an effective 1D exciton diffusion. Numerical solution of the exciton diffusion model shows that the crown size independent localization efficiency can be attributed to selective trapping of holes at the CdSe/CdS interface, which leads to a crown size independent branching ratio of exciton localization and hole trapping pathways. This model also suggests that the excitation wavelength dependent excitation localization efficiency can be accounted for by including hot excitons with larger diffusion constants. Our finding suggests that these nanosheet heterostructures are promising materials for solar concentrator applications and identifies pathways for further improving their properties.

Appendix 3.1

TEM images and the dimensional analysis of CC NSs

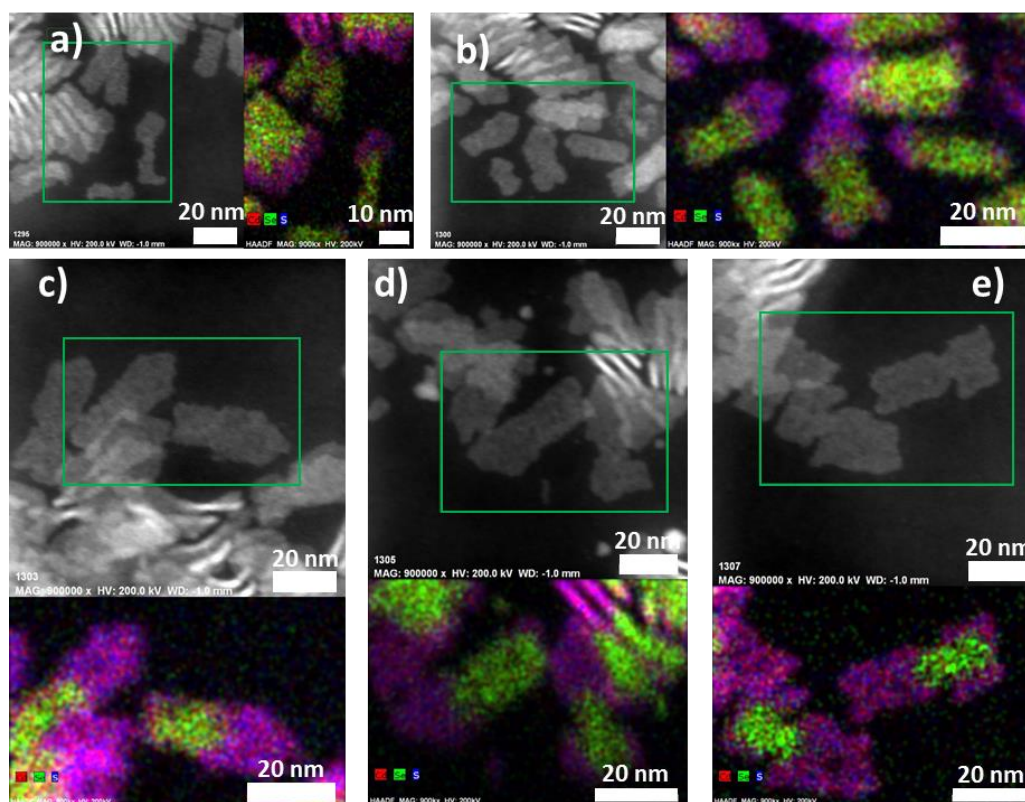


Figure 3.8. The HAADF scanning TEM images and EDX images in the green selected area of (a) CC1, (b) CC2, (c) CC3, (d) CC4, (e) CC5.

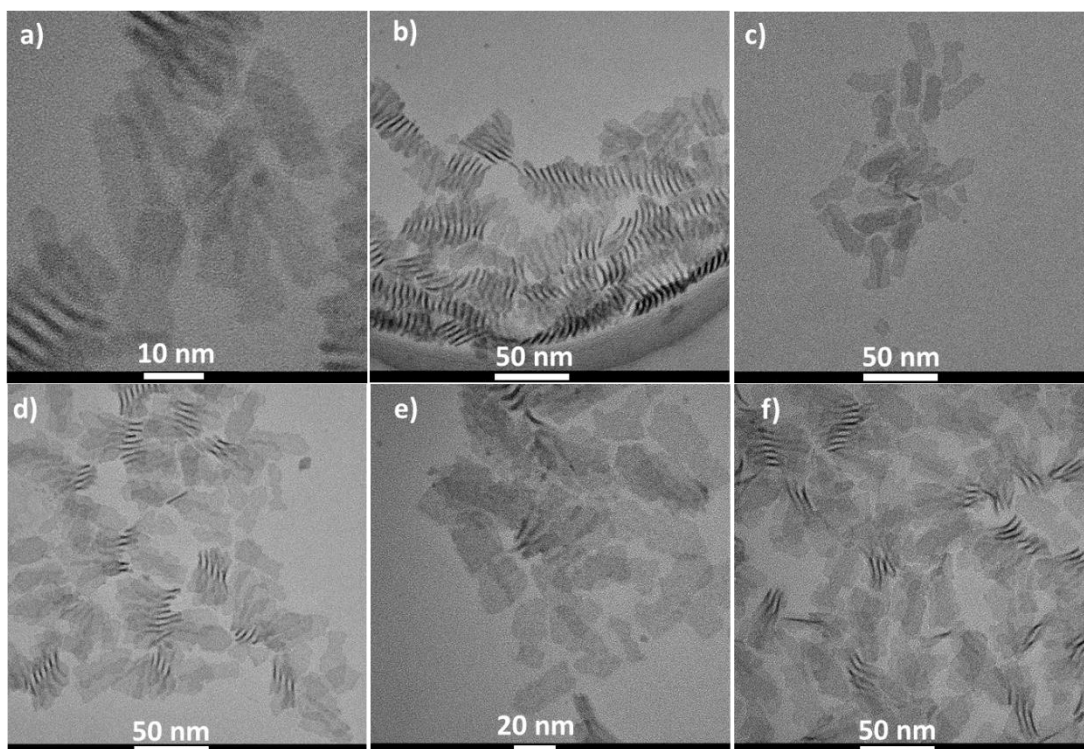


Figure 3.9. TEM images of (a) CdSe core, (b) CC1, (c) CC2, (d) CC3, (e) CC4, (f) CC5.

Table 3.1. The length, width, and crown length with errors of CdSe core and CC NSs

	Count	Length/nm	Width/nm	Crown length(L)/nm
CdSe	25	21.2 ± 2.1	11.1 ± 2.2	—
CC1	50	33.9 ± 1.4	10.1 ± 1.2	12.7 ± 1.3
CC2	30	35.6 ± 2.0	11.2 ± 1.1	14.4 ± 1.5
CC3	40	38.3 ± 3.6	11.3 ± 2.0	17.1 ± 2.5
CC4	25	39.7 ± 5.6	11.7 ± 1.8	18.5 ± 3.2
CC5	40	42.0 ± 3.2	13.7 ± 1.4	20.8 ± 2.3

Appendix 3.2.

The CdSe/CdS CC NSs band edge position estimation

The CB (VB) band edge position of bulk CdSe and CdS are -4.0 eV (-5.7 eV) and -3.7 eV (-6.2 eV), respectively.^{79, 111, 156} In two dimensional NSs, if we only consider the effect of quantum confinement, the band gap would shift according to the following equation:¹⁴⁴

$$E_{\text{exciton}} = E_g + (E_{k(h)} + E_{k(e)}) \quad (3.5)$$

where E_g is the band gap in bulk materials (1.7 eV for CdSe and 2.5 eV for CdS),^{111, 157-158} $E_{k(e)}$ and $E_{k(h)}$ are quantum confinement energy of the conduction band (CB) and valence band (VB) conduction band electron and valence band holes, respectively. We consider the electron and hole can move freely in x, y direction but confined in z direction within a well of thickness L: $V(z) = 0$ in the region $0 < z < L$, $V = \infty$ elsewhere. So the kinetics energy of the particles inside this well is:

$$E_k = \frac{h^2 n^2}{8m^* L^2} \quad (3.6)$$

where m^* is the effective mass of electron or hole. The ratio of confinement energies in CB and VB are $1/m_e^*$ to $1/m_h^*$.

$$\frac{E_{k(e)}}{E_{k(h)}} = \frac{m_h^*}{m_e^*} \quad (3.7)$$

We determined E_{exciton} from the lowest energy absorption peak of NSs in the UV/VIS absorption spectra: 2.4 eV for CdSe NSs and 3.0 eV for CdS NSs. The calculated CB (VB) edge positions are \sim -3.4 eV (-5.8 eV) and -3.3 eV (-6.3 eV) for CdSe and CdS, respectively.

Appendix 3.3.

485 nm excitation T1 bleach kinetics fitting

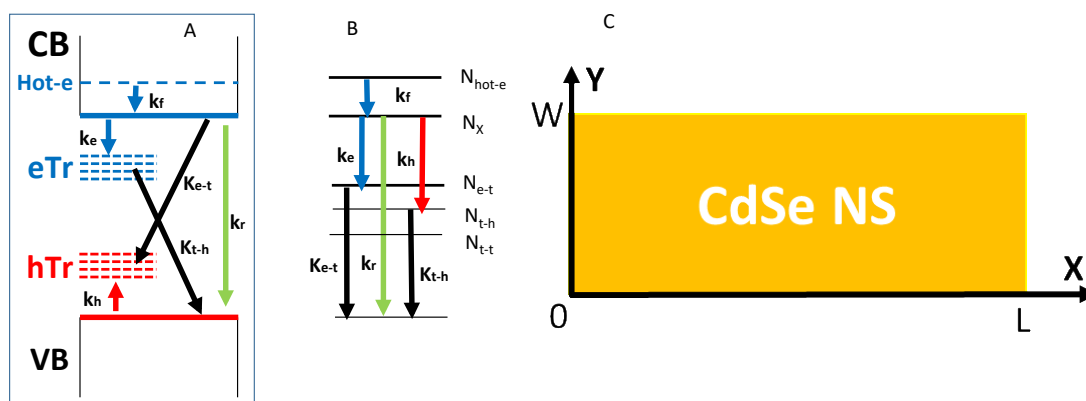


Figure 3.10. Carrier decay pathways in CC NSs at 485 nm excitation: (A) single particle (electron and hole) representation, (B) state representation. See the text for the notations of various states and carrier trapping and decay process. (C) Morphology and coordinate system of CdSe NS core. The surrounding CdS crown is not depicted because there is not net carrier transport from CdSe core to CdS crown at 485 nm excitation.

At 485 nm excitation, only CdSe core was excited and because of the type I band alignment between CdSe and CdS, the carriers remain in CdSe. This is confirmed by the transient spectra shown in Figure 3.2b. The carriers in CdSe core undergo diffusion in a rectangular NS with length L and width W (Figure 3.10c), as well as various relaxation, trapping and/ recombination processes (Figure 3.10a). Because of strong electron-hole interaction in NSs, the carriers diffuse as a bound pair after its initial formation. Furthermore, because the TA signals at T1 peak of CC NSs are dominated by the concentrations of electrons at the CB edge, we only need to consider three species that affect its concentration: hot-electrons (N_{hot-e}), band edge excitons (N_X , with both electron and hole in the band edge), and trapped exciton (N_{eo} , band-edge electron and a trapped hole). Hot-electrons (N_{hot-e}) represents initially excited carriers that decay to form

band-edge exciton with a rate constant of k_f . The band-edge excitons can decay through radiative recombination with a rate constant k_r or via electron trapping with a rate constant k_e , (to form trapped exciton N_{t-h}) and hole trapping with a rate constant of k_h (to form trapped excitons N_{e-t}). The trapped excitons can decay by electron trapping (k_e) and radiative and nonradiative recombination (k_{e-t}). The spatial distribution of these species is governed by the following rate equations:

$$\frac{dN_{\text{hot-e}}(x, y, t)}{dt} = D_{\text{hot-e}} \left(\frac{\partial^2 N_{\text{hot-e}}}{\partial x^2} + \frac{\partial^2 N_{\text{hot-e}}}{\partial y^2} \right) - k_f N_{\text{Hot-e}} \quad (3.8)$$

$$\frac{dN_X(x, y, t)}{dt} = D_X \left(\frac{\partial^2 N_X}{\partial x^2} + \frac{\partial^2 N_X}{\partial y^2} \right) + k_f N_{\text{Hot-e}} - (k_r + k_e + k_h) N_X \quad (3.9)$$

$$\frac{dN_{e-t}(x, y, t)}{dt} = D_{e-t} \left(\frac{\partial^2 N_{eoe-t}}{\partial x^2} + \frac{\partial^2 N_{e-t}}{\partial y^2} \right) + k_h N_X - (k_{e-t} + k_e) N_{e-t} \quad (3.10)$$

where D_i ($i=\text{Hot-e}, X, e$) are the diffusion constants of hot-electron, exciton, and band edge electron respectively. As discussed before, TA kinetics of T1 bleach represents the band edge electron decay. Hence, T1 signal is given by:

$$\Delta A(t) \propto - \left(\int_0^W \int_0^L [N_X(x, y, t) + N_{e-t}(x, y, t)] dx dy \right) \quad (3.11)$$

The rate equation 3.8 to 3.10 have a general form as:

$$\frac{dN(x, y, t)}{dt} = D \left(\frac{\partial^2 N}{\partial x^2} + \frac{\partial^2 N}{\partial y^2} \right) - kN + \sum_i f_i(t) \quad (3.12)$$

This differential equation can be solved by Variable Separation Method by assuming:^{70, 159}

$$N(x, y, t) = X(x)Y(y)T(t) + \sum_i F_i(t) \quad (3.13)$$

The equation becomes:

$$\frac{dT(t)}{DT(t)dt} = \left(\frac{d^2 X(x)}{X(x)dx^2} + \frac{d^2 Y(y)}{Y(y)dy^2} \right) - \frac{k}{D} \quad \text{and} \quad \sum_i \frac{dF_i(t)}{dt} = \sum_i f_i(t) \quad (3.14)$$

Since there is no exciton diffuse outside the CdSe core, the flux crossing the core edge is 0, which gives boundary condition 1:

$$\frac{\partial N(0, y, t)}{\partial x} = \frac{\partial N(L, y, t)}{\partial x} = \frac{\partial N(x, 0, t)}{\partial y} = \frac{\partial N(x, W, t)}{\partial y} = 0 \quad (3.15)$$

which gives:

$$N(x, y, t) = e^{-\left(\frac{k}{D}\right)t} \sum_n B_n \cos\left(\frac{n\pi}{L}x\right) e^{-\left(\frac{n\pi^2}{L}\right)t} \sum_n B'_n \cos\left(\frac{n\pi}{L}y\right) e^{-\left(\frac{n\pi^2}{W}\right)t} + \sum_i F_i(t) \quad (3.16)$$

where n are Integers. Due to the randomly photo-generated excitons in CdS crown, we also have boundary condition 2:

$$N(x, y, t = 0) = \text{Constant} \quad (3.17)$$

which requires:

$$B_n = \frac{1}{L} \int_0^L C_1 \cos\left(\frac{n\pi}{L}x\right) dx = 0 \quad \text{and} \quad B'_n = \frac{1}{W} \int_0^W C_2 \cos\left(\frac{n\pi}{W}y\right) dy = 0 \quad (3.18)$$

where C_1 and C_2 are constants. Therefore, boundary condition 2 requires $X(x)$ and $Y(y)$ are all constants, meaning when the electron cannot diffuse outside CdSe core, the diffusion process won't change the total concentration of charges. The rate equation 3.8 to 3.10 then become:

$$\frac{dN_{\text{hot-e}}(t)}{dt} = -k_f N_{\text{Hot-e}} \quad (3.19)$$

$$\frac{dN_X(t)}{dt} = k_f N_{\text{Hot-e}} - (k_r + k_e + k_h) N_X \quad (3.20)$$

$$\frac{dN_{e-t}(t)}{dt} = k_h N_X - (k_{e-t} + k_e) N_{e-t} \quad (3.21)$$

The solution of rate equations 3.19 to 3.21 gives:

$$\begin{aligned} \Delta A(t) &\propto N_X(t) + N_{e-t}(t) \\ &\propto e^{-k_f t} - A_1 \frac{(k_{e-t} - k_r)(k_f - k_{nre-t} - k_e)(k_f - k_r - k_e - k_h)}{(k_{e-t} - k_r - k_h)k_f(k_{e-t} + k_e + k_h - k_f)} e^{-(k_r + k_e + k_h)t} \\ &\quad - A_2 \frac{(k_f - k_{e-t} - k_e)(k_f - k_r - k_e - k_h)}{k_f(k_{e-t} + k_e + k_h - k_f)} e^{-(k_{e-t} + k_e)t} \quad (3.22) \end{aligned}$$

where A_1 and A_2 are constants that satisfy:

$$A_1 \frac{k_{e-t} - k_r}{k_{e-t} - k_r - k_h} + A_2 = \frac{k_f(k_{e-t} + k_e + k_h - k_f)}{(k_f - k_{nr} - k_e)(k_f - k_r - k_e - k_h)} \quad (3.23)$$

This model shows that TA kinetics of CB edge electron can be effectively described by multi-exponential functions. The above model did not consider the distribution of trap states and initial hot carriers and the rate constants should be taken as average rate constants. Therefore, we fitted the T1 bleach formation and recovery at 485 nm excitation with three-exponential functions convoluted with instrument response function (IRF):

$$T1(485ex) = A_{T1} [e^{-\frac{t}{\tau_f}} - a_1 \cdot e^{-\frac{t}{\tau_{d1}}} - a_2 \cdot e^{-\frac{t}{\tau_{d2}}}] \otimes IRF \quad (3.24)$$

where τ_f is the formation time constant, a_i (τ_{di}) are exciton decay time constants. The IRF (~ 150 fs) is determined from the scattering signals of the solvent (hexane). All the fitting parameters are listed in Table 3.2.

Table 3.2. The fitting parameters and errors for T1 kinetics (485 nm excitation)

τ_f/ps	τ_{d1}/ns (a_1)	τ_{d2}/ns (a_2)
0.10 ± 0.02	0.83 ± 0.02 ($83.0 \pm 1.8\%$)	50.4 ± 4.4 ($17.0 \pm 1.9\%$)

Appendix 3.4

Comparison of the absorbance, PLE and extinction spectra of CdSe and CC NSs

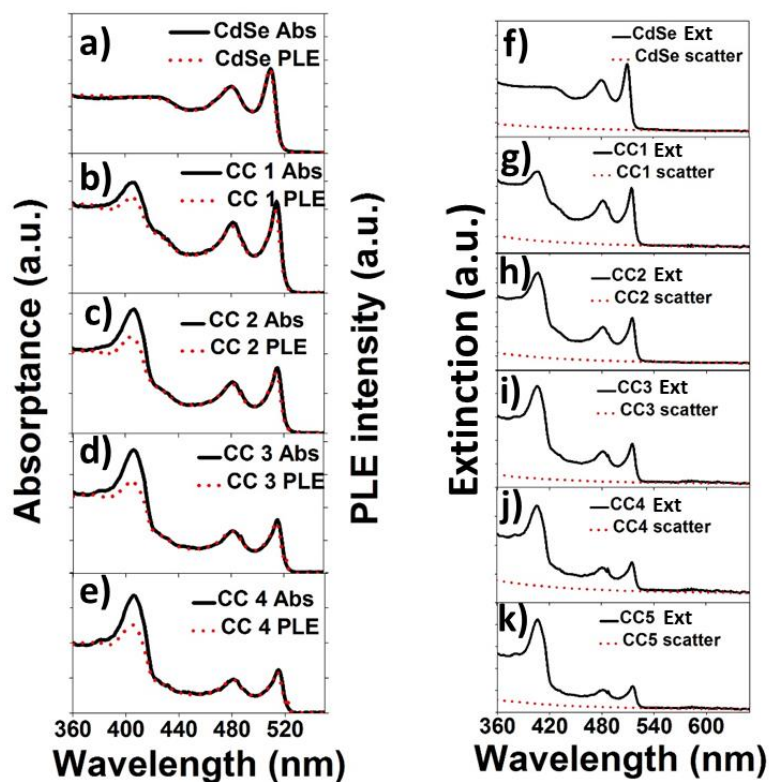


Figure 3.11. (a-e) Absorbance (black solid lines) and PLE spectra (red dashed lines) of CdSe NSs and CC1 to CC5. All spectra have been scaled to the same height at 515 nm. (f-k) Extinction and (estimated) scattering spectra of CdSe NS and CC1 to CC5.

Appendix 3.5

Kinetics of T1S and T3 bleach measured with 400 nm excitation.

In order to obtain T1S bleach kinetics, we have assumed the kinetics of direct CdSe excitation is the same as those measured with 485 nm excitation. The relative contributions of CdS crown and CdSe core to the total signal were determined from the absorption spectra of CC1-CC5 and the CdSe core-only NSs. T3 and T1S bleach kinetics of all samples were normalized by the absorbed photons by the CdS crowns at 400 nm excitation. The kinetics of T3 and T1S bleach of CC NSs were fit by the following equations:

$$T3 = A_{\text{initial}} \left[e^{-\frac{t}{\tau_{T3}}} - a_{\text{XL}} \cdot e^{-\frac{t}{\tau_1}} - a_{\text{XI},1} \cdot e^{-\frac{t}{\tau_2}} - a_{\text{XI},2} \cdot e^{-\frac{t}{\tau_3}} \right] \otimes \text{IRF} \quad (3.25)$$

$$T1S = A_{\text{max}} \left[(a_{\text{XL}} \cdot e^{-\frac{t}{\tau_f}} - b_1 \cdot e^{-\frac{t}{\tau_{d1}}} - b_2 \cdot e^{-\frac{t}{\tau_{d2}}}) + (a_{\text{XI},1} \cdot e^{-\frac{t}{\tau_2}} + a_{\text{XI},2} \cdot e^{-\frac{t}{\tau_3}} - b_r \cdot e^{-\frac{t}{\tau_r}}) \right] \otimes \text{IRF} \quad (3.26)$$

where τ_1 is the exciton localization (XL) time; τ_2, τ_3 are two components of exciton ionization (XI) process. τ_{T3} is the CdS T3 formation time constant, which is the same as the T3 bleach formation time constant of free CdS NSs, as shown in Table S3. The amplitudes a_{XL} and a_{XI} are constrained by the PLE result:

$$a_{\text{XL}} = 0.7, a_{\text{XI},1} + a_{\text{XI},2} = 0.3 \quad (3.27)$$

b_1 (τ_{d1}) and b_2 (τ_{d2}) are amplitude (time constants) of CdSe exciton decay (created by the XL process), which is the same as the XB bleach decay kinetics measured at 485 nm excitation (Table 3.2). b_r (τ_r) is the amplitude (recombination time constant) of the charge separated state (generated by XI process). The amplitude of XL and XI components are given by:

$$b_1 + b_2 = 0.7, b_r = 0.3 \quad (3.28)$$

and

$$b_1 = 0.58, b_2 = 0.12 \quad (3.29)$$

The T3 and T1S kinetics were fitted at the same time. All the fitting parameters and errors are listed in Table 3.3. The fitting results of T3 and T1S bleaches of CC1 to CC5 are plotted in Figure 3.12. The area weighted average lifetime (τ_{ave}) of XI process was calculated as:

$$\tau_{ave} = \frac{a_{XI,1}\tau_2^2 + a_{XI,2}\tau_3^2}{a_{XI,1}\tau_2 + a_{XI,2}\tau_3} \quad (3.30)$$

Table 3.3. Fitting parameters and errors for bleach kinetics

	CC1	CC2	CC3	CC4	CC5
τ_{T3}/ps	0.17±0.07	0.17±0.07	0.17±0.07	0.17±0.07	0.17±0.07
τ_1/ps (a_{XL})	0.31±0.03 (70.0±0.3%)	0.35±0.01 (70.0±0.7%)	0.42±0.03 (70.0±1.7%)	0.53±0.03 (70.0±1.0%)	0.65±0.04 (70.0±1.2%)
τ_2/ps ($a_{XI,1}$)	1.67±0.13 (25.6±0.1%)	3.57±0.23 (27.0±0.6%)	4.35±0.04 (26.0±0.7%)	5.63±0.31 (26.5±0.4%)	6.67±0.08 (25.0±2.0%)
τ_3/ps ($a_{XI,2}$)	16.3±3.2 (4.4±0.2%)	18.3±1.7 (3.0±0.3%)	33.0±5.2 (4.0±3.5%)	45.3±8.3 (3.5±1.0%)	55.8±7.5 (5.0±2.0%)
τ_{ave}/ps	7.68±2.09	8.91±1.01	19.8±3.5	26.1±4.1	37.4±5.2
τ_{d1}/ns (b_1)	0.83±0.02 (58.0±2.3%)	0.83±0.02 (58.0±2.3%)	0.83±0.02 (58.0±2.3%)	0.83±0.02 (58.0±2.3%)	0.83±0.02 (58.0±2.3%)
τ_{d2}/ns (b_2)	50.4±4.4 (12.0±0.8%)	50.4±4.4 (12.0±0.8%)	50.4±4.4 (12.0±0.8%)	50.4±4.4 (12.0±0.8%)	50.4±4.4 (12.0±0.8%)
τ_r/ns (b_r)	1570±240 (30.0±0.3%)	1570±240 (30.0±0.3%)	1570±240 (30.0±0.3%)	1570±240 (30.0±0.3%)	1570±240 (30.0±0.3%)

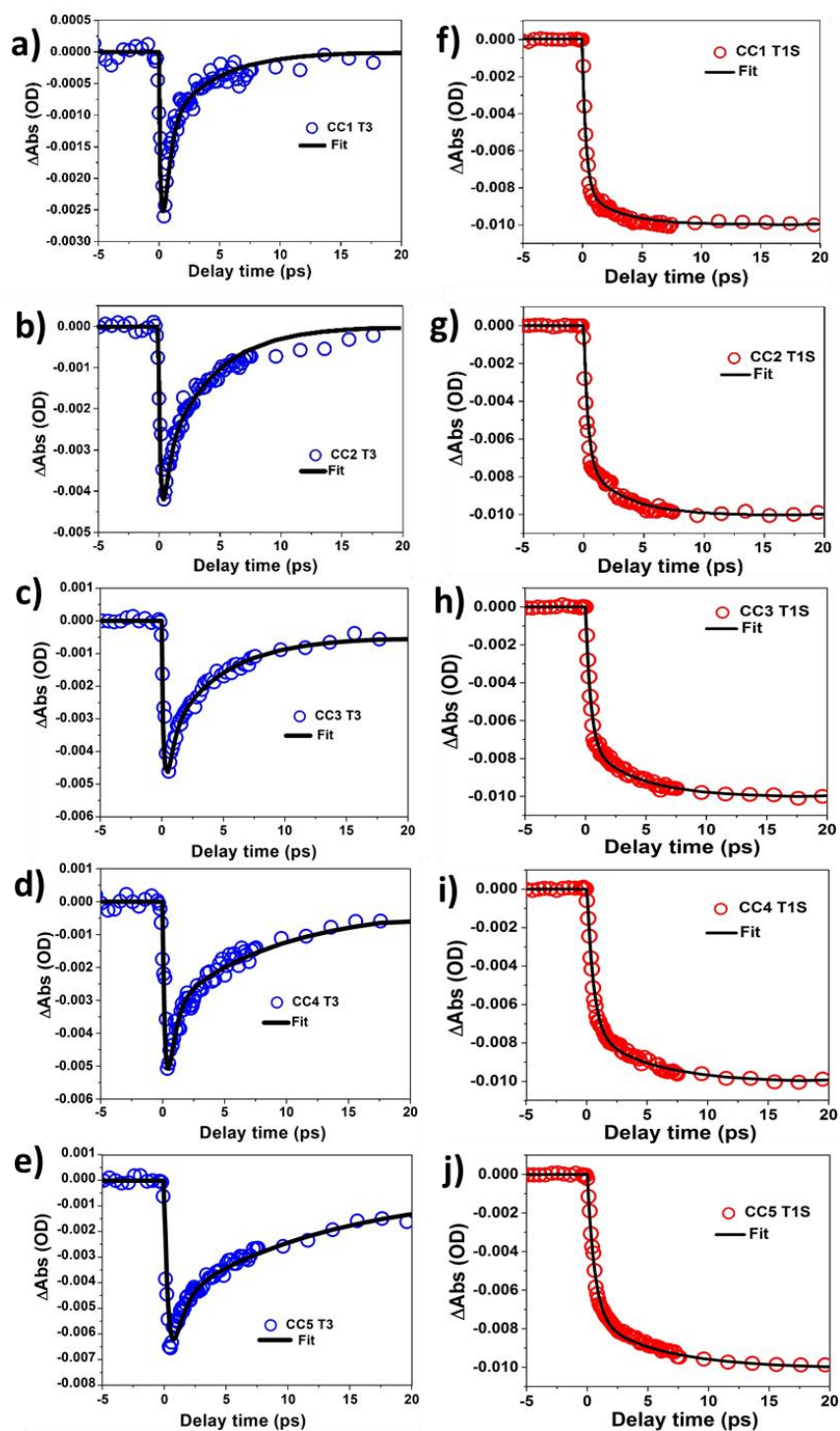


Figure 3.12. The T3 (a-e) and T1S (f-j) bleach kinetics and fittings of (a, f) CC1, (b, g) CC2, (c, h) CC3, (d, i) CC4, (e, j) CC5 within 20 ps.

Appendix 3.6

Diffusive exciton localization model

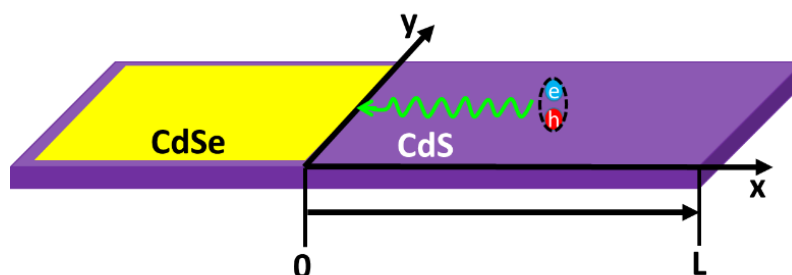


Figure 3.13. The schematic exciton in-plane diffusion model for CC NSs.

The size distribution obtained by TEM and EDX images showed the same width of all CC NSs with the CdS crown extending mainly along the length direction of CdSe core (+x direction in Figure 3.13). As shown in Figure 3.14, the crown length L (Table 3.1) depends linearly on crown absorbance at 410 nm (Figure 3.3c in the main text), consistent with morphology depicted in Figure 3.13. The fit is not perfect, which can be attributed to a small degree of growth of CdS crown along y-axis or along the $-x$ direction (Figure 3.13).

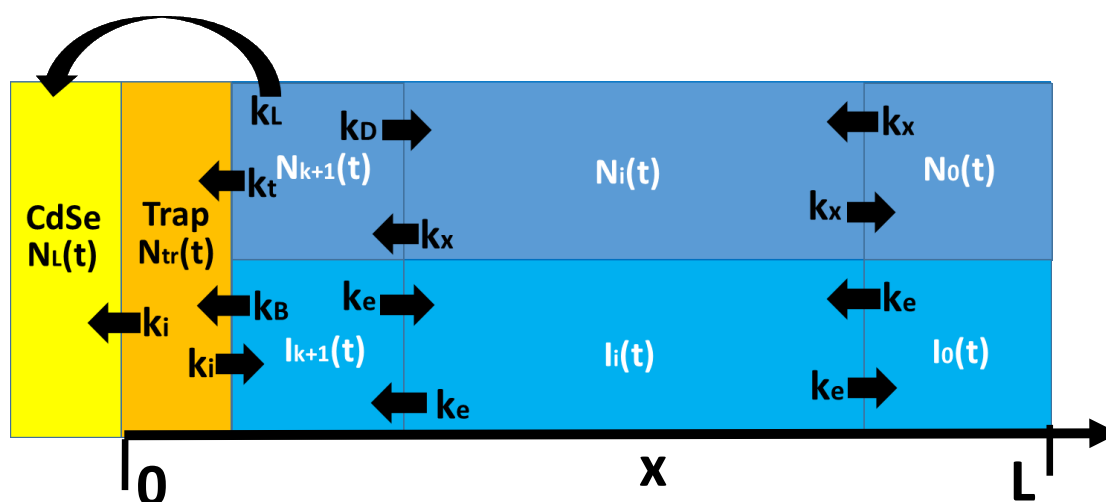


Figure 3.14. Schematic of CdSe/CdS CC core/crown structures used for solving the diffusion equations. Key carrier/exciton processes at different spatial region along x are indicated. Top half: exciton diffusion, interfacial transfer and trapping process. Bottom half: trapped exciton ionization, electron diffusion, and recapture processes.

The CdSe/CdS core crown can be divided into three areas: the CdS crown, CdSe core and the interface region where hole is trapped, as shown in Figure 3.14. The diffusion equations governing these regions are given below. We consider free excitons (with density N) in CdS with diffusion constant D_x . At the interface these excitons can either move into CdSe (with localization rate k_L) or trapped at the interface (k_t) to form trapped excitons (N_{tr}). The trapped excitons can ionize (with rate constant $2k_i$) to generate half of the electrons in the CdSe and the other half in CdS. The resulting electron in the CdS conduction band (with concentration of I_i) can diffuse within the CdS domain (with diffusion constant D_e) and be recaptured by the trapped hole at the interface (with rate constant k_B).

In CdS region, there exist free excitons and electron,

$$\frac{dN(x, t)}{dt} = D_x \frac{\partial^2 N}{\partial x^2} \quad (3.31)$$

$$\frac{dI(x, t)}{dt} = D_e \frac{\partial^2 I}{\partial x^2} \quad (3.32)$$

At the interface ($x=0$):

$$\frac{dN(x=0, t)}{dt} = D_x \frac{\partial^2 N}{\partial x^2} - k_t N - k_L N \quad (3.33)$$

$$\frac{dN_{tr}(t)}{dt} = k_t N(x=0, t) - 2k_i N_{tr} + k_B I(x=0, t) \quad (3.34)$$

$$\frac{dI(x=0, t)}{dt} = D_e \frac{\partial^2 I}{\partial x^2} + k_i N_{tr} - k_B I \quad (3.35)$$

In CdSe:

$$\frac{dN_L(t)}{dt} = k_i N_{tr} + k_L N \quad (3.36)$$

Those equations can be solved numerically by dividing the CdS sheet into small segments (Figure 3.5c) and making the following approximation for derivatives.

$$\begin{aligned} D \frac{\partial^2 N}{\partial x^2} &= D \lim_{\Delta L \rightarrow 0} \frac{\frac{N(x + \Delta L, t) - N(x, t)}{\Delta L} - \frac{N(x, t) - N(x - \Delta L, t)}{\Delta L}}{\Delta L} \\ &\cong D \frac{N(x + \Delta L, t) + N(x - \Delta L, t) - 2N(x, t)}{\Delta L^2} \quad (3.37) \end{aligned}$$

The CdS crown has been divided 10, 11, 13, 14, 16 equal segments for CC1 to CC5 respectively, with each part has length of ΔL . According to the 2D exciton size (a_{2D}), we set $\Delta L = a_{2D} = a_0/4 = 1.32$ nm, using 2D hydrogen model, where a_0 is the Bohr radius of the bulk CdS crystals.¹⁵³⁻¹⁵⁴ The exciton (ionized electron) density in each segment, N_k (I_k), is given by:

$$\frac{dN_0(t)}{dt} = k_X N_1(t) - k_X N_0(t) \quad (3.38)$$

$$\frac{dN_i(t)}{dt} = k_X (N_{i+1}(t) + N_{i-1}(t) - 2N_i(t)) \quad (i \text{ from } 1 \text{ to } k) \quad (3.39)$$

$$\frac{dN_{k+1}(t)}{dt} = k_X N_k(t) - (k_L + k_t + k_X) N_{k+1}(t) \quad (3.40)$$

$$\frac{dI_0(t)}{dt} = k_e I_1(t) - k_e I_0(t) \quad (3.41)$$

$$\frac{dI_i(t)}{dt} = k_e (I_{i+1}(t) + I_{i-1}(t) - 2I_i(t)) \quad (i \text{ from } 1 \text{ to } k) \quad (3.42)$$

$$\frac{dI_{k+1}(t)}{dt} = k_i N_{tr}(t) + k_e I_k(t) - (k_B + k_e) I_{k+1}(t) \quad (3.43)$$

$$\frac{dN_{tr}(t)}{dt} = k_t N_{k+1}(t) + k_B I_{k+1}(t) - 2k_i N_{tr}(t) \quad (3.44)$$

$$\frac{dN_L(t)}{dt} = k_L N_{k+1}(t) + k_i N_{tr}(t) \quad (3.45)$$

where $k_X = D_X/\Delta L^2$, $k_e = D_e/\Delta L^2$. We assume at $t = 0$, one exciton is generated randomly on the NS, meaning each part have the same exciton density $N_k(0) = 1/n$, where n is the number of the parts.

Solution of these equations lead to $N_L(t)$, the conduction band electrons in CdSe. To account for the limited instrument response of the measurement, the calculated $N_L(t)$ value is convoluted with IRF response function at 400 nm excitation according to Eq. 3.46.

$$T1S = N_L(t) \otimes \text{IRF} \quad (3.46)$$

The convoluted CdSe population kinetics was used to fit the rise kinetics of T1S exciton bleach of all CC NSs. The best fitting results are shown in Figure 3.14 and the fitting parameters and error bars are listed in Table 3.4. There are five independent fitting parameters. Because the diffusion constants are proportional to the mobility of charges, the ratio of D_X and D_e was constrained by the ratio of exciton and electron mobilities in the bulk.¹⁶⁰ The values of k_L and k_t determine the branching ratio between the exciton localization and trapping; The value of k_X and crown size L determined the size dependent exciton localization kinetics (i.e. the fast XL component in T1S formation). The value of k_i , k_e and k_B determines the slow XI component in T1S kinetics.

Table 3.4. The fitting parameters for T1S kinetics (400 nm excitation)

k_X/ps^{-1}	k_t/ps^{-1}	k_L/ps^{-1}	k_i/ps^{-1}	k_B/ps^{-1}	k_e/ps^{-1}
125 ± 25	25 ± 5	100 ± 20	0.2 ± 0.2	200 ± 20	413 ± 82

From the k_X and k_e values obtained from the fit, this relationship, $D_i = k_i \Delta L^2$ ($i = X$ or e), was used to calculate the diffusion constant of excitons ($D_X = 2.2 \pm 0.2 \text{ cm}^2/\text{s}$) and electrons (D_e of $7.3 \pm 0.6 \text{ cm}^2/\text{s}$). The diffusion constant of excitons in bulk CdS single crystals (D_{Bulk}) is:¹⁶⁰

$$D_{\text{bulk},X} = \frac{\mu_x kT}{e} \quad (3.47)$$

where k is Boltzmann constant, T is the room temperature as 300K. μ_x is the center-of-mass drift mobility of exciton, and it equals:

$$\mu_x = \frac{\mu_e m_e + \mu_h m_h}{m_e + m_h} \quad (3.48)$$

The $m_e = 0.21m_0$ ($m_h = 0.8m_0$) is the effective mass of electron (hole) in bulk CdS.¹¹⁶⁻¹¹⁷ μ_e (μ_h) is the mobility of electron (hole) in the bulk CdS and we have used the upper limits of reported values, 400 (48) $\text{cm}^2/(\text{Vs})$.^{70, 160-162} The calculated results for $D_{\text{Bulk},X}$ and $D_{\text{Bulk},e}$ are 3.2 cm^2/s and 10.5 cm^2/s , respectively, which is in reasonable agreement with the values for the CdS nanosheet determined from the fit.

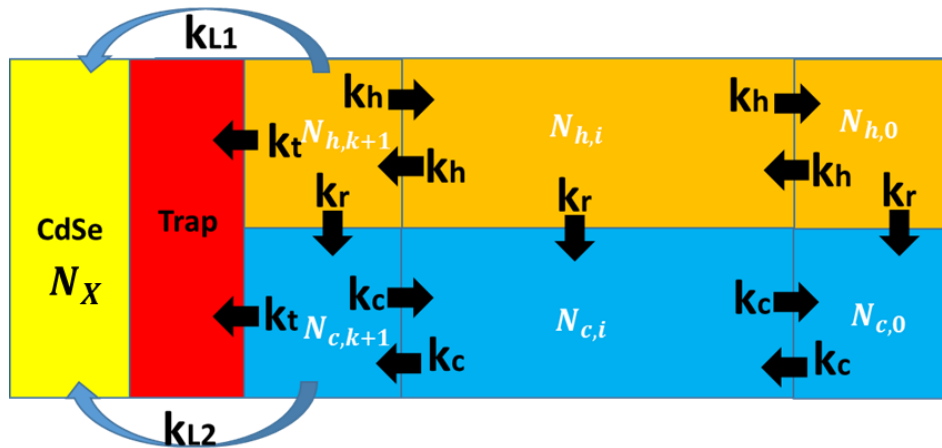


Figure 3.15. Schematic of solving hot exciton diffusion equations for CdSe/CdS CC structure.

To account for the excitation wavelength dependent exciton localization efficiency, we add in wavelength dependent hot exciton transport and relaxation into our diffusion model. As shown in Figure 3.15, similar to our last model in Figure 3.14, the hot excitons (N_h) are generated randomly in CdS crown after excitation. As shown in Eq. 3.49 and 3.50, they

simultaneously diffuse in the crown with a diffusion constant D_h and relax to cold exciton (N_c) with a relaxation rate constant k_r :

$$\frac{dN_h(x, t)}{dt} = D_h \frac{\partial^2 N_h}{\partial x^2} - k_r N_h \quad (3.49)$$

$$\frac{dN_c(x, t)}{dt} = D_c \frac{\partial^2 N_c}{\partial x^2} + k_r N_h \quad (3.50)$$

Cold excitons diffuse in crown with diffusion constant D_c . When move to the interface, both hot and cold exciton can either localize to CdSe core with localization rate (k_{L1} and k_{L2} for hot and cold exciton respectively) or get trapped with a rate constant k_t .

$$\frac{dN_h(x = 0, t)}{dt} = D_h \frac{\partial^2 N_h}{\partial x^2} - k_r N_h - k_t N_h - k_{L1} N_h \quad (3.51)$$

$$\frac{dN_c(x = 0, t)}{dt} = D_c \frac{\partial^2 N_c}{\partial x^2} + k_r N_h - k_t N_c - k_{L2} N_c \quad (3.52)$$

The localized excitons in CdSe (N_x):

$$\frac{dN_x(t)}{dt} = k_{L1} N_h + k_{L2} N_c \quad (3.53)$$

We solve these equations numerically using the same method described above, the hot and cold exciton density in each segment, $N_{h,i}$ ($I_{c,i}$), is given by:

$$\frac{dN_{h,0}(t)}{dt} = k_h N_{h,1}(t) - (k_h + k_r) N_0(t) \quad (3.54)$$

$$\frac{dN_{h,i}(t)}{dt} = k_h (N_{h,i-1}(t) + N_{h,i+1}(t)) - (2k_h + k_r) N_{h,i}(t) \quad (i \text{ from } 1 \text{ to } k) \quad (3.55)$$

$$\frac{dN_{h,k+1}(t)}{dt} = k_h N_{h,k}(t) - (k_t + k_h + k_r + k_{L1}) N_{h,k+1}(t) \quad (3.56)$$

$$\frac{dN_{c,0}(t)}{dt} = k_c N_{c,1}(t) - k_e I_0(t) \quad (3.57)$$

$$\frac{dN_{c,i}(t)}{dt} = k_c (N_{c,i-1}(t) + N_{c,i+1}(t)) - 2k_c N_{c,i}(t) + k_r N_{h,i}(t) \quad (i \text{ from } 1 \text{ to } k) \quad (3.58)$$

$$\frac{dN_{c,k+1}(t)}{dt} = k_c N_{c,k}(t) - (k_c + k_t + k_{L2}) N_{c,k+1} + k_h N_{h,k+1}(t) \quad (3.59)$$

$$\frac{dN_x(t)}{dt} = k_{L1}N_{h,k+1} + k_{L2}N_{c,k+1} \quad (3.60)$$

where $k_h = D_h/\Delta L^2$, $k_c = D_c/\Delta L^2$.

Solving the equations gave localization efficiency (N_x). The rate constants for exciton trapping (k_t), cold exciton diffusion (D_c), and cold exciton localization rate (k_{L2}) are kept to the same values Table 3.4:

$$k_c = k_x, k_{L2} = k_L \quad (3.61)$$

We assume that with increased excessive excitation energy, the hot exciton diffusion rate (k_h) is larger and the relaxation rate (k_r) is slower. The latter assumption is supported by excitation wavelength dependent TA study of CdSe NSs (see below). With this assumption, the calculated exciton localization efficiency increases from 70% to 95% and the localization rate become faster at higher excitation energy for all CC NS samples (Figure 3.7a). The simulated exciton localization efficiency cannot reach 100% because of the presence of the trapping pathway. The fitting parameters and errors for hot exciton transport at each excitation wavelength are listed in Table 3.5.

Table 3.5. The fitting parameters for hot exciton transport simulation at different excitation wavelength

Excitation wavelength	400nm (70% LE)	390 nm (80% LE)	380 nm (90% LE)	370 nm (95% LE)
Excessive energy	–	119 meV	203meV	289 meV
k_h/ps^{-1}	–	300 ± 20	500 ± 50	1000 ± 50
k_r/ps^{-1}	–	4 ± 1	3 ± 1	2 ± 1
k_{L1}/ps^{-1}	100 ± 20	250 ± 20	600 ± 50	2000 ± 100
k_c/ps^{-1}	125 ± 25	125 ± 25	125 ± 25	125 ± 25

k_t/ps^{-1}	25 ± 5	25 ± 5	25 ± 5	25 ± 5
k_{L2}/ps^{-1}	100 ± 20	100 ± 20	100 ± 20	100 ± 20

This simulation result provides a reasonable explanation for the experimentally observed excitation wavelength dependent excitation localization efficiency. This model predicts that the exciton localization rate should increase with excitation energy from 400 to 370 nm. Unfortunately, we are not able to test this prediction because our TA system cannot provide these tunable wavelengths. These predictions are direct consequence of the assumption of excess energy dependent hot exciton relaxation and diffusion rates. To provide experimental support of excitation wavelength dependent hot exciton relaxation rates, we studied the T1 bleach formation kinetics of free CdSe NSs at different excitation wavelength. Again, similar measurements cannot be done for CdS NSs because of the limited tunability of the laser system. As shown in Figure 3.7b, the T1 bleach kinetics decay is excitation wavelength independent, but the formation kinetics becomes slower at higher excitation energy, suggesting that the hot exciton relaxation to band edge is slower with higher excessive energy. We fitted the T1 kinetics of CdSe by multi-exponential functions convoluted with IRF:

$$\text{T1}(\text{Free CdSe}) = A_{\text{T1}} \left(e^{-\frac{t}{\tau_r}} - d_1 e^{-\frac{t}{\tau_{d1}}} - d_2 e^{-\frac{t}{\tau_{d2}}} - d_3 e^{-\frac{t}{\tau_{d3}}} \right) \otimes \text{IRF} \quad (3.62)$$

where τ_r is the hot exciton relaxation time constant, τ_{di} ($i = 1, 2, 3$) are the decay time constants. The fitting parameters and error bars are listed in Table 3.6. The fitting result shows that hot exciton relaxation time constant increases from ~ 0 at 510 nm to 125 ± 10 fs at 400 nm. The observed trend is supportive of the assumption of hot electron relaxation used in our model.

Table 3.6. Fitting parameters and errors for free CdSe T1 bleach kinetics

Excitation	τ_r/fs	τ_{d1}/ps (d_1)	τ_{d2}/ps (d_2)	τ_{d3}/ps (d_3)
------------	--------------------	---------------------------------	---------------------------------	---------------------------------

400 nm	125±10	2.07±0.26 (13.5±2.6%)	65.4±4.8 (22.8±2.8%)	8728±427 (63.7±4.0%)
485 nm	88±10	2.07±0.26 (13.5±2.6%)	65.4±4.8 (22.8±2.8%)	8728±427 (63.7±4.0%)
510 nm	0±10	2.07±0.26 (13.5±2.6%)	65.4±4.8 (22.8±2.8%)	8728±427 (63.7±4.0%)

Chapter 4. Efficient Diffusive Transport of Hot and Cold Excitons in CdSe/CdS Type-II Core/Crown Nanoplatelet Heterostructures

Reproduced with permission from *ACS Energy Lett.* **2017**, 2, 174. Copyright 2017 American Chemical Society.

4.1. Introduction

Cadmium chalcogenide CdX (X=Se, S, Te) colloidal quantum wells (QWs), also known as nanoplatelets (NPLs), are a novel class of 2-dimensional (2D) materials with atomically precise thickness,^{19-21, 26, 32, 61, 69, 95, 108-109, 143, 145, 150-152, 155, 163-166} and many potential applications in photocatalysis,^{42, 62} light-emitting diodes,¹⁶⁷ photo transistors,¹⁶⁸⁻¹⁶⁹ and lasing.^{30-33, 146} Unlike 0D quantum dots (QDs), these NPLs, with thickness of a few CdX layers (1-2 nm) and lateral dimensions of 10s nm, are strongly quantum confined only in the thickness direction.^{145, 150} Similar to other two-dimensional (2D) materials (such as transition metal dichalcogenides¹⁷⁰⁻¹⁷¹), strong electron-hole Coulomb interaction and large exposed surfaces leads to fast exciton radiative and nonradiative decay, hindering their application as light harvesting or light emitting materials.¹⁷² It has been well demonstrated that in 0D quantum dots and 1D nanorods, exciton lifetimes can be lengthened by forming type II heterostructures.¹⁷³⁻¹⁸⁰ Following this concept, type II CdSe/CdTe core/crown NPL heterostructures (Figure 4.1a), in which a CdTe NPL crown extends laterally on a CdSe NPL core of the same number of layers, has been synthesized; and the excited state lifetime are indeed extended by forming long-lived charge transfer (CT) exciton states with electron and hole separated across the

core/crown interface.^{109, 155, 181} Such approach for extending excited state lifetime requires efficient transport of excitons from the CdTe crown and CdSe core to the core/crown interface prior to trapping of excitons at defect sites.

The extent of exciton in-plane delocalization and mechanism of exciton transport in NPLs are still poorly understood, although they are among the most important properties of these materials. They affect the efficiency of crown-to-core exciton transport in core/crown NPLs mentioned above as well as many other fundamental processes of NPLs, such as energy transfer, charge separation and recombination, and multi-exciton dynamics. The uniform exciton confinement energy across NPLs of 10s of nanometer and larger has been speculated to enable the delocalization of the exciton center-of-mass over the entire NPL, suggestive of ballistic transport.^{26, 182} A previous study of single CdSe quantum belts (of $\sim 1.2 \mu\text{m}$ in length) shows that the spatial distribution of emission intensity is independent of excitation location and attributes this phenomenon to effective delocalization of excitons over the entire length of the crystal at room temperature.¹⁸² However, in a previous study of type I CdSe/CdS core/crown NPL, we showed that the transport time of excitons generated in the CdS crown to the CdSe core increases with crown size, consistent with diffusive transport of localized exciton.⁶⁹ Because of these contradictory findings, the mechanism of exciton transport in NPLs remains to be fully understood.

In this chapter, we report a study of exciton in-plane transport in type II CdSe/CdTe core/crown (CC) colloidal NPL heterostructures to establish that 2D diffusion is the dominant exciton transport mechanism in NPL materials at room temperature. The type II band alignment drives the photogenerated excitons in the CdTe crown to the core/crown interface to form the long-lived CT exciton (Figure 4.1a).^{109, 155, 181} By photoluminescence excitation (PLE) measurement, we showed that the exciton transport quantum efficiency is unity, free from competition with carrier trapping. Transient absorption (TA) spectroscopy study revealed that

the thermalized exciton transport time strongly depends on the crown size and can be well described as a classical 2D diffusion. Finally, through excitation energy dependent studies, we observed a minor but notable contribution of hot exciton transport in these materials at room temperatures. These results suggest that ultrafast diffusive hot and cold exciton transports can be exploited for designing core/crown NPL heterostructures for efficient light harvesting and emission. Furthermore, because CdSe/CdTe differs from the previously studied type I CdSe/CdS NPLs (Chapter 3) in both the crown material (CdTe vs CdS) and band alignment (type II vs type I), taken together, these results show that exciton diffusion is the dominant transport mechanism in 2D NPLs.⁶⁹

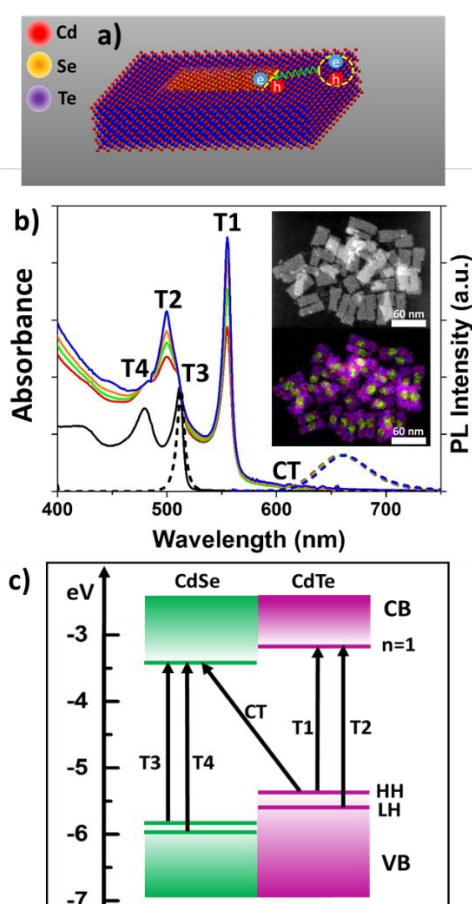


Figure 4.1. (a) Type II CdSe/CdTe core/crown NPL heterostructures with CdTe crown extending laterally on CdSe core. (b) Absorption (solid lines) and photoluminescence (dashed lines) of CdSe core (black), CC1 (red), CC2 (green), CC3 (orange), and CC4 (blue). Inset:

HAADF-STEM and EDX images of CC2 with Cd in red, Se in green, and Te in blue. (c) Band alignment and exciton transitions (see main text for further details)

4.2. Results and Discussion

4.2.1. Sample characterization.

The CdSe/CdTe CC NPLs were synthesized *via* the methods reported in literature with slight modifications.¹⁰⁹ We first synthesized 4 monolayer (ML) CdSe NPLs as the core, which have zinc blend structure with 4 selenium layers and 5 cadmium layers and a thickness of ~ 1.8 nm.²¹ The CdTe crown with the same number of layers were then extended laterally around the CdSe core by injecting additional Cd and Te precursors into CdSe-octadecene (ODE) solutions. The lateral size of CdTe crown can be tuned by changing the crown growth time. Four CdSe/CdTe CC NPL samples, named CC1 to CC4 in the order of increasing crown sizes, were prepared using the same CdSe core. The inset of Figure 4.1b inset and Figure 4.7 in Appendix 4.1 showed the high-angle annular dark-field (HAADF) scanning TEM images and energy-dispersive X-ray (EDX) images of CC2 and rest of the samples, respectively. These images show rectangular shaped CC colloidal NPLs. The EDX images confirm the core/crown heterostructure with Se in the core, Te in the crown, and Cd spread all over the NPL. From these images, the lateral sizes of all CC NPL samples and CdSe core were determined and listed in Table 4.1 in Appendix 4.1. The CC NPLs have a CdSe core in an approximately rectangular shape with 13.9 ± 2.7 nm in length and 9.7 ± 1.4 nm in width. The lateral size of CC NPLs extends from $(38.9 \pm 3.8) \times (17.5 \pm 4.0)$ nm² in CC1 to $(58.2 \pm 7.1) \times (28.1 \pm 7.0)$ nm² as in CC4, while their thickness remains the same according to their exciton peak position in UV-Vis absorption spectra (Figure 4.1b). The crown sizes of CC1 to CC4 were determined by subtracting CdSe core area from the whole CC NPL area.

The normalized absorption spectra and the steady-state photoluminescence (PL) spectra of CC NPLs and CdSe core are shown in Figure 4.1b. Four exciton features, T1 to T4, are clearly observed in absorption spectra. As shown in Figure 4.1c, T1 (~555 nm) and T2 (~500 nm) are the electron-heavy hole (e-hh) and electron-light hole (e-lh) transition of the CdTe crown, respectively; T3 (~512 nm) and T4 (~485 nm) are the e-hh and e-lh transitions of the CdSe cores, respectively.^{21, 109, 155, 181} Compared to the CdSe core, the CdTe crown absorption strength increases from CC1 to CC4, consistent with the increase of the crown size observed by TEM. All CC samples show a broad charge transfer (CT) band emission at ~660 nm.^{109, 155, 181} The type-II band alignment of CdSe/CdTe CC colloidal NPLs can be estimated according to the bulk band edge positions of CdSe and CdTe, quantum confinement effect, self-image energy due to dielectric confinement effect, and the exciton binding energy due to Coulomb interaction.^{21, 61, 144-145} Because the band edge shifts due to exciton binding energy (~100 meV) and the self-image energy (~100 meV) almost cancel out each other,^{21, 61, 145} we only consider the quantum confinement effect in this calculation. With this approximation, the ratio of the shifts of the conduction band (CB) to valence band (VB) edges is equal to the ratio of the hole to electron effective masses.^{21, 69, 144} The estimated CB and VB band edge positions of CdSe (CdTe) are at -3.4 eV (-3.1 eV) and -5.8 eV (-5.3 eV), respectively. The estimated light hole position is at -6.0 eV in CdSe and -5.6 eV in CdTe according to the energy difference between the e-hh and e-lh exciton peaks. The calculation details can be found in the Appendix 4.2.

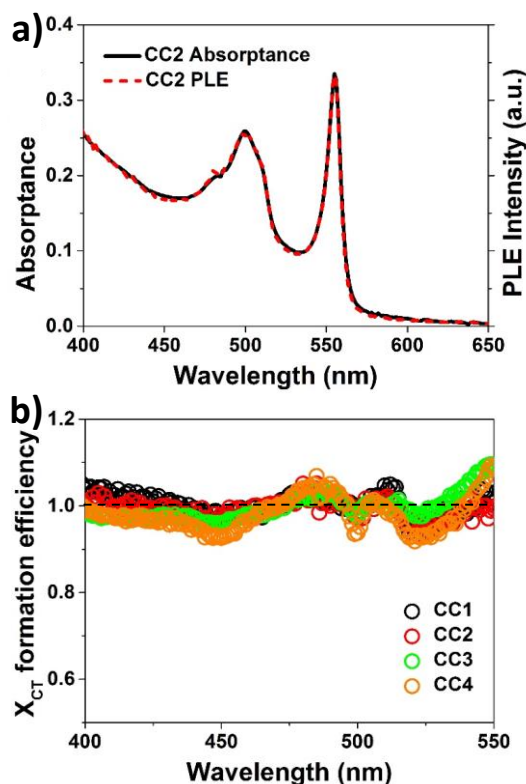


Figure 4.2. CT exciton formation efficiency in CdSe/CdTe core/crown NPLs. (a) Comparison of normalized absorbance and PLE spectrum of CC2. (b) CT exciton formation efficiency of CC1 to CC4.

4.2.2. Unity CT exciton formation efficiency.

We first examined the crown-to-core exciton transport efficiency by photoluminescence excitation (PLE) spectroscopy. In CdSe/CdTe NPLs, the type II band alignment should drive excitons, regardless their initial locations in the core or crown, to the core/crown interface, where interfacial transfer of the electron to CdSe or hole to CdTe forms charge transfer (CT) excitons. The efficiency of forming CT excitons can be measured by the photoluminescence excitation (PLE) spectra that monitors CT band emission (~ 660 nm) intensity as a function of excitation wavelength. As shown in Figure 4.2a (CC2) and Figure 4.8 in Appendix 4.3 (other samples), the PLE spectra agree well with the absorbance spectra. The

absorptance ($1 - 10^{-\text{Optical Density}}$) represents the percentage of photons absorbed. Thus, the ratio of PLE to absorptance, as shown in Figure 4.2b, gives the CT exciton formation efficiency as a function of excitation wavelength (with the localization efficiency set to 1 when directly exciting the CT band). All CC NPL samples show an unity CT exciton formation efficiency, consistent with our previous work.¹⁰⁹ The unity CT exciton formation efficiency indicates fast and efficient exciton and carrier transport and interfacial transfer prior to carrier trapping and charge recombination.

4.2.3. Size dependent exciton in-plane transport.

To determine the exciton transport mechanism in NPLs, we studied the crown size dependent CT exciton formation time by ultrafast pump-probe transient absorption (TA) spectroscopy in CC1 to CC4 at room temperature. All TA measurements were carried out with a low pump fluence ($\sim 4 \mu\text{J}/\text{cm}^2$) to ensure single exciton conditions and negligible contribution of multi-exciton dynamics. Our recent TA studies on cadmium chalcogenides colloidal NPLs have shown that both exciton bleach of CdSe and CdTe are caused by electron state-filling on the CB levels.^{62, 69, 109} Hole state-filling contributions to the exciton bleach are negligible because of the mixing and degeneracy of denser hole levels in VB, similar to cadmium chalcogenide quantum dots (QDs) and nanorods (NRs).^{78, 110, 148, 183} Take CC2 as an example, the TA spectra of CC2 at 530 nm pump are shown in Figure 4.3a. At this excitation wavelength, only cold excitons at the band edge of CdTe crown are generated. The TA spectra show the recovery of CdTe exciton bleach, T1 (~ 555 nm) and T2 (~ 500 nm), and the accompany formation of CdSe exciton bleach, T3 (~ 512 nm) and T4 (~ 485 nm), and CT exciton bleach (~ 640 nm, inset of Figure 3a). The recovery of T1 and T2 bleach indicates the transfer of electron from the $n=1$ conduction band level of the crown and the corresponding growth of the T3, T4 and CT bleach indicates the increase of the population at the CdSe $n=1$ level.¹⁰⁹ We

note that the energy difference between T1 and CT exciton (~ 292 meV) is approximately the CB band offset between CdTe and CdSe, which is consistent with the estimated values (~ 300 meV) shown in Figure 4.1c.

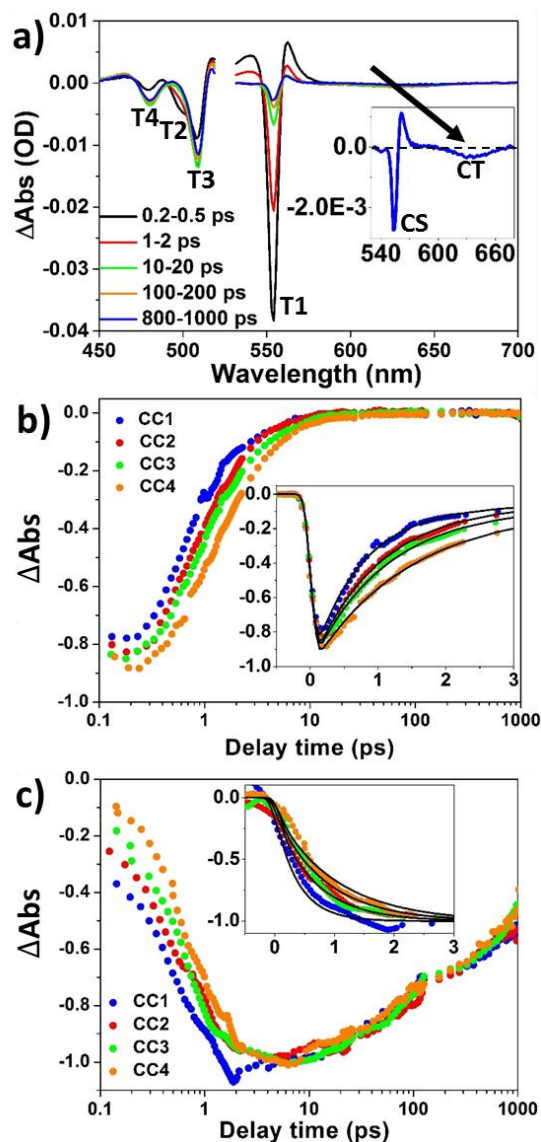


Figure 4.3. TA spectra and kinetics of CdSe/CdTe CC NPLs at 530 nm excitation. Inset: TA spectrum from 530 to 680 nm at 800-1000 ps. (a) The TA spectra of CC2 at different delay time. (b) Comparison of the T1S bleach decay kinetics of CC1 to CC4. Insets in b): expanded view of the kinetics (dots) with their multi-exponential fit (black lines) at early delay times (<3ps). (c) Comparison of the CT bleach formation kinetics of CC1 to CC4. Insets in (c):

expanded view of the kinetics (dots) with their 2D diffusion model fit (black lines) at early delay times (<3 ps).

To follow the kinetics of electron transfer from CdTe crown and arrival at the CdSe, we plot the T1-subtracted (see below) and CT kinetics Figure 4.3b and 4.3c, respectively, as a function of crown size. The CT bleach reflects the state-filling of the CdSe CB level. T1 signal contains both CdTe electron state-filling induced bleach and the charge-separated (CS) state signal. The latter appears as a derivative of the T1 exciton band and can be clearly seen in the spectra at long delay time (inset of Figure 4.3a), when CS feature dominates. The CS signal results from the shifting of the T1 exciton band in the presence of a CT exciton,^{62, 109-110} and its kinetics should be the same as CT exciton kinetics. Thus, to remove the contribution of CS state signal, we scaled the T1 and CT kinetics of CC1 to CC4 such that their scaled CT bleach after 20 ps have the same value (Figure 4.4), which corresponds to the generation of the same number CT excitons in these samples. We then subtracted the scaled CT kinetics from the scaled T1 kinetics to obtain the T1-subtracted (T1S) kinetics, which depends only on electron population at the $n=1$ CB level in the CdTe crown. As shown in Figure 4.3b, the T1S bleach recovers to zero within 15 ps, reflecting the completion of electron transport from CdTe. Corresponding to the T1S bleach recovery, the CT kinetics (Figure 4.3c) shows a growth on time scales consistent with the T1S bleach, reflecting the transport of electrons into CdSe. Both T1S and CT kinetics show clearly that the electron transport time increases with the crown size.

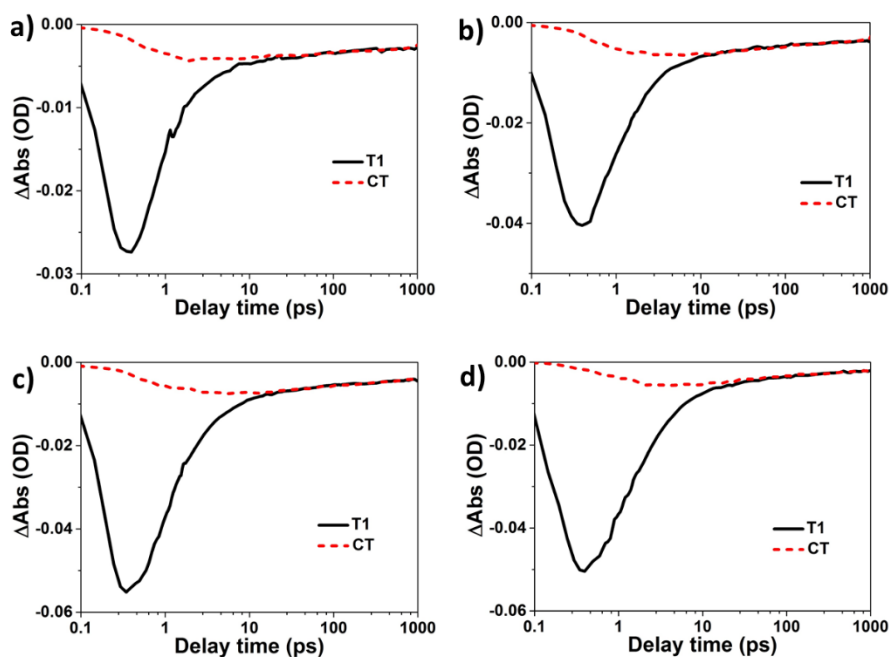


Figure 4.4. Normalized T1 and CT kinetics of (a) CC1, (b) CC2, (c) CC3, (d) CC4 at 530 nm pump.

To obtain an effective time constant for the crown-to-core exciton transport, both T1S and CT kinetics were fit to multi-exponential functions (with convolution with instrument response function, IRF), as shown in the inset of Figure 4.3b and Figure 4.9 in Appendix 4.4. Because the decay of T1S kinetics and the formation of CT kinetics resulted from the same exciton transport process, they are constrained to the same bi-exponential functions (with a < 1 ps and few ps component). The fitting details and parameters can be found in Appendix 4.4 (Table 4.2). The averaged transport time constants obtained from the best fits increase from ~ 2.71 ps in CC1 to ~ 5.57 ps in CC4. It is important to note that because of the limited instrument response function, such ultrafast exciton transport process also leads to an initial amplitude of T1S bleach that decreases from CC4 to CC1 (see Figure 4.9 in Appendix 4.4).

4.2.4. 2D exciton diffusion model.

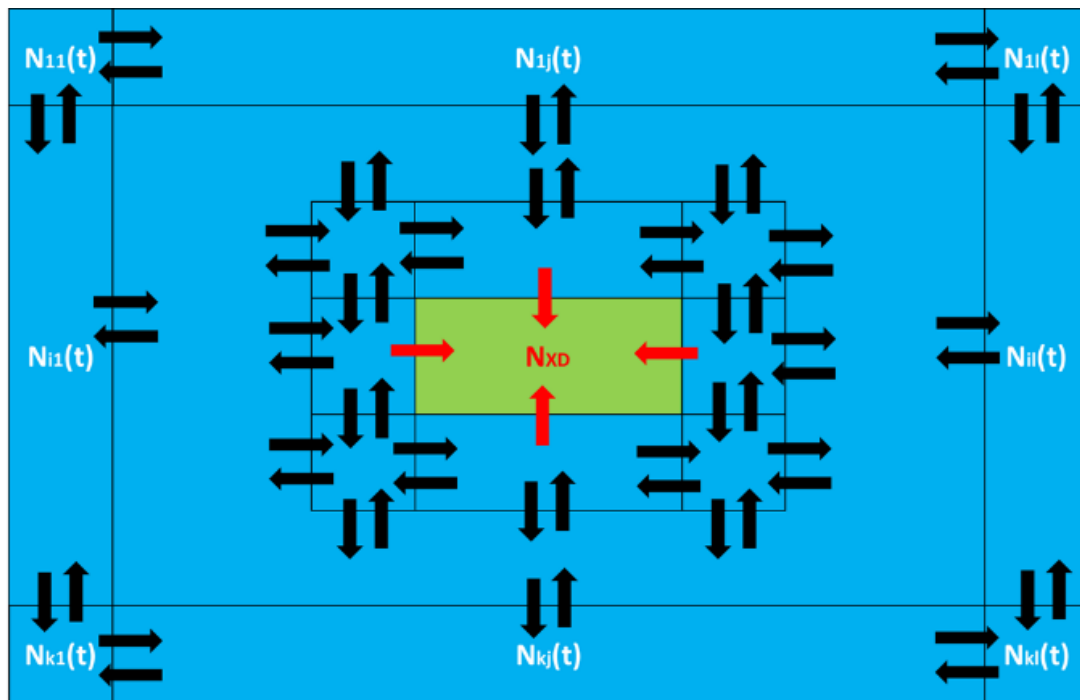


Figure 4.5. 2D diffusional model for exciton transport. Schematic of CdSe/CdTe core/crown quantum well heterostructures used for solving the 2D exciton diffusion equations. The black arrows represent exciton transport with rate constant k_x and the red arrows represent exciton interfacial dissociation with rate constant k_{XD} .

The overall crown-to-interface exciton localization time in CdSe/CdTe contains the contribution of exciton transport in the CdTe crown and electron transfer from CdTe to CdSe at the core/crown interface. Because the crown and core exciton peak positions are the same in CC1 to CC4 (Figure 4.1b), there is negligible crown size dependence in the band offset between the CdSe and CdTe and their interfacial structure. Thus, the interfacial electron transfer step should be crown size independent; and the measured crown size dependent exciton localization kinetics can only be caused by exciton transport within the crown. Furthermore, because

ballistic transport time should be size independent, only diffusive exciton transport in the CdTe crown are considered here.

To model the diffusive transport process, we fit the size dependent CT kinetics by solving the exciton 2D diffusion equation in CdSe/CdTe core/crown NPLs. Although the TA kinetics follows directly the CB electron signal, it should reflect motion of the exciton because the electron and hole are expected to move as a pair (exciton) on the CdTe crown as a result of the strong electron-hole Coulomb interaction in NPLs (with binding energy of ~ 100 eV).^{21, 61} We assumed that excitons are generated by the pump randomly in the crown and diffuse classically with a diffusion constant D_X in the CdTe crown. At the CdTe crown outer edges, excitons are reflected elastically back (with net flux=0). When excitons reach the core/crown interface, they dissociate with an exciton dissociation (XD) rate constant k_{XD} . To solve the diffusion equations numerically, we assumed that the CdSe core is at the CC NPL center (Figure 4.5), and divided CdTe crown into square segments (N_{ij}) with length ΔL , which was set to the 2D exciton of CdTe QWs Bohr radius (a_{2D}). In bulk CdTe, the 3D exciton Bohr radius (a_0), which represents the relative distance between electron-hole pair, is:¹⁵³⁻¹⁵⁴

$$a_0 = \frac{4\pi\epsilon\hbar^2}{\mu e^2} \quad (4.1)$$

where μ is the reduced mass of exciton:

$$\mu = \frac{m_e m_h}{m_e + m_h} \quad (4.2)$$

where m_e and m_h are electron and hole effective mass of bulk CdTe. Thus, μ is calculated as $0.078m_0$ (m_0 is free electron mass). ϵ is the relative dielectric constant of bulk CdTe as 10.3.¹⁸⁴ Then the a_0 is calculated as 6.9 nm. If we consider the exciton as a quasi-2D hydrogen atom move only in the 2D plane, the 2D exciton Bohr radius (a_{2D}) is equal to a quarter of 3D exciton Bohr radius of Bulk CdTe:¹⁵³⁻¹⁵⁴

$$a_{2D} = \frac{a_0}{4} \quad (4.3)$$

which is calculated as 1.7 nm ($=\Delta L$). The exciton transport rate between segments was set as k_x , which equals to $D_x/\Delta L^2$. Exciton recombination and trapping process are ignored in the diffusion equation because of the observed unity exciton transport efficiency. With k_x and k_{XD} as fitting parameters, we solved the exciton 2D diffusion equation numerically to yield the population kinetics of electrons in CdSe, which were used to fit the measured CT kinetics (Figure 4.3c inset and Figure 4.12 in Appendix 4.5) after proper convolution with IRF. Modeling details and fitting parameters and errors can be found in Appendix 4.5. Figure 4.3c inset and Figure 4.12 in Appendix 4.5 show that the CT kinetics is well fitted by the 2D diffusion model, indicating the exciton in-plane motion in CdTe crown can be well described as diffusive transport at room temperature. The fitting result yields an exciton diffusion constant of $2.5 \pm 0.3 \text{ cm}^2/\text{s}$ in CdTe crown, similar to the diffusion constant in CdS colloidal NPLs ($2.2 \text{ cm}^2/\text{s}$) measured in Chapter 3.⁶⁹ The exciton diffusion constant is smaller than the estimated value of bulk CdTe crystal ($D_{\text{bulk},X} = \frac{\mu_x kT}{e} = 6.7 \text{ cm}^2/\text{s}$, where k is the Boltzmann constant, $T=300 \text{ K}$, $\mu_x = \frac{\mu_e m_e + \mu_h m_h}{m_e + m_h}$, $\mu_e=880 \text{ cm}^2/\text{V}\cdot\text{s}$ and $\mu_h=90 \text{ cm}^2/\text{V}\cdot\text{s}$ are reported drift mobility of electron and hole in the bulk CdTe, respectively).^{62, 160, 185-186} The smaller diffusion constant in NPLs may be caused by extra scattering channels induced by large surface area of NPL nanostructures.^{70, 187-188}

4.2.5. Hot exciton transport.

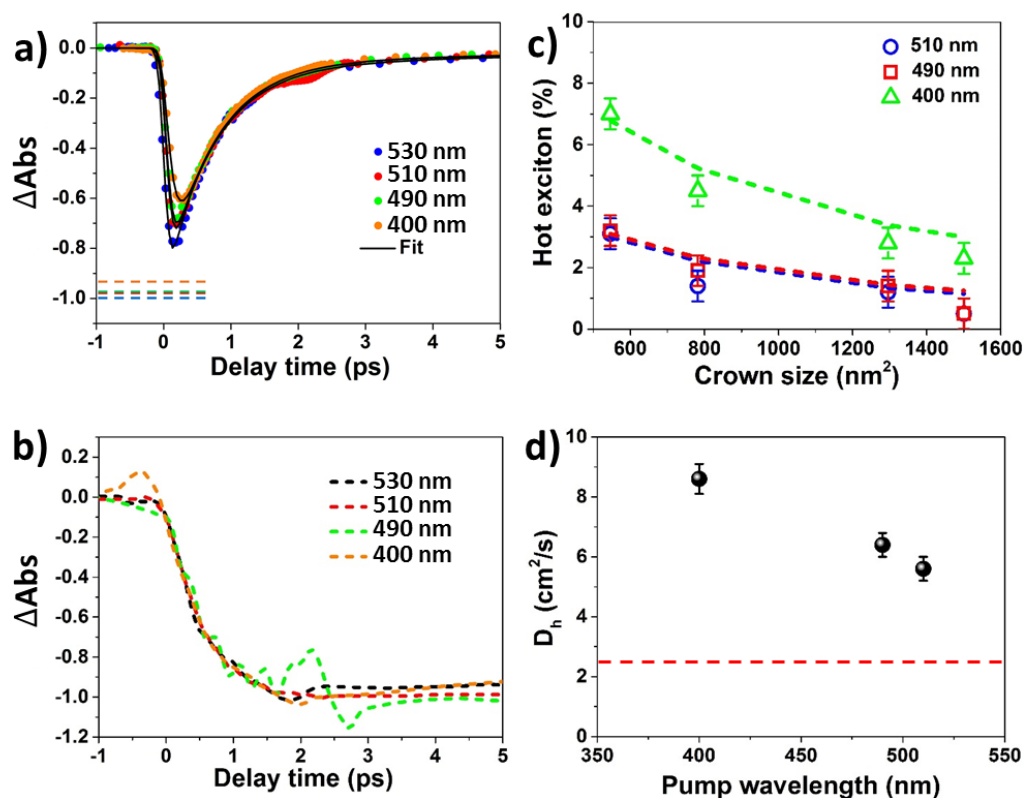


Figure 4.6. Hot exciton transport. (a) Normalized TIS kinetics of CC1 at indicated excitation wavelength. The dashed lines are initial TIS bleach amplitude at 530 nm (blue), 510 nm (red), 490 nm (green), and 400 nm (orange) excitation, obtained after de-convolution of the IRF, representing the number of cold excitons at band edge. (b) Comparison of normalized CT kinetics of CC1 at different pump wavelength. (c) The percentage of hot exciton transport in CC1 to CC4 as a function of crown sizes at 510 nm (blue circles), 490 nm (red squares), and 400 nm (green triangles) pump. The dashed lines represented the estimated percentage of hot exciton transport according to 2D hot exciton diffusion model. (d) The effective hot exciton diffusion constant as a function of pump wavelength. The red dashed line represented the value of cold exciton diffusion constant.

To examine the role of hot exciton transport in NPLs at room temperature, we studied the transport dynamics as a function of excitation wavelength. It will be shown below that the contribution of hot exciton transport can be determined by comparing the relative amplitude of T1S exciton bleach when the same number of photons is absorbed. To do that, we normalize the TA signals measured at different excitation wavelengths for all samples to the same maximal CT bleach amplitude, which reflects the same number of CT excitons and same number of absorbed photons per NPL (because of the unity and wavelength independent transport efficiency determined by the PLE results shown in Figure 2). The resulting normalized kinetics of T1S and CT bands are shown in Figure 4.6a&b, respectively, for CC1 and Figure 4.10 in Appendix 4.4 for CC2 to CC4. Negligible difference was observed in normalized CT kinetics (Figure 4.6b), confirming the formation of the same CT excitons in these CCs. The decay kinetics of the normalized T1S signal are also identical, although the initial amplitude and the formation time are excitation wavelength dependent. The normalized T1S bleach recovery kinetics probes the cold CB electrons at the $n=1$ level, which monitors the transport of thermalized excitons from the CdTe crown (because of the strong e-h binding in these materials). Its transport kinetics should be independent of excitation wavelength, as shown in Figure 4.6a and Figure 4.10d-f in Appendix 4.4.

The observed normalized T1S bleach kinetics show amplitudes smaller than unity for two reasons: (1) the convolution of a finite instrument response time with fast transport of cold excitons, and (2) the presence of hot exciton transport, prior to the relaxation of CB electron to the $n=1$ level in CdTe. To separate the contributions of these two factors, we fitted the normalized T1S kinetics by multi-exponential function convoluted with IRF (see Eq. 4.6 in Appendix 4.4). Their decay components (both ratio and time constants) were fixed to the parameters obtained from the 530 nm pump results. The only fitting parameters are the formation time constants and the initial amplitudes (A_{ini}) of normalized T1S kinetics. In this

analysis, we have assumed 100% thermalized exciton transport at 530 nm excitation, therefore, the initial amplitude of T1S at 530 nm pump was set to 1 (blue dashed line in Figure 4.6a). The initial amplitudes at other wavelengths obtained from the fit reflect the percentage of cold exciton transport and the percentage of hot exciton transport (HET) is calculated from ($\phi_{\text{HET}}=1-A_{\text{ini}}$). The best fit shows that the formation time of the normalized T1S bleach increases from 0 fs at 530 nm to 107 ± 10 fs at 400 nm (see Table 4.3 in Appendix 4.4). This rise time, reflecting the cooling time of the hot electron to the CdTe band edge, becomes slower at higher carrier excess energy, consistent with literature reports.⁶⁹ The fit also reveals that the initial amplitude of normalized T1S becomes less than 1 and the percentage of hot exciton transport (ϕ_{HET}) of CC1 increases at higher excitation energy (up to $\sim 7.0\%$ at 400 nm pump), as shown in Figure 4.6a&c. Similar analysis of CC2 to CC4 samples (with larger crowns) shows decreasing ϕ_{HET} in larger crown: from $\sim 4\%$ to $\sim 2\%$ at 400 nm pump (Figure 4.6c, Figure 4.10 and Table S4 in Appendix 4.4). This result suggests with increasing crown size, hot exciton transport becomes less competitive with fast exciton cooling in these materials and the transport is dominated by thermalized excitons at room temperature.

To understand the mechanism of hot exciton transport, we modified the 2D exciton diffusion equations discussed above to include the effect of hot excitons. Although there exists a continuum of hot exciton states with different excess energies, we modeled the system with only two states: an average hot exciton state and a thermalized (cold) exciton state. The hot exciton transport diffusively in the crown with an effective diffusion constant, D_{h} , and this process competes with its relaxation to form cold exciton with a time constant τ_{f} . The hot exciton relaxation time is set to be the same as the formation time of cold excitons, which has been determined experimentally from the T1 bleach formation (see Table 4.3 in Appendix 4.4). When the hot exciton reaches to the core/crown interface, the electron is ionized from the hole in CdTe and transferred to the CdSe core region near the interface with a rate constant k_{I} . The

electron transported to the core region can also diffuse along the interface and relax with time constants the same as for hot excitons in the crown. The ionized electron can also move back to the crown with a rate constant k_B due to the Coulomb attraction, competing with their relaxation in the core region. The amount of transported hot excitons is calculated from the amount of hot electrons that thermalized in the core. Using D_h , k_I , and k_B as the fitting parameters, we fit the experimentally observed size dependent hot electron transfer quantum efficiency at each pump wavelength. The details of 2D hot exciton diffusion model can be found in Appendix 4.5. The crown size dependent ϕ_{HET} obtained by 2D hot exciton diffusion model (dashed lines in Figure 4.6c) agrees reasonably well with our experimental data. As shown in Figure 4.6d, the fit also reveals that the hot exciton diffusion constants are larger at higher excitation photon energy: from $5.6 \pm 0.4 \text{ cm}^2/\text{s}$ at 510 nm pump to $8.6 \pm 0.5 \text{ cm}^2/\text{s}$ at 400 nm pump, over 2-folds larger than cold exciton diffusion constant. This is consistent with higher exciton excessive energy at shorter pump wavelength observed in our previous work.⁶⁹

In Chapter 3, we showed that exciton diffusive transport from the CdS crown to CdSe core competes with hole trapping at the interface.⁶⁹ Furthermore, the transfer efficiency increases at higher excitation energy above the CdS bandgap (from 70% at 400 nm to ~100% at 370 nm), also suggesting a role of hot exciton transport. Taken together, these results reveal that in CC colloidal NPLs of 10s nm in size, notable contributions of hot exciton transport can be observed at room temperature, even though cold exciton diffusive transport still dominates. It is interesting to note the much more pronounced role of hot exciton transport in CdSe/CdS NPLs (up to 30% at 370 nm excitation). The key difference is that in CdSe/CdS the VB hole is also transferred across the interface while only the CB electron is transferred across the CdSe/CdTe interface. This likely indicates that excess hot hole energy is needed to overcome interfacial barriers/hole trapping in CdSe/CdS.⁶⁹ In CdSe/CdTe, although excess hot electron energy increases the rate of exciton localization, it does not alter the overall efficiency, indicating

negligible barrier for interfacial electron transfer. It is interesting to compare exciton transport in CC NPLs to heterostructures of lower dimension: 0D core/shell QDs, 1D dot-in-rods and barbell heterostructures. For type-II CdSe/CdTe core/shell QDs, exciton is completely confined in all three dimensions, exciton transport is ballistic, leading to much faster ($<1\text{ps}$) formation of the CT exciton state.^{177, 189-190} In CdSe/CdS (type I and Quasi-type II) and CdSe/CdTe (type II) dot-in-rod nanorods, the wurtzite structure results in surface defects along the rod induced, which trap the exciton and reduce the efficiency of exciton diffusive transport.^{70, 175}

Our finding may also be relevant to a previous study of single CdSe quantum belts, in which it is shown that exciton radiative recombination probability is uniform over the length ($\sim 1.2\ \mu\text{m}$) of the quantum belt.¹⁸² This phenomenon can be attributed to a coherent delocalization of the exciton throughout the whole belt or *via* fast diffusion transport. Our studies suggest that the latter is the more likely mechanism. For example, the exciton diffusion constants on CdTe and CdS NPL crowns are near the values of bulk single crystals. Using the diffusion constant of $2.5 \pm 0.3\ \text{cm}^2/\text{s}$ measured for the CdTe crown, we estimate that mean displacement length for 2D exciton diffusion can reach $0.6\ \mu\text{m}$ within $360\ \text{ps}$. Thus, it is possible that the spatial distribution of excitons on single quantum belts can become uniform through fast exciton diffusion, independent of the excitation location.¹⁸² Our result suggests that despite atomically uniform thickness, the wavefunction of exciton center-of-mass motion does not delocalize coherently over the entire NPL, indicating that there exist fluctuations of exciton energy in the lateral dimension. We speculate that this energetic variation may be caused by interaction of NPLs with surface ligand and surrounding solvent.

The observation of hot exciton transport in CdSe/CdTe and CdSe/CdS NPLs differ from exciton transport mechanisms in more extensively studied multiple-quantum-well (MQW) materials grown by molecular beam epitaxy that consist of an active layer of few nanometers in thickness sandwiched by barrier layers.^{64, 191-193} In these MQW materials exciton transport

at room temperature can be described by diffusion of thermalized excitons (i.e. classical transport), and non-classical transport (ballistic transport and hot exciton diffusion) becomes notable only at low temperature. The difference may be attributed to the very different lateral dimension studied in these materials. These previous studies of MQWs utilized PL imaging methods with sub-micrometer spatial resolution and investigated exciton transport across lateral dimensions of 100s nm to a few micrometers. It is likely that because of the relative smaller lateral dimension of NPLs (10s nm), the time scale of exciton transport starts to approach hot exciton relaxation, which increases the contribution of hot exciton transport at room temperature.

4.3. Conclusion

In summary, exciton in-plane transport mechanisms in colloidal nanoplatelets have been studied in four CdSe/CdTe core/crown type II heterostructures of the same core and varying crown size at room temperature. Excitons generated in the CdTe crown are transported to the core/crown interface to form charge transfer (CT) excitons (in which the electron in the CdSe core is bound to the hole in the CdTe crown). PLE measurements reveal a unity crown to CT exciton exciton transport efficiency, independent of the CdTe crown size, suggesting efficient transport prior to exciton trapping or recombination. At near band edge excitation (530 nm), TA spectroscopy studies show that exciton in-plane transport time increases in larger crowns (from 2.7 ps in CC1 to 5.6 ps in CC4). This size dependence can be well described by 2D diffusive transport of thermalized excitons with a diffusion constant of $2.5 \pm 0.3 \text{ cm}^2/\text{s}$ (about a factor of 1.6 times smaller than the bulk value). At excitation energy above the band edge, TA studies reveal a minor contribution of hot excitons (up to 7 % of the total excitons at 400 nm excitation in CC1) with diffusion constant that are over twice that of cold excitons. The contribution of hot excitons decreases with increasing NPL sizes and decreasing excess

excitation photon energy. These results indicate that diffusive transport of thermalized exciton dominates in-plane motion in CdTe crown at room temperature in NPLs of 10s nm in size. This ultrafast and efficient diffusive transport of hot and cold excitons to the type II interface in cadmium chalcogenide colloidal NPLs suggests their potential for light harvesting applications.

Appendix 4.1

The TEM images and lateral sizes of samples

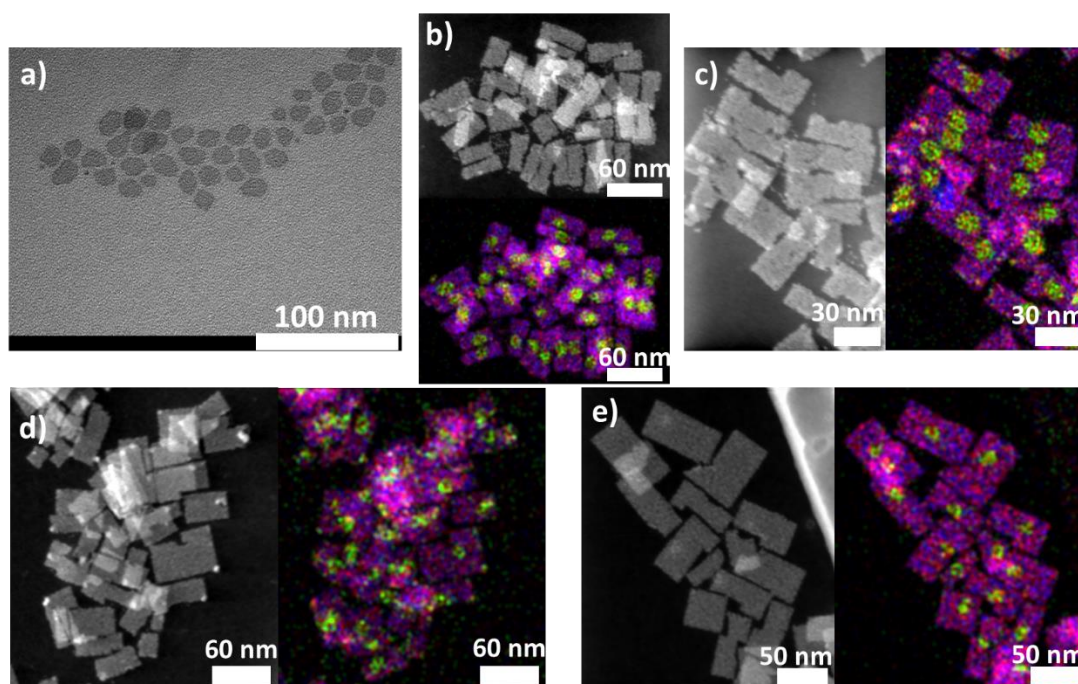


Figure 4.7. (a) The TEM images of CdSe core. The HAADF-STEM images with EDX mapping of (b) CC1, (c) CC2, (d) CC3, (e) CC4. In core/crown samples, CdTe crown and CdSe core were shown in purple and green, respectively.

Table 4.1. The length, width, and area with errors of CdSe core and CC NPLs

	Length/nm	Width/nm	NPL Area/nm ²	Crown area/nm ²
CdSe core	13.9±2.7	9.7±1.4	134.8±31.7	–
CC1	38.9±3.8	17.5±4.0	680.8±177.7	546.0±146.0
CC2	52.1±6.8	17.6±4.1	917.0±262.1	782.2±230.4

CC3	54.4 ± 5.4	26.3 ± 6.0	1430.7 ± 363.2	1295.9 ± 331.5
CC4	58.2 ± 7.1	28.1 ± 7.0	1635.4 ± 481.6	1500.6 ± 449.9

Appendix 4.2

Type-II band alignment estimation

The band alignment of CdSe/CdTe CC colloidal NPLs were calculated from their bulk band-gap and the 1D quantum confinement effect as described in the main text. The band edge position (relative to vacuum) were calculated by the following equations:

$$E_{CB} = E_{\text{bulk,CB}} + \frac{m_h}{m_e + m_h} (E_X - E_g) \quad (4.4)$$

$$E_{VB} = E_{\text{bulk,VB}} - \frac{m_e}{m_e + m_h} (E_X - E_g) \quad (4.5)$$

where E_{CB} and E_{VB} are conduction band (CB) and valence band (VB) edge positions of colloidal NPLs, respectively. The $E_{\text{bulk,CB}}$ and $E_{\text{bulk,VB}}$ are CB and VB edge position in bulk crystals, respectively. m_e and m_h are effective mass of electron and hole, respectively. E_X represents the first exciton peak energy of colloidal NPLs and E_g is the bulk band gap.

The CB (VB) edge position of bulk CdSe and bulk CdTe is -4.0 eV (-5.7 eV) and -3.7 eV (-5.2 eV), respectively.¹⁹⁴⁻¹⁹⁵ This results in the bulk bandgap of 1.7 eV in CdSe and 1.5 eV in CdTe. The effective mass of electron (hole) is $0.13m_0$ ($0.45m_0$) in bulk CdSe,¹⁹⁵⁻¹⁹⁶ and $0.1m_0$ ($0.35m_0$) in bulk CdTe,¹⁹⁵ where m_0 is the free electron mass. Thus, the CB and VB band edge position of CdSe (CdTe) colloidal NPLs were calculated roughly as -3.4 eV (-3.1 eV) and -5.8 eV (-5.3 eV), respectively. The light hole position can be calculated as -6.0 eV in CdSe and -5.6 eV in CdTe colloidal NPLs according to the energy difference between the e-hh and e-lh exciton peaks.

Appendix 4.3

Comparison of Absorbance and PLE spectra

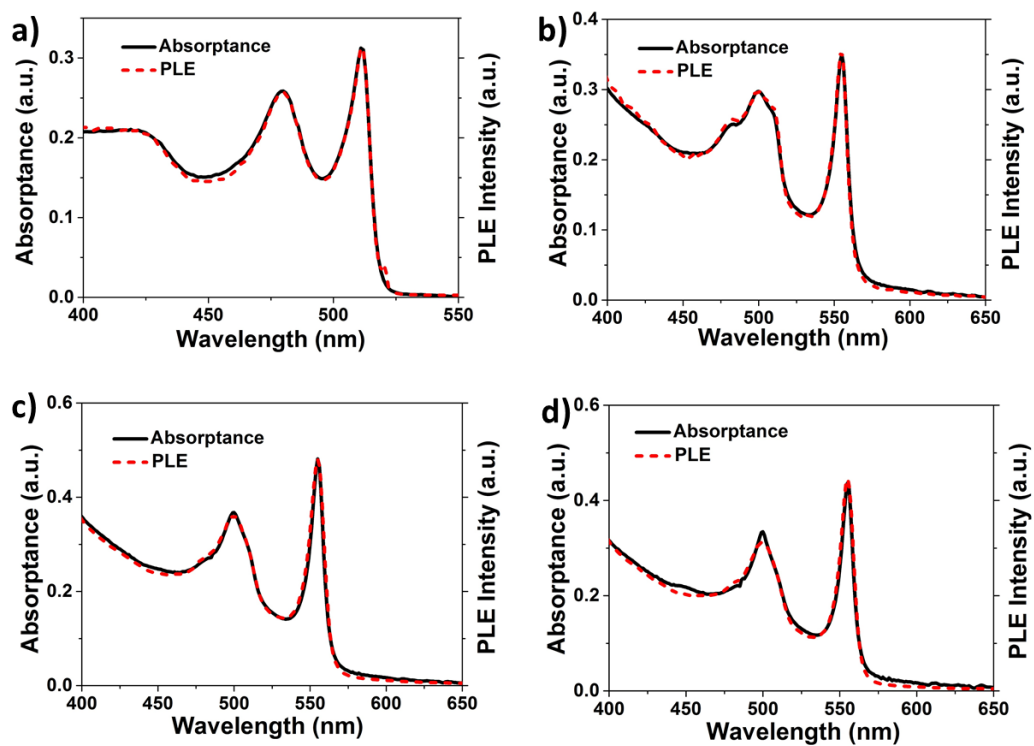


Figure 4.8. The comparison of normalized absorbance and PLE spectra of (a) CdSe core, (b) CC1, (c) CC3, and (d) CC4.

Appendix 4.4

Transient absorption bleach kinetics and the fits

The T1S kinetics of all samples were obtained by subtracting normalized CT kinetics from T1 kinetics as described in Chapter 4.2.3. We fitted both T1S and CT kinetics of all samples within 1 ns at 530 nm pump by multi-exponential functions convoluted with instrument response function (IRF, ~150 fs) using the same set of parameters:

$$\text{T1S}(t) = A_{\text{initial}}[e^{-\frac{t}{\tau_f}} - a_1 \cdot e^{-\frac{t}{\tau_1}} - a_2 \cdot e^{-\frac{t}{\tau_2}}] \otimes \text{IRF} \quad (4.6)$$

$$\text{CT}(t) = A_{\text{max}}[(a_1 \cdot e^{-\frac{t}{\tau_1}} + a_2 \cdot e^{-\frac{t}{\tau_2}}) - b_1 \cdot e^{-\frac{t}{\tau_3}} - b_2 \cdot e^{-\frac{t}{\tau_4}}] \otimes \text{IRF} \quad (4.7)$$

where τ_f is the formation time constant of T1S kinetics, which is fixed as 0 fs due to band edge excitation. a_1, a_2 (τ_1, τ_2) are the two exciton transport components (time constant), which were shown as decay in T1S and growth in CT kinetics, respectively. b_1, b_2 (τ_3, τ_4) are the two CT kinetics decay components (time constants), representing the CT exciton recombination process. The area weighted average lifetime (τ_{ave}) of exciton transport process was calculated as:

$$\tau_{\text{ave}} = \frac{a_1 \tau_1^2 + a_2 \tau_2^2}{a_1 \tau_1 + a_2 \tau_2} \quad (4.8)$$

The fitting parameters and errors were listed in Table 4.2, and the fitting results were shown in Figure 4.9. We also plotted the same multi-exponential functions for fitting T1S and CT kinetics without convolution with IRF as gray dashed lines in Figure 4.9. Compared to the fit with (black solid lines) and without (gray dashed lines) convolution, we clearly observed that the fast decay components (<1 ps) of in T1S kinetics were missing due to the limited instrument response function; while the fit with or without convolution of CT kinetics remained the same with a negligible difference at time zero.

Table 4.2. The fitting parameters and errors of bleach kinetics at 530 nm pump

	CC1	CC2	CC3	CC4
τ_f/fs	0 ± 10	0 ± 10	0 ± 10	0 ± 10
τ_1/ps	0.72 ± 0.07	0.94 ± 0.05	1.06 ± 0.05	1.38 ± 0.08
(a ₁)	(0.90 ± 0.03)	(0.88 ± 0.02)	(0.89 ± 0.03)	(0.86 ± 0.01)
τ_1/ps	5.24 ± 0.85	7.25 ± 0.68	8.19 ± 0.61	9.34 ± 1.07
(a ₂)	(0.10 ± 0.03)	(0.12 ± 0.02)	(0.11 ± 0.03)	(0.14 ± 0.02)
$\tau_{\text{ave}}/\text{ps}$	2.71	4.11	4.56	5.57
τ_3/ps	25.7 ± 5.0	25.7 ± 5.0	25.7 ± 5.0	25.7 ± 5.0
(b ₁)	(0.35 ± 0.06)	(0.35 ± 0.06)	(0.35 ± 0.06)	(0.35 ± 0.06)
τ_4/ps	2151 ± 608	2151 ± 608	2151 ± 608	2151 ± 608
(b ₂)	(0.65 ± 0.06)	(0.65 ± 0.06)	(0.65 ± 0.06)	(0.65 ± 0.06)

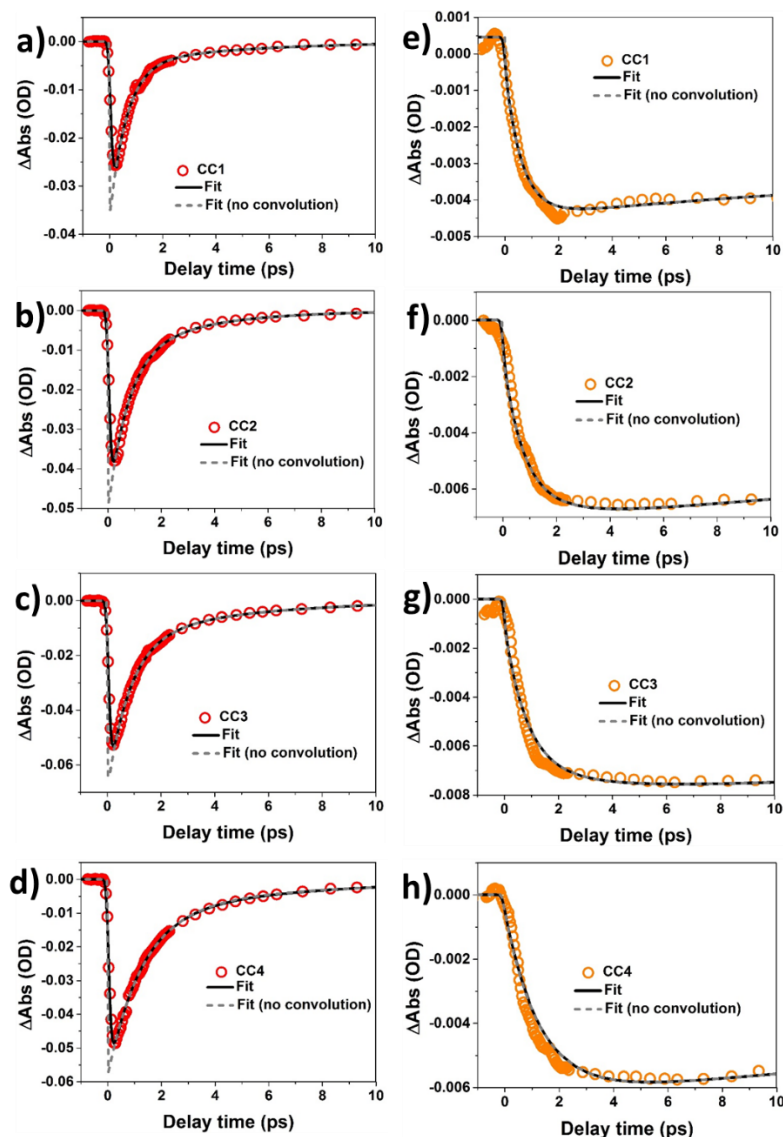


Figure 4.9. T1S kinetics (red dots) and their fits (black lines) of (a) CC1, (b) CC2, (c) CC3, (d) CC4; and CT kinetics (orange dots) and their fits with (black lines) of (e) CC1, (f) CC2, (g) CC3, (h) CC4. All kinetics were measured at 530 nm excitation. Also shown are fit functions (dashed line) without convolution with instrument response.

The T1S kinetics of CC1 to CC4 at different pump wavelength were normalized as in the main text. They were fitted by Eq. 4.6, and all the fitting parameters were fixed as in Table 4.2 except for the formation time constant and initial amplitude (A_{initial}). The best fitted formation time constant and errors at different pump wavelength were listed in Table 4.3. The normalized

T1S and CT kinetics of CC1 to CC4 at different pump wavelength were plotted in Figure 4.6 and 4.10. The percentage of hot exciton transport (ϕ_{HET}) of CC1 to CC4 at different excitation wavelength were shown in Table 4.4.

Table 4.3. The formation time constants and errors of T1S kinetics at different pump

	400 nm	490 nm	510 nm	530 nm
τ_f/fs	107 ± 10	55 ± 10	40 ± 10	0 ± 10

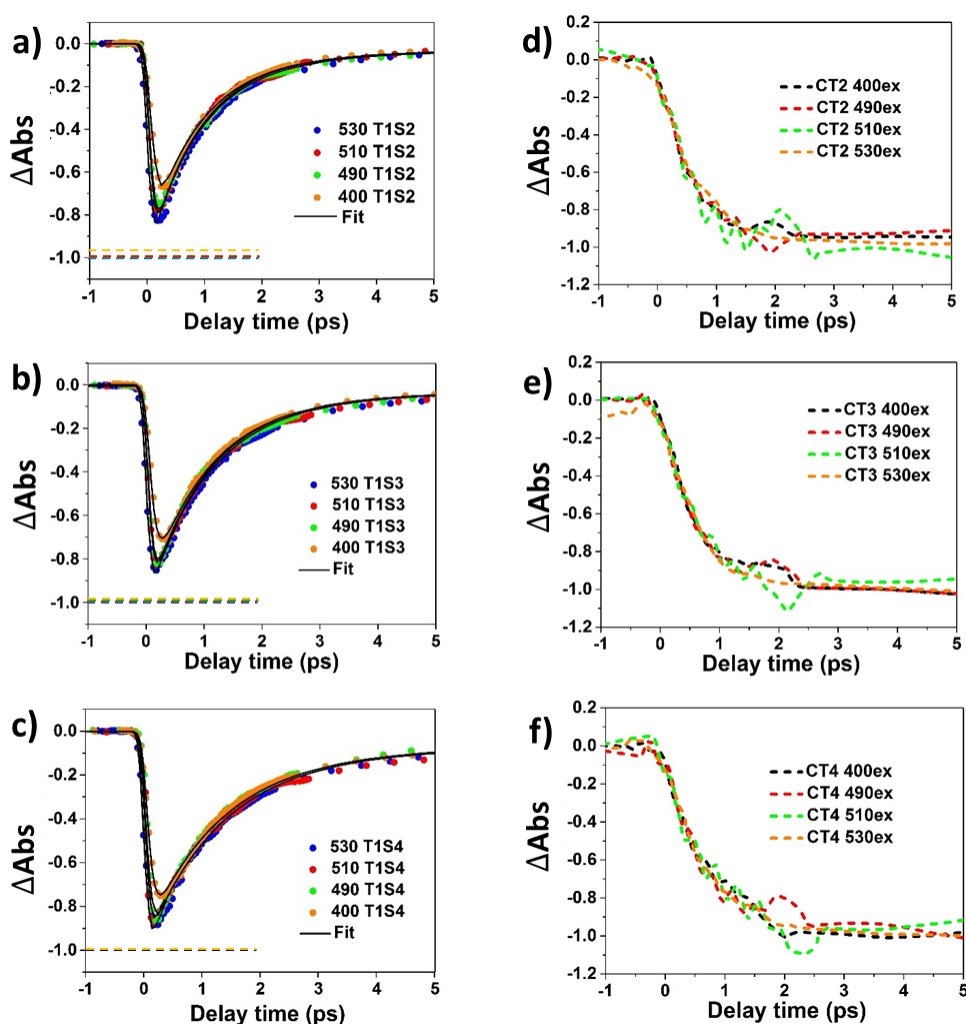


Figure 4.10. (a-c) The comparison of normalized T1S kinetics of (a) CC2, (b) CC3, (c) CC4 at different pump wavelength. Horizontal dashed lines are the initial amplitude of T1S bleach

at different pump wavelength. (d-f) The comparison of normalized CT kinetics of (d) CC2, (e) CC3, (f) CC4 at different pump wavelength.

Table 4.4. The percentage of hot exciton transport (ϕ_{HET}) at different pump

	400 nm pump	490 nm pump	510 pump
CC1 ϕ_{HET} /%	7.0 ± 0.5	3.2 ± 0.5	3.1 ± 0.5
CC2 ϕ_{HET} /%	4.5 ± 0.5	1.9 ± 0.5	1.4 ± 0.5
CC3 ϕ_{HET} /%	2.8 ± 0.5	1.4 ± 0.5	1.2 ± 0.5
CC4 ϕ_{HET} /%	2.3 ± 0.5	0.5 ± 0.5	0.5 ± 0.5

Appendix 4.5

2D exciton diffusion model

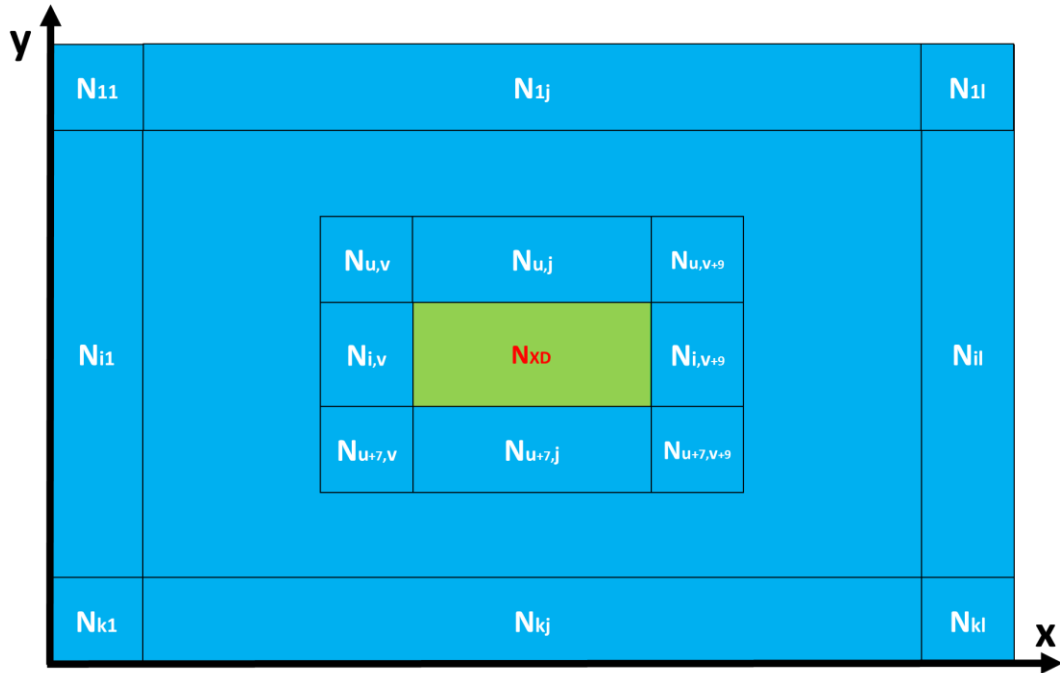


Figure 4.11. Schematic of CdSe/CdTe core/crown NPL heterostructures used for solving the 2D cold exciton diffusion equations numerically.

According to rectangular shape for both core and the crown, we put length along x-axis and the width along y-axis with the CdSe core at the center of NPL as shown in Figure 4.11. The length (width) for the core and the crown were set as L_{core} (W_{core}) and L_{crown} (W_{crown}), respectively, the exact value of which for all samples were listed in Table 4.1. The CdSe/CdTe CC NPL can be divided into four areas: the core area, the crown area, the edges of crown, and the core/crown interface. We consider free excitons (with density N) in CdTe crown with diffusion constant D_x in both x and y direction according to the homogeneous environment for 2D excitons in NPLs. At the interface, these excitons dissociate (XD) and transfer electrons into CdSe with rate k_{XD} . At crown outer edges, no excitons can diffuse outside the crown so that the flux crossing the edges were set to zero.

Typically, in crown region, the excitons diffuse following the 2D diffusion equation:

$$\frac{dN(x, y, t)}{dt} = D_x \left(\frac{\partial^2 N}{\partial x^2} + \frac{\partial^2 N}{\partial y^2} \right) \quad (4.9)$$

At the interface:

$$\frac{dN \left(x = \frac{L_{\text{crown}} - L_{\text{core}}}{2} \text{ or } \frac{L_{\text{crown}} + L_{\text{core}}}{2}, y, t \right)}{dt} = D_x \left(\frac{\partial^2 N}{\partial x^2} + \frac{\partial^2 N}{\partial y^2} \right) - kN$$

$$\text{where } \frac{W_{\text{crown}} - W_{\text{core}}}{2} < y < \frac{W_{\text{crown}} + W_{\text{core}}}{2} \quad (4.10)$$

$$\frac{dN \left(x, y = \frac{W_{\text{crown}} - W_{\text{core}}}{2} \text{ or } \frac{W_{\text{crown}} + W_{\text{core}}}{2}, t \right)}{dt} = D_x \left(\frac{\partial^2 N}{\partial x^2} + \frac{\partial^2 N}{\partial y^2} \right) - kN$$

$$\text{where } \frac{L_{\text{crown}} - L_{\text{core}}}{2} < x < \frac{L_{\text{crown}} + L_{\text{core}}}{2} \quad (4.11)$$

At crown edges:

$$\frac{\partial N(x = 0 \text{ or } L_{\text{crown}}, y, t)}{\partial x} = 0 \quad (4.12)$$

$$\frac{\partial N(x, y = 0 \text{ or } W_{\text{crown}}, t)}{\partial y} = 0 \quad (4.13)$$

In CdSe core:

$$\frac{dN_{\text{XD}}(t)}{dt} = kN(x, y, t) \quad (x, y \in \text{interface}) \quad (4.14)$$

Those equations can be solved numerically by dividing the CdTe crown into square segments as shown in Figure 4.11 under the following approximation for derivatives:

$$\begin{aligned} D \frac{\partial^2 N}{\partial x^2} &= D \lim_{\Delta L \rightarrow 0} \frac{\frac{N(x + \Delta L, y, t) - N(x, y, t)}{\Delta L} - \frac{N(x, y, t) - N(x - \Delta L, y, t)}{\Delta L}}{\Delta L} \\ &\cong D \frac{N(x + \Delta L, y, t) + N(x - \Delta L, y, t) - 2N(x, y, t)}{\Delta L^2} \quad (4.15) \end{aligned}$$

$$D \frac{\partial^2 N}{\partial y^2} = D \lim_{\Delta L \rightarrow 0} \frac{\frac{N(x, y + \Delta L, t) - N(x, y, t)}{\Delta L} - \frac{N(x, y, t) - N(x, y - \Delta L, t)}{\Delta L}}{\Delta L}$$

$$\cong D \frac{N(x, y + \Delta L, t) + N(x, y - \Delta L, t) - 2N(x, y, t)}{\Delta L^2} \quad (4.16)$$

The CC NPLs were divided into $k \times l$ square segments, in particular, 24×10 , 30×10 , 32×15 , 34×16 segments with a core at the center (8×6 segments) for CC1 to CC4, respectively. The segment length was set to 2D exciton Bohr radius of CdTe as 1.7 nm. The exciton density in each segment was N_{ij} , whose order were shown in Figure 4.11. Then, the diffusion equations for segments were divided into four parts, the segments at the crown edges, the segments along the interface, the rest crown segments, and the CdSe core.

For the segment at the crown edges:

$$\frac{dN_{11}(t)}{dt} = k_X(N_{12}(t) + N_{21}(t) - 2N_{11}(t)) \quad (4.17)$$

$$\frac{dN_{1j}(t)}{dt} = k_X(N_{1,j+1}(t) + N_{1,j-1}(t) + N_{2j}(t) - 3N_{1j}(t)) \quad (j \text{ from } 2 \text{ to } l - 1) \quad (4.18)$$

$$\frac{dN_{1l}(t)}{dt} = k_X(N_{1,l-1}(t) + N_{2l}(t) - 2N_{1l}(t)) \quad (4.19)$$

$$\frac{dN_{i1}(t)}{dt} = k_X(N_{i-1,1}(t) + N_{i+1,1}(t) + N_{i2}(t) - 3N_{i1}(t)) \quad (i \text{ from } 2 \text{ to } k - 1) \quad (4.20)$$

$$\frac{dN_{il}(t)}{dt} = k_X(N_{i-1,1}(t) + N_{i+1,1}(t) + N_{i,l-1}(t) - 3N_{il}(t)) \quad (i \text{ from } 2 \text{ to } k - 1) \quad (4.21)$$

$$\frac{dN_{k1}(t)}{dt} = k_X(N_{k-1,1}(t) + N_{k2}(t) - 2N_{k1}(t)) \quad (4.22)$$

$$\frac{dN_{kj}(t)}{dt} = k_X(N_{k,j+1}(t) + N_{k,j-1}(t) + N_{k-1,j}(t) - 3N_{kj}(t)) \quad (j \text{ from } 2 \text{ to } l - 1) \quad (4.23)$$

$$\frac{dN_{kl}(t)}{dt} = k_X(N_{k-1,l}(t) + N_{k,l-1}(t) - 2N_{kl}(t)) \quad (4.24)$$

For the segments along the interface start near N_{uv} :

$$\begin{aligned} \frac{dN_{uj}(t)}{dt} = & k_X \left(N_{u-1,j}(t) + N_{u,j-1}(t) + N_{u,j+1}(t) - 3N_{uj}(t) \right) \\ & - k_{XD} N_{uj}(t) \quad (j \text{ from } v+1 \text{ to } v+8) \quad (4.25) \end{aligned}$$

$$\begin{aligned} \frac{dN_{iv}(t)}{dt} = & k_X \left(N_{i-1,v}(t) + N_{i+1,v}(t) + N_{i,v-1}(t) - 3N_{iv}(t) \right) \\ & - k_{XD} N_{iv}(t) \quad (i \text{ from } u+1 \text{ to } u+6) \quad (4.26) \end{aligned}$$

$$\begin{aligned} \frac{dN_{i,v+9}(t)}{dt} = & k_X \left(N_{i-1,v}(t) + N_{i+1,v}(t) + N_{i,v+10}(t) - 3N_{i,v+9}(t) \right) \\ & - k_{XD} N_{i,v+9}(t) \quad (i \text{ from } u+1 \text{ to } u+6) \quad (4.27) \end{aligned}$$

$$\begin{aligned} \frac{dN_{u+7,j}(t)}{dt} = & k_X \left(N_{u+8,j}(t) + N_{u+7,j-1}(t) + N_{u+7,j+1}(t) - 3N_{u+7,j}(t) \right) \\ & - k_{XD} N_{u+7,j}(t) \quad (j \text{ from } v+1 \text{ to } v+8) \quad (4.28) \end{aligned}$$

For the rest crown segments:

$$\begin{aligned} \frac{dN_{ij}(t)}{dt} = & k_X \left(N_{i-1,j}(t) + N_{i+1,j}(t) + N_{i,j-1}(t) + N_{i,j+1}(t) - 4N_{ij}(t) \right) \quad (i, j \\ & \in \text{other crown segments}) \quad (4.29) \end{aligned}$$

For CdSe core, the density of dissociated excitons, N_{XD} :

$$\frac{dN_{XD}}{dt} = \sum_{j=v+1}^{v+8} k_{XD} [N_{uj}(t) + N_{u+7,j}(t)] + \sum_{i=u+1}^{u+6} k_{XD} [N_{iv}(t) + N_{i,v+9}(t)] \quad (4.30)$$

where $k_X = D_X/\Delta L^2$. We assume at time zero, single exciton was generated randomly on CdTe crown, meaning each crown segment has the same exciton density at $t = 0$:

$$N_{ij}(0) = \frac{1}{n} \quad (4.31)$$

n is the number of crown segments, which equals the total CC NPL segments subtract the CdSe core segments: $k \times l - 48$.

The solution of these equations gave the $N_{XD}(t)$, which reflected the exciton transport kinetics and was convoluted with IRF and fitted the CT kinetics:

$$CT(t) = N_{XD}(t) \otimes IRF \quad (4.32)$$

The best fits were shown in Figure 4.3c inset and 4.12 with k_X as $90 \pm 10 \text{ ps}^{-1}$ and k_{XD} as $100 \pm 12 \text{ ps}^{-1}$. The k_{XD} is very large due to the ultrafast exciton dissociation at the interface, consistent with our recent estimation in CdS nanorods.⁷⁰ The D_X of CdTe crown was calculated from $k_X = D_X/\Delta L^2$ as $2.5 \pm 0.3 \text{ cm}^2/\text{s}$.

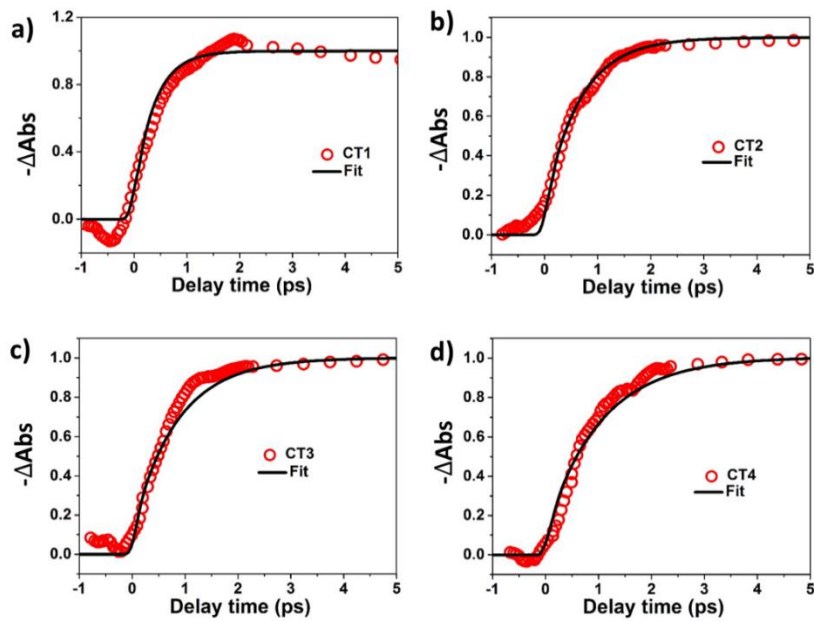


Figure 4.12. The CT kinetics at 530 nm pump of (a) CC1, (b) CC2, (c) CC3, (d) CC4 and the fit using 2D diffusion model.

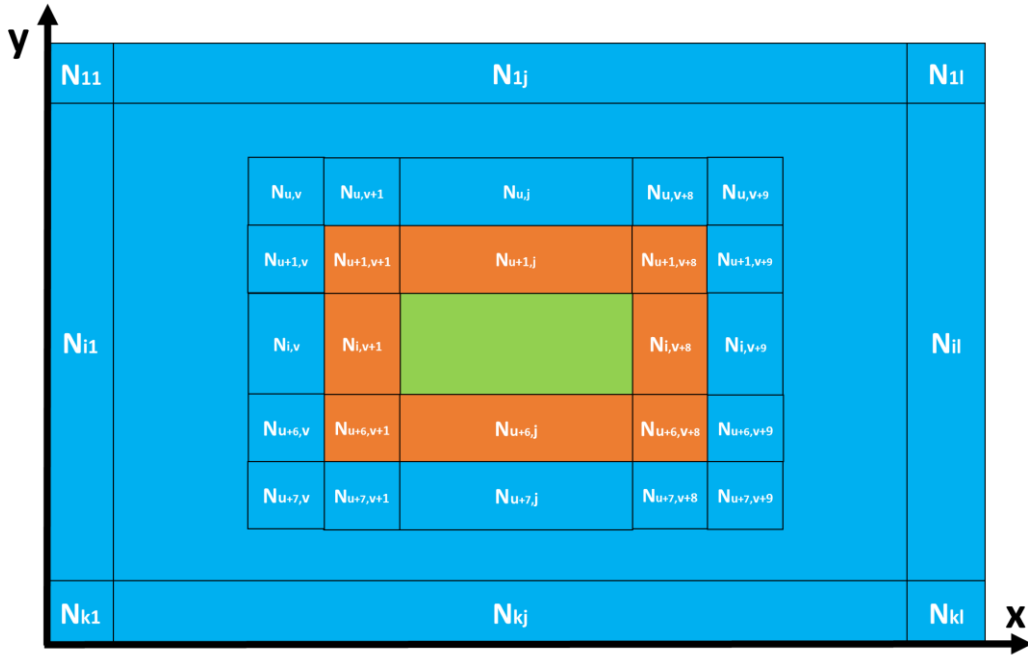


Figure 4.13. Schematic of CdSe/CdTe core/crown NPL heterostructures used for solving the 2D hot exciton diffusion equations numerically.

Similarly, we also simulated the hot exciton transport process at shorter pump wavelength by considering an effective hot exciton species transports diffusively with an effective diffusion constant, D_h , in the crown. The hot exciton can also relax to form cold exciton with an effective relaxation time τ_f that is determined experimentally (Table 4.3). As shown in Figure 4.13, we divided the CC NPLs into four areas: the crown edges, the core/crown interface, the core region near the interface (orange area), and the rest of the crown region. The hot exciton was generated randomly in the crown at $t=0$. The hot exciton diffused between segments with a rate constant: $k_h = D_h/\Delta L^2$, and decayed to cold exciton in each segment with a rate constant: $k_f = 1/\tau_f$. When the hot exciton reached to the core/crown interface, the electron in the exciton can be ionized into the core region near the interface with a rate constant k_I , the ionized electron in core region can also move back to the crown at the interface with a rate constant k_B before it is relaxed. We ignored the hole crown-to-core transfer at the interface due to the massive VB

offset. We assumed the ionized electron in core region have the same relaxation rate, k_f , and diffusion rate, k_h , as hot exciton in the crown, and it cannot move deeper inside the core due to its Coulomb interaction with the hole at the interface.

For the segment at the crown edges:

$$\frac{dN_{11}(t)}{dt} = k_h(N_{12}(t) + N_{21}(t) - 2N_{11}(t)) - k_f N_{11}(t) \quad (4.33)$$

$$\begin{aligned} \frac{dN_{1j}(t)}{dt} = k_h & \left(N_{1,j+1}(t) + N_{1,j-1}(t) + N_{2,j}(t) - 3N_{11}(t) \right) \\ & - k_f N_{1j}(t) \quad (j \text{ from } 2 \text{ to } l - 1) \quad (4.34) \end{aligned}$$

$$\frac{dN_{1l}(t)}{dt} = k_h(N_{1,l-1}(t) + N_{2l}(t) - 2N_{1l}(t)) - k_f N_{1l}(t) \quad (4.35)$$

$$\begin{aligned} \frac{dN_{i1}(t)}{dt} = k_h & \left(N_{i-1,1}(t) + N_{i+1,1}(t) + N_{i2}(t) - 3N_{i1}(t) \right) \\ & - k_f N_{i1}(t) \quad (i \text{ from } 2 \text{ to } k - 1) \quad (4.36) \end{aligned}$$

$$\begin{aligned} \frac{dN_{il}(t)}{dt} = k_h & \left(N_{i-1,1}(t) + N_{i+1,1}(t) + N_{i,l-1}(t) - 3N_{il}(t) \right) \\ & - k_f N_{il}(t) \quad (i \text{ from } 2 \text{ to } k - 1) \quad (4.37) \end{aligned}$$

$$\frac{dN_{k1}(t)}{dt} = k_h(N_{k-1,1}(t) + N_{k2}(t) - 2N_{k1}(t)) - k_f N_{k1}(t) \quad (4.38)$$

$$\begin{aligned} \frac{dN_{kj}(t)}{dt} = k_h & \left(N_{k,j+1}(t) + N_{k,j-1}(t) + N_{k-1,j}(t) - 3N_{kj}(t) \right) - k_f N_{kj}(t) \quad (j \text{ from } 2 \text{ to } l \\ & - 1) \quad (4.39) \end{aligned}$$

$$\frac{dN_{kl}(t)}{dt} = k_h(N_{k-1,l}(t) + N_{k,l-1}(t) - 2N_{kl}(t)) - k_f N_{kl}(t) \quad (4.40)$$

For the crown segments along the core/crown interface start near N_{uv} :

$$\begin{aligned} \frac{dN_{u,v+1}(t)}{dt} = k_h & \left(N_{u,v}(t) + N_{u,v+2}(t) + N_{u-1,v+1}(t) - 3N_{u,v+1}(t) \right) - (k_f + k_l)N_{u,v+1}(t) \\ & + k_B N_{u+1,v+1}(t) \quad (4.41) \end{aligned}$$

$$\begin{aligned} \frac{dN_{uj}(t)}{dt} &= k_h \left(N_{u-1,j}(t) + N_{u,j-1}(t) + N_{u,j+1}(t) - 3N_{uj}(t) \right) - (k_f + k_I)N_{uj}(t) \\ &\quad + k_B N_{u+1,j}(t) \quad (j \text{ from } v+2 \text{ to } v+7) \quad (4.42) \end{aligned}$$

$$\begin{aligned} \frac{dN_{u,v+8}(t)}{dt} &= k_h \left(N_{u,v+7}(t) + N_{u,v+9}(t) + N_{u-1,v+8}(t) - 3N_{u,v+8}(t) \right) - (k_f + k_I)N_{u,v+8}(t) \\ &\quad + k_B N_{u+1,v+8}(t) \quad (4.43) \end{aligned}$$

$$\begin{aligned} \frac{dN_{u+1,v}(t)}{dt} &= k_h \left(N_{u,v}(t) + N_{u+1,v-1}(t) + N_{u+2,v}(t) - 3N_{u+1,v}(t) \right) - (k_f + k_I)N_{u+1,v}(t) \\ &\quad + k_B N_{u+1,v}(t) \quad (4.44) \end{aligned}$$

$$\begin{aligned} \frac{dN_{iv}(t)}{dt} &= k_h \left(N_{i-1,v}(t) + N_{i+1,v}(t) + N_{i,v-1}(t) - 3N_{iv}(t) \right) - (k_I + k_f)N_{iv}(t) \\ &\quad + k_B N_{i,v+1}(t) \quad (i \text{ from } u+2 \text{ to } u+5) \quad (4.45) \end{aligned}$$

$$\begin{aligned} \frac{dN_{u+6,v}(t)}{dt} &= k_h \left(N_{u+5,v}(t) + N_{u+7,v}(t) + N_{u+6,v-1}(t) - 3N_{u+6,v}(t) \right) - (k_f + k_I)N_{u+6,v}(t) \\ &\quad + k_B N_{u+1,v+1}(t) \quad (4.46) \end{aligned}$$

$$\begin{aligned} \frac{dN_{u+1,v+9}(t)}{dt} &= k_h \left(N_{u,v+9}(t) + N_{u+2,v+9}(t) + N_{u+1,v+10}(t) - 3N_{u+1,v+9}(t) \right) \\ &\quad - (k_f + k_I)N_{u+1,v+9}(t) + k_B N_{u+1,v+8}(t) \quad (4.47) \end{aligned}$$

$$\begin{aligned} \frac{dN_{i,v+9}(t)}{dt} &= k_h \left(N_{i+1,v+9}(t) + N_{i-1,v+9}(t) + N_{i,v+10}(t) - 3N_{i,v+9}(t) \right) - (k_I + k_f)N_{i,v+9}(t) \\ &\quad + k_B N_{i,v+8}(t) \quad (i \text{ from } u+2 \text{ to } u+5) \quad (4.48) \end{aligned}$$

$$\begin{aligned} \frac{dN_{u+6,v+9}(t)}{dt} &= k_h \left(N_{u+5,v+9}(t) + N_{u+7,v+9}(t) + N_{u+6,v+10}(t) - 3N_{u+6,v+9}(t) \right) \\ &\quad - (k_f + k_I)N_{u+6,v+9}(t) + k_B N_{u+1,v+8}(t) \quad (4.49) \end{aligned}$$

$$\begin{aligned} \frac{dN_{u+7,v+1}(t)}{dt} &= k_h \left(N_{u+7,v}(t) + N_{u+7,v+2}(t) + N_{u+8,v+1}(t) - 3N_{u+7,v+1}(t) \right) \\ &\quad - (k_f + k_I)N_{u+7,v+1}(t) + k_B N_{u+6,v+1}(t) \quad (4.50) \end{aligned}$$

$$\begin{aligned} \frac{dN_{u+7,j}(t)}{dt} = & k_h \left(N_{u+8,j}(t) + N_{u+7,j-1}(t) + N_{u+7,j+1}(t) - 3N_{u+7,j}(t) \right) - (k_f + k_I)N_{u+7,j}(t) \\ & + k_B N_{u+6,j}(t) \text{ (j from } v+2 \text{ to } v+7) \end{aligned} \quad (4.51)$$

$$\begin{aligned} \frac{dN_{u+7,v+8}(t)}{dt} = & k_h \left(N_{u+7,v+7}(t) + N_{u+7,v+9}(t) + N_{u+8,v+8}(t) - 3N_{u+7,v+8}(t) \right) \\ & - (k_f + k_I)N_{u+7,v+8}(t) + k_B N_{u+6,v+8}(t) \end{aligned} \quad (4.52)$$

For the core segments near the interface (orange area):

$$\begin{aligned} \frac{dN_{u+1,v+1}(t)}{dt} = & k_h \left(N_{u+1,v+2}(t) + N_{u+2,v+1}(t) - 2N_{u,v+1}(t) \right) - (k_f + 2k_B)N_{u,v+1}(t) \\ & + k_I(N_{u,v+1}(t) + N_{u+1,v}(t)) \end{aligned} \quad (4.53)$$

$$\begin{aligned} \frac{dN_{u+1,j}(t)}{dt} = & k_h \left(N_{u+1,j+1}(t) + N_{u+1,j-1}(t) - 2N_{u+1,j}(t) \right) - (k_f + k_B)N_{u,j}(t) \\ & + k_I N_{u,j}(t) \text{ (j from } v+2 \text{ to } v+7) \end{aligned} \quad (4.54)$$

$$\begin{aligned} \frac{dN_{u+1,v+8}(t)}{dt} = & k_h \left(N_{u+1,v+7}(t) + N_{u+2,v+8}(t) - 2N_{u+1,v+7}(t) \right) - (k_f + 2k_B)N_{u+1,v+8}(t) \\ & + k_I(N_{u,v+8}(t) + N_{u+1,v+9}(t)) \end{aligned} \quad (4.55)$$

$$\begin{aligned} \frac{dN_{i,v+1}(t)}{dt} = & k_h \left(N_{i+1,v+1}(t) + N_{i-1,v+1}(t) - 2N_{i,v+1}(t) \right) - (k_f + k_B)N_{i,v+1}(t) \\ & + k_I N_{i,v}(t) \text{ (i from } u+2 \text{ to } u+5) \end{aligned} \quad (4.56)$$

$$\begin{aligned} \frac{dN_{i,v+8}(t)}{dt} = & k_h \left(N_{i+1,v+8}(t) + N_{i-1,v+8}(t) - 2N_{i,v+8}(t) \right) - (k_f + k_B)N_{i,v+8}(t) \\ & + k_I N_{i,v+9}(t) \text{ (i from } u+2 \text{ to } u+5) \end{aligned} \quad (4.57)$$

$$\begin{aligned} \frac{dN_{u+6,v+1}(t)}{dt} = & k_h \left(N_{u+5,v}(t) + N_{u+6,v+2}(t) - 2N_{u+6,v+1}(t) \right) - (k_f + 2k_B)N_{u+6,v+1}(t) \\ & + k_I(N_{u+6,v}(t) + N_{u+7,v+1}(t)) \end{aligned} \quad (4.58)$$

$$\begin{aligned} \frac{dN_{u+6,j}(t)}{dt} = & k_h \left(N_{u+6,j+1}(t) + N_{u+6,j-1}(t) - 2N_{u+6,j}(t) \right) - (k_f + k_B)N_{u+6,j}(t) \\ & + k_I N_{u+7,j}(t) \text{ (j from } v+2 \text{ to } v+7) \end{aligned} \quad (4.59)$$

$$\begin{aligned} \frac{dN_{u+6,v+8}(t)}{dt} = & k_h \left(N_{u+6,v+7}(t) + N_{u+5,v+8}(t) - 2N_{u+6,v+8}(t) \right) - (k_f + 2k_B)N_{u+6,v+8}(t) \\ & + k_I(N_{u+7,v+8}(t) + N_{u+6,v+9}(t)) \quad (4.60) \end{aligned}$$

For the rest crown segments:

$$\begin{aligned} \frac{dN_{ij}(t)}{dt} = & k_h \left(N_{i-1,j}(t) + N_{i+1,j}(t) + N_{i,j-1}(t) + N_{i,j+1}(t) - 4N_{ij}(t) \right) \quad (i, j \\ & \in \text{other crown segments}) \quad (4.61) \end{aligned}$$

Transported hot exciton (N_h) was calculated as the percentage of the relaxed ionized electron in the core region near the interface:

$$\frac{dN_h}{dt} = \sum_{j=v+1}^{v+8} k_f [N_{u+1,j}(t) + N_{u+6,j}(t)] + \sum_{i=u+2}^{u+5} k_f [N_{i,v+1}(t) + N_{i,v+8}(t)] \quad (4.62)$$

We solved the diffusion equations above numerically and used Eq. 4.62 to fit the percentage of hot exciton transport (ϕ_{HET}) of CC1 to CC4 at different pump wavelength (as listed in Table 4.4) by tuning the k_h , k_I , and k_B . The simulated hot exciton transport kinetics of CC1 to CC4 at different pump wavelength according to Eq. 4.62 are shown in Figure 4.14. The fitting parameters and errors with estimated percentage of hot exciton transport ($\phi_{\text{HET, Est}}$) are listed in Table 4.5.

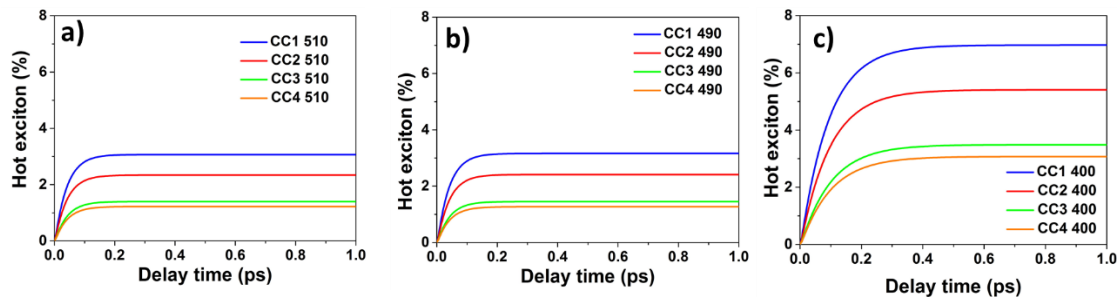


Figure 4.14. The simulated hot exciton transport kinetics of CC1 to CC4 at (a) 510 nm, (b) 490 nm, and (c) 400 nm excitation.

Table 4.5. The fitting parameters and errors with the estimated $\phi_{\text{HET}} / \%$

	510 nm pump	490 nm pump	400 nm pump
k_h/ps^{-1}	200 ± 12	230 ± 13	308 ± 16
$D_h/(\text{cm}^2/\text{s})$	5.6 ± 0.4	6.4 ± 0.4	8.6 ± 0.5
k_l/ps^{-1}	100 ± 10	103 ± 10	291 ± 15
k_B/ps^{-1}	330 ± 20	330 ± 20	330 ± 20
CC1 $\phi_{\text{HET, Est}} / \%$	3.1 ± 0.2	3.2 ± 0.2	7.0 ± 0.3
CC2 $\phi_{\text{HET, Est}} / \%$	2.3 ± 0.2	2.4 ± 0.2	5.4 ± 0.3
CC3 $\phi_{\text{HET, Est}} / \%$	1.4 ± 0.2	1.5 ± 0.2	3.5 ± 0.3
CC4 $\phi_{\text{HET, Est}} / \%$	1.2 ± 0.2	1.3 ± 0.2	3.1 ± 0.3

Chapter 5. Area- and Thickness-Dependent Biexciton Auger Recombination in CdSe Nanoplatelets

Reproduced with permission from *Nano Lett.* **2017**, *17*, 3152. Copyright 2017 American Chemical Society.

5.1. Introduction

Compared to zero-dimensional (0D) quantum dots (QDs) and one-dimensional (1D) nanorods (NRs), two-dimensional (2D) zinc-blend CdSe nanoplatelets (NPLs) have sharper absorption and emission peaks (due to a more uniform quantum confinement), larger absorption cross-section (due to larger lateral dimension), and larger radiative decay rate (due to strong dielectric confinement).^{19-21, 26, 31} Owing to these novel properties, CdSe NPLs have shown great potentials as low gain threshold lasing materials.^{30-34, 146} Optical gain threshold is determined in part by the lifetime of multiple exciton states.³¹ Multi-excitons decay predominantly by Auger recombination, in which an electron-hole pair recombines non-radiatively by exciting a third particle (electron or hole) to a higher energy level to conserve energy and momentum.^{16, 30-33, 95, 146, 197-198} In addition to its importance in lasing applications, Auger recombination of excitons also affects many other important properties of semiconductors, such as carrier multiplication,^{29, 80, 82, 84, 90, 199-201} and multi-exciton dissociation.^{76, 78-79} However, unlike Auger recombination times in QDs and NRs, which have been reported to follow “universal volume scaling law”,^{29, 90, 96-99} the dependence of Auger recombination time on size, thickness and volume in 2D NPLs and other 2D materials remains unclear. Further study of Auger recombination in CdSe NPLs is required for both fundamental

understanding of exciton-exciton interaction in low dimensional materials and rational material engineering for better lasing and other applications.

In this chapter, we report a systematic study of the dependence of biexciton Auger recombination lifetime on the lateral size and thickness of CdSe NPLs at room temperature *via* transient absorption (TA) spectroscopy. We show that the biexciton Auger lifetime increases linearly with the lateral area for NPLs of the same thickness but depends much more strongly on the thickness d (scaling nearly linearly with d^7). The biexciton Auger lifetimes do not show a simple dependence on NPL volumes, inconsistent with the “universal volume scaling law” reported for QDs.^{29, 90, 96-99} The observed dependence can be well explained by a model that accounts for both lateral size dependent collision frequency and thickness dependent Auger recombination probability.

5.2. Results and Discussion

5.2.1. Sample characterization

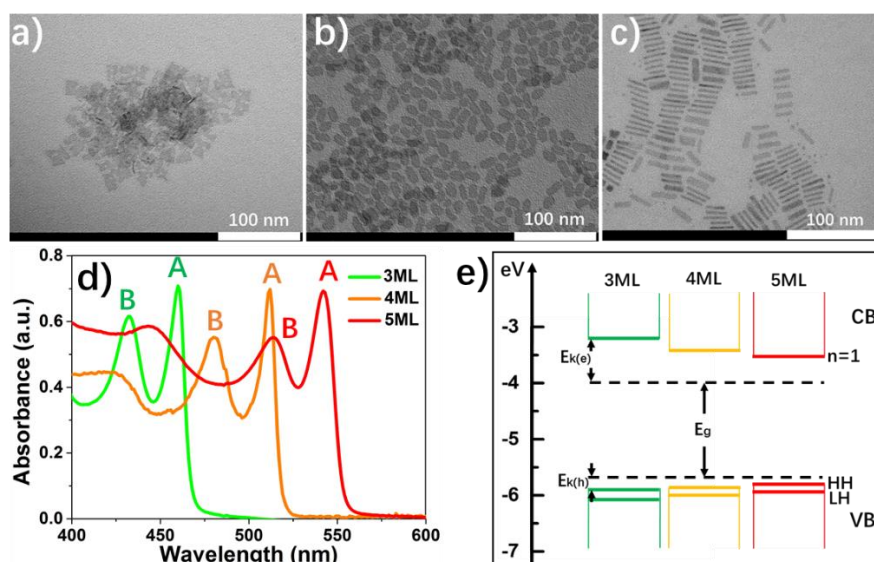


Figure 5.1. TEM images of (a) 3MLb, (b) 4MLc, and (c) 5MLb CdSe NPL samples. (d) Absorption spectra of CdSe NPLs. (e) Schematic energy levels of CdSe NPLs.

The colloidal zinc-blend CdSe NPLs with different thicknesses and lateral sizes were synthesized following reported procedures with slight modifications.²¹ The thickness of CdSe NPLs was tuned by changing the amount of Cd precursors and synthesis temperature while the lateral size was mainly controlled by the reaction time. Because of zinc-blend structure, NPLs with n monolayers (MLs) of CdSe contain n Se layers and $n+1$ Cd layers, with Cd as the terminating layers. NPLs with 3, 4, 5 CdSe MLs were prepared, which correspond to thicknesses of ~ 1.5 , ~ 1.8 and ~ 2.1 nm, respectively.^{21, 32, 143, 165} For each thickness, NPLs with different lateral area (x) were also prepared, producing a set of samples labeled as $n\text{ML}_x$ ($n=3$, $x=a, b$; $n=4$, $x=a-d$; $n=5$, $x=a, b$). TEM images of 3ML_b , 4ML_c and 5ML_b are shown in Figure 5.1a, 5.1b, and 5.1c, respectively, and TEM images of all other samples are shown in Figure 5.4 in Appendix 5.1. These images show that the NPLs have approximately rectangular shapes with length and width ranging from 11.9 ± 2.1 to 32.6 ± 3.5 nm, and from 4.8 ± 1.0 to 10.6 ± 2.9 nm, respectively (see Table 5.1 in Appendix 5.1 for details). The thickness of these samples was determined from the exciton peak positions in their UV-Vis absorption spectra (see below).

The UV-Vis absorption spectra (Figure 5.1d) show sharp A exciton (~ 460 , ~ 512 , ~ 546 nm) and B exciton (~ 431 , ~ 480 , ~ 520 nm) peaks for 3, 4, 5 ML CdSe NPLs, respectively. These exciton bands can be attributed to electron-heavy hole (e-hh) and electron-light hole (e-lh) exciton transitions, respectively.²¹ The conduction (CB) and valence (VB) band edge positions of these NPLs can be estimated from these exciton peak positions, reported bulk band edge and band gap (E_g), and estimated electron ($E_{k(e)}$) and hole ($E_{k(h)}$) quantum confinement energy, as shown in Figure 5.1e.^{21, 61, 144-145} Similar to the estimation in Chapter 3&4, the estimated conduction band (CB) and valence band (VB) edge positions for 3ML, 4ML, and 5ML CdSe NPLs are -3.20 eV, -3.41 eV, -3.53 eV, and -5.87 eV, -5.82 eV, -5.79 eV, respectively. The light hole levels for 3ML, 4ML, and 5ML NPLs are calculated as -6.05 eV,

-5.96 eV, and -5.91 eV, respectively, according to the energy difference between A and B exciton (see Appendix 5.2 for details).

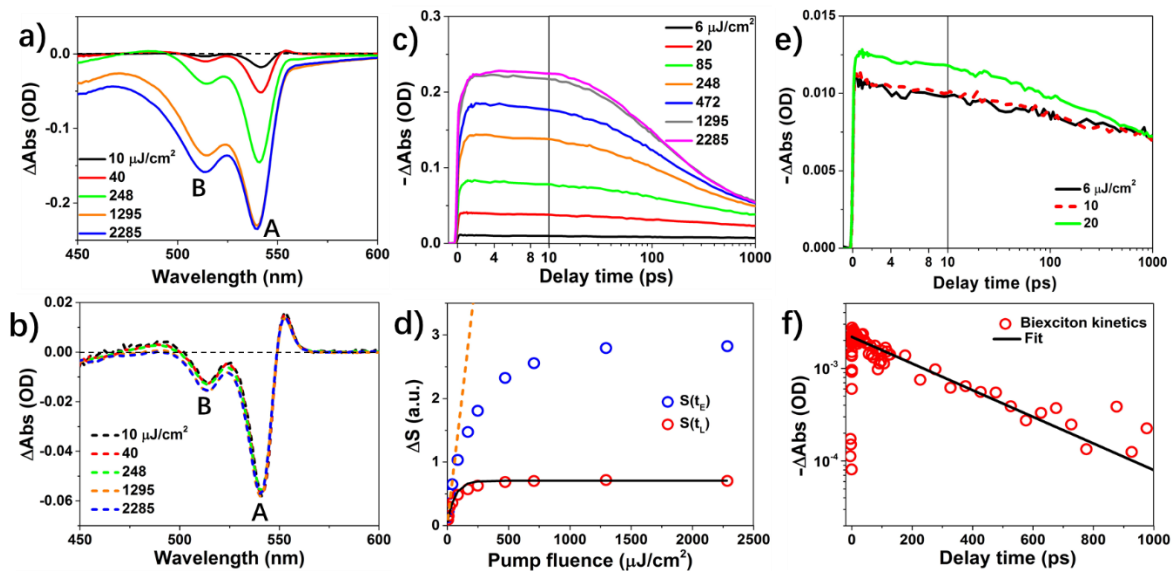


Figure 5.2. Transient absorption (TA) spectra and kinetics of 5MLb NPLs. TA spectra at (a) early delay time (2-4 ps) and (b) long delay time (800-1000 ps) at indicated pump fluences. (c) A exciton bleach kinetics at indicated pump fluences. (d) Normalized A exciton bleach amplitude at early (2-4 ps, blue circles) and long (800-1000 ps, red circles) delay times. The solid line shows a fit to the probability of excited NPLs at long delay time (800-1000 ps) according to a Poisson distribution model (see Appendix 5.3). The dashed line represents the initial average number of excitons per NPL as a function of pump fluence. (e) Comparison of normalized A exciton kinetics at low pump fluences ($<20 \mu\text{J}/\text{cm}^2$). These kinetics have been scaled to the same amplitude at long delay time (800-1000ps). (f) Biexciton decay kinetics (circles) and fit (solid line).

5.2.2. Transient absorption spectroscopy on colloidal CdSe NPLs

To quantify biexcitons Auger recombination time, we carried out TA study of exciton dynamics in CdSe NPLs (dissolved in hexane) as a function of lateral sizes and thicknesses at

room temperature. Figure 5.2a shows the TA spectra of 5MLb sample at different pump fluences at early delay time (t_E at 2-4 ps). At t_E , the exciton bleach amplitude reaches the maximum, because hot excitons have relaxed to the band edge and multi-exciton recombination is negligible. According to our previous work on cadmium chalcogenide NPLs, both A (~546 nm) and B (~515 nm) exciton bleach signals are due to the electron state-filling at the CB edge, directly probing the dynamics of CB edge electrons.^{62, 69, 109} The contribution of VB hole state-filling to the exciton bleach signals is negligible due to degeneracy and strong mixing between denser VB hole levels, similar to cadmium chalcogenide quantum dots and nanorods.^{78, 110, 148} A comparison of TA spectra of at different pump fluences at long delay time (t_L at 800-1000 ps), as shown in Figure 5.2b, reveals that these spectra are identical upon applying a power dependent scaling factor, indicating that at t_L multi-exciton annihilation has completed and only single excitons remain in excited NPLs. A comparison of the A exciton bleach kinetics at different pump fluences (Figure 5.2c) show that kinetics are dependent on the excitation power at pump fluence $<1295 \mu\text{J}/\text{cm}^2$, reflecting the pump fluence dependence of the number of excitons per NPL in the sample. At higher pump fluences, the A exciton bleach kinetics saturates, indicating the saturation of the number of initially generated A excitons in these samples.

The pump fluence dependence of the TA signal amplitude can be better seen in Figure 5.2d, which shows the normalized A exciton bleach amplitude (ΔS) of 5MLb at early (blue circles) and long (red circles) delay time as a function of pump fluence. These amplitudes are normalized according to the following model. At high pump fluence ($>1295 \mu\text{J}/\text{cm}^2$), A exciton bleach amplitude at long delay time saturates, indicating that all NPLs are excited. According to the kinetics at single exciton conditions (pump fluence of $6 \mu\text{J}/\text{cm}^2$, Figure 5.2e), only 70.5% of the excited NPL population remains at excited state at long delay time. Thus, the saturated A exciton bleach amplitude at long delay time (800-1000 ps) is normalized to 0.705 (by a

scaling factor), to reflect the probability of finding excited NPLs at that time. The A exciton bleach amplitude at early delay time (2-4 ps) is normalized by the same scaling factor to represent the average initial number of A excitons per NPL. Assuming a Poisson distribution of the initial number of excitons, the normalized A exciton bleach amplitude as a function of pump fluence at long delay time can be fitted (black solid line) to obtain the average exciton number per NPL ($\langle N \rangle$) as a function of pump fluence (orange dashed line). The details of the fitting procedure can be found in the Appendix 5.3.

Biexciton Auger recombination kinetics can be obtained by normalizing the A exciton bleach kinetics at low pump fluence ($<20 \mu\text{J}/\text{cm}^2$) to the same value after 500 ps, as shown in Figure 5.2e. Below $10 \mu\text{J}/\text{cm}^2$, normalized A exciton kinetics is pump fluence independent, indicating that the TA signal is dominated by single exciton kinetics. At $20 \mu\text{J}/\text{cm}^2$ pump fluence, in addition to the single exciton decay observed at lower fluences, the normalized kinetics show a faster decay component, which can be attributed to biexciton decay kinetics. From the estimated average exciton number per NPL of 0.33 at $20 \mu\text{J}/\text{cm}^2$ (Figure 5.2d), the number of excited NPLs with single, bi-exciton and higher-exciton (>2) states are 84.4%, 13.9% and 1.7% according to the Poisson distribution, indicating that A exciton bleach signal is dominated by the contributions of single and bi-exciton states. The pure biexciton kinetics (Figure 5.2f) can be obtained by subtracting the normalized single exciton kinetics at $6 \mu\text{J}/\text{cm}^2$ from the normalized kinetics (single + bi- exciton) at $20 \mu\text{J}/\text{cm}^2$. The bi-exciton decay kinetics can be fitted to a single exponential function (black solid line) to obtain the biexciton lifetime of 380.8 ± 25.0 ps for 5MLb. The details of the procedure can be found in Appendix 5.4.

5.2.3. Lateral size and thickness dependent Auger recombination

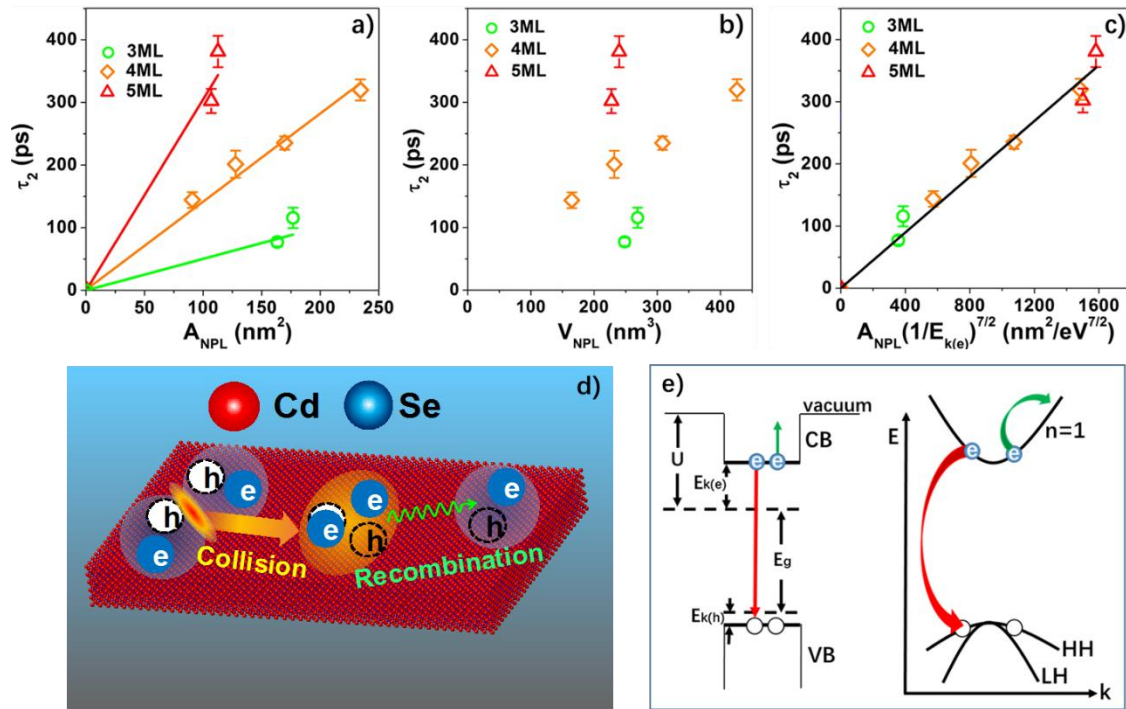


Figure 5.3. Size and thickness dependence of biexciton lifetimes in NPLs. (a) Biexciton lifetime (symbols) as a function of NPL lateral area (A_{NPL}) and their linear fits for 3, 4 and 5 ML NPLs. (b) Biexciton lifetime of different NPL samples as a function of NPL volume (V_{NPL}). (c) Biexciton lifetime of different NPL samples as a function of the product of NPL lateral area (A_{NPL}) and the reciprocal of electron quantization energy ($E_{k(e)}$) to the 7/2 order. The black solid line is the best linear fit according to Eq. 5.3. (d) Schematic of bi-exciton annihilation process in colloidal CdSe NPLs, showing both the collision and Auger recombination processes (e) Relevant energy levels and band diagrams in exciton Auger recombination process in NPLs.

The biexciton lifetimes of all other CdSe NPL samples (see Table 5.3 in Appendix 5.4) were extracted using the same method as discussed above. As shown in Figure 5.3a, bi-exciton lifetimes increase linearly with NPL lateral area (A_{NPL}) with a slope that increases with NPL thickness. For NPLs with similar lateral area, the bi-exciton recombination time increases with NPL thickness. Biexciton lifetimes in many 0D QDs have been reported to increase linearly

with volume, following the so-called “universal volume scaling law”.^{29, 96-99} A plot of the biexciton Auger lifetimes as a function of volume (Figure 5.3b) shows no obvious relationships. For NPLs of similar volume ($\sim 250 \text{ nm}^3$), the lifetime increases from $\sim 77 \text{ ps}$ in 3ML NPLs to $\sim 380 \text{ ps}$ in 5ML NPLs, showing a sensitive dependence on NPL thickness. These data clearly show that biexciton lifetimes in NPLs increase with both area and thickness, and these dependences cannot be understood by considering the volume change alone. Our measured biexciton lifetimes of CdSe NPLs are consistent with recent reported values of CdSe NPLs *via* TA measurements,¹⁴⁶ and time-resolved photoluminescence (TR-PL) measurements with time resolution of $\sim 10 \text{ ps}$,⁹⁵ but are much shorter than the earlier reported values measured by TR-PL, which is $\sim 14 \text{ ns}$ for 5 ML CdSe NPLs with similar lateral dimension ($\sim 150 \text{ nm}^2$).²⁶ The origin for this deviation is unclear, although the latter TR-PL measurement has a much slower instrument response function, IRF, of $\sim 150 \text{ ps}$,²⁶ approaching the biexciton lifetime of NPLs.

We now consider Auger recombination models that can describe the observed size and thickness dependences of biexciton lifetimes. Although excitons in NPLs are strongly quantum confined in the thickness direction, they are free to move in the lateral direction (within the plane of the NPL). Furthermore, due to strong e-h Coulomb interaction, an e-h pair is strongly bound and is expected to move together as an exciton at room temperature. Thus, as shown in Figure 5.3d, bi-exciton Auger recombination involves the binary collision of two excitons to form a bi-exciton complex and Auger recombination within the complex. Chapter 3&4 have shown that in CdTe and CdS NPLs, the exciton diffusion constants ($\sim 2.5 \text{ cm}^2/\text{s}$) are near their values in bulk crystals, and excitons can diffuse throughout NPLs of $10 \text{ nm} \times 10 \text{ nm}$ area within $\sim 1.1 \text{ ps}$, which is much shorter than the measured Auger recombination time.⁶⁸⁻⁶⁹ Thus, Auger recombination times in CdSe NPLs are not exciton diffusion rate limited, which is consistent

with a previous report,²⁶ suggesting that Auger recombination of biexcitons likely requires many binary collisions of excitons.

Following a previous model for exciton Auger recombination in 1D materials,⁹² we propose that the exciton-exciton Auger recombination time of a N exciton state is given by:

$$\frac{1}{\tau_N} = F_C P_{\text{Aug}} = a\bar{v} \frac{(N-1)N}{A_{\text{NPL}}} P_{\text{Aug}} \quad (5.1)$$

where F_C is the binary collision frequency between 2D excitons, P_{Aug} is the Auger recombination probability per collision, a is the diameter of a 2D exciton, \bar{v} is the average relative motion velocity of exciton center of mass. The details of the derivation of F_C are provided in Appendix 5.5. According to Eq. 5.1, the observed linear increase of Auger lifetime with NPL lateral area (Figure 5.3a) reflects the fact that the binary collision frequency decreases at larger NPL size for biexciton states.

According to Eq. 5.1, the NPL thickness dependent slopes in Figure 5.3a reflect thickness dependent Auger recombination probabilities (P_{Aug}). Because exciton lateral motion has a well-defined momentum in NPLs, Auger recombination should satisfy both energy and momentum conservation, similar to the extensively studied multiple-well quantum well materials (with much larger lateral sizes of a few μms) produced by molecular beam epitaxy.²⁰²⁻²⁰³ According to an earlier theoretical study of InP/InGaAsP/InP quantum wells (with InGaAsP sandwiched between InP), among all possible Auger recombination pathways for a biexciton state with two band edge excitons, the CCCH recombination pathway dominates (Figure 5.3e), in which the Auger process leads to a final state with an excited electron at a higher CB energy level. The Auger rate for CHHH pathway (involving the excitation of a heavy hole to higher heavy hole states) is much smaller because the large effective mass of heavy hole ($m_{\text{hh}}^*=0.45m_0$, $m_e^*=0.045m_0$) requires larger momentum increase, which is more difficult to satisfy.²⁰² The Auger rate for CHHL pathway (involving the excitation of a heavy hole to higher light hole state) is also much smaller because of the small hole wavefunction amplitude at the interface,

where Auger coupling matrix elements is the largest.²⁰² It is interesting to note that in 0D QDs Auger processes involving VB holes are often thought to be more efficient than those involving CB electrons due to a larger density of hole states.²⁰⁴⁻²⁰⁵ It is likely that in 0D QDs, quantum confinement in all three dimensions relaxes the requirement of momentum conservation in the Auger process, whereas in 2D quantum wells, electrons and holes still have well defined momentums in the non-quantum- confined dimension and the requirement of momentum conservation leads to very different dominating Auger pathways.

In light of similar band structures and ratios of electron and hole effective masses in CdSe ($m_e^*=0.18m_0$, $m_{lh}^*=0.19m_0$, $m_{hh}^*=0.89m_0$),²¹ it is reasonable to assume that the bi-exciton Auger recombination in CdSe NPLs also follows the bi-exciton CCCH pathway and the Auger probability P_{Aug} is given by:²⁰²

$$P_{Aug} \propto \frac{U}{kT} \left(\frac{E_{k(e)}}{E_g} \right)^{\frac{7}{2}} \quad (5.2)$$

where U is well depth (~ 4 eV), k Boltzmann constant, T temperature, $E_{k(e)}$ confinement energy of electron, and E_g bulk band gap (Figure 5.3e). Combining Eq. 5.1 and 5.2, the Auger recombination rate of a biexciton (N=2) state becomes:

$$\frac{1}{\tau_2} = C \frac{1}{A_{NPL}} \frac{U}{kT} \left(\frac{E_{k(e)}}{E_g} \right)^{\frac{7}{2}} \quad (5.3)$$

where C is a proportionality constant.

As shown in Figure 5.3c, the measured biexciton lifetime shows a linear dependence to the product of A_{NPL} and $(1/E_{k(e)})^{7/2}$, agreeing well with Eq. 5.3, the trend predicted by the CCCH recombination process. It is worth noting, if we consider electron quantization energy to be:

$E_{k(e)} = \frac{h^2}{8m_e^*d^2}$ (d is NPL thickness),²⁰² CCCH recombination time should be proportional to d^7 . Using d values of 1.52, 1.82, 2.13 nm for 3, 4, 5 ML NPLs as reported,²¹ biexciton lifetimes of CdSe NPLs show a reasonable linear dependence on $A_{NPL}d^7$ (see Figure 5.10 in Appendix

5.5), although the deviation is noticeably larger compared with the plot *vs.* $A_{\text{NPL}} (1/E_{\text{k}(\text{e})})^{7/2}$ (Figure 5.3b). This result suggests that treating electrons in NPLs as particles confined in an infinite potential well is qualitatively reasonable but quantitatively inaccurate for calculating the thickness dependent Auger recombination rates.

It is interesting to compare the size dependence of Auger recombination rates in 2D NPLs to other low dimensional nanocrystals, such as 0D QDs, and 1D NRs or nanotubes. Bi-exciton Auger recombination times in many direct and indirect band gap 0D QDs, such as CdSe, PbSe, InAs, and Ge QDs, have been reported to scale with R^3 (R is QD radius), following a “universal volume scaling law”.^{29, 96-99} Although this volume dependence may resemble the concentration dependence of Auger lifetimes in bulk materials, the physical meaning for such comparison is unclear, since 0D excitons are confined in nanocrystal volume and interact with each other without diffusion or collision process. The QD volume dependence has been attributed to three possible reasons: (1) $1/R$ dependence of the degree of confinement-induced mixing of different momentum states;²⁰⁶⁻²⁰⁸ (2) $1/R$ dependence of Coulomb coupling of biexcitons; and finally (3) $1/R$ dependence of surface-to-volume ratio (with surface enhancing the Auger process).⁹⁶ Deviations from the “universal volume scaling law” have also been reported. Theoretical studies have shown that abrupt confinement potentials, which break strict momentum conservation, enhance the Auger recombination rate, while smooth confinement potentials suppress Auger recombination.^{89, 209-212} The latter has been confirmed in core/shell QDs with alloyed interface, which leads to suppressed QD blinking (caused by Auger ionization).²¹³⁻²¹⁵ For CdSe QDs with an abrupt 3D confinement potential, the Auger recombination lifetime is calculated to be $R^{4.5}$ dependent,²⁰⁹ giving rise to “superlinear volume scaling”. It should be noted that the dependence of Auger rates on interface sharpness in core/shell QDs has also been attributed to variations in interfacial hole traps.²¹⁶ Moreover, “sublinear volume scaling” of

biexciton lifetime in CsPbX (X=Br or I) perovskite QDs has also been reported recently, although the origin for this dependence remains unclear.²¹⁷

Our result suggests that the “universal volume scaling law”, which has been reasonably successful for accounting Auger lifetime trend in QDs, does not hold for 2D NPLs. Our result is consistent with the trend of Auger lifetimes in 1D materials. A theoretical model similar to Eq. 5.1 has been proposed for carbon nanotubes (NTs), in which the calculated Auger recombination rate is proportional to E_b^3/L (E_b is the exciton binding energy and L the NT length).⁹² The inverse length dependence of Auger recombination rate reflects the length dependent collision frequency of 1D excitons. This model is supported by the experimental observation of a linear increase of biexciton Auger lifetime on rod length in PbSe NRs.⁹⁰ The dependence on binding energy is attributed to the fact the strongly bound excitons involve large momentum states, which facilitates momentum conservation in the Auger process. We speculate that similar reasons can be invoked to explain the observed increase of Auger recombination rates in thinner NPLs of similar area or volume (Figure 5.3a&b), because the exciton binding energy also increases in thinner NPLs.^{61, 145}

Although the number of examples is still limited, biexciton Auger recombination rates in 1D and 2D materials appear to be consistent with a model that accounts for both exciton collision and Auger recombination steps, as described above. In 1D and 2D materials, the concept of volume dependence appears to be not useful, because there are two very different dependences on the quantum confined (thickness in 2D and diameter in 1D materials) and non-confined (lateral area in 2D and length in 1D materials) dimensions and their dependences should be considered separately. The size dependence in the non-confined dimension can be accounted for by the binary collision frequency for forming bi-exciton complexes, which gives rise to $1/\text{area}$ and $1/\text{length}$ dependences of Auger recombination rate in 2D and 1D materials, respectively. The dependence on the quantum-confined dimension reflects how the Auger

recombination probability of bi-exciton complexes is enhanced by quantum confinement. We argue that 2D NPLs are an ideal model system for testing how size, interface and confinement affect Auger recombination rates because these parameters can be tuned independently. For example, the lateral size of the NPLs can be changed to tune the area/volume without affecting the degree of quantum confinement or surface curvature. Similarly, the degree of quantum confinement can be tuned while maintaining the volume or lateral area. Although similar independent tunings can in principle be done in 1D nanorods, it is practically difficult to achieve uniform rod diameter throughout the length of the nanorod and to maintain the same diameter while tuning the rod length. Although we have only presented an *ad hoc* model to account for the trend, we hope our results will motivate comprehensive theoretical studies that can quantitatively explain the observed rates, their dependence on lateral size and thickness, and the general applicability of the proposed model.

5.3. Conclusion

In summary, we have studied the dependence of bi-exciton Auger recombination times of CdSe NPLs on their thicknesses and lateral areas by TA spectroscopy. Bi-exciton Auger lifetimes increase linearly with the NPL lateral area with slopes that increase with the NPL thickness. Interestingly, comparison of NPLs with different thicknesses shows that the Auger lifetime does not increase linearly with the NPL volume, contradictory to previous observations in QDs. The observed dependences can be explained by a model that accounts for both the frequency of binary exciton collision to form bi-exciton complexes and Auger recombination probability of the bi-exciton complexes. The linear increase of Auger lifetimes with NPL lateral areas reflects the $1/\text{area}$ dependence of exciton-exciton binary collision frequency. The change of Auger lifetimes on NPL thickness (d) can be well described by a linear dependence on $(1/E_{k(e)})^{7/2}$, and a nearly linear dependence on d^7 , indicating its strong dependence on the degree

of quantum confinement. Our results provide guidance for controlling Auger recombination rates through tailoring NPL lateral area and thickness. We suggest that the proposed model to account for the different dependences on the quantum confined and nonconfined dimensions may be generally applicable to many 1D and 2D materials. Furthermore, these NPLs are ideal model systems for critically testing exciton Auger recombination models in quantum confined low dimensional nanomaterials, because their size and degree of quantum confinement can be independently tuned.

Appendix 5.1

The TEM images and the lateral dimensions of CdSe nanoplatelets

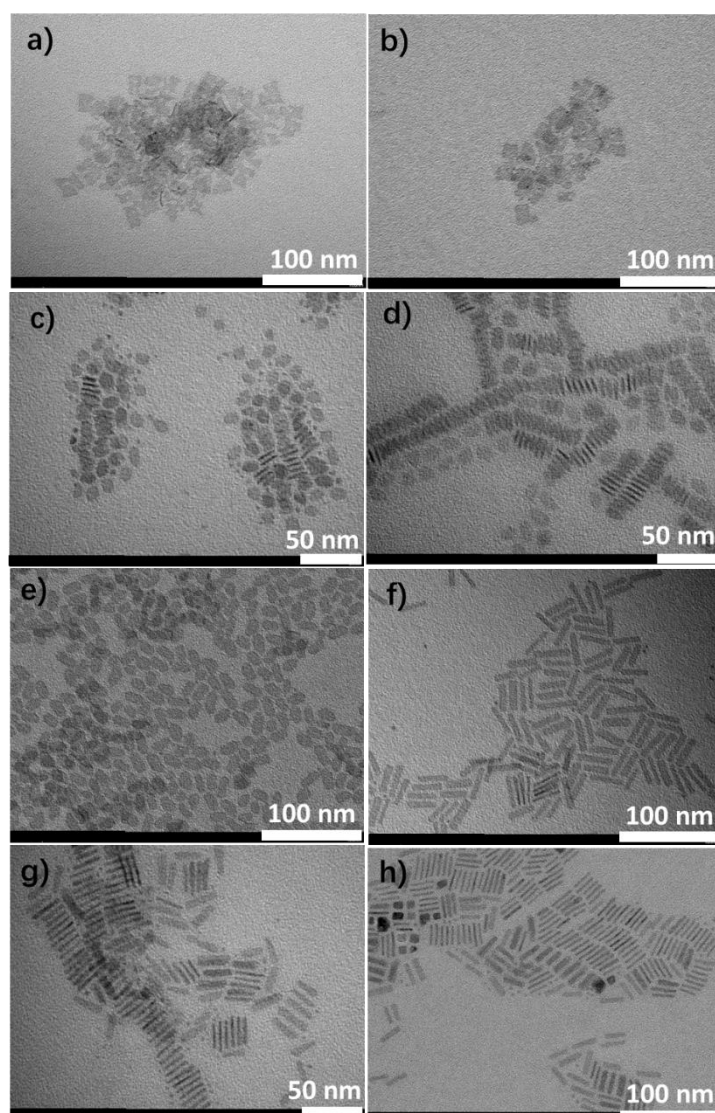


Figure 5.4. TEM images of NPL samples. (a) 3MLa, (b) 3MLb, (c) 4MLa, (d) 4MLb, (e) 4MLc, (f) 4MLd, (g) 5MLa, and (h) 5MLb.

Table 5.1. Averages and standard deviations (error bar) of length, width and area distributions of CdSe colloidal NPLs

	Length/nm	Width/nm	Area/nm ²
3MLa	16.7±3.3	9.8±1.9	163.4±50.5
3MLb	16.6±3.6	10.6±2.9	176.8±58.4
4MLa	11.9±2.1	7.6±0.9	90.5±21.4
4MLb	14.8±1.7	8.6±1.0	127.4±22.6
4MLc	18.0±2.7	9.4±1.0	169.4±35.0
4MLd	32.6±3.5	7.1±1.0	234.2±41.9
5MLa	22.5±2.9	4.8±1.0	106.8±26.9
5MLb	20.6±3.3	5.5±0.9	112.5±26.4

Appendix 5.2

Band edge position estimation of CdSe nanoplatelets

The band gaps of CdSe colloidal NPLs (E_{exciton}), given by the A exciton peak energy shown in absorption spectra, are 2.67, 2.41, and 2.26 eV for 3ML, 4ML, and 5ML NPLs, respectively. Considering only the quantum confinement effect on the band edge shifts, the E_{exciton} can be calculated as:^{21, 144, 218}

$$E_{\text{exciton}} = E_g + (E_{k(h)} + E_{k(e)}) \quad (5.4)$$

where E_g (1.7 eV) is the band gap of bulk CdSe with conduction band (CB) edge at -4.0 eV and valence band (VB) edge at -5.7 eV.^{21, 218} $E_{k(e)}$ and $E_{k(h)}$ are quantization energy of CB electrons and VB holes, respectively. We consider the electron and hole move freely in x-y plane but confined in z direction in NPL. The potential is set as zero and infinity inside and outside the NPL, respectively. Thus, the quantization energy of carriers in the NPL is:^{144, 218}

$$E_k = \frac{h^2 n^2}{8m^* d^2} \quad (5.5)$$

where m^* is the effective mass for electron or hole of CdSe NPLs, d is NPL thickness.

Therefore, the ratio of CB to VB edge shifts is equal to the ratio of electron to hole quantization energies and we calculated $E_{k(e)}$ ($E_{k(h)}$) as 0.80 (0.17), 0.59 (0.12), and 0.47 (0.09) eV for 3, 4, 5 ML NPLs. The CB (VB) edge position for 3ML, 4ML, and 5ML NPLs are then -3.20 eV (-5.87 eV), -3.41 eV (-5.82 eV), and -3.53 eV (-5.79 eV), respectively.

Appendix 5.3

Estimation of average exciton number per NPL according to Poisson distribution

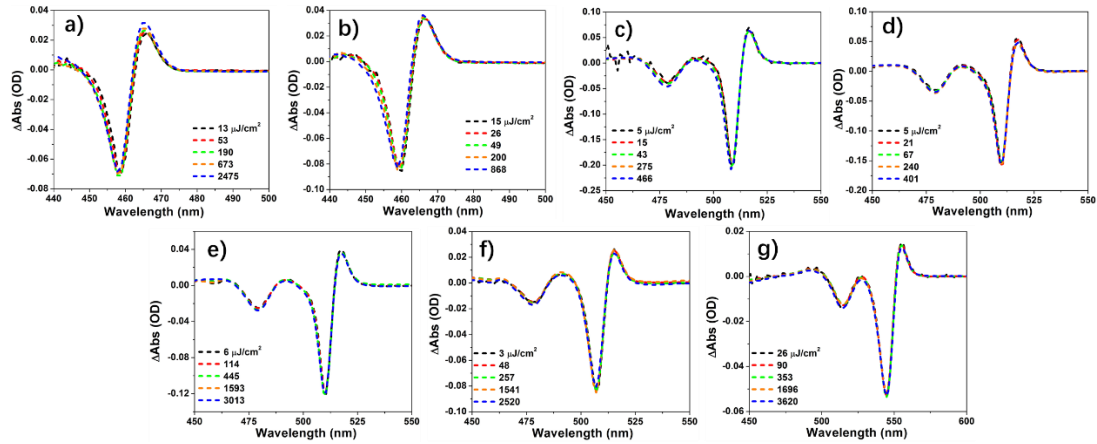


Figure 5.5. The normalized TA spectra at long delay time (800-1000 ps) at different pump fluences of (a) 3MLa, (b) 3MLb, (c) 4MLa, (d) 4MLb, (e) 4MLc, (f) 4MLd, and (g) 5MLa.

To estimate the average exciton number per NPL, we measured pump fluence dependent A exciton kinetics on different NPLs. At long delay time (800-1000 ps), when multiple exciton annihilation completed, only single exciton states remain. Indeed, as shown in Figure 5.5, the normalized TA spectra at 800-1000 ps measured at different pump fluences agreed well with each other in all NPL samples. The A exciton bleach amplitude at this long delay time as a function of pump fluence can be used to calculate the average exciton numbers per NPL, following previously published procedure.⁷⁶ Generally, the probability of finding NPLs with n absorbed photons is governed by the Poisson distribution:

$$P_n(m) = \frac{m^n e^{-m}}{n!} \quad (5.6)$$

where m is the average number of photons absorbed per NPL. m can be related to the pump fluence (I) through a scaling factor C that is dependent on the absorption cross section:

$$m(I) = CI \quad (5.7)$$

At long delay time (t_L), all multiple excitons have annihilated, and only single exciton states remained. Therefore, at long delay time, the TA signal amplitudes ($\Delta A(\lambda, t_L)$) are proportional to the number of excited NPLs: $\gamma(1 - P_0(m))$, where γ is the percentage of excited NPLs remained at long delay time caused by the decay of single exciton states, and can be determined from the A exciton kinetics at lowest pump fluence. We define the normalized TA signal at long delay time as:

$$\Delta S(\lambda, t_L) = \frac{\Delta A(\lambda, t_L)}{\alpha(\lambda)} = \gamma(1 - P_0(m)) = \gamma(1 - e^{-m}) = \gamma(1 - e^{-CI}) \quad (5.8)$$

where λ is wavelength. These normalized TA signals represent the probability of finding excited NPLs in the solution sample. At high excitation intensities, when all NPLs were excited, $\Delta S(\lambda, t_L)$ approached γ from which the normalization factor $\alpha(\lambda)$ was determined. Fitting $\Delta S(t_L)$ at A exciton wavelength as a function of pump fluence I to Eq. 5.8 (black solid lines in Figure 5.3d and 5.6) yields the value of parameter C as listed in Table 5.2. From the parameter C , the average number of photons absorbed by NPL at any pump fluence (m) can be determined by Eq. 5.7 (orange dashed line in Figure 5.2d and 5.6).

Table 5.2. Fitting parameter C of all NPL samples

	C ($\text{cm}^2/\mu\text{J}$)
3MLa	0.0054
3MLb	0.0056
4MLa	0.0316
4MLb	0.0329
4MLc	0.0108
4MLd	0.0181

5MLa	0.0043
5MLb	0.0165

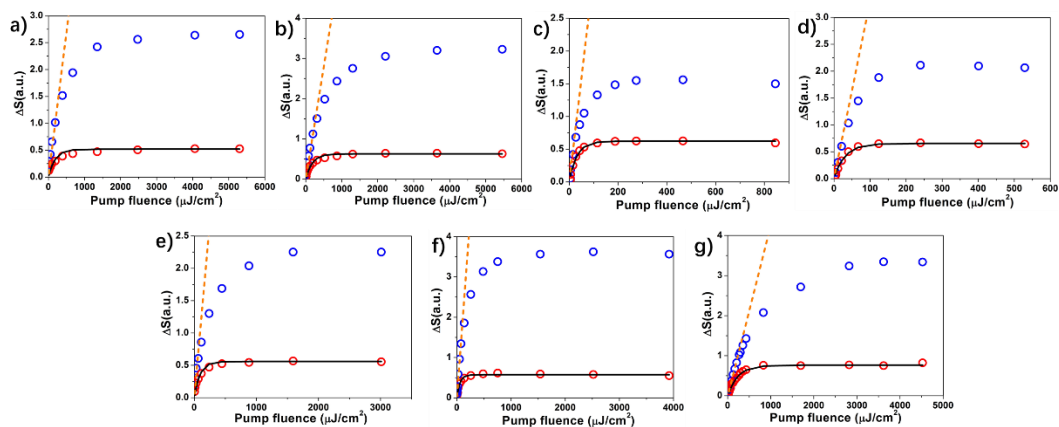


Figure 5.6. Normalized A exciton bleach amplitude (ΔS) at early (2-4 ps, blue circles) and long (800-1000 ps, red circles) delay times. (a) 3MLa, (b) 3MLb, (c) 4MLa, (d) 4MLb, (e) 4MLc, (f) 4MLd, and (g) 5MLa. The black solid lines are fit of ΔS at long delay time as a function of fluence to Eq. 5.8. Orange dashed lines are the average exciton number per NPL as a function of pump fluence obtained from the fit and Eq. 5.7.

Appendix 5.4

Measurement of biexciton lifetime

At low pump fluence, we consider conditions in which the TA signal is dominated by single and bi-excitons states, with probability of $\rho_1(t)$ and $\rho_2(t)$, respectively. Biexciton states decay to single exciton states with time constant of τ_2 , while single exciton states decay with a time constant of τ_1 . Then, the rate equations considering single and bi-exciton state decay are shown below:

$$\frac{d\rho_2(t)}{dt} = -\frac{1}{\tau_2}\rho_2(t) \quad (5.9)$$

$$\frac{d\rho_1(t)}{dt} = \frac{1}{\tau_2}\rho_2(t) - \frac{1}{\tau_1}\rho_1(t) \quad (5.10)$$

Solutions to Eq. 5.9 and 5.10 are:

$$\rho_2(t) = \rho_2(0)e^{-\frac{t}{\tau_2}} \quad (5.11)$$

$$\rho_1(t) = (\rho_1(0) + \frac{\tau_1}{\tau_1 - \tau_2}\rho_2(0))e^{-\frac{t}{\tau_1}} - \frac{\tau_1}{\tau_1 - \tau_2}\rho_2(0)e^{-\frac{t}{\tau_2}} \quad (5.12)$$

where $\rho_1(0)$ and $\rho_2(0)$ are initial probability of finding NPLs in single and bi-exciton states, respectively, which is assumed to be given by Poisson statistics. Because the A exciton (AX) bleach amplitude is proportional to the average electron concentration at NPL CB edge, its time dependence is given by:

$$AX(t) \propto [\rho_1(t) + 2\rho_2(t)] = (\rho_1(0) + \frac{\tau_1}{\tau_1 - \tau_2}\rho_2(0))e^{-\frac{t}{\tau_1}} + \left(2 - \frac{\tau_1}{\tau_1 - \tau_2}\right)\rho_2(0)e^{-\frac{t}{\tau_2}} \quad (5.13)$$

To extract τ_2 , we need to separate $e^{-\frac{t}{\tau_2}}$ (fast decay) from $e^{-\frac{t}{\tau_1}}$ (slower decay) term in A exciton bleach kinetics. Therefore, we normalized single exciton kinetics, which was obtained from A exciton bleach kinetics at the lowest pump fluence, and the A exciton kinetics at higher fluences when biexciton decay components also present, to the same value at long delay time (800-1000 ps) as shown in Figure 5.7. We subtracted the former from the latter to obtain the subtracted A

exciton bleach kinetics (S-AX), which only contains $e^{-\frac{t}{\tau_2}}$ term. Then, we fitted the decay part of S-AX kinetics with a single-exponential function to extract biexciton lifetime (τ_2) as shown in Figure 5.8. The fitting parameters and errors were shown in Table 5.3.

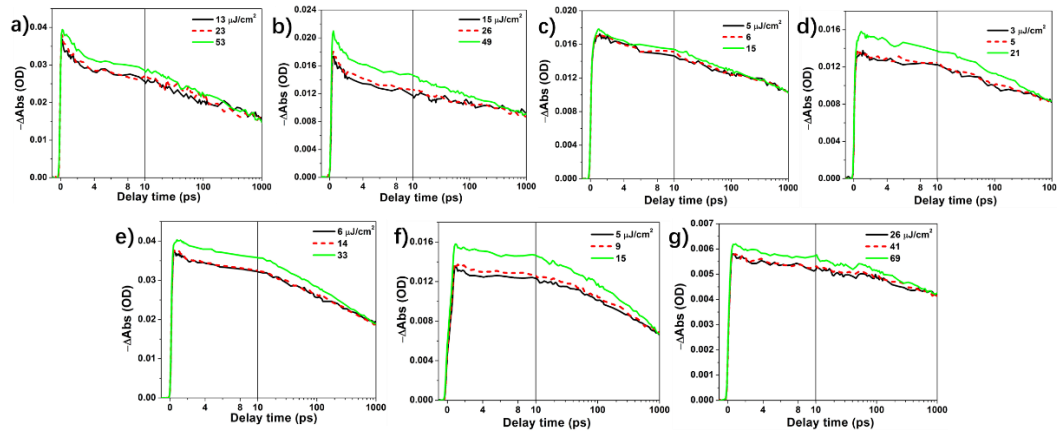


Figure 5.7. Normalized A exciton bleach kinetics at different pump fluences of (a) 3MLa, (b) 3MLb, (c) 4MLa, (d) 4MLb, (e) 4MLc, (f) 4MLd, and (g) 5MLa.

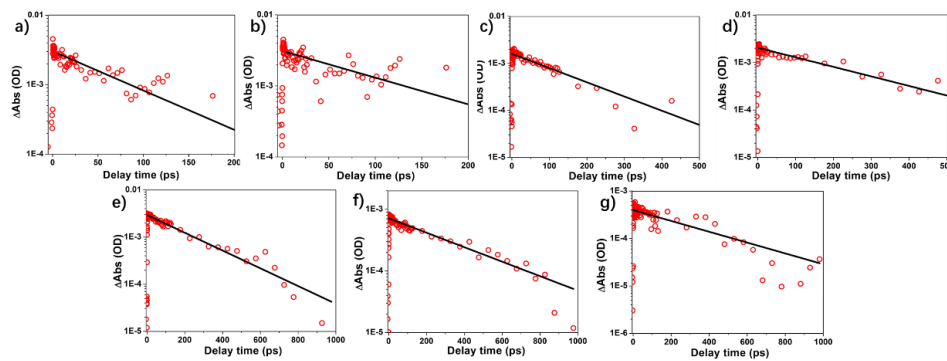


Figure 5.8. Subtracted A exciton bleach kinetics (red circles) and their single-exponential fits (black lines) of (a) 3MLa, (b) 3MLb, (c) 4MLa, (d) 4MLb, (e) 4MLc, (f) 4MLd, and (g) 5MLa.

Table 5.3. Biexciton lifetime and errors of all NPL samples.

	τ_2 (ps)
3MLa	77.00 ± 6.88
3MLb	115.7 ± 16.3
4MLa	143.7 ± 12.6
4MLb	201.3 ± 21.6
4MLc	235.4 ± 10.8
4MLd	320.1 ± 17.1
5MLa	302.1 ± 19.3
5MLb	380.8 ± 25.0

Appendix 5.5

2D bi-exciton Auger recombination rate

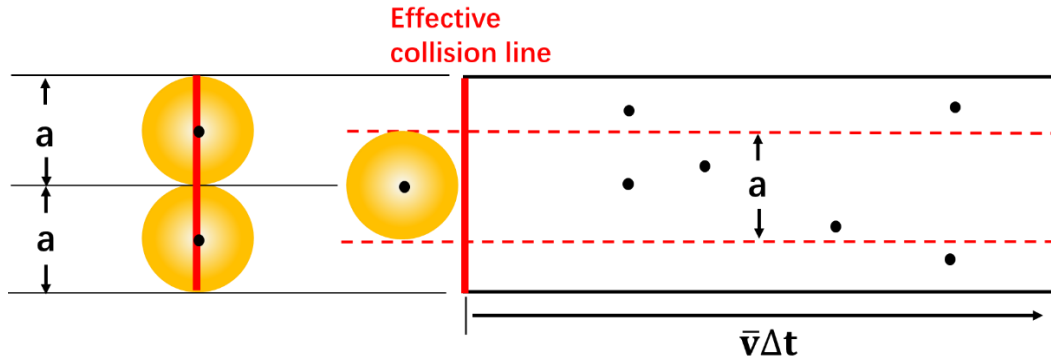


Figure 5.9. Scheme of 2D exciton collision theory.

As shown in Figure 5.9, we considered 2D excitons (orange circles) of CdSe NPLs have a diameter of a . Then, the effective cross-section for exciton collision in 2D system can be modeled by a line with a length of $2a$ (red solid lines), similar to effective collision area in molecular collision theory of a 3D system.²¹⁹⁻²²⁰ With an exciton in the middle of effective collision line, within time interval Δt , it can collide with any excitons whose center (black dots) is in the area of collisional square, S_C ,

$$S_C = 2a\bar{v}\Delta t \quad (5.14)$$

where \bar{v} is mean relative speed of excitons. The collision frequency, f_C , is

$$f_C = \frac{S_C(N-1)}{\Delta t A_{\text{NPL}}} = \frac{2a\bar{v}(N-1)}{A_{\text{NPL}}} \quad (5.15)$$

where N is number of excitons in a NPL with a lateral area of A_{NPL} .

The total binary exciton collision frequency is:

$$F_C = \frac{Nf_C}{2} = \frac{a\bar{v}(N-1)N}{A_{\text{NPL}}} \quad (5.16)$$

The Auger recombination rate constant for a N exciton state is:

$$\frac{1}{\tau_N} = F_C P_{\text{Aug}} = a\bar{v} \frac{(N-1)N}{A_{\text{NPL}}} P_{\text{Aug}} \quad (5.17)$$

where P_{Aug} is the Auger recombination probability per collision.

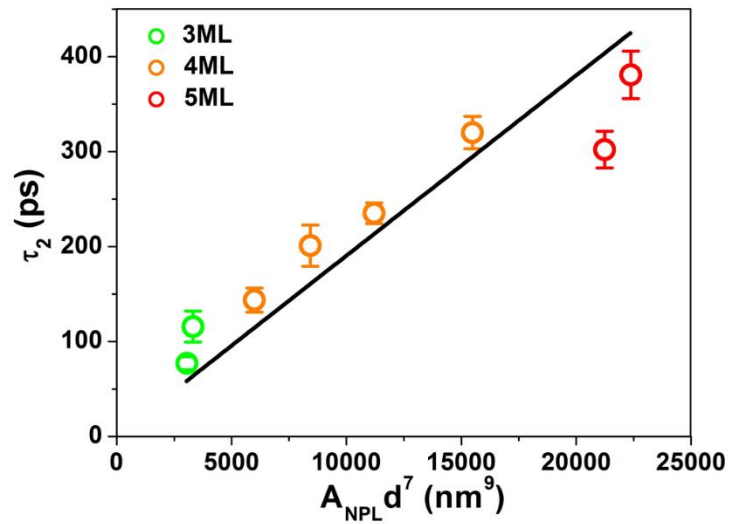


Figure 5.10. Biexciton lifetime of NPLs as a function of $A_{\text{NPL}}d^7$, where A_{NPL} and d are lateral area and thickness of NPLs, respectively. Black line is the linear fit.

Chapter 6. A Model for Optical Gain in CdSe Nanoplatelets

Reproduced with permission from *Chem. Sci.* **2018**, 9, 728. Copyright 2018 Royal Society of Chemistry.

6.1. Introduction

Cadmium chalcogenide nanoplatelets (NPLs), CdX (X=Se, S, Te), and their heterostructures have shown many novel properties, such as large absorption cross-sections, uniform 1D quantum confinement, long biexciton Auger lifetimes, and giant oscillator strength.^{19-21, 26, 61, 109, 145, 150, 155, 165, 181, 221-223} These materials have attracted intense interest for lasing applications due to reported large gain coefficients and low optical gain (OG) threshold.^{30-39, 146} For example, the reported threshold of amplified spontaneous emission (ASE) of CdSe NPLs is as low as $6 \mu\text{J}/\text{cm}^2$,¹⁴⁶ which is over an order of magnitude lower than that in cadmium chalcogenide quantum dots (QDs) or QD heterostructures.¹⁵⁻¹⁶ Although OG models for QDs are well understood, it is unclear whether they are applicable to 1D nanorods (NRs) and 2D NPLs, because of fundamental differences in their exciton properties. In 0D QDs, excitons are confined in all three dimensions, whereas in 2D NPLs and 1D NRs, excitons are free to move in the plane and along the long axis, respectively, which increases the degree of degeneracy of band edge exciton states and may alter their gain mechanism. So far, there lacks an OG model for 2D NPLs or 1D NRs, and reasons for the superior OG properties in NPLs remain unclear. In addition, many other interesting differences between NPLs and QDs may also contribute to their different OG properties. For example, because of the atomically precise thickness, NPLs have uniform quantum confinement energy and narrow exciton

transition linewidth, which should reduce the overlap between stimulated absorption (loss) and emission (gain) transitions.²¹ It has also been argued that exciton transition oscillator strength in NPLs may be enhanced by coherent delocalization of exciton center-of-mass in the lateral direction, which should affect the stimulated emission cross-section.³ The bi-exciton Auger recombination lifetimes in NPLs are much longer than QDs,^{26, 31} and have been shown to increase linearly with their lateral size.^{27, 68-69} It has been proposed that the low OG thresholds in NPLs can be attributed to their longer Auger lifetime.^{31, 33} These observations would suggest that one of the key difference between NPLs and QDs is the possibility of tuning their OG performance through their lateral size. Olutas et al. have reported ASE threshold of CdSe NPLs increases with their lateral area.³² However, She et al. reported a lateral area-independent ASE threshold of the same materials.³³ These contradictory observations and a lack of understanding of OG mechanisms in NPLs suggests the need for a systematic study and a model for optical gain in these materials.

In this Chapter, we report a systematic study of the dependence of OG on the lateral area and optical density at pump wavelength in 4 monolayer (ML) CdSe NPLs. We investigate the OG characteristics by femtosecond transient absorption (TA) spectroscopy of colloidal NPLs samples and ASE measurements of NPL films at room temperature. We show that OG thresholds are independent on the lateral area of NPLs, while the saturation OG amplitude increases linearly with the area, when comparing samples of the same optical density at the excitation wavelength. For NPLs of the same size, their OG and ASE thresholds increase with optical density at the excitation wavelength. We propose a biexciton gain model that can satisfactorily account for the experimental observations in NPL and explain the origin for their much lower OG thresholds compared to QDs. We believe that this model should also be applicable to other 2D nanosheets and 1D nanorods.

6.2. Results and Discussion

6.2.1. Sample characterization.

4 ML CdSe NPLs (with 5 Cd layer and 4 Se layer and a thickness of ~ 1.8 nm) were synthesized according to reported procedures with slight modifications.²¹ The lateral size of NPL was tuned by changing the synthesis temperature and the reaction time. NPL samples with different lateral sizes were named NPLa to NPLd with increasing lateral size. The same batch of samples have been used in Chapter 5 for the lateral size dependent biexciton Auger lifetime in NPLs.²⁷ Figure 6.1a shows the TEM image of NPLd (NPLa to NPLc in Figure 6.6 in Appendix 6.1), from which we determined the lateral size of approximately rectangular shaped NPLs to be from 80.2 ± 12.4 nm² in NPLa to 205.1 ± 35.3 nm² in NPLd (see Table 6.1 in Appendix 6.1). The absorption spectra of NPLa to NPLd (solid lines, Figure 6.1b) show A (~ 512 nm) and B (~ 480 nm) exciton peaks that correspond to electron-heavy hole (e-hh) and electron-light hole (e-lh) transition, respectively. All NPL samples of different lateral sizes have the same A and B exciton transition energy. Static photoluminescence (PL) spectrum of NPLb (blue dashed line in Figure 6.1b) shows a sharp band edge (e-hh) emission peak at ~ 518 nm and a full width at half maximum width (FWHM) of ~ 38 meV. The PL spectra of NPLa to NPLd are compared in Figure 6.1c, showing that the band edge emission is independent on the lateral size.

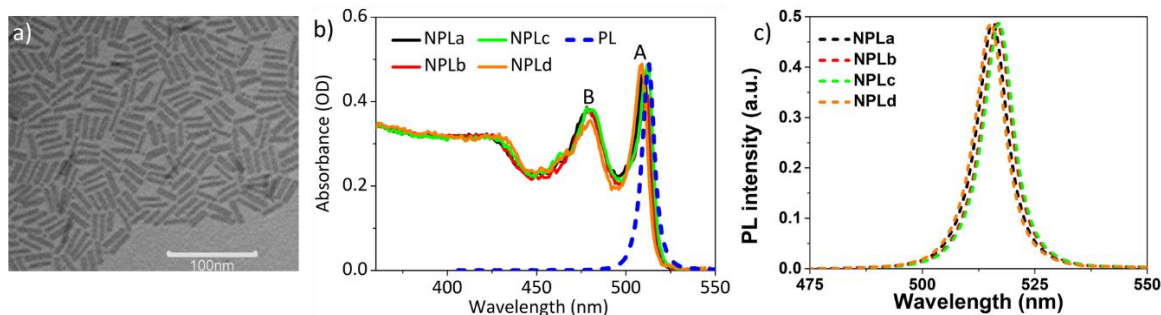


Figure 6.1. (a) TEM image of NPLd. (b) Absorption spectra of all CdSe samples of different sizes (NPLa-d) in hexane (solid lines). The blue dashed line is the static photoluminescence spectrum of NPLb. (c) Comparison of static PL spectra of all CdSe NPL samples.

6.2.2. Lateral area independent optical gain threshold

To determine OG threshold, we carried out pump fluence dependent TA spectroscopy study of NPLa to NPLd in hexane at room temperature. In a TA measurement, the optical density of samples under illumination is given by $\Delta A(\lambda, t) + A_0(\lambda)$, where $\Delta A(\lambda, t)$ is pump-induced absorbance change shown in TA spectra and $A_0(\lambda)$ is the static absorbance prior to excitation. Thus OG is achieved when $\Delta A(\lambda, t) + A_0(\lambda) < 0$. Because the OG threshold is dependent on the optical density of the sample (see below), to enable the comparison of NPLs samples of different lateral areas, their optical density at the pump wavelength (400 nm) was controlled to the same value to ensure the same number of absorbed photons (Figure 6.1b). The TA spectra of NPLc at the lowest pump fluence ($3 \mu\text{J}/\text{cm}^2$, Figure 6.2a) show long-lived bleach of A (~ 512 nm) and B (~ 480 nm) exciton. According to our previous work on CdSe NPLs, both exciton bleaches can be attributed to the state-filling on the first electron level in conduction band (CB), and the contribution of hole state-filling in valence band (VB) is negligible due to degeneracy and strong mixing between denser hole levels in VB,^{62, 69, 109} similar to cadmium chalcogenide quantum dots and nanorods.^{78, 110, 148} Figure 6.2b shows the TA spectra of NPLc at the highest pump fluence ($629 \mu\text{J}/\text{cm}^2$) when the bleach amplitudes of A and B exciton states at early delay time have saturated. Compared to those at low pump fluence, these spectra show an additional broad negative peak, $\Delta A(\lambda, t) < 0$, at energy lower than the A exciton (~ 520 - 560 nm), which can be attributed to optical gain (OG) signal,³³ similar to that reported in CdSe quantum dots (QDs).¹⁶

Gain spectra ($-\Delta A(\lambda, t) - A_0(\lambda)$) at 3-4 ps of NPLc at different pump fluences are shown in Figure 6.2c and an expanded view of the gain spectra (Figure 6.2c inset) shows a broad OG peak with maximum at ~ 528 nm. The kinetics of gain signal of NPLc at OG peak wavelength (~ 528 nm) at different pump fluences are compared in Figure 6.2d. All kinetics show a negative signal around time zero (< 1 ps), which reflects a red-shifted exciton absorption caused by exciton-exciton interaction.^{27, 34, 62, 68-69, 109} After 1ps, the OG amplitude remains negative, indicating no OG, for pump fluences below $27 \mu\text{J}/\text{cm}^2$. OG amplitude increases with increasing pump fluence, and becomes positive, indicating gain, after pump fluence of $84 \mu\text{J}/\text{cm}^2$. The OG amplitude saturates after pump fluence reaches $506 \mu\text{J}/\text{cm}^2$. NPL samples with different lateral areas were also studied and their OG kinetics at ~ 528 nm are shown in Figure 6.7 in Appendix 6.2.

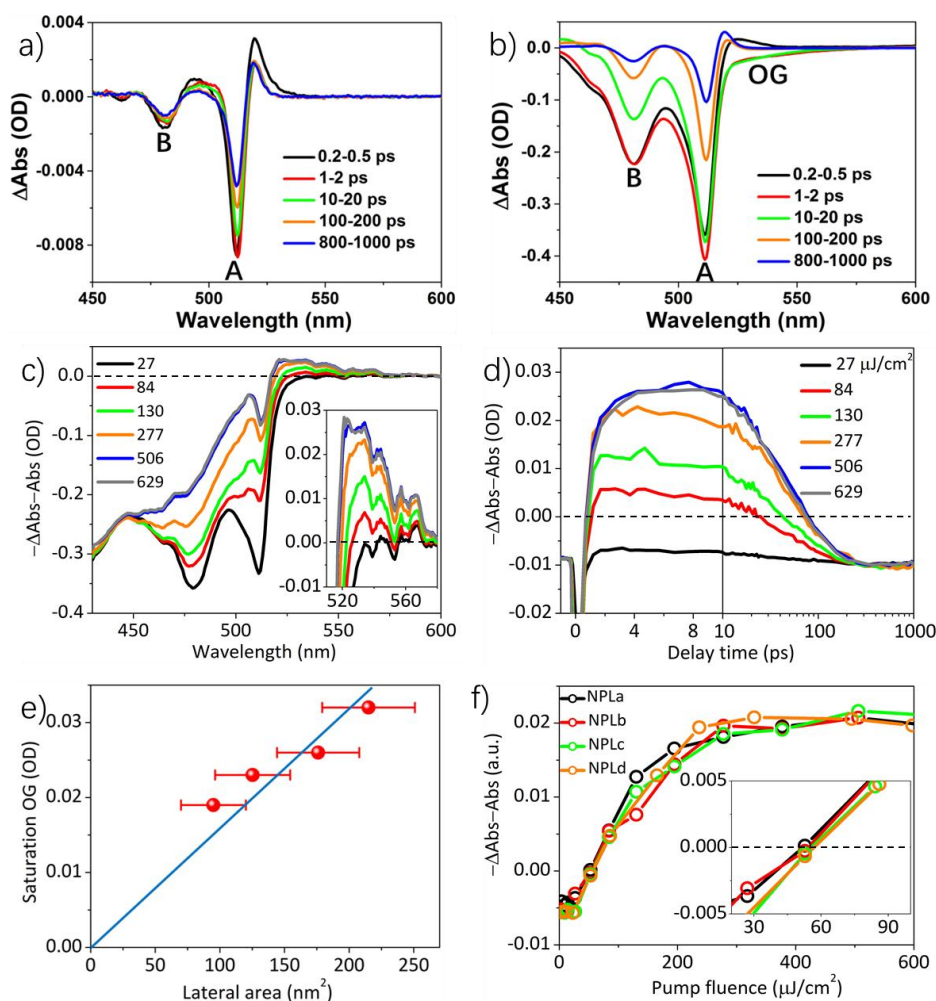


Figure 6.2. TA spectra of NPLc at indicated delay times after 400 nm pump measured at a pump fluence of (a) $3 \mu\text{J}/\text{cm}^2$ and (b) $629 \mu\text{J}/\text{cm}^2$. (c) Gain spectra, $-(\Delta A(\lambda, t) + A_0(\lambda))$, of NPLc at 3-4 ps at indicated fluences of 400 nm excitation. (d) OG kinetics (probed at 528 nm) of NPLc at different pump fluences. (e) Saturation OG amplitudes (at 3-4 ps) of different NPL samples as a function of lateral area. (f) Normalized OG amplitude (at 3-4 ps) of all NPL samples as a function of pump fluences. Inset shows the OG amplitude at low pump fluence ($20\text{-}100 \mu\text{J}/\text{cm}^2$), where the intercept on x-axis gives OG threshold.

As shown in Figure 6.2d and Figure 6.7 in Appendix 6.2, the OG amplitude of all samples reach highest value at delay time 3-4 ps, after which OG signals decay due to multiple exciton Auger recombination.²⁷ A plot of the maximum OG amplitudes (at 3-4 ps) as a function of

pump fluence (Figure 6.9b in Appendix 6.3) shows that for all NPL samples, OG reaches saturation at high pump fluences, but the saturation OG value increases linearly with their lateral area (Figure 6.2e). To facilitate comparison of gain threshold, we have scaled the OG of different samples to the same saturation amplitude and plotted the normalized OG as a function of pump fluence in Figure 6.2f. The comparison shows that the normalized OG of all NPL samples exhibit the same dependence on the pump fluence: linear increase of OG with pump fluence between 15-150 $\mu\text{J}/\text{cm}^2$, and reaching saturation between 150-500 $\mu\text{J}/\text{cm}^2$. As shown in the inset of Figure 6.2f, the intercept of OG amplitude on x-axis yields the same OG threshold of $54.6 \pm 1.8 \mu\text{J}/\text{cm}^2$ for all four samples under our experimental conditions (optical density of 0.31 ± 0.01 at 400 nm pump), independent on their lateral area.

6.2.3. Optical density dependent OG threshold.

To investigate how OG threshold changes with sample optical density, we carried out TA study of NPLc samples in hexane solution with different concentrations, named NPLc1 to NPLc4 in the order of increasing NPL concentration (NPLc3 is the sample used in Figure 6.2). The absorption spectra of NPLc1 to NPLc4 (Figure 6.3a) show that the optical density at 400 nm increases from 0.12 to 0.49 from sample NPLc1 to NPLc4. These samples were investigated using the same pump fluence dependent TA measurement and analysis method described above. Their OG kinetics as a function of pump fluence are shown in Figure 6.7 in Appendix 6.2. Their peak OG amplitudes at 3-4 ps and ~ 528 nm are plotted as a function of pump fluence in Figure 6.3b. The intercept of these data on x-axis yields OG thresholds of 43.0 ± 1.6 , 52.5 ± 1.7 , 54.6 ± 1.8 , and $63.5 \pm 2.2 \mu\text{J}/\text{cm}^2$ for NPLc1 to NPLc4, respectively. As shown in Figure 6.3c, these OG threshold values increases with the optical density at the pump wavelength (400 nm). Figure 6.3d shows the saturation OG amplitude increases linearly with optical density at 400 nm, indicating more gain at saturation if absorbed more photons.

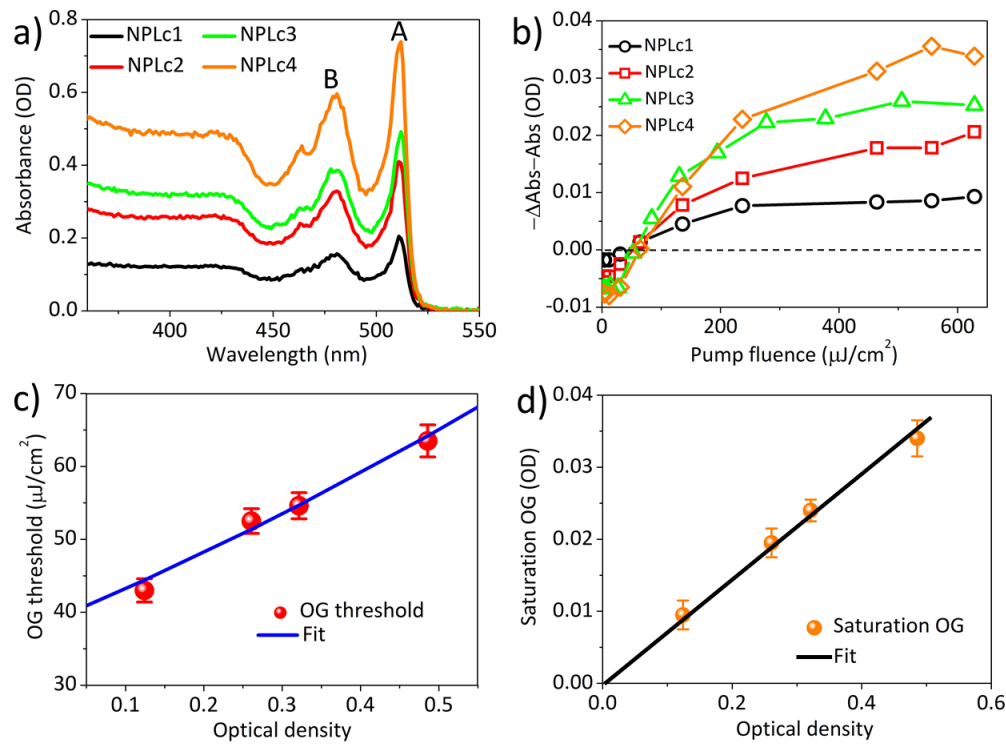


Figure 6.3. Optical density dependent optical gain threshold. (a) Absorption spectra of NPLc samples with different concentrations (and optical density at 400 nm). (b) OG amplitudes as a function of pump fluence for NPLc samples with different concentrations. (c) OG thresholds as a function of NPLc optical density at pump wavelength (400 nm). The blue solid line is the fit according to the OG threshold model described in the main text. (d) Saturation OG amplitude as a function of NPLc optical density at 400 nm. Black line is a linear fit.

6.2.4. Amplified spontaneous emission measurements

As another way of characterizing potential laser performance of NPLs, we also studied how ASE threshold depends on the optical density of the sample. For this study, three NPLc films, named Film1 to Film3 with increasing absorbance (Figure 6.4a), were prepared by spin-coating NPLc solution with increasing concentrations on a glass substrate. ASE measurement was carried out using the same 400 nm pulse excitation that was also used for the TA

measurement. The pump beam was focused into a stripe along the film plane using a cylindrical lens. The emission was detected at the film edge along the stripe direction. The emission spectra of Film1 to Film3 as a function of fluence are shown in Figure 6.4b-d, respectively. The emission spectra can be assigned to ASE, consistent with previous reports.³²⁻³³ Unlike previous reports, no single exciton band edge emission, which is centered at ~ 518 nm, was observed in the ASE measurement. This likely indicates that single exciton band edge emission intensity is too small to be observed under our experimental conditions. As shown in Figure 6.4e, the ASE peak intensity of all films increases linearly with pump fluence within 1 mJ/cm^2 . The intercepts on the x-axis of the linear fits of these data reveal ASE thresholds of 44.8 ± 4.0 , 50.0 ± 4.7 , and $112.4 \pm 4.2 \text{ } \mu\text{J/cm}^2$ for Film1 to Film3, respectively. As shown in Figure 6.4f, the ASE threshold shows the same dependence on NPL optical density as the OG threshold: it increases in films of higher optical density. Furthermore, the slope of the linear increase of ASE with pump fluence increases with the optical density at the excitation wavelength, also similar to OG threshold.

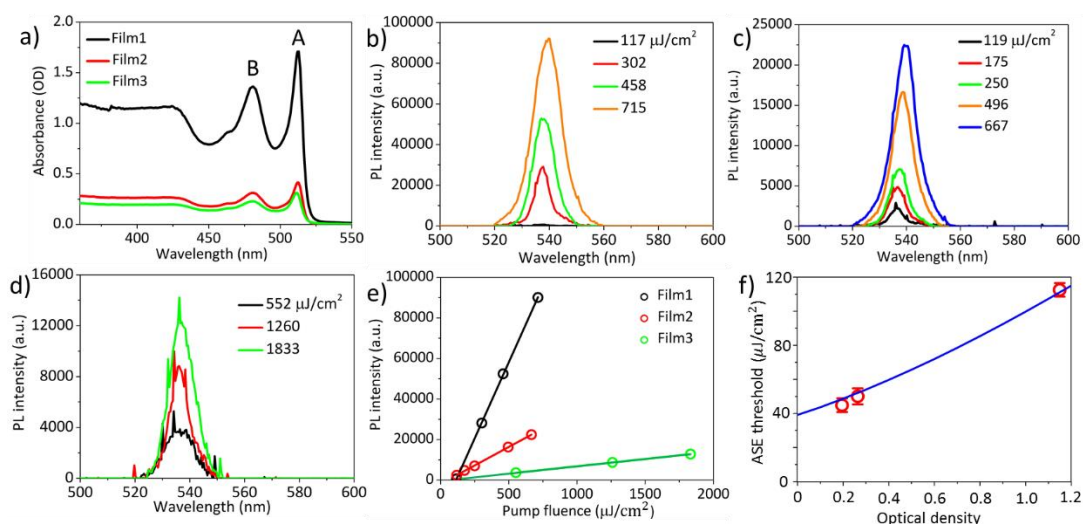


Figure 6.4. (a) Absorption spectra of different NPLc films. ASE spectra of NPLc (b) Film1, (c) Film2, and (d) Film3 at different pump fluences. (e) ASE peak intensity (circles) as a function of pump fluence for NPLc films. The solid lines are linear fits. (f) ASE thresholds as

a function of NPLc film absorbance at pump wavelength (400 nm). The blue solid line is a fit according to the OG threshold model described in the main text.

6.2.5. Model of optical gain threshold

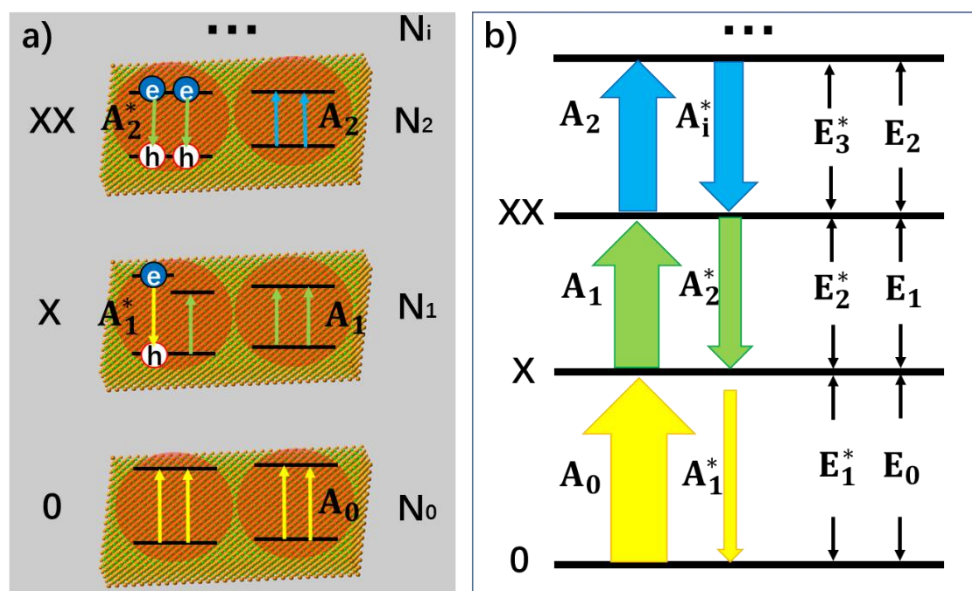


Figure 6.5. A model for biexciton optical gain in colloidal CdSe NPLs. Relevant states and transitions in (a) single particle (electron or hole) and (b) exciton state representations, respectively. N_0 (0), N_1 (X) and N_2 (XX) are population probabilities (and label) of NPL states with 0, 1 and 2 excitons, respectively. Color of arrows indicates transition energy of stimulated absorptions (upward arrow, A_i) and emissions (downward arrow, A_i^*) from state i ; Figure 4a shows an example NPLs that can contain up to 4 conduction band edge excitons ($N_s=4$).

To explain the experimental results described above, we propose a model for OG in NPLs. The details of this OG model can be found in Appendix 6.3 and only the key aspects are summarized here. This model is an extension of the previous gain model proposed for QDs,¹⁵ which, because of confinement in all three dimensions, can only accommodate two band edge excitons. In this model, we assume that because of the large (unconfined) lateral dimension of NPLs, the number (N_s) of band edge (or A) excitons can exceed 2, increasing the complexity

of the number of transitions associated with single and multiple band edge exciton states, as shown in Figure 6.5 (for an example of $N_s=4$). This assumption is based on our previous observations on NPLs,³⁴ and 2D hydrogen like exciton model in 2D structures.¹⁵³⁻¹⁵⁴ On the basis of the redshift of OG and ASE from NPL emission, it has been proposed that OG or ASE in NPLs can be attributed to stimulated emission from band edge bi-exciton states,³¹⁻³³ similar to QDs.¹⁶ Therefore, our model only considers band edge exciton states with 0, 1, ..., N_s band edge excitons, which are labeled as 0, X, XX, ... states respectively, and their population probabilities are indicated by N_i ($i=0$ to N_s). Each exciton state (i) can undergo stimulated absorption (upward arrows in Figure 6.5) or emission (downward arrows in Figure 6.5) with partial cross-sections per NPL of A_i ($i=0$ to N_s-1) and A_i^* ($i=1$ to N_s), respectively, given by Eq. 6.1&6.2:

$$A_i(E) = A_T \frac{8\pi^2 E N_s - i}{h n_r c N_s} \frac{\gamma_i}{(E - E_i)^2 + \gamma_i^2}, \quad i \text{ from } 0 \text{ to } N_s - 1, \quad (6.1)$$

$$A_i^*(E) = -A_T \frac{8\pi^2 E i}{h n_r c N_s} \frac{\gamma_i^*}{(E - E_i^*)^2 + \gamma_i^{*2}}, \quad i \text{ from } 1 \text{ to } N_s, \quad (6.2)$$

In Eq. 6.1&6.2, h is Planck's constant, n_r is the refractive index, and c is the speed of light. A_T is the transition strength of bandedge excitons (e-hh) per NPL, which is proportional to NPL lateral area, A_{QW} . $2\gamma_i$ and $2\gamma_i^*$ are the full width of the half maximum (FWHM) of absorption and emission spectra of N_i species, respectively. E_i and E_i^* are stimulated absorption and emission peak energy for N_i species, respectively. We set both γ_0 and γ_1^* to be ~ 19 meV for both single band edge exciton absorption and emission according to Figure 6.1b. We assume other γ_{i-1} and γ_i^* (i from 2 to N_s) to be the same as the broad OG spectra (~ 50 meV) shown in Figure 6.2c. E_0 and E_1^* are 2.42 eV and 2.39 eV according to A exciton absorption (512 nm) and emission (518 nm) wavelengths in Figure 6.1b, respectively. The energy of bi-exciton absorption (E_1) and emission (E_2^*) is assumed to be the optical gain energy, E_{OG} , which is set to OG peak value (2.35 eV, 528 nm) according to Figure 6.2c. The inhomogeneous distribution

of E_{OG} is ignored due to the uniform 1D quantum confinement of NPLs. The shift (from E_{OG}) of transition energies for tri and higher exciton states is assumed to be much smaller than the transition line width: $|E_{i-1} - E_{OG}| \sim |E_i^* - E_{OG}| \ll \gamma_i$ (for $i > 2$). This assumption is based on broad transition width for tri and higher exciton states and Coulomb screening of multi-excitons reported in other 2D materials,²²⁴ although these values have not been observed directly in our NPLs.

The absorption coefficient of the NPL ensemble at OG energy is:

$$\alpha(E_{OG}) = N_{en} \sum_{i=0}^{N_s} [A_i(E_{OG}) + A_i^*(E_{OG})] N_i \quad (6.3)$$

where N_{en} is the number of NPL in ensemble, which is proportional to NPL molar concentration, C_m . The population probability of NPL species (N_i) is assumed to follow Poisson distribution: $P_n(m) = \frac{m^n e^{-m}}{n!}$, which represents the possibility of finding NPLs with n excitons when the average number of excitons per NPL is m . Optical gain threshold is achieved when $\alpha(E_{OG})=0$. Solving Eq. 6.3 numerically under this condition leads to $m_{th}(N_s)$, the average number of excitons per NPL at OG threshold, of $0.49(\pm 0.01)N_s$ (see Figure 6.8 and Table 6.2 in Appendix 6.3). The result suggests that OG is reached when about half of the band edge exciton states are occupied. Under this condition, the gain (emission from excited states) equals to the loss (absorption from ground states). In the limit of QDs ($N_s=2$), $m_{th} \sim 1$, which is consistent with previous findings in QDs.¹⁵

Because m is proportional to pump fluence (I) and the optical density at the pump wavelength following the Beer's law, m_{th} value can be converted to threshold pump fluence, i.e. the OG threshold (I_{th}), according to Eq. 6.4.

$$I_{th} = \frac{h\nu N_A}{\epsilon z A_X} \frac{m_{th}}{N_s} \frac{OD}{1 - 10^{-OD}} \quad (6.4)$$

In Eq. 6.4, $OD = \varepsilon z A_{QW} C_m L$, $h\nu$ is pump photon energy (3.1 eV), N_A is Avogadro constant, and $A_X = A_{QW}/N_s$, ε is molar absorption coefficient per unit NPL volume, z is NPL thickness (~1.8 nm), L is light path of cuvette (1 mm) and $m_{th}/N_s = 0.49 \pm 0.01$. Details of the derivation can be found in Appendix 6.3. According to Eq. 6.4, when comparing NPL samples of the same thickness, their OG thresholds are independent on NPL lateral area as long as the optical densities at the pump wavelength are the same. This prediction is consistent with the experimental result shown in Figure 6.2f. Moreover, the observed OD dependent OG and ASE thresholds can be well fitted by Eq. 6.4, as shown in Figure 6.3c and 6.4f, respectively, providing further support for our OG model.

At the limit of large m , the optical gain reach saturation with a gain amplitude given by Eq. 6.5:

$$\lim_{m \rightarrow \infty} \alpha(E_{OG}) \propto -N_{en} A_T \frac{N_s}{2} \propto -C_m A_{QW} \frac{N_s}{2} = -\frac{OD}{\varepsilon z L} \frac{N_s}{2} \quad (6.5)$$

It predicts that the saturation gain amplitude increases linearly with both the lateral area (proportional to N_s) and optical density (OD) of the NPL (Figure 6.9a in Appendix 6.3), both of which are consistent with the experimental findings as shown in Figure 6.2e and 6.3d, respectively.

Finally, our model (Eq. 6.3) also predicts that how OG increases with the pump fluence. The observed OG amplitude as a function of m can be reasonably well fitted by our model (Figure 6.9h in Appendix 6.3), although the simulated OG saturates at lower m compared to the experimental results for NPLs with large N_s ($N_s > 3$). The origin of this deviation is not well understood, but it indicates that some loss factors are not fully accounted for in our model. It is likely due to the lack of consideration of a transition width distribution from higher exciton states in our model, which have not been experimentally observed.

There have been two contradicting reports on whether ASE threshold depends on NPL lateral area.³²⁻³³ In Ref,³³ optical density at pump wavelength of different NPL samples were

controlled to similar values, and lateral area-independent ASE thresholds were observed, which is consistent with our experimental results and OG model. In Ref,³² lateral area dependent ASE threshold was observed, but it is unclear whether the optical density at pump wavelength for samples of different NPL area were controlled to the same values.

Our result suggests that OG is achieved when average number of excitons per NPL is close to half (0.49) of the band edge exciton states, which is similar to the OG requirement in QDs. Despite this similarity, OG thresholds in QDs have been reported to be more than an order of magnitude higher than those in NPLs.^{15-16, 146} According to our model, the lower OG threshold of NPLs can be attributed to the following reasons. First, the intrinsic absorption cross-section of NPLs, i.e. the absorption coefficient per unit volume (ϵ), is larger than that of QDs, which according to Eq. 6.4, leads to lower OG threshold. Recently, Achtstein et al. have reported that the intrinsic absorption coefficient of CdSe NPLs is over 3 folds larger than that in CdSe QDs due to larger aspect ratio of NPLs.¹¹ Second, the ratio of biexciton binding energy (~ 40 meV) and transition linewidth (~ 38 meV), $(E_1^* - E_2^*)/2\gamma_1^*$, in NPLs (~ 1.0) is larger than that in QDs (< 0.3) whose biexciton binding energy is < 30 meV and transition linewidth is ~ 100 meV.¹⁵ This reduces the overlap between gain and loss transitions, decreasing the OG threshold in NPLs. The latter can be attributed to atomically precise uniform thickness of NPLs, which reduces inhomogeneous broadening of exciton transition energy. Such sharp transitions are difficult to achieve in QDs because of the broad size distribution and large inhomogeneous distribution of transition energies. In addition, the symmetry of the NPLs dictates that both the electric field of the exciton and the dipole moments lie within the lateral plane,²²⁵ which may account for the observed large Stark effect induced shift of transition energy between bi-exciton and single exciton states.

6.3. Conclusions

In summary, we have systematically studied the dependence of OG properties of CdSe NPLs on their lateral area and optical density at pump wavelength using TA spectroscopy and ASE measurements. We show that OG threshold is lateral area independent when comparing samples of the same optical density at the excitation wavelength, although the saturation OG amplitude increases with the lateral area. Furthermore, for samples of the same NPL size, the OG and ASE threshold increases with their optical density at the pump wavelength. To account for these observations, we proposed an optical gain model for 2D CdSe NPLs. This model assumes that the number of band edge excitons scales with the NPL lateral area (and can exceed 2) and optical gain results from stimulated emission from biexciton states. Our model successfully explains the experimental observations. The model also reveals that OG is achieved when the average number of excitons reaches ~49% of the band edge exciton states. This OG requirement is similar to that in QDs, despite that the observed OG threshold in NPLs is an order of magnitude smaller than that in QDs. According to our model, the lower OG threshold of NPLs can be attributed to their unique 2D morphology, which leads to larger intrinsic absorption coefficient, narrower transition linewidth and larger shift between bi- and single-exciton state. This work provides not only important insights on how crystal morphology affects OG properties of colloidal nanocrystals, but also guidance on rational improvement of OG and ASE in NPL materials for lasing applications. Finally, we believe that this OG model should be applicable to other 2D and 1D nanocrystals.

Appendix 6.1

The TEM images and lateral size of samples

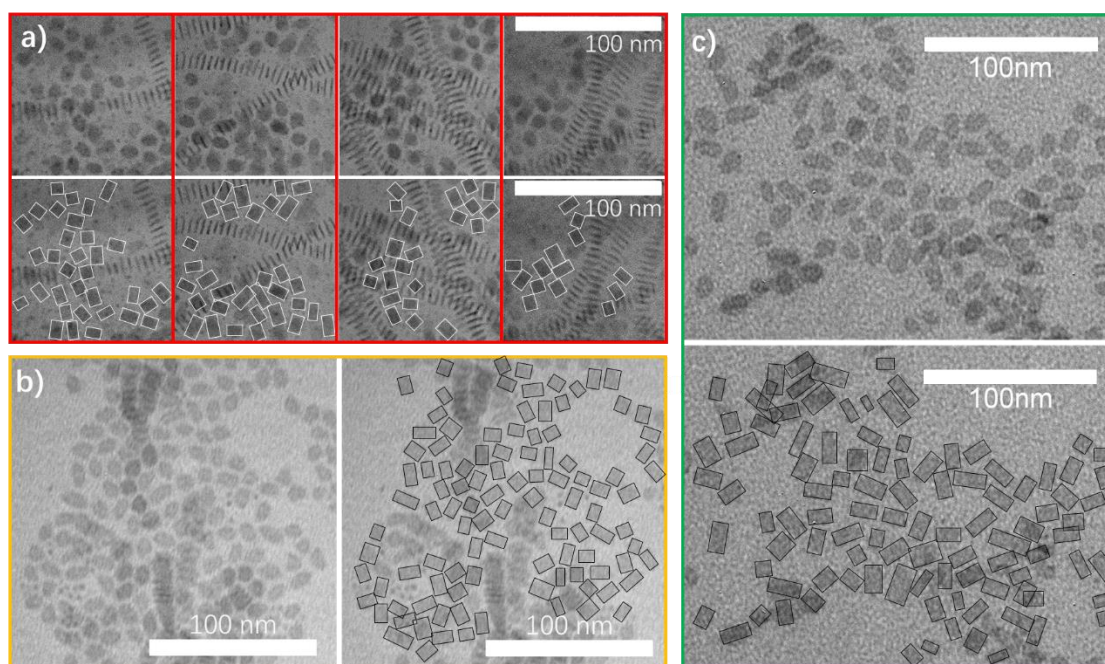


Figure 6.6. TEM images of (a) NPLa, (b) NPLb, and (c) NPLc. The length and width of all samples are determined by the solid lines marked in lower panels of (a) for NPLa, right panel of (b) for NPLb, and lower panel of (c) for NPLc.

Table 6.1. The length, width, and area with errors of CdSe colloidal NPLs

	Length/nm	Width/nm	Area/nm ²
NPLa	11.8±1.4	6.8±0.7	80.2±12.4
NPLb	14.0±1.9	8.8±1.2	123.2±23.8
NPLc	18.2±3.0	9.5±1.5	172.9±35.6
NPLd	29.3±2.6	7.0±1.1	205.1±35.3

Appendix 6.2

The optical gain kinetics

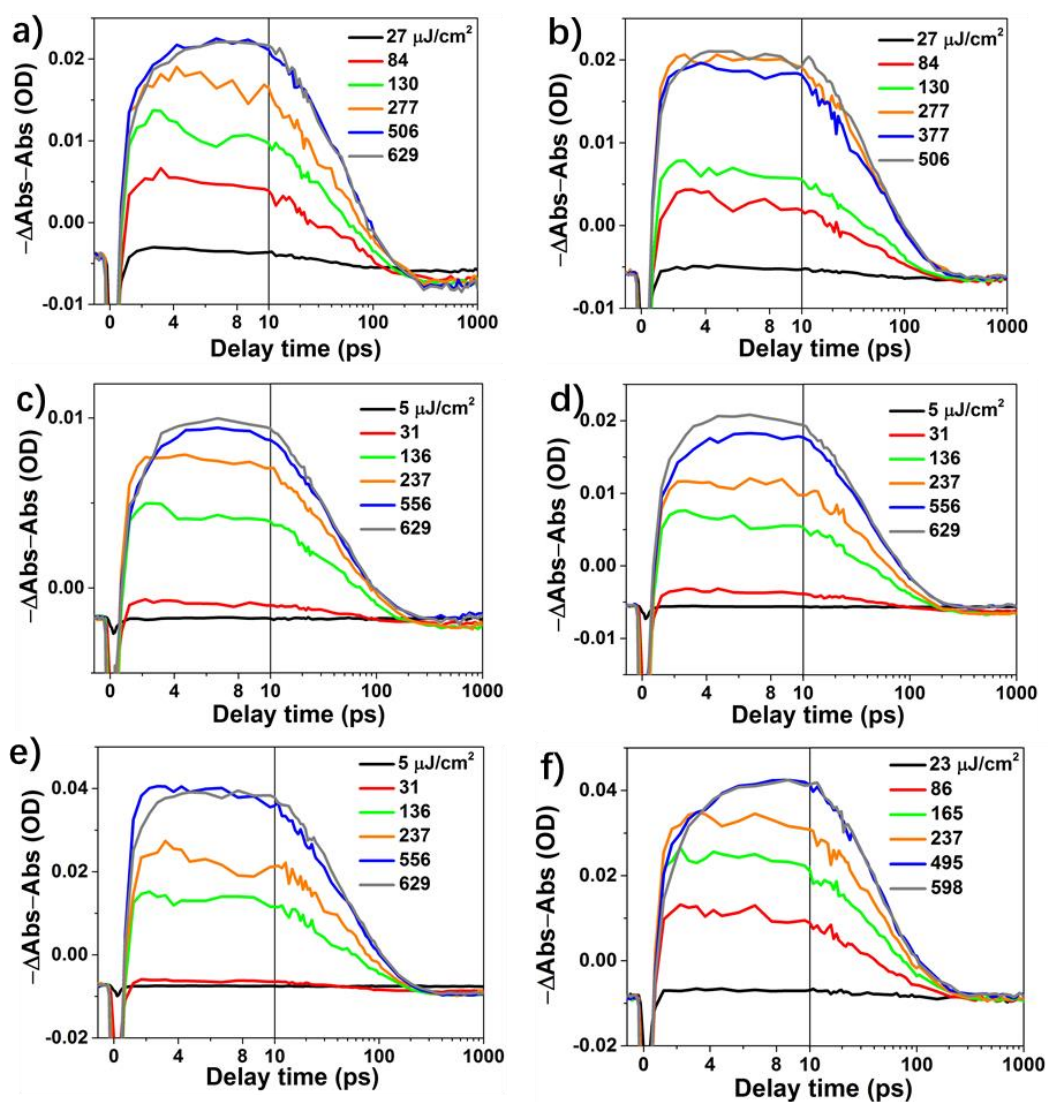


Figure 6.7. Optical gain kinetics at ~ 528 nm at different pump fluences of (a) NPLa, (b) NPLb, (c) NPLd, (d) NPLc1, (e) NPLc2, and (f) NPLc4.

Appendix 6.3

Optical gain mechanisms and threshold model

The absorption coefficient (α) at OG energy E_{OG} of the NPL ensemble, following Eq. 6.3 of the main text, is given by:

$$\begin{aligned}\alpha(E_{OG}) &= N_{en} \sum_{i=0}^{N_S} [A_i(E_{OG}) + A_i^*(E_{OG})] N_i \\ &\propto N_{en} A_T \left[\sum_{i=0}^{N_S} \left(\frac{N_S}{2} - 1 \right) N_i - 0.42 N_S N_0 + 0.3 N_1 \right] \quad (6.6)\end{aligned}$$

Assumed a Poisson distribution of exciton numbers in NPLs, Eq. 6.6 becomes:

$$\alpha(E_{OG}) \propto N_{en} A_T \left[\frac{N_S}{2} - \left[\sum_{i=0}^{N_S} i P_i + N_S \left(1 - \sum_{i=0}^{N_S} P_i \right) \right] - 0.42 N_S N_0 + 0.3 N_1 \right] \quad (6.7)$$

$P_n(m)$, the Poisson distribution possibility of finding NPLs with n excitons when the average number of excitons per NPL is m . Gain threshold is reached when $\alpha(E_{OG}) = 0$. The solution to Eq. 6.7 under this condition gives the average number of excitons per NPL at OG threshold, $m_{th}(N_S)$, which is a function of N_S . We numerically solved Eq. 6.7 and all m_{th} values are listed in Table 6.2. We plotted $m_{th}(N_S)$ as a function of N_S in Figure 6.8, where we clearly observed a linear increase of m_{th} with N_S . The linear fit reveals a $m_{th}(N_S)/N_S$ ratio of 0.49 ± 0.01 .

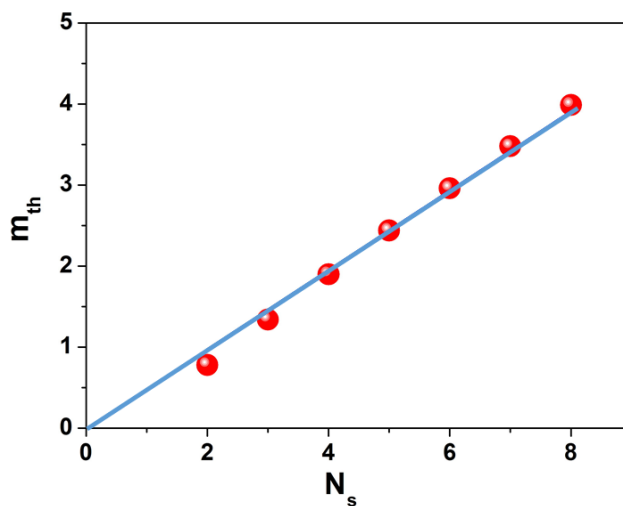


Figure 6.8. The average number of photons encountered with NPLs at OG threshold (m_{th}) as a function of N_s (red dots) and the linear fit (blue line).

Table 6.2. The average number of photons encountered with NPLs at OG threshold

N_s	m_{th}
2	0.78 ± 0.01
3	1.34 ± 0.01
4	1.90 ± 0.01
5	2.44 ± 0.01
6	2.96 ± 0.01
7	3.48 ± 0.01
8	3.99 ± 0.01

The average number of photons in NPLs can be related to pump fluence I:

$$m = \frac{(1 - 10^{-\epsilon z A_{QW} C_m L})}{C_m N_A L} \frac{I}{h\nu} \quad (6.8)$$

where $h\nu$ is pump photon energy, N_A is Avogadro constant, ε is molar absorption coefficient per unit NPL volume, z is NPL thickness, A_{QW} is NPL lateral area, L is light path of cuvette (1 mm), and C_m is molar concentration of NPL solution. From Eq. 6.8, we can obtain the pump fluence at OG threshold, i.e. the OG threshold I_{th} :

$$I_{th} = \frac{h\nu N_A}{\varepsilon z A_X} \frac{m_{th}(N_s)}{N_s} \frac{OD}{1 - 10^{-OD}} \quad (6.9)$$

where $OD = \varepsilon z A_{QW} C_m L$ is optical density at pump wavelength. Substituting in $m_{th}(N_s)/N_s \sim 0.49$, Eq. 6.9 can be rewritten as:

$$I_{th} = B \frac{OD}{1 - 10^{-OD}} \quad (6.10)$$

We used Eq. 6.10 to fit the optical density dependent OG threshold and ASE threshold as shown in Figure 6.3c and 6.4f, respectively. The best fit gave the fitting parameter, B , as $88.9 \mu\text{J}/\text{cm}^2$ in Figure 6.3c and $89.7 \mu\text{J}/\text{cm}^2$ in Figure 6.4f.

Eq. 6.7 also predicts how optical gain increase with m . Shown in Figure 6.9a is a plot of normalized $-\alpha(E_{OG})$ as a function of m for different N_s (from 1 to 8). To compare with the pump fluence dependence of optical gain, we need to determine the average number of excitons per NPL, m , at any given pump fluence, using a well-established procedure. Following our previous TA studies on the same NPL samples,²⁷ only NPLs with single exciton remained at long delay time (t_L , 800-1000 ps). Therefore, the A exciton bleach at t_L (800-1000 ps) is proportional to the percentage of excited NPLs: $1 - P_0(m)$. Following the same analyzing methods as reported in our previous work,³⁴ we define the normalized TA signal at t_L as:

$$\Delta S(\lambda, t_L) = \frac{\Delta \text{Abs}(\lambda, t_L)}{S(\lambda)} = 1 - P_0(m) = 1 - e^{-m} \quad (6.11)$$

where λ is A exciton wavelength (~ 512 nm). These normalized TA signals represent the probability of finding excited NPLs in the solution sample. At high excitation intensities, when

all NPLs were excited, $\Delta S(\lambda, t_L)$ approached one, from which the scaling factor $S(\lambda)$ was determined. According to Eq. 6.8, m is proportional to pump fluence: $m=CI$, and C is the photon encountering cross-section, which is proportional to lateral area (A_{QW}). Therefore, Eq. 6.11 becomes:

$$\Delta S(\lambda, t_L) = 1 - e^{-CI} \quad (6.12)$$

As shown in Figure 6.9c-f, fitting $\Delta S(512\text{nm}, t_L)$ as a function of pump fluence I to Eq. 6.12 yields the value of parameter C of 0.023, 0.031, 0.040, and 0.045 $\text{cm}^2/\mu\text{J}$ for NPLa to d, respectively. Parameter C as a function of lateral area is plotted in Figure 6.9g, which confirms its linear increase with lateral area.

Our experimental OG amplitude as a function of m of all NPL samples were fitted to Eq. 6.7 with N_S as the fitting parameter. The fitting results is plotted in Figure 6.9h. This plot agrees well with the measured OG saturation process and average exciton number at threshold (m_{th}) with different N_S .

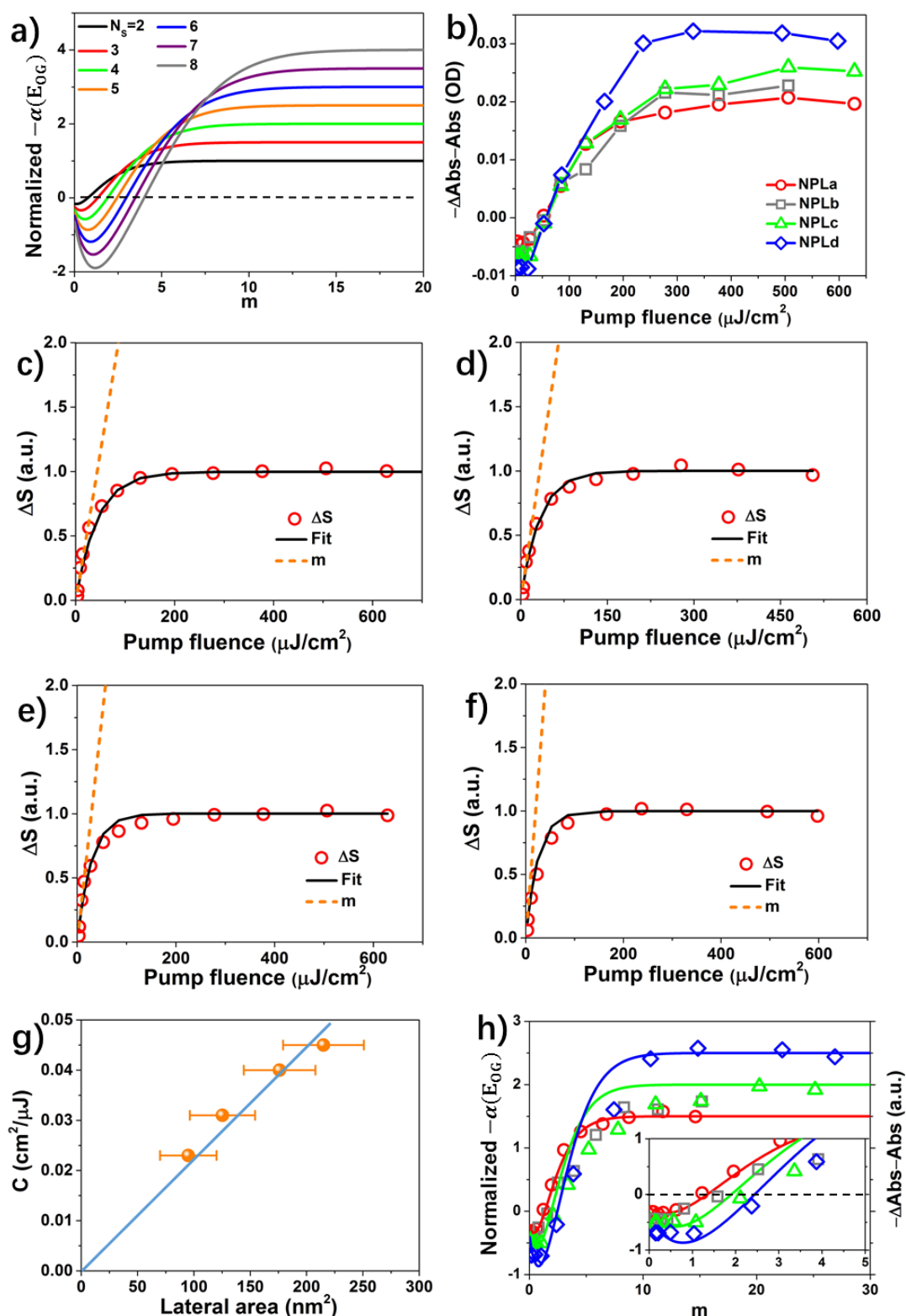


Figure 6.9. OG as a function of excitation fluence. (a) Simulated OG amplitude as a function of average number of excitons per NPL (m). (b) OG amplitude (at 3-4 ps) as a function of pump fluence of NPLa to NPLd. (c-f) Normalized A exciton bleach amplitude at long delay time

(800-1000 ps) as a function of pump fluence (open circles) and their fits (lines) for (c) NPLa, (d) NPLb, (e) NPLc, and (f) NPLd. (g) Photon encountering cross-section (C) of NPLs as a function of lateral area. Blue line is the linear fit. (h) Normalized OG amplitude of NPLa (red circles), NPLb (gray squares), NPLc (green triangles), and NPLd (blue rhombus) as a function of m . Solid lines are their fits according to Eq. 6.7: red line for $N_S=3$, green line for $N_S=4$, and blue line for $N_S=5$.

Chapter 7. Reducing Optical Gain Threshold in Two-Dimensional CdSe Nanoplatelets by Giant Oscillator Strength Transition Effect

Reproduced with permission from *J. Phys. Chem. Lett.* **2019**, *10*, 1624. Copyright 2019 American Chemical Society.

7.1. Introduction

Compared to conventional bulk semiconductor lasers, quantum dot (QD) lasers have many potential advantages induced by the quantum confinement along all three dimensions, including the tunable lasing wavelength through size dependent quantum confinement effects.¹⁶ Moreover, the density of states of QDs near the band-edge reduce to a Dirac delta function-like distribution so that carriers are concentrated to fewer states, which reduces the optical gain (OG) threshold as fewer injected carriers are required for population inversion.²²⁶⁻²²⁷ QD lasers have shown promise in recent years and continuous-wave lasing²²⁸ and direct-current electrical pumped optical gain¹⁴ in QD films have been reported. Cadmium chalcogenide (CdX, X=Se, S, Te) nanoplatelets (NPLs), with atomic-precise thickness (of ~1.2-1.8 nm) and large lateral dimension (100s nm²), are an emerging class of nanocrystals²¹ and, by some metrics, have shown even greater potential for lasing applications than QDs.^{28,31,35-36} The continuous-wave lasing of CdSe NPLs has been reported and the best-reported threshold of amplified spontaneous emission (ASE) of CdSe NPLs is as low as 6 $\mu\text{J}/\text{cm}^2$,²⁸ which is over an order of magnitude lower than that in similar QDs¹⁵⁻¹⁶ and nanorods (NRs).²²⁹ The low optical gain (OG) threshold of NPLs is attributed to low multiple exciton Auger

recombination rates,^{26-27, 94} large absorption cross-sections,¹¹ and narrow emission peaks (due to precise confinement energy)²³ of these materials, all of which are a consequence of their unique 2D morphology. Compared to QDs, 2D NPLs have much larger absorption cross-section per unit volume,¹¹ and biexciton Auger lifetimes in NPLs have been shown to increase with their lateral dimension,²⁷ which would suggest that increasing lateral size as a potential approach for further reducing the OG threshold. However, the extended lateral dimension of NPLs allows spatially separated excitons, which increases the maximum number of band-edge exciton states (N_S) to be >2 . Previous studies have shown that in cadmium chalcogenide QDs¹⁵ and NPLs,^{34, 230-231} optical gain is achieved when the band-edge exciton states are just over half-occupied. Thus, OG threshold corresponds to an average number of excitons per nanocrystal (m_{th}) of >1 for QDs and $>N_S/2$ for NPLs (Figure 7.1a). As a result, OG in NPLs is achieved at higher order (>2) multi-exciton states. These higher multi-exciton states are generated by the absorption of multiple photons (>2) and are much shorter-lived compared to the biexciton state, both of which increases the OG threshold intensity.

Here, we demonstrate a new strategy for reducing OG threshold in NPLs by exploiting the giant oscillator strength transition (GOST) effect in these 2D colloidal quantum well materials.^{21, 58, 60} Because of the atomically precise thickness of 2D CdSe NPLs, the confinement energy is the same along the lateral dimension. It has been speculated that, in the absence of scattering by phonons and surface imperfections, the exciton center-of-mass (COM) can coherently delocalize over the entire NPL, giving rise to the GOST effect.^{21, 58, 60} This notion is supported by the observation of increased radiative decay rate at lower temperature.^{21, 58} Note that this COM spatial coherence is different from the temporal coherence of excitonic states, which have been shown to be short lived (<1 ps).²³²⁻²³⁴ The extent of COM coherent delocalization is often characterized by a coherent spatial area (S_x). We hypothesize that at low temperature, the COM coherent spatial area can extend to the whole NPL, which results in a

doubly degenerate band-edge exciton state (Figure 7.1b), similar to QDs, and a much enhanced exciton radiative decay rate (the GOST effect). The combination of these factors without reducing the large absorption cross-section of 2D NPLs should further reduce the OG threshold in 2D NPLs.

In this chapter, we report a study of temperature-dependent OG threshold and exciton COM coherent delocalization in colloidal CdSe NPLs using pump fluence-dependent transient absorption (TA) spectroscopy. We observe ~4-fold lower OG threshold at 4K compared to that at room temperature (298K). We develop a new method for direct measurement of S_X in colloidal NPLs based on the TA spectroscopic study of the saturation number of band-edge excitons. We show that S_X is smaller than the CdSe NPL lateral area at room temperature but increases at lower temperatures until it extends to nearly the NPL lateral area at 4K. Our results demonstrate the strategy of reducing OG threshold by the extension of exciton COM spatial coherence and the resulting GOST effect in colloidal NPLs.

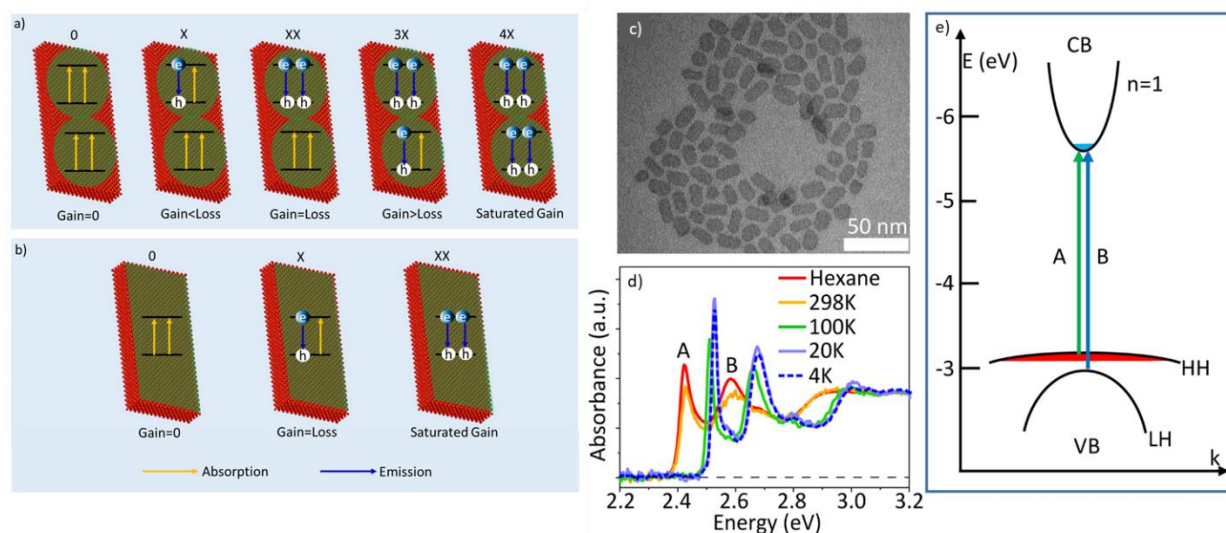


Figure 7.1. (a) Scheme of different exciton states in NPLs at room temperature with the saturation number of the band-edge exciton (N_s) as 4. (b) Scheme of different exciton states in NPLs at low temperature (<4K). The exciton COM coherence delocalized throughout the

whole NPL due to GOST effect, giving $N_S=2$. Sample characterization of CdSe NPLs. (c) TEM image of NPL1. (d) Selected absorption spectra of NPL1 in hexane (at 298K) and PMAO at indicated temperatures. (e) The scheme of band structure and band-edge transitions of NPL1 at 298K. HH and LH represent heavy hole and light hole, respectively.

7.2. Results and Discussion

7.2.1. Sample characterization

For OG studies, we synthesized CdSe NPLs with a thickness of 4 monolayers (MLs) (~ 1.2 nm)¹⁵² following reported procedures with slight modifications.²¹ These CdSe NPLs have a zinc-blend structure with 4 Se layers and 5 Cd layers^{21, 143} and are labeled as NPL1. The TEM image of NPL1 (Figure 7.1c) shows its rectangular shape, from which its lateral size is determined as 167.8 ± 27.0 nm². Measurements at room temperature (298K) were carried out in solution samples of NPL1 dispersed in hexane. Temperature dependent measurements (4-298K) were carried out in thin films of NPL1 dispersed in poly (maleic anhydride-*alt*-1-octadecene) (PMAO). The sample preparation details are shown in Chapter 2. These polymer dispersed NPL films instead of solid films of NPLs were used for low-temperature study to reduce stacking of NPLs, which has been reported to cause additional inter-NPL exciton relaxation pathway, such as Forster energy transfer between NPLs.^{166, 225, 235} The normalized UV-Vis absorption spectra of NPL1 at selected temperatures (Figure 7.1d) shows two sharp peaks that can be attributed to the band-edge electron-heavy hole (A) and electron-light hole (B) exciton transitions, respectively (Figure 7.1e). The exciton peaks of NPL1 in PMAO drop compared to that in hexane at 298K, which is likely due to the scattering from the NPL-polymer film. Both A and B exciton peaks shift to higher energy at a lower temperature (from ~ 2.42 eV at 298K to ~ 2.53 eV at 4K) due to Varshni behavior.²³⁶⁻²³⁷

7.2.2. Temperature-dependent OG threshold by GOST effect

The OG thresholds of NPL1 temperatures from 4K to 298 K were measured by pump fluence-dependent TA spectroscopy studies using 3.1 eV excitation. The optical density of the sample under illumination is $\Delta\text{Abs}(E,t)+\text{Abs}(E)$, where $\Delta\text{Abs}(E,t)$ is photo-induced absorbance change measured in TA spectra and $\text{Abs}(E)$ is the static absorbance before pump at energy, E . Therefore, OG threshold is reached when the gain is larger than the loss, i.e. $\Delta\text{Abs}(E,t)+\text{Abs}(E) < 0$. The gain spectra, expressed as $-(\Delta\text{Abs}(E,t)+\text{Abs}(E))$, at 2-3 ps of NPL1 in hexane (298K) at different pump fluences (Figure 7.2a) show a broad positive peak centered at ~ 2.34 eV, indicating the presence of OG in these samples.^{33, 230} The kinetics of NPL1 at OG peak energy (~ 2.34 eV) for different pump fluences are compared in Figure 7.2b. These kinetics show a negative signal around time zero ($< \sim 1$ ps), which reflects a red-shifted exciton absorption caused by exciton-exciton interaction.^{27, 34, 62} After ~ 1 ps, the OG amplitude remains negative at low pump fluences ($< 3 \mu\text{J}/\text{cm}^2$), indicating gain < loss, while OG amplitude becomes positive at higher pump fluence ($> 65 \mu\text{J}/\text{cm}^2$), indicating gain > loss. NPL1 in PMAO at different temperatures were also studied with the same analysis (Figure 7.7 in Appendix 7.2) and their OG peaks are at ~ 2.44 eV, ~ 2.45 eV, and ~ 2.46 eV at 100K, 50K, and 4-20K, respectively. Note that at low temperature ($\leq 100\text{K}$), an additional peak at ~ 50 meV higher than the OG peak appears at high pump fluence ($> 100 \mu\text{J}/\text{cm}^2$), which is attributed to the OG from the excited state (p-state) of A exciton (Figure 7.7b-f in Appendix 7.2).²²³

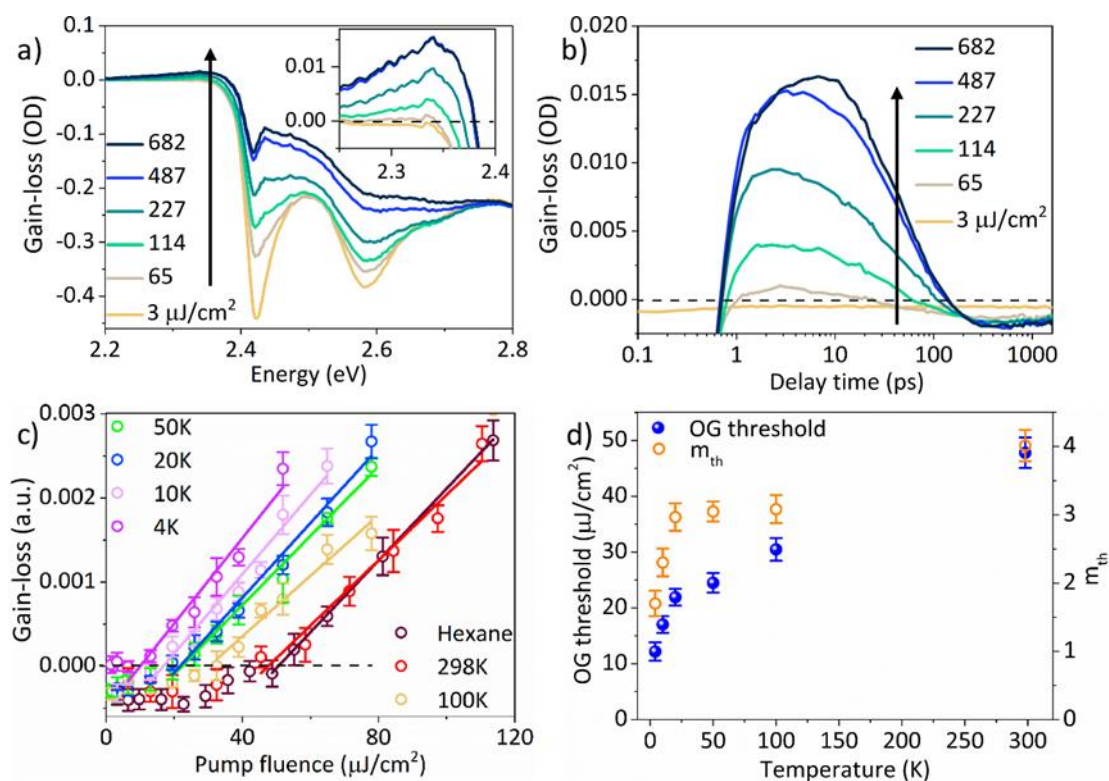


Figure 7.2. Temperature-dependent optical gain (OG) thresholds of CdSe NPLs. (a) Gain spectra, $-\Delta\text{Abs}(E,t)-\text{Abs}(E)$ (gain-loss), of NPL1 in hexane at 2-3 ps at indicated pump fluences of 3.1 eV excitation. The inset is the same spectra at OG region. (b) OG kinetics (probed at ~ 2.34 eV) of NPL1 in hexane at different pump fluences. (c) Normalized OG amplitude (at ~ 2.34 eV, 2-3 ps) at different temperatures as a function of pump fluences, where the intercept on the x-axis (black dashed line) gives OG threshold. (d) The OG threshold and the average exciton number per NPL at the OG threshold (m_{th}) of NPL1 in hexane as a function of temperature.

The OG amplitude reaches its maximum at a delay time of 2-3 ps (Figure 7.2b and 7.7g-l in Appendix 7.2), after which it decays due to multi-exciton annihilation.^{27, 230} A plot of the peak OG amplitudes as a function of pump fluence (Figure 7.2c) shows a linear dependence for gain >0 . We fit the peak OG amplitudes in their linear growth region for all temperatures (solid lines in Figure 7.2c) and extract the intercepts to determine the OG threshold fluence,

which, as shown in Figure 7.2d, decreases from $47.8 \pm 2.7 \mu\text{J}/\text{cm}^2$ at 298K to $12.2 \pm 1.6 \mu\text{J}/\text{cm}^2$ at 4K (Table 7.1). The OG threshold at 298K is consistent with previously reported values for CdSe NPLs,^{33, 238} even though a quantitative comparison of OG threshold values among different reports is difficult due to variations in optical densities, excitation wavelengths and sample qualities.

The measured OG threshold fluence is related to the average exciton number per NPL at the OG threshold (m_{th}) through Eq. 7.1.

$$I_{\text{th}} = m_{\text{th}} N_{\text{NPL}} L \frac{h\nu}{1 - 10^{-\text{OD}}} = m_{\text{th}} \frac{h\nu}{\varepsilon V_{\text{NPL}}} \frac{\text{OD}}{1 - 10^{-\text{OD}}} \quad (7.1)$$

In Eq. 7.1, I_{th} is the pump fluence (energy per unit excited area per pulse) at the OG threshold, $h\nu$ is the excitation photon energy (3.1 eV), N_{NPL} is the number of NPLs per unit volume. $\text{OD} = \varepsilon V_{\text{NPL}} N_{\text{NPL}} L$ (Beer's law) is the optical density at excitation energy, ε is the single NPL extinction coefficient per unit NPL volume, L is the sample thickness (1 mm in this work), and V_{NPL} is the volume of NPLs, which is calculated from its area ($201.4 \pm 32.4 \text{ nm}^2$, Figure 7.1c) and thickness (1.2 nm^{152}). ε (at 3.1 eV) is estimated to be $1.17 \times 10^5 \text{ cm}^{-1}$ at 298 K according to the reported extinction coefficient of the A exciton peak,¹¹ and its values at lower temperatures are estimated by both comparing the optical density of the same spot on the NPL1-PMAO film at different temperatures (Figure 7.9b in Appendix 7.4 and Table 7.1) as well as comparing to absorption studies at reduced temperature.²³⁷ From the measured threshold fluence and using Eq. 7.1, the average number of excitons at the gain threshold, m_{th} , is determined to decrease from 4.01 ± 0.23 at 298K (in PMAO) to 1.70 ± 0.19 at 4K (Figure 7.2d and Table 7.1), indicating that four- and higher-exciton states are required to reach the OG threshold at room temperature while the bi-exciton state is enough to achieve net OG at 4K.

Table 7.1. Exciton and gain parameters of NPL1 as a function of temperature. These parameters include the temperature-dependent OG threshold (I_{th}), optical density (OD) at 3.1

eV, NPL extinction coefficient per unit NPL volume (ε) at 3.1 eV, average exciton number per NPL at the OG threshold (m_{th}), band-edge exciton coherent area (S_X), and saturation number of band-edge excitons per NPL (N_S).

	Hexane (298K)	PMAO (298K)	PMAO (100K)	PMAO (50K)	PMAO (20K)	PMAO (10K)	PMAO (4K)
I_{th} ($\mu\text{J}/\text{cm}^2$)	50.7 \pm 2.1	47.8 \pm 2.7	30.5 \pm 2.0	24.5 \pm 1.2	21.9 \pm 1.5	17.0 \pm 1.5	12.2 \pm 1.6
OD	0.34	0.24	0.29	0.18	0.12	0.15	0.19
ε (10^5 cm^{-1})	1.17	1.17	1.48	1.62	1.66	1.71	1.85
m_{th}	3.83 \pm 0.16	4.01 \pm 0.23	3.08 \pm 0.20	3.05 \pm 0.15	2.97 \pm 0.20	2.30 \pm 0.20	1.70 \pm 0.19
S_X (nm^2)	95.9 \pm 15.4	95.3 \pm 15.3	115.7 \pm 15.6	123.4 \pm 14.8	130.1 \pm 13.9	137.5 \pm 14.1	155.3 \pm 12.5
N_S	3.50 \pm 0.02	3.52 \pm 0.02	2.90 \pm 0.02	2.72 \pm 0.02	2.58 \pm 0.02	2.44 \pm 0.02	2.16 \pm 0.02

According to optical gain models of NPLs and QDs,^{15,230} OG requires that the band-edge exciton states are at least half-filled, at which point the probability of stimulated emission equals the probability of absorption. As shown in Figure 7.2d, the average number of excitons per NPL at the OG threshold decreases with reduced temperature. This would suggest that the number of band-edge exciton states decreases at lower temperature, which is possible if the exciton COM coherent spatial area increases at lower temperatures, as indicated in Figure 7.1b.

7.2.3. Measurement of exciton coherent area.

To provide experimental support for temperature-dependent exciton coherent spatial area (S_X), we develop a new method to directly measure its value in CdSe NPLs at different temperatures by pump fluence-dependent TA spectroscopy (at 3.1 eV excitation). This method is based on the determination of the number of band-edge excitons at saturation fluences. The comparison of TA spectra of NPL1 at early delay time ($t_E=2-3$ ps) measured with different pump fluences (Figure 7.3a) shows the bleach of A and B exciton bands, which can be attributed to the state-filling of the lowest CB electron level,⁶² similar to cadmium chalcogenide

QDs.^{148, 239} This conclusion differs from some studies which report that the VB hole contributes to the exciton bleach signal.²⁴⁰⁻²⁴¹ The lack of hole state-filling induced exciton bleach signals has often been attributed to the higher degeneracy of VB levels,^{148, 239} which is also likely to be valid in NPLs due to the non-confined lateral dimensions with a large effective-mass of the heavy hole.²¹ With increasing pump fluences, both A and B exciton bleach amplitudes increase because of both more excited NPLs and more excitons per NPL. At pump fluences $>1267 \mu\text{J}/\text{cm}^2$, the A exciton bleach amplitude saturates, indicating the complete filling of the band-edge exciton states. Although the B exciton bleach should follow the same dependence on the pump fluence as the A exciton, its saturation behavior cannot be observed because this signal overlaps with a continuum feature associated with the A exciton band as shown in Appendix 7.4. Furthermore, in addition to exciton bleach, the presence of multi-excitons introduces other spectral features that give rise to the pump fluence-dependent TA spectral shape (Figure 7.3a).

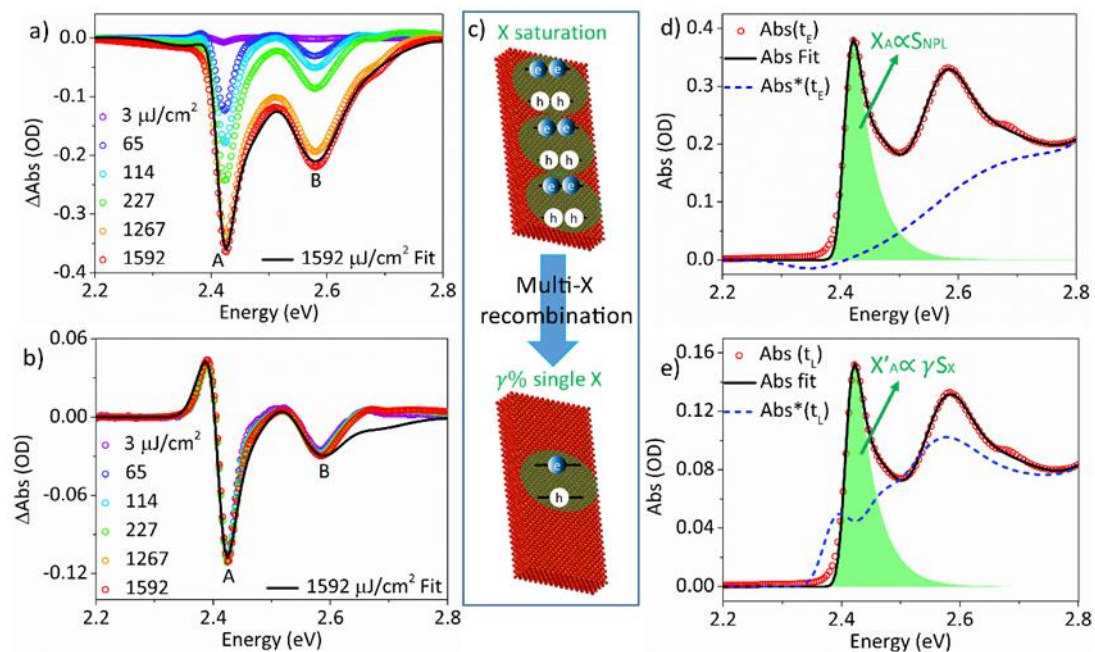


Figure 7.3. (a) TA spectra of early delay time ($t_E=2-3$ ps) and (b) normalized TA spectra at long delay time ($t_L=800-1000$ ps) of NPL1 at indicated pump fluences (circles). Solid lines are the fits of TA spectra at the highest pump fluence ($1592 \mu\text{J}/\text{cm}^2$). (c) Schematic depiction of

decay from the initial multi-exciton state with a saturated number of band-edge excitons to final single exciton state. The saturation number of the initial band-edge exciton is determined by the exciton spatial area (S_X) and lateral size of NPLs (S_{NPL}) determined by TEM. (d, e) The fits of the absorption spectra of the excited region in NPL1 NPLs before pump (Abs, solid black lines) and after pump (Abs*, blue dashed lines) at (d) early delay time ($t_E=2-3$ ps) and (e) long delay time ($t_L=800-1000$ ps) at the highest pump fluence ($1592 \mu\text{J}/\text{cm}^2$). Red circles are the normalized static absorption spectra of NPL1. Green shaded regions represent the A exciton absorbance in NPL1 NPLs before pump.

The normalized TA spectra at long delay time (800-1000 ps) measured at different pump fluences are identical (Figure 7.3b), indicating that at this delay time, multi-exciton states generated at high pump fluences have recombined, and only the single-exciton state remains.^{26-27, 57} This multi-exciton decay process can be better seen in the A exciton bleach kinetics at different pump fluences (Figure 7.8a in Appendix 7.3), which clearly shows an increase of the amplitude of the fast decay components at higher pump fluences, consistent with the expected increase of multiple-exciton populations. It also shows that both the amplitudes at early delay time (2-3 ps) and long delay time (800-1000 ps) saturate at high pump fluences when all NPLs in the probe beam path are excited, suggesting that all band-edge A exciton states are occupied at early delay time, and these multi-exciton states decay to a single-exciton state at long delay time (Figure 7.3c). Even at the lowest pump fluence ($3 \mu\text{J}/\text{cm}^2$), with an estimated average exciton number per NPL as 0.04 (see Appendix 7.3), the A exciton bleach decays to only $\gamma\%$ (68.9% in NPL1) of its initial amplitude at 1 ns. Note that this $\gamma\%$ factor accounts for both radiative and non-radiative decay of band-edge excitons. It may also contain relaxation between exciton fine-structure states, particularly, from bright to dark exciton state with a reported splitting energy of ~ 5 meV for 4ML NPLs,²⁴² and exciton trapping with the electron

in the CB-edge and hole localized at a defect site within 1 ns.¹⁵¹ The latter is expected to have a small or negligible effect on the exciton bleach amplitude.

The static absorption spectra of NPLs (black solid lines), can be well fitted to a model that consists of four absorption features: exciton bands along with continuous absorption bands of electron-heavy hole (A) and electron-light hole (B) transitions (Figure 7.3d&e).²⁸ The absorption spectra after excitation (denoted as Abs*, blue dashed lines) can be fit to a model that accounts for the state-filling induced bleach of A and B excitons bands, shift of A and B exciton frequency (due to exciton-exciton interaction), the bleach of the continuous absorption features, and band-gap renormalizations (dashed lines in Figure 7.3d&e).²⁴³ Differences between these spectra (Abs*-Abs) yields the fit of the TA spectra at saturation pump fluence (1592 $\mu\text{J}/\text{cm}^2$) shown in Figure 7.3a&b (solid lines). Details of the fitting procedures and results for all samples are shown in Appendix 7.4&7.5. According to the fit, at early delay time and saturation pump fluence (Figure 7.3d), when the A exciton is saturated, the A exciton bleach amplitude at E_X (peak of A exciton transition) equals to the A exciton absorbance of the whole NPL, $X_A(E_X)$, and is proportional to the area of the NPL (S_{NPL}) as shown in upper panel of Figure 7.3c.¹¹ At long delay time (Figure 7.3e), a single A exciton blocks half of the band-edge transitions within the exciton coherent area (due to 2-fold spin degeneracy in the CB level), leading to the bleach of half of the A exciton transitions in the same spatial area.²⁴³ The A exciton transitions outside the occupied area are unaffected so that they have no contributions to TA spectra at long delay time. Therefore, the A exciton absorbance of the excited region (i.e., the exciton coherent area) in an NPL at long delay time, $X_A'(E_X)$, which represents $\gamma\%$ of total NPLs with a single exciton, is proportional to $\gamma\% \cdot S_X$ (lower panel of Figure 7.3c). This relationship is given by:

$$\frac{X_A(E_X)}{\left[\frac{X_A'(E_X)}{\gamma\%}\right]} = \frac{S_{\text{NPL}}}{S_X} = \frac{N_S}{2} \quad (7.2)$$

From the value of $X_A(E_X)/[\frac{X_A'(E_X)}{\gamma\%}]$ (1.75 ± 0.01) and S_{NPL} ($167.8 \pm 27.0 \text{ nm}^2$, Figure 7.1c), the value of S_X for NPL1 in hexane is determined to be $95.9 \pm 15.4 \text{ nm}^2$.

7.2.4. Temperature-dependent S_X

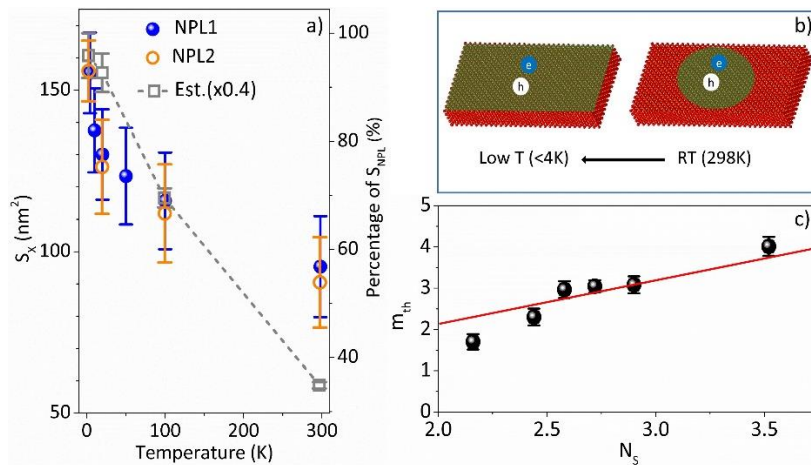


Figure 7.4. Temperature- and size-dependent S_X of CdSe NPLs. (a) Comparison of experimental S_X of NPL1 (blue spheres) and NPL2 (orange circles) and estimated S_X (Est., gray squares) as a function of temperature. The y-axis of the right side represents the percentage of the lateral area of NPL1. (b) Scheme of S_X of CdSe NPLs at room temperature (RT, 298K) and low temperature (low T, <4K). (c) The average exciton number per NPL at gain threshold (m_{th}) as a function of the saturation number of band-edge exciton of NPLs (N_s).

The TA spectra of NPL1 in PMAO at different temperatures were analyzed with the same method as described above, and all the fitting results (Figure 7.13 in Appendix 7.5) and parameters (Table 7.6 in Appendix 7.5) are shown in Appendix 7.5. S_X as a function of temperature is shown in Figure 7.4a, and their values are listed in Table 7.1. The result shows that S_X at low temperature (4K) occupies over 90% of the NPL, extending nearly to the whole NPL area, as illustrated in Figure 7.4b. It also shows that the saturation number of band-edge excitons per NPL (N_s) is ~ 3.5 at room temperature and only ~ 2 at 4K (Table 7.1). This is

consistent with the change of m_{th} values determined by temperature dependent OG threshold measurement (Figure 7.4c and Table 7.1), supporting the proposed gain model shown in Figure 7.1a&b. We observed similar temperature-dependent S_X of another 4ML CdSe NPL sample (NPL2) of a similar lateral area ($165.3 \pm 25.8 \text{ nm}^2$, Figure 7.6e in Appendix 7.1) in a different polymer, poly(methyl methacrylate) (PMMA), as shown in Figure 7.4a and Table 7.9 in Appendix 7.6.

Although temperature changes can also affect the dielectric environment of the NPL, its effects on S_X can be excluded for two reasons. (1) The dielectric constant of non-polar solids such as CdSe and PMAO changes negligibly with temperature.²⁴⁴ (2) The measured S_X values do not show significant changes in solvents of different dielectric constants either (Figure 7.16 and Table 7.9 in Appendix 7.6). Exciton-phonon scattering, which decreases at low temperature due to a reduced phonon population, affects the exciton spatial coherence. The average spatial area resulted from this dephasing pathway can be estimated from the exciton linewidth according to this relationship: $S_X = 4h^2 / \Delta(T)M$,⁵⁷⁻⁵⁸ where h is the Planck's constant, $\Delta(T)$ is the transition linewidth at temperature T , and M is the sum of the effective-masses of the band-edge electron ($0.13m_0$, m_0 is free electron mass) and hole ($0.89m_0$).²¹ Using emission linewidth of NPL2 at different temperatures as $\Delta(T)$ (Figure 7.5a), the estimated S_X calculated here (Figure 7.4a) and in a previous study⁵⁷ are over 2-fold larger than our experimentally determined S_X . This indicates that other factors besides exciton-phonon scattering play an essential role in reducing exciton spatial coherence. It has been suggested previously that the inhomogeneity of the interaction between the surface capping ligand and NPL may also play an important role.²⁴⁵

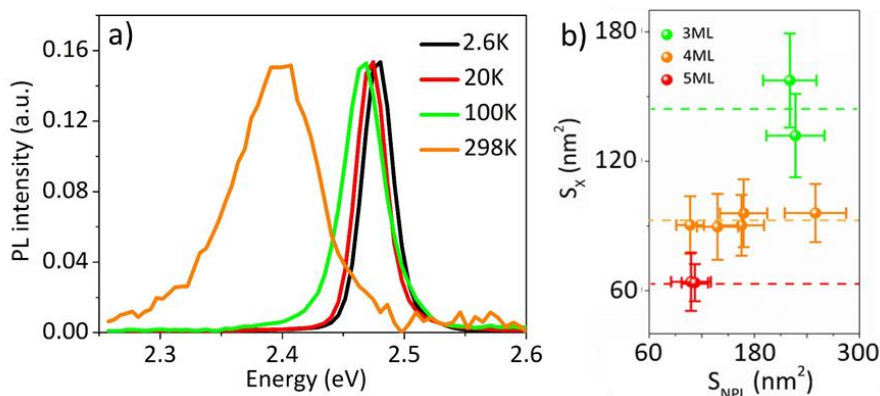


Figure 7.5. (a) Photoluminescence spectra of NPL2 in PMMA at different temperatures. (b) The S_x of CdSe NPLs with different thicknesses as a function of NPL lateral area. The dashed lines represent the average S_x for 3 (green), 4 (orange), and 5ML (red) CdSe NPLs.

We also studied how NPL thickness and lateral area affects S_x at room temperature using 3ML CdSe NPLs of two different sizes (3MLa&b), 4 ML CdSe NPLs of three additional sizes (4MLa-c) besides NPL1&2, and 5ML NPLs of two different sizes (5MLa&b). These NPLs have increasing lateral sizes from a to c (Figure 7.6 in Appendix 7.1), and their lateral sizes are determined in Table 7.2 in Appendix 7.1. The same set of samples have been used in studies of Auger recombination and optical gain of CdSe NPLs.^{27, 230} Using the same method, we extract the S_x of these NPLs in hexane at room temperature (Table 7.2 in Appendix 7.1), which is independent to the lateral size but increases at smaller NPL thickness (Figure 7.5b). This indicates thinner NPLs may lead to lower OG thresholds. It is also important to note that our method for direct determination of exciton COM coherence applies to other semiconductor 2D and 1D materials, which complements a previously reported method for estimation of exciton Bohr radius in 1D nanotubes.²⁴⁶⁻²⁴⁷

7.2.5. Temperature-dependence of gain threshold in 0D, 1D, 2D, and bulk materials

It is interesting to compare the temperature-dependence of gain threshold in materials of different dimensionality. Nearly temperature-independent OG and ASE thresholds have been reported in 0D CdSe QDs¹⁶ and 1D CdSe/CdS NRs.²²⁹ 0D QDs are quantum-confined in all dimensions in which the exciton COM and the degeneracy of band-edge exciton states are temperature independent; while 1D cadmium chalcogenide NRs usually have ununiform quantum-confinement along their length direction and this disorder reduces the exciton spatial coherence length dramatically. In conventional bulk semiconductor lasers, it has been reported that the gain threshold increases exponentially with temperature, which is due to the exponential absorption edge within the band-gap induced by doping/defect states and the thermal spreading of carriers over a wide range of accessible electronic states near the band-edge.²⁴⁸⁻²⁴⁹ However, this does not apply to 2D NPLs, in which excitonic rather than free carrier transitions dominate at the band-edge because of their large exciton binding energy (~100 meV).²¹ Unlike bulk semiconductors, the OG threshold of NPLs is determined by the relative populations of NPL species with different A excitons (Figure 7.1a&b). Furthermore, it is important to emphasize that this exciton coherent area extension strategy reduces the OG threshold by achieving bi-exciton gain and enhancing the radiative recombination rate (GOST effect) without reducing the absorption cross-section of 2D NPLs. We anticipate that this strategy for lowering gain thresholds is applicable in other 2D and 1D semiconductor nanomaterials which possess (1) uniform quantum confinement to enable large exciton spatial coherence, and (2) large exciton binding energy so that sharp excitonic transitions dominate at the band-edge.

7.3. Conclusion

In summary, we report reducing OG threshold of 2D NPLs by exciton COM coherence extension and GOST effect. The OG threshold of 4ML CdSe NPLs decreases nearly 4-fold from $\sim 48 \mu\text{J}/\text{cm}^2$ at room temperature to $\sim 12 \mu\text{J}/\text{cm}^2$ at 4K. TA spectroscopy studies show that the exciton COM coherent spatial area in CdSe NPLs is smaller than the NPL lateral size at room temperature and increases to nearly encompass the whole NPL at 4K. Our result also shows that the exciton COM coherent spatial area at room temperature is independent to NPL lateral size but decreases in NPLs of larger thickness. The reduction of the OG threshold at low temperature is attributed to the extension of exciton COM coherent area in NPLs, which reduces the saturation number of band-edge excitons to enable bi-exciton gain and increases the oscillator strength through the GOST effect. This work demonstrates a new approach for designing low threshold optical gain materials.

Appendix 7.1

The TEM images and lateral size of samples

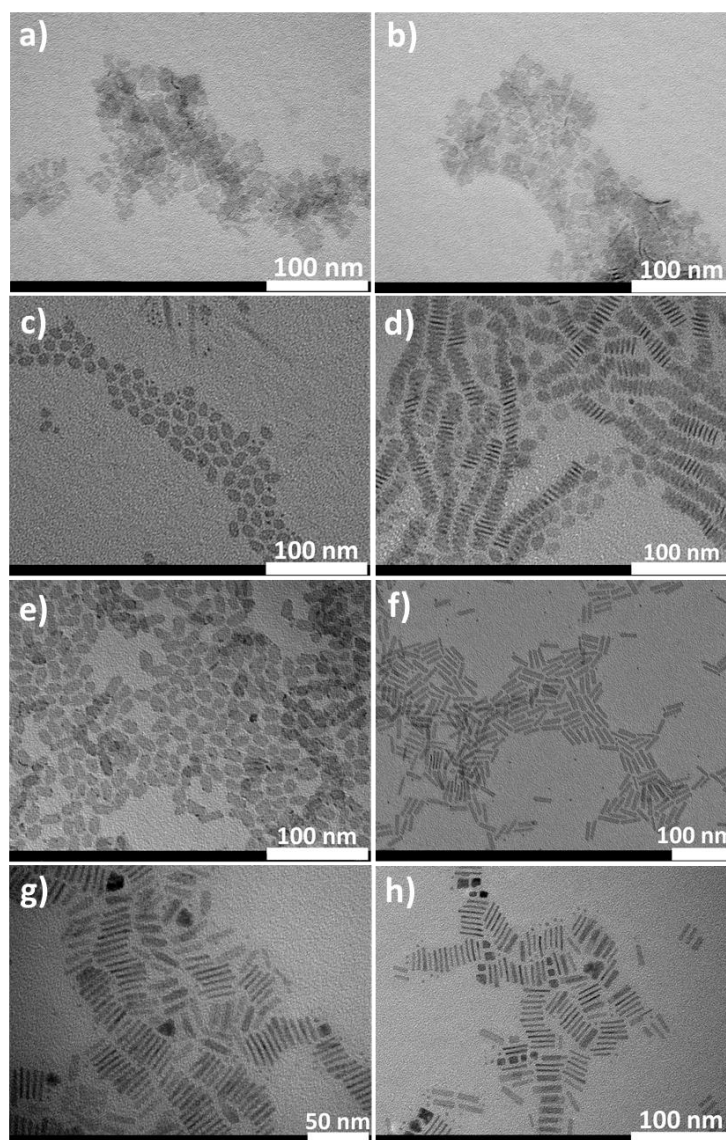


Figure 7.6. The TEM images of (a) 3MLa, (b) 3MLb, (c) 4MLa, (d) 4MLb, (e) NPL2, (f) 4MLc, (g) 5MLa, and (h) 5MLb

Table 7.2. The average length, width, area (S_{NPL}), saturation number of the band-edge exciton (N_s), and band-edge exciton coherent area (S_x) with errors of CdSe NPLs in hexane

	Length/nm	Width/nm	S_{NPL}/nm^2	N_s	S_x/nm^2	Average S_x/nm^2
3MLa	18.4±3.1	11.8±2.3	220.5±30.5	2.80±0.02	157.5±21.8	144.7±20.6
3MLb	19.9±3.8	11.4±2.0	226.8±33.2	3.44±0.02	131.9±19.3	
NPL1	17.4±2.3	9.7±1.1	167.8±27.0	3.50±0.02	95.9±15.4	92.4±14.4
NPL2	17.5±2.7	9.5±1.0	165.3±25.8	3.66±0.02	90.3±14.1	
4MLa	13.1±1.2	8.1±0.8	106.7±15.8	2.36±0.02	90.4±13.4	
4MLb	14.4±1.7	9.6±1.0	138.0±23.6	3.08±0.02	89.6±15.3	
4MLc	32.0±2.5	7.8±1.1	249.7±35.1	5.20±0.02	96.0±13.5	
5MLa	19.9±2.5	5.4±0.8	107.7±22.7	3.36±0.02	64.1±13.5	63.9±11.1
5MLb	19.8±2.0	5.7±0.6	112.1±15.1	3.52±0.02	63.7±8.6	

Appendix 7.2

Gain spectra and kinetics

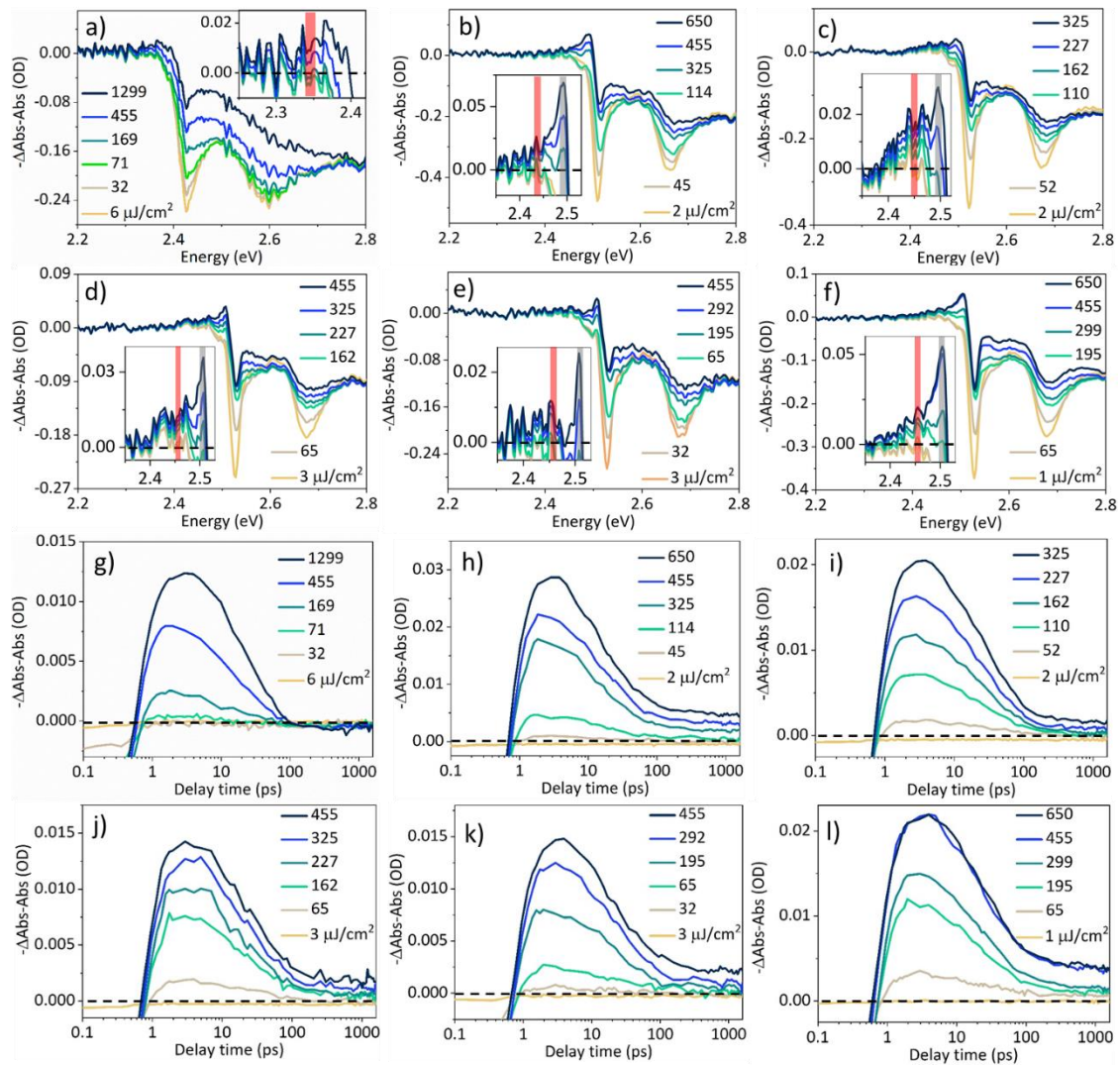


Figure 7.7. The gain spectra at early delay time (2-3 ps) of NPL1 in PMAO at (a) 298K, (b) 100K, (c) 50K, (d) 20K, (e) 10K, and (f) 4K. The insets are the same spectra at the optical gain (OG) region, where the shaded areas represent the OG from s-state (red) and p-state (gray) of A exciton, respectively. The gain kinetics at the s-state OG peak energy (marked by the red shaded area in (a)-(f)) of NPL1 in PMAO at (g) 298K, (h) 100K, (i) 50K, (j) 20K, (k) 10K, and (l) 4K.

Appendix 7.3

The estimation of the average exciton number

The A exciton kinetics of sample NPL1 in hexane at different pump fluences are shown in Figure 7.8a. Following the main text, only NPLs with single exciton remained at long delay time (t_L , 800-1000 ps) for all pump fluences. Therefore, the A exciton bleach at t_L (800-1000 ps) is proportional to the percentage of excited NPLs: $\gamma(1-P_0(m))$, where $P_n(m)$ is Poisson distribution that represents the possibility of finding n excitons per NPL if the average exciton number per NPL is m . Following the same analyzing methods as reported in our previous work,^{27, 34} we define the normalized TA signal at t_L as:

$$\Delta S(E_X, t_L) = \frac{\Delta \text{Abs}(E_X, t_L)}{\beta(E_X)} = \gamma(1 - P_0(m)) = \gamma(1 - e^{-m}) = \gamma(1 - e^{-CI}) \quad (7.3)$$

where E_X is A exciton peak energy (~ 2.42 eV). At high pump fluence, when all NPLs were excited, $\Delta S(E_X, t_L)$ approached γ (0.689 for NPL1 in hexane, see Table 7.6), from which the scaling factor $\beta(E_X)$ was determined. m is assumed proportional to pump fluence: $m=CI$ with C is the photon encountering cross-section.²⁷ As shown in Figure 7.8b, fitting $\Delta S(E_X, t_L)$ of NPL1 in hexane as a function of pump fluence I to Eq. 7.3 yields the value of parameter C of $0.013 \text{ cm}^2/\mu\text{J}$. At the lowest pump fluence ($3 \mu\text{J}/\text{cm}^2$), the average exciton number per NPL is determined as 0.04.

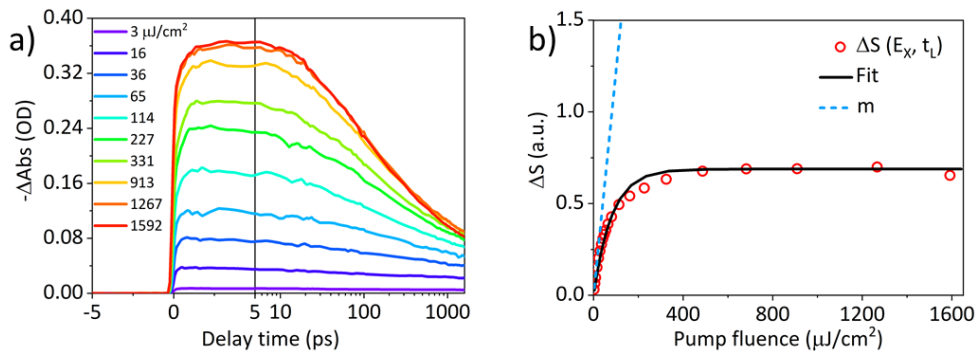


Figure 7.8. (a) The A exciton kinetics of NPL1 in hexane at selected pump fluences. (b) Normalized A exciton bleach amplitude at long delay time (800-1000 ps) as a function of pump fluence (open circles) and their fits (solid black line) for NPL1 in hexane. Blue dashed line is the average exciton number per NPL (m) as a function of pump fluence.

Appendix 7.4

UV-Vis absorption spectra fit

The UV-Vis absorption spectra of CdSe colloidal NPLs were fitted according to a well-established NPL absorption model.^{28, 250-251} Near the band-edge, the absorption is given by,

$$\text{Abs}(E) = C_A \alpha_A(E) + C_B \alpha_B(E) \quad (7.4)$$

where C_i and $\alpha_i(E)$ are the weights and absorption strength of the electron-heavy hole ($i=A$) and electron-light hole ($i=B$) transitions, respectively. These absorptions include contributions of both band-edge excitons, $X_i(E)$, and continuous band absorption, $\text{Cont}_i(E)$, as shown in Eq. 7.5:

$$\alpha_i(E) = X_i(E) + \text{Cont}_i(E) \quad (i = A \text{ or } B) \quad (7.5)$$

$X_i(E)$ represents A and B excitons for $i=A$ and B. The exciton line shape and the continuous band absorption line shape are given by Eq. 7.6-7.8, respectively:

$$\begin{aligned} X_A(E) &= X_S(E) + X_P(E) \\ &= \frac{1}{2\eta_S} \left[\text{erf} \left(\frac{E - E_{X,S}}{W_{X,S}} - \frac{W_{X,S}}{2\eta_S} \right) + 1 \right] \exp \left(\frac{W_{X,S}^2}{4\eta_S^2} - \frac{E - E_{X,S}}{\eta_S} \right) \\ &\quad + \frac{C_P}{2\eta_P} \left[\text{erf} \left(\frac{E - E_{X,P}}{W_{X,P}} - \frac{W_{X,P}}{2\eta_P} \right) + 1 \right] \exp \left(\frac{W_{X,P}^2}{4\eta_P^2} - \frac{E - E_{X,P}}{\eta_P} \right) \end{aligned} \quad (7.6)$$

$$X_B(E) = \frac{1}{2\eta_B} \left[\text{erf} \left(\frac{E - E_{X,B}}{W_{X,B}} - \frac{W_{X,B}}{2\eta_B} \right) + 1 \right] \exp \left(\frac{W_{X,B}^2}{4\eta_B^2} - \frac{E - E_{X,B}}{\eta_B} \right) \quad (7.7)$$

$$\text{Cont}_i(E) = \frac{H_i}{2} \left[\text{erf} \left(\frac{(E - E_{X,i}) - E_{b,i}}{W_{C,i}} \right) + 1 \right] \quad (i = A \text{ or } B) \quad (7.8)$$

In Eq. 7.6-7.8, $X_S(E)$ and $X_P(E)$ are exciton peaks for s- and p-state of A exciton, respectively. $E_{X,i}$ ($i=S, P, A$ or B) and $E_{b,i}$ ($i=A$ or B) are exciton transition energy and exciton binding energy, respectively, and we consider $E_{X,A} = E_{X,S}$ in Eq. 7.8. $W_{X,i}$ ($i=S, P,$ or B) and $W_{C,i}$ ($i=A$ or B) are exciton peak width and continuum edge width, respectively. H_i ($i=A$ or B) is the continuum edge step height and η_i ($i=S, P,$ or B) is the asymmetric broadening. C_P is the

relative weight of p-state of A exciton. Note that we consider the s-state/p-state splitting of A excitons,²²³ which is supported by both s- and p-state OG observed at low temperatures as shown in Figure 7.7b-f. We don't consider the same splitting for B exciton because it is far from the spectral region of interest (at the band-edge) and there lacks reliable experimental or reported results. The exciton binding energies for A exciton ($E_{b,A}$) at room temperature (298K) are fixed as reported: 289, 231, and 193 meV for 3, 4, and 5 ML NPLs, respectively.⁶¹ At low temperatures ($\leq 100\text{K}$), the exciton binding energy is not known and was assumed to be the same as the value at room temperature in our fit. The s-state/p-state splitting ($E_{X,P}-E_{X,S}$) for 4 ML NPLs is fixed as 50 ± 2 meV according to the energy difference between s- and p-state OG peaks in Figure 7.7b-f. The s-state/p-state splitting is proportional to the exciton binding energy according to the Rydberg series,^{153-154, 252} so the s-state/p-state splitting for 3 and 5 ML NPLs are set as 63 and 42 meV, respectively.

The absorption spectra of NPL1 in PMAO and NPL2 in poly(methyl methacrylate) (PMMA) and solid film at different temperatures are shown and fitted in Figure 7.9 and 7.10, respectively. Although scattering affects the static absorption spectra of NPL2 in PMMA (Figure 7.10a), its effect on TA spectra is negligible as shown by the TA spectra in PMMA, which agrees excellently with those in hexane at 298K (Figure 7.10b). Moreover, aside from the scattering features for the samples in PMMA, their spectra agree well with those of NPL2 solid films (Figure 7.10c-f), which are not affected by scattering. We have thus assumed that the absorption spectra of solid films can approximate those of NPL2 in PMMA and the latter can be fit to obtain the temperature dependence of the static absorption spectra in PMMA (Figure 7.10c-f). The fitting parameters and errors for NPL1 and NPL2 at different temperatures are listed in Table 7.3 and 7.4, respectively. The absorption spectra and the fitting results of 3, 4, and 5 ML CdSe colloidal NPLs in solution are shown in Figure 7.11, which indicates negligible effects of the lateral size and solvents on absorption spectra. Therefore, we

report only the average fitting parameters and errors for the 3 to 5 ML NPLs in solution, which are listed in Table 7.5.

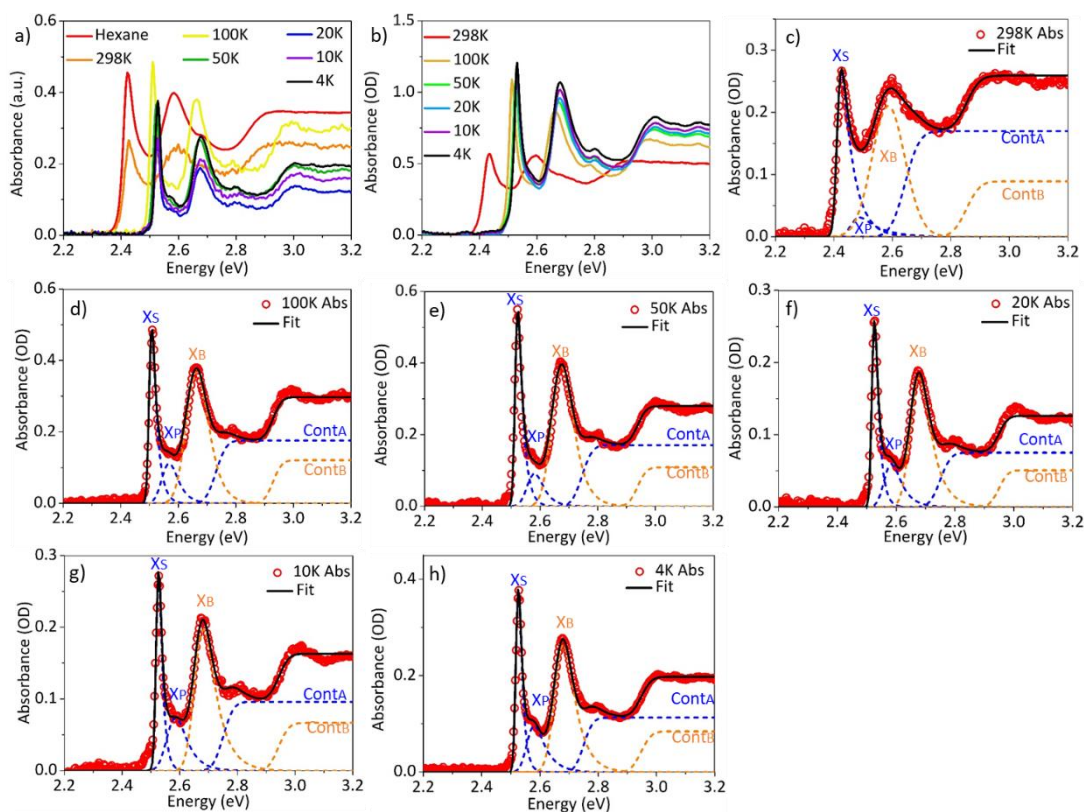


Figure 7.9. (a) Absorption spectra of NPL1 in hexane and PMAO at different temperatures for optical gain studies. (b) Absorption spectra of the same spot on NPL1 PMAO film at different temperatures. Absorption spectra and fits of NPL1 in PMAO at (c) 298K, (d) 100K, (e) 50K, (f) 20K, (g) 10K, and (h) 4K.

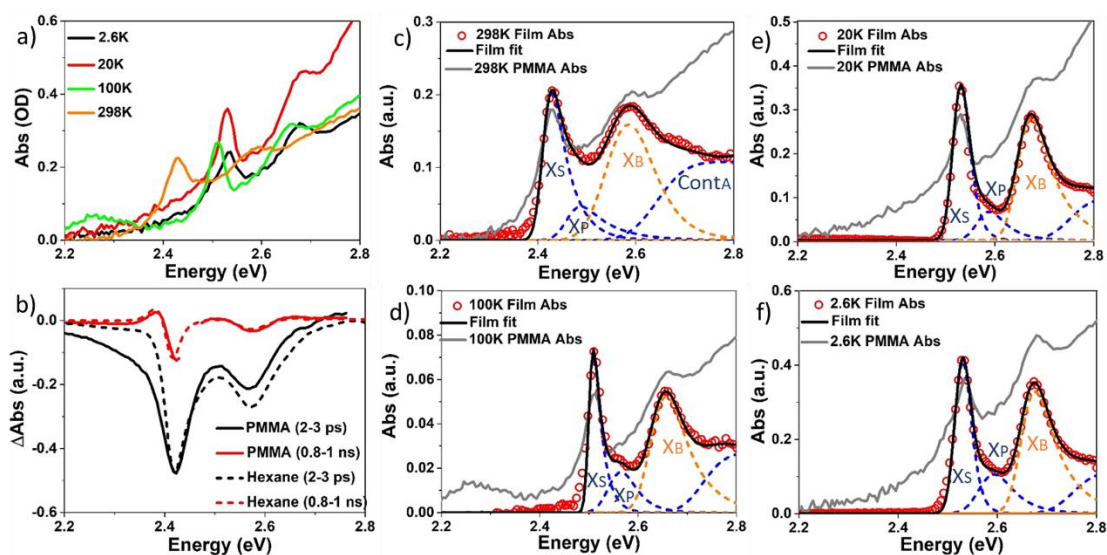


Figure 7.10. (a) The absorption spectra of NPL2 in PMMA at different temperatures. (b) Comparison of TA spectra of NPL2 in PMMA (solid lines) and hexane (dashed lines) at room temperature (298K). The comparison of absorption spectra of NPL2 in PMMA (solid gray lines) and NPL2 solid films (red circles) at (c) 298K, (d) 100K, (e) 20K, and (f) 2.6K. Black solid lines and dashed lines are the fits of absorption spectra of NPL2 solid films.

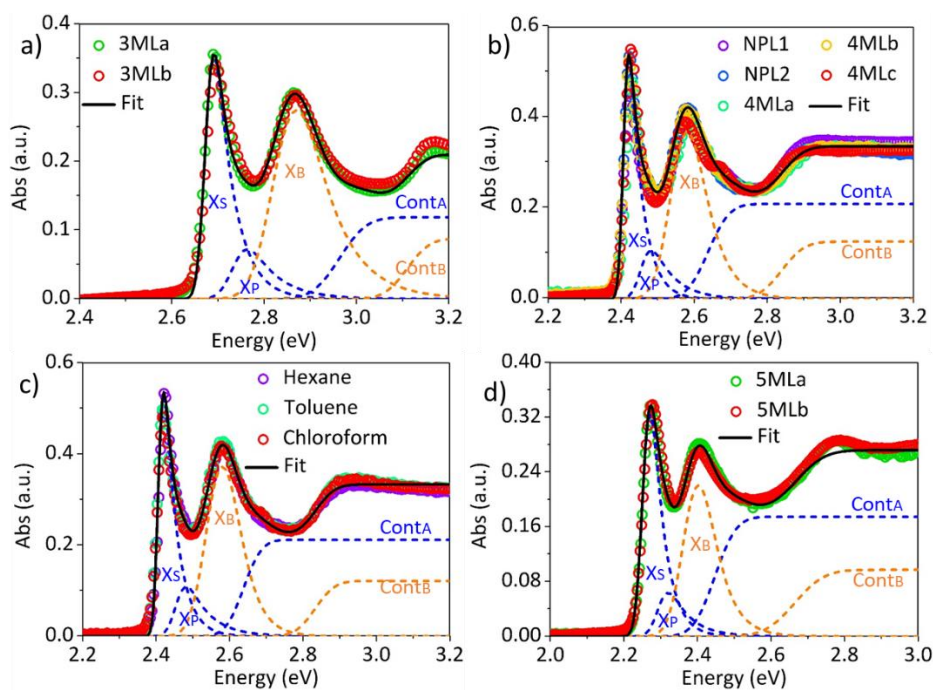


Figure 7.11. (a) Scaled absorption spectra of 3MLa&b (circles) and the fit. (b) Scaled absorption spectra of NPL1&2 and 4MLa-c (circles) and the fit. (c) Scaled absorption spectra of NPL2 in hexane, toluene, and chloroform (circles) and the fit. (d) Scaled absorption spectra of 5MLa&b (circles) and the fit.

Table 7.3. Fitting parameters and errors for absorption spectra of NPL1 in PMAO at different temperatures

	298K	100K	50K	20K	10K	4K
$E_{X,S}/\text{meV}$	2408 ± 2	2500 ± 2	2515 ± 2	2519 ± 2	2520 ± 2	2520 ± 2
$E_{X,P}/\text{meV}$	2458 ± 2	2550 ± 2	2565 ± 2	2569 ± 2	2570 ± 2	2570 ± 2
$E_{b,A}/\text{meV}$	231	231	231	231	231	231
$W_{X,S}/\text{meV}$	15 ± 1	10 ± 1	10 ± 1	10 ± 1	10 ± 1	10 ± 1
$W_{X,P}/\text{meV}$	30 ± 1	30 ± 1	30 ± 1	30 ± 1	30 ± 1	30 ± 1
$W_{C,A}/\text{meV}$	55 ± 1	40 ± 1	40 ± 1	40 ± 1	40 ± 1	35 ± 1
η_S/meV	40 ± 1	18 ± 1	18 ± 1	15 ± 1	13 ± 1	13 ± 1
η_P/meV	68 ± 1	30 ± 1	30 ± 1	35 ± 1	40 ± 1	40 ± 1
H_A/meV	10000 ± 100	10700 ± 100	9200 ± 100	9600 ± 100	12500 ± 100	10500 ± 100
C_P	0.21 ± 0.01	0.52 ± 0.01	0.38 ± 0.01	0.60 ± 0.01	0.85 ± 0.01	0.75 ± 0.01
C_A	0.017 ± 0.00	0.017 ± 0.00	0.019 ± 0.00	0.0078 ± 0.000	0.0077 ± 0.000	0.011 ± 0.00
	1	1	1	1	1	1
$E_{X,B}/\text{meV}$	2568 ± 2	2641 ± 2	2653 ± 2	2656 ± 2	2658 ± 2	2658 ± 2
$E_{b,B}/\text{meV}$	285 ± 5	288 ± 5	285 ± 5	293 ± 5	285 ± 5	290 ± 5
$W_{X,B}/\text{meV}$	75 ± 1	45 ± 1	42 ± 1	35 ± 1	35 ± 1	35 ± 1
$W_{C,B}/\text{meV}$	65 ± 1	35 ± 1	35 ± 1	35 ± 1	40 ± 1	40 ± 1
η_B/meV	25 ± 1	33 ± 1	35 ± 1	40 ± 1	40 ± 1	40 ± 1
H_B/meV	3000 ± 100	3200 ± 100	2800 ± 100	3000 ± 100	3400 ± 100	3400 ± 100
C_B	0.030 ± 0.00	0.038 ± 0.00	0.039 ± 0.00	0.017 ± 0.001	0.020 ± 0.001	0.025 ± 0.00
	1	1	1			1

Table 7.4. Fitting parameters and errors for absorption spectra of NPL2 solid films at different temperatures

	298K	100K	20K	2.6K
$E_{X,S}/\text{meV}$	2412 ± 2	2502 ± 2	2520 ± 2	2521 ± 2
$E_{X,P}/\text{meV}$	2462 ± 2	2552 ± 2	2570 ± 2	2571 ± 2
$E_{b,A}/\text{meV}$	231	231	231	231
$W_{X,S}/\text{mV}$	20 ± 1	10 ± 1	20 ± 1	20 ± 1
$W_{X,P}/\text{mV}$	30 ± 1	30 ± 1	28 ± 1	35 ± 1
$W_{C,A}/\text{mV}$	65 ± 1	50 ± 1	50 ± 1	50 ± 1
η_S/meV	35 ± 1	18 ± 1	15 ± 1	13 ± 1
η_P/meV	60 ± 1	30 ± 1	35 ± 1	40 ± 1
H_A/meV	8000 ± 100	11000 ± 100	6000 ± 100	6200 ± 100
C_P	0.37 ± 0.01	0.57 ± 0.01	0.31 ± 0.01	0.55 ± 0.01
C_A	0.014 ± 0.001	0.0025 ± 0.0001	0.016 ± 0.001	0.018 ± 0.001
$E_{X,B}/\text{meV}$	2555 ± 2	2633 ± 2	2650 ± 2	2653 ± 2
$E_{b,B}/\text{meV}$	290 ± 5	288 ± 5	293 ± 5	290 ± 5
$W_{X,B}/\text{mV}$	56 ± 1	35 ± 1	35 ± 1	30 ± 1
$W_{C,B}/\text{mV}$	52 ± 1	35 ± 1	35 ± 1	40 ± 1
η_B/meV	45 ± 1	50 ± 1	50 ± 1	50 ± 1
H_B/meV	2500 ± 100	3900 ± 100	4200 ± 100	4000 ± 100
C_B	0.021 ± 0.001	0.0055 ± 0.0001	0.027 ± 0.001	0.032 ± 0.001

Table 7.5. Fitting parameters and errors for absorption spectra of 3ML, 4ML and 5 ML NPLs in solution

	3ML	4ML	5ML
$E_{X,S}/\text{meV}$	2675 ± 2	2408 ± 2	2255 ± 2
$E_{X,P}/\text{meV}$	2738 ± 2	2458 ± 2	2297 ± 2
$E_{b,A}/\text{meV}$	289	231	193
$W_{X,S}/\text{meV}$	20 ± 1	15 ± 1	23 ± 1
$W_{X,P}/\text{meV}$	35 ± 1	30 ± 1	30 ± 1
$W_{C,A}/\text{meV}$	65 ± 1	60 ± 3	65 ± 2
η_S/meV	40 ± 1	35 ± 1	35 ± 1
η_P/meV	40 ± 1	60 ± 1	55 ± 1
H_A/meV	4700 ± 100	6800 ± 100	7600 ± 100
C_P	0.33 ± 0.01	0.37 ± 0.01	0.28 ± 0.01
C_A	0.025 ± 0.001	0.034 ± 0.001	0.023 ± 0.001
$E_{X,B}/\text{meV}$	2832 ± 2	2550 ± 2	2375 ± 2
$E_{b,B}/\text{meV}$	278 ± 5	290 ± 5	290 ± 5
$W_{X,B}/\text{meV}$	58 ± 1	55 ± 2	50 ± 2
$W_{C,B}/\text{meV}$	55 ± 1	65 ± 2	90 ± 2
η_B/meV	70 ± 1	45 ± 3	45 ± 2
H_B/meV	2000 ± 100	2550 ± 100	3600 ± 100
C_B	0.044 ± 0.001	0.054 ± 0.001	0.027 ± 0.001

Appendix 7.5

Transient absorption spectra fit

TA spectra are difference spectra of the sample after pump and before pump, and only excited NPLs contribute to the signal. The absorption spectra of contributing NPLs in solution and polymer samples before pump, $Abs(t, E)$, which are their static absorption spectra, can be well fitted using NPL absorption model as discussed above (Table 7.3-7.5). For NPL2 in PMMA, strong light scattering hinders a reliable fit to their spectra, and we assume that they have the same absorption line shape of NPL2 solid films (Figure 7.10). The time dependence of this signal reflects the change of contributing populations as a function of time (due to excited state decay). The absorption spectra of contributing NPLs after pump, $Abs^*(t, E)$, contain the contributions of the decrease of absorption strength due to electron state-filling and shift of exciton band caused by exciton-exciton interaction (or Stark shift).^{224, 253} For TA spectra measured with the highest pump fluence at early delay time (t_E , 2-3 ps), the CB edge is fully occupied with electrons, and the exciton transitions are entirely blocked. Therefore, the excited state absorption bands of A and B exciton, X_A^* and X_B^* respectively, are set to zero. We attribute the additional negative signals between A and B exciton bleach, which only show up at high pump fluence, to the state-filling of continuum band of A exciton, $Cont_A^*$. $Cont_B$ is far from the TA spectra region of interest, and its spectral change can be ignored. There is also a broad negative absorption feature at the low energy side of A exciton peak under high pump fluence, which can be attributed to the optical gain of semiconductor NPLs.^{33, 224} We fit this optical gain with a negative asymmetric peak, G , in excited state absorption. Thus, the absorbance of excited NPLs at early delay time is given by:

$$Abs^*(t_E, E) = C_G G(E) + C_A Cont_A^*(t_E, E) + C_B Cont_B \quad (7.9)$$

$$G(E) = -\frac{1}{2\eta_G} \left[\operatorname{erf} \left(\frac{E - E_G}{W_G} - \frac{W_G}{2\eta_G} \right) + 1 \right] \exp \left(\frac{W_G^2}{4\eta_G^2} - \frac{E - E_G}{\eta_G} \right) \quad (7.10)$$

$$\text{Cont}_A^*(t_E, E) = \frac{H_A}{2} \left[\text{erf} \left(\frac{[E - (E_{X,S} - \Delta_{\text{Cont},A})] - E_{b,A}}{W_{C,A}^*} \right) + 1 \right] \quad (7.11)$$

where C_G is the amplitude of optical gain, η_G is the asymmetric broadening, E_G is the gain peak energy, W_G is the gain width, and $\Delta_{\text{Cont},A}$ is band gap renormalization.^{224, 243}

At long delay time (t_L , 800-1000 ps) and highest pump fluence, all NPLs are in the single-exciton state.²⁷ With only one electron in the NPL, occupying the CB edge level, both the strengths of A and B exciton transitions are reduced by half due to the Pauli exclusion principle.²⁴³ The A and B exciton transitions (X_A^* and X_B^*) are shifted to lower energy (by $\Delta_{X,S}$ and $\Delta_{X,P}$ for s- and p-state of A exciton, respectively, and $\Delta_{X,B}$ for B exciton) and the s-state of A exciton is broadened after pump (with $W_{X,S}^*$ and η_S^* are width and asymmetric broadening after pump, respectively) due to exciton-exciton interaction.^{224, 243, 253} The amplitude of the continuous band A (Cont_A^*) remains unaffected and its energy redshifts by $\Delta_{\text{Cont},A}$ due to band-gap renormalization.^{224, 243} The occupation probability for s-state ($P_{s\text{-state}}$) and p-state ($P_{p\text{-state}}$) of A exciton follows Boltzmann distribution: $\frac{P_{p\text{-state}}}{P_{s\text{-state}}} = e^{-\frac{E_{X,P} - E_{X,S}}{k_B T}}$, where k_B is the Boltzmann constant, T is the temperature, and $P_{s\text{-state}} + P_{p\text{-state}} = 1$. Thus, the absorbance of excited NPLs at long delay time is given by:

$$\text{Abs}^*(t_L, E) = C_A [X_A^*(t_L, E) + \text{Cont}_A^*(t_L, E)] + C_B [X_B^*(t_L, E) + \text{Cont}_B(t_L, E)] \quad (7.12)$$

where:

$$\begin{aligned}
X^*_A(t_L, E) &= P_{s\text{-state}} \left(\frac{X^*_S(t_L, E)}{2} + X^*_P(t_L, E) \right) + P_{p\text{-state}} \left(X^*_S(t_L, E) + \frac{X^*_P(t_L, E)}{2} \right) \\
&= \left(\frac{P_{s\text{-state}}}{2} \right. \\
&\quad \left. + P_{p\text{-state}} \right) \frac{1}{2\eta_S^*} \left[\operatorname{erf} \left(\frac{E - (E_{X,S} - \Delta_{X,S})}{W_{X,S}^*} - \frac{W_{X,S}^*}{2\eta_S^*} \right) \right. \\
&\quad \left. + 1 \right] \exp \left(\frac{W_{X,S}^{*2}}{4\eta_S^{*2}} - \frac{E - (E_{X,S} - \Delta_{X,S})}{\eta_S^*} \right) + (P_{s\text{-state}} \\
&\quad + \frac{P_{p\text{-state}}}{2}) \frac{C_P}{2\eta_P} \left[\operatorname{erf} \left(\frac{E - (E_{X,P} - \Delta_{X,P})}{W_{X,P}} - \frac{W_{X,P}}{2\eta_P} \right) \right. \\
&\quad \left. + 1 \right] \exp \left(\frac{W_{X,P}^2}{4\eta_P^2} - \frac{E - (E_{X,P} - \Delta_{X,P})}{\eta_P} \right) \quad (7.13)
\end{aligned}$$

$$\begin{aligned}
X^*_B(t_L, E) &= \frac{1}{4\eta_B} \left[\operatorname{erf} \left(\frac{E - (E_{X,B} - \Delta_{X,B})}{W_{X,B}} - \frac{W_{X,B}}{2\eta_B} \right) \right. \\
&\quad \left. + 1 \right] \exp \left(\frac{W_{X,B}^2}{4\eta_B^2} - \frac{E - (E_{X,B} - \Delta_{X,B})}{\eta_B} \right) \quad (7.14)
\end{aligned}$$

$$\operatorname{Cont}_A^*(t_L, E) = \frac{H_A}{2} \left[\operatorname{erf} \left(\frac{[E - (E_{X,S} - \Delta_{\operatorname{Cont},A})] - E_{b,A}}{W_{C,A}} \right) + 1 \right] \quad (7.15)$$

At room temperature (298K), $P_{s\text{-state}}$ ($P_{p\text{-state}}$) for 3, 4, and 5 ML NPLs are estimated as 92.1% (7.9%), 87.5% (12.5%), and 83.7% (16.3%), respectively. At low temperatures ($\leq 100\text{K}$), $P_{p\text{-state}}$ is estimated $\leq 0.3\%$ for 4 ML NPLs so that we approximate $P_{s\text{-state}}=1$ and $P_{p\text{-state}}=0$ for 4 ML NPLs at low temperatures ($\leq 100\text{K}$).

The TA spectra then are fitted by:

$$\Delta\text{Abs}(t, E) = \text{Abs}^*(t, E) - \text{Abs}(t, E) \quad (7.16)$$

The peak values of contributing A exciton absorption of the excited region in NPL before pump at early and long delay time are used to calculate the S_X :

$$\frac{X_A(t_E, E_{X,S})}{X_A(t_L, E_{X,S})} = \frac{S_{\text{NPL}}}{\gamma\% \cdot S_X} \quad (7.17)$$

where S_{NPL} is NPL lateral area (Table 7.2) and $\gamma\%$ is the population of excited NPLs remaining at t_L . The fitting parameters for absorption spectra before pump are all fixed as in Table 7.3-7.5 to keep the absorption line-shape, except for C_A and C_B , which determine the actual amplitude of the contributing NPLs before pump. The fitting results of Abs, Abs*, and TA spectra for NPL1 in hexane are shown as an example for the complete fitting process in Figure 7.12. TA spectra and the fits of all NPL samples are shown in Figure 7.13 (for NPL1), 7.14 (for NPL2), and 7.15 (for 3MLa&b, 4MLa-c, and 5MLa&b) with the fitting parameters listed in Table 7.6 (for NPL1), 7.7 (for NPL2), and 7.8 (for 3MLa&b, 4MLa-c, and 5MLa&c).

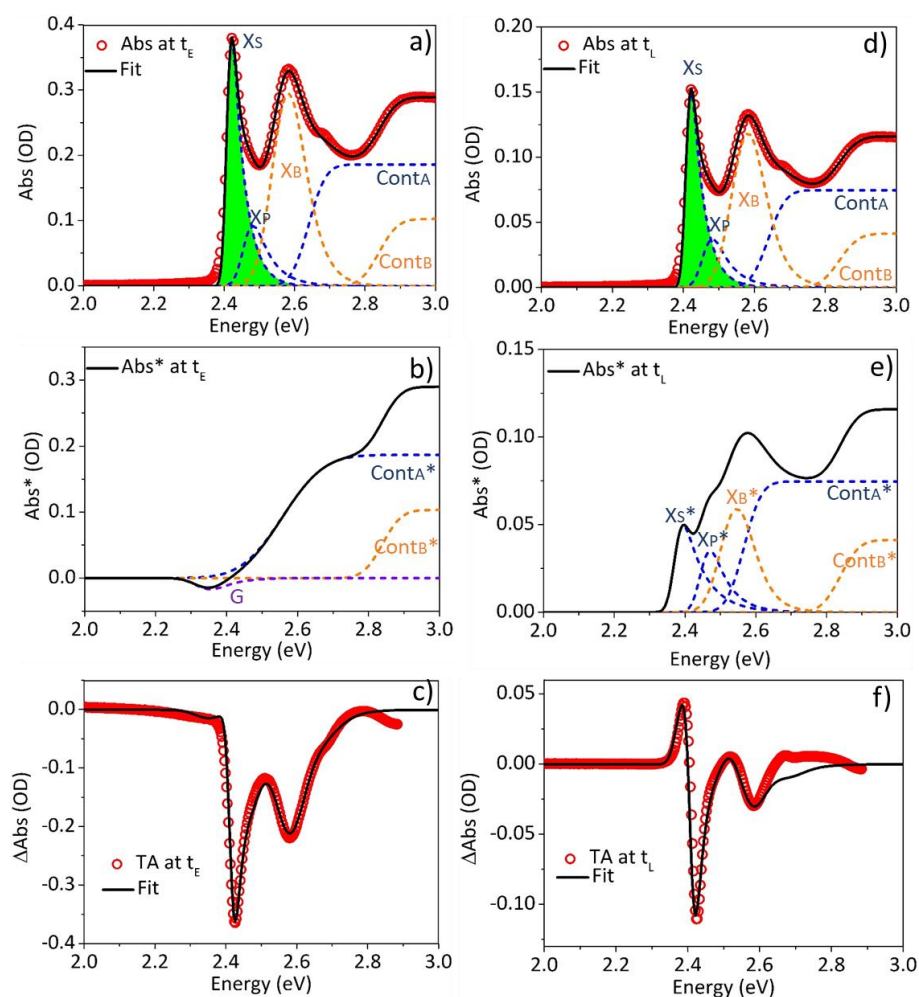


Figure 7.12. The absorption spectra (a) before pump, (b) after pump, and (c) the TA spectra of NPL1 in hexane at early delay time (t_E , 2-3 ps). The absorption spectra (d) before pump, (e) after pump, and (f) the TA spectra of NPL1 in hexane at long delay time (t_L , 800-1000 ps).

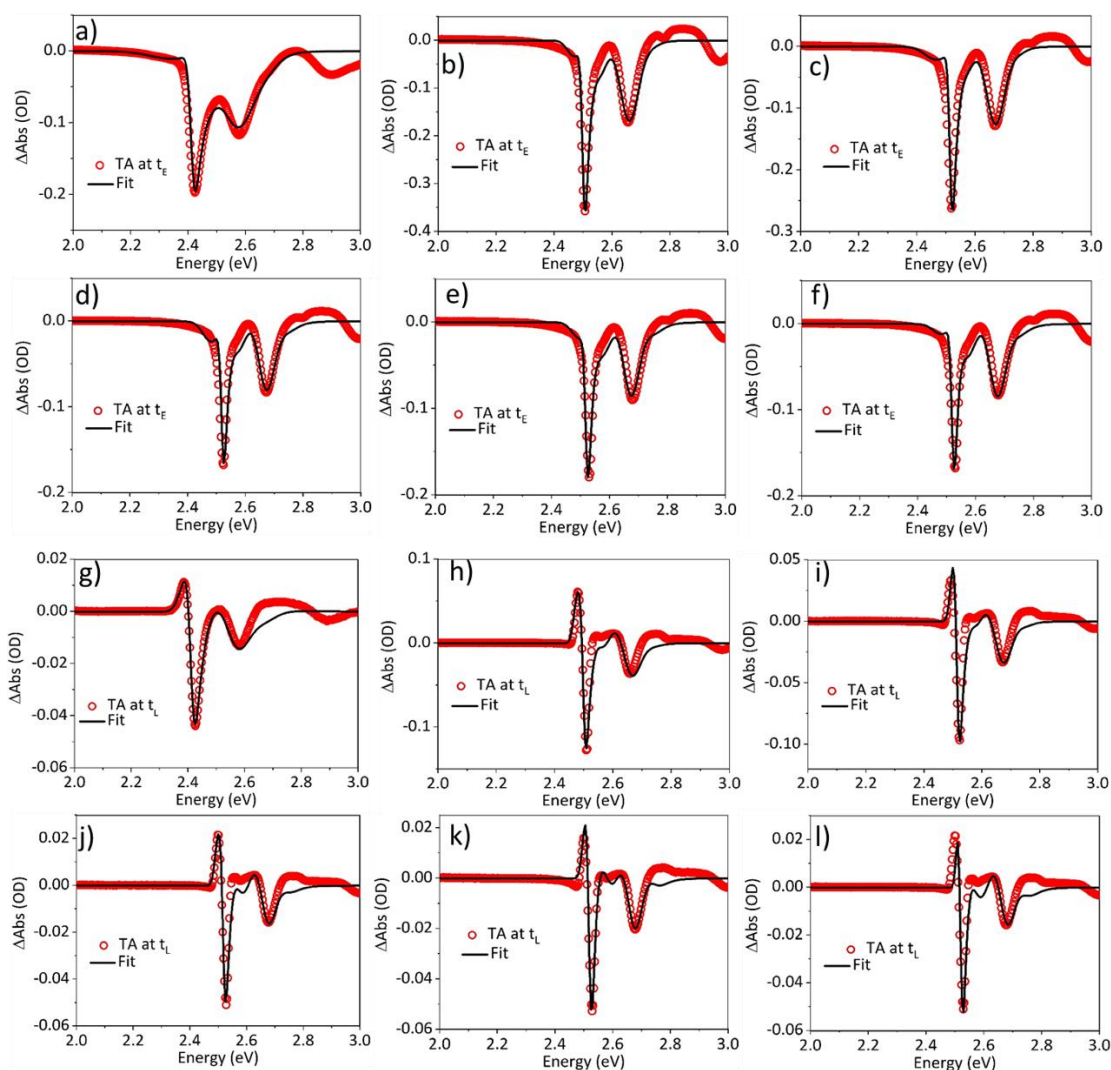


Figure 7.13. The TA spectra at early delay time (circles) and the fits (solid lines) of NPL1 in PMAO at (a) 298K, (b) 100K, (c) 50K, (d) 20K, (e) 10K, and (f) 4K. The TA spectra at long delay time (circles) and the fits (solid lines) of NPL1 in PMAO at (g) 298K, (h) 100K, (i) 50K, (j) 20K, (k) 10K, and (l) 4K.

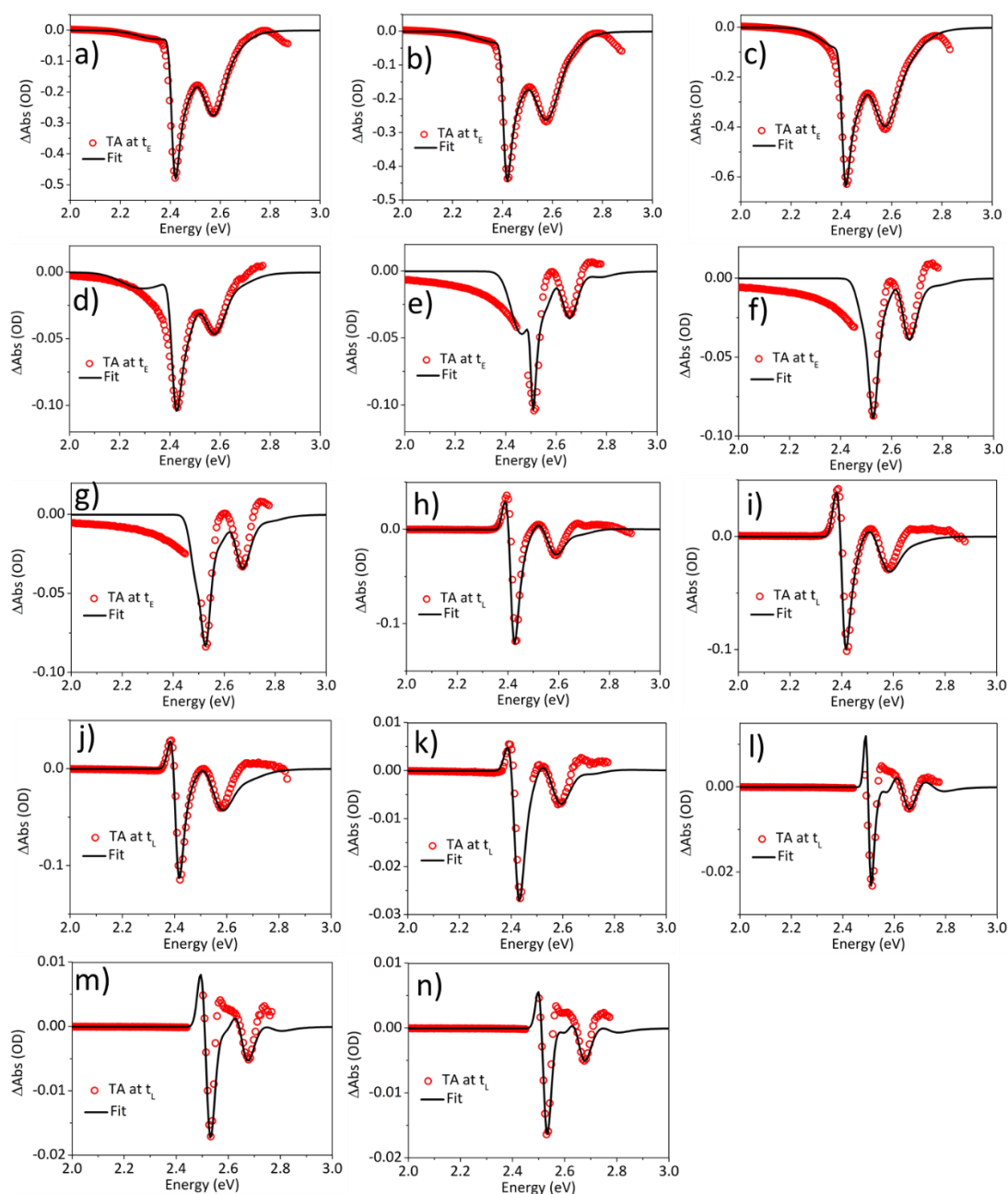


Figure 7.14. The TA spectra at early delay time (circles) and the fits (solid lines) of NPL2 in (a) hexane, (b) toluene, (c) chloroform, (d) PMMA at 298K, (e) PMMA at 100K, (f) PMMA at 20K, and (g) PMMA at 2.6K. The TA spectra at long delay time (circles) and the fits (solid lines) of NPL2 in (h) hexane, (i) toluene, (j) chloroform, (k) PMMA at 298K, (l) PMMA at 100K, (m) PMMA at 20K, and (n) PMMA at 2.6K.

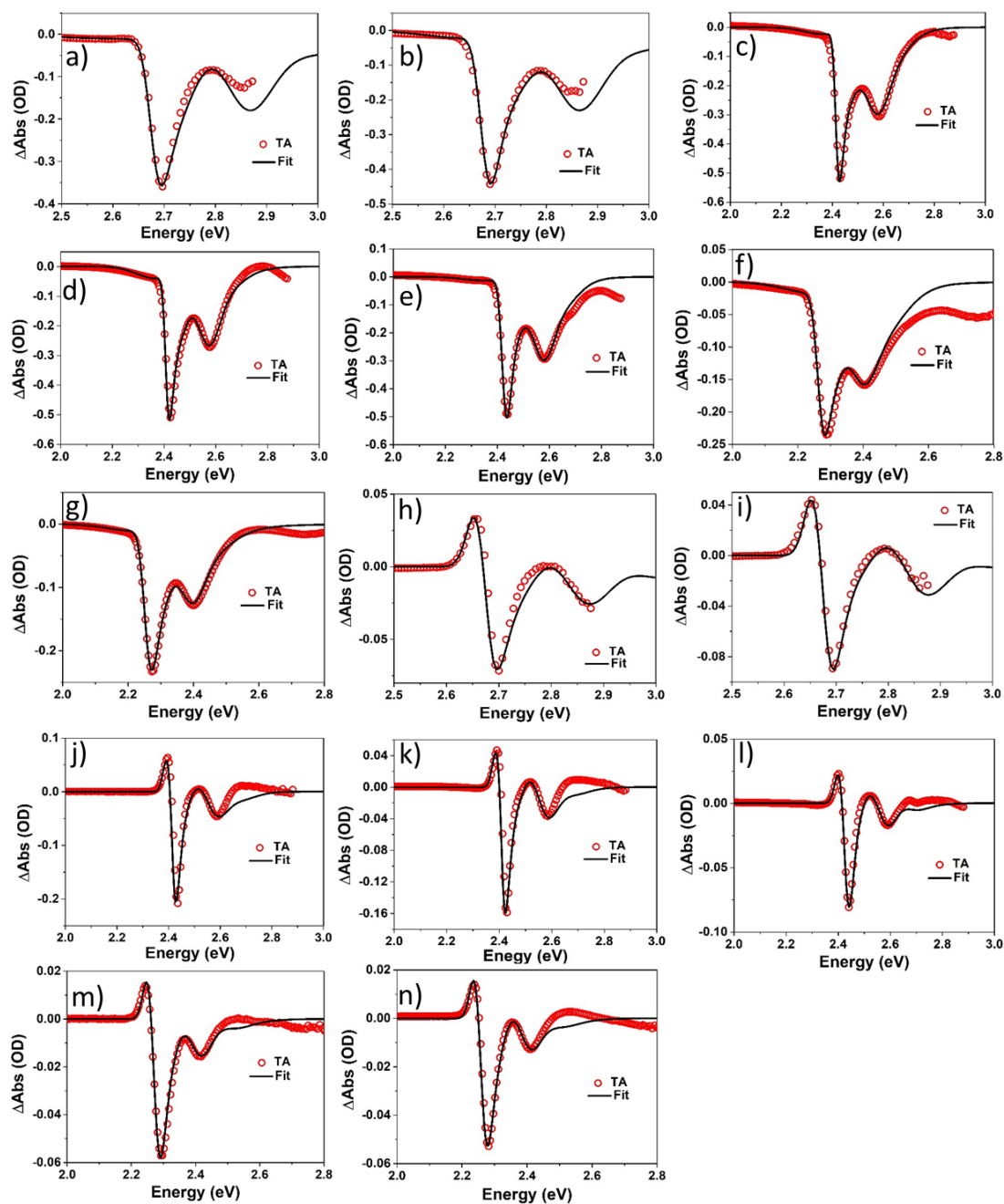


Figure 7.15. The TA spectra at early delay time (circles) and the fits (solid lines) of (a) 3MLa, (b) 3MLb, (c) 4MLa, (d) 4MLb, (e) 4MLc, (f) 5MLa, and (g) 5MLb. The TA spectra at long delay time (circles) and the fits (solid lines) of (h) 3MLa, (i) 3MLb, (j) 4MLa, (k) 4MLb, (l) 4MLc, (m) 5MLa, and (n) 5MLb.

Table 7.6. Fitting parameters and errors of TA spectra of NPL1 at different temperatures

		Hexane (298K)	PMAO (298K)	PMAO (100K)	PMAO (50K)	PMAO (20K)	PMAO (10K)	PMAO (4K)
t _E	E _G /meV	2200±10	2200±10	2420±10	2420±10	2430±10	2400±10	2380±10
	W _G /meV	300±2	300±2	100±2	100±2	100±2	200±2	200±2
	B _G /meV	50±5	100±5	30±5	50±5	35±5	35±5	35±2
	Δ _{Cont,A} /meV	131±5	116±5	171±5	171±5	161±5	151±5	171±5
	W _{C,A*} /meV	130±5	130±5	90±5	90±5	100±5	100±5	100±5
	C _A	0.022±0.00 1	0.012±0.0 01	0.012±0. 001	0.0089±0 .0001	0.0048±0 .0001	0.0047±0 .0001	0.0047±0 .0001
	C _B	0.038±0.00 1	0.021±0.0 01	0.027±0. 001	0.019±0. 001	0.010±0. 001	0.012±0. 001	0.011±0. 001
	C _G	0.000004± 0.000001	0.0015±0. 001	0.0010±0 .0001	0.005±0. 001	0.0015±0 .0001	0.00001± 0.00001	0.00001± 0.00001
X _A (Ex)/OD	0.386	0.191	0.343	0.256	0.155	0.162	0.163	
t _L	Δ _{X,S} /meV	35±1	35±1	30±1	20±1	25±1	20±1	10±1
	Δ _{X,P} /meV	10±1	10±1	18±1	18±1	18±1	15±1	15±1
	W _{X,S*} /meV	25±1	30±1	15±1	15±1	15±1	15±1	11±1
	η _{S*} /meV	60±1	100±1	20±1	20±1	19±1	20±1	14±1
	Δ _{Cont,A} /meV	72±1	55±1	80±1	80±1	75±1	60±1	80±1
	C _A	0.0088±0.0 001	0.0036±0. 0001	0.0053±0 .0001	0.0047±0 .0001	0.0020±0 .0001	0.0020±0 .0001	0.0024±0 .0001
	Δ _{X,B} /meV	35±1	48±1	30±2	25±2	20±2	15±2	15±3
	C _B	0.015±0.00 1	0.0063±0. 0001	0.012±0. 001	0.0098±0 .0001	0.0043±0 .0001	0.0052±0 .0001	0.0057±0 .0001
	X _A (Ex)/OD	0.152	0.061	0.155	0.134	0.064	0.070	0.085
	γ%	68.9%	56.2%	65.4%	71.3%	53.3%	52.8%	56.4%

Table 7.7. Fitting parameters and errors of TA spectra NPL2 at different temperatures

		Hexane (298K)	Toluene (298K)	Chloroform (298K)	PMMA (298K)	PMMA (100K)	PMMA (20K)	PMMA (2.6K)
t _E	E _G /meV	2100±10	2120±10	2130±10	2100±10	2420±10	2450±10	2470±10
	W _G /meV	500±2	510±2	540±2	550±2	80±2	100±2	50±2
	B _G /meV	100±5	97±5	97±5	100±5	50±5	35±5	30±2
	Δ _{Cont,A} /meV	111±5	106±5	101±5	171±5	171±10	141±5	170±5
	W _{C,A*} /meV	100±5	120±5	120±5	80±5	90±5	90±5	50±5
	C _A	0.027±0.00 1	0.024±0.0 01	0.032±0.00 1	0.0066± 0.0001	0.0025± 0.0001	0.0029± 0.0001	0.0024±0 .0001
	C _B	0.040±0.00 1	0.040±0.0 01	0.057±0.00 1	0.010±0. 001	0.005±0. 001	0.0049± 0.0001	0.0043±0 .0001
	C _G	0.00013±0. 00001	0.00009±0 .00001	0.00012±0. 00001	0.00002 ±0.0000 1	0.0055± 0.0001	0.0013± 0.0001	0.0031±0 .0001
X _A (E _X)/OD	0.458	0.409	0.544	0.104	0.073	0.064	0.055	
t _L	Δ _{X,S} /meV	35±1	35±1	30±1	35±1	20±1	30±1	20±1
	Δ _{X,P} /meV	10±1	10±1	10±1	10±1	15±1	10±1	15±1
	W _{X,S*} /meV	15±1	18±1	20±1	20±1	11±1	20±1	20±1
	η _S [*] /meV	100±1	70±1	80±1	100±1	20±1	15±1	13±1
	Δ _{Cont,A} /meV	68±1	65±1	50±1	60±1	95±1	95±1	95±1
	C _A	0.0082±0.0 001	0.0071±0. 0001	0.0093±0.0 001	0.0020± 0.0001	0.0011± 0.0001	0.0010± 0.0001	0.0010±0 .0001
	Δ _{X,B} /meV	30±1	35±1	25±1	30±1	20±1	15±1	10±1
	C _B	0.012±0.00 1	0.012±0.0 01	0.017±0.00 1	0.0032± 0.0001	0.0024± 0.00001	0.0016± 0.0001	0.0017±0 .0001
	X _A (E _X)/OD	0.140	0.134	0.156	0.032	0.032	0.021	0.022
	γ%	55.9%	61.8%	60.3%	56.0%	65.9%	42.9%	42.3%

Table 7.8. Fitting parameters and errors of TA spectra of 3MLa&b, 4MLa-c, and 5MLa&b in hexane

		3MLa	3MLb	4MLa	4MLb	4MLc	5MLa	5MLb
t _E	E _G /meV	2550±10	2600±10	2120±10	2130±10	2100±10	2230±10	2200±10
	W _G /meV	200±2	100±2	500±2	500±2	500±2	90±5	180±5
	B _G /meV	200±5	100±5	100±5	100±5	100±5	130±5	130±5
	Δ _{Cont,A} /meV	204±5	199±5	121±5	151±5	161±5	5±5	93±5
	W _{C,A*} /meV	50±5	80±5	120±5	120±5	100±5	120±5	130±5
	C _A	0.029±0. 001	0.030±0. 001	0.030±0. 001	0.029±0. 001	0.030±0. 001	0.015±0. 001	0.016±0. 001
	C _B	0.046±0. 001	0.053±0. 001	0.053±0. 001	0.045±0. 001	0.043±0. 001	0.017±0. 001	0.018±0. 001
	C _G	0.006±0. 001	0.006±0. 001	0.00012± 0.00001	0.00022± 0.00001	0.00006± 0.00001	0.006±0. 001	0.007±0. 001
	X _A (E _X)/OD	0.347	0.421	0.507	0.484	0.490	0.209	0.221
t _L	Δ _{X,S} /meV	28±1	28±1	35±1	35±1	35±1	25±1	25±1
	Δ _{X,P} /meV	15±1	15±1	10±1	10±1	10±1	10±1	10±1
	W _{X,S*} /meV	25±1	23±1	18±1	18±1	22±1	30±1	23±1
	η _S [*] /meV	55±1	45±1	100±1	100±1	80±1	60±1	60±1
	Δ _{Cont,A} /meV	125±1	135±1	75±1	70±1	75±1	50±1	60±1
	C _A	0.0097± 0.001	0.010±0. 001	0.016±0. 001	0.012±0. 001	0.0067±0 .0001	0.0067±0 .0001	0.0062±0 .0001
	Δ _{X,B} /meV	40±1	40±1	37±1	30±1	37±1	20±1	28±1
	C _B	0.015±0. 001	0.018±0. 001	0.029±0. 001	0.019±0. 001	0.0094±0 .0001	0.0079±0 .0001	0.0073±0 .0001
	X _A (E _X)/OD	0.116	0.141	0.269	0.206	0.109	0.096	0.088
	γ%	46.9%	46.9%	62.5%	65.5%	57.7%	77.1%	70.0%

Appendix 7.6

Dielectric environment dependent exciton coherent area

The temperature-dependent S_x and N_s of NPL2 in poly(methyl methacrylate) (PMMA) are listed in Table 7.9. We changed the dielectric environment of NPL2 by dispersing NPL2 in different solvents: hexane, toluene, and chloroform with a dielectric constant of 1.9, 2.4, and 4.8, respectively.²⁵⁴ The S_x of NPL2 in various solvents are obtained as 90.3 ± 14.1 nm² in hexane, 87.5 ± 13.7 nm² in toluene, and 78.7 ± 12.3 nm² in chloroform (Figure 7.16 and Table 7.9).

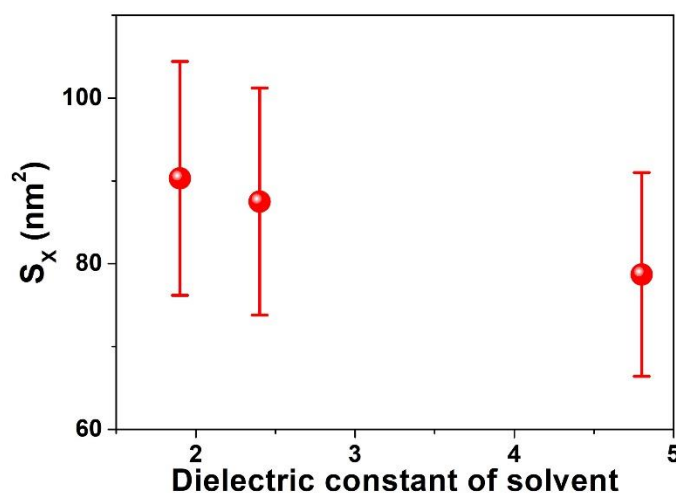


Figure 7.16. Exciton coherent spatial area of 4MLc as a function of solvent dielectric constant.

Table 7.9. Temperature- and solvent-dependent band-edge exciton coherent area (S_x) and the saturation number of band-edge excitons per NPL (N_s) of NPL2.

	S_x (nm ²)	N_s
Hexane	90.3±14.1	3.66±0.02
Toluene	87.5±13.7	3.78±0.02
Chloroform	78.7±12.3	4.20±0.02
PMMA 298K	90.4±14.5	3.66±0.02
PMMA 100K	111.8±15.2	3.00±0.02
PMMA 20K	126.2±14.6	2.62±0.02
PMMA 2.6K	155.9±9.4	2.12±0.02

Chapter 8. Low Threshold Multi-Exciton Optical Gain in CdSe/CdTe Core/Crown Type-II Nanoplatelets Heterostructures

Reproduced with permission from *ACS Nano* **2017**, *11*, 2545. Copyright 2017 American Chemical Society.

8.1. Introduction

Colloidal cadmium chalcogenide nanoplatelets (NPLs) have shown novel physical properties such as uniform 1D quantum confinement, high luminescent quantum yield, and giant oscillator strength.^{19-21, 32, 61, 69, 95, 109, 145, 150, 152, 164, 166} These properties have led to many promising applications, including lasing,^{30-33, 146} photocatalysis,^{42, 62} light-emitting diodes,¹⁶⁷ and phototransistors.¹⁶⁸⁻¹⁶⁹ The properties of these materials can be further improved in NPL heterostructures with type-I or type II band alignment.^{26, 30, 69, 108-109, 143, 151, 155, 165, 181, 221-222} For example, CdSe/CdTe core/crown (CC) NPLs form type-II heterostructures, in which both the conduction band (CB) and valence band (VB) of CdSe are lower with respect to those of CdTe, excitons are driven with unity quantum efficiency to form long-lived charge transfer (CT) exciton states across the CdSe/CdTe interface, extending the exciton lifetime compared to single component materials.^{68, 109, 155, 181} A previous study of type-II core/shell quantum dots (QDs) has demonstrated that single-exciton optical gain can be achieved due to large energy blue shift of the second CT exciton, suggesting great potentials of type-II heterostructures for low threshold lasing.¹⁵ Unlike core/shell QDs, core/crown type-II NPLs can achieve larger spatial separation between the core and crown excitons, which may prolong the lifetime of multiple exciton states. Coupled with their large absorption cross-section, type-II NPLs may

be promising materials for low threshold multiple exciton lasing. Rational design and optimization of NPL heterostructures for lasing and other light emitting applications requires fundamental understanding of multi-exciton structure and dynamics and the optical gain (OG) state in these materials, which remains poorly understood.

In this chapter, we report a study of the energetics, spatial distribution and dynamics of one to six exciton states in CdSe/CdTe CC NPL heterostructures. By excitation fluence and wavelength dependent ultrafast transient absorption (TA) spectroscopy, we have identified three types of excitons, *i.e.* interface localized X_{CT} , CdTe crown-localized X_{CdTe} , and CdSe core-localized X_{CdSe} excitons (in the order of increasing energies). These exciton levels, with each accommodating up to two excitons, can be sequentially filled at high excitation energy and flux to generate one to six exciton states. The spatial arrangement and formation and decay dynamics of these single and multiple exciton states are discussed. OG can be achieved in tri- ($XX_{CT}X_{CdTe}$) and four- ($XX_{CT}XX_{CdTe}$) exciton states. Although OG requires multiple excitons in CC NPLs, their large absorption cross-section results in over 40 folds lower OG threshold ($\sim 43 \mu\text{J}/\text{cm}^2$ at 550 nm pump) compared to reported single-exciton gain threshold in type-II core/shell QDs ($\sim 2 \text{ mJ}/\text{cm}^2$).¹⁵ Moreover, unlike in type II core/shell QDs, 2D morphology extends the spatial separation of different excitons, which lengthens the multi-exciton state and gain lifetimes, suggesting potential applications of these materials in low threshold lasing and high power light emitting devices.

8.2. Results and Discussion

8.2.1. Sample characterization

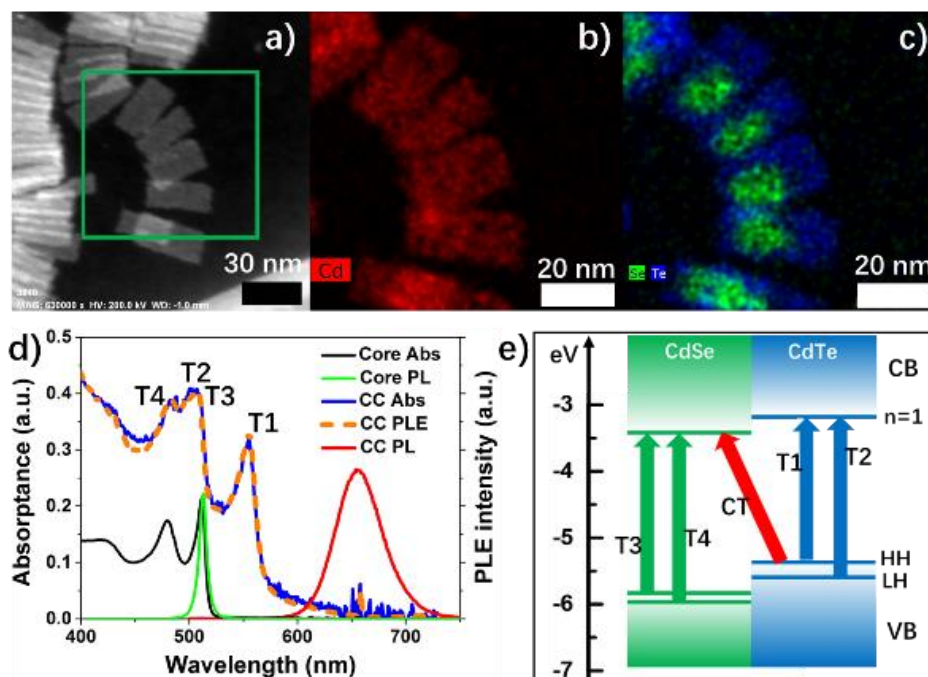


Figure 8.1. TEM images, absorption spectra and band alignment. (a) HAADF-STEM images and (b,c) EDX images of elemental distribution of Cd (red), Se (green), and Te (blue) of CdSe/CdTe CC NPLs. (d) Absorbance spectra of CdSe core (black solid line) and CdSe/CdTe CC (blue solid line), photoluminescence spectra (right vertical axis) of CdSe core (green solid lines) and CdSe/CdTe CC (red solid lines), and PLE spectrum of CC NPLs (orange dashed line). (e) Relevant energy levels, type-II band alignment and exciton transitions in CdSe/CdTe CC NPLs.

Colloidal CdSe/CdTe CC NPLs were synthesized following the reported procedures with slight modifications.¹⁰⁹ 4 monolayer (ML) CdSe NPL cores, which has a zinc blend structure with 4 Se layers, 5 Cd layers and a thickness of ~ 1.8 nm,²¹ were first synthesized. High-angle annular dark-field (HAADF) scanning TEM (STEM) images of CdSe/CdTe CC NPL solution sample (Figure 8.1a) show rectangular shaped CC NPLs. Energy-dispersive X-ray (EDX) images of selected areas in Figure 8.1a (green square) show Cd in both the core and crown (Figure 8.1b) and Se and Te in the core, and crown, respectively (Figure 8.1c). From TEM

images (Figure 8.8a&b in Appendix 8.1), the lateral sizes of CC NPL and CdSe core were determined. The rectangular CdSe core has an average length of 18.6 ± 2.4 nm and width of 8.5 ± 1.6 nm (Table 8.1 in Appendix 8.1). In CC NPLs, the size is extended to 33.0 ± 3.4 nm in length and 14.1 ± 1.5 nm in width, while their thickness remains the same according to the exciton peak positions in the absorbance spectra (Figure 8.1d).

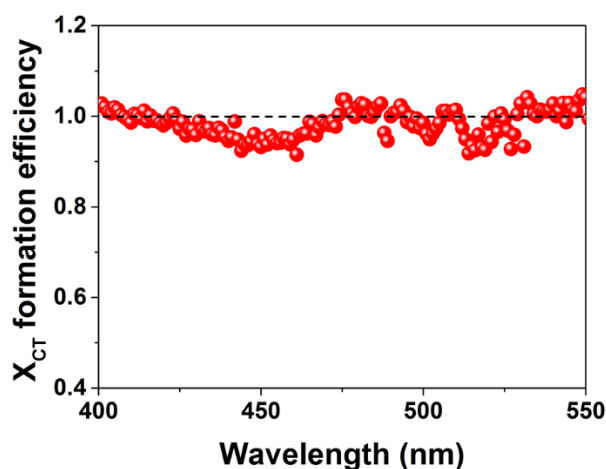


Figure 8.2. The CT exciton formation efficiency of CdSe/CdTe CC NPLs according to the ratio of the normalized PLE to absorbance spectra in Figure 8.1c.

The absorbance ($1 - 10^{-\text{Optical Density}}$, the percentage of absorbed photons) and steady-state photoluminescence (PL) spectra of CC NPLs and CdSe core are shown in Figure 8.1d. Four sharp exciton features are observed in the absorbance spectra of CC NPLs: T1 (~554 nm) and T2 (~500 nm) are the electron-heavy hole (e-hh) and electron-light hole (e-lh) transitions, respectively, in the CdTe crown, while T3 (~512 nm) and T4 (~485 nm) are the corresponding transitions in the CdSe core, as shown in Figure 8.1e.^{21, 109, 155, 181} In addition, there is a broad absorption feature from 570 to 650 nm, which is absent in either CdSe or CdTe NPLs alone and has been attributed to the transition to the CT exciton state (with an electron in CdSe CB edge and hole in CdTe VB edge).^{109, 155, 181} The PL spectrum of CC NPLs shows a broad CT

exciton emission at ~ 660 nm with no observable CdSe or CdTe emissions. The normalized photoluminescence excitation (PLE) spectra of CC NPLs (monitoring the CT band emission) match their absorbance spectra (Figure 8.1d and Figure 8.2), indicating unity CT exciton formation efficiency, consistent with reported in Chapter 4.^{109, 155}

8.2.2. Charge transfer exciton state

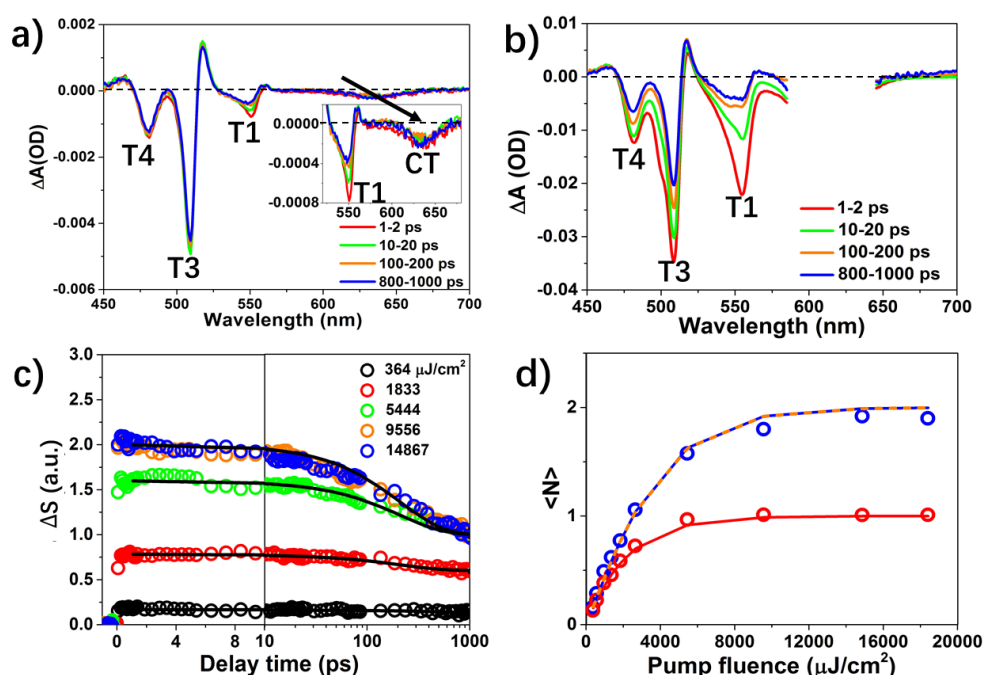


Figure 8.3. Transient absorption spectra and kinetics of CdSe/CdTe CC NPLs measured at 620 nm excitation. The TA spectra at indicated delay times measured at a pump fluence of (a) $364 \mu\text{J}/\text{cm}^2$ and (b) $14867 \mu\text{J}/\text{cm}^2$. (c) Normalized T4 kinetics at selected pump fluences (circles) and their fits (solid lines). (d) Average electron number per NPL in CdSe core at 1-2 ps (blue circles) and 800-1000 ps (red circles), their fits (solid line, see the main text and the Appendix 8.3 for details), and average total initial exciton number per CC NPL (orange dashed line).

To determine the nature and energy order of different exciton states in CdSe/CdTe CC NPLs, we carried out pump fluence and wavelength dependent transient absorption (TA)

spectroscopy studies. We started out with 620 nm excitation of the lowest energy CT exciton band, directly promoting an electron from the CdTe crown VB heavy hole level into CdSe core CB edge.¹⁰⁹ As shown in Figure 8.3a, the TA spectra at the lowest pump fluence ($364 \mu\text{J}/\text{cm}^2$) show bleaches of CdSe (T3 and T4) and CT (broad feature centered at 630 nm, inset of Figure 8.3a) exciton bands. Our previous TA studies of colloidal NPLs and heterostructures have shown that both exciton bleach of CdSe and CdTe are caused by state-filling of the CB electron levels,^{62, 69, 109} with negligible contribution of hole state-filling due to the mixing and degeneracy of denser hole levels in VB, similar to cadmium chalcogenide quantum dots (QDs) and nanorods (NRs).^{78, 110, 148, 183} Indeed, the T3, T4, and CT bleaches show the same kinetics (Figure 8.10 in Appendix 8.3), indicating that they probe the same electron state-filling effect in n=1 level of CdSe core.¹⁰⁹ These signals are formed instantaneously upon optical excitation and show negligible decay within 1 ns, consistent with the direct formation of long-lived single CT exciton state (Figure 8.10 in Appendix 8.3). The TA spectra at the highest pump fluence ($14867 \mu\text{J}/\text{cm}^2$, Figure 8.3b) also show T3 and T4 exciton bleach features, similar to those observed at low pump fluences. However, the CT bleach signals cannot be clearly observed due to the interference of the scattered 620 nm excitation pulse. In addition, because of the larger spectral overlap between the CdSe T3 exciton and CdTe T2 exciton bleaches, we will use the T4 bleach to follow the electron dynamics in CdSe core.

A comparison of the normalized TA spectra at difference pump fluences (Figure 8.9 in Appendix 8.2) shows that at long delay time (800-1000 ps), all excited CC NPLs (with bi- and single-excitons) decay to the long-lived single CT exciton state. Thus, the amplitude of the T4 bleach at 800-1000 ps is proportional to the probability of finding excited CC NPLs and can be scaled to one at the highest fluence, when all NPLs are excited. The same scaling factor is applied to the T4 bleach amplitude at other delay time and the scaled bleach amplitude represents the average number of electrons in the n=1 level of CdSe core. The scaled T4 bleach

kinetics at different pump fluences are compared in Figure 8.3c. At low pump fluences, the signal is dominated by the slow decay of a long-lived single CT exciton state ($\gg 1$ ns). With increasing pump fluences, the amplitude of T4 bleach increases and there appears a faster decay component, which can be attributed bi-exciton Auger recombination (see below). At even higher pump fluences, the T4 kinetics become independent of the pump fluence ($>9556 \mu\text{J}/\text{cm}^2$), indicating the saturation of CT exciton states. The scaled T4 kinetics can be well fit to a model that assumes the existence of only single CT exciton (X_{CT}) and bi-CT exciton (XX_{CT}) states (with lifetime of $\gg 1$ ns, and 209 ± 4 ps, respectively). The details of the fitting model (fitting parameters) can be found in Appendix 8.3 (Table 8.3).

The scaled T4 bleach amplitudes at early delay time (1-2 ps, when exciton-exciton annihilation is negligible) and long delay time (800-1000 ps, when exciton-exciton annihilation is completed) as a function of pump fluences are compared in Figure 8.3d. The signal amplitudes saturate at 1 and 2 at late (800-1000 ps) and early (1-2 ps) delay times, respectively, at high fluences when all NPLs are excited. This result reveals that the CT exciton states can accommodate up to two excitons (due to two-fold spin degeneracy in the CB electron level). As shown in Figure 8.3d, the early and long delay time bleach amplitudes as a function of pump fluence can be fit to $P_1(m) + 2[1 - P_0(m) - P_1(m)]$, and $1 - P_0(m)$, respectively, where $P_n(m)$ is the Poisson distribution probability of encountering n photons when the average number of encountered photons is m . The fits also reveal the total average number of excitons (w) per CC NPL in the sample at any pump fluences (Figure 8.3d, orange dashed line),^{69, 76} which also saturates at 2 because the maximum number of photons that can be absorbed is two per NPL at this excitation wavelength. The details of this fit can be found in Appendix 8.2. The same analysis procedure will be applied to all pump fluence dependent signal amplitudes measured at shorter excitation wavelengths to be discussed below.

The TA spectra (Figure 8.3a) show a derivative feature of the CdSe T1 exciton band, which can be attributed to the red shift of T1 exciton band in the presence of CT exciton (*i.e.* T1 and CT biexciton interaction).¹⁰⁹ In addition, the TA spectra also show a T1 exciton bleach signal at high fluence. The origin of this signal is not clear. It can be attributed to small probability of direct excitation of electrons to the CdTe CB band edge from filled defect states above the VB edge, because the CdTe nanoplatelets show an absorption tail below the T1 exciton band, extending to 620 nm.^{21, 255} Unfortunately, this contribution cannot be easily quantified in CdSe/CdTe heterostructures due to its overlap with the CT band.

8.2.3. Long-lived excitons in the CdTe crown

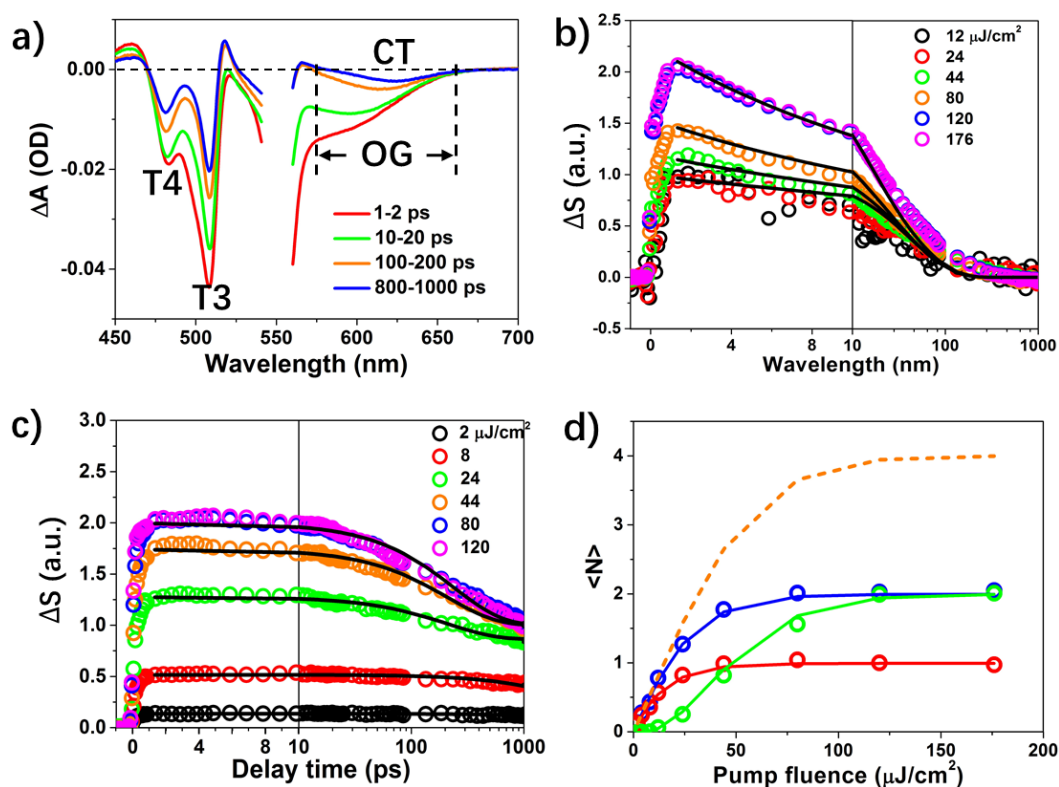


Figure 8.4. Transient absorption spectra and kinetics of CdSe/CdTe CC NPLs measured at 550 nm excitation. (a) TA spectra at indicated delay times measured at a pump fluence of 80 $\mu\text{J}/\text{cm}^2$. (b) Normalized optical gain (OG) kinetics at selected pump fluences (circles) and their

fits (solid lines), where ΔS represents normalized TA signal. (c) Normalized T4 kinetics at selected pump fluences (circles) and their fits (solid lines), where ΔS represents normalized TA signal. (d) Average electron number in CdSe core per CC NPL as a function of pump fluence at 1-2 ps (blue circles) and 800-1000 ps (red circles), average number of long-lived electrons in CdTe crown at 1-2 ps, and fits (solid lines) to these data according to a Poisson distribution model (see Supporting Information). Dashed orange line represents the average total initial exciton number per CC NPL as a function of pump fluence.

To investigate higher energy exciton states above the CT exciton band, we measured the TA spectra of CC NPLs by exciting the CdTe crown T1 band at 550 nm. TA spectra and kinetics measured at low pump fluence ($2 \mu\text{J}/\text{cm}^2$) are shown in Figure 8.11a-c in Appendix 8.3. The comparison of T1, CT, T3, and T4 exciton bleach kinetics (Figure 8.11b&c in Appendix 8.3) shows a fast T1 bleach recovery (0.30 ± 0.02 ps) and a corresponding formation of the CT, T3, and T4 bleaches, indicating an ultrafast electron transfer from the CdTe crown to CdSe core to form the long-lived single CT exciton state. This result is consistent with our previous finding in similar CdSe/CdTe NPLs.¹⁰⁹ Details of the fitting model and parameters are shown in Appendix 8.3 (Figure 8.11 and Table 8.2). At higher pump fluences, as shown in Figure 8.4a (pump fluence of $80 \mu\text{J}/\text{cm}^2$), a broad negative TA feature between T1 and CT exciton bleach is also present in the first 100 ps, in addition to the T3, T4 and CT exciton bleach features observed under low fluences. This signal can be attributed to the OG signal of CC NPLs, which has also been observed in QDs,¹⁶ and other colloidal NPLs.³³ The OG kinetics can be conveniently followed by the TA signal amplitude at 580-582 nm, because, at this wavelength, the TA signal was \sim zero after 100 ps (Figure 8.4a), and the signal at < 100 ps can be attributed exclusively to OG.

The normalized T4 bleach kinetics at selected pump fluences, scaled according to the procedure described above and in Appendix 8.2, are compared in Figure 8.4c. As shown in Figure 8.4d, the scaled T4 amplitudes at early (1-2 ps, when the crown to core electron transfer is completed and multiple exciton annihilation is negligible) and long delay times (800-1000 ps, when multi-exciton annihilation is completed) increase with the pump fluence until they saturate at 2 and 1, respectively, confirming the initial number of CT excitons also saturates at 2 at 550 nm excitation. The pump fluence dependent kinetics in Figure 8.4c can be fit to the same kinetics model shown in Figure 8.3c, consisting of single- and bi- CT exciton states with lifetime of > 1 ns and 209 ± 4 ps (Table 8.4 in Appendix 8.3), respectively. Indeed, a comparison of the T4 bleach kinetics measured with 550 nm and 620 nm excitation (Figure 8.5c, Table 8.3&8.5 in Appendix 8.3) at saturation pump fluences confirms that the same CT exciton states are generated regardless of the excitation wavelength. These kinetics differ in the initial formation phase (not shown) due to the crown to core electron transfer at 550 nm excitation, as discussed above.

It will be shown below (Figure 8.12c and 8.13b in Appendix 8.3, transient kinetics measured at 525 and 400 nm excitation, respectively) that the OG kinetics follow the T1 kinetics after the initial crown to core electron transfer is completed, revealing that the OG is due to additional excitons in CdTe crown. It is reasonable to assume the same origin for the OG signal at 550 nm excitation, although a direct comparison of OG and T1 kinetics cannot be established in this case because the T1 signal contains strong interference of scattered 550 nm excitation photons at high pump fluences. Figure 8.4b shows the comparison of the normalized OG kinetics at different pump fluences, in which the OG signals have been normalized to the same amplitude at 150-1000 ps. The normalized OG kinetics are the same at low pump fluences ($< 44 \mu\text{J}/\text{cm}^2$), reflecting the dominance of single crown exciton state (in addition to two excitons in the CT state) that decays with a lifetime of 43.5 ± 4.3 ps (see below). With increasing

pump fluence, a fast decay component (11.8 ± 0.3 ps, see below) appears in addition to the slower decay component observed at low fluences, which is attributed to the multiple crown exciton annihilation process. The amplitude of the fast decay component increases with pump fluence until it saturates at a pump fluence of $120 \mu\text{J}/\text{cm}^2$, after which the kinetics became independent of pump fluence and the initial signal amplitude saturates at \sim twice of that of the slow component.

The pump fluence dependent OG signal amplitudes can be scaled using the procedures described above (see Appendix 8.2). The scaled OG signal at 1-2 ps reflects the average number of excitons in the CdTe crown, after crown-to-core transfer has completed and before significant exciton-exciton annihilation has occurred. A plot of this signal as a function of pump fluence (Figure 8.4d) shows a delay onset of crown excitons compared to CT excitons. It can be well fit (Figure 8.4d, green solid line) by this expression: $P_3(m) + 2 \sum_{n=4}^{\infty} P_n(m)$, where the first term is a tri-exciton state ($XX_{\text{CT}}X_{\text{CdTe}}$) with two CT excitons and one CdTe crown exciton and second term is a four-exciton state ($XX_{\text{CT}}XX_{\text{CdTe}}$) with two CT excitons and two crown excitons. This result confirms that up to two additional relatively long-lived excitons can be generated in the CdTe crown after the saturation of the two CT exciton states. The fit of these data also reveals the average number of excitons in the NPL at any pump fluences (orange dashed line in Figure 8.4d), which saturates at 4, accounting for two CT excitons and two crown excitons. The excitation fluence dependence of the OG gain kinetics (Figure 8.4b) can be fit to a model that contains a long-lived tri-exciton ($XX_{\text{CT}}X_{\text{CdTe}}$, with lifetime of 43.5 ± 4.3 ps) and four exciton ($XX_{\text{CT}}XX_{\text{CdTe}}$, 11.8 ± 0.3 ps) states in the NPL. Compared to tri-exciton and four-exciton states in QDs,^{29, 179} the relatively long lifetimes of these multiple exciton states in CdSe/CdTe NPLs can be attributed to the spatial separation of CT and crown-based excitons.

8.2.4. Higher energy excitons in the CdSe core

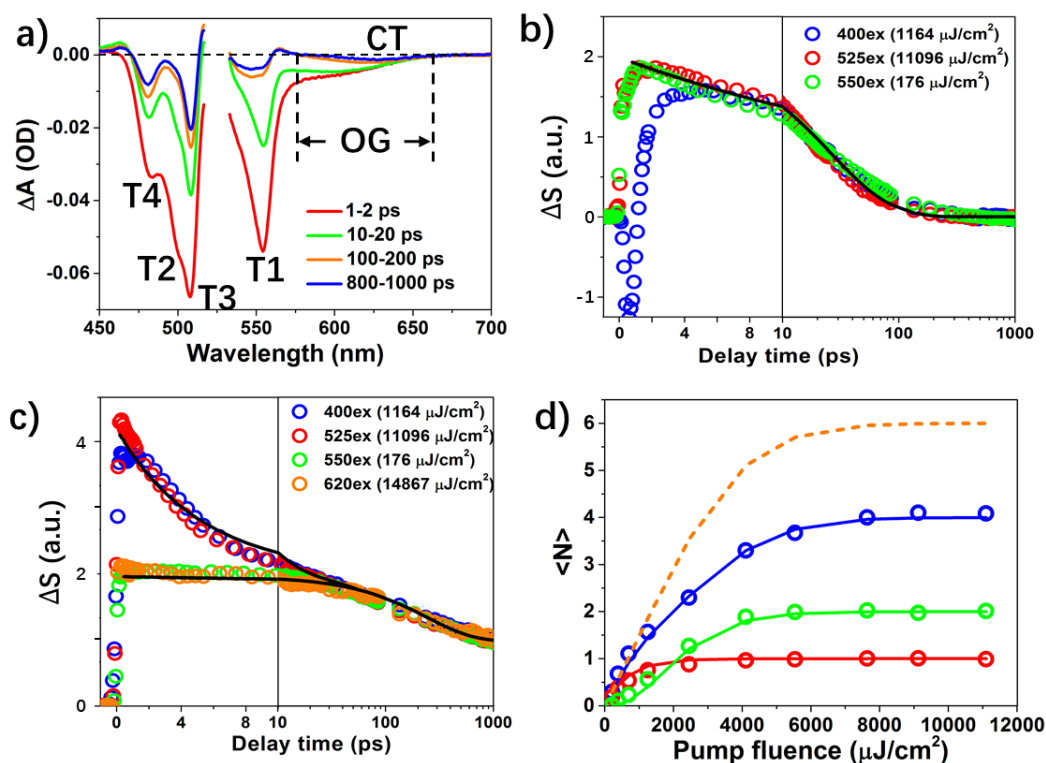


Figure 8.5. Transient absorption spectra and kinetics of CdSe/CdTe CC NPLs measured at 520 nm excitation (a) The TA spectra indicated delay times measured at a high pump fluence (11096 $\mu\text{J}/\text{cm}^2$). (b) Comparison of OG kinetics measured at 400, 525 and 550 nm excitation at saturation fluences, where ΔS represents normalized TA signal. (c) Comparison of T4 bleach kinetics measured at 400, 525, 550 and 620 nm excitation at saturation fluences, where ΔS represents normalized TA signal. (d) Average electron number in CdSe core per CC NPL as a function of 525 nm pump fluence at 1-2 ps (blue circles) and 800-1000 ps (red circles), average number of additional CdTe crown excitons per CC NPL at 1-2 ps (Green circles), fits to these data (solid lines) according to Poisson distribution model (see Supporting information), and is the total average exciton number per CC NPL as a function of pump fluence (dashed line) obtained from the fit.

To access even higher exciton states, we carried out TA studies at 525 nm and 400 nm excitation. At these wavelengths both the CdTe crown and CdSe core-based transitions can be excited. The TA spectra and kinetics for 525 nm (Figure 8.5 and Figure 8.12 in Appendix 8.3) and 400 nm (Figure 8.13 in Appendix 8.3) excitation are qualitatively similar and only the former is discussed in detail here. As shown in Figure 8.5a, the TA spectra at indicated delay times at 525 nm pump fluence of $11096 \mu\text{J}/\text{cm}^2$ show spectral features similar to those measured at 550 nm. The comparison of T1 and OG kinetics at selected pump fluences are shown in Figure 8.12c in Appendix 8.3. At low pump fluences, OG signal is negligible; T1 bleach shows an ultrafast ($< 1\text{ps}$) decay (caused by the fast crown-to-core electron transfer driven by the type-II band alignment), similar to those measured at 550 nm (Figure 8.11c in Appendix 8.3).¹⁰⁹ At higher pump fluences, an additional decay component with a time constant of $43.5 \pm 4.3 \text{ ps}$ (see below) appear in the T1 kinetics, which is attributed to the presence of long-lived excitons in CdTe crown after the completion of the initial ultrafast crown-to-core electron transfer (Figure 8.12a&c in Appendix 8.3). The appearance of this signal coincides with the OG, and these features show the same decay kinetics, indicating that the optical gain results from the additional excitons in the CdTe crown. The power dependence of these signals are similar to those of OG kinetic measured at 550 nm and can be fit by the same kinetic model that accounts for a long lived tri-exciton state ($\text{XX}_{\text{CT}}\text{X}_{\text{CdTe}}$, $43.5 \pm 4.3 \text{ ps}$) and four exciton state ($\text{XX}_{\text{CT}}\text{XX}_{\text{CdTe}}$, $11.8 \pm 0.3 \text{ ps}$). As shown in Figure 8.5b, at saturation fluences, the OG kinetics measured at 400 and 525 nm excitation are identical to those measured at 550 nm excitation (Figure 8.4b). The pump fluence dependence of the signal amplitudes at early delay time (1-2 ps) (Figure 8.5d) can be analyzed in the same way as the result shown in Figure 8.4d, confirming the crown exciton number saturates at 2. These results suggest that at excitation energy above the crown band gap (550, 525 and 400 nm), up to two

excitons can be accommodated in the crown after both CT states are filled. These crown excitons cannot be populated by direct excitation of the CT excitation.

The scaled T4 kinetics at selected 525 (400) nm pump fluences are shown in Figure 8.12b in Appendix 8.3 (Figure 8.13d in Appendix 8.3). A comparison of the kinetics at saturation fluences measured with 400, 525 and 550 nm excitations show that these signals at longer delay time (50 ps -1 ns) are identical, dominated by the long-lived bi-CT exciton (XX_{CT}) state (Figure 8.5c). The kinetics at 400 and 525 nm excitation show additional fast decay components with time constants of 5.86 ± 0.12 ps and 4.5 ± 0.2 ps, and an initial amplitude that are twice as large (see Table 8.5 in Appendix 8.3). As shown in Figure 8.5d (and Figure 8.13e in Appendix 8.3), the scaled T4 bleach amplitudes at late (800-1000 ps) and early (1-2 ps) delay times saturate at 1 and 4, respectively. These results suggest that at high 525 and 400 nm excitation fluence, there exist two additional electrons at the CB edge of the CdSe core in addition to the two electrons associated with CT excitons. Because these excitons cannot be created at lower excitation wavelength (620 and 550 nm, below the CdSe band edge), we attribute them to CdSe core-based excitons created by direct excitation of the CdSe exciton bands. The initial scaled T4 bleach amplitude (at 1-2 ps) as a function of pump fluence is well fit by $P_1(m) + 2[P_2(m) + P_3(m) + P_4(m)] + 3P_5(m) + 4 \sum_{n=6}^{\infty} P_n(m)$, where the first and the second terms are the probability of creating 1 and 2 CT excitons, and third and fourth terms are probability of creating additional 1 and 2 excitons in the CdSe core, *i.e.* five ($XX_{CT}XX_{CdTe}X_{CdSe}$) and six ($XX_{CT}XX_{CdTe}XX_{CdSe}$) exciton states, respectively). The fitting details are described in Appendix 8.2. This result suggests that when the excitation energy is above the CdSe band edge, two additional excitons can be created at the core after the saturation of the two CT excitons and two crown excitons.

8.2.5. Spatial distribution and energetics of exciton states

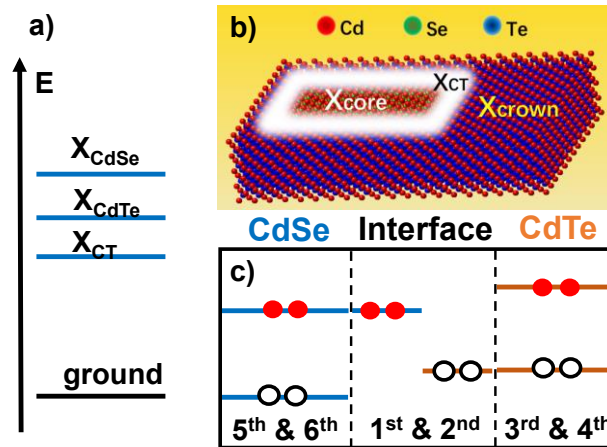


Figure 8.6. Three exciton states in CC NPL. (a) Scheme of the three energetically separated exciton states in CdSe/CdTe CC NPLs. (b, c) Three spatially separated exciton states in CdSe/CdTe CC NPLs.

The result above shows three distinct types of excitons with interesting spatial arrangement in CdSe/CdTe type II CC NPLs. These are interface localized X_{CT} , crown-localized X_{CdTe} , core-localized X_{CdSe} excitons in the order of increasing energy, as shown in Figure 8.6a. This energy order is consistent with the band gap and band alignment of these materials. Each exciton level can be doubly occupied, due to the 2-fold spin degeneracy of the CB electron levels. Although excitons in the core and crown are not strongly quantum confined in the lateral direction, the numbers of band edge excitons are limited by their size (18.5 nm x 8.5 nm and 15 nm x 14 nm for the core and crown, respectively). Both interface-localized X_{CT} excitons (exciton 1& 2) and crown-localized X_{CdTe} , excitons (exciton 5&6) have electrons in the $n=1$ level of the CdSe core (because the formation of both leads to the bleach of the T4 transition). It suggests that the CdSe core has the spatial area to accommodate 4 electrons in the $n=1$ level. However, only two X_{CT} excitons can be generated (with only two electrons at the CdSe core), suggesting that the electrons in this exciton state cover only half of the space available in the

CdSe core, localizing at the core/crown interface (Figure 8.6b). This is consistent with the expectation of strong Coulomb interaction between the electron in the CdSe and hole in CdTe (Figure 8.6b). In tri- ($XX_{CT}X_{CdTe}$) and four- ($XX_{CT}XX_{CdTe}$) exciton states generated with excitation wavelength above the CdTe band edge (Figure 8.4&8.5), the crown-based X_{CdTe} excitons do not undergo electron transfer to the CdSe core despite a favorable 0.3 eV band offset (Figure 8.1e). The driving force for electron transfer is reduced if one considers the loss of strong attractive e-h Coulomb interaction in crown and increase e-e and h-h repulsion accompanying such transfer. It is possible that such transfer is prevented because of the full occupancy of the CdSe interface region by the electrons associated with the CT excitons, prolonging the lifetime of the crown-based exciton states. Similarly, we speculate that the CT exciton is also responsible for the localization of exciton 5 and 6 in the CdSe core, despite the large driving force for moving the hole from the CdSe to CdTe.

8.2.6. Pump wavelength dependent optical gain threshold

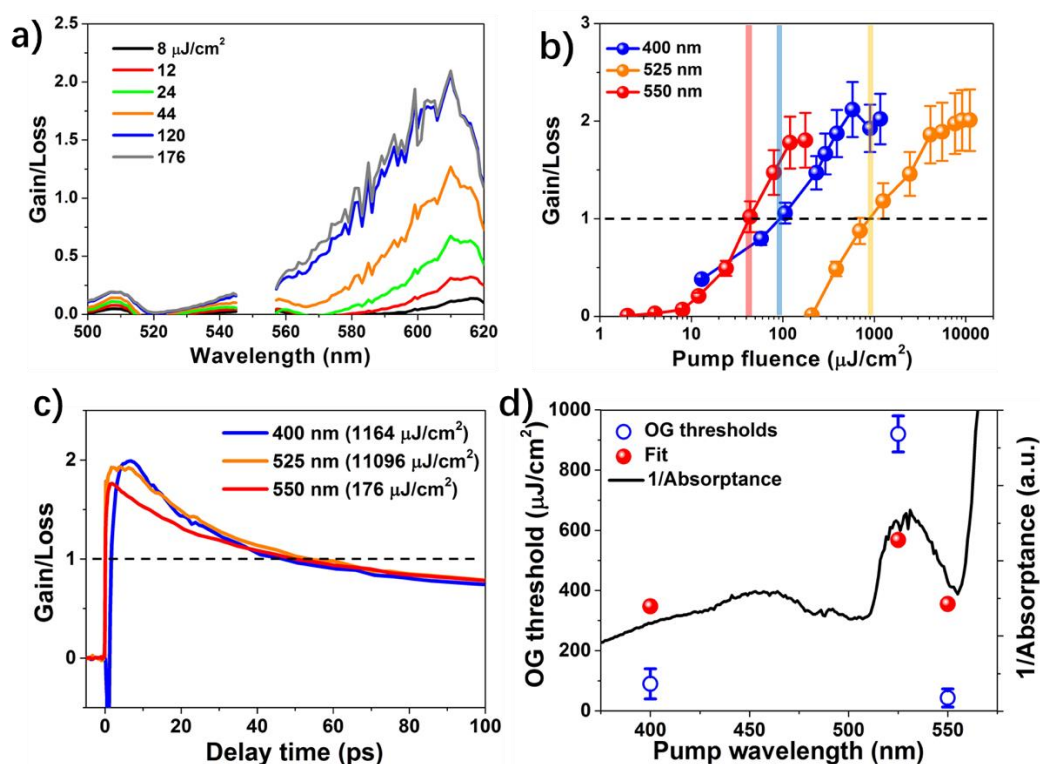


Figure 8.7. OG in CC NPLs. (a) The gain/loss ratio spectra at early delay time of different 550 nm pump fluences. (b) The gain/loss ratio at ~607 nm (1-2 ps) as a function of pump fluence at different pump wavelengths. The point of intersection of the black dashed line and the shaded areas represent the OG thresholds. (c) The gain/loss ratio kinetics at ~607 nm at the highest pump fluence with different pump wavelengths. (d) The optical gain threshold as a function of pump wavelength (blue circles) and their fit (red dots). The black line represents the reciprocal of relative absorptance of CC NPLs.

The optical density of samples under illumination is given by $\Delta A(\lambda, t) + A_0(\lambda)$, where $\Delta A(\lambda, t)$ is pump-induced absorbance change shown in transient absorption spectra and $A_0(\lambda)$ is the static absorbance prior to excitation. Thus, optical gain is achieved when $\Delta A(\lambda, t) + A_0(\lambda) < 0$ or $-\Delta A(\lambda, t)/A_0(\lambda) > 1$. We plot $-\Delta A(\lambda, t_{\max})/A_0(\lambda)$, t_{\max} is the delay time with maximum gain (1-2 ps), at different 550 nm pump fluences in Figure 8.7a. We refer these as maximum gain/loss ratio spectra. Similar $-\Delta A(\lambda, t_{\max})/A_0(\lambda)$ spectra at 400 and 525 nm pump (at $t_{\max}=1-2$ ps and 4-5 ps, respectively) are shown in Figure 8.14 in Appendix 8.4. The gain peaks at ~607 nm regardless of the excitation wavelength, confirming that the same tri- and four- exciton states are responsible for the gain. The peak gain/loss ratio at ~607 nm as a function of pump fluence at different pump wavelength is shown in Figure 8.7b. The OG threshold, defined as the pump fluence when the peak gain/loss ratio at ~607 nm reaches 1, is determined from Figure 8.7b to be 90 ± 50 , 920 ± 60 , and $43 \pm 30 \mu\text{J}/\text{cm}^2$ at 400 nm, 525 nm, and 550 nm pump, respectively. The time evolution of the gain/loss ratio at ~607 nm at the highest pump fluence is shown in Figure 8.7c. The gain lifetime for CC NPL, defined as the time range when gain/loss ratio is larger than 1, was determined to be 46.3 ± 3.1 ps regardless of the pump wavelength, which is consistent with the tri-exciton lifetime (~43.5 ps).

The OG thresholds as a function of pump wavelength are shown in Figure 8.7d (blue circles). To understand the origin of the pump wavelength dependence, we develop a model that accounts for the stimulated absorption and emission of the first four exciton states. The details of this model can be found in Appendix 8.4. Because the same tri-exciton state is responsible for the OG regardless of the pump wavelength, the OG threshold is related to the average number of excitons per NPL. Accounting for pump photon energy and CC NPL optical density at different pump wavelength, the OG threshold in the unit of pump fluence (P_{th}) is found to be proportional to the ratio of pump photon energy to sample absorbance at the pump wavelength: $P_{th} \propto \frac{hv}{1-10^{-\text{Optical Density}}}$. As shown in Figure 8.7d, this model provides a reasonable fit to the wavelength dependent OG thresholds data, revealing that the main threshold-determining factor is the wavelength dependent absorbance of the sample with minor contribution from the wavelength dependent photon energy.

The lowest OG threshold of our CC NPL sample ($\sim 43 \mu\text{J}/\text{cm}^2$ at 550 nm) is over 40 folds lower than the reported single-exciton gain threshold in type-II core/shell quantum dots ($\sim 2 \text{ mJ}/\text{cm}^2$).¹⁵ This indicates that although CC NPLs requires at least 3 excitons per NPL to reach the OG threshold, the large absorption cross-section makes it much easier to absorb multiple photons in NPLs compared to QDs, resulting to a lower optical gain threshold.

8.3. Conclusion

In summary, we have determined three energetically and spatially distinct types of excitons in CdSe/CdTe CC NPL heterostructures *via* pump fluence and wavelength dependent ultrafast transient absorption spectroscopy. These exciton states increase in energy from interface localized X_{CT} , crown-localized X_{CdTe} , to core-localized X_{CdSe} excitons. With increasing excitation energy and fluence, these excitons states can be sequentially filled, with each accommodating two excitons due to the 2-fold spin degeneracy of the electron level. The

lifetime of one to six exciton states (X_{CT} , XX_{CT} , $XX_{CT}X_{CdTe}$, $XX_{CT}XX_{CdTe}$, $XX_{CT}XX_{CdTe}X_{CdSe}$, and $XX_{CT}XX_{CdTe}XX_{CdSe}$) are $\gg 1000$, 209, 43.5, 11.8, 5.9, and 4.5 ps, respectively.

The OG state was determined to be tri-exciton ($XX_{CT}X_{CdTe}$) and four exciton states ($XX_{CT}XX_{CdTe}$), with gain lifetimes of 46.3 ± 3.1 ps. The OG threshold was pump wavelength dependent: ~ 90 , ~ 920 , and $\sim 43 \mu\text{J}/\text{cm}^2$ at 400, 525, and 550 nm pump, respectively. Modeling of the OG threshold reveals that the wavelength dependence is caused mainly by the variation of absorptance at the pump wavelength, and the large absorption cross section of these materials leads to small gain threshold. Furthermore, because of the spatial separation of X_{CT} , X_{CdTe} , and X_{CdSe} excitons, the multiple exciton states are relatively long lived compared to those in QDs, giving rise to long multiple exciton gain lifetime in these materials. Furthermore, the rich complexity of energetically and spatially separated excitons provides exciting opportunities for further engineering their multiple exciton state properties for applications as lasing materials.

Appendix 8.1

The TEM images and lateral size of samples

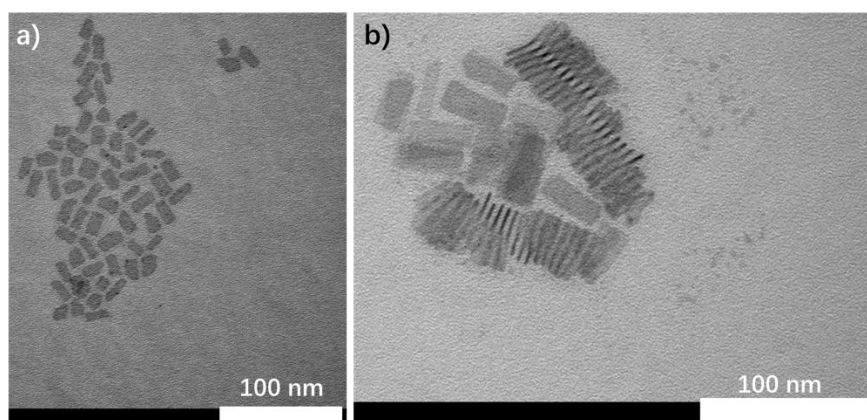


Figure 8.8. The TEM images of (a) CdSe core and (b) CdSe/CdTe CC NPLs.

Table 8.1. The length and width with errors of CdSe core and CC NPLs

	Length/nm	Width/nm
CdSe core	18.6 ± 2.4	8.5 ± 1.6
CC NPL	33.0 ± 3.4	14.1 ± 1.5

Appendix 8.2

Estimation of average exciton number per nanoplatelet according to Poisson distribution

To estimate average exciton number per NPL, we measured pump fluence dependent TA kinetics at different excitation wavelength on CdSe/CdTe CC NPLs. At long delay time (800-1000 ps), when multiple exciton annihilation completed, only single exciton states remained. As shown in Figure 8.9, the normalized TA spectra at 800-1000 ps measured at different pump fluences agreed well with each other in CC NPL samples at all excitations. The signal amplitude at this long delay time as a function of pump fluence can be used to calculate the average exciton numbers per NPL, following previously published procedure.^{69, 76}

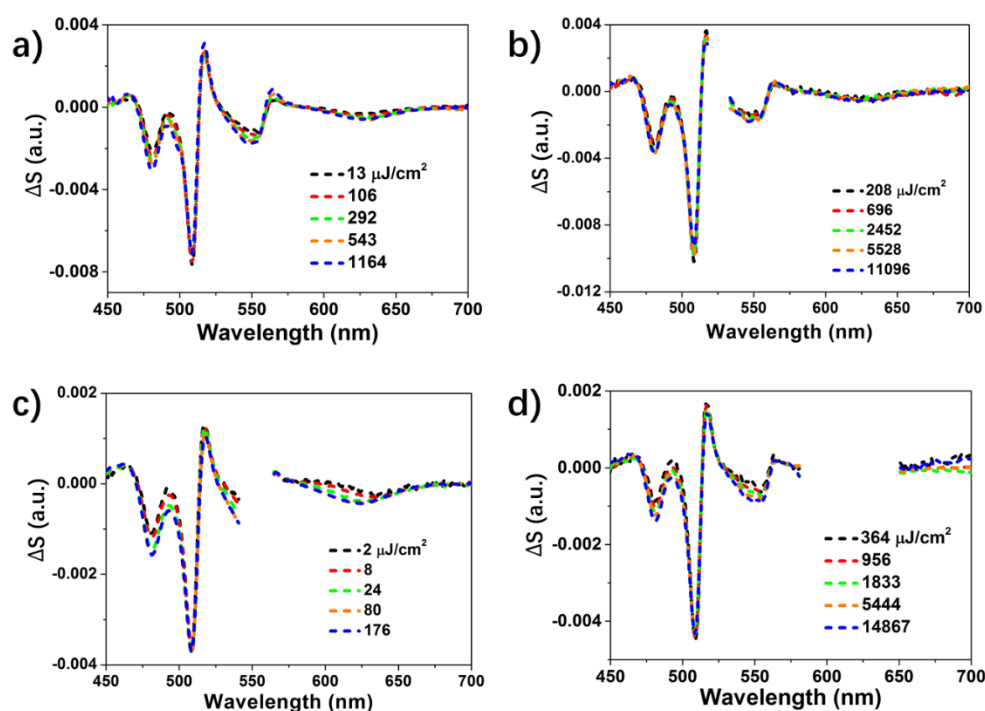


Figure 8.9. The normalized TA spectra of CdSe/CdTe CC NPLs at long delay time (800-1000 ps) at different pump fluences with (a) 400 nm, (b) 525 nm, (c) 550 nm, and (d) 620 nm excitation, where ΔS represents normalized TA signal.

Generally, the probability of a NPL encountering with n photons after initial optical excitation is governed by the Poisson distribution:

$$P_n(m) = \frac{m^n e^{-m}}{n!} \quad (8.1)$$

where m is the average number of photons encountered with NPLs. m can be related to the pump fluence (I) through a scaling factor C is dependent on the absorption cross section:

$$m(I) = CI \quad (8.2)$$

At long delay time (t_L), all multiple excitons have annihilated, and only single exciton states remained. Therefore, at long delay time, the TA signal amplitudes ($\Delta A(\lambda, t_L)$) are proportional to the number of excited NPLs: $1 - P_0(m)$. We define the normalized TA signal at late delay time as:

$$\Delta S(\lambda, t_L) = \frac{\Delta A(\lambda, t_L)}{\alpha(\lambda)} = 1 - P_0(m) = 1 - e^{-m} = 1 - e^{-CI} \quad (8.3)$$

where λ is wavelength. These normalized TA signals represent the probability of finding excited NPLs in the solution sample. At high excitation intensities, when all NPLs were excited, $\Delta S(\lambda, t_L)$ approached one, from which the normalization factor $\alpha(\lambda)$ was determined. Fitting $\Delta S(480\text{nm}, t_L)$ as a function of pump fluence I to Eq. 8.2 (red solid lines in Figure 8.3d, 8.4d, 8.5d, and 8.13e) yields the value of parameter C of 0.0005, 0.0672, 0.0015, and 0.0128 $\text{cm}^2/\mu\text{J}$ for CC NPLs at 620, 550, 525, and 400 nm excitation, respectively. From the parameter C , the average number of photons encountered with NPL at any pump fluence can be determined by Eq. 8.2.

At early delay time (1-2 ps), the normalized T4 amplitudes represented the average electron number in CdSe core using the same normalization factor $\alpha(\lambda)$. For 550 nm and 620 nm excitation, the CdSe core contained 2 electrons in CT excitons at saturation. Therefore, the normalized T4 amplitudes at early delay time (t_E), $\Delta S_{550/600\text{ex}}(480\text{nm}, t_E)$, is:

$$\begin{aligned}\Delta S_{550/600\text{ex}}(480\text{nm}, t_E) &= \frac{\Delta A_{550/600\text{ex}}(480\text{nm}, t_E)}{\alpha(480\text{nm})} = P_1(m) + 2[1 - P_0(m) - P_1(m)] \\ &= 2 - 2e^{-m} - me^{-m} = 2 - (2 + CI)e^{-CI} \quad (8.4)\end{aligned}$$

For 525 nm and 400 nm excitation, CdSe core contained 4 electrons at saturation (as shown in Figure 8.5d and 8.13e): two from CT exciton, which are the first and second excitons, and another two from CdSe core excitons, which were the 5th and 6th excitons after both CT and CdTe crown exciton states saturated. The normalized TA signal at early delay time (t_E) is:

$$\begin{aligned}\Delta S_{400/525\text{ex}}(480\text{nm}, t_E) &= \frac{\Delta A_{400/525\text{ex}}(480\text{nm}, t_E)}{\alpha(480\text{nm})} \\ &= P_1(m) + 2 \left[\sum_{n=2}^4 P_n(m) \right] + 3P_5(m) + 4 \left[1 - \sum_{n=0}^5 P_n(m) \right] \\ &= 4 - \left(4 + 3m + m^2 + \frac{m^3}{3} + \frac{m^4}{12} + \frac{m^5}{120} \right) e^{-m} \\ &= 4 - \left[4 + 3CI + (CI)^2 + \frac{(CI)^3}{3} + \frac{(CI)^4}{12} + \frac{(CI)^5}{120} \right] e^{-CI} \quad (8.5)\end{aligned}$$

The normalized gain signal depends on the number of excitons in the crown after formation of two CT excitons. Thus, its signal amplitude at early delay time (1-2 ps, after crown-to-core transport and before multi-exciton annihilation) is given by:

$$\begin{aligned}\Delta S_{\lambda\text{ex}}(\text{OG}, t_E) &= \frac{\Delta A_{\lambda\text{ex}}(\text{OG}, t_E)}{\alpha(\text{OG})} = P_3(m) + 2 \left[1 - \sum_{n=0}^3 P_n(m) \right] \\ &= 2 - \left(2 + 2m + m^2 + \frac{m^3}{6} \right) e^{-m} \\ &= 2 - \left[2 + 2CI + (CI)^2 + \frac{(CI)^3}{6} \right] e^{-CI} \quad (8.6)\end{aligned}$$

To estimate the total average exciton numbers per NPLs (w), we considered, at each excitation wavelength, there existed the maximum number of excitons can be generated in NPLs (N_{max}) by absorbing the same number of photons. The NPL stopped absorbing more

photons after containing N_{\max} excitons. Then the total average number of excitons per NPL can be described as:

$$w = \sum_{n=1}^{N_{\max}-1} nP_n(m) + N_{\max} \sum_{n=N_{\max}}^{\infty} P_n(m) \quad (8.7)$$

The N_{\max} at 620, 550, and 525 nm excitation were 2, 4, and 6, respectively, according to the highest exciton states they excited. This gave the orange dashed lines in Figure 8.3d, 8.4d, and 8.5d as:

$$w_{620\text{ex}} = P_1(m) + 2[1 - P_0(m) - P_1(m)] \quad (8.8)$$

$$w_{550\text{ex}} = \sum_{n=1}^3 nP_n(m) + 4[1 - \sum_{n=0}^3 P_n(m)] \quad (8.9)$$

$$w_{525\text{ex}} = \sum_{k=1}^5 nP_n(m) + 6[1 - \sum_{n=0}^5 P_n(m)] \quad (8.10)$$

For 400 nm excitation, we assumed the continuous CB band can keep absorbing encountered photons with pump fluence increasing, thus, as shown in Figure 8.13e (orange dashed line):

$$w_{400\text{ex}} = m = CI \quad (8.11)$$

Appendix 8.3

The analysis of TA bleach kinetics

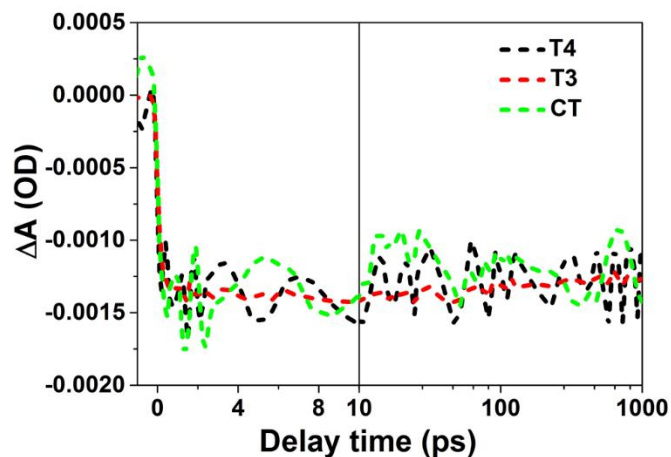


Figure 8.10. The comparison of T3, T4, and CT kinetics at $364 \mu\text{J}/\text{cm}^2$ with 620 nm excitation.

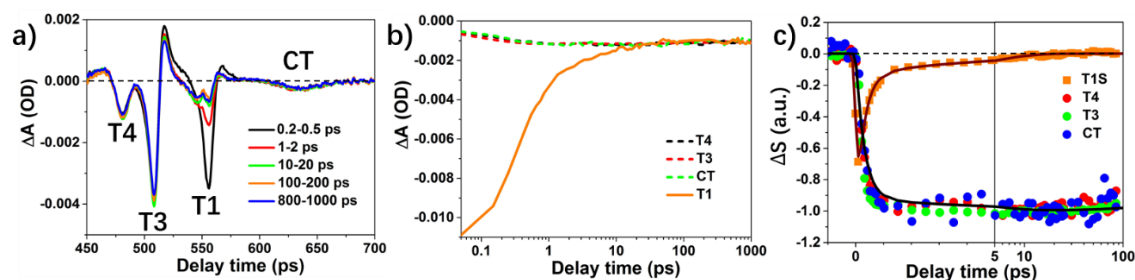


Figure 8.11. (a) The TA spectra at $2 \mu\text{J}/\text{cm}^2$ with 550 nm excitation. (b) The comparison of T3, T4, CT and T1 kinetics after normalized them at 100-1000 ps time region. (c) The normalized T1S (squares), T4, T3, and CT kinetics (dots) with their fits (solid lines), where ΔS represents normalized TA signal.

At the lowest pump fluence ($2 \mu\text{J}/\text{cm}^2$) with 550 nm excitation, the average exciton number per CC NPL was 0.13 as shown in Figure 8.4d, indicating the single exciton condition. The details of estimation of average exciton number were shown in Appendix 8.2. The T1 kinetics

contained both CdTe electron state-filling signal and the charge-separation (CS) signal, the latter was induced by CT exciton. So, the CS signal kinetics should be the same as CT exciton kinetics. Figure 8.11a showed the TA spectra at different delay times at $2 \mu\text{J}/\text{cm}^2$ 550 nm pump. We normalized the T3, T4, CT kinetics, and T1 kinetics at the long delay time (100-1000 ps) in Figure 8.11b. T1S (T1-subtracted) kinetics, which represented the CdTe electron state-filling only, was obtained by subtracting normalized T4 kinetics from normalized T1 kinetics as shown in Figure 8.11b. The decay of T1S kinetics should be the same as the growth of T4 kinetics due to the crown-to-core electron transfer.¹⁰⁹ We fitted the T1S and T4 (T3, CT) kinetics using multi-exponential function convoluted with instrument response function (IRF) with the same set of parameters:

$$\text{T1S}(t) = A_{\text{initial}} \left[e^{-\frac{t}{\tau_f}} - a_1 e^{-\frac{t}{\tau_1}} - a_2 e^{-\frac{t}{\tau_2}} \right] \otimes \text{IRF} \quad (8.12)$$

$$\text{T4}(t) = A_{\text{initial}} \left[a_1 e^{-\frac{t}{\tau_1}} + a_2 e^{-\frac{t}{\tau_2}} - e^{-\frac{t}{\tau_{\text{CT}}}} \right] \otimes \text{IRF} \quad (8.13)$$

where τ_f was the T1 exciton formation time and we set it as 0 fs due to band edge excitation. $\tau_1(a_1)$ and $\tau_2(a_2)$ were electron transfer time constant (components), which were also the growth time constant (components) in T4 kinetics. τ_{CT} was the CT exciton decay time constant. The fitting results were shown in Figure 8.11c and the fitting parameters with errors were listed in Table 8.2.

Table 8.2. Fitting parameters and errors of T1S and T4 kinetics at 550 nm excitation

τ_f/fs	$\tau_1/\text{ps} (a_1)$	$\tau_2/\text{ps} (a_2)$	$\tau_{\text{CT}}/\text{ps}$
0 ± 10 fs	0.30 ± 0.02 (0.86 ± 0.01)	4.46 ± 0.03 (0.14 ± 0.02)	$\gg 1000$

The T4 and OG kinetics at different pump wavelength and fluences were normalized using Eq. 8.3 and the methods described in the main text, respectively. Then their decay processes can be well fitted by multi-exponential functions with the same set of parameters:

$$\text{T4 decay}_{\text{nor}}(t) = d_1 e^{-\frac{t}{\tau_{\text{CT}}}} + d_2 e^{-\frac{t}{\tau_{\text{CT,XX}}}} + d_3 e^{-\frac{t}{\tau_{\text{CdSe},1}}} + d_4 e^{-\frac{t}{\tau_{\text{CdSe},2}}} \quad (8.14)$$

$$\text{OG decay}_{\text{nor}}(t) = b_1 e^{-\frac{t}{\tau_{\text{OG}}}} + b_2 e^{-\frac{t}{\tau_{\text{crown,XX}}}} \quad (8.15)$$

where d_i ($i=1$ to 4) represented the different decay components of normalized T4 kinetics. $\tau_{\text{CT,XX}}$ is the CT biexciton time constant. $\tau_{\text{CdSe},i}$ ($i=1,2$) was the time constants for additional i^{th} CdSe core excitons. b_i ($i=1$ to 2) represented the decay components for normalized optical gain kinetics. τ_{OG} was the time constant for single exciton condition of crown excitons. $\tau_{\text{crown,XX}}$ was the time constant of biexciton states in crown (in addition to two CT excitons). The best fits were shown as black solid lines in Figure 8.3c, 8.4b, 8.4c, 8.5b, 8.5c, 8.12a, and 8.12b. The fitting parameters and errors were listed in Table 8.3 to 8.7.

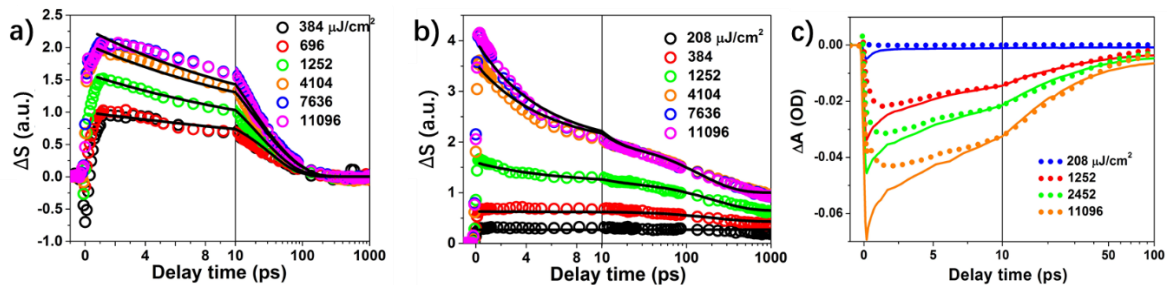


Figure 8.12. Transient kinetics of CdSe/CdTe NPLs measured at 525 nm excitation. (a) Normalized OG kinetics at indicated pump fluences (circles) and their fits (solid lines), where ΔS represents normalized TA signal. (b) Normalized T4 kinetics measured at indicated pump fluences (circles) and their fits, where ΔS represents normalized TA signal. (c) The comparison of OG (dots) and T1 (solid lines) kinetics at different pump fluences.

Table 8.3. Fitting parameters and errors of normalized T4 kinetics at 620 nm pump

Pump fluence/ $\mu\text{J}/\text{cm}^2$	$\tau_{\text{CT}}/\text{ps}$ (d ₁)	$\tau_{\text{CT,XX}}/\text{ps}$ (d ₂)	$\tau_{\text{CdSe,1}}/\text{ps}$ (d ₃)	$\tau_{\text{CdSe,2}}/\text{ps}$ (d ₄)
364	$\gg 1000$	–	–	–
1833	$\gg 1000$	209 \pm 4 (0.17 \pm 0.01)	–	–
5444	$\gg 1000$	209 \pm 4 (0.60 \pm 0.01)	–	–
9556	$\gg 1000$	209 \pm 4 (1 \pm 0.01)	–	–
14867	$\gg 1000$	209 \pm 4 (1 \pm 0.01)	–	–

Table 8.4. Fitting parameters and errors of normalized T4 kinetics at 550 nm pump

Pump fluence/ $\mu\text{J}/\text{cm}^2$	$\tau_{\text{CT}}/\text{ps}$ (d ₁)	$\tau_{\text{CT,XX}}/\text{ps}$ (d ₂)	$\tau_{\text{CdSe,1}}/\text{ps}$ (d ₃)	$\tau_{\text{CdSe,2}}/\text{ps}$ (d ₄)
2	$\gg 1000$	–	–	–
8	$\gg 1000$	–	–	–
24	$\gg 1000$	209 \pm 4 (0.41 \pm 0.02)	–	–
44	$\gg 1000$	209 \pm 4 (0.74 \pm 0.01)	–	–
80	$\gg 1000$	209 \pm 4 (1 \pm 0.01)	–	–
120	$\gg 1000$	209 \pm 4	–	–

		(1±0.01)		
--	--	----------	--	--

Table 8.5. Fitting parameters and errors of normalized T4 kinetics at 525 nm pump

Pump fluence/ $\mu\text{J}/\text{cm}^2$	$\tau_{\text{CT}}/\text{ps}$ (d ₁)	$\tau_{\text{CT,XX}}/\text{ps}$ (d ₂)	$\tau_{\text{CdSe,1}}/\text{ps}$ (d ₃)	$\tau_{\text{CdSe,2}}/\text{ps}$ (d ₄)
208	$\gg 1000$	–	–	–
384	$\gg 1000$	209±4 (0.20±0.01)	–	–
1252	$\gg 1000$	209±4 (0.58±0.01)	5.86±0.12 (0.37±0.02)	4.45±0.20 (0.20±0.01)
4104	$\gg 1000$	209±4 (1±0.01)	5.86±0.12 (0.79±0.02)	4.45±0.20 (0.55±0.01)
7636	$\gg 1000$	209±4 (1±0.01)	5.86±0.12 (1±0.01)	4.45±0.20 (1±0.01)
11096	$\gg 1000$	209±4 (1±0.01)	5.86±0.12 (1±0.01)	4.45±0.20 (1±0.01)

Table 8.6. Fitting parameters and errors of normalized OG kinetics at 550 nm pump

Pump fluence/ $\mu\text{J}/\text{cm}^2$	$\tau_{\text{OG}}/\text{ps}$ (b ₁)	$\tau_{\text{crown,XX}}/\text{ps}$ (b ₂)
12	43.5±4.3 (1±0.01)	–
24	43.5±4.3	–

	(1±0.01)	
44	43.5±4.3 (1±0.01)	11.8±0.3 (0.22±0.02)
80	43.5±4.3 (1±0.01)	11.8±0.3 (0.54±0.02)
120	43.5±4.3 (1±0.01)	11.8±0.3 (1±0.01)
176	43.5±4.3 (1±0.01)	11.8±0.3 (1±0.01)

Table 8.7. Fitting parameters and errors of normalized OG kinetics at 525 nm pump

Pump fluence/ $\mu\text{J}/\text{cm}^2$	$\tau_{\text{OG}}/\text{ps}$ (b_1)	$\tau_{\text{crown,XX}}/\text{ps}$ (b_2)
384	43.5±4.3 (1±0.01)	–
696	43.5±4.3 (1±0.01)	–
1252	43.5±4.3 (1±0.01)	11.8±0.3 (0.56±0.01)
4104	43.5±4.3 (1±0.01)	11.8±0.3 (0.97±0.01)
7636	43.5±4.3 (1±0.01)	11.8±0.3 (1±0.01)

11096	43.5 ± 4.3	11.8 ± 0.3
	(1 ± 0.01)	(1 ± 0.01)

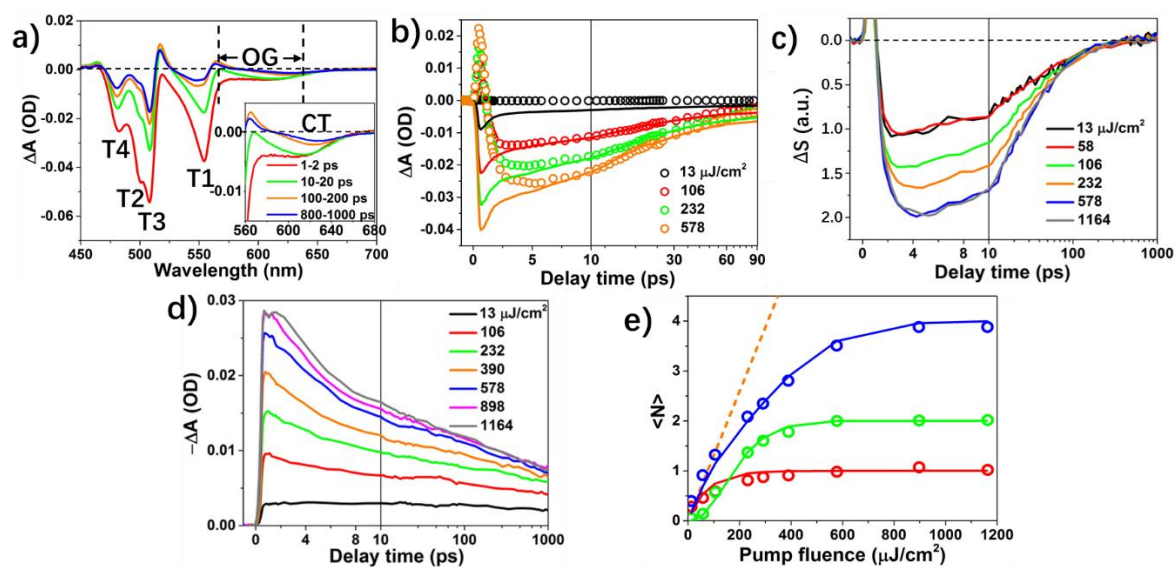


Figure 8.13. The pump fluence dependent TA results of CdSe/CdTe CC NPLs at 400 nm excitation. (a) The TA spectra of CdSe/CdTe CC NPLs at different delay times with 400 nm excitation and pump fluence of $1164 \mu\text{J}/\text{cm}^2$. (b) The comparison of T1 (solid lines) and OG (circles) kinetics of CdSe/CdTe CC NPLs at selected pump fluence with 400 nm excitation. (c) The normalized OG kinetics of CdSe/CdTe CC NPLs at different pump fluences with 400 nm excitation, where ΔS represents normalized TA signal. (d) The T4 kinetics of different 400 nm pump fluences. (e) The average electron number in CdSe core per CC NPL as a function of pump fluence at 1-2 ps (blue circles) and 800-1000 ps (red circles) with 400 nm excitation. Green circles are the average number of additional CdTe crown excitons per CC NPL at 1-2 ps with 400 nm excitation. Solid lines are the fits according to Poisson distribution. Dashed line is the total average exciton number per CC NPL as a function of pump fluence at 400 nm excitation.

Appendix 8.4

Pump wavelength dependent optical gain threshold model

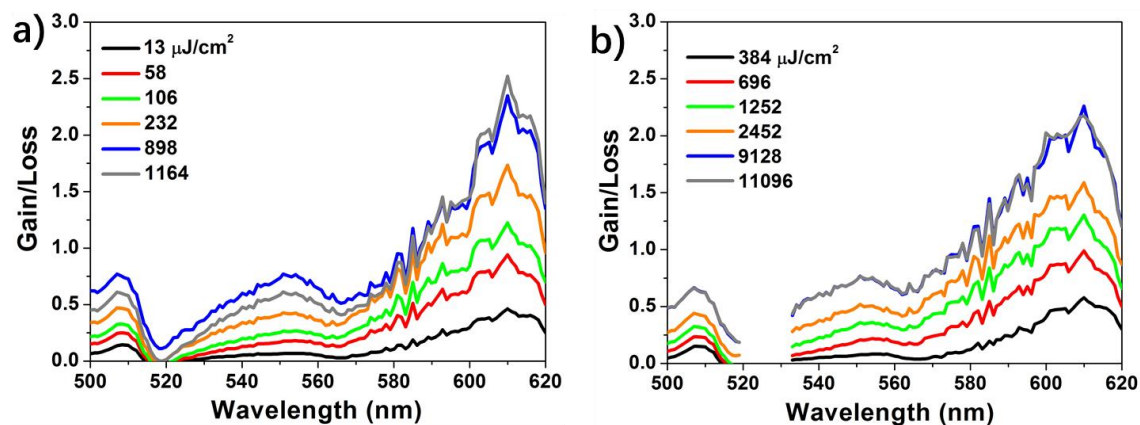


Figure 8.14. The gain/loss ratio spectra at 1-2 ps at different (a) 400 nm and (b) 525 nm pump fluences.

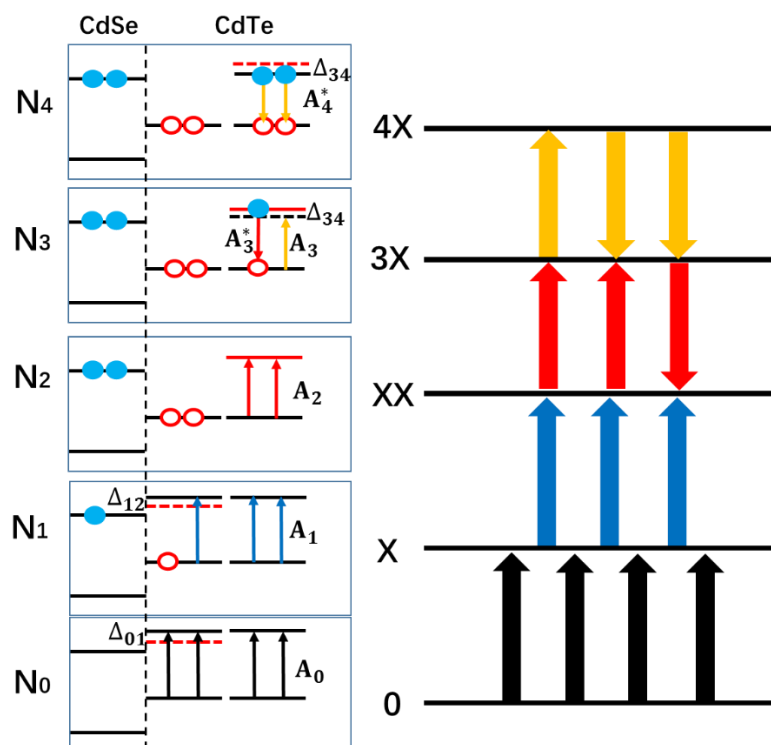


Figure 8.15. The schematic of the optical gain mechanisms in CdSe/CdTe CC NPLs. The left and right panel shows the exciton states in single particle (electron and hole) representation and state representation, respectively.

The exciton states that affect optical gain are shown in Figure 8.15 in both single particle (electron or hole) and state representations. N_i ($i=0$ to 4) is the population of NPL species which contains i excitons after excitation. The arrows with different colors show the stimulated absorption (upward) and emission (downward) of different NPL species. As shown in Figure 8.15, only exciton transitions of NPL species of the 4 lowest energy exciton states are considered here because TA studies have revealed that higher exciton states do not contribute to the optical gain (OG). The absorption (A_i) and emission (A_i^*) cross-section of i -exciton state at optical gain transition energy, E_0 , is¹⁵

$$A_0(E) = A \frac{\gamma^2}{(E - (E_0 + \Delta_{01}))^2 + \gamma^2} \quad (8.16)$$

$$A_1(E) = A \frac{3}{4} \frac{\gamma^2}{(E - (E_0 + \Delta_{12}))^2 + \gamma^2} \quad (8.17)$$

$$A_2(E) = A \frac{1}{2} \frac{\gamma^2}{(E - E_0)^2 + \gamma^2} \quad (8.18)$$

$$A_3(E) = A \frac{1}{4} \frac{\gamma^2}{(E - (E_0 - \Delta_{34}))^2 + \gamma^2} \quad (8.19)$$

$$A_3^*(E) = -A \frac{1}{4} \frac{\gamma^2}{(E - E_0)^2 + \gamma^2} \quad (8.20)$$

$$A_4^*(E) = -A \frac{1}{2} \frac{\gamma^2}{(E - (E_0 - \Delta_{34}))^2 + \gamma^2} \quad (8.21)$$

where $A = \frac{4E}{h n_r c \gamma}$, h is Plank's constant, n_r is the refractive index, and c is the speed of light. We

have assumed the transition line width, γ , is the same for all 4 lowest energy exciton states.

The size distribution of E_0 is ignored due to the uniform 1D quantum confinement of NPLs. Because OG results from tri-exciton state, the transition energy between tri- and four exciton states were determined as OG transition energy, E_0 . Δ_{ij} ($i, j=0$ to 4) is the energy shift of the transition energy between i and j exciton states relative to E_0 . Therefore, the partial absorption coefficient (α) of the NPL ensemble due to the first four lowest exciton transitions is:

$$\alpha(E) = N_0 A_0(E) + N_1 A_1(E) + N_2 A_2(E) + N_3 [A_3(E) + A_3^*(E)] + N_4 A_4^*(E) \quad (8.22)$$

OG threshold is reached when stimulated emission is larger than absorption, i.e., $\alpha(E_0) < 0$, which is given by Eq. 8.23.

$$-\frac{N_4}{2\left(1 + \frac{\Delta_{34}^2}{\gamma^2}\right)} - \frac{N_3}{4} + \frac{N_3}{4\left(1 + \frac{\Delta_{34}^2}{\gamma^2}\right)} + \frac{N_2}{2} + \frac{3N_1}{4\left(1 + \frac{\Delta_{12}^2}{\gamma^2}\right)} + \frac{N_0}{1 + \frac{\Delta_{01}^2}{\gamma^2}} < 0 \quad (8.23)$$

As shown in Figure 8.4a, 8.5a and 8.6a, OG peak is far away from the first two exciton transitions (~ 550 nm) of CdTe, indicating $\Delta_{01}, \Delta_{12} \gg \gamma$. Because tri-exciton lifetime (~ 43.5 ps) is consistent with gain lifetime (~ 46.3 ps), which is much longer than four-exciton lifetime (~ 11.8 ps), it indicates that the OG remains after all four-exciton state decay to tri-exciton states. It can be shown that in absence of four exciton states (no N_4 term in Eq. 8.23), OG can be achieved only when $\Delta_{34} \gg \gamma$ and when:

$$N_3 > 2N_2 \quad (8.24)$$

According to truncated Poisson distribution, Eq. 8.24 becomes:

$$1 - P_0(m) - P_1(m) - P_2(m) > 2P_2(m) \quad (8.25)$$

where $P_n(m)$ follows Eq. 8.1. The numerical solution of Eq. 8.25 gives: $m > 2.656$. The average number of encountered photons per NPL, m , can also be represented as:

$$m = \frac{(1 - 10^{-\varepsilon(\lambda)SL}) \frac{P}{h\nu}}{SN_A L} > 2.656 \quad (8.26)$$

where $\varepsilon(\lambda)$ is molar absorption coefficient of CC NPLs at wavelength λ . S is the molar concentration of CC NPL solution. L is the light path of the cuvette (1 mm). P is the pump

fluence and $h\nu$ is pump photon energy. N_A is Avogadro constant. Therefore, to reach OG threshold, we need the pump fluence:

$$P > 2.656SN_A L \frac{h\nu}{1 - 10^{-\text{Optical Density}}} \quad (8.27)$$

$$P_{\text{th}} = B \frac{h\nu}{1 - 10^{-\text{Optical Density}}} \quad (8.28)$$

Therefore, we used Eq. 8.28 to fit the OG threshold, P_{th} , as shown in Figure 8.7c. The best fitting parameter B is $53.3 \pm 2.5 \mu\text{J}/(\text{cm}^2 \text{ eV})$.

Chapter 9. Two-Dimensional Morphology Enhances Light-Driven H₂ Generation Efficiency in CdS Nanoplatelet-Pt Heterostructures

Reproduced with permission from *J. Am. Chem. Soc.* **2018**, *140*, 11726. Copyright 2018 American Chemical Society.

9.1. Introduction

Catalytic conversion of solar energy to green fuels, such as hydrogen, is one of the most promising approaches for generating renewable clean energy.²⁵⁶ Light-driven H₂ production using quantum-confined semiconductor nanocrystal-metal heterostructures, such as zero-dimensional semiconductor quantum dots (QDs) and one-dimensional (1D) nanorods (NRs) functionalized with catalytic metal (Ni or Pt) particles, have been intensively studied because they combine the tunable light harvesting and charge separation abilities of robust semiconductor nanocrystals with the efficient catalytic properties of metal nanoparticles.^{42, 102-104, 110, 112-114, 257-266} These studies have shown that although charge separation in these nanoheterostructures, with conduction band (CB) electron transfer (ET) and valence band (VB) hole transfer (HT) to the metal tip and sacrificial hole acceptor, respectively, is efficient, recombination of the transferred electron with hole is the main loss pathway due to the slow H₂ evolution reaction (the reduction of H⁺ at low pH or water at high pH) on the metal catalyst.^{63, 102-103} Thus, reducing charge recombination loss is a key approach for improving H₂ generation efficiency in these nanocrystal-based solar energy conversion systems.

One way to suppress charge recombination is to irreversibly remove the hole by using hole acceptors that can undergo rapid reactions upon oxidation. This approach has been successfully demonstrated for CdSe/CdS NR-Pt and CdS NR-Ni with OH^- as hole acceptors and redox shuttles, which upon hole transfer forms hydroxyl radicals that rapidly react with ethanol (as the sacrificial donor).^{114, 259} Although internal quantum efficiency (IQE) for hydrogen generation can reach near unity at high pH (~ 15), it decreases rapidly to $<30\%$ at pH below 13.¹¹ Furthermore, such schemes do not work for lower band gap materials that have better overlap with the solar spectrum (such as CdSe), because their VB holes are not energetic enough to oxidize OH^- . Thus, alternative approaches to suppress charge recombination are needed. A previous study using 1D CdSe/CdS NR-Pt of varying lengths (in water with ethanol as a sacrificial electron donor) has shown that the highest light-driven H_2 generation IQE ($\sim 20\%$) was obtained with a rod length of ~ 60 nm.¹¹³ More recently, Kuno and coworkers have reported the apparent quantum efficiency of light-driven H_2 generation performances of Ni-decorated CdS nanoplatelets (in water with ethanol as sacrificial electron donor) can reach $\sim 64\%$ in the first 2h and $\sim 25\%$ over 40h,⁴² considerably higher than the reported performance of CdS NR-Ni at near neutral pH.¹¹⁴ Although these studies suggest the efficiency of light-driven H_2 generation can be improved by the morphology of the nanocrystals, the mechanism of the morphological dependence remains unclear.

In this chapter, we report how 2D morphology can be used to increase the lifetime of charge-separated (CS) state and improve light-driven H_2 generation efficiency. 2D zinc-blend cadmium chalcogenide nanoplatelets (NPLs) possess large absorption cross-section, uniform quantum confinement along the *c* crystal axis, and giant oscillator strength compared to NRs and QDs, making them better light absorbing materials.^{19-21, 106, 267-268} In this work, we systematically study the pH dependent light-driven H_2 generation performances of CdS NPL-Pt heterostructures. We observed that, compared to the best reported NR-Pt performance,²⁵⁹

CdS NPL-Pt heterostructures show improved H₂ generation IQE over a wide pH range, achieving IQE of ~42% at pH = 8.8 and near unity (~99.5%) at pH = 14.7. Based on insights gained from detailed time-resolved spectroscopic studies of ET and HT rates and numerical simulation of charge recombination processes, we propose a mechanism that accounts for the improved H₂ generation performance in 2D NPLs.

9.2. Results and Discussion

9.2.1. Sample characterization

Colloidal zinc-blend CdS NPLs with 4 layers of sulfur, 5 layers of cadmium, and a thickness of ~1.8 nm^{21, 106} were synthesized following reported procedures.¹⁰⁶ Pt particles were deposited on NPLs by thermal reduction of Pt (II) acetylacetonate following the reported procedures of Pt deposition on CdSe NPLs,⁶² and CdS NRs.¹¹⁰ Details of sample synthesis can be found in Chapter 2.1. The absorption and photoluminescence spectra of free CdS NPLs and CdS NPL-Pt heterostructures in hexane (aqueous solution) are shown in Figure 9.1a (Figure 9.1b). The absorption peak centered at ~412 nm corresponds to the overlapping electron-heavy hole and electron-light hole transitions of CdS NPLs (Figure 9.1a).²¹ The absorption spectra of CdS NPL-Pt can be considered as the sum of contributions of isolated Pt particles and CdS NPLs (Figure 9.8a in Appendix 9.1). A sharp emission at the band-edge (~417 nm) is attributed to band-edge exciton emission and two broad emission peaks centered at ~448 and ~600 nm are attributed to trapped exciton emissions following the assignments of similar emissions in CdS NRs.²⁶⁹ The emission of CdS NPL-Pt is strongly quenched, indicative of ultrafast ET from the CdS to Pt (see below). Transmission electron microscopy (TEM) images of free CdS NPLs (Figure 9.7a in Appendix 9.1) and CdS NPL-Pt in hexane (Figure 9.1c) show that the rectangular shaped CdS NPLs tend to slightly roll up and the Pt particles are mainly deposited randomly on the NPL edges. The latter is similar to CdSe NPL-Pt heterostructures,⁶² and is due

to two reasons: (1) NPL edges have higher surface energy than basal plane, thus, higher reactivity;²⁷⁰ (2) NPL edges have reduced ligand coverage compared to basal plane, facilitating Pt growth.²⁷¹ Due to the overlaps and roll-ups among NPLs, we can only estimate the NPL length along the rolling axis as 58.9 ± 9.9 nm according to their TEM images (Figure 9.7a in Appendix 9.1). Water soluble samples for pH dependent light-driven H₂ generation experiments were produced *via* ligand exchange of CdS NPLs and CdS NPL-Pt heterostructures by replacing oleic acid (OA) capping ligand to L-cysteine (see Chapter 2.1 for details). The absorption peaks of CdS NPLs in aqueous solution (pH=10) are broadened and shifted to ~ 430 nm due to the change of the dielectric environment (Figure 9.1b), and the absorption spectrum of CdS NPL-Pt can still be described by the sum of isolated Pt and free CdS NPLs (Figure 9.8b-e in Appendix 9.1). The band-edge and trapped emission bands of free CdS NPLs are also red shifted compared to CdS NPLs in hexane. The emission of CdS NPL-Pt heterostructures is still fully quenched. The TEM images for free CdS NPLs (Figure 9.7b in Appendix 9.1) and CdS NPL-Pt heterostructures (Figure 9.1d) in pH 10 solution show corrosion of NPLs and different distribution of Pt particles at the NPL edges. Their TEM images (Figure 9.1d, Figure 9.7b&d in Appendix 9.1) give the average values of length and width as 57.7 ± 13.4 nm and 33.4 ± 9.4 nm, respectively. Similar NPL lengths are observed in hexane and water, indicating NPLs tend to roll up along their long axis in hexane and 2D morphology is maintained after ligand exchange. According to TEM images (Figure 9.1c&d, Figure 9.7c&d in Appendix 9.1), the average numbers of Pt particles per NPL before and after ligand exchange are 24.5 ± 5.4 and 13.4 ± 7.7 , respectively. Despite large error associated with these values (due to overlapping sheets in the TEM image), this result suggests that some Pt particles detached from the NPL during the ligand exchange process. The average diameter of Pt particles in hexane and water with pH of 10 are 3.31 ± 0.50 nm and 3.27 ± 0.54 nm, respectively. Although both Pt size²⁷² and number per NPL²⁷³ are reported to affect H₂

generation performance, we did not attempt to optimize these parameters. Instead, this paper focuses on the pH dependence of H₂ generation performances of CdS NPL-Pt with a fixed Pt size (~3.3 nm).

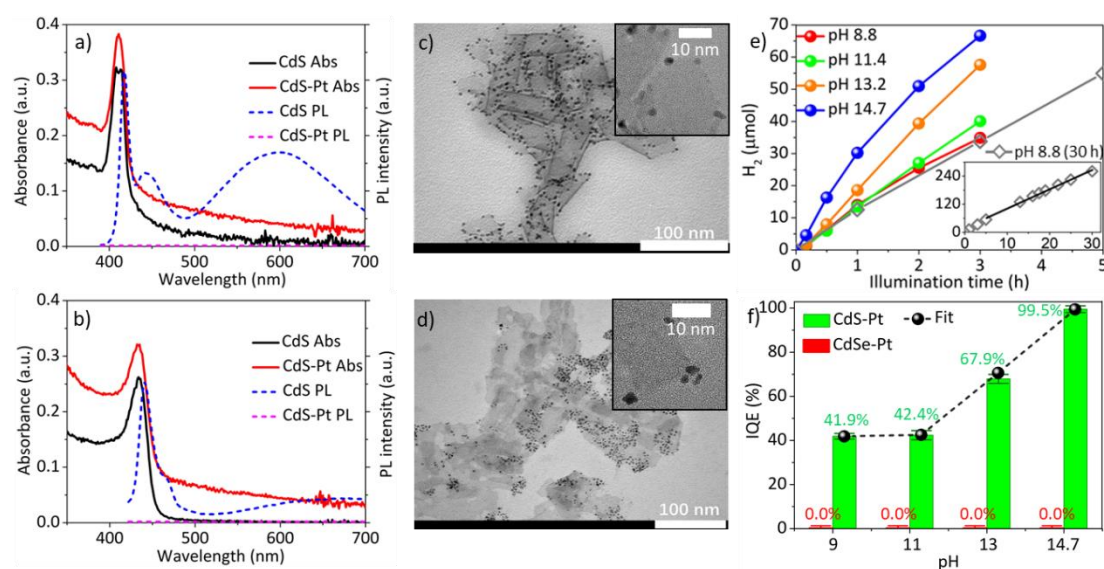


Figure 9.1. Absorption (Abs) and static-photoluminescence (PL) spectra of CdS NPLs, CdS NPL-Pt heterostructures dispersed in (a) hexane and (b) water (pH=10). TEM images of CdS NPL-Pt heterostructures in (c) hexane and (d) water. Insets in (c) and (d): TEM images showing preferential deposition of Pt at the CdS NPL edge. (e) Normalized H₂ production amount as a function of illumination time of CdS NPL-Pt heterostructures at different pH values. Inset: H₂ generation kinetics of CdS NPL-Pt at pH 8.8 up to 30 h. The black line is the linear fit for data between 5-30 h. (f) The pH dependent light-driven H₂ generation IQE of CdS NPL-Pt (green column) and CdSe NPL-Pt (red column). The black dots with dashed line is the fit of pH dependent IQE of CdS NPL-Pt.

9.2.2. Enhanced H₂ generation internal quantum efficiency

The pH dependent light-driven H₂ generation measurement was conducted with CdS NPL-Pt heterostructures in ethanol/KOH aqueous solution (volume ratio of 1:9) inside a

cylindrical cuvette with a light path of 1 cm. 405 nm LED light (5 mW) was focused on the cuvette with a beam area of 0.78 cm^2 and illumination intensity of 6.4 mW/cm^2 . The pH of the solution was adjusted by KOH concentration with the highest pH (14.7) achieved using 5 mol/L KOH solution. The amount of H_2 was detected by gas chromatography (see Chapter 2.3 for details). To enable comparison of H_2 generation rates of different samples, the H_2 amounts is normalized by the percentages of photons absorbed by CdS domain in the CdS NPL-Pt heterostructures ($1 - 10^{-\text{optical density}}$), such that they correspond to the same rate of light absorption. The normalized H_2 amount grows linearly with illumination time in the first 2h (Figure 9.1e), and the slope of their linear fits, representing the internal H_2 generation rate, increases from $12.8 \pm 0.2 \mu\text{mol/h}$ at pH 8.8 to $30.3 \pm 0.3 \mu\text{mol/h}$ at pH 14.7. IQEs is calculated from the ratio of H_2 generation to photon absorption rates after correcting for light absorption and scattering loss resulting from the cuvette and Pt particles (see Chapter 2.2 for calculation details). As shown in Figure 9.1f (green column), the IQE of light-driven H_2 generation of CdS NPL-Pt increases from $41.9 \pm 1.3\%$ at pH 8.8 to $99.5 \pm 0.5\%$ at pH 14.7. Under the same conditions, negligible amount of H_2 was detected in CdSe NPL-Pt systems, which corresponds to an estimated IQE of $0.0 \pm 1.0\%$ in the same pH range. This result indicates that CdS NPL-Pt system can achieve not only a unity solar-to- H_2 conversion efficiency at high pH (14.7), but also efficient H_2 generation over a wide pH range (IQE > 40% at pH > 8.8). Similarly efficient H_2 generation (apparent quantum efficiency of ~64% in the first 2h) has also been reported using Ni-decorated CdS NPLs.⁴² At pH < 13, the IQE of CdS NPL-Pt is significantly better than those reported for CdS NR based heterostructures (Table 9.1), including CdSe/CdS NR-Pt (apparent quantum efficiency < 30% at pH < 13),²⁵⁹ CdS NR-Ni (IQE < 20% at pH < 14),¹¹⁴ although at pH 14.7 near unity IQE has also been reported for CdSe/CdS NR-Pt heterostructures.²⁵⁹ The long-time stability of CdS NPL-Pt heterostructures was tested at pH 8.8 (inset of Figure 9.1e), which shows that the IQE is stable ($29.4 \pm 1.2\%$) from 5 to 30 h,

which is smaller than the initial value of ~42% (in the first two hour). Similar decreases in IQE have also observed in CdS NPL-Ni heterostructures,⁹ and CdS NR-Ni,¹⁰ and have been attributed to photo-corrosion of CdS.^{42, 274} A comparison of the UV-Vis absorption spectra of the CdS NPL-Pt (Figure 9.9a in Appendix 9.1) shows that the exciton peak becomes broader after a longer duration of photocatalysis measurement. Fitting these absorption spectra in Figure 9.9b (Appendix 9.1) shows exciton peak width, W_x , extends from 45 ± 2 meV to 57 ± 2 meV (Table 9.2 in Appendix 9.1) after 30h illumination (see Appendix 9.1 for fitting details). This can be attributed to the variation of NPL thickness resulting from photo-corrosion of NPL basal planes. Indeed, TEM images of CdS NPL-Pt show irregular shaped NPLs with holes on the basal planes after 30 hours of illumination (Figure 9.9c&d in Appendix 9.1), indicating both NPL edges and basal planes are corroded. Interestingly, despite photo-corrosion, CdS NPL-Pt still maintains 2D morphology (Figure 9.9c&d in Appendix 9.1), 2D electronic structures (Figure 9.9a&b in Appendix 9.1), and relatively stable and efficient H₂ generation IQE after 30 h.

Table 9.1. Comparison of the initial H₂ generation efficiency of CdS Nanorods (NRs) or NPL based heterostructures at pH < 12

Components	pH	Efficiency	Ref.
CdS NR-Ni	11	<5% at 447 nm	Ref ¹¹⁴
CdS NR-Pt	9	<3% at 447 nm	Ref ²⁷⁵
CdSe/CdS NR-Pt	–	~20% at 450 nm	Ref ¹¹³
CdSe/CdS NR-Pt	–	~27% at 455 nm	Ref ²⁷³
CdSe/CdS NR-Pt	9.5	~11% at 455 nm	Ref ²⁵⁹
CdS NPL-Ni	–	~64% at 405 nm	Ref ⁴²

9.2.3. Ultrafast charge separation.

Although 2D NPLs have been predicted²⁷⁶ and shown^{42, 277} to have promising solar-to-H₂ conversion performances previously, and our results show that their performance is better than 1D NRs at pH<13, the mechanism for the improved performance remains unclear. As shown in Figure 9.2a, for CdS NPL-Pt heterostructures in aqueous solution, Pt serves as both the electron acceptor and catalyst; while valence band or trapped holes can be transferred to surface covered hole acceptors such as thiol ligands (L-cysteine) or redox shuttle (OH⁻). Although HT to Pt is energetically allowed, ultrafast trapping of the hole to hole traps within the NPL (with time constant of τ_t) enables selective transfer of electrons to Pt (see below), similar to that observed previously in CdS NR-Pt.⁶ Thus, efficient light-driven H₂ generation requires both efficient exciton dissociation by ET (with time constant of τ_{ET}) from CdS NPL to Pt and HT (τ_{HT}) from CdS NPL to sacrificial electron donors to generate long-lived CS state (Figure 9.2a). H₂ evolution requires the accumulation of two electrons in the Pt on the time scale of catalytic turnover (>10 ms).²⁵⁹ This in turn requires effective suppression of charge recombination of the CS states (with time constant of τ_{CS}), especially the recombination of the transferred electron in Pt with transferred hole in hole acceptors (Figure 9.2b). To provide insight into the observed pH dependent and enhanced H₂ generation IQE of 2D NPLs, we directly measured the processes of ET (τ_{ET}), hole trapping (τ_t), HT (τ_{HT}), and charge recombination (in both CdS NPL-Pt and CdS NPL-methyl viologen complexes) using time-resolved absorption and emission spectroscopy.

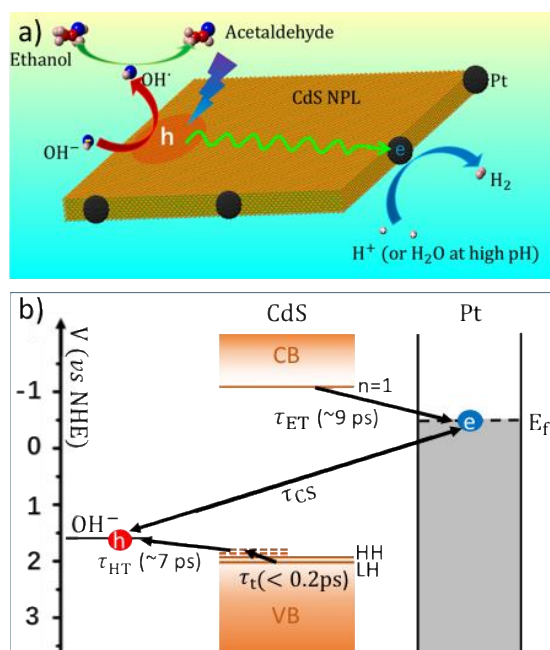


Figure 9.2. Mechanism of efficient light-driven H₂ generation in CdS NPL-Pt heterostructures. (a) Schematic depiction of key forward processes. (b) Simplified energy level diagram and charge separation and recombination processes. All band-edge positions and redox potentials correspond to aqueous solution at pH = 14.7.

We first carried out time-resolved transient absorption (TA) studies of free CdS NPLs and CdS NPL-Pt heterostructures in hexane to quantify the rates of ET from the CdS NPL to Pt. The TA measurements were conducted at a low pump fluence ($\sim 5 \mu\text{J}/\text{cm}^2$) to avoid multiple exciton generation in these samples.^{27, 69} As shown in Figure 9.3a&b, the TA spectra at early delay times ($< 0.1 \text{ ns}$) is dominated by the decrease of absorbance of the exciton band (at $\sim 412 \text{ nm}$), referred to as exciton bleach (XB). XB of CdS NPLs can be attributed to the state-filling of the conduction band electron levels with negligible contribution of hole state-filling according to our previous TA studies of colloidal NPLs,^{34, 62, 68-69, 109} similar to cadmium chalcogenide QDs and NRs.^{78, 110, 148, 183} The comparison of XB kinetics of CdS and CdS-Pt (Figure 9.3c) shows a much faster decay in the latter, suggesting a shorter CdS conduction band

electron lifetime in the presence of Pt. This observation is consistent with PL quenching shown in Figure 9.1a.

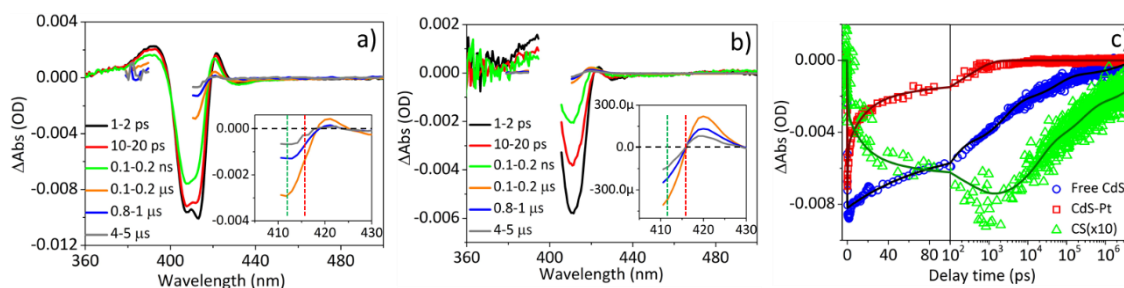


Figure 9.3. Average TA spectra at indicated delay time windows of (a) free CdS NPLs and (b) CdS NPL-Pt heterostructures in hexane. Inset in (a) and (b): expanded view of the TA spectra at long delay times (0.1-0.2, 0.8-1 and 4-5 μ s). The dashed lines mark the wavelength of 412 nm (green) and 416 nm (red). (c) Comparison of exciton bleach (XB) kinetics at 416 nm of CdS NPLs (blue circles) and CdS NPL-Pt heterostructures (red squares), and the scaled charge separated state (CS) kinetics (green triangles). Their fits according to the model in the Appendix 9.3 are shown in solid lines.

The mechanism of PL quenching in CdS NPL-Pt is revealed by the TA spectra of CdS NPL-Pt at long delay times ($>0.8 \mu$ s, Figure 9.3b inset), which are clearly different from that of free CdS NPLs ($>0.8 \mu$ s, Figure 9.3a inset), and from the spectra of CdS NPL-Pt at early delay times (<0.1 ns). They show derivative-like spectral feature around exciton transition, which is indicative of a red-shifted exciton peak and can be attributed to the CS state (with the electron transferred to the Pt particle at the NPL edge and the hole remained in the CdS NPL) following previous assignment in similar NPLs.^{62, 69} Thus, the TA signals of CdS NPL-Pt at ~ 412 nm and delay times $<0.8 \mu$ s is the sum of contributions of excited NPL (electron state-filling induced XB) and the CS state signals. As shown in Figure 9.3b inset, because the CS signal has zero amplitude at 416 nm, the kinetics at this wavelength probe selectively the pure

electron state-filling of CdS. Thus, the kinetics of pure CS state signal can be obtained by the difference between the kinetics at 412 nm (containing both XB and CS) and 416 nm (containing only XB), as shown in Figure 9.13b in Appendix 9.3. This procedure of obtaining pure CS state kinetics is supported by similar analysis in free CdS NPLs, where the CS spectral feature is not observed (inset of Figure 9.3a) and the TA kinetics at 416 nm and 412 nm are identical (Figure 9.13a in Appendix 9.3). This analysis is further supported by the comparison in Figure 9.3c, which shows that the growth of CS signal agrees with the decay of XB signal in CdS NPL-Pt. This agreement also confirms that ET from the CdS NPL to the attached Pt particle is the main exciton quenching pathway. The CS kinetics decays on the 1 ns to μ s time scale, which can be attributed to charge recombination, transferring the electron from the Pt tip back to NPL. The XB and CS kinetics were fitted globally to a model that includes both ET and recombination processes in CdS NPL-Pt (Figure 9.13e&f in Appendix 9.3), in addition to the intrinsic decay processes within CdS NPLs. The latter is assumed to be the same as free CdS NPLs (Figure 9.13c&d in Appendix 9.3). The best fit gives average times of 426 ± 13 ps and 8.7 ± 1.7 μ s (or half-lifetimes of 8.84 ± 0.50 ps and 96.2 ± 4.8 ns) for ET and charge recombination processes, respectively (Table 9.3 in Appendix 9.3). From the ET rate and the intrinsic exciton decay rate, the ET yield is calculated to be 99.4 ± 0.6 %. The details of the fitting model and calculation of ET yield are shown in the Appendix 9.3.

Similar TA measurements of CdS NPL-Pt heterostructures in aqueous solution were not possible because their limited solubility resulted in low concentration and large scattering. However, TA studies of related CdS NR-Pt heterostructures in aqueous solution (see Appendix 9.2) show that ET rates are pH independent (Figure 9.12 in Appendix 9.2). Furthermore, electrochemical measurements show similar conduction band edge positions of CdS NRs and CdS NPLs (see Chapter 2.4), suggesting similar driving forces for ET in CdS NR-Pt and NPL-Pt heterostructures. For these reasons, we assume that the ET in CdS NPL-Pt is also pH

independent and has a rate and quantum efficiency similar to those measured in hexane solution. It is also interesting to note that the exciton quenching mechanism in CdS NPL-Pt differs significantly from that in CdSe NPL-Pt. In the latter, 87% of excitons is quenched by energy transfer to Pt because of rapidly exciton diffusion in these materials; only 13% of excitons are rapidly trapped and undergo charge separation according to our previous study.⁶² The difference in exciton quenching mechanism in these materials is consistent with their performance in light-driven H₂ generation. Negligible amount of H₂ was detected after 1h of illumination at pH 9 to 14.7 using CdSe NPL-Pt heterostructures under the same experimental conditions as those for CdS NPL-Pt (red columns in Figure 9.1f).

9.2.4. Ultrafast and pH dependent hole removal

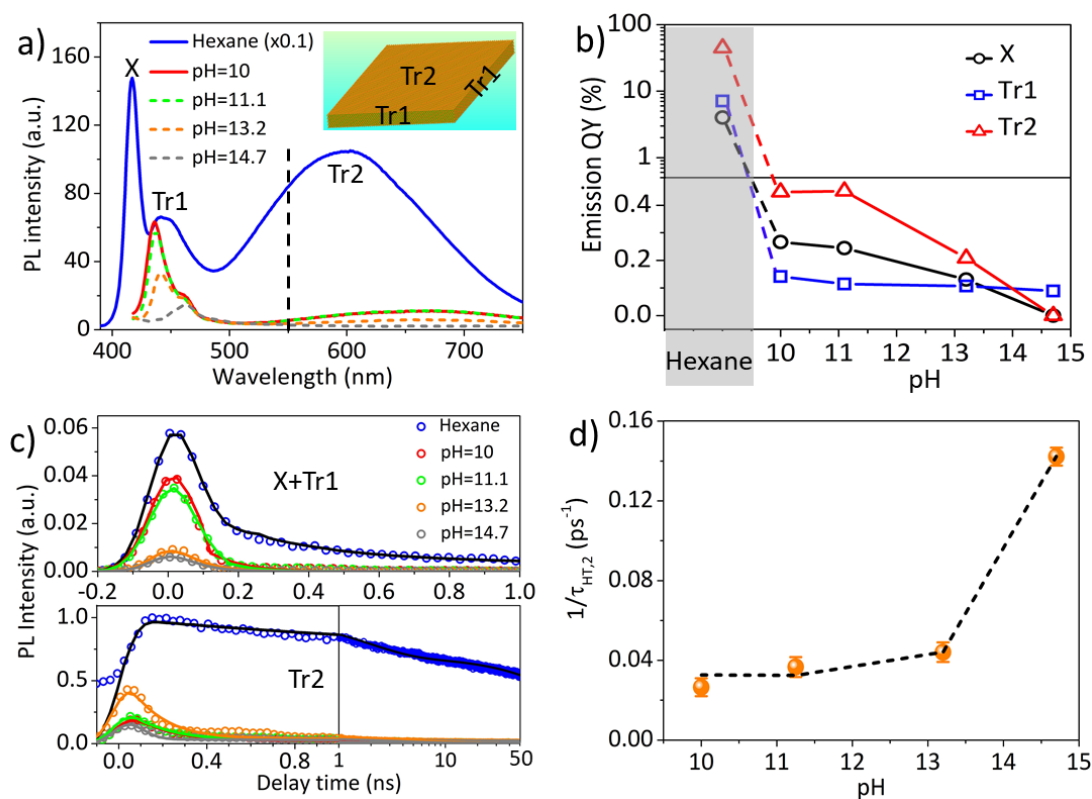


Figure 9.4. pH dependent hole removal. (a) The static-PL spectra of CdS NPLs dispersed in hexane and aqueous solution with different pH. Inset shows the location of two types of hole

traps (Tr1 and Tr2). (b) The quantum yield (QY) of band-edge (X) and trap state (Tr1, Tr2) emissions of CdS NPLs in hexane (shaded area) and aqueous solution at pH 10 to 14.7. (c) The PL decay kinetics (circles) and fits (solid lines) of the emission of the band-edge excitons and the 1st type of trapped excitons (Tr1+X, upper panel) and 2nd type of trapped excitons (Tr2, lower panel) in CdS NPLs dispersed in hexane and aqueous solution. (d) The HT rate ($1/\tau_{HT,2}$) of 2nd type of trapped excitons (Tr2) in CdS NPLs dispersed in aqueous solution as a function of pH. The black dashed line is a fit to a model that described in Appendix 9.4.

To investigate the HT process from CdS NPLs, we carried out both static-PL and TR-PL measurements on free CdS NPLs, in which HT leads to PL quenching. These measurements cannot be done in NPL-Pt, because ET to Pt also quenches the PL. The static PL spectra of CdS NPLs in different solutions (Figure 9.4a) show a band-edge exciton emission (X) and two trapped exciton emissions (Tr1 and Tr2), which can be well fitted by a sum of Gaussian functions (Figure 9.14a-f in Appendix 9.4). Emission quantum yield (QY) of each species (Figure 9.4b) were determined by comparing the integrated emission peak area to that of Coumarin 343 (QY ~63%).²⁷⁸ For PL QY measurement, all samples were adjusted to the same optical density at the excitation wavelength (390 nm). Comparison of band-edge (X) PL decay and XB recovery shows that PL decay is instrument response time limited, much faster than XB recovery (Figure 9.17b-f in Appendix 9.4), suggesting that PL decay is caused mainly by ultrafast hole trapping, similar to related CdS NRs (~780 fs).^{63, 70, 110, 279} The emission QYs of all species decrease at higher pH (Figure 9.4b), although the change of Tr1 emission is not as pronounced as the other two emissions. We attribute Tr1 and Tr2 to trapped exciton states at the NPL edges and basal plane, respectively (inset of Figure 9.4a). We speculate that at higher pH, OH⁻ can replace the ligands on CdS NPL basal plane to decrease the L-cysteine coverage and increase the number of trapped states, which accounts for the pH dependent band-edge

exciton and Tr2 PL decay. Because the NPL edges, consisting of (010) and (100) planes, have lower ligand coverage than the basal plane,²⁷¹ the Tr1 trap state density does not depend strongly on the pH (or OH).

The PL decay kinetics of X+Tr1 and Tr2 emissions are shown in the upper and lower panel of Figure 9.4c, respectively. The X and Tr1 emissions are measured together because of their strong spectral overlap. It is clear that in aqueous solution of all pH, the PL decay rates are much faster than those in hexane, consistent with the much lower static PL intensity in the former solution (Figure 9.4a&b). To quantify the HT rates, we fit the TR-PL decay kinetics of X+Tr1 and Tr2 emissions to a model described in Appendix 9.4. This model assumes that the reduced X emission intensity in aqueous solution is caused by faster hole trapping, and faster Tr1 and Tr2 emission decays in aqueous solution reflect ultrafast HT (Figure 9.16a&b in Appendix 9.4) to L-cysteine or OH. The best fits show that the hole trapping time decreases from 200 ± 20 fs in hexane to 125 ± 20 fs in pH 10 and 10 ± 10 in pH 14.7. The HT time decreases from 76.9 ± 5.5 ps to 54.1 ± 1.8 ps for Tr1 and from 37.7 ± 1.7 ps to 7.03 ± 0.20 ps for Tr2 when solution pH increases from 10.0 to 14.7 (Figure 9.4d). Note that there was a small amount (<5%) of slow Tr2 quenching with HT time constant of several ns at all pH. From the HT rate and the intrinsic decay rates of Tr1 and Tr2 emissions in hexane, the HT QY can be calculated to range from $81.3 \pm 1.0\%$ to $85.9 \pm 0.4\%$ for Tr1 and from $99.4 \pm 0.6\%$ to $99.9 \pm 0.1\%$ for Tr2, respectively, at pH 10 to 14.7 (Table 9.6 in Appendix 9.4).

9.2.5. pH and morphology dependent charge recombination in NPL-MV²⁺ complexes

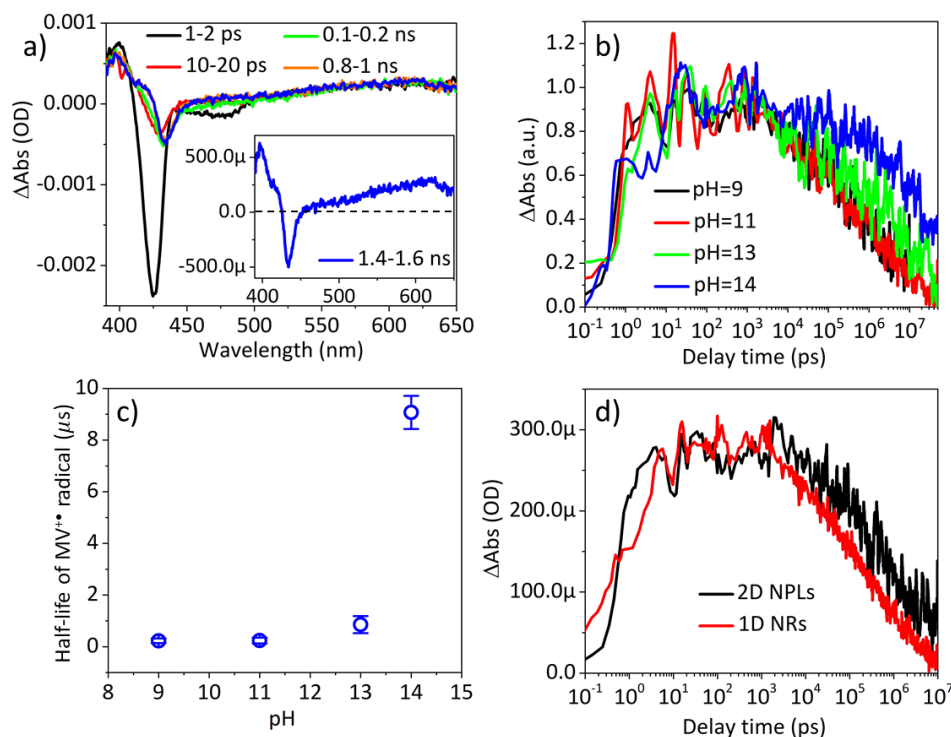


Figure 9.5. pH and morphology dependent charge recombination kinetics in CdS-methyl viologen (MV²⁺) complexes. (a) TA spectra of CdS NPL-MV²⁺ complexes in aqueous pH=9 solution at indicated delay times after 400 nm excitation. Inset: expanded view of the TA spectrum at 1.4-1.6 ns. (b) Comparison of normalized MV⁺• radical kinetics of CdS NPL-MV²⁺ complexes at different pH. (c) The half-life of MV⁺• radicals of CdS NPL-MV²⁺ complexes as a function of pH. (d) Comparison of MV⁺• radical kinetics of CdS NR-MV²⁺ (red line) and NPL-MV²⁺ complexes (black line) at pH 9.

The above TA and PL studies show that initial ET from NPL to Pt and HT to adsorbed acceptor molecules are ultrafast and efficient. Thus, the key factor that limits the overall H₂ generation efficiency is most likely the lifetime of the CS state (Figure 9.2b), i.e. the recombination of the transferred electron in Pt with the hole in the oxidized ligand. Unfortunately, it is not possible to directly measure this charge recombination time because CdS NPL-Pt has limited solubility in aqueous solution, which causes large scattering, and there

lacks clear spectral signal for probing the transferred electron in the Pt and hole in the oxidized ligand. Therefore, we use CdS NPL-methyl viologen (MV^{2+}) complexes to mimic the CdS NPL-Pt heterostructure by substituting Pt tips with MV^{2+} . MV^{2+} is frequently used as an one-electron acceptor that can adsorb on nanocrystal surfaces,^{44, 76, 78, 104, 110, 280} and while MV^{2+} has no absorption from 400 to 800 nm, its reduced radical has a distinct absorption features centered at ~400 and 600 nm, making it a convenient spectroscopic probe for the ET and charge recombination processes.^{12, 102} We study the lifetime of CS state with transferred electron on the reduced MV^{2+} (or $MV^{+\bullet}$ radical) and transferred hole on surface covered ligands (L-cysteine or OH^-) in CdS NPL- MV^{2+} complexes in ethanol/KOH (volume ratio of 1:9) aqueous solution of different pH. The static absorption spectra of these samples are shown in Figure 9.19a in Appendix 9.5. The TA spectra at pH=9 are shown in Figure 9.5a and the spectra at other pH (from 11 to 14) are shown in Figure 9.19b-d in Appendix 9.5. The complete recovery of XB signal (~430 nm) and the growth of $MV^{+\bullet}$ radical signal (at ~600 nm and ~400 nm) within 10 ps indicates ET from the CdS NPL to MV^{2+} . The $MV^{+\bullet}$ radical signal decay can be used to probe the charge recombination process. The normalized $MV^{+\bullet}$ radical kinetics at different pH are shown in Figure 9.5b, from which we obtain the CS state half-lifetime of $0.23 \pm 0.09 \mu s$, $0.24 \pm 0.11 \mu s$, $0.86 \pm 0.33 \mu s$, and $9.07 \pm 0.64 \mu s$ at pH of 9, 11, 13, and 14, respectively. As shown in Figure 9.5c, the CS state lifetime changes negligibly from pH 9 to 13 and increases by a factor of ~10.5 from pH 13 to pH 14, indicating much more effective suppression of charge recombination at pH 14. Unfortunately, the NPL- MV^{2+} is only stable at pH 14, and a direct comparison with the pH 14.7 condition for H_2 generation is not possible. Nevertheless, the observed trend supports the hypothesis that although fast and efficient HT to both OH^- and L-cysteine at pH 10 to 14.7 can be achieved, the fast removal of the hydroxyl radical (by reaction with ethanol) is the key to suppress charge recombination and enhance H_2 generation quantum efficiency at pH>13.

To provide insight into how morphology can influence charge recombination, we also compare this process in 1D CdS NR-MV²⁺ and 2D CdS NPL-MV²⁺ complexes under the same experimental conditions. We use CdS NRs with length of ~55 nm (see TEM image in Figure 9.20a in Appendix 9.5), similar to the length of CdS NPLs, and their absorption spectra are shown in Figure 9.20b in Appendix 9.5. TA spectra (Figure 9.20c in Appendix 9.5) show the recovery of CdS NR XB and the corresponding formation of MV^{+•} radical signal, confirming ET from CdS NRs to MV²⁺. Comparison of the MV^{+•} radical decay kinetics of 1D NR- MV²⁺ and 2D NPL-MV²⁺ complexes at pH 9 (Figure 9.5d) show a much shorter-lived CS state with half-lifetime of $0.07 \pm 0.02 \mu\text{s}$ in the NR-MV²⁺ complexes, which is ~3.3 folds shorter than that in NPL-MV²⁺ complexes.

9.2.6. A Model for pH dependent H₂ generation IQE

As shown in Figure 9.1f, H₂ generation IQE of CdS NPL-Pt decreases from near unity to ~42% when pH decreases from 14.7 to 8.8, which is much larger than the variation of hole transfer efficiency over a similar pH range. Moreover, as shown in Figure 9.5c, the charge recombination time is pH dependent with a dramatic increase of CS state lifetime at pH=14. These results suggest that at pH<14.7, the steady state H₂ generation efficiency is limited by charge recombination between the transferred electron at the Pt nanoparticles and the transferred hole in the hole acceptor. To account for the observed pH dependent H₂ generation efficiency, we propose that at pH>13, OH⁻ is the main hole acceptor. Upon hole transfer, it generates hydroxyl radicals that can undergo rapid ethanol oxidation and irreversibly removes the photogenerated hole from NPLs.¹¹⁴ This process suppresses charge recombination and enables the transferred electron on Pt to efficiently carry out relatively slow H₂ evolution reactions. At pH<13, L-cysteine is the main hole acceptor because of the limited OH⁻ concentration. It has been shown that similar HT processes from QDs to other thiols (3-

mercaptopropionic acid) generate thiol radicals which are followed by disulfide formation on QD surfaces,²⁸¹⁻²⁸² or further oxidation of alcohol.²⁸³ Although the time scales of these thiol radical reactions in our NPLs are unknown, they likely compete with the recombination of the transferred hole (in L-cysteine) with the electron on Pt, which reduces the H₂ generation IQE. This proposal is supported by several previous studies of similar QDs and NRs.^{63, 103-104} Therefore, the observed rapid decrease in H₂ generation IQE efficiency (Figure 9.1f) at pH<13 can be attributed to decreased OH⁻ concentration in aqueous solution. The proposed model is further supported by the excellent fits of the pH dependent IQE (Figure 9.1f) and average Tr2 HT time (Figure 9.4d) to a model that accounts for the pH dependent surface coverage of and different HT rates to L-cysteine and OH⁻ (see Appendix 9.4 for details). The best fits lead to HT time constants of 0.700 ± 0.005 ns and 1.19 ± 0.03 ns per surface adsorbed OH⁻ and L-cysteine, respectively.

9.2.7. A Model for Enhanced H₂ IQE in 2D NPL-Pt Heterostructures

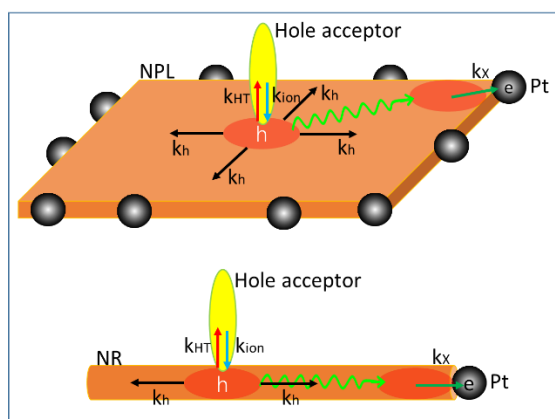


Figure 9.6. Scheme of charge recombination processes in 2D NPL-Pt and 1D NR-Pt heterostructures in aqueous solution at pH <13.

Our results show that at $\text{pH} < 13$, the H_2 generation IQE of NPLs is much larger than NRs. There are several possibilities that could result in this enhanced H_2 generation efficiency of 2D NPLs. One possibility is the different numbers of Pt on NPLs and NRs. In a previous study of H_2 generation in CdS NR-Pt, the presence of multiple Pt particles on the NR surface is shown to reduce the H_2 generation quantum efficiency, which is attributed to decrease of the average distance between the separated electron and hole,²⁷⁵ Although the presence of multiple Pt particles on NPL edges doesn't affect the average charge separation distance, it can affect the rate of accumulating two electrons on a single particle.²⁷³ It has been reported that in CdSe/CdS NR-Pt, a higher H_2 generation efficiency was observed in longer NRs, suggesting a higher absorber volume per catalyst may lead to higher H_2 generation efficiency through faster two electron accumulation.³ Considering a CdS NPL with lateral dimension of $\sim 58 \times 33 \text{ nm}^2$ and thickness of $\sim 1.8 \text{ nm}$,^{23,24} decorated by ~ 13 Pt particles with diameter of $\sim 3.3 \text{ nm}$ (Figure 9.7b&d in Appendix 9.1), the volume of CdS NPL absorber per Pt catalyst is $\sim 265 \text{ nm}^3$. However, for typical CdSe/CdS NR-Pt heterostructures used in Ref²⁵⁹ with rod length of $\sim 50 \text{ nm}$, rod diameter of $\sim 5 \text{ nm}$, and one Pt tip with diameter of $\sim 4 \text{ nm}$,²⁵⁹ the absorber volume per Pt catalyst is $\sim 981 \text{ nm}^3$, ~ 3.7 folds larger than that of NPL-Pt. This indicates different absorber volume per catalyst is not the main reason for the observed enhanced H_2 generation efficiency of 2D NPLs.

Another possibility is different surface passivation between 1D and 2D nanostructures, which is induced by different crystal structures with different exposed atoms on the surface. In particular, 1D wurtzite NRs have both Cd and S exposed along NR surface while 2D zinc-blend NPLs only have Cd exposed on the basal planes. This could affect ET and HT rates in NPLs and NRs, which can be directly probed by their XB and TR-PL decay kinetics, respectively, as discussed above. For example, ET time from NPL to Pt (as measured by the

half-lifetime of XB) of CdS NPL-Pt (~ 8.8 ps, Figure 9.3c) is ~ 2.6 folds longer than that of CdS NR-Pt (~ 3.4 ps),⁶ while the HT time (as measured by the half-lifetime of TR-PL) of 2D NPLs (Figure 9.4c and Figure 9.15f in Appendix 9.4) is over 8 folds shorter than that of 1D NRs (Figure 9.15e in Appendix 9.4) at all pH (Table 9.5 in Appendix 9.4). Although the ET and HT times are different in NRs and NPLs, they are both in the ps timescale and do not affect the initial HT and ET efficiency because they are much faster than the intrinsic exciton lifetime.

We propose that the 2D morphology in NPLs can enhance the lifetime of charge-separated state compared to 1D NRs and play a key role in enhancing the H₂ generation quantum efficiency. As discussed above, at pH < 13, when OH⁻ is no longer the dominant hole acceptor, charge recombination becomes the key efficiency limiting factor. This hypothesis is supported by the experimental comparison of charge recombination times in NR-MV²⁺ and NPL-MV²⁺ complexes shown in Figure 9.5d. Because we cannot directly measure the charge recombination time in NPL-Pt system, we numerically simulated this process in both CdS NR-Pt and CdS NPL-Pt heterostructures. In the simulation, we assume that charge recombination proceeds by an activated diffusion of the transferred hole. As shown in Figure 9.6 and described in detail in Appendix 9.6, this model accounts for trapped hole transfer to L-cysteine (with rate constant k_{HT} , see Appendix 9.4), ionization of the hole in L-cysteine back to NPLs valence band (k_{ion}), trapped hole diffusion (k_h), and recombination with electron (k_x) at CdS-Pt interface. Our simulation shows that, with the same rate constants for elementary steps and lateral size (same length for NRs and square NPLs), charge recombination in 2D NPLs is over 5 folds slower than 1D NRs regardless of fast ($k_h/k_x \gg 1$) or slow ($k_h/k_x \ll 1$) trapped hole diffusion (Figure 9.22 and Table 9.7 in Appendix 9.6). Our model is similar to a hole hopping model has been applied successfully in previous studies of electron-trapped hole recombination in CdS and CdSe NRs.²⁸⁴⁻²⁸⁷ Compared to 1D NRs, the 2D morphology requires many more random walk steps before the hole finds the recombination (Pt) site, leading to slower charge

recombination. In our simulation, recombination can occur only at the Pt site to which the electron has been transferred, although there are several Pt particles per NPL (Figure 9.1c&d). Including hole transfer to other Pt particles, which interrupts the random walk of trapped hole, will further extend the lifetime of the CS state in NPL-Pt. It is likely that charge recombination and the reaction of the transferred hole with ethanol in solution occur on similar time scales, which reduce H₂ generation IQE and leads to its sensitive dependence on the nanocrystal morphology. Although compared to 1D NRs, 2D morphology also slows down the initial electron transfer to Pt, this does not affect the charge separation efficiency because, as shown in Figure 9.3c, the ET rate is much faster than intrinsic exciton decay within NPL. It is important to note that our simulation is focused on how 1D and 2D diffusion can affect the charge recombination without accounting for possible differences in the nature of hole trap states and trapped hole diffusion time constant. More in-depth studies will be needed to fully account for the many differences in these systems and identify all contributing factors to the observed enhanced H₂ generation efficiency in 2D NPL-Pt heterostructures.

9.3. Conclusion

In summary, we have demonstrated an efficient light-driven H₂ generation system using CdS NPL-Pt heterostructures in aqueous solution with ethanol as a sacrificial electron donor. We show that the IQE of H₂ production increases from ~41.9% at pH 8.8 to unity at pH 14.7. This 2D NPL based system shows much improved IQE at pH 8-13 compared to previously reported performance using 1D CdS and CdSe/CdS NR heterostructures, although both 1D and 2D systems achieve similar near unity IQE at pH 14.7. Detailed TA as well as static and time-resolved PL studies show that the initial charge separation process (electron transfer to Pt and hole transfer to acceptors) is ultrafast and efficient at all pH, the recombination of the CS state (electron in Pt and hole on surface adsorbed hole acceptor) is the key efficiency limiting factor.

We propose that at extremely high pH of 14.7, OH^- is the main hole acceptor, which upon oxidation can react rapidly and irreversibly with ethanol to suppress charge recombination and enable H_2 generation with near unity IQE. At $\text{pH} < 13$, L-cysteine is the main hole acceptor and the charge recombination process likely competes with the subsequent reaction of the oxidized L-cysteine, lowering the H_2 generation IQE. This proposed model is consistent with the observed pH dependent HT time and H_2 generation efficiency. Our numerical simulation result shows that compared to 1D CdS NRs, the 2D morphology of CdS NPLs slows down charge recombination, which is the dominant factor that enhances their IQE at $\text{pH} < 13$ compared to CdS NRs. Further support for the proposed model is provided by the study of charge recombination time in 2D NPL/ MV^{2+} complexes, which shows a pronounced lengthening of CS state lifetime at $\text{pH} > 13$, and a longer lived CS state compared to that in 1D NR/ MV^{2+} complexes at pH 9. Our result demonstrates that 2D morphology provides an additional control for designing nanoscale systems with improved charge separation and light-driven catalytic reactions. We believe this insight can be extended to other 2D materials and can be used to improve the solar energy conversion efficiencies of other artificial photosynthetic systems.

Appendix 9.1

Additional characterizations (Size distribution, absorption spectra, and photostability) of CdS NPL-Pt heterostructures

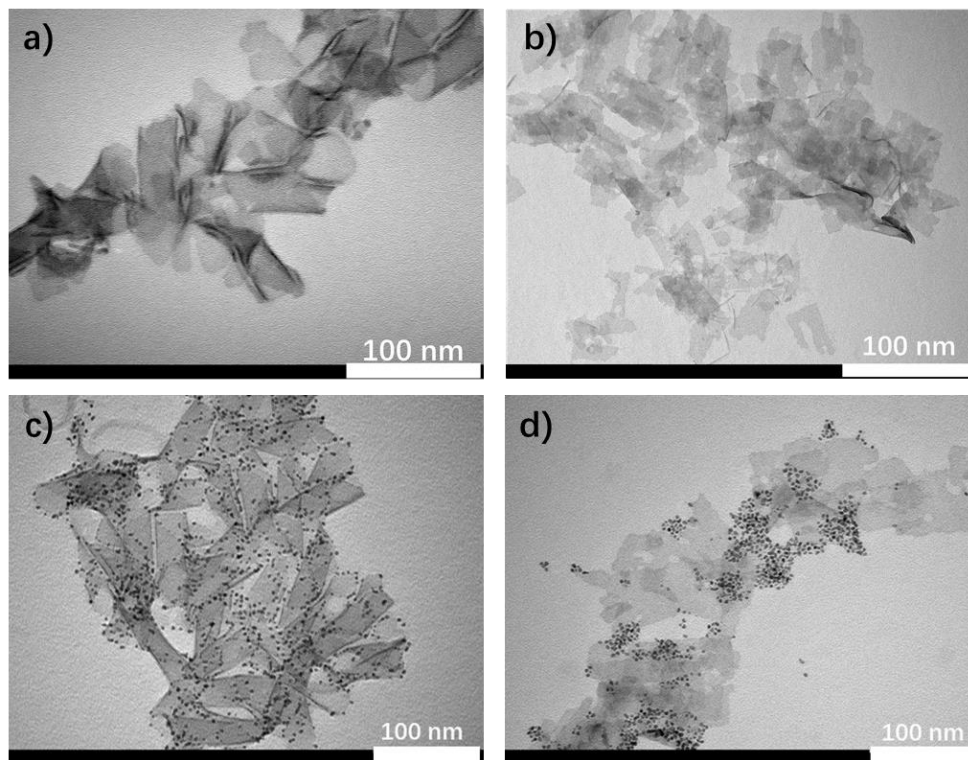


Figure 9.7. The TEM images of free CdS NPLs in (a) hexane and (b) aqueous solution with pH of 10. The TEM images of CdS NPL-Pt heterostructures in (c) hexane and (d) aqueous solution with pH of 10.

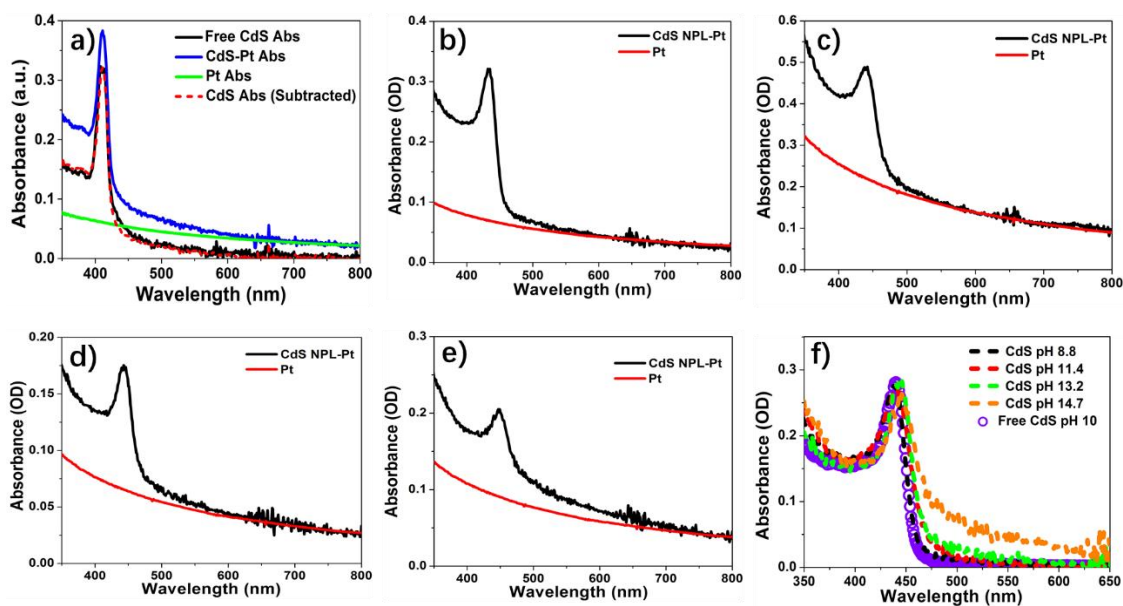


Figure 9.8. (a) The absorption spectra of CdS NPL-Pt heterostructures in hexane (blue solid line), which can be considered as the sum of the absorption spectrum of Pt particles (green solid line) and the CdS NPLs (red dashed line). The latter is consistent with the absorption spectrum of free CdS NPLs (black solid line). The absorption spectra of CdS NPL-Pt heterostructures in aqueous solution with pH of (b) 8.8, (c) 11.4, (d) 13.2, and (e) 14.7 for H_2 generation. The red lines are the normalized Pt absorption. (f) The comparison of subtracted CdS NPL absorption (dashed lines) obtained from (b-e) and the free CdS NPL absorption at pH of 10 (purple circles).

The comparison of CdS NPL-Pt absorption spectra at aqueous solution with pH of 8.8 before and after 5, 19, 25, and 30 h's illumination is shown in Figure 9.9a. The absorption spectra of CdS NPL-Pt heterostructures are fitted as the sum of CdS NPL and Pt particle absorptions. CdS NPL absorption spectra are fitted according to a well-established NPL absorption model.^{28, 250-251} The CdS NPL-Pt absorption can be represented by the following equation:

$$\text{Abs}(E) = \text{Pt}(E) + A_{\text{NPL}}[\text{X}(E) + \text{Cont}(E)] \quad (9.1)$$

where $Pt(E)$ is scaled Pt particle absorption (in water) measured by UV/Vis spectrometer, A_{NPL} is scaling parameter that determines the CdS NPL absorption intensity. $X(E)$ is band-edge exciton peak, $Cont(E)$ is continuous band absorption, and they are fitted as:

$$X(E) = \frac{1}{2\eta} \left[\operatorname{erf} \left(\frac{E - E_X}{W_X} - \frac{W_X}{2\eta} \right) + 1 \right] \exp \left(\frac{W_X^2}{4\eta^2} - \frac{E - E_X}{\eta} \right) \quad (9.2)$$

$$Cont(E) = \frac{H}{2} \left[\operatorname{erf} \left(\frac{(E - E_X) - E_b}{W_C} \right) + 1 \right] \quad (9.3)$$

In Eq. 9.2 and 9.3, E_X and E_b are exciton transition energy and exciton binding energy, respectively. W_X and W_C are exciton peak width and continuum edge width, respectively. H is the continuum edge step height and η is the asymmetric broadening. Note that we only consider one exciton peak and one continuous band absorption near CdS NPL band edge due to the strong overlaps between electron-heavy hole and electron-light hole transitions in CdS NPLs.²¹

We fit the CdS NPL-Pt absorption spectra (red circles) at aqueous solution with pH of 8.8 before and after 5, 19, 25, and 30 h's illumination as shown in Figure 9.9b. The Pt absorption are in gray solid lines, exciton peak and continuous band are in green solid lines, and the total absorption fits are in black dashed lines. The fitting parameters with errors are listed in Table 9.2.

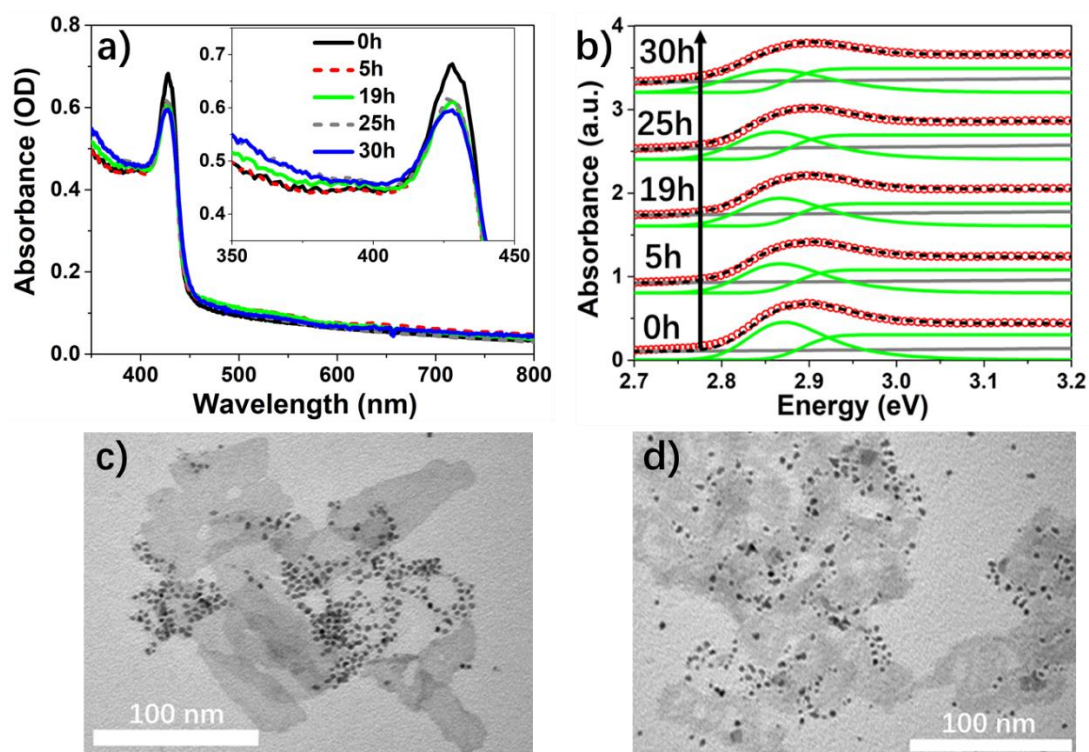


Figure 9.9. (a) The comparison of CdS NPL-Pt absorption spectra at aqueous solution with pH of 8.8 before and after 5, 19, 25, and 30 h's illumination. The inset shows the same spectra near exciton peak region. (b) The CdS NPL-Pt absorption spectra (red circles) with fit (lines) at aqueous solution with pH of 8.8 before and after 5, 19, 25, and 30 h's illumination. The Pt absorption are in gray solid lines, exciton peak and continuous band are in green solid lines, and the total absorption fits are in black dashed lines. The TEM image of CdS NPL-Pt at aqueous solution with pH of 8.8 (c) before and (d) after 30 h's illumination.

Table 9.2. Fitting parameters with errors of CdS NPL-Pt absorption spectra before and after photocatalysis

	0h	5h	19h	25h	30h
E_x/eV	2.83 ± 0.01				
E_b/meV	50 ± 2				

W_X/meV	45 ± 2	49 ± 2	51 ± 2	52 ± 2	57 ± 2
W_C/meV	35 ± 1				
η/meV	52 ± 2				
H/eV	5.5 ± 0.1	5.9 ± 0.1	6.0 ± 0.1	6.5 ± 0.1	6.8 ± 0.1
A_{NPL}	0.048 ± 0.001	0.046 ± 0.001	0.045 ± 0.001	0.045 ± 0.001	0.044 ± 0.001

Appendix 9.2

Electron transfer in CdS nanorod (NR)-Pt heterostructures

The pH dependent electron transfer (ET) is studied using CdS nanorods (NRs) tipped with Pt particles. The CdS NR-Pt heterostructures were transferred to aqueous solution with different pH *via* ligand exchange reaction mentioned above. The absorption spectra of CdS NR-Pt heterostructures with different pH (dashed lines) are shown in Figure 9.10. The long tail below the first exciton peak (~463 nm) is due to Pt absorption as compared as gray solid line. The CdS NR-Pt has more scattering when pH>14, which is attributed to the reduced solubility and NRs were etched at high pH (>14).

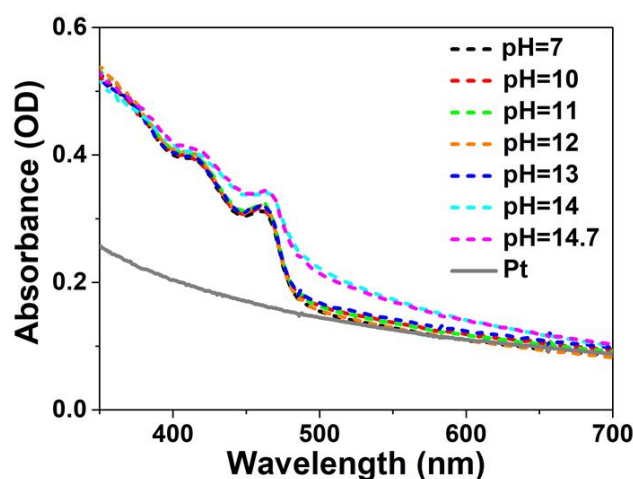


Figure 9.10. The absorption spectra of CdS NR-Pt heterostructures in aqueous solution with different pH (dashed lines) and the absorption of Pt particles in water (gray solid line).

We carried out TA spectroscopy on these CdS NR-Pt heterostructures to quantify the pH dependent ET process from CdS NR to Pt, and their TA spectra are shown in Figure 9.11. All TA spectra show exciton bleach (XB) at ~463 nm, which is due to electron state-filling on conduction band edge.^{63, 70, 102, 110} Their XB kinetics are compared in Figure 9.12, which shows identical decay kinetics within errors due to the small optical density differences between

samples. This shows pH independent electron transfer from CdS NR to Pt, although at pH=14.7, small difference shows near the time zero, which is likely due to CdS NR is etched and unstable at such high pH.

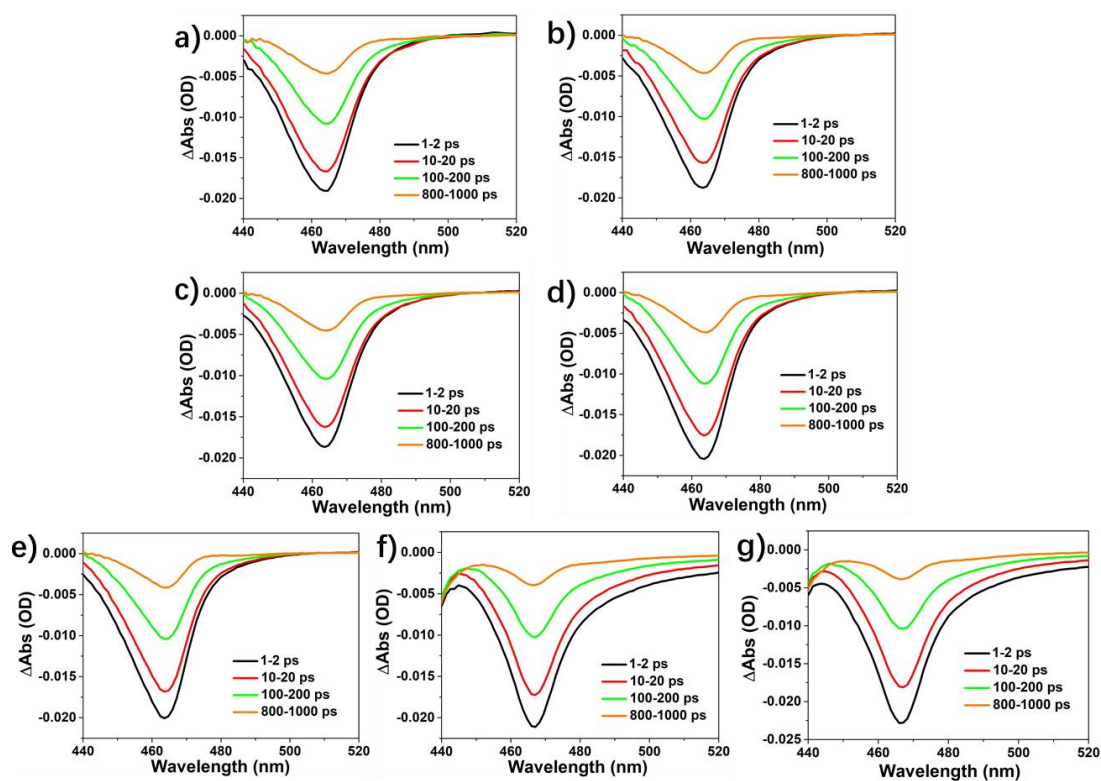


Figure 9.11. The TA spectra of CdS NR-Pt heterostructures in aqueous solution with (a) pH=7, (b) pH=10, (c) pH=11, (d) pH=12, (e) pH=13, (f) pH=14, and (g) pH=14.7.

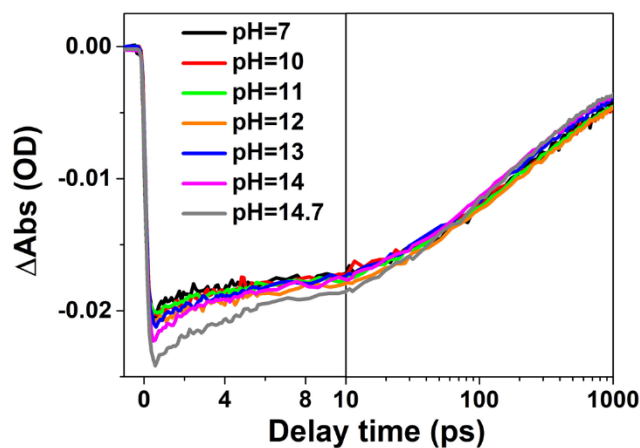


Figure 9.12. The comparison of XB kinetics of CdS NR-Pt heterostructures in aqueous solution with different pH.

Appendix 9.3

Fits of the TA bleach kinetics

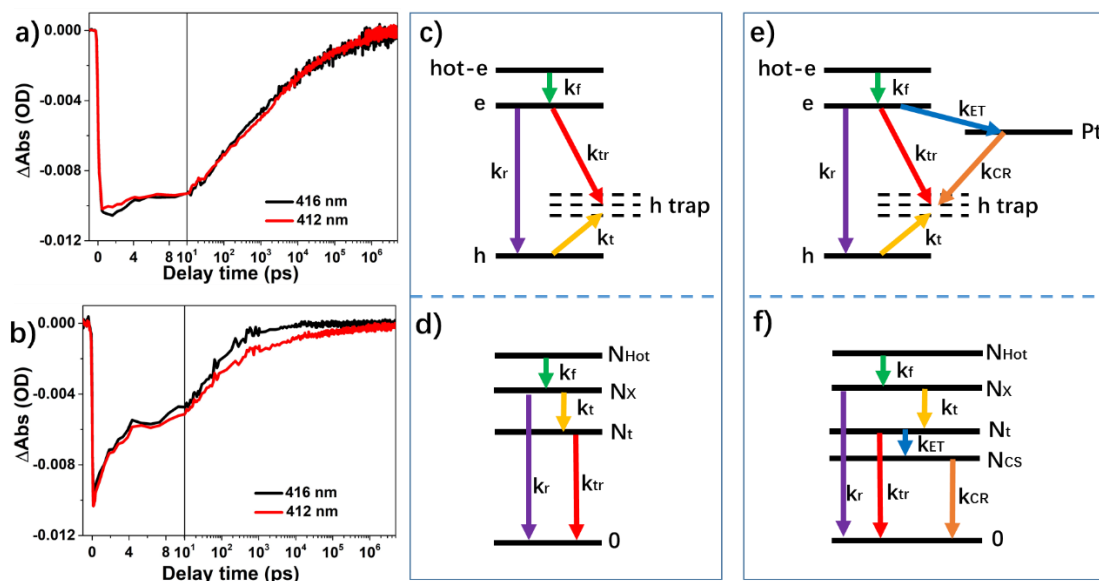


Figure 9.13. The comparison of normalized XB kinetics at different wavelength (412 and 416 nm) of (a) free CdS NPLs and (b) CdS NPL-Pt heterostructures. Carrier decay pathways in free CdS NPLs in (c) single particle (electron and hole) representation and (d) state representation at 400 nm excitation. Carrier decay pathways in CdS NPL-Pt heterostructures in (e) single particle (electron and hole) representation and (f) state representation at 400 nm excitation.

The XB kinetics at different wavelength of free CdS NPLs and CdS NPL-Pt heterostructures were normalized at the time zero and compared in Figure 9.13a and 9.13b, respectively. In free CdS NPLs, the XB kinetics at 416 nm was identical to XB kinetics at 412 nm. In CdS NPL-Pt heterostructures, the XB at 416 nm represented the pure electron state-filling signals on CdS CB edge, while XB at 412 nm contained both electron state-filling and charge-separated (CS) state signals.

At 400 nm excitation, the carriers in CdS NPLs undergo various relaxation, trapping and recombination processes (Figure 9.13c&d). Because the TA signals at exciton peak of CdS

NPLs are dominated by the concentrations of electrons at the CB edge, we only need to consider three species that affect its concentration: hot-electrons (N_{hot}), band edge excitons (N_X , with both electron and hole in the band edge), and trapped exciton (N_t , band edge electron and a trapped hole). As shown in Figure 9.13c&d, hot-electrons (N_{hot}) represents initially excited carriers that decay to form band edge exciton with a rate constant of k_f . The band edge excitons can decay through radiative recombination with a rate constant k_r or *via* hole trapping with a rate constant k_t (to form trapped exciton N_t). The trapped excitons can decay by radiative and nonradiative recombination (k_{tr}). As shown in Figure 9.13e&f, CdS NPL-Pt heterostructures have an additional decay pathway for trapped excitons (N_t): the electron transfers to Pt with a rate constant k_{ET} after the hole gets trapped, which generates a CS state, N_{CS} . The charge-separated state decays by electron in Pt recombining with the trapped hole in CdS NPL with a charge recombination (CR) rate of k_{CR} .

For free CdS NPLs, these species are governed by the following rate equations:

$$\frac{dN_{\text{Hot}}}{dt} = -k_f N_{\text{Hot}} \quad (9.4)$$

$$\frac{dN_X}{dt} = k_f N_{\text{Hot}} - (k_r + k_t) N_X \quad (9.5)$$

where total hole trapping rate, k_t , is the sum of hole trapping rate, $k_{t,i}$, for different trap states, $N_{t,i}$:

$$k_t = \sum_i k_{t,i} \quad (9.6)$$

Each trap state, $N_{t,i}$, has a formation rate the same as hole trapping rate, $k_{t,i}$, and a recombination rate of $k_{\text{tr},i}$:

$$\frac{dN_{t,i}}{dt} = k_{t,i} N_X - k_{\text{tr},i} N_{t,i} \quad (9.7)$$

The solution of Eq. 9.4 to 9.7 are:

$$N_{\text{Hot}} = N_0 e^{-k_f t} \quad (9.8)$$

$$N_X(t) = \frac{N_0 k_f}{k_f - (k_r + k_t)} [e^{-(k_r + k_t)t} - e^{-k_f t}] \quad (9.9)$$

$$N_{t,i}(t) = \frac{N_0 k_f}{k_f - (k_r + k_t)} \left[\left(\frac{k_{t,i}}{k_r + k_t - k_{tr,i}} - \frac{k_{t,i}}{k_f - k_{tr,i}} \right) e^{-k_{tr,i}t} + \frac{k_{t,i}}{k_f - k_{tr,i}} e^{-k_f t} - \frac{k_{t,i}}{k_r + k_t - k_{tr,i}} e^{-(k_r + k_t)t} \right] \quad (9.10)$$

where N_0 is the initial amount of excitons generated after pump. Due to $k_f \gg k_{tr,i}$, considering trapped exciton recombination is not competitive to the hot exciton relaxation, Eq. 9.10 is approximated to:

$$N_{t,i}(t) = \frac{N_0 k_f}{k_f - k_t} \frac{k_{t,i}}{k_t} \left[\frac{k_f - k_t}{k_f} e^{-k_{tr,i}t} + \frac{k_t}{k_f} e^{-k_f t} - e^{-(k_r + k_t)t} \right] \quad (9.11)$$

and the sum of all the trapped excitons is:

$$\sum_i N_{t,i}(t) = \frac{N_0 k_f}{k_f - k_t} \left[\frac{k_f - k_t}{k_f} \sum_i \frac{k_{t,i}}{k_t} e^{-k_{tr,i}t} + \frac{k_t}{k_f} e^{-k_f t} - e^{-(k_r + k_t)t} \right] \quad (9.12)$$

The TA exciton bleach kinetics of free CdS NPLs is the sum of the population change of band-edge excitons and trapped excitons:

$$\begin{aligned} \text{TA}_{\text{free CdS}}(t) &\propto N_X(t) + \sum_i N_{t,i}(t) = \frac{N_0 k_f}{k_f - k_t} \left[\frac{k_f - k_t}{k_f} \sum_i \frac{k_{t,i}}{k_t} e^{-k_{tr,i}t} + \left(\frac{k_t}{k_f} - 1 \right) e^{-k_f t} \right] \\ &= N_0 \left[\sum_i \frac{k_{t,i}}{k_t} e^{-k_{tr,i}t} - e^{-k_f t} \right] \quad (9.13) \end{aligned}$$

For CdS NPL-Pt heterostructures, the rate equation for trapped exciton is different from the one for the free CdS NPLs:

$$\frac{dN_{t,i}}{dt} = k_{t,i} N_X - (k_{tr,i} + k_{ET,i}) N_{t,i} \quad (9.14)$$

This gives:

$$N_{t,i}(t) = \frac{N_0 k_f}{k_f - k_t} \frac{k_{t,i}}{k_t} \left[\frac{k_f - k_t}{k_f} e^{-(k_{tr,i} + k_{ET,i})t} + \frac{k_t}{k_f} e^{-k_f t} - e^{-(k_r + k_t)t} \right] \quad (9.15)$$

$$\sum_i N_{t,i}(t) = \frac{N_0 k_f}{k_f - k_t} \left[\frac{k_f - k_t}{k_f} \sum_i \frac{k_{t,i}}{k_t} e^{-(k_{tr,i} + k_{ET,i})t} + \frac{k_t}{k_f} e^{-k_f t} - e^{-(k_r + k_t)t} \right] \quad (9.16)$$

The corresponding CS state, $N_{CS,i}$, decays as:

$$\frac{dN_{CS,i}}{dt} = k_{ET,i} N_{t,i} - k_{CR,i} N_{CS,i} \quad (9.17)$$

which gives:

$$N_{CS,i}(t) = \frac{N_0 k_f}{k_f - k_t} \frac{k_{t,i}}{k_t} \left[\frac{k_{ET,i}}{k_r + k_t - k_{CR,i}} e^{-(k_r + k_t)t} + \gamma e^{-k_{CS,i}t} - \frac{k_{ET,i}}{k_f - k_{CR,i}} \frac{k_t}{k_f} e^{-k_f t} - \frac{k_{ET}}{k_{tr,i} + k_{ET} - k_{CR,i}} \frac{k_f - k_t}{k_f} e^{-(k_{tr,i} + k_{ET,i})t} \right] \quad (9.18)$$

$$\gamma = \frac{k_{ET,i}}{k_{tr,i} + k_{ET} - k_{CR,i}} \frac{k_f - k_t}{k_f} - \frac{k_{ET,i}}{k_r + k_t - k_{CR,i}} + \frac{k_{ET,i}}{k_f - k_{CR,i}} \frac{k_t}{k_f} \quad (9.19)$$

Due to $k_f, k_t \gg k_{ET} \gg k_r, k_{tr,i}, k_{CS,i}$, the Eq. 9.19 is approximated as:

$$N_{CS,i}(t) = N_0 \frac{k_{t,i}}{k_t} [e^{-k_{CS,i}t} - e^{-k_{ET,i}t}] \quad (9.20)$$

$$\sum_i N_{CS,i}(t) = N_0 \sum_i \frac{k_{t,i}}{k_t} [e^{-k_{CS,i}t} - e^{-k_{ET,i}t}] \quad (9.21)$$

The TA exciton bleach kinetics at 416 nm of CdS NPL-Pt heterostructures then becomes:

$$\begin{aligned} TA_{CdS-Pt}(t) &\propto N_X(t) + \sum_i N_{t,i}(t) \\ &= N_0 \left[\sum_i \frac{k_{t,i}}{k_t} e^{-k_{ET,i}t} - e^{-k_f t} \right] + \alpha N_0 \sum_i \frac{k_{t,i}}{k_t} [e^{-k_{CR,i}t} - e^{-k_{ET,i}t}] \end{aligned} \quad (9.22)$$

where α is the relative signal amplitude for CS state.

According to Eq. 9.13, 9.21, and 9.22, we fitted the normalized XB kinetics at 416 nm and the CS state kinetics of free CdS NPLs and CdS NPL-Pt heterostructures with multi-exponential functions convoluted with instrument response function (IRF, ~150 fs), which is determined from the scattering signals of the solvent (hexane):

$$XB_{\text{free CdS}}(t) = A_X \left[\sum_{i=1}^4 C_i e^{-\tau_{\text{tr},i}t} - e^{-\tau_f t} \right] \otimes \text{IRF} \quad (9.23)$$

$$XB_{\text{CdS-Pt}}(t) = A_X \left[\sum_{i=1}^4 C_i e^{-\tau_{\text{ET},i}t} - e^{-\tau_f t} \right] \otimes \text{IRF} \quad (9.24)$$

$$CS_{\text{CdS-Pt}}(t) = A_{\text{CS}} \sum_{i=1}^4 C_i [e^{-\tau_{\text{CR},i}t} - e^{-\tau_{\text{ET},i}t}] \otimes \text{IRF} \quad (9.25)$$

where A_X and A_{CS} are the initial amplitudes for XB and CS state signal, respectively. C_i ($i=1$ to 4) are different decay components, the sum of which equals 1. τ is the time constant of corresponding decay rate, k : $\tau = \frac{1}{k}$. The fitting parameters with errors are listed in Table 9.3.

Table 9.3. TA exciton bleach kinetics fitting parameters with errors

i	1	2	3	4
$C_i/\%$	41.2 ± 2.2	30.8 ± 1.1	17.9 ± 3.7	10.1 ± 1.6
$\tau_{\text{tr},i}/\text{ps}$	81.5 ± 1.4	2570 ± 250	56787 ± 2131	2419017 ± 57365
$\tau_{\text{ET},i}/\text{ps}$	0.68 ± 0.20	16.1 ± 1.3	486 ± 16	87.5 ± 8.3
$\tau_{\text{CR},i}/\text{ns}$	19.0 ± 1.3	255 ± 90	8987 ± 1793	
τ_f/fs	10 ± 10			

The average time constant of ET (CR) is calculated as: $\tau_{\text{ave}} = \frac{\sum_{i=1}^4 C_i \tau_{\text{ET(CR)},i}^2}{\sum_{i=1}^4 C_i \tau_{\text{ET(CR)},i}} = 426 \pm 13$

ps ($8.7 \pm 1.7 \mu\text{s}$), and the electron transfer yield (ET.Y.) is calculated considering the competition between trapped exciton recombination and ET: ET.Y. =

$$\sum_{i=1}^4 C_i \frac{\tau_{\text{tr},i}}{\tau_{\text{ET},i} + \tau_{\text{tr},i}} = 99.4 \pm 0.6 \%$$

Appendix 9.4

Fits of the static PL spectra and TR-PL decay kinetics

The static PL spectra of CdS NPLs were fitted by three Gaussian functions:

$$PL(\lambda) = BG + \frac{A_X e^{-\frac{4\ln 2(\lambda-\lambda_X)^2}{w_X^2}}}{w_X \sqrt{\frac{\pi}{4\ln 2}}} + \frac{A_{Tr1} e^{-\frac{4\ln 2(\lambda-\lambda_{Tr1})^2}{w_{Tr1}^2}}}{w_{Tr1} \sqrt{\frac{\pi}{4\ln 2}}} + \frac{A_{Tr2} e^{-\frac{4\ln 2(\lambda-\lambda_{Tr2})^2}{w_{Tr2}^2}}}{w_{Tr2} \sqrt{\frac{\pi}{4\ln 2}}} \quad (9.26)$$

where BG is the background, λ is the wavelength. A_i , λ_i , and w_i ($i=X, Tr1, Tr2$) are the amplitude, peak center, and peak width of the band edge emission (X), the 1st type of trapped state emission (Tr1), and the 2nd type of trapped state emission (Tr2), respectively. The fitting results are shown in Figure S14 and the fitting parameters and errors were listed in Table 9.4.

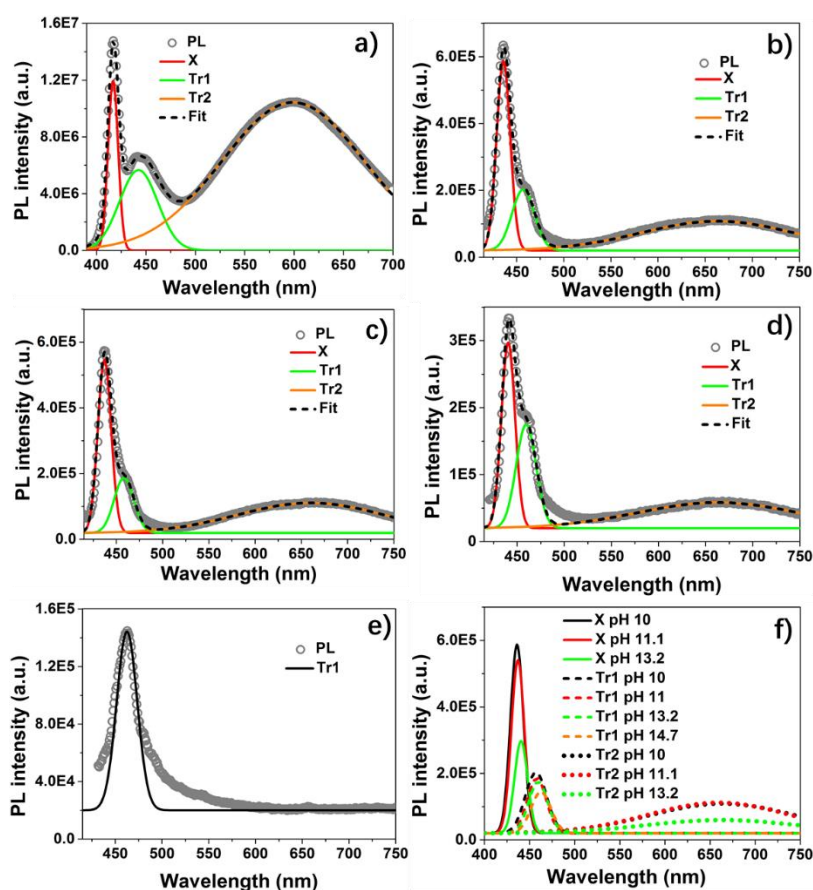


Figure 9.14. The static PL spectra and the fits of CdS NPLs in (a) hexane and aqueous solution with pH of (b) 10, (c) 11.1, (d) 13.2, and (e) 14.7. (f) The comparison of band edge emission

(solid lines), Tr1 emission (dashed lines), and Tr2 emission (dots) in aqueous solution with pH of 10 (black), 11.1 (red), 13.2 (green), and 14.7 (orange).

Table 9.4. Static PL spectra fitting parameters and errors

	Hexane	pH 10	pH 11.1	pH 13.2	pH 14.7
λ_X/nm	416.7 ± 0.1	436.0 ± 0.1	437.1 ± 0.1	440.5 ± 0.1	–
w_X/nm	10.3 ± 0.1	17.2 ± 0.2	17.2 ± 0.2	17.2 ± 0.2	–
$A_X/10000\text{nm}$	15400 ± 145	1820 ± 30	1690 ± 20	890 ± 5	–
$\lambda_{\text{Tr1}}/\text{nm}$	442.5 ± 0.2	457.2 ± 0.3	458.0 ± 0.4	459.5 ± 0.2	462.0 ± 0.1
w_{Tr1}/nm	38.7 ± 0.3	28.0 ± 0.4	25.0 ± 0.5	25.0 ± 0.3	29 ± 0.3
$A_{\text{Tr1}}/10000\text{nm}$	27474 ± 247	965 ± 15	790 ± 15	730 ± 10	660 ± 10
$\lambda_{\text{Tr2}}/\text{nm}$	599.0 ± 1.0	663.0 ± 3.0	663.0 ± 3.0	663.0 ± 3.0	–
w_{Tr2}/nm	143.5 ± 0.3	190 ± 0.3	185 ± 0.3	200 ± 0.4	–
A_{Tr2}/nm	187597 ± 318	3150 ± 100	3200 ± 100	1450 ± 50	–
BG/10000	2	2	2	2	2

We use static- and TR-PL spectroscopy to probe hole transfer (HT) process in CdS NRs and NPLs. CdS NRs used for PL study are characterized in Figure 9.15a (TEM image) and Figure 9.15b (absorption spectra). The static-PL spectra (Figure 9.15c&d) and TR-PL kinetics (Figure 9.15e) of CdS NPLs in hexane and aqueous solution with different pH are shown in Figure 9.15. The TR-PL decay kinetics of all emissions (both band-edge and trap state emissions) from CdS NPLs in hexane and aqueous solution with different pH are shown in Figure 9.15f (same set of results used in Figure 4c with different normalization). The half-life, $\tau_{1/2}$, of TR-PL decay kinetics of CdS NPLs and NRs were determined according to the initial

TR-PL intensity without hole acceptors, which is the initial TR-PL intensity of CdS NRs (NPLs) in chloroform (hexane) considering different NPL or NR samples absorbed the same number of photons at 390 nm pump. The half-life, $\tau_{1/2}$, of both CdS NRs and NPLs in different solutions are extracted from Figure 9.15e&f. They are listed in Table 9.5 with errors. The hole transfer rate, k_{HT} , from NRs or NPLs is estimated by: $k_{HT} = 1/\tau_{1/2}$, for charge recombination simulation in Appendix 9.6.

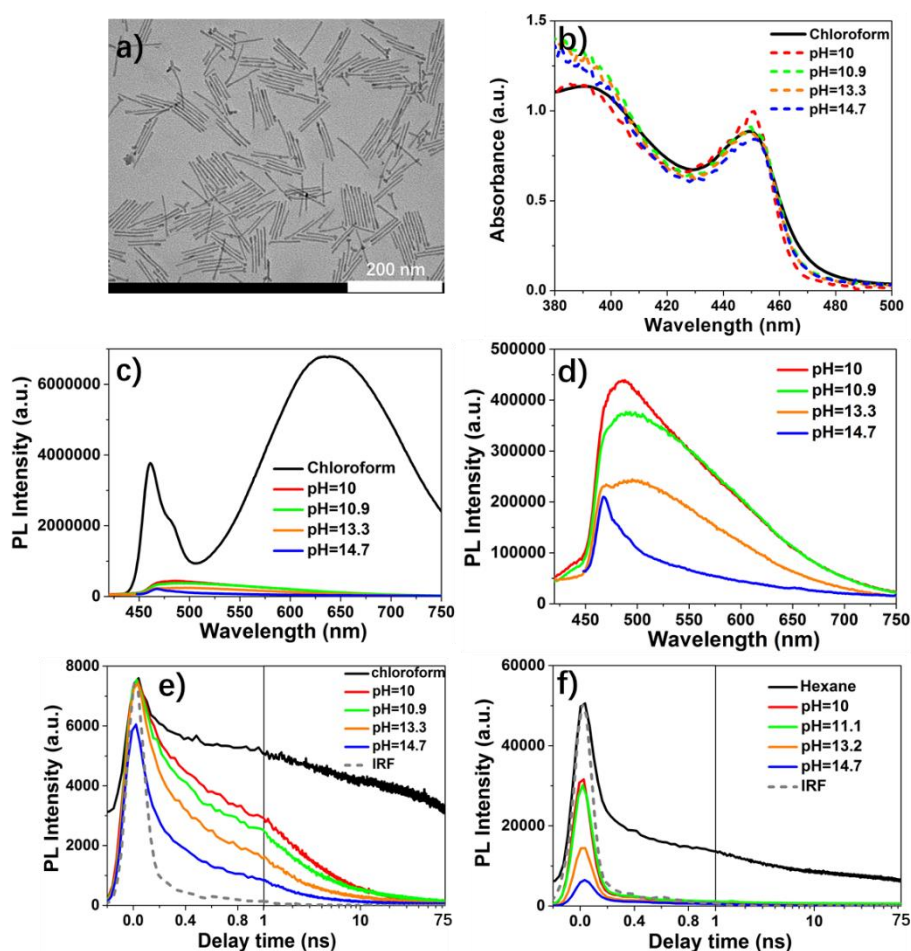


Figure 9.15. (a) The TEM image of CdS NRs in hexane. (b) The absorption spectra of CdS NRs in chloroform and aqueous solution with different pH. (c) The static PL spectra of CdS NRs in chloroform and KOH aqueous solution with different pH. (d) The pH dependent static-PL spectra of CdS NR in KOH aqueous solution. (e) The TR-PL decay kinetics (solid lines) with IRF (dashed line) of CdS NRs in chloroform and KOH aqueous solution with different

pH. (f) The TR-PL decay kinetics (solid lines) with IRF (dashed line) of CdS NPLs in hexane and KOH aqueous solution with different pH.

Table 9.5. The half-life of TR-PL decay of CdS NRs and NPLs.

	Chloroform	pH 10	pH 10.9	pH 13.3	pH 14.7
NRs $\tau_{1/2}/\text{ps}$	30500 ± 2300	585 ± 45	487 ± 15	273 ± 16	132 ± 16
	Hexane	pH 10	pH 11.1	pH 13.2	pH 14.7
NPLs $\tau_{1/2}/\text{ps}$	178 ± 15	72.8 ± 7.5	65.2 ± 8.0	$\ll \text{IRF}$	$\ll \text{IRF}$

To extract the pH dependent hole transfer rates from different trap states, we first collected the total emissions after 400 nm (X+Tr1+Tr2) at 390 nm pump using a 400 nm long-pass filter (Figure 9.15f). Then we used a 550 nm long-pass filter to selectively collect the Tr2 emissions as shown in Figure 9.4c lower panel. We subtracted the Tr2 kinetics from the total PL decay kinetics to obtain the X+Tr1 decay kinetics as shown in Figure 9.4c upper panel.

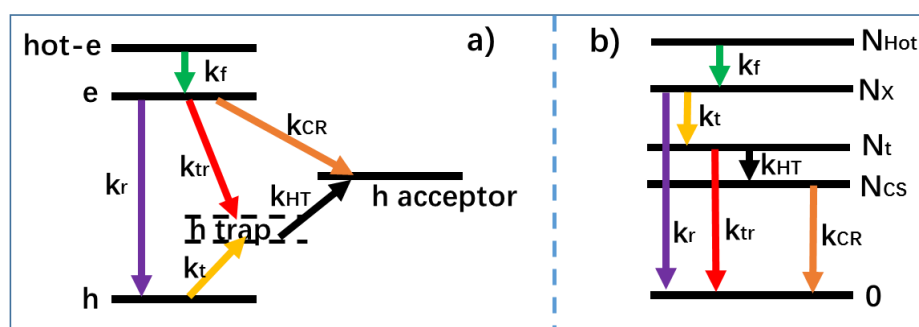


Figure 9.16. Carrier decay pathways in (a) single particle (electron and hole) representation and (b) state representation of CdS NPLs in aqueous solution at 400 nm excitation.

Similar to CdS NPL-Pt heterostructures, the carriers in CdS NPLs in aqueous solution undergo various relaxation, trapping, charge transfer and recombination processes (Figure 9.16a&b). Because the TR-PL signals of CdS NPLs are dominated by the three different emissions: band-edge emission (X), Tr1 emission, and Tr2 emission, we only need to consider three species that affect their concentration: hot-electrons (N_{hot}), band edge excitons (N_X , with both electron and hole in the band edge), and trapped excitons (N_t , band edge electron and a trapped hole). Most carrier pathways are the same as in CdS NPLs dispersed in hexane, CdS NPLs in aqueous solution have an additional decay pathway for trapped excitons (N_t): the hole transfer to hydroxyl anion or L-cysteine with a rate constant k_{HT} . We didn't consider the hole transfer directly from VB edge due to the ultrafast hole trapping time reported in similar NPLs (~ 30 fs),⁶² and CdS NRs (~ 780 fs).⁷⁰ For CdS NPLs in aqueous solution, N_X decays the same as in Eq. 9.9, and $N_{t,i}$ decays following:

$$\frac{dN_{t,i}}{dt} = k_{t,i}N_X - (k_{tr,i} + k_{HT,i})N_{t,i} \quad (9.27)$$

considering hole trapping is much faster than band-edge exciton radiative recombination ($k_t \gg k_r$) and trapped hole removal is also much faster than it recombines with CB electron ($k_{HT,i} \gg k_{tr,i}$), Eq. 9.27 gives:

$$N_{t,i}(t) = \frac{N_0 k_f}{k_f - k_t} \frac{k_{t,i}}{k_t} \left[\frac{k_f - k_t}{k_f} e^{-k_{HT,i}t} + \frac{k_t}{k_f} e^{-k_f t} - e^{-k_t t} \right] \quad (9.28)$$

For free CdS NPLs in hexane, there is no hole transfer, so the sum of band-edge emission and Tr1 emission TR-PL kinetics follows:

$$\begin{aligned}
\text{TR} - \text{PL}_{\text{hexane, X+Tr1}}(t) &= AN_X + \sum_i B_i N_{t,1i} \\
&= A \frac{N_0 k_f}{k_f - k_t} [e^{-k_t t} - e^{-k_f t}] + \sum_i B_i \frac{k_{t,1i}}{k_t} \frac{N_0 k_f}{k_f - k_t} \left[\frac{k_f - k_t}{k_f} e^{-k_{tr,1i} t} + \frac{k_t}{k_f} e^{-k_f t} - e^{-k_t t} \right] \\
&= A \frac{N_0 k_f}{k_f - k_t} [e^{-k_t t} - e^{-k_f t}] \\
&+ N_0 \frac{\text{Sum}_{\text{Bk}}}{k_t} \left[\sum_i \frac{B_i k_{t,1i}}{\text{Sum}_{\text{Bk}}} e^{-k_{tr,1i} t} + \frac{k_t}{k_f - k_t} e^{-k_f t} - \frac{k_f}{k_f - k_t} e^{-k_t t} \right] \quad (9.29)
\end{aligned}$$

$$\text{Sum}_{\text{Bk}} = \sum_i B_i k_{t,1i} \quad (9.30)$$

where $N_{t,1i}$ represents the i^{th} trapped exciton among the 1^{st} type of trapped excitons (Tr1) and its corresponding trapping rate, $k_{t,1i}$, follows: $\sum_i k_{t,1i} = k_{t,1}$. A and B_i represent the PL intensity weight for band edge emission and the i^{th} Tr1 state emission, respectively. Similarly, the Tr2 emission TR-PL kinetics follows:

$$\begin{aligned}
\text{TR} - \text{PL}_{\text{hexane, Tr2}}(t) &= \sum_i D_i N_{t,2i} = \sum_i D_i \frac{k_{t,2i}}{k_t} \frac{N_0 k_f}{k_f - k_t} \left[\frac{k_f - k_t}{k_f} e^{-k_{tr,2i} t} + \frac{k_t}{k_f} e^{-k_f t} - e^{-k_t t} \right] \\
&= N_0 \frac{\text{Sum}_{\text{Dk}}}{k_t} \left[\sum_i \frac{D_i k_{t,2i}}{\text{Sum}_{\text{Dk}}} e^{-k_{tr,2i} t} + \frac{k_t}{k_f - k_t} e^{-k_f t} - \frac{k_f}{k_f - k_t} e^{-k_t t} \right] \quad (9.31)
\end{aligned}$$

$$\text{Sum}_{\text{Dk}} = \sum_i D_i k_{t,2i} \quad (9.32)$$

where D_i represents the PL intensity weight of the i^{th} Tr2 state emission and $k_{t,2i}$ represents VB hole trapping rate to the i^{th} Tr2 state: $\sum_i k_{t,2i} = k_{t,2}$, and $\sum_i k_{t,1i} + \sum_i k_{t,2i} = k_t$.

For CdS NPLs in aqueous solution, the hole transfers to hydroxyl anion or L-cysteine so that its TR-PL kinetics of band-edge emission and Tr1 emission follows:

$$\begin{aligned}
\text{TR} - \text{PL}_{\text{aqueous, X+Tr1}}(t) &= A \frac{N_0 k_f}{k_f - k_t} [e^{-k_t t} - e^{-k_f t}] \\
&+ N_0 \frac{\text{Sum}_{\text{Bk}}}{k_t} \left[\sum_i \frac{B_i k_{t,1i}}{\text{Sum}_{\text{Bk}}} e^{-k_{HT,1i} t} + \frac{k_t}{k_f - k_t} e^{-k_f t} - \frac{k_f}{k_f - k_t} e^{-k_t t} \right] \quad (9.33)
\end{aligned}$$

where $k_{HT,1i}$ represents the rate constant of hole transfer from the i th trapped exciton state among Tr1 states. Similarly, the Tr2 emission TR-PL kinetics of CdS NPLs in aqueous solution follows:

$$TR - PL_{\text{aqueous, Tr2}}(t) = N_0 \frac{\text{Sum}_{Dk}}{k_t} \left[\sum_i \frac{D_i k_{t,2i}}{\text{Sum}_{Dk}} e^{-k_{HT,2i}t} + \frac{k_t}{k_f - k_t} e^{-k_f t} - \frac{k_f}{k_f - k_t} e^{-k_t t} \right] \quad (9.34)$$

where $k_{HT,2i}$ represents the rate constant of hole transfer from the i th Tr2 state. The trapping rates $k_{t,1}$ and $k_{t,2}$ both increase with pH due to hydroxyl anion reduces the ligand coverage (L-cysteine) on CdS NPLs in aqueous solution. However, Tr2 states, whose hole is considered trapped on the (001) surface, is affected by pH more than Tr1 states, whose hole is considered trapped on NPL edges. Thus, $k_{t,2}$ increases with pH faster than $k_{t,1}$ does, resulting in Sum_{Dk}/k_t increases with pH and Sum_{BK}/k_t decreases with pH. We also assumed the trapping rates, $k_{t,1i}$ ($k_{t,2i}$) for different Tr1 (or Tr2) states, increase with pH at the same ratio so that $\frac{B_i k_{t,1i}}{\text{Sum}_{BK}} \left(\frac{D_i k_{t,2i}}{\text{Sum}_{DK}} \right)$ is independent on pH.

According to Eq. 9.29 to 9.34, we fitted the TR-PL decay kinetics of CdS NPLs in hexane and aqueous solution by multi-exponential function convoluted with IRF (~ 110 ps):

$$\begin{aligned} TR - PL_{\text{hexane, X+Tr1}}(t) &= I_X \frac{\tau_t}{\tau_t - \tau_f} [e^{-\tau_t t} - e^{-\tau_f t}] \\ &+ I_{Tr1} B \left[X_1 e^{-\tau_{tr,1a} t} + X_2 e^{-\tau_{tr,1b} t} + \frac{\tau_f}{\tau_t - \tau_f} e^{-\tau_f t} - \frac{\tau_t}{\tau_t - \tau_f} e^{-\tau_t t} \right] \otimes \text{IRF} \quad (9.35) \end{aligned}$$

$$\begin{aligned} TR - PL_{\text{aqueous, X+Tr1}}(t) &= I_X \frac{\tau_t}{\tau_t - \tau_f} [e^{-\tau_t t} - e^{-\tau_f t}] + I_{Tr1} B \left[e^{-\tau_{HT,1} t} + \frac{\tau_f}{\tau_t - \tau_f} e^{-\tau_f t} - \frac{\tau_t}{\tau_t - \tau_f} e^{-\tau_t t} \right] \\ &\otimes \text{IRF} \quad (9.36) \end{aligned}$$

$$\begin{aligned} TR - PL_{\text{hexane, Tr2}}(t) &= I_{Tr2} D \left[Y_1 e^{-\tau_{tr,2a} t} + Y_2 e^{-\tau_{tr,2b} t} + \frac{\tau_f}{\tau_t - \tau_f} e^{-\tau_f t} - \frac{\tau_t}{\tau_t - \tau_f} e^{-\tau_t t} \right] \otimes \text{IRF} \quad (3.37) \end{aligned}$$

$$\begin{aligned} & \text{TR} - \text{PL}_{\text{aqueous, Tr2}}(t) \\ &= I_{\text{Tr2}} D \left[Y_1' e^{-\tau_{\text{HT},2a}t} + Y_2' e^{-\tau_{\text{HT},2a}t} + \frac{\tau_f}{\tau_t - \tau_f} e^{-\tau_f t} - \frac{\tau_t}{\tau_t - \tau_f} e^{-\tau_t t} \right] \\ & \otimes \text{IRF} \quad (3.38) \end{aligned}$$

where I_X , I_{Tr1} , and I_{Tr2} are the initial PL intensity at time zero of band-edge exciton, Tr1, and Tr2 emission, respectively, and they are pH independent. B and D correspond to $\text{Sum}_{\text{Bk}}/k_t$ and $\text{Sum}_{\text{Dk}}/k_t$, respectively. They are fixed as 1 for TR-PL decay of CdS NPLs in hexane, and B decreases while D increases with pH for CdS NPLs in aqueous solution. X_i , Y_i , and Y_i' ($i=1, 2$) are the different decay components. τ is the time constant of corresponding decay rate, k : $\tau = \frac{1}{k}$. τ_f is kept the same as in Table 9.3.

For the TR-PL of CdS NPLs with the highest pH (14.7), no band edge emission was observed as shown in Figure 9.14e, thus, we assumed the $\tau_t = \tau_f$ at pH of 14.7 considering ultrafast VB hole trapping after relaxation. Thus, Eq. 9.36 and 9.38 are approximated as:

$$\text{TR} - \text{PL}_{\text{pH } 14.7, X+\text{Tr1}}(t) = I_{\text{Tr1}} B [e^{-\tau_{\text{HT},1}t} - e^{-\tau_t t}] \otimes \text{IRF} \quad (9.39)$$

$$\text{TR} - \text{PL}_{\text{pH } 14.7, \text{Tr2}}(t) = I_{\text{Tr2}} D [Y_1' e^{-\tau_{\text{HT},2a}t} + Y_2' e^{-\tau_{\text{HT},2a}t} - e^{-\tau_t t}] \otimes \text{IRF} \quad (9.40)$$

The fitting parameters with errors are listed in Table 9.6. The hole transfer quantum yield (HT QY) for Tr1 and Tr2 are calculated considering the competition between trapped exciton recombination and HT:

$$\text{HT. Y. (Tr1)} = X_1 \frac{\tau_{\text{tr},1a}}{\tau_{\text{HT},1} + \tau_{\text{tr},1a}} + X_2 \frac{\tau_{\text{tr},1b}}{\tau_{\text{HT},1} + \tau_{\text{tr},1b}} \quad (9.41)$$

$$\text{HT. Y. (Tr2)} = Y_1 \frac{\tau_{\text{tr},2a}}{\tau_{\text{HT},2a} + \tau_{\text{tr},2a}} + Y_2 \frac{\tau_{\text{tr},2b}}{\tau_{\text{HT},2a} + \tau_{\text{tr},2b}} \quad (9.42)$$

Table 9.6. TR-PL decay kinetics fitting parameters and errors

	Hexane	pH 10	pH 11.1	pH 13.2	pH 14.7

B	1.00±0.01	1.00±0.02	0.98±0.04	0.81±0.04	0.62±0.05
D	1.00±0.01	1.02±0.02	1.04±0.04	1.86±0.23	2.53±0.20
τ_t /fs	200±20	125±20	112±15	29±10	10±10
$\tau_{tr,1a}$ /ps (X_1 /%)	272±5 (82.9±0.5)	–	–	–	–
$\tau_{tr,1b}$ /ps (X_2 /%)	2898±120 (17.1±0.1)	–	–	–	–
$\tau_{HT,1}$ /ps	–	76.9±5.5	64.5±4.2	60.6±2.3	54.1±1.8
HT. Y. (Tr1)/%	–	81.3±1.0	83.7±0.9	84.5±0.5	85.9±0.4
$\tau_{tr,2a}$ /ns (Y_1 /%)	1.90±0.32 (31.1±0.3)	–	–	–	–
$\tau_{tr,2b}$ /ns (Y_2 /%)	209±7 (68.9±0.2)	–	–	–	–
$\tau_{HT,2a}$ /ps (Y_1' /%)	–	37.7±1.7 (95.7±0.3)	27.3±0.8 (95.7±0.2)	22.7±2.3 (96.5±0.3)	7.03±0.20 (98.3±0.2)
$\tau_{HT,2b}$ /ns (Y_2' /%)	–	4.04±0.83 (4.3±0.2)	3.63±0.35 (4.3±0.2)	2.79±0.22 (3.5±0.5)	2.37±0.10 (1.7±0.4)
HT. Y. (Tr2)/%	–	99.4±0.6	99.5±0.5	99.6±0.4	99.9±0.1

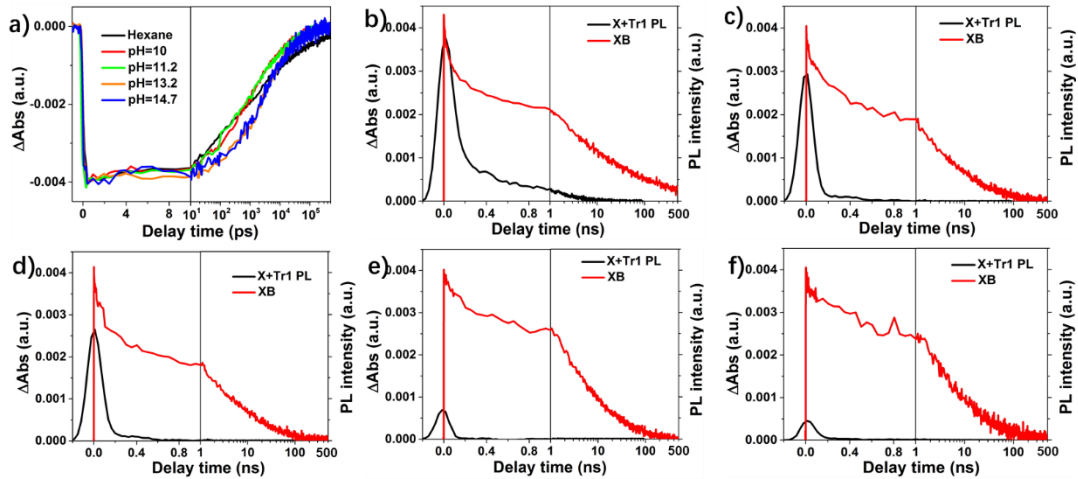


Figure 9.17. (a) The comparison of exciton bleach (XB) kinetics of free CdS NPLs in hexane and aqueous solution with different pH. The comparison of XB kinetics and TR-PL decay kinetics (400 to 550 nm) of free CdS NPLs in (b) hexane and aqueous solution with pH of (c) 10.0, (d) 11.0, (e) 13.2, and (f) 14.7. X and Tr1 represent the band-edge exciton and the first trap state, respectively.

To distinguish HT to L-cysteine and to OH^- at different pH, we fitted the pH dependent H_2 generation IQE and apparent HT rate for Tr2 ($1/\tau_{\text{HT},2}$) according to the proposal in the main text. To remove the hole, the OH^- has to adsorb on NPL surface first, and we assume the adsorption of OH^- on NPL surfaces following the Langmuir adsorption isotherm as reported in similar QDs with slight modifications for competitive adsorption between OH^- and L-cysteine:²⁸⁸⁻²⁸⁹

$$\frac{m_{\text{OH}}}{N_{\text{total}}} = \theta_{\text{OH}} = \theta_{\text{max}} \frac{K_{\text{OH}}[\text{OH}]}{1 + K_{\text{OH}}[\text{OH}] + K_{\text{C}}[\text{C}]} \quad (9.43)$$

$$\frac{m_{\text{C}}}{N_{\text{total}}} = \theta_{\text{C}} = \theta_{\text{max}} \frac{K_{\text{C}}[\text{C}]}{1 + K_{\text{OH}}[\text{OH}] + K_{\text{C}}[\text{C}]} \quad (9.44)$$

where θ_{OH} and θ_{C} are the mean fractional surface coverages of OH^- and L-cysteine on NPLs, respectively. m_{OH} and m_{C} are the average number of OH^- and cysteine per NPL, respectively.

N_{total} is the total number of adsorption sites available per NPL; θ_{max} the maximum fractional surface coverage of hole acceptors on NPLs. K_{OH} and K_{C} are the binding constants of OH^- and cysteine, respectively. $[\text{OH}]$ and $[\text{C}]$ are the concentrations of free (unbound) OH^- and cysteine in NPL aqueous solution at adsorption equilibrium, respectively. $[\text{OH}]$ can be approximated by pH, and all cysteines in NPL solution come from those covered on NPL surfaces after ligand exchange. Therefore, m_{OH} and m_{C} can be represented by:

$$m_{\text{OH}} = N_{\text{max}} \frac{K_{\text{OH}}[\text{OH}]}{1 + K_{\text{OH}}[\text{OH}] + K_{\text{C}}[\text{C}]} \quad (9.45)$$

$$m_{\text{C}} = N_{\text{max}} \frac{K_{\text{C}}[\text{C}]}{1 + K_{\text{OH}}[\text{OH}] + K_{\text{C}}[\text{C}]} \quad (9.46)$$

where $N_{\text{max}} = N_{\text{total}}\theta_{\text{max}}$ is the maximum number of bound hole acceptors on the NPL surface.

At any pH, the H_2 generation IQE then can be represented as:

$$\frac{m_{\text{C}}\tau_{\text{OH}}}{m_{\text{C}}\tau_{\text{OH}} + m_{\text{OH}}\tau_{\text{C}}}\eta + \frac{m_{\text{OH}}\tau_{\text{C}}}{m_{\text{C}}\tau_{\text{OH}} + m_{\text{OH}}\tau_{\text{C}}} = \text{IQE} \quad (9.47)$$

where τ_{OH} and τ_{C} are hole transfer rate per molecular acceptor for HT to OH^- and to L-cysteine, respectively. η is the percentage of transferred holes to L-cysteine that don't recombine so that contribute to H_2 generation:

$$\eta = \frac{\tau_{\text{HR}}}{\tau_{\text{turnover}} + \tau_{\text{HR}}} \quad (9.48)$$

where τ_{turnover} and τ_{HR} are catalytic H_2 turnover time on Pt particles and recombination time of transferred hole on L-cysteine, respectively. We also attribute the apparent HT rate for Tr2 measured by TR-PL ($1/\tau_{\text{HT},2}$) to the sum of rates of HT to L-cysteine and to OH^- :

$$\frac{1}{\tau_{\text{HT},2}} = m_{\text{C}}\frac{1}{\tau_{\text{C}}} + m_{\text{OH}}\frac{1}{\tau_{\text{OH}}} \quad (9.49)$$

Substituting Eq. 9.45&9.46 to Eq. 9.47&9.49 gives:

$$\frac{\eta\tau_{\text{OH}}K_{\text{C}}[\text{C}] + K_{\text{OH}}[\text{OH}]\tau_{\text{C}}}{\tau_{\text{OH}}K_{\text{C}}[\text{C}] + K_{\text{OH}}[\text{OH}]\tau_{\text{C}}} = \text{IQE} \quad (9.50)$$

$$\frac{1}{\tau_{\text{HT},2}} = N_{\text{max}} \left[\frac{K_{\text{C}}[\text{C}]}{(1 + K_{\text{OH}}[\text{OH}] + K_{\text{C}}[\text{C}])\tau_{\text{C}}} + \frac{K_{\text{OH}}[\text{OH}]}{(1 + K_{\text{OH}}[\text{OH}] + K_{\text{C}}[\text{C}])\tau_{\text{OH}}} \right] \quad (9.51)$$

We approximate $\tau_{\text{HT},2}$ to $\tau_{\text{HT},2a}$ as listed in Table 9.6, and then fit IQE and $1/\tau_{\text{HT},2}$ at different pH using Eq. 9.50 and 9.51, respectively, with τ_{OH} , τ_{C} , K_{OH} , η , N_{max} , and $K_{\text{C}}[\text{C}]$ are the fitting parameters. The best fits are shown as black dots in Figure 9.1f and dashed lines in 9.4d for pH dependent IQE and $1/\tau_{\text{HT},2}$, respectively. They give τ_{OH} as 700 ± 5 ps, τ_{C} as 1.19 ± 0.03 ns, K_{OH} as $1.31 \pm 0.15 \text{ M}^{-1}$, η as $41.9 \pm 0.8\%$, N_{max} as 115 ± 2 , and $K_{\text{C}}[\text{C}]$ as 0.51 ± 0.08 , 0.50 ± 0.05 , 0.36 ± 0.04 , and 0.09 ± 0.03 for pH at 10.0, 11.2, 13.2, and 14.7, respectively. Taking the τ_{turover} as 10 ms reported in literature,²⁵⁹ the τ_{HR} is estimated using Eq. 9.48 as 14.0 ± 0.3 ms. The m_{OH} and m_{C} as a function of pH are plotted in Figure 9.18, which clearly shows L-cysteine dominates at low pH (<13) while OH⁻ starts to replace L-cysteine at pH>13 and finally dominates at pH>14.

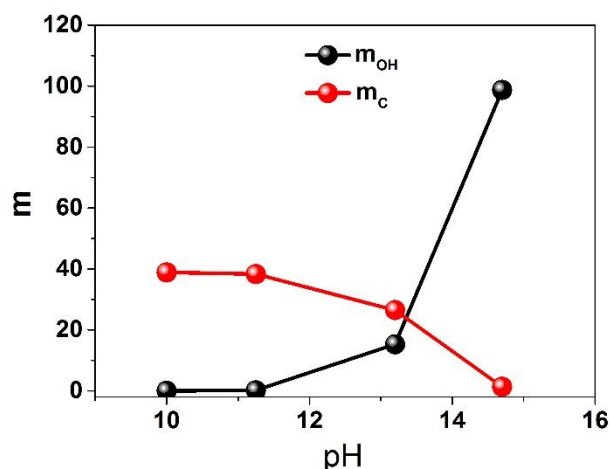


Figure 9.18. The average number of OH⁻ (m_{OH}) and L-cysteine (m_{C}) per NPL as a function of pH.

Appendix 9.5

Charge recombination in CdS NPL- and NR-methyl viologen (MV^{2+}) complexes

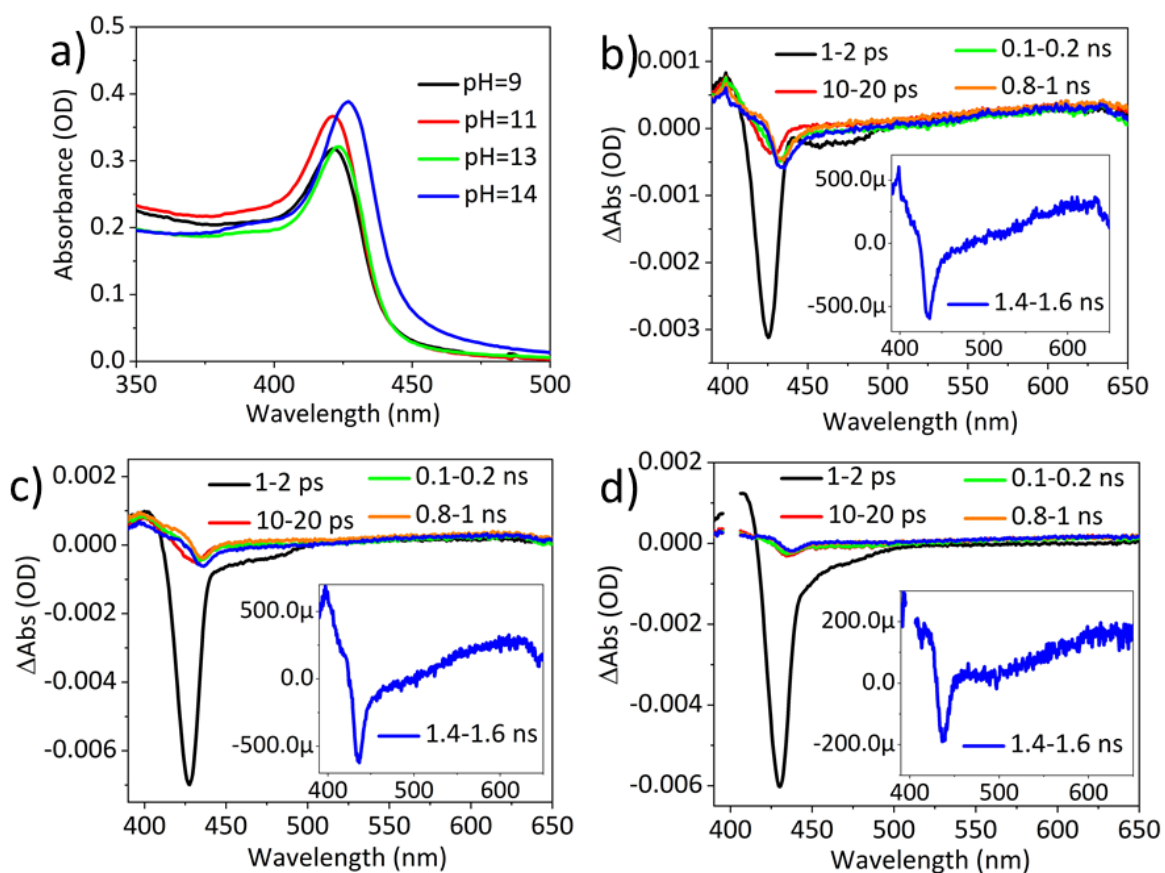


Figure 9.19. (a) Absorption of CdS NPL- MV^{2+} complexes aqueous solution with different pH. The TA spectra of CdS NPL- MV^{2+} complexes aqueous solution with (b) pH=11, (c) pH=13, and (d) pH=14 at indicated delay times. The insets show the same spectra at 1.4-1.6 ns.

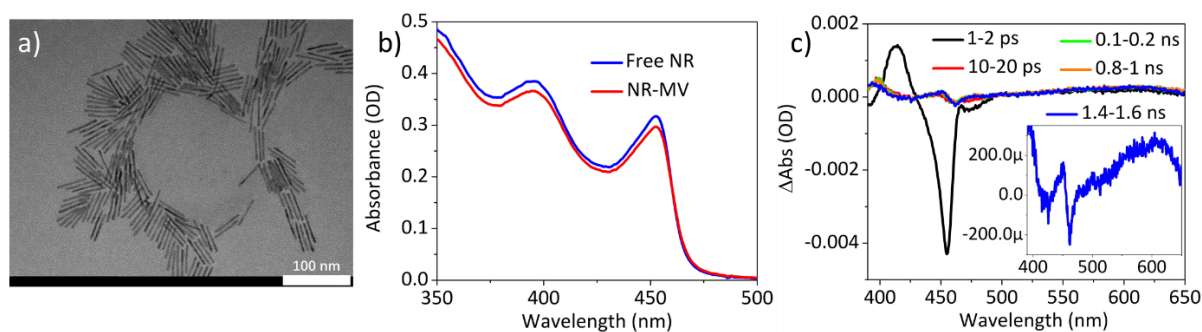


Figure 9.20. (a) TEM image of CdS NRs used for charge recombination study. (b) Absorption spectra of free CdS NRs and CdS NR-MV²⁺ complexes in aqueous solution with pH of 9. (c) TA spectra of CdS NR-MV²⁺ complexes in aqueous solution with pH of 9 at indicated delay times. Inset shows the same spectra at 1.4-1.6 ns.

Appendix 9.6

Simulation of charge recombination in CdS NPL-Pt heterostructures

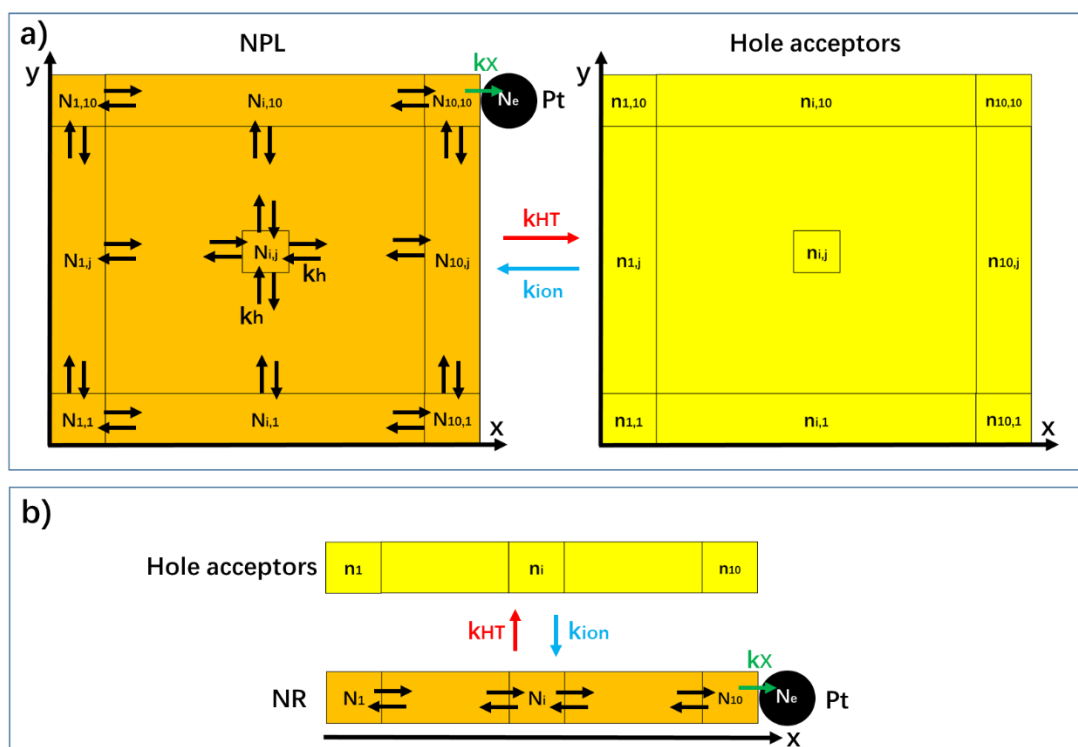


Figure 9.21. Scheme of charge recombination process in (a) CdS NPL-Pt and (b) CdS NR-Pt heterostructures with presence of hole acceptors on NPL and NR surfaces.

We consider the charge recombination between a trapped hole in CdS NPLs and a transferred electron on one Pt particle. This process is dominated by trapped hole diffusion to Pt, similar to CdS NRs.²⁸⁴ In CdS NPLs, the probability density of trapped hole follows the 2D diffusion equation:

$$\frac{dN(x, y, t)}{dt} = D \left(\frac{\partial^2 N}{\partial x^2} + \frac{\partial^2 N}{\partial y^2} \right) \quad (9.52)$$

where $N(x, y, t)$ is the trapped hole probability density in NPL at position (x, y) at time t . D is the diffusion constant for both x and y direction due to zinc-blend NPLs are isotropic along basal plane. In the presence of hole acceptors (L-cysteine at $\text{pH} < 13$) on NPL basal plane, we

propose the trapped hole in NPLs can transfer to L-cysteine at the same position with rate constant k_{HT} and be ionized back to NPLs with rate constant k_{ion} many times before it diffuses to electron at Pt tip. We assume NPLs are fully covered with hole acceptors so that Eq. 9.52 becomes:

$$\frac{dN(x, y, t)}{dt} = D \left(\frac{\partial^2 N}{\partial x^2} + \frac{\partial^2 N}{\partial y^2} \right) - k_{HT}N(x, y, t) + k_{ion}n(x, y, t) \quad (9.53)$$

where $n(x, y, t)$ represents the transferred hole on L-cysteine at position (x, y) at time t :

$$\frac{dn(x, y, t)}{dt} = k_{HT}N(x, y, t) - k_{ion}n(x, y, t) \quad (9.54)$$

We also assume the transferred electron is on the Pt at the corner of a NPL with a length of L and a width of W . So, when the hole diffuses to the corner, in addition to hole transfer and ionization processes, it recombines with electron on Pt with a rate constant of k_X :

$$\frac{dN(L, W, t)}{dt} = D \left(\frac{\partial^2 N}{\partial x^2} + \frac{\partial^2 N}{\partial y^2} \right) \Big|_{x=L, y=W} - (k_{HT} + k_X)N(L, W, t) + k_{ion}n(L, W, t) \quad (9.55)$$

The survival probability of electron on Pt, N_e , only decreases by recombination at NPL-Pt interface:

$$\frac{dN_e}{dt} = -k_X N(L, W, t) \quad (9.56)$$

We solve Eq. 9.56 numerically to simulate charge recombination kinetics (N_e as a function of time) by dividing NPL into several square segments as shown in Figure 9.21a under the following approximation for derivatives:⁶⁸

$$\begin{aligned} D \frac{\partial^2 N}{\partial x^2} &= D \lim_{\Delta L \rightarrow 0} \frac{\frac{N(x + \Delta L, y, t) - N(x, y, t)}{\Delta L} - \frac{N(x, y, t) - N(x - \Delta L, y, t)}{\Delta L}}{\Delta L} \\ &\cong D \frac{N(x + \Delta L, y, t) + N(x - \Delta L, y, t) - 2N(x, y, t)}{\Delta L^2} \quad (9.57) \end{aligned}$$

$$D \frac{\partial^2 N}{\partial y^2} = D \lim_{\Delta L \rightarrow 0} \frac{\frac{N(x, y + \Delta L, t) - N(x, y, t)}{\Delta L} - \frac{N(x, y, t) - N(x, y - \Delta L, t)}{\Delta L}}{\Delta L}$$

$$\cong D \frac{N(x, y + \Delta L, t) + N(x, y - \Delta L, t) - 2N(x, y, t)}{\Delta L^2} \quad (9.58)$$

The segment length, ΔL , is set to exciton Bohr radius of bulk CdS as 5.5 nm.¹⁰² We assume square shaped NPL with length of ~55 nm according to the TEM images of CdS NPLs shown in Figure 9.1 and 9.7. Then, the NPL is divided into 10×10 segments with the hole probability density in each segment is $N_{i,j}$ (i, j from 1 to 10). The diffusion equations for segments of NPLs become:

$$\frac{dN_{i,j}(t)}{dt} = k_h \left(N_{i-1,j}(t) + N_{i+1,j}(t) + N_{i,j-1}(t) + N_{i,j+1}(t) - 4N_{i,j}(t) \right) - k_{HT} N_{i,j}(t)$$

$$+ k_{ion} n_{i,j}(t), \text{ when } i, j \text{ from } 2 \text{ to } 9 \quad (9.59)$$

$$\frac{dN_{1,1}(t)}{dt} = k_h \left(N_{1,2}(t) + N_{2,1}(t) - 2N_{1,1}(t) \right) - k_{HT} N_{1,1}(t) + k_{ion} n_{1,1}(t) \quad (9.60)$$

$$\frac{dN_{1,j}(t)}{dt} = k_h \left(N_{1,j+1}(t) + N_{1,j-1}(t) + N_{2,j}(t) - 3N_{1,1}(t) \right) - k_{HT} N_{1,j}(t)$$

$$+ k_{ion} n_{1,j}(t), \text{ when } j \text{ from } 2 \text{ to } 9 \quad (9.61)$$

$$\frac{dN_{1,10}(t)}{dt} = k_h \left(N_{1,9}(t) + N_{2,10}(t) - 2N_{1,10}(t) \right) - k_{HT} N_{1,10}(t) + k_{ion} n_{1,10}(t) \quad (9.62)$$

$$\frac{dN_{i,1}(t)}{dt} = k_h \left(N_{i-1,1}(t) + N_{i+1,1}(t) + N_{i,2}(t) - 3N_{i,1}(t) \right) - k_{HT} N_{i,1}(t)$$

$$+ k_{ion} n_{i,1}(t), \text{ when } i \text{ from } 2 \text{ to } 9 \quad (9.63)$$

$$\frac{dN_{i,10}(t)}{dt} = k_h \left(N_{i-1,1}(t) + N_{i+1,1}(t) + N_{i,9}(t) - 3N_{i,10}(t) \right) - k_{HT} N_{i,10}(t)$$

$$+ k_{ion} n_{i,10}(t), \text{ when } i \text{ from } 2 \text{ to } 9 \quad (9.64)$$

$$\frac{dN_{10,1}(t)}{dt} = k_h \left(N_{9,1}(t) + N_{10,2}(t) - 2N_{10,1}(t) \right) - k_{HT} N_{10,1}(t) + k_{ion} n_{10,1}(t) \quad (9.65)$$

$$\begin{aligned} \frac{dN_{10,j}(t)}{dt} = & k_h(N_{10,j+1}(t) + N_{10,j-1}(t) + N_{9,j}(t) - 3N_{10,j}(t)) - k_{HT}N_{10,j}(t) \\ & + k_{ion}n_{10,j}(t), \text{ when } j \text{ from } 2 \text{ to } 9 \quad (9.66) \end{aligned}$$

$$\begin{aligned} \frac{dN_{10,10}(t)}{dt} = & k_h(N_{9,10}(t) + N_{10,9}(t) - 2N_{10,10}(t)) - (k_{HT} + k_X)N_{10,10}(t) \\ & + k_{ion}n_{10,10}(t) \quad (9.67) \end{aligned}$$

where $k_h=D/\Delta L^2$ is the 2D diffusion rate constant. The diffusion equations for hole probability density on hole acceptors become:

$$\frac{dn_{i,j}(t)}{dt} = k_{HT}n_{i,j}(t) - k_{ion}n_{i,j}(t), \text{ when } i, j \text{ from } 1 \text{ to } 10 \quad (9.68)$$

and the survival probability of electron on Pt follows:

$$\frac{dN_e}{dt} = -k_X N_{10,10}(t) \quad (9.69)$$

To unveil how morphology (2D vs 1D) affects charge recombination process, we consider NR-Pt heterostructures with Pt at the NR tip and NR has the same length as NPL. Similarly, we solve the 1D diffusion equations for trapped holes in NRs numerically by dividing NR into 10 segments as shown in Figure 9.21b. We assume all the segments of NR are covered with hole acceptors, and the hole diffusion, transfer, and ionization rates of NRs are the same as those of NPLs. The hole also recombines with electron at NR tip with a rate constant of k_X . The hole probability density of each segments in NR and hole acceptors are N_i and n_i (i from 1 to 10), respectively. The probability density equations are:

$$\begin{aligned} \frac{dN_i(t)}{dt} = & k_h[N_{i-1}(t) + N_{i+1}(t) - 2N_i(t)] - k_{HT}N_i(t) \\ & + k_{ion}n_i(t), \text{ when } i \text{ from } 2 \text{ to } 9 \quad (9.70) \end{aligned}$$

$$\frac{dN_1(t)}{dt} = k_h[N_2(t) - N_1(t)] - k_{HT}N_1(t) + k_{ion}n_1(t) \quad (9.71)$$

$$\frac{dN_{10}(t)}{dt} = k_h[N_9(t) - N_{10}(t)] - (k_{HT} + k_X)N_{10}(t) + k_{ion}n_{10}(t) \quad (9.72)$$

$$\frac{dn_i(t)}{dt} = k_{HT}N_i(t) - k_{ion}n_i(t), \text{ when } i \text{ from } 1 \text{ to } 10 \quad (9.73)$$

The survival probability of electron on Pt tip on 1D NRs is:

$$\frac{dN_e}{dt} = -k_X N_{10}(t) \quad (9.74)$$

In both 1D and 2D cases, we assume that the initial hole distribution are random so that the probability density on each segments of NPL and NR are the same: $N_{i,j}(0)=1/100=0.01$ (i, j from 1 to 10), $N_i(0)=1/10=0.1$ (i from 1 to 10). The hole transfer hasn't started at time zero so that $n_{i,j}(0)=0$ (i, j from 1 to 10), $n_i(0)=0$ (i from 1 to 10), and the electron survival probability is 1 at time zero: $N_e(0)=1$. k_{HT} , k_{ion} , and k_X are set as the reciprocal of half-life of TR-PL decay of NPL at pH=10 (see Appendix 9.4, Table 9.5), XB kinetics of NPL at pH=10 (Figure 9.17a&c), and XB kinetics of NPL in hexane (Figure 9.3c), respectively. We compare the charge recombination kinetics (N_e as a function of time) for 2D and 1D morphologies in both slow ($k_h/k_X \ll 1$) and fast ($k_h/k_X \gg 1$) trapped hole diffusion conditions in Figure 9.22. The simulation parameters and the half-life ($\tau_{1/2}$) of $N_e(t)$ decay for 2D and 1D morphologies are listed in Table 9.7.

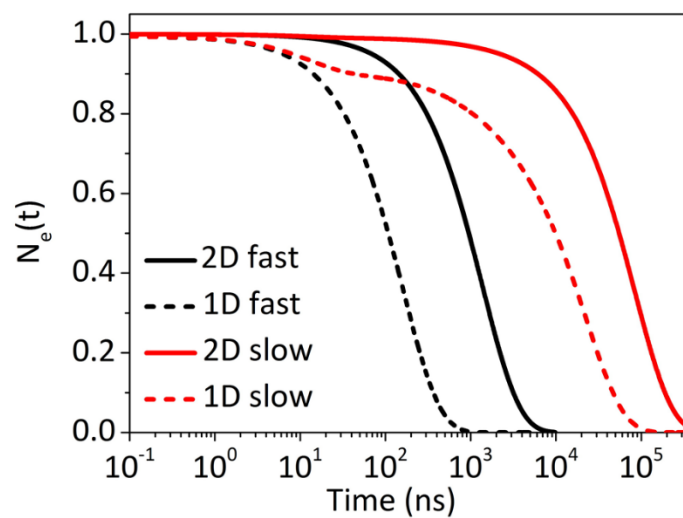


Figure 9.22. The survival probability of electron on Pt tip of 2D NPL-Pt (solid lines) and 1D NR-Pt (dashed lines) heterostructures under fast ($k_h/k_X \gg 1$, black) and slow ($k_h/k_X \ll 1$, red) trapped hole diffusion conditions.

Table 9.7. The simulation parameters and half-life of $N_e(t)$ for 2D and 1D morphologies

	Fast diffusion	Slow diffusion
k_h/ns^{-1}	10.0	0.02
k_{HT}/ns^{-1}	13.7	
k_{ion}/ns^{-1}	1.20	
k_X/ns^{-1}	1.00	
$\tau_{1/2}$ of N_e (2D)/ns	954.1 ± 0.1	55000 ± 5
$\tau_{1/2}$ of N_e (1D)/ns	107.8 ± 0.1	9905 ± 5

Chapter 10. Efficient Charge Separation in Two-Dimensional CsPbBr₃ Perovskite Nanoplatelets

Reproduced with permission from *J. Phys. Chem. Lett.* **2019**, *10*, 566. Copyright 2019 American Chemical Society.

10.1. Introduction

Perovskite semiconductors, including hybrid (MAPbX₃, where MA=methyl ammonium, X=Cl, Br, I) and all-inorganic (CsPbX₃, X=Cl, Br, I) perovskites, are a new class of materials with great potentials for optoelectrical applications.²⁹⁰⁻²⁹³ Their high luminescent quantum yield, long carrier lifetime, and long carrier diffusion length have led to impressive performances for light emitting diodes,²⁹⁴⁻³⁰² lasing,³⁰³⁻³¹⁶ and low-cost photovoltaics³¹⁷⁻³¹⁹ (with solar-to-electricity conversion efficiency exceeding 20%³²⁰⁻³²⁹). Two-dimensional (2D) CsPbX₃ (X=Cl, Br, I) colloidal nanoplatelets (NPLs) were introduced into the perovskite family recently with tunable emission from 2.0 to 3.0 eV.^{52, 330-333} These colloidal NPLs can be synthesized in ambient condition at room temperature,^{52, 330, 332} and their 2D morphology gives rise to unique excitonic features, such as large exciton binding energy,⁵⁴ sharp absorption and emission peaks,^{52, 330, 332, 334-335} and large absorption coefficient.³³⁶ These properties make perovskite NPLs even more promising materials for photocatalysis and optoelectrical applications. However, the properties of charge separation and recombination in these 2D NPLs, which are the key processes during photocatalytic and photovoltaic reactions, remain unclear. On the one hand, the 2D morphology of NPLs is reported to effectively extend the charge-separated state compared to the 0D and 1D nanostructures⁴³ and enhance the solar-to-

H₂ conversion efficiency.⁴²⁻⁴⁴ On the other hand, the large exciton binding energy due to dielectric confinement effect in 2D morphology^{54, 337} is not favorable for exciton dissociation and charge separation. Moreover, charge separation/recombination properties are determined by the band-edge 2D exciton behaviors in these NPLs. Therefore, systematic studies on exciton and charge transfer dynamics in CsPbBr₃ NPLs are important to both fundamental understanding of 2D excitons in these 2D perovskite materials and rational improvements of their photocatalysis and optoelectrical performances.

In this chapter, we report a systematic study of exciton and interfacial charge transfer dynamics of CsPbBr₃ colloidal NPLs *via* transient absorption (TA) spectroscopy. The NPL absorption features before and after excitation were analyzed to reveal the binding energy of excitons (~260 meV). The origin of band edge exciton bleach (XB) signal was examined. The dissociation of excitons by selective interfacial electron transfer (ET) and hole transfer (HT) from the NPL to adsorbed benzoquinone (BQ) and phenothiazine (PTZ), respectively, was studied as a function of acceptor concentration to reveal the time constants for the charge separation and recombination processes.

10.2. Results and Discussion

10.2.1. Sample characterization

CsPbBr₃ NPLs were synthesized following reported procedures with slight modifications.⁵² TEM image of CsPbBr₃ NPLs (Figure 10.1a) shows rectangular morphology with a lateral size of $(26.7 \pm 6.4) \times (8.1 \pm 1.6)$ nm². The CsPbBr₃ NPLs dispersed in toluene were used for all measurements in this work. The static absorption (Abs, blue dots in Figure 10.1b) spectrum of NPLs can be fit according to the well-established model for quantum wells (QWs) and consists of the exciton and continuous band transitions (see Appendix 10.2).^{27, 54, 146, 250-251} The sharp absorption peak at ~2.76 eV (~448 nm) is assigned to the band-edge excitonic

transition (X) of 5 monolayer CsPbBr₃ NPLs with a thickness of ~3 nm,⁵² and the sharp photoluminescence (PL, blue solid line in Figure 10.1b) peak at ~2.70 eV (~459 nm) is attributed to band edge emission.^{52, 54} The full-width-at-the-half-maximum of PL peak is 90±2 meV, which is 1.4 fold narrower than CsPbBr₃ QDs (~130 meV),²⁸⁹ indicating more uniform quantum confinement along NPL thickness direction. From the peak position and the onset of the continuous absorption band (Con, from 2.9 to 3.2 eV), the exciton binding energy is determined to be 260±10 meV, which is much larger than that in CsPbBr₃ QDs (~40 meV),³³⁴ and bulk perovskites (~10 meV).^{243, 293} This binding energy value in CsPbBr₃ NPLs is consistent with recently reported (C₆H₅(CH₂)₂NH₃)₂PbI₄ nanosheets (200–260 meV),³³⁷ but is about 2 folds larger than previous reported CsPbBr₃ NPLs (~120 meV).⁵⁴ The band edge positions (vs. vacuum) of the conduction band (CB) and valence band (VB) are estimated as -3.59 eV and -6.34 eV, respectively, which differ from bulk values due mainly to quantum confinement effect (see Appendix 10.1). With the reported reduction potential of BQ at -4.3 eV,³³⁸ and the reported oxidation potential of PTZ at -5.5 eV,¹⁸³ electrons and holes can be selectively transferred from NPLs to BQ and PTZ, respectively (Figure 10.1c).

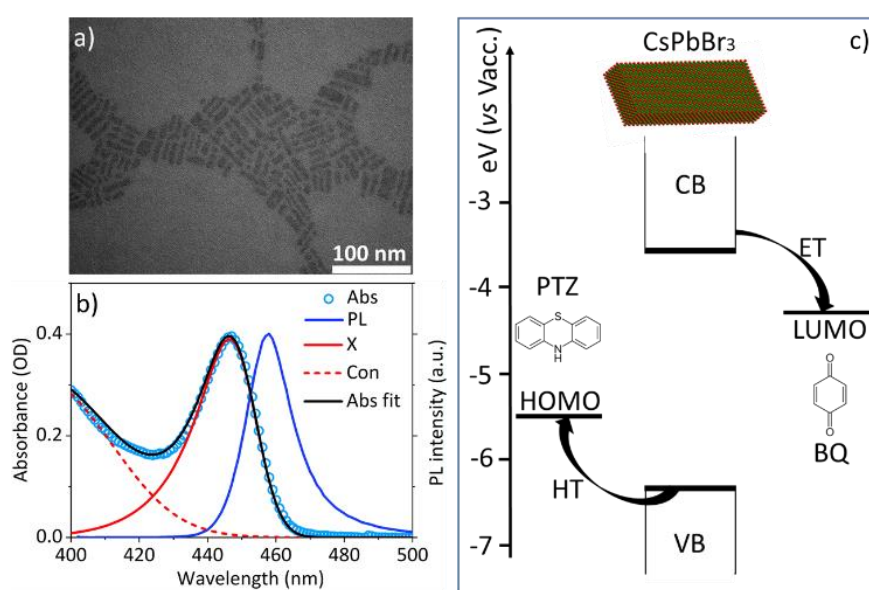


Figure 10.1. CsPbBr₃ NPLs. (a) The TEM image of CsPbBr₃ NPLs. (b) The photoluminescence (solid blue line) and absorption (blue dots) spectra of CsPbBr₃ NPLs. Black solid line is the fit of the absorption spectrum. (c) The scheme of energy levels of CsPbBr₃ NPLs, the oxidation potential (HOMO) of PTZ, the reduction potential (LUMO) of BQ, and the interfacial ET and HT pathways from NPL to molecular acceptors (BQ or PTZ).

10.2.2. Spectroscopy of CsPbBr₃ NPLs

We first investigated the exciton dynamics in CsPbBr₃ NPLs by TA spectroscopy. All TA measurements in this work were conducted at room temperature with low pump fluence ($\sim 5 \mu\text{J}/\text{cm}^2$) so that multi-exciton generation is negligible and only single exciton dynamics is considered. The TA spectra of free NPLs (Figure 10.2a) show a negative exciton bleach (XB) signal at ~ 448 nm, which can be attributed to blocking of the band edge transitions by the presence of a photogenerated band edge exciton. Comparison of normalized TA spectra at all delay times (Figure 10.4 in Appendix 10.2) shows that the spectral shape is independent of delay time from 1 ps - 1.2 ns, consistent with the presence of only long-lived single exciton states. The spectra also show a broad photo-induced absorption (PA) signal from 480-680 nm (inset of Figure 10.2a), similar to many other low dimensional semiconductor nanocrystals.^{62, 76, 110, 183, 289} The TA spectra (Figure 10.2a) can be fit to the difference between the absorption of the excited NPL (Abs*) and ground state (Abs), accounting for exciton-state filling, exciton-exciton interaction, and band gap renormalization (BGR), similar to bulk perovskites,²⁴³ and other 2D NPLs.^{27, 146} State filling of continuous band is ignored at the low excitation conditions in which only the single exciton state is occupied. Abs (solid lines) is obtained by fitting the ground state spectrum as shown in Figure 10.1b. Compared to Abs, Abs* (dashed lines, Figure 10.2b) has a lower exciton peak intensity due to the state filling of band edge exciton state, broadened peak width, and red-shifted peak position due to exciton-exciton interaction.²⁷ The

continuous feature in the excited NPLs (Con*) is shifted to lower energy due to the BGR.^{224, 243} (See Appendix 10.2 for details). The best fits (black solid lines in Figure 10.2a) give an exciton shift of 10 ± 2 meV, similar to CsPbBr₃ QDs,³³⁵ but smaller than that in CdSe NPLs (~ 20 meV).²⁷ This shift is a net result of exciton-exciton interactions (Δ_{XX}), which contains: (1) red shift due to exciton-exciton Coulomb attraction, also known as the bi-exciton binding energy,³³⁹⁻³⁴⁰ and (2) blue shift due to Coulomb screening effect, which reduces the exciton binding energy at a higher exciton density.²²⁴

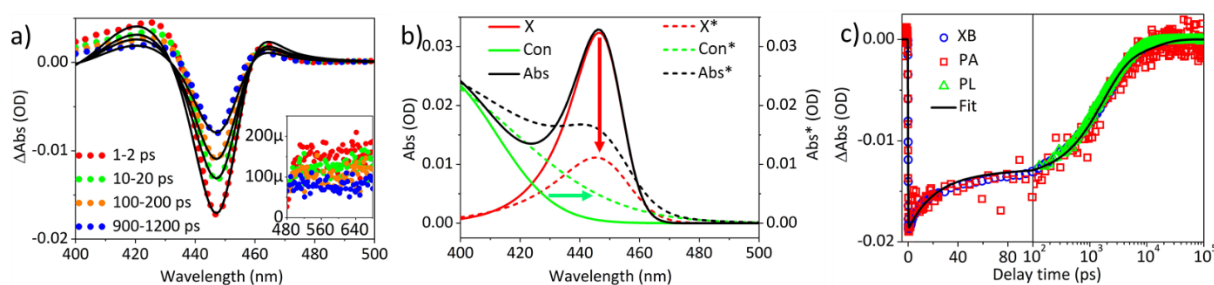


Figure 10.2. TA spectra and kinetics of free CsPbBr₃ NPLs. (a) TA spectra at indicated delay times (dots) and their fits (solid black lines). Inset: the expanded view of the TA spectra at low energy range (480–680 nm). (b) Fits of absorption spectra before pump (Abs, solid lines) and after pump (Abs*, dashed lines) that contribute to TA spectra. The arrows show the state-filling (red) and BGR (green) effects on absorption after pump. (c) The comparison of XB, PA, and PL decay kinetics. The solid line is the fit.

The XB (~ 448 nm), PA (500–650 nm), and PL decay kinetics agree with each other (Figure 10.2c), indicating that both XB and PL probe exciton decay processes. PL decay kinetics before 120 ps is not compared due to the limited instrument response time of time-resolved PL measurement (~ 110 ps). The best fit of the XB kinetics gives a formation time of 101 ± 20 fs (see Appendix 10.3), indicating fast hot exciton relaxation to the band edge, consistent with recently reported of CsPbBr₃ NPLs³⁴¹ and similar to CsPbBr₃ QDs.^{289, 335} The decay time

constants are 20.8 ± 1.2 ps ($26.8 \pm 2.1\%$), 1664 ± 156 ps ($53.2 \pm 4.4\%$), and 11.4 ± 1.3 ns ($20.0 \pm 4.2\%$) (Table 10.2 in Appendix 10.3) and the half-life of XB kinetics is 804 ± 25 ps, which is faster than the band edge exciton decay reported in CsPbBr₃ QDs (half-life ~ 2.8 ns).²⁸⁹ This may be attributed to enhanced radiative decay rates of band edge excitons in 2D materials,^{21, 58-59} and additional nonradiative pathways in NPLs based on a lower PL quantum yield of NPLs ($\sim 31\%$)⁴³ compared to QDs ($\sim 79\%$).⁵⁴

10.2.3. Charge separation in CsPbBr₃ NPLs

Electron and hole transfer from NPLs were investigated in NPL-BQ and NPL-PTZ complexes, respectively, with varying NPL/adsorbate ratio by transient absorption spectroscopy. These complexes were prepared by adding different amounts of BQ (PTZ) to NPL toluene solution followed by sonication, and the total BQ (PTZ) concentrations vary from 0.55 (1.12) to 9.25 (7.53) mM. The transient spectra of NPL-PTZ complexes with the highest PTZ concentration (7.53 mM) are shown in Figure 10.3a. At long delay time (>0.2 μ s), when TA signal of free NPL decays to zero, a broad peak of NPL-PTZ sample centered at ~ 525 nm can be seen (inset of Figure 10.3a), which is attributed to the oxidized PTZ signal.¹⁸³ This long-lived oxidized PTZ signal shows that the exciton in NPL dissociates by hole transfer to PTZ to form a charge-separated state with electron remained in NPL and hole in PTZ. Comparison of XB kinetics of free NPLs and NPL-PTZ show a faster recovery of the latter in the < 1 ns time scale. Interestingly, these samples show the same decay kinetics (Figure S4a) at long delay time (>10 ns), indicating that there exists some free NPLs in NPL-PTZ sample. The contribution NPLs with adsorbed PTZ can be represented by the subtracted XB kinetics (SXB), which is obtain by subtracting normalized XB kinetics of free NPL from total XB kinetics of NPL-PTZ (Figure 10.5a in Appendix 10.3). Due to the overlap between PA and oxidized PTZ signals (Figure 10.5b in Appendix 10.3), we subtract the normalized PA kinetics (600-650 nm)

from the total signal at ~ 525 nm, to obtain the pure oxidized PTX signal, referred to as the subtracted oxidized PTZ kinetics (SPTZ). As shown in Figure 10.3b, SXB decays faster than XB of free NPLs, consistent with HT from NPL to PTZ. Furthermore, the formation of SPTZ signal agrees with the decay of SXB signal, confirming that exciton decays by HT from NPL to PTZ. It is important to note that the XB decays to zero at long delay time (>1 ns), when the electron remains in the NPL and hole is transferred to PTZ, indicating that the VB hole is required for observing an XB signal.

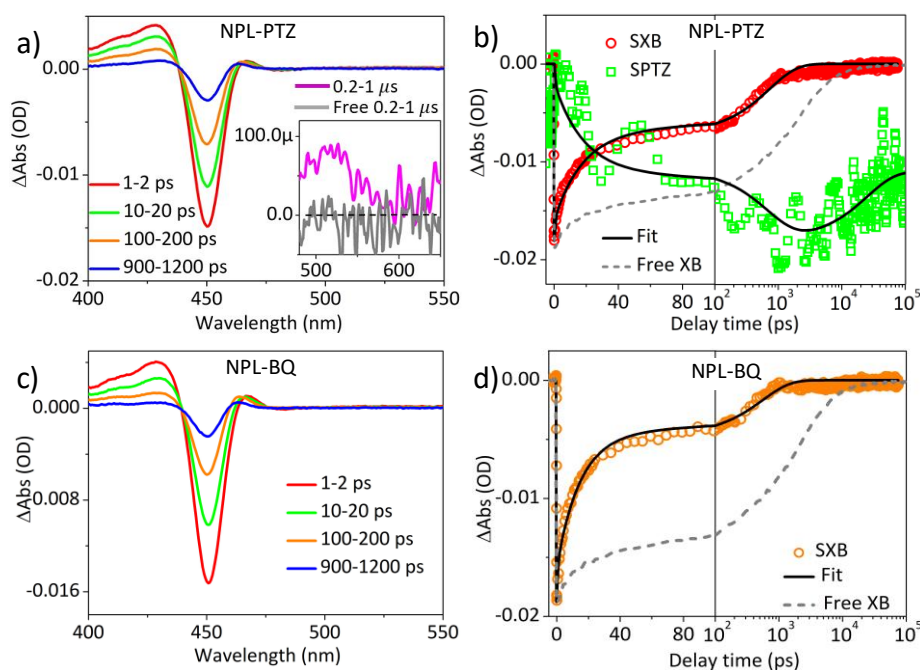


Figure 10.3. Electron and hole transfer from NPLs. (a) TA spectra of NPL-PTZ complexes at indicated delay times. Inset: a comparison of TA spectra of NPL-PTZ and free NPL at long delay time (0.2-1 μs). (b) Comparison of kinetics of subtracted exciton bleach of NPL-PTZ (SXB, red circles), exciton bleach of free NPLs (free XB, gray dashed line) and subtracted oxidized PTZ signals (SPTZ, green squares). The black lines are the fits of SXB and SPTZ kinetics of NPL-PTZ. (c) TA spectra of NPL-BQ complexes at indicated delay times. (d) Comparison of kinetics of subtracted exciton bleach of NPL-BQ (SXB, red circles) and exciton

bleach of free NPLs (free XB, gray dashed line). The black lines are the fits of SXB kinetics of NPL-BQ.

The transient spectra of NPL-BQ complexes with the highest BQ concentration (9.25 mM) are shown in Figure 10.3c. Similar to the NPL-PTZ sample, the NPL-BQ sample also contains a contribution of free NPLs, whose contribution can be removed by subtracting normalized XB kinetics of free NPL from the XB kinetics of NPL-BQ (Figure 10.5c in Appendix 10.3). As shown in Figure 10.3d, the subtracted exciton bleach kinetics (SXB) of NPL-BQ complexes decays faster than XB of free NPLs (Figure 10.3d), indicating ET from NPL to BQ. Surprisingly, the SXB of NPL-BQ also decays to zero at long delay time (>1 ns), indicating CB electron is also required for the observation of XB.

The results above show that the selective removal of either the CB electron or VB hole results in the complete recovery of XB, which suggest that the band edge exciton transition is blocked by the exciton and the presence of only the CB electron or hole leads to negligible contribution to XB. This is different from either cadmium chalcogenide nanocrystals (QDs,^{148, 239, 342-343} NRs,^{63, 102, 140} and NPLs,^{34, 62, 68-69, 109}) where electron state-filling dominates XB, or CsPbBr₃ QDs, where both electron (~67%) and hole (~33%) state-filling contribute to XB.²⁸⁹ Although the origin of this difference is unclear, it is likely due to two properties of CsPbBr₃ NPLs. (1) The effective mass of the electron ($m_e=0.215m_0$) is similar to that of the hole ($m_h=0.211m_0$) in CsPbBr₃ NPLs,⁵² so that the CB and VB edges likely have similar density of states and phase space-filling behaviors at a thermal equilibrium. (2) The band edge exciton in CsPbBr₃ NPLs is strongly bound (with a binding energy of ~260 meV) so that the exciton wavefunction is a superposition of many single electron and hole levels. Because the band edge single electron or hole level make only small contributions to the exciton wavefunction, neither

the CB electron (VB hole) in the charge-separated state, with the electron (hole) in NPL and the transferred hole (electron) in the acceptor, leads to significant exciton bleach.

We fit the XB kinetics of free CsPbBr₃ NPL, SXB kinetics of NPL-BQ/PTZ complexes, and SPTZ kinetics (black solid lines in Figure 10.2c, 10.3b, and 10.3d) using multi-exponential functions with the same set of parameters accounting for band edge recombination, carrier trapping, and CS processes (see Appendix 10.3 for details). The best multi-exponential fits give time constants (amplitudes) of 0.55 ± 0.02 ps ($26.8 \pm 2.1\%$), 17.7 ± 3.8 ps ($53.2 \pm 4.4\%$), and 724 ± 84 ps ($20.0 \pm 4.2\%$) for HT and 0.66 ± 0.03 ps ($26.8 \pm 2.1\%$), 14.7 ± 2.6 ps ($53.2 \pm 4.4\%$), and 552 ± 67 ps ($20.0 \pm 4.2\%$) for ET in samples with the highest PTZ (7.53 mM) and BQ (9.25 mM) concentrations, respectively. From these time constants, the HT and ET half-life can be estimated to be 24.1 ± 2.5 ps and 10.6 ± 1.0 ps, respectively. Accounting for the competition between charge separation (CS) and recombination, the HT and ET yields are estimated to be $97.6 \pm 0.1\%$ in NPL-PTZ complexes and $97.8 \pm 0.1\%$ in NPL-BQ complexes, respectively (see Appendix 10.3). The fits also reveal that the charge-separated state in NPL-PTZ is long-lived, whose decay can be fit to a biexponential function with time constants (amplitudes) of 31 ± 3 ns ($42.8 \pm 3.0\%$) and 4887 ± 241 ns ($57.2 \pm 3.1\%$) and described by a half-life $\gg 100$ ns.

Because both the ET and HT times depend on the number of acceptors per NPL, it is useful to quantify these time constants for complexes with one acceptor (BQ or PTZ), referred to as the intrinsic ET and HT time constants. To do this, we analyzed the XB kinetics of NPL-BQ (PTZ) as a function of BQ(PTZ) concentrations using a previously-reported model for colloidal QDs (see Appendix 10.4).^{269, 288-289} This model assumes: 1) the number of acceptors on NPL surfaces follows a Poisson distribution;³⁴⁴⁻³⁴⁵ 2) the adsorption of acceptors on NPL surfaces follows the Langmuir adsorption isotherm;²⁸⁸ and 3) exciton diffusion within 2D NPLs is fast⁶⁸⁻⁶⁹ and ET and HT rates scale linearly with the number of adsorbed acceptors on the NPL surface.²⁸⁹ The apparent exciton quenching rate (the reciprocal of the half-life of XB kinetics:

$1/\tau_{1/2}$) as a function of acceptor concentration (Figure 10.7c in Appendix 10.4) can be fit well according to this model, from which the average number of acceptor per NPL at different acceptor concentrations (Figure 10.7d in Appendix 10.4) can be obtained. The best fits (solid lines in Figure 10.7c in Appendix 10.4) yield the intrinsic ET (HT) time constant per BQ (PTZ) of 248 ± 69 ps (670 ± 90 ps), which is similar to those in CsPbBr₃ QDs.²⁸⁹ This indicates that strong electronic coupling between charge carriers in NPLs and surface adsorbed acceptors results in efficient charge transfer, similar to QDs and nanorods.^{12, 76, 78-79, 269, 280, 346}

Compared to CsPbBr₃ QDs, the 2D morphology of CsPbBr₃ NPLs results in following distinguishing advantages. (1) The strong dielectric confinement effect gives large exciton binding energy so that the exciton rather than free carriers dominates at the band-edge, which increases the oscillator strength of band-edge transitions and is promising for emitting applications. (2) The charge-separated state lifetime of CsPbBr₃ NPL-PTZ complexes (with half-life $\gg 100$ ns) is over 100 folds longer than that in CsPbBr₃ QD-PTZ complexes (with half-life of that ~ 1 ns).²⁸⁹ We attribute the longer charge separated state lifetime to the 2D morphology, on the basis of our previous findings of 2D CdS NPLs.⁴³ Although for the same reason, we also expect a longer charge-separated state lifetime in NPL-electron acceptor complexes than that in QD-electron acceptor complexes, we are unable to probe the charge-separated state in NPL-BQ complexes because the reduced form of BQ does not have an absorption feature in visible region (400-800 nm). Considering charge recombination is the main loss pathway for solar-to-fuel conversion,⁴³ the longer-lived charge-separated state in CsPbBr₃ NPL-acceptor complexes shows greater potentials than perovskite QDs for photocatalysis. (3) NPLs have larger absorption coefficient,³³⁶ making NPLs potentially better sensitizers in photovoltaics. Therefore, with near unity CS yield, high CS rate, long CS distance, and large absorption cross-section, CsPbBr₃ NPLs are promising as a novel class of photocatalysis and optoelectrical materials.^{333, 347-348}

10.3. Conclusion

In summary, we have studied the exciton dynamics and charge transfer processes in CsPbBr₃ NPLs *via* TA spectroscopy. The binding energy of exciton (~260 meV) are determined *via* detailed analysis on static and transient absorption spectra. The XB of CsPbBr₃ NPLs requires exciton at band edge, and single carriers (electron or hole) have negligible contributions to XB, which is different from either CsPbBr₃ QDs or low dimensional cadmium chalcogenide nanocrystals. ET and HT from NPLs to electron (BQ) and hole (PTZ) acceptors, respectively, were observed and their rates increase at higher acceptor concentrations. The ET and HT time constants are determined to be 248 ± 69 ps and 670 ± 90 ps per BQ and PTZ, respectively, and reaches 24.1 ± 2.5 ps and 10.6 ± 1.0 ps, respectively, at the highest PTZ (7.53 mM) and BQ (9.25 mM) concentrations studied in our work. At these concentrations, the HT and ET yields are estimated to be $97.6 \pm 0.1\%$ in NPL-PTZ complexes and $97.8 \pm 0.1\%$ in NPL/BQ complexes and the half-life time of charge separated state in NPL/PTZ complexes exceeds 100 ns, which is over 100 folds longer than that in CsPbBr₃ QD/PTZ complexes. The findings in this work enhances fundamental understanding of exciton properties and carrier dynamics in 2D perovskite nanomaterials. Moreover, the observation of ultrafast interfacial charge transfer and long-lived charge-separated state of NPL/acceptor complexes suggest they are also promising materials for photocatalysis and solar cell applications.

Appendix 10.1

Band edge position estimation of CsPbBr₃ NPLs

The band-edge exciton energy of CsPbBr₃ colloidal NPLs (E_X) is given by the exciton peak energy shown in absorption spectra as 2.76 eV. According to well-known quantum well (QW) model, the exciton energy equals to the sum of the bulk band gap of CsPbBr₃, carrier (electron and hole) quantization energy induced by quantum confinement effect, exciton binding energy induced by Coulomb interaction, and self-image energy induced by dielectric confinement effect:¹⁴⁴

$$E_X = E_g + (E_{k(h)} + E_{k(e)}) + E_b + E_S \quad (10.1)$$

where E_g is the band gap of bulk CsPbBr₃. $E_{k(e)}$ and $E_{k(h)}$ are the quantization energy of conduction band (CB) electrons and valence band (VB) holes, respectively. E_b is exciton binding energy, and E_S is ground state electron and hole self-image energy.

Considering the CB and VB edges are contributed by p orbitals of Pb and Br, respectively,³³⁴ we assumed that bulk CsPbBr₃ have similar band edge position as bulk CH₃NH₃PbBr₃ perovskite with -4.0 and -5.96 eV (vs. vacuum) for CB and VB edge, respectively,²⁸⁹ and E_g is estimated at 1.96 eV. Considering the electron and hole moved freely in x-y plane but confined in the z-direction in NPL. The potential is set as zero and infinity inside and outside the NPL, respectively. Thus, the quantization energy of carriers in the NPL is:^{27, 144}

$$E_{k(i)} = \frac{\hbar^2 n^2}{8m_i d^2} \quad (10.2)$$

where m_i ($i=e$ or h) is the effective mass for electron or hole of CsPbBr₃ NPLs, d is NPL thickness. The ratio of CB to VB edge shifts due to quantum confinement effect is equal to the ratio of electron to hole quantization energies:

$$\frac{\text{CB shift}}{\text{VB shift}} = \frac{E_{k(e)}}{E_{k(h)}} = \frac{m_h}{m_e} \quad (10.3)$$

Due to the similar effective mass for electron ($m_e=0.215m_0$) and hole ($m_h=0.211m_0$, m_0 is free electron mass),⁵² we assumed the CB and VB shifts evenly due to E_b and E_s . Therefore, the estimated CB and VB edge position for NPLs are -3.59 eV and -6.34 eV (vs. vacuum), respectively.

Appendix 10.2

Static and transient absorption spectra and their fits

The static absorption spectrum of NPLs was fitted according to a well-established QW absorption model:^{146, 250-251}

$$\text{Abs}(E) = C\alpha(E) \quad (10.4)$$

where C and $\alpha(E)$ are the weights and absorption strength of the band-edge transitions, respectively. These absorptions include contributions of both band-edge excitons, $X(E)$, and continuous band absorption, $\text{Con}(E)$:

$$\alpha(E) = X(E) + \text{Con}(E) \quad (10.5)$$

The exciton line shape and the continuous band absorption line shape are given by Eq. 10.6 and 10.7, respectively.

$$X(E) = \frac{1}{2\eta} \left[\text{erf} \left(\frac{E - E_X}{W_X} - \frac{W_X}{2\eta} \right) + 1 \right] \exp \left(\frac{W_X^2}{4\eta^2} - \frac{E - E_X}{\eta} \right) \quad (10.6)$$

$$\text{Con}(E) = \frac{H}{2} \left[\text{erf} \left(\frac{(E - E_X) - E_b}{W_C} \right) + 1 \right] \quad (10.7)$$

In Eq. 10.6 and 10.7, E_X and E_b are exciton transition energy and exciton binding energy, respectively. W_X and W_C are exciton peak width and continuum edge width, respectively. H is the continuum edge step height and η is the asymmetric broadening.

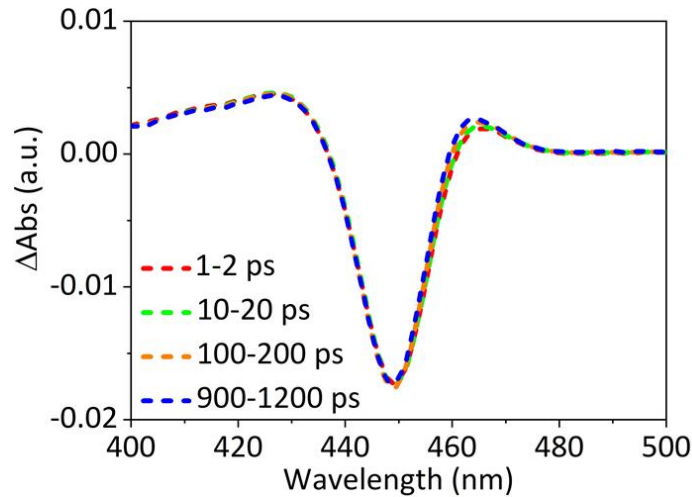


Figure 10.4. The normalized TA spectra of NPLs at different delay times.

For TA measurements with low pump fluence, NPLs are in the single-exciton condition. This is supported by the delay time independent TA spectra as shown in Figure 10.4. With one exciton occupying the band edge state, the strengths of band-edge exciton transitions are reduced by half due to the Pauli exclusion principle, the band-edge exciton transitions after pump (X^*) is shifted to lower energy (by Δ_{XX}) and get broadened due to exciton-exciton interaction.^{224, 253} The amplitude of the continuous band after pump (Con^*) remains unaffected, and we consider the energy-dependent band gap renormalization (BGR) by adding a shift on transition energy (Δ_{Con}) and broadening the edge width as W_C^* . Thus, the absorbance after pump is given by:

$$Abs^*(E) = C[X^*(E) + Con^*(E)] \quad (10.8)$$

where:

$$X^*(E) = \frac{1}{4\eta^*} \left[\operatorname{erf} \left(\frac{E - (E_X - \Delta_{XX})}{W_X^*} - \frac{W_X^*}{2\eta^*} \right) + 1 \right] \exp \left(\frac{W_X^{*2}}{4\eta^{*2}} - \frac{E - (E_X - \Delta_{XX})}{\eta^*} \right) \quad (10.9)$$

$$Con^*(E) = \frac{H}{2} \left[\operatorname{erf} \left(\frac{[E - (E_X - \Delta_{Con})] - E_b}{W_C^*} \right) + 1 \right] \quad (10.10)$$

The TA spectra then are fitted by:

$$\Delta\text{Abs}(E) = \text{Abs}^*(E) - \text{Abs}(E) \quad (10.11)$$

By tuning C, we can fit TA spectra at different delay times because they have the same lineshape and only differ in amplitude. The best fit of the static absorption spectrum is shown in Figure 10.1b, the fitting results for TA spectra are shown in Figure 10.2a-b, and the fitting parameters and errors are listed in Table 10.1.

Table 10.1. The fitting parameters and errors of static and TA spectra

Static absorption parameters		TA parameters	
E_X/meV	2750 ± 10	Δ_{XX}/meV	10 ± 2
E_b/meV	260 ± 10	$\Delta_{\text{Con}}/\text{meV}$	53 ± 2
W_X/meV	50 ± 2	W_X^*/meV	70 ± 5
W_C/meV	150 ± 5	W_C^*/meV	250 ± 5
η/meV	78 ± 3	η^*/meV	117 ± 5
H/meV	5600 ± 100		
C	0.061 ± 0.001		

Appendix 10.3

Transient absorption kinetics and the fits

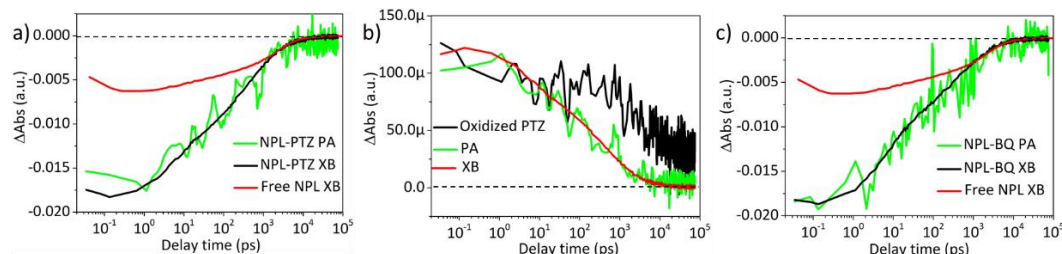


Figure 10.5. The comparison of (a) XB and PA kinetics of NPL-PTZ complexes and XB kinetics free NPLs, (b) total kinetics at ~ 525 nm, PA kinetics (600-650 nm), and XB kinetics of NPL-PTZ complexes, and (c) XB and PA kinetics of NPL-BQ complexes and XB kinetics of free NPLs

As shown in Figure 10.5a&c, XB kinetics of free NPL and NPL-BQ/PTZ were normalized to the same at long delay time (> 1 ns), and the subtracted exciton bleach (SXB) kinetics of NPL-BQ/PTZ were obtained as the differences of the two kinetics. The ratio of the initial amplitude between the two kinetics gives the free NPL percentage in NPL-BQ (PTZ) complexes as $33.1 \pm 0.5\%$ ($34.2 \pm 0.5\%$). Similarly, subtracted oxidized PTZ kinetics is obtained by normalizing PA and total kinetics at oxidized PTZ wavelength at the time zero as shown in Figure 10.5b, which is due to no hole transfer so that no oxidized PTZ at time zero, and taking the difference of the two kinetics. PA kinetics also show excellent agreement with XB kinetics in both NPL-BQ and PTZ complexes.

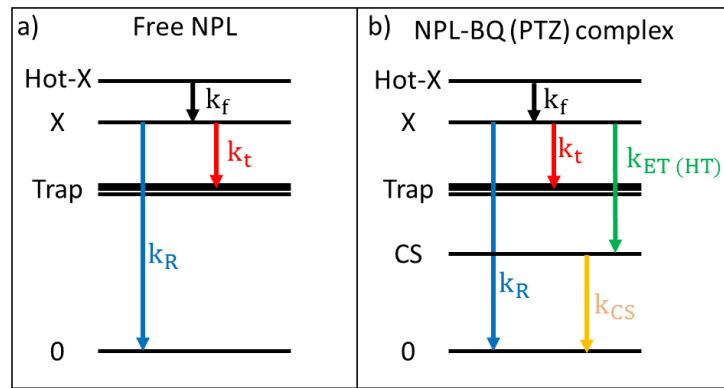


Figure 10.6. Carrier decay pathways in (1) free CsPbBr₃ NPLs and (b) NPL-BQ (or NPL-PTZ) complexes in state representation.

Exciton bleach signal requires band-edge exciton with electron and hole in CB and VB edge, respectively. Thus, we schemed the exciton decay pathways in free NPLs and NPL-acceptor complexes in Figure 10.6. For free NPLs (Figure 10.6a), after 400 nm (3.1 eV) pump, hot exciton relaxes to band edge to form the A exciton with a rate constant k_f . The band edge exciton can either decay *via* electron-hole recombination with a rate constant k_R or becomes trapped exciton with a trapping rate of k_t . For NPL-acceptor complexes (Figure 10.6b), in addition to the free NPL decay pathways, the band edge exciton can also dissociate and become charge-separation (CS) state with an electron (hole) transferred to BQ (PTZ) with a transfer rate of k_{ET} (k_{HT}). The CS state finally decays to the ground state (0) due to electron-hole recombination with a rate constant of k_{CS} . According to these exciton decay pathways, we fitted the free NPL XB kinetics using multi-exponential function convoluted with the instrument response function (IRF):

$$TA_{\text{free NPL}}(t) = A_{\text{initial}} \left[e^{-\frac{t}{\tau_f}} - \sum_{i=1}^3 a_i e^{-\frac{t}{\tau_i}} \right] \otimes \text{IRF} \quad (10.12)$$

where A_{initial} is the initial bleach amplitude, $\tau_f = 1/k_f$ is the formation time constant. a_i ($i=1$ to 3) is the weight of different NPL populations that decays with a different time constant of $\tau_i = (\frac{1}{k_t+k_R})_i$. Similarly, for NPL-BQ or PTZ complexes, we fitted their SXB kinetics as:

$$TA_{\text{NPL-PTZ}}(t) = A_{\text{initial}} \left[e^{-\frac{t}{\tau_f}} - \sum_{i=1}^3 a_i e^{-\left(\frac{t}{\tau_i} + \frac{t}{\tau_{\text{HT},i}}\right)} \right] \otimes \text{IRF} \quad (10.13)$$

$$TA_{\text{NPL-BQ}}(t) = A_{\text{initial}} \left[e^{-\frac{t}{\tau_f}} - \sum_{i=1}^3 a_i e^{-\left(\frac{t}{\tau_i} + \frac{t}{\tau_{\text{ET},i}}\right)} \right] \otimes \text{IRF} \quad (10.14)$$

where $\tau_{\text{HT},i} = 1/k_{\text{HT},i}$ and $\tau_{\text{ET},i} = 1/k_{\text{ET},i}$ are the hole transfer and electron transfer time constant, respectively, of the different components ($i=1$ to 3). In NPL-acceptor complexes, the decay time constant of SXB is the formation rate of CS state, which is probed by oxidized PTZ signals (SPTZ). Therefore, the SPTZ kinetics was fitted as:

$$TA_{\text{SPTZ}}(t) = A_{\text{initial}} \left[\sum_{i=1}^3 a_i e^{-\frac{t}{\tau_{\text{ET},i}}} - \sum_{i=1}^2 b_i e^{-\frac{t}{\tau_{\text{CS},i}}} \right] \otimes \text{IRF} \quad (10.15)$$

where b_i ($i=1$ and 2) represents different CS state decay component with the decay time constant of $\tau_{\text{CS},i} = 1/k_{\text{CS},i}$. We used Eq. 10.12 to 10.15 to fit XB kinetics of free NPLs, SXB kinetics of NPL-PTZ and NPL-BQ with the highest BQ (9.25 mM) or PTZ (7.53 mM) concentration, and SPTZ kinetics of NPL-PTZ with the highest PTZ concentration (7.53 mM), respectively, as shown in Figure 10.2c, 10.3b, and 10.3d. The fitting parameters and errors are listed in Table 10.2.

Table 10.2. Fitting parameters and errors of TA kinetics

τ_f/fs	101 ± 20
a_1 (τ_1/ps)	0.268 ± 0.021 (20.8 ± 1.2)
a_2 (τ_2/ps)	0.532 ± 0.044 (1664 ± 156)

a_1 (τ_3/ps)	0.200 ± 0.042 (11406 ± 1030)
$\tau_{\text{HT},1}/\text{ps}$ ($\tau_{\text{ET},1}/\text{ps}$)	0.55 ± 0.02 (0.66 ± 0.03)
$\tau_{\text{HT},2}/\text{ps}$ ($\tau_{\text{ET},2}/\text{ps}$)	17.7 ± 3.8 (14.7 ± 2.6)
$\tau_{\text{HT},3}/\text{ps}$ ($\tau_{\text{ET},3}/\text{ps}$)	724 ± 84 (552 ± 67)
b_1 ($\tau_{\text{CS},1}/\text{ns}$)	0.428 ± 0.030 (31 ± 3)
b_2 ($\tau_{\text{CS},2}/\text{ns}$)	0.572 ± 0.031 (4887 ± 241)

The ET (HT) yields are estimated by: $\sum_{i=1}^3 a_i \frac{\tau_i}{\tau_i + \tau_{\text{ET}}} \left(\sum_{i=1}^3 a_i \frac{\tau_i}{\tau_i + \tau_{\text{HT}}} \right)$.

Appendix 10.4

Molecular acceptor concentration-dependent TA kinetics

We analyzed the molecular acceptor concentration-dependent XB kinetics of NPL-BQ (Figure 10.7a) and NPL-PTZ (Figure 10.7b) using a previously-reported model for colloidal QDs.^{269, 288-289} It assumes the distribution of acceptor number on NPL surfaces following the Poisson distribution:³⁴⁴⁻³⁴⁵

$$P_m(n) = \frac{e^{-m} m^n}{n!} \quad (10.16)$$

where $P_m(n)$ is the possibility of finding n acceptors on NPL surface when the average acceptor number is m . We also assumed the charge transfer rate scales linearly with the acceptor number on NPL surface similar to QDs so that the total charge transfer rate with n acceptor per NPL (k_n) is n times as charge transfer rate per acceptor (k_1):^{288-289, 345}

$$k_n = nk_1 \quad (10.17)$$

In this case, the excited NPL population, $N(t)$, decays as:²⁸⁰

$$N(t) = N(0) \sum_i a_i \sum_{n=0}^{\infty} P_m(n) e^{-(k_i+k_n)t} = N(0) \cdot g(t) \cdot e^{-m} \cdot e^{(me^{-k_1 t})} \quad (10.18)$$

where $g(t) = \sum_i a_i e^{-k_i t}$ and k_i (the reciprocal of τ_i as in Table 10.2) is the exciton recombination rate without acceptors. When the excited NPL population decays to half, Eq. 10.18 gives the half-life ($\tau_{1/2}$) as:

$$\frac{1}{\tau_{1/2}} = - \frac{k_1}{\text{Ln} \left[1 - \frac{\text{Ln} \left(2g \left(\frac{\tau_1}{2} \right) \right)}{m} \right]} = - \frac{1}{\text{Ln} \left[1 - \frac{\text{Ln} \left(2g \left(\frac{\tau_1}{2} \right) \right)}{m} \right]} \frac{1}{\tau_m} \quad (10.19)$$

where $g(\tau_{1/2})$ is the percentage of remained XB amplitude of free NPLs at the half-life of XB kinetics of NPL-acceptor complexes. τ_m is the charge transfer time constant per acceptor. The

model also assumes the adsorption of acceptors on NPL surfaces following the Langmuir adsorption isotherm:²⁸⁸

$$\frac{m}{N_{\text{total}}} = \theta = \theta_{\text{max}} \frac{K_A[A]}{1 + K_A[A]} \quad (10.20)$$

where θ is the mean fractional surface coverage of acceptors on NPLs. N_{total} is the total number of adsorption sites available per NPL; θ_{max} the maximum fractional surface coverage of acceptors on NPLs. K_A is the binding constant of acceptors; and $[A]$ the total concentration of acceptors in NPL-acceptor complex solution. Therefore, m can be represented by:

$$m = N_{\text{max}} \frac{K_A[A]}{1 + K_A[A]} \quad (10.21)$$

where $N_{\text{max}} = N_{\text{total}}\theta_{\text{max}}$ is the maximum number of bound acceptors on the NPL surface.

Using Eq. 10.19 and 10.21, we fitted the $1/\tau_{1/2}$ of XB kinetics as a function of acceptor concentration in Figure 10.7c by tuning N_{max} , K_A , and τ_m , where our model fits reasonably well to our experimental results. The best fits give N_{max} as 30 ± 1 for NPLs, which is over 2 folds larger than that of CsPbBr₃ QDs (~ 14) as reported.²⁸⁹ This is attributed to the large surface area of NPL due to the 2D morphology that can adsorb more acceptors compared to QDs. K_A is determined as $15.7 \pm 1.2 \text{ M}^{-1}$ and $16.1 \pm 1.0 \text{ M}^{-1}$ for BQ and PTZ, respectively, which are both smaller than those for CsPbBr₃ QDs.²⁸⁹ This is very likely due to the larger and stronger original ligand coverage on NPLs surface due to flat basal plane of NPLs compared to QDs so that it is more difficult to replace them to BQ or PTZ. τ_m is fitted to $248 \pm 69 \text{ ps}$ and $670 \pm 90 \text{ ps}$ for electron and hole transfer, respectively, which are similar to those reported in CsPbBr₃ QDs.²⁸⁹ The estimated m of NPL-BQ and NPL-PTZ as a function of acceptor concentration are shown in Figure 10.7d, and the values of $\tau_{1/2}$ and m with errors are listed in Table 10.3.

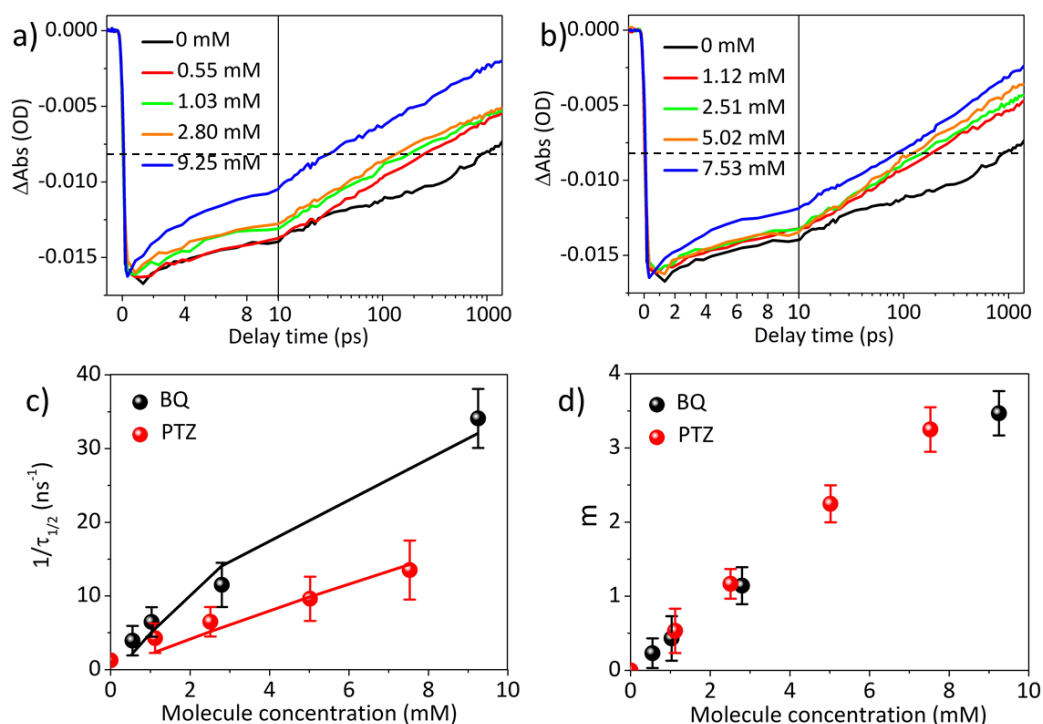


Figure 10.7. The XB kinetics of (a) NPL-BQ and (b) NPL-PTZ at different BQ and PTZ concentrations, respectively. The dashed lines represent the half bleach amplitude. (c) The apparent decay rate ($1/\tau_{1/2}$) of XB kinetics of NPL-BQ (black dots) and NPL-PTZ (red dots) as a function of acceptor concentration. Solid lines are the fits according to the model. (d) The average number of BQ or PTZ per NPL as a function of acceptor concentration.

Table 10.3. Acceptor concentration-dependent XB decay half-life and m with errors

[BQ]/mM ([PTZ]/mM)	$\tau_{1/2}$ /ps for BQ (for PTZ)	m for BQ (for PTZ)
0 (0)	804 ± 25 (804 ± 25)	0 (0)
0.55 (1.12)	254 ± 25 (234 ± 25)	0.23 ± 0.20 (0.53 ± 0.30)
1.03 (2.51)	154 ± 5 (153 ± 5)	0.43 ± 0.30 (1.17 ± 0.30)
2.80 (5.02)	90.5 ± 3.5 (104 ± 5)	1.14 ± 0.25 (2.25 ± 0.25)
9.25 (7.53)	29.3 ± 1.0 (74.0 ± 3.5)	3.47 ± 0.30 (3.25 ± 0.30)

Chapter 11. Conclusion and Outlooks

Reproduced in part with permission from *Nano Research* **2018**, *11*, 3031. Copyright 2018 Springer Nature.

In summary, 2D cadmium chalcogenide (CdX, X=Se, S, Te) NPLs exhibit many unique properties, such as uniform quantum confinement, large binding energy, and giant oscillator strength transition effect, long Auger lifetime, and high quantum yield, and have been intensively investigated for potential applications as optoelectrical (e.g., lasing, light-emitting diodes) and photocatalytic applications (e.g., solar-to-H₂ conversion). Many of their performances and optical properties are determined by the physical properties of 2D excitons in these NPLs. In this dissertation, we have systematically studied the physical properties and dynamics of 2D excitons in cadmium chalcogenide NPLs, and how 2D exciton properties affect their OG properties (e.g., OG mechanism and threshold) and their performances of solar-to-H₂ conversion.

First, we investigated three of the most important physical properties of 2D excitons, i.e. exciton spatial area, exciton transport, and Auger annihilation, in cadmium chalcogenide NPLs. We have developed a method of measuring the exciton COM coherent area by transient absorption spectroscopy. The exciton COM coherent area in CdSe NPLs is smaller than NPL lateral area at room temperature but extends throughout the whole NPL at low temperature (<4K) giving rise to the GOST effect. We also showed that at room temperature, both hot and cold (band-edge) excitons transport diffusively in the plane of NPLs, and the diffusion constant of the band-edge exciton is close to that of their bulk counterpart. Moreover, we demonstrated

a new model for Auger recombination in 2D NPLs. Because of this fast in-plane diffusion of excitons, multi-excitons collide with each other frequently in CdSe NPLs before annihilation. We revealed that the Auger recombination lifetime is determined by the exciton binary collision frequency and the Auger probability per collision, the former scales linearly with NPL lateral area and the latter increases drastically with NPL thickness. These works advance the fundamental understandings of 2D excitons in 2D materials.

Second, we have systematically examine the OG mechanism and threshold in cadmium chalcogenide NPLs and their heterostructures. We showed that the OG threshold of CdSe NPLs depends on optical density, and temperature, but is independent to NPL lateral area. When absorbing the same number of photons, although larger NPLs can generate multiple excitons per NPL easier, they are also capable of holding more band-edge excitons. In this case, higher exciton states are required to reach the OG threshold in larger NPLs so that the OG threshold is independent to NPL lateral area. We also found that larger optical density at excitation wavelength increases the OG threshold by introducing more loss (absorption). Moreover, exciton coherent area extension due to GOST effect at low temperature effectively reduces the degree of band-edge exciton degeneracy without changing the large absorption cross-section of NPLs and achieves lower OG threshold. For NPL heterostructures, unlike type-II QDs, which can realize a single-exciton gain, OG is achieved at the tri-exciton state in CdSe/CdTe type-II CC NPLs with two CT-exciton at core/crown interface and one CdTe crown exciton. Although the multi-exciton is needed for OG type-II NPLs, the threshold is still much lower than that of type-II QDs due to the larger absorption cross-section induced by 2D morphology. These works improved our understanding of OG properties of 2D NPLs and provide insights and directions for rational design and improvement of NPL lasing properties.

At last, we investigated the exciton dissociation in both CdS and CsPbBr₃ perovskite NPLs decorated with electron and hole acceptors. We found the charge separation are efficient and

ultrafast, moreover, the 2D morphology of NPLs efficiently suppresses the charge recombination process, which is the main loss pathway for light-driven H₂ generation, in both cadmium chalcogenide (CdS) and perovskite (CsPbBr₃) 2D NPL-acceptor systems and is the key of the enhanced solar-to-H₂ conversion efficiency of 2D CdS NPL-Pt heterostructures compared with 1D NR-Pt heterostructures. With the unique properties of 2D excitons resulted from the 2D morphology, we herein conclude that 2D NPLs are promising for both optoelectrical applications (e.g., low-threshold lasing materials) and photocatalysis (e.g., solar-to-H₂ conversion).

Although promising optoelectrical performances of 2D NPLs have been reported, there remain challenges on the synthesis and further understanding of fundamental exciton properties and OG mechanisms. First, NPLs with larger lateral area is needed to reduce the binary exciton collision frequency and increase multi-exciton lifetime. However, controlling and extending lateral dimension of 2D NPLs are still challenging, and larger NPLs usually have more defect/trap states.³⁴⁹ Second, further understanding of factors that limits the exciton COM area is needed. For example, the measured exciton coherent area is smaller than the estimated value according to exciton-phonon scattering, indicating important contributions of yet to be identified factors. One possible reason is the inhomogeneity of the interaction between the surface capping ligand and NPL.²⁴⁵ Our results show that exciton coherent area increases in NPLs with smaller thickness (and stronger quantum confinement). Further exploration of NPL quantum confinement strength and uniformity, and surface chemistry could be the key to extend the exciton coherent area at the room temperature, which if successful would further reduce the lasing threshold.²³⁰

Similarly, many challenges remain for photocatalysis using 2D NPLs. Significant advances in material synthesis are needed. High quality NPLs are often synthesized and dispersed in organic solvents. Transferring NPLs to aqueous solution by ligand exchange often

results in poor ligand coverage and low solubility in aqueous solution.³⁵⁰ This problem is further worsened by the relatively large volume of NPLs compared to QDs and NRs. Therefore, new methods for aqueous solution synthesis of NPLs and improved ligand exchange methods are required to increase the solubility of NPLs in aqueous solution for practical solar energy harvesting. Moreover, H₂ generation quantum efficiencies of NPL-Pt heterostructures at neutral pHs reported so far are still far from unity, indicating either non-unity initial charge separation and/or recombination of separated electrons and holes prior to H₂ formation. One approach for suppressing charge recombination is to increase the rate of irreversible hole removal by a sacrificial hole acceptor. Moreover, since nanocrystal decorated graphene nanosheets have shown strong electronic coupling and promising performances for solar-to-H₂ conversion,³⁵¹⁻³⁵³ 2D/2D heterostructures, such as NPL decorated graphene with 2D catalyst/electron acceptor, show great potentials for further enhancement of solar-to-H₂ conversion efficiency. Finally, so far most light-driven H₂ generation studies has focused on the reduction half reaction, employing sacrificial hole acceptors to complete the oxidation half reaction. Chai et al. have reported recently an efficient photosynthetic system that is consisted of Ni-modified giant CdS nanoparticles and alcohol and converts alcohol into H₂ and aldehyde (or ketone) with a H₂ generation AQE reaching ~40%.²⁵⁸ This work demonstrates that there exist interesting opportunities to couple the proton (water) reduction half reaction with non-sacrificial oxidation half reaction to drive more interesting and useful chemical transformations.

References

- (1) Alivisatos, A. P. Semiconductor Clusters, Nanocrystals, and Quantum Dots. *Science* **1996**, *271*, 933-937.
- (2) Burda, C.; Chen, X.; Narayanan, R.; El-Sayed, M. A. Chemistry and Properties of Nanocrystals of Different Shapes. *Chem. Rev.* **2005**, *105*, 1025-1102.
- (3) Henry, C., Size Effects on Structure and Morphology of Free or Supported Nanoparticles. In *Nanomaterials and Nanochemistry*, Bréchnignac, C.; Houdy, P.; Lahmani, M., Eds. Springer Berlin Heidelberg: Berlin, Heidelberg, 2007; pp 3-34.
- (4) Reimann, S. M.; Manninen, M. Electronic structure of quantum dots. *Reviews of Modern Physics* **2002**, *74*, 1283-1342.
- (5) Efros, A. L.; Rosen, M. THE ELECTRONIC STRUCTURE OF SEMICONDUCTOR NANOCRYSTALS¹. *Annu. Rev. Mater. Sci.* **2000**, *30*, 475-521.
- (6) Murray, C. B.; Norris, D. J.; Bawendi, M. G. Synthesis and characterization of nearly monodisperse CdE (E = sulfur, selenium, tellurium) semiconductor nanocrystallites. *J. Am. Chem. Soc.* **1993**, *115*, 8706-8715.
- (7) Yu, W. W.; Qu, L.; Guo, W.; Peng, X. Experimental Determination of the Extinction Coefficient of CdTe, CdSe, and CdS Nanocrystals. *Chem. Mat.* **2003**, *15*, 2854-2860.
- (8) Li, J.; Chen, J.; Shen, Y.; Peng, X. Extinction coefficient per CdE (E = Se or S) unit for zinc-blende CdE nanocrystals. *Nano Res*, **2018**, *11*, 3991-4004.
- (9) Hens, Z.; Moreels, I. Light absorption by colloidal semiconductor quantum dots. *J. Mater. Chem.* **2012**, *22*, 10406-10415.
- (10) Yeltik, A.; Delikanli, S.; Olutas, M.; Kelestemur, Y.; Guzel Turk, B.; Demir, H. V.

Experimental Determination of the Absorption Cross-Section and Molar Extinction Coefficient of Colloidal CdSe Nanoplatelets. *J. Phys. Chem. C* **2015**, *119*, 26768-26775.

(11) Achtstein, A. W.; Antanovich, A.; Prudnikau, A.; Scott, R.; Woggon, U.; Artemyev, M. Linear Absorption in CdSe Nanoplates: Thickness and Lateral Size Dependency of the Intrinsic Absorption. *J. Phys. Chem. C* **2015**, *119*, 20156-20161.

(12) Zhu, H. M.; Lian, T. Q. Wavefunction engineering in quantum confined semiconductor nanoheterostructures for efficient charge separation and solar energy conversion. *Energy & Environ. Sci.* **2012**, *5*, 9406-9418.

(13) Wu, K.; Park, Y.-S.; Lim, J.; Klimov, V. I. Towards zero-threshold optical gain using charged semiconductor quantum dots. *Nat. Nanotechnol.* **2017**, *12*, 1140.

(14) Lim, J.; Park, Y.-S.; Klimov, V. I. Optical gain in colloidal quantum dots achieved with direct-current electrical pumping. *Nat. Mater.* **2017**, *17*, 42-49.

(15) Klimov, V. I.; Ivanov, S. A.; Nanda, J.; Achermann, M.; Bezel, I.; McGuire, J. A.; Piryatinski, A. Single-exciton Optical Gain in Semiconductor Nanocrystals. *Nature* **2007**, *447*, 441-446.

(16) Klimov, V.; Mikhailovsky, A.; Xu, S.; Malko, A.; Hollingsworth, J.; Leatherdale, C.; Eisler, H. J.; Bawendi, M. Optical gain and stimulated emission in nanocrystal quantum dots. *Science* **2000**, *290*, 314-317.

(17) Chen, X.; Li, C.; Gratzel, M.; Kostecki, R.; Mao, S. S. Nanomaterials for renewable energy production and storage. *Chem. Soc. Rev.* **2012**, *41*, 7909-7937.

(18) Wu, K.; Lian, T. Quantum confined colloidal nanorod heterostructures for solar-to-fuel conversion. *Chem. Soc. Rev.* **2016**, *45*, 3781-3810.

(19) Ithurria, S.; Dubertret, B. Quasi 2D Colloidal CdSe Platelets with Thicknesses Controlled at the Atomic Level. *J. Am. Chem. Soc.* **2008**, *130*, 16504-16505.

(20) Ithurria, S.; Bousquet, G.; Dubertret, B. Continuous Transition from 3D to 1D

Confinement Observed during the Formation of CdSe Nanoplatelets. *J. Am. Chem. Soc.* **2011**, *133*, 3070-3077.

(21) Ithurria, S.; Tessier, M. D.; Mahler, B.; Lobo, R. P. S. M.; Dubertret, B.; Efros, A. Colloidal nanoplatelets with two-dimensional electronic structure. *Nat. Mater.* **2011**, *10*, 936-941.

(22) Nasilowski, M.; Mahler, B.; Lhuillier, E.; Ithurria, S.; Dubertret, B. Two-Dimensional Colloidal Nanocrystals. *Chem. Rev.* **2016**, *116*, 10934-10982.

(23) Tessier, M. D.; Javaux, C.; Maksimovic, I.; Loriette, V.; Dubertret, B. Spectroscopy of Single CdSe Nanoplatelets. *ACS Nano* **2012**, *6*, 6751-6758.

(24) Chen, O.; Zhao, J.; Chauhan, V. P.; Cui, J.; Wong, C.; Harris, D. K.; Wei, H.; Han, H.-S.; Fukumura, D.; Jain, R. K.; Bawendi, M. G. Compact High-quality CdSe–CdS Core–Shell Nanocrystals with Narrow Emission Linewidths and Suppressed Blinking. *Nat Mater* **2013**, *12*, 445-451.

(25) Singh, S.; Tomar, R.; ten Brinck, S.; De Roo, J.; Geiregat, P.; Martins, J. C.; Infante, I.; Hens, Z. Colloidal CdSe Nanoplatelets, A Model for Surface Chemistry/Optoelectronic Property Relations in Semiconductor Nanocrystals. *J. Am. Chem. Soc.* **2018**, *140*, 13292-13300.

(26) Kunneman, L. T.; Tessier, M. D.; Heuclin, H.; Dubertret, B.; Aulin, Y. V.; Grozema, F. C.; Schins, J. M.; Siebbeles, L. D. A. Bimolecular Auger Recombination of Electron-Hole Pairs in Two-Dimensional CdSe and CdSe/CdZnS Core/Shell Nanoplatelets. *J. Phys. Chem. Lett.* **2013**, *4*, 3574-3578.

(27) Li, Q.; Lian, T. Area- and Thickness-Dependent Biexciton Auger Recombination in Colloidal CdSe Nanoplatelets: Breaking the “Universal Volume Scaling Law”. *Nano Lett.* **2017**, *17*, 3152-3158.

(28) Grim, J. Q.; Christodoulou, S.; Di Stasio, F.; Krahne, R.; Cingolani, R.; Manna, L.; Moreels, I. Continuous-wave biexciton lasing at room temperature using solution-processed

quantum wells. *Nat. Nanotechnol.* **2014**, *9*, 891-895.

- (29) Klimov, V. I.; Mikhailovsky, A. A.; McBranch, D. W.; Leatherdale, C. A.; Bawendi, M. G. Quantization of multiparticle Auger rates in semiconductor quantum dots. *Science* **2000**, *287*, 1011-1013.
- (30) Guzelturk, B.; Kelestemur, Y.; Olutas, M.; Delikanli, S.; Demir, H. V. Amplified Spontaneous Emission and Lasing in Colloidal Nanoplatelets. *ACS Nano* **2014**, *8*, 6599-6605.
- (31) She, C. X.; Fedin, I.; Dolzhenkov, D. S.; Demortiere, A.; Schaller, R. D.; Pelton, M.; Talapin, D. V. Low-Threshold Stimulated Emission Using Colloidal Quantum Wells. *Nano Lett.* **2014**, *14*, 2772-2777.
- (32) Olutas, M.; Guzelturk, B.; Kelestemur, Y.; Yeltik, A.; Delikanli, S.; Demir, H. V. Lateral Size-Dependent Spontaneous and Stimulated Emission Properties in Colloidal CdSe Nanoplatelets. *ACS Nano* **2015**, *9*, 5041-5050.
- (33) She, C.; Fedin, I.; Dolzhenkov, D. S.; Dahlberg, P. D.; Engel, G. S.; Schaller, R. D.; Talapin, D. V. Red, Yellow, Green, and Blue Amplified Spontaneous Emission and Lasing Using Colloidal CdSe Nanoplatelets. *ACS Nano* **2015**, *9*, 9475-9485.
- (34) Li, Q.; Xu, Z.; McBride, J. R.; Lian, T. Low Threshold Multiexciton Optical Gain in Colloidal CdSe/CdTe Core/Crown Type-II Nanoplatelet Heterostructures. *ACS Nano* **2017**, *11*, 2545-2553.
- (35) Yang, Z.; Pelton, M.; Fedin, I.; Talapin, D. V.; Waks, E. A room temperature continuous-wave nanolaser using colloidal quantum wells. *Nat. Commun.* **2017**, *8*, 143.
- (36) Li, M.; Zhi, M.; Zhu, H.; Wu, W.-Y.; Xu, Q.-H.; Jhon, M. H.; Chan, Y. Ultralow-threshold multiphoton-pumped lasing from colloidal nanoplatelets in solution. **2015**, *6*, 8513.
- (37) Diroll, B. T.; Talapin, D. V.; Schaller, R. D. Violet-to-Blue Gain and Lasing from Colloidal CdS Nanoplatelets: Low-Threshold Stimulated Emission Despite Low Photoluminescence Quantum Yield. *Acs Photonics* **2017**, *4*, 576-583.

- (38) Kelestemur, Y.; Dede, D.; Gungor, K.; Usanmaz, C. F.; Erdem, O.; Demir, H. V. Alloyed Heterostructures of CdSexS1-x Nanoplatelets with Highly Tunable Optical Gain Performance. *Chem. Mat.* **2017**, *29*, 4857-4865.
- (39) Kelestemur, Y.; Guzelurk, B.; Erdem, O.; Olutas, M.; Gungor, K.; Demir, H. V. Platelet-in-Box Colloidal Quantum Wells: CdSe/CdS@CdS Core/Crown@Shell Heteronanoplatelets. *Adv. Funct. Mater.* **2016**, *26*, 3570-3579.
- (40) Pelton, M. Carrier Dynamics, Optical Gain, and Lasing with Colloidal Quantum Wells. *J. Phys. Chem. C* **2018**, *122*, 10659-10674.
- (41) Guzelurk, B.; Pelton, M.; Olutas, M.; Demir, H. V. Giant Modal Gain Coefficients in Colloidal II-VI Nanoplatelets. *Nano Lett.* **2018**, *19*, 277-282.
- (42) Zhukovskyi, M.; Tongying, P.; Yashan, H.; Wang, Y.; Kuno, M. Efficient Photocatalytic Hydrogen Generation from Ni Nanoparticle Decorated CdS Nanosheets. *ACS Catalysis* **2015**, *5*, 6615-6623.
- (43) Li, Q.; Zhao, F.; Qu, C.; Shang, Q.; Xu, Z.; Yu, L.; McBride, J. R.; Lian, T. Two-Dimensional Morphology Enhances Light-Driven H₂ Generation Efficiency in CdS Nanoplatelet-Pt Heterostructures. *J. Am. Chem. Soc.* **2018**, *140*, 11726-11734.
- (44) Li, Q.; Lian, T. Exciton dissociation dynamics and light-driven H₂ generation in colloidal 2D cadmium chalcogenide nanoplatelet heterostructures. *Nano Res.* **2018**, *11*, 3031-3049.
- (45) Aerts, M.; Bielewicz, T.; Klinke, C.; Grozema, F. C.; Houtepen, A. J.; Schins, J. M.; Siebbeles, L. D. A. Highly efficient carrier multiplication in PbS nanosheets. *Nat. Commun.* **2014**, *5*, 3789.
- (46) Kubie, L.; King, L. A.; Kern, M. E.; Murphy, J. R.; Kattel, S.; Yang, Q.; Stecher, J. T.; Rice, W. D.; Parkinson, B. A. Synthesis and Characterization of Ultrathin Silver Sulfide Nanoplatelets. *ACS Nano* **2017**, *11*, 8471-8477.

- (47) Yan, Y.; Crisp, R. W.; Gu, J.; Chernomordik, B. D.; Pach, G. F.; Marshall, Ashley R.; Turner, J. A.; Beard, M. C. Multiple exciton generation for photoelectrochemical hydrogen evolution reactions with quantum yields exceeding 100%. *Nature Energy* **2017**, *2*, 17052.
- (48) Izquierdo, E.; Dufour, M.; Chu, A.; Livache, C.; Martinez, B.; Amelot, D.; Patriarche, G.; Lequeux, N.; Lhuillier, E.; Ithurria, S. Coupled HgSe Colloidal Quantum Wells through a Tunable Barrier: A Strategy To Uncouple Optical and Transport Band Gap. *Chem. Mat.* **2018**.
- (49) Izquierdo, E.; Robin, A.; Keuleyan, S.; Lequeux, N.; Lhuillier, E.; Ithurria, S. Strongly Confined HgTe 2D Nanoplatelets as Narrow Near-Infrared Emitters. *J. Am. Chem. Soc.* **2016**, *138*, 10496-10501.
- (50) Bekenstein, Y.; Koscher, B. A.; Eaton, S. W.; Yang, P.; Alivisatos, A. P. Highly Luminescent Colloidal Nanoplates of Perovskite Cesium Lead Halide and Their Oriented Assemblies. *J. Am. Chem. Soc.* **2015**, *137*, 16008-16011.
- (51) Tyagi, P.; Arveson, S. M.; Tisdale, W. A. Colloidal Organohalide Perovskite Nanoplatelets Exhibiting Quantum Confinement. *J. Phys. Chem. Lett.* **2015**, *6*, 1911-1916.
- (52) Akkerman, Q. A.; Motti, S. G.; Srimath Kandada, A. R.; Mosconi, E.; D'Innocenzo, V.; Bertoni, G.; Marras, S.; Kamino, B. A.; Miranda, L.; De Angelis, F.; Petrozza, A.; Prato, M.; Manna, L. Solution Synthesis Approach to Colloidal Cesium Lead Halide Perovskite Nanoplatelets with Monolayer-Level Thickness Control. *J. Am. Chem. Soc.* **2016**, *138*, 1010-1016.
- (53) Shamsi, J.; Dang, Z.; Bianchini, P.; Canale, C.; Di Stasio, F.; Brescia, R.; Prato, M.; Manna, L. Colloidal Synthesis of Quantum Confined Single Crystal CsPbBr₃ Nanosheets with Lateral Size Control up to the Micrometer Range. *J. Am. Chem. Soc.* **2016**, *138*, 7240-7243.
- (54) Li, J.; Luo, L.; Huang, H.; Ma, C.; Ye, Z.; Zeng, J.; He, H. 2D Behaviors of Excitons in Cesium Lead Halide Perovskite Nanoplatelets. *J. Phys. Chem. Lett.* **2017**, *8*, 1161-1168.
- (55) Xiao, P.; Huang, J.; Yan, D.; Luo, D.; Yuan, J.; Liu, B.; Liang, D. Emergence of

Nanoplatelet Light-Emitting Diodes. *Materials* **2018**, *11*, 1376.

(56) Scholes, G. D.; Rumbles, G. Excitons in nanoscale systems. *Nat. Mater.* **2006**, *5*, 683-696.

(57) Ma, X.; Diroll, B. T.; Cho, W.; Fedin, I.; Schaller, R. D.; Talapin, D. V.; Gray, S. K.; Wiederrecht, G. P.; Gosztola, D. J. Size-Dependent Biexciton Quantum Yields and Carrier Dynamics of Quasi-Two-Dimensional Core/Shell Nanoplatelets. *ACS Nano* **2017**, *11*, 9119-9127.

(58) Feldmann, J.; Peter, G.; Göbel, E. O.; Dawson, P.; Moore, K.; Foxon, C.; Elliott, R. J. Linewidth dependence of radiative exciton lifetimes in quantum wells. *Phys. Rev. Lett.* **1987**, *59*, 2337-2340.

(59) 't Hooft, G. W.; van der Poel, W. A. J. A.; Molenkamp, L. W.; Foxon, C. T. Giant oscillator strength of free excitons in GaAs. *Phys. Rev. B* **1987**, *35*, 8281-8284.

(60) Naeem, A.; Masia, F.; Christodoulou, S.; Moreels, I.; Borri, P.; Langbein, W. Giant exciton oscillator strength and radiatively limited dephasing in two-dimensional platelets. *Phys. Rev. B* **2015**, *91*, 121302.

(61) Benchamekh, R.; Gippius, N. A.; Even, J.; Nestoklon, M. O.; Jancu, J. M.; Ithurria, S.; Dubertret, B.; Efros, A. L.; Voisin, P. Tight-binding calculations of image-charge effects in colloidal nanoscale platelets of CdSe. *Phys. Rev. B* **2014**, *89*, 035307.

(62) Wu, K.; Li, Q.; Du, Y.; Chen, Z.; Lian, T. Ultrafast exciton quenching by energy and electron transfer in colloidal CdSe nanosheet-Pt heterostructures. *Chemical Science* **2015**, *6*, 1049-1054.

(63) Wu, K.; Zhu, H.; Lian, T. Ultrafast Exciton Dynamics and Light-Driven H₂ Evolution in Colloidal Semiconductor Nanorods and Pt-Tipped Nanorods. *Accounts Chem. Res.* **2015**, *48*, 851-859.

(64) Zhao, H.; Moehl, S.; Wachter, S.; Kalt, H. Hot exciton transport in ZnSe quantum wells.

Appl. Phys. Lett. **2002**, *80*, 1391-1393.

(65) Zhao, H.; Moehl, S.; Kalt, H. Coherence length of excitons in a semiconductor quantum well. *Phys. Rev. Lett.* **2002**, *89*, 097401.

(66) Kalt, H.; Zhao, H.; Dal Don, B.; Schwartz, G.; Bradford, C.; Prior, K. Quasi-ballistic transport of excitons in quantum wells. *J. Lumin.* **2005**, *112*, 136-141.

(67) Liu, Y.-H.; Wayman, V. L.; Gibbons, P. C.; Loomis, R. A.; Buhro, W. E. Origin of High Photoluminescence Efficiencies in CdSe Quantum Belts. *Nano Lett.* **2010**, *10*, 352-357.

(68) Li, Q.; Zhou, B.; McBride, J. R.; Lian, T. Efficient Diffusive Transport of Hot and Cold Excitons in Colloidal Type II CdSe/CdTe Core/Crown Nanoplatelet Heterostructures. *ACS Energy Letters* **2017**, *2*, 174-181.

(69) Li, Q.; Wu, K.; Chen, J.; Chen, Z.; McBride, J. R.; Lian, T. Size-Independent Exciton Localization Efficiency in Colloidal CdSe/CdS Core/Crown Nanosheet Type-I Heterostructures. *ACS Nano* **2016**, *10*, 3843-3851.

(70) Wu, K.; Hill, L. J.; Chen, J.; McBride, J. R.; Pavlopolous, N. G.; Richey, N. E.; Pyun, J.; Lian, T. Universal Length Dependence of Rod-to-Seed Exciton Localization Efficiency in Type I and Quasi-Type II CdSe@CdS Nanorods. *ACS Nano* **2015**, *9*, 4591-4599.

(71) Liu, B.; Delikanli, S.; Gao, Y.; Dede, D.; Gungor, K.; Demir, H. V. Nanocrystal light-emitting diodes based on type II nanoplatelets. *Nano Energy* **2018**, *47*, 115-122.

(72) Giovanella, U.; Pasini, M.; Lorenzon, M.; Galeotti, F.; Lucchi, C.; Meinardi, F.; Luzzati, S.; Dubertret, B.; Brovelli, S. Efficient Solution-Processed Nanoplatelet-Based Light-Emitting Diodes with High Operational Stability in Air. *Nano Lett.* **2018**, *18*, 3441-3448.

(73) Vitukhnovsky, A. G.; Lebedev, V. S.; Selyukov, A. S.; Vashchenko, A. A.; Vasiliev, R. B.; Sokolikova, M. S. Electroluminescence from colloidal semiconductor CdSe nanoplatelets in hybrid organic-inorganic light emitting diode. *Chem. Phys. Lett.* **2015**, *619*, 185-188.

(74) Selyukov, A. S.; Vitukhnovskii, A. G.; Lebedev, V. S.; Vashchenko, A. A.; Vasiliev, R.

B.; Sokolikova, M. S. Electroluminescence of colloidal quasi-two-dimensional semiconducting CdSe nanostructures in a hybrid light-emitting diode. *J Exp Theor Phys* **2015**, *120*, 595-606.

(75) Vashchenko, A. A.; Vitukhnovskii, A. G.; Lebedev, V. S.; Selyukov, A. S.; Vasiliev, R. B.; Sokolikova, M. S. Organic light-emitting diode with an emitter based on a planar layer of CdSe semiconductor nanoplatelets. *Jetp Lett* **2014**, *100*, 86-90.

(76) Zhu, H. M.; Song, N. H.; Rodriguez-Cordoba, W.; Lian, T. Q. Wave Function Engineering for Efficient Extraction of up to Nineteen Electrons from One CdSe/CdS Quasi-Type II Quantum Dot. *J. Am. Chem. Soc.* **2012**, *134*, 4250-4257.

(77) Yang, Y.; Rodriguez-Cordoba, W.; Lian, T. Q. Multiple Exciton Generation and Dissociation in PbS Quantum Dot-Electron Acceptor Complexes. *Nano Lett.* **2012**, *12*, 4235-4241.

(78) Zhu, H. M.; Lian, T. Q. Enhanced Multiple Exciton Dissociation from CdSe Quantum Rods: The Effect of Nanocrystal Shape. *J. Am. Chem. Soc.* **2012**, *134*, 11289-11297.

(79) Zhu, H. M.; Yang, Y.; Lian, T. Q. Multiexciton Annihilation and Dissociation in Quantum Confined Semiconductor Nanocrystals. *Accounts Chem. Res.* **2013**, *46*, 1270-1279.

(80) Klimov, V. I. Multicarrier Interactions in Semiconductor Nanocrystals in Relation to the Phenomena of Auger Recombination and Carrier Multiplication. *Annual Review of Condensed Matter Physics* **2014**, *5*, 285-316.

(81) Robel, I.; Gresback, R.; Kortshagen, U.; Schaller, R. D.; Klimov, V. I. Universal Size-Dependent Trend in Auger Recombination in Direct-Gap and Indirect-Gap Semiconductor Nanocrystals. *Phys. Rev. Lett.* **2009**, *102*, 177404.

(82) McGuire, J. A.; Joo, J.; Pietryga, J. M.; Schaller, R. D.; Klimov, V. I. New Aspects of Carrier Multiplication in Semiconductor Nanocrystals. *Accounts Chem. Res.* **2008**, *41*, 1810-1819.

(83) Klimov, V. I.; McGuire, J. A.; Schaller, R. D.; Rupasov, V. I. Scaling of multiexciton

lifetimes in semiconductor nanocrystals. *Phys. Rev. B* **2008**, *77*, 195324.

(84) Klimov, V. I. Spectral and Dynamical Properties of Multiexcitons in Semiconductor Nanocrystals. *Annu. Rev. Phys. Chem.* **2007**, *58*, 635-673.

(85) Barzykin, A. V.; Tachiya, M. Stochastic models of charge carrier dynamics in semiconducting nanosystems. *J Phys-Condens Mat* **2007**, *19*, 065105.

(86) Barzykin, A. V.; Tachiya, M. Stochastic models of carrier dynamics in single-walled carbon nanotubes. *Phys. Rev. B* **2005**, *72*, 075425.

(87) Klimov, V. I.; McBranch, D. W. Auger-process-induced charge separation in semiconductor nanocrystals. *Phys. Rev. B* **1997**, *55*, 13173-13179.

(88) Ghanassi, M.; Schanneklein, M. C.; Hache, F.; Ekimov, A. I.; Ricard, D.; Flytzanis, C. Time-Resolved Measurements of Carrier Recombination in Experimental Semiconductor-Doped Glasses - Confirmation of the Role of Auger Recombination. *Appl. Phys. Lett.* **1993**, *62*, 78-80.

(89) Chepic, D. I.; Efros, A. L.; Ekimov, A. I.; Vanov, M. G.; Kharchenko, V. A.; Kudriavtsev, I. A.; Yazeva, T. V. Auger Ionization of Semiconductor Quantum Drops in a Glass Matrix. *J. Lumin.* **1990**, *47*, 113-127.

(90) Padilha, L. A.; Stewart, J. T.; Sandberg, R. L.; Bae, W. K.; Koh, W.-K.; Pietryga, J. M.; Klimov, V. I. Aspect Ratio Dependence of Auger Recombination and Carrier Multiplication in PbSe Nanorods. *Nano Lett.* **2013**, *13*, 1092-1099.

(91) Rajadell, F.; Climente, J. I.; Planelles, J.; Bertoni, A. Excitons, Biexcitons, and Trions in CdSe Nanorods. *The Journal of Physical Chemistry C* **2009**, *113*, 11268-11272.

(92) Wang, F.; Wu, Y.; Hybertsen, M. S.; Heinz, T. F. Auger recombination of excitons in one-dimensional systems. *Phys. Rev. B* **2006**, *73*, 245424.

(93) Robel, I.; Bunker, B. A.; Kamat, P. V.; Kuno, M. Exciton Recombination Dynamics in CdSe Nanowires: Bimolecular to Three-Carrier Auger Kinetics. *Nano Lett.* **2006**, *6*, 1344-1349.

- (94) Pelton, M.; Andrews, J. J.; Fedin, I.; Talapin, D. V.; Leng, H.; O’Leary, S. K. Nonmonotonic Dependence of Auger Recombination Rate on Shell Thickness for CdSe/CdS Core/Shell Nanoplatelets. *Nano Lett.* **2017**, *17*, 6900-6906.
- (95) Baghani, E.; O’Leary, S. K.; Fedin, I.; Talapin, D. V.; Pelton, M. Auger-Limited Carrier Recombination and Relaxation in CdSe Colloidal Quantum Wells. *J. Phys. Chem. Lett.* **2015**, *6*, 1032-1036.
- (96) Robel, I.; Gresback, R.; Kortshagen, U.; Schaller, R. D.; Klimov, V. I. Universal Size-Dependent Trend in Auger Recombination in Direct-Gap and Indirect-Gap Semiconductor Nanocrystals. *Phys. Rev. Lett.* **2009**, *102*, 177404.
- (97) Padilha, L. A.; Stewart, J. T.; Sandberg, R. L.; Bae, W. K.; Koh, W. K.; Pietryga, J. M.; Klimov, V. I. Carrier Multiplication in Semiconductor Nanocrystals: Influence of Size, Shape, and Composition. *Accounts Chem. Res.* **2013**, *46*, 1261-1269.
- (98) Schaller, R. D.; Klimov, V. I. High efficiency carrier multiplication in PbSe nanocrystals: Implications for solar energy conversion. *Phys. Rev. Lett.* **2004**, *92*, 186601.
- (99) Schaller, R. D.; Pietryga, J. M.; Klimov, V. I. Carrier multiplication in InAs nanocrystal quantum dots with an onset defined by the energy conservation limit. *Nano Lett.* **2007**, *7*, 3469-3476.
- (100) Li, Y.; Ding, T.; Luo, X.; Chen, Z.; Liu, X.; Lu, X.; Wu, K. Biexciton Auger recombination in mono-dispersed, quantum-confined CsPbBr₃ perovskite nanocrystals obeys universal volume-scaling. *Nano Res.* **2019**, *12*, 619-623.
- (101) Gratzel, M. Photoelectrochemical cells. *Nature* **2001**, *414*, 338-344.
- (102) Wu, K.; Lian, T. Quantum confined colloidal nanorod heterostructures for solar-to-fuel conversion. *Chem. Soc. Rev.* **2016**, *45*, 3781-3810.
- (103) Wu, K.; Chen, Z.; Lv, H.; Zhu, H.; Hill, C. L.; Lian, T. Hole Removal Rate Limits Photodriven H₂ Generation Efficiency in CdS-Pt and CdSe/CdS-Pt Semiconductor Nanorod–

Metal Tip Heterostructures. *J. Am. Chem. Soc.* **2014**, *136*, 7708-7716.

(104) Zhu, H. M.; Song, N. H.; Lv, H. J.; Hill, C. L.; Lian, T. Q. Near Unity Quantum Yield of Light-Driven Redox Mediator Reduction and Efficient H₂ Generation Using Colloidal Nanorod Heterostructures. *J. Am. Chem. Soc.* **2012**, *134*, 11701-11708.

(105) Li, Q.; Lian, T. Ultrafast Charge Separation in Two-Dimensional CsPbBr₃ Perovskite Nanoplatelets. *J. Phys. Chem. Lett.* **2019**, *10*, 566-573.

(106) Li, Z.; Qin, H.; Guzun, D.; Benamara, M.; Salamo, G.; Peng, X. Uniform thickness and colloidal-stable CdS quantum disks with tunable thickness: Synthesis and properties. *Nano Res.* **2012**, *5*, 337-351.

(107) Tessier, M. D.; Spinicelli, P.; Dupont, D.; Patriarche, G.; Ithurria, S.; Dubertret, B. Efficient Exciton Concentrators Built from Colloidal Core/Crown CdSe/CdS Semiconductor Nanoplatelets. *Nano Lett.* **2014**, *14*, 207-213.

(108) Prudnikau, A.; Chuvilin, A.; Artemyev, M. CdSe-CdS Nanoheteroplatelets With Efficient Photoexcitation of Central CdSe Region through Epitaxially Grown CdS Wings. *J. Am. Chem. Soc.* **2013**, *135*, 14476-14479.

(109) Wu, K.; Li, Q.; Jia, Y.; McBride, J. R.; Xie, Z.-x.; Lian, T. Efficient and Ultrafast Formation of Long-Lived Charge-Transfer Exciton State in Atomically Thin Cadmium Selenide/Cadmium Telluride Type-II Heteronanoshells. *ACS Nano* **2015**, *9*, 961-968.

(110) Wu, K. F.; Zhu, H. M.; Liu, Z.; Rodriguez-Cordoba, W.; Lian, T. Q. Ultrafast Charge Separation and Long-Lived Charge Separated State in Photocatalytic CdS-Pt Nanorod Heterostructures. *J. Am. Chem. Soc.* **2012**, *134*, 10337-10340.

(111) Müller, J.; Lupton, J. M.; Lagoudakis, P. G.; Schindler, F.; Koeppe, R.; Rogach, A. L.; Feldmann, J.; Talapin, D. V.; Weller, H. Wave Function Engineering in Elongated Semiconductor Nanocrystals with Heterogeneous Carrier Confinement. *Nano Lett.* **2005**, *5*, 2044-2049.

- (112) Acharya, K. P.; Khnayzer, R. S.; O'Connor, T.; Diederich, G.; Kirsanova, M.; Klinkova, A.; Roth, D.; Kinder, E.; Imboden, M.; Zamkov, M. The Role of Hole Localization in Sacrificial Hydrogen Production by Semiconductor–Metal Heterostructured Nanocrystals. *Nano Lett.* **2011**, *11*, 2919-2926.
- (113) Amirav, L.; Alivisatos, A. P. Photocatalytic Hydrogen Production with Tunable Nanorod Heterostructures. *J. Phys. Chem. Lett.* **2010**, *1*, 1051-1054.
- (114) Simon, T.; Bouchonville, N.; Berr, M. J.; Vaneski, A.; Adrović, A.; Volbers, D.; Wyrwich, R.; Döblinger, M.; Susha, A. S.; Rogach, A. L.; Jäckel, F.; Stolarczyk, J. K.; Feldmann, J. Redox shuttle mechanism enhances photocatalytic H₂ generation on Ni-decorated CdS nanorods. *Nat Mater* **2014**, *13*, 1013-1018.
- (115) Zhao, J.; Holmes, M. A.; Osterloh, F. E. Quantum Confinement Controls Photocatalysis: A Free Energy Analysis for Photocatalytic Proton Reduction at CdSe Nanocrystals. *ACS Nano* **2013**, *7*, 4316-4325.
- (116) Brus, L. E. Electron--electron and electron-hole interactions in small semiconductor crystallites: The size dependence of the lowest excited electronic state. *J. Chem. Phys.* **1984**, *80*, 4403-4409.
- (117) Brus, L. E. A simple model for the ionization potential, electron affinity, and aqueous redox potentials of small semiconductor crystallites. *J. Chem. Phys.* **1983**, *79*, 5566-5571.
- (118) Markus, T. Z.; Wu, M.; Wang, L.; Waldeck, D. H.; Oron, D.; Naaman, R. Electronic Structure of CdSe Nanoparticles Adsorbed on Au Electrodes by an Organic Linker: Fermi Level Pinning of the HOMO. *J. Phys. Chem. C* **2009**, *113*, 14200-14206.
- (119) Pandey, A.; Guyot-Sionnest, P. Intraband spectroscopy and band offsets of colloidal II-VI core/shell structures. *J. Chem. Phys.* **2007**, *127*, 104710.
- (120) Nagoya, A.; Asahi, R.; Kresse, G. First-principles study of Cu₂ZnSnS₄ and the related band offsets for photovoltaic applications. *Journal of Physics: Condensed Matter* **2011**, *23*,

404203.

- (121) Nirmal, M.; Murray, C. B.; Bawendi, M. G. FLUORESCENCE-LINE NARROWING IN CDSE QUANTUM DOTS - SURFACE LOCALIZATION OF THE PHOTOGENERATED EXCITON. *Phys. Rev. B* **1994**, *50*, 2293-2300.
- (122) Norris, D. J.; Bawendi, M. G. Measurement and assignment of the size-dependent optical spectrum in CdSe quantum dots. *Phys. Rev. B* **1996**, *53*, 16338-16346.
- (123) Peng, X. G.; Manna, L.; Yang, W. D.; Wickham, J.; Scher, E.; Kadavanich, A.; Alivisatos, A. P. Shape control of CdSe nanocrystals. *Nature* **2000**, *404*, 59-61.
- (124) Leatherdale, C. A.; Woo, W. K.; Mikulec, F. V.; Bawendi, M. G. On the Absorption Cross Section of CdSe Nanocrystal Quantum Dots. *J. Phys. Chem. B* **2002**, *106*, 7619-7622.
- (125) Kim, S.; Fisher, B.; Eisler, H.-J.; Bawendi, M. Type-II Quantum Dots: CdTe/CdSe(Core/Shell) and CdSe/ZnTe(Core/Shell) Heterostructures. *J. Am. Chem. Soc.* **2003**, *125*, 11466-11467.
- (126) Kumar, S.; Jones, M.; Lo, S. S.; Scholes, G. D. Nanorod Heterostructures Showing Photoinduced Charge Separation. *Small* **2007**, *3*, 1633-1639.
- (127) Li, L.-s.; Hu, J.; Yang, W.; Alivisatos, A. P. Band Gap Variation of Size- and Shape-Controlled Colloidal CdSe Quantum Rods. *Nano Lett.* **2001**, *1*, 349-351.
- (128) Hu, J.; Wang; Li, L.-s.; Yang, W.; Alivisatos, A. P. Semiempirical Pseudopotential Calculation of Electronic States of CdSe Quantum Rods. *J. Phys. Chem. B* **2002**, *106*, 2447-2452.
- (129) Kan, S.; Mokari, T.; Rothenberg, E.; Banin, U. Synthesis and size-dependent properties of zinc-blende semiconductor quantum rods. *Nat Mater* **2003**, *2*, 155-158.
- (130) Meinardi, F.; Colombo, A.; Velizhanin, K. A.; Simonutti, R.; Lorenzon, M.; Beverina, L.; Viswanatha, R.; Klimov, V. I.; Brovelli, S. Large-area luminescent solar concentrators based on 'Stokes-shift-engineered' nanocrystals in a mass-polymerized PMMA matrix. *Nat Photonics*

2014, *8*, 392-399.

(131) Coropceanu, I.; Bawendi, M. G. Core/Shell Quantum Dot Based Luminescent Solar Concentrators with Reduced Reabsorption and Enhanced Efficiency. *Nano Lett.* **2014**, *14*, 4097-4101.

(132) Erickson, C. S.; Bradshaw, L. R.; McDowall, S.; Gilbertson, J. D.; Gamelin, D. R.; Patrick, D. L. Zero-Reabsorption Doped-Nanocrystal Luminescent Solar Concentrators. *ACS Nano* **2014**, *8*, 3461-3467.

(133) Bradshaw, L. R.; Knowles, K. E.; McDowall, S.; Gamelin, D. R. Nanocrystals for Luminescent Solar Concentrators. *Nano Lett.* **2015**, *15*, 1315-1323.

(134) Bomm, J.; Buchtemann, A.; Fiore, A.; Manna, L.; Nelson, J. H.; Hill, D.; van Sark, W. G. J. H. M. Fabrication and spectroscopic studies on highly luminescent CdSe/CdS nanorod polymer composites. *Beilstein J Nanotech* **2010**, *1*, 94-100.

(135) Bronstein, N. D.; Li, L.; Xu, L.; Yao, Y.; Ferry, V. E.; Alivisatos, A. P.; Nuzzo, R. G. Luminescent Solar Concentration with Semiconductor Nanorods and Transfer-Printed Micro-Silicon Solar Cells. *ACS Nano* **2014**, *8*, 44-53.

(136) Hines, M. A.; Guyot-Sionnest, P. Synthesis and Characterization of Strongly Luminescing ZnS-Capped CdSe Nanocrystals. *J. Phys. Chem.* **1996**, *100*, 468-471.

(137) Dabbousi, B. O.; Rodriguez-Viejo, J.; Mikulec, F. V.; Heine, J. R.; Mattoussi, H.; Ober, R.; Jensen, K. F.; Bawendi, M. G. (CdSe)ZnS Core-Shell Quantum Dots: Synthesis and Characterization of a Size Series of Highly Luminescent Nanocrystallites. *J. Phys. Chem. B* **1997**, *101*, 9463-9475.

(138) Luo, Y.; Wang, L.-W. Electronic Structures of the CdSe/CdS Core-Shell Nanorods. *ACS Nano* **2009**, *4*, 91-98.

(139) Zhu, H. M.; Song, N. H.; Lian, T. Q. Controlling Charge Separation and Recombination Rates in CdSe/ZnS Type I Core-Shell Quantum Dots by Shell Thicknesses. *J. Am. Chem. Soc.*

2010, *132*, 15038-15045.

(140) Wu, K. F.; Rodriguez-Cordoba, W. E.; Liu, Z.; Zhu, H. M.; Lian, T. Q. Beyond Band Alignment: Hole Localization Driven Formation of Three Spatially Separated Long-Lived Exciton States in CdSe/CdS Nanorods. *ACS Nano* **2013**, *7*, 7173-7185.

(141) She, C.; Bryant, G. W.; Demortière, A.; Shevchenko, E. V.; Pelton, M. Controlling the spatial location of photoexcited electrons in semiconductor CdSe/CdS core/shell nanorods. *Phys. Rev. B* **2013**, *87*, 155427.

(142) Kunneman, L. T.; Zanella, M.; Manna, L.; Siebbeles, L. D. A.; Schins, J. M. Mobility and Spatial Distribution of Photoexcited Electrons in CdSe/CdS Nanorods. *J. Phys. Chem. C* **2013**, *117*, 3146-3151.

(143) Mahler, B.; Nadal, B.; Bouet, C.; Patriarche, G.; Dubertret, B. Core/Shell Colloidal Semiconductor Nanoplatelets. *J. Am. Chem. Soc.* **2012**, *134*, 18591-18598.

(144) Kumagai, M.; Takagahara, T. Excitonic and nonlinear-optical properties of dielectric quantum-well structures. *Phys. Rev. B* **1989**, *40*, 12359-12381.

(145) Achtstein, A. W.; Schliwa, A.; Prudnikau, A.; Hardzei, M.; Artemyev, M. V.; Thomsen, C.; Woggon, U. Electronic Structure and Exciton-Phonon Interaction in Two-Dimensional Colloidal CdSe Nanosheets. *Nano Lett.* **2012**, *12*, 3151-3157.

(146) Grim, J. Q.; Christodoulou, S.; Di Stasio, F.; Krahne, R.; Cingolani, R.; Manna, L.; Moreels, I. Continuous-wave biexciton lasing at room temperature using solution-processed quantum wells. *Nat Nano* **2014**, *9*, 891-895.

(147) Wu, K.; Li, Q.; Jia, Y.; McBride, J. R.; Xie, Z.-x.; Lian, T. Efficient and Ultrafast Formation of Long-Lived Charge-Transfer Exciton State in Atomically Thin Cadmium Selenide/Cadmium Telluride Type-II Heteronanosheets. *ACS Nano* **2015**, *9*, 961-968.

(148) Klimov, V. I. Optical Nonlinearities and Ultrafast Carrier Dynamics in Semiconductor Nanocrystals. *J. Phys. Chem. B* **2000**, *104*, 6112-6123.

- (149) Huang, J.; Stockwell, D.; Huang, Z. Q.; Mohler, D. L.; Lian, T. Q. Photoinduced ultrafast electron transfer from CdSe quantum dots to re-bipyridyl complexes. *J. Am. Chem. Soc.* **2008**, *130*, 5632-5633.
- (150) Tessier, M. D.; Mahler, B.; Nadal, B.; Heuclin, H.; Pedetti, S.; Dubertret, B. Spectroscopy of Colloidal Semiconductor Core/Shell Nanoplatelets with High Quantum Yield. *Nano Lett.* **2013**, *13*, 3321-3328.
- (151) Kunneman, L. T.; Schins, J. M.; Pedetti, S.; Heuclin, H.; Grozema, F. C.; Houtepen, A. J.; Dubertret, B.; Siebbeles, L. D. A. Nature and Decay Pathways of Photoexcited States in CdSe and CdSe/CdS Nanoplatelets. *Nano Lett.* **2014**, *14*, 7039-7045.
- (152) Biadala, L.; Liu, F.; Tessier, M. D.; Yakovlev, D. R.; Dubertret, B.; Bayer, M. Recombination Dynamics of Band Edge Excitons in Quasi-Two-Dimensional CdSe Nanoplatelets. *Nano Lett.* **2014**, *14*, 1134-1139.
- (153) Schmitt-Rink, S.; Chemla, D. S.; Miller, D. A. B. Theory of transient excitonic optical nonlinearities in semiconductor quantum-well structures. *Phys. Rev. B* **1985**, *32*, 6601-6609.
- (154) Shinada, M.; Sugano, S. Interband Optical Transitions in Extremely Anisotropic Semiconductors .I. Bound and Unbound Exciton Absorption. *J Phys Soc Jpn* **1966**, *21*, 1936-1946.
- (155) Pedetti, S.; Ithurria, S.; Heuclin, H.; Patriarche, G.; Dubertret, B. Type-II CdSe/CdTe Core/Crown Semiconductor Nanoplatelets. *J. Am. Chem. Soc.* **2014**, *136*, 16430-16438.
- (156) Borys, N. J.; Walter, M. J.; Huang, J.; Talapin, D. V.; Lupton, J. M. The Role of Particle Morphology in Interfacial Energy Transfer in CdSe/CdS Heterostructure Nanocrystals. *Science* **2010**, *330*, 1371-1374.
- (157) Garcia-Santamaria, F.; Chen, Y. F.; Vela, J.; Schaller, R. D.; Hollingsworth, J. A.; Klimov, V. I. Suppressed Auger Recombination in "Giant" Nanocrystals Boosts Optical Gain Performance. *Nano Lett.* **2009**, *9*, 3482-3488.

- (158) Brovelli, S.; Schaller, R. D.; Crooker, S. A.; García-Santamaría, F.; Chen, Y.; Viswanatha, R.; Hollingsworth, J. A.; Htoon, H.; Klimov, V. I. Nano-engineered Electron–hole Exchange Interaction Controls Exciton Dynamics in Core–Shell Semiconductor Nanocrystals. *Nat Commun* **2011**, *2*, 280.
- (159) Yang, Y.; Liu, Z.; Lian, T. Q. Bulk Transport and Interfacial Transfer Dynamics of Photogenerated Carriers in CdSe Quantum Dot Solid Electrodes. *Nano Lett.* **2013**, *13*, 3678-3683.
- (160) Warman, J. M.; De Haas, M. P.; Van Hovell tot Westerflier, S. W. F. M.; Binsma, J. J. M.; Kolar, Z. I. Electronic processes in semiconductor materials studied by nanosecond time-resolved microwave conductivity. 1. Cadmium sulfide macroscopic crystal. *J. Phys. Chem.* **1989**, *93*, 5895-5899.
- (161) Spear, W. E.; Mort, J. Electron and Hole Transport in CdS Crystals. *Proceedings of the Physical Society* **1963**, *81*, 130.
- (162) Mort, J.; Spear, W. E. Hole Drift Mobility and Lifetime in CdS Crystals. *Phys. Rev. Lett.* **1962**, *8*, 314-315.
- (163) Pelton, M.; Ithurria, S.; Schaller, R. D.; Dolzhenkov, D. S.; Talapin, D. V. Carrier Cooling in Colloidal Quantum Wells. *Nano Lett.* **2012**, *12*, 6158-6163.
- (164) Tessier, M. D.; Biadala, L.; Bouet, C.; Ithurria, S.; Abecassis, B.; Dubertret, B. Phonon Line Emission Revealed by Self-Assembly of Colloidal Nanoplatelets. *ACS Nano* **2013**, *7*, 3332-3340.
- (165) Tessier, M. D.; Spinicelli, P.; Dupont, D.; Patriarche, G.; Ithurria, S.; Dubertret, B. Efficient Exciton Concentrators Built from Colloidal Core/Crown CdSe/CdS Semiconductor Nanoplatelets. *Nano Lett.* **2014**, *14*, 207-213.
- (166) Guzelturk, B.; Erdem, O.; Olutas, M.; Kelestemur, Y.; Demir, H. V. Stacking in Colloidal Nanoplatelets: Tuning Excitonic Properties. *ACS Nano* **2014**, *8*, 12524-12533.

- (167) Chen, Z.; Nadal, B.; Mahler, B.; Aubin, H.; Dubertret, B. Quasi-2D Colloidal Semiconductor Nanoplatelets for Narrow Electroluminescence. *Adv. Funct. Mater.* **2014**, *24*, 295-302.
- (168) Lhuillier, E.; Robin, A.; Ithurria, S.; Aubin, H.; Dubertret, B. Electrolyte-Gated Colloidal Nanoplatelets-Based Phototransistor and Its Use for Bicolor Detection. *Nano Lett.* **2014**, *14*, 2715-2719.
- (169) Lhuillier, E.; Pedetti, S.; Ithurria, S.; Heuclin, H.; Nadal, B.; Robin, A.; Patriarche, G.; Lequeux, N.; Dubertret, B. Electrolyte-Gated Field Effect Transistor to Probe the Surface Defects and Morphology in Films of Thick CdSe Colloidal Nanoplatelets. *ACS Nano* **2014**, *8*, 3813-3820.
- (170) Geim, A. K.; Grigorieva, I. V. Van der Waals heterostructures. *Nature* **2013**, *499*, 419-425.
- (171) Hong, X.; Kim, J.; Shi, S.-F.; Zhang, Y.; Jin, C.; Sun, Y.; Tongay, S.; Wu, J.; Zhang, Y.; Wang, F. Ultrafast charge transfer in atomically thin MoS₂/WS₂ heterostructures. *Nat Nano* **2014**, *9*, 682-686.
- (172) Ithurria, S.; Tessier, M. D.; Mahler, B.; Lobo, R. P. S. M.; Dubertret, B.; Efros, A. L. Colloidal nanoplatelets with two-dimensional electronic structure. *Nat Mater* **2011**, *10*, 936-941.
- (173) Kim, S.; Fisher, B.; Eisler, H.-J.; Bawendi, M. Type-II Quantum Dots: CdTe/CdSe(Core/Shell) and CdSe/ZnTe(Core/Shell) Heterostructures. *J. Am. Chem. Soc.* **2003**, *125*, 11466-11467.
- (174) Peng, P.; Milliron, D. J.; Hughes, S. M.; Johnson, J. C.; Alivisatos, A. P.; Saykally, R. J. Femtosecond spectroscopy of carrier relaxation dynamics in type II CdSe/CdTe tetrapod heteronanostructures. *Nano Lett.* **2005**, *5*, 1809-1813.
- (175) Jones, M.; Kumar, S.; Lo, S. S.; Scholes, G. D. Exciton Trapping and Recombination

in Type II CdSe/CdTe Nanorod Heterostructures. *Journal of Physical Chemistry C* **2008**, *112*, 5423-5431.

(176) Hewa-Kasakarage, N. N.; El-Khoury, P. Z.; Tarnovsky, A. N.; Kirsanova, M.; Nemitz, I.; Nemchinov, A.; Zamkov, M. Ultrafast Carrier Dynamics in Type II ZnSe/CdS/ZnSe Nanobarbells. *ACS Nano* **2010**, *4*, 1837-1844.

(177) Zhu, H.; Song, N.; Lian, T. Wave Function Engineering for Ultrafast Charge Separation and Slow Charge Recombination in Type II Core/Shell Quantum Dots. *J. Am. Chem. Soc.* **2011**, *133*, 8762-8771.

(178) Ivanov, S. A.; Piryatinski, A.; Nanda, J.; Tretiak, S.; Zavadil, K. R.; Wallace, W. O.; Werder, D.; Klimov, V. I. Type-II Core/Shell CdS/ZnSe Nanocrystals: Synthesis, Electronic Structures, and Spectroscopic Properties. *J Am Chem Soc* **2007**, *129*, 11708.

(179) Zhu, H.; Yang, Y.; Lian, T. Multiexciton Annihilation and Dissociation in Quantum Confined Semiconductor Nanocrystals. *Accounts Chem Res* **2013**, *46*, 1270-1279.

(180) Zhu, H.; Lian, T. Wavefunction engineering in quantum confined semiconductor nanoheterostructures for efficient charge separation and solar energy conversion. *Energy Environ. Sci.* **2012**, *5*, 9406-9418.

(181) Antanovich, A. V.; Prudnikau, A. V.; Melnikau, D.; Rakovich, Y. P.; Chuvilin, A.; Woggon, U.; Achtstein, A. W.; Artemyev, M. V. Colloidal synthesis and optical properties of type-II CdSe-CdTe and inverted CdTe-CdSe core-wing heteronano-platelets. *Nanoscale* **2015**, *7*, 8084-8092.

(182) Liu, Y.-H.; Wayman, V. L.; Gibbons, P. C.; Loomis, R. A.; Buhro, W. E. Origin of High Photoluminescence Efficiencies in CdSe Quantum Belts. *Nano Lett.* **2009**, *10*, 352-357.

(183) Huang, J. E.; Huang, Z. Q.; Jin, S. Y.; Lian, T. Q. Exciton Dissociation in CdSe Quantum Dots by Hole Transfer to Phenothiazine. *J. Phys. Chem. C* **2008**, *112*, 19734-19738.

(184) Strzalkowski, I.; Joshi, S.; Crowell, C. R. Dielectric constant and its temperature

dependence for GaAs, CdTe, and ZnSe. *Appl. Phys. Lett.* **1976**, *28*, 350-352.

(185) Sellin, P. J.; Davies, A. W.; Lohstroh, A.; Ozsan, M. E.; Parkin, J. Drift mobility and mobility-lifetime products in CdTe:Cl grown by the travelling heater method. *IEEE Transactions on Nuclear Science* **2005**, *52*, 3074-3078.

(186) Suzuki, K.; Seto, S.; Sawada, T.; Imai, K. In *Carrier transport properties of HPB CdZnTe and THM CdTe:Cl*, Nuclear Science Symposium Conference Record, 2001 IEEE, 2001; 2001; pp 2391-2395.

(187) Long, Q.; Dinca, S. A.; Schiff, E. A.; Yu, M.; Theil, J. Electron and hole drift mobility measurements on thin film CdTe solar cells. *Appl. Phys. Lett.* **2014**, *105*, 042106.

(188) Portella-Oberli, M. T.; Ciulin, V.; Haacke, S.; Ganière, J. D.; Kossacki, P.; Kutrowski, M.; Wojtowicz, T.; Deveaud, B. Diffusion, localization, and dephasing of trions and excitons in CdTe quantum wells. *Phys. Rev. B* **2002**, *66*, 155305.

(189) Rawalekar, S.; Kaniyankandy, S.; Verma, S.; Ghosh, H. N. Effect of Surface States on Charge-Transfer Dynamics in Type II CdTe/ZnTe Core–Shell Quantum Dots: A Femtosecond Transient Absorption Study. *J. Phys. Chem. C* **2011**, *115*, 12335-12342.

(190) Chuang, C. H.; Lo, S. S.; Scholes, G. D.; Burda, C. Charge Separation and Recombination in CdTe/CdSe Core/Shell Nanocrystals as a Function of Shell Coverage: Probing the Onset of the Quasi Type-II Regime. *J. Phys. Chem. Lett.* **2010**, *1*, 2530-2535.

(191) Zhao, H.; Moehl, S.; Kalt, H. Coherence Length of Excitons in a Semiconductor Quantum Well. *Phys. Rev. Lett.* **2002**, *89*, 097401.

(192) Zhao, H.; Dal Don, B.; Moehl, S.; Kalt, H.; Ohkawa, K.; Hommel, D. Spatiotemporal dynamics of quantum-well excitons. *Phys. Rev. B* **2003**, *67*, 035306.

(193) Kalt, H.; Zhao, H.; Don, B. D.; Schwartz, G.; Bradford, C.; Prior, K. Quasi-ballistic transport of excitons in quantum wells. *J. Lumin.* **2005**, *112*, 136-141.

(194) Wei, S.-H.; Zunger, A. Calculated natural band offsets of all II--VI and III--V

semiconductors: Chemical trends and the role of cation d orbitals. *Appl. Phys. Lett.* **1998**, *72*, 2011-2013.

(195) Zhu, H. M.; Song, N. H.; Lian, T. Q. Wave Function Engineering for Ultrafast Charge Separation and Slow Charge Recombination in Type II Core/Shell Quantum Dots. *J. Am. Chem. Soc.* **2011**, *133*, 8762-8771.

(196) Peng, X.; Schlamp, M. C.; Kadavanich, A. V.; Alivisatos, A. P. Epitaxial Growth of Highly Luminescent CdSe/CdS Core/Shell Nanocrystals with Photostability and Electronic Accessibility. *J. Am. Chem. Soc.* **1997**, *119*, 7019-7029.

(197) Park, Y.-S.; Bae, W. K.; Baker, T.; Lim, J.; Klimov, V. I. Effect of Auger Recombination on Lasing in Heterostructured Quantum Dots with Engineered Core/Shell Interfaces. *Nano Lett.* **2015**, *15*, 7319-7328.

(198) Htoon, H.; Hollingsworth, J. A.; Dickerson, R.; Klimov, V. I. Effect of Zero- to One-Dimensional Transformation on Multiparticle Auger Recombination in Semiconductor Quantum Rods. *Phys. Rev. Lett.* **2003**, *91*, 227401.

(199) Schaller, R. D.; Klimov, V. I. High Efficiency Carrier Multiplication in PbSe Nanocrystals: Implications for Solar Energy Conversion. *Phys. Rev. Lett.* **2004**, *92*, 186601.

(200) Schaller, R. D.; Sykora, M.; Pietryga, J. M.; Klimov, V. I. Seven Excitons at a Cost of One: Redefining the Limits for Conversion Efficiency of Photons into Charge Carriers. *Nano Lett.* **2006**, *6*, 424-429.

(201) Cirloganu, C. M.; Padilha, L. A.; Lin, Q.; Makarov, N. S.; Velizhanin, K. A.; Luo, H.; Robel, I.; Pietryga, J. M.; Klimov, V. I. Enhanced carrier multiplication in engineered quasi-type-II quantum dots. *Nat Commun* **2014**, *5*, 4148.

(202) Dyakonov, M. I.; Kachorovskii, V. Y. Nonthreshold Auger recombination in quantum wells. *Phys. Rev. B* **1994**, *49*, 17130-17138.

(203) Taylor, R. I.; Abram, R. A.; Burt, M. G.; Smith, C. A detailed study of Auger

recombination in 1.3 μm InGaAsP/InP quantum wells and quantum well wires. *Semicond Sci Tech* **1990**, *5*, 90.

(204) Park, Y.-S.; Bae, W. K.; Pietryga, J. M.; Klimov, V. I. Auger Recombination of Biexcitons and Negative and Positive Trions in Individual Quantum Dots. *ACS Nano* **2014**, *8*, 7288-7296.

(205) Cohn, A. W.; Rinehart, J. D.; Schimpf, A. M.; Weaver, A. L.; Gamelin, D. R. Size Dependence of Negative Trion Auger Recombination in Photodoped CdSe Nanocrystals. *Nano Lett.* **2014**, *14*, 353-358.

(206) Kovalev, D.; Heckler, H.; Ben-Chorin, M.; Polisski, G.; Schwartzkopff, M.; Koch, F. Breakdown of the k-conservation rule in Si nanocrystals. *Phys. Rev. Lett.* **1998**, *81*, 2803-2806.

(207) Hybertsen, M. S. Absorption and Emission of Light in Nanoscale Silicon Structures. *Phys. Rev. Lett.* **1994**, *72*, 1514-1517.

(208) Sykora, M.; Mangolini, L.; Schaller, R. D.; Kortshagen, U.; Jurbergs, D.; Klimov, V. I. Size-dependent intrinsic radiative decay rates of silicon nanocrystals at large confinement energies. *Phys. Rev. Lett.* **2008**, *100*, 067401.

(209) Vaxenburg, R.; Rodina, A.; Shabaev, A.; Lifshitz, E.; Efros, A. L. Nonradiative Auger Recombination in Semiconductor Nanocrystals. *Nano Lett.* **2015**, *15*, 2092-2098.

(210) Vaxenburg, R.; Lifshitz, E.; Efros, A. Suppression of Auger-stimulated efficiency droop in nitride-based light emitting diodes. *Appl. Phys. Lett.* **2013**, *102*, 031120.

(211) Climente, J. I.; Movilla, J. L.; Planelles, J. Auger Recombination Suppression in Nanocrystals with Asymmetric Electron-Hole Confinement. *Small* **2012**, *8*, 754-759.

(212) Cragg, G. E.; Efros, A. L. Suppression of Auger Processes in Confined Structures. *Nano Lett.* **2010**, *10*, 313-317.

(213) Efros, A. L.; Nesbitt, D. J. Origin and control of blinking in quantum dots. *Nat Nano* **2016**, *11*, 661-671.

- (214) Bae, W. K.; Padilha, L. A.; Park, Y.-S.; McDaniel, H.; Robel, I.; Pietryga, J. M.; Klimov, V. I. Controlled Alloying of the Core–Shell Interface in CdSe/CdS Quantum Dots for Suppression of Auger Recombination. *ACS Nano* **2013**, *7*, 3411-3419.
- (215) Wang, X.; Ren, X.; Kahen, K.; Hahn, M. A.; Rajeswaran, M.; Maccagnano-Zacher, S.; Silcox, J.; Cragg, G. E.; Efros, A. L.; Krauss, T. D. Non-blinking semiconductor nanocrystals. *Nature* **2009**, *459*, 686-689.
- (216) Beane, G. A.; Gong, K.; Kelley, D. F. Auger and Carrier Trapping Dynamics in Core/Shell Quantum Dots Having Sharp and Alloyed Interfaces. *ACS Nano* **2016**, *10*, 3755-3765.
- (217) Makarov, N. S.; Guo, S.; Isaienko, O.; Liu, W.; Robel, I.; Klimov, V. I. Spectral and Dynamical Properties of Single Excitons, Biexcitons, and Trions in Cesium–Lead-Halide Perovskite Quantum Dots. *Nano Lett.* **2016**, *16*, 2349-2362.
- (218) Li, Q.; Wu, K.; Chen, J.; Chen, Z.; McBride, J. R.; Lian, T. Size-Independent Exciton Localization Efficiency in Colloidal CdSe/CdS Core/Crown Nanosheet Type-I Heterostructures. *ACS Nano* **2016**, *10*, 3843-3851.
- (219) Atkins, P. Physical Chemistry: Sixth Edition. *Physical Chemistry: Sixth Edition*, W.H. Freeman and Company. **2000**.
- (220) Atkins, P.; Paula, J. d. Physical Chemistry for the Life Sciences. *Physical Chemistry for the Life Sciences.*, W.H. Freeman and Company. **2006**.
- (221) Ithurria, S.; Talapin, D. V. Colloidal Atomic Layer Deposition (c-ALD) using Self-Limiting Reactions at Nanocrystal Surface Coupled to Phase Transfer between Polar and Nonpolar Media. *J. Am. Chem. Soc.* **2012**, *134*, 18585-18590.
- (222) Delikanli, S.; Guzelurk, B.; Hernández-Martínez, P. L.; Erdem, T.; Kelestemur, Y.; Olutas, M.; Akgul, M. Z.; Demir, H. V. Continuously Tunable Emission in Inverted Type-I CdS/CdSe Core/Crown Semiconductor Nanoplatelets. *Adv. Funct. Mater.* **2015**, *25*, 4282-4289.

- (223) Achtstein, A. W.; Scott, R.; Kickhöfel, S.; Jagsch, S. T.; Christodoulou, S.; Bertrand, G. H. V.; Prudnikau, A. V.; Antanovich, A.; Artemyev, M.; Moreels, I.; Schliwa, A.; Woggon, U. π -State Luminescence in CdSe Nanoplatelets: Role of Lateral Confinement and a Longitudinal Optical Phonon Bottleneck. *Phys. Rev. Lett.* **2016**, *116*, 116802.
- (224) Chernikov, A.; Ruppert, C.; Hill, H. M.; Rigosi, A. F.; Heinz, T. F. Population inversion and giant bandgap renormalization in atomically thin WS₂ layers. *Nat Photon* **2015**, *9*, 466-470.
- (225) Gao, Y.; Weidman, M. C.; Tisdale, W. A. CdSe Nanoplatelet Films with Controlled Orientation of their Transition Dipole Moment. *Nano Lett.* **2017**, *17*, 3837-3843.
- (226) Asada, M.; Miyamoto, Y.; Suematsu, Y. Gain and the threshold of three-dimensional quantum-box lasers. *Ieee J Quantum Elect* **1986**, *22*, 1915-1921.
- (227) Coleman, J. J.; Young, J. D.; Garg, A. Semiconductor Quantum Dot Lasers: A Tutorial. *Journal of Lightwave Technology* **2011**, *29*, 499-510.
- (228) Fan, F.; Voznyy, O.; Sabatini, R. P.; Bicanic, K. T.; Adachi, M. M.; McBride, J. R.; Reid, K. R.; Park, Y.-S.; Li, X.; Jain, A.; Quintero-Bermudez, R.; Saravanapavanantham, M.; Liu, M.; Korkusinski, M.; Hawrylak, P.; Klimov, V. I.; Rosenthal, S. J.; Hoogland, S.; Sargent, E. H. Continuous-wave lasing in colloidal quantum dot solids enabled by facet-selective epitaxy. *Nature* **2017**, *544*, 75-79.
- (229) Iwan, M.; Gabriele, R.; Raquel, G.; Zeger, H.; Thilo, S.; F., M. R. Nearly Temperature - Independent Threshold for Amplified Spontaneous Emission in Colloidal CdSe/CdS Quantum Dot - in - Rods. *Adv. Mater.* **2012**, *24*, OP231-OP235.
- (230) Li, Q.; Lian, T. A model for optical gain in colloidal nanoplatelets. *Chemical Science* **2018**, *9*, 728-734.
- (231) Guzelurk, B.; Kelestemur, Y.; Olutas, M.; Li, Q.; Lian, T.; Demir, H. V. High-Efficiency Optical Gain in Type-II Semiconductor Nanocrystals of Alloyed Colloidal Quantum

Wells. *J. Phys. Chem. Lett.* **2017**, *8*, 5317-5324.

(232) Griffin, G. B.; Ithurria, S.; Dolzhenkov, D. S.; Linkin, A.; Talapin, D. V.; Engel, G. S. Two-dimensional electronic spectroscopy of CdSe nanoparticles at very low pulse power. *J. Chem. Phys.* **2013**, *138*, 014705.

(233) Caram, J. R.; Zheng, H.; Dahlberg, P. D.; Rolczynski, B. S.; Griffin, G. B.; Dolzhenkov, D. S.; Talapin, D. V.; Engel, G. S. Exploring size and state dynamics in CdSe quantum dots using two-dimensional electronic spectroscopy. *J. Chem. Phys.* **2014**, *140*, 084701.

(234) Cassette, E.; Pensack, R. D.; Mahler, B.; Scholes, G. D. Room-temperature exciton coherence and dephasing in two-dimensional nanostructures. *Nat. Commun.* **2015**, *6*, 6086.

(235) Rowland, C. E.; Fedin, I.; Zhang, H.; Gray, S. K.; Govorov, A. O.; Talapin, D. V.; Schaller, R. D. Picosecond energy transfer and multiexciton transfer outpaces Auger recombination in binary CdSe nanoplatelet solids. *Nat. Mater.* **2015**, *14*, 484.

(236) Varshni, Y. P. Temperature dependence of the energy gap in semiconductors. *Physica* **1967**, *34*, 149-154.

(237) Diroll, B. T.; Fedin, I.; Darancet, P.; Talapin, D. V.; Schaller, R. D. Surface-Area-Dependent Electron Transfer Between Isoenergetic 2D Quantum Wells and a Molecular Acceptor. *J. Am. Chem. Soc.* **2016**, *138*, 11109-11112.

(238) Olutas, M.; Guzelturk, B.; Kelestemur, Y.; Yeltik, A.; Delikanli, S.; Demir, H. V. Lateral Size-Dependent Spontaneous and Stimulated Emission Properties in Colloidal CdSe Nanoplatelets. *ACS Nano* **2015**, *9*, 5041-5050.

(239) Hunsche, S.; Dekorsy, T.; Klimov, V.; Kurz, H. Ultrafast dynamics of carrier-induced absorption changes in highly-excited CdSe nanocrystals. *Applied Physics B* **1996**, *62*, 3-10.

(240) Cassette, E.; Pedetti, S.; Mahler, B.; Ithurria, S.; Dubertret, B.; Scholes, G. Ultrafast exciton dynamics in 2D in-plane hetero-nanostructures: delocalization and charge transfer. *Phys. Chem. Chem. Phys.* **2017**, *19*, 8373-8379.

- (241) Morgan, D. P.; Maddux, C. J. A.; Kelley, D. F. Transient Absorption Spectroscopy of CdSe Nanoplatelets. *J. Phys. Chem. C* **2018**, *122*, 23772-23779.
- (242) Shornikova, E. V.; Biadala, L.; Yakovlev, D. R.; Sapega, V. F.; Kusrayev, Y. G.; Mitioglu, A. A.; Ballottin, M. V.; Christianen, P. C. M.; Belykh, V. V.; Kochiev, M. V.; Sibeldin, N. N.; Golovatenko, A. A.; Rodina, A. V.; Gippius, N. A.; Kuntzmann, A.; Jiang, Y.; Nasilowski, M.; Dubertret, B.; Bayer, M. Addressing the exciton fine structure in colloidal nanocrystals: the case of CdSe nanoplatelets. *Nanoscale* **2018**, *10*, 646-656.
- (243) Yang, Y.; Ostrowski, D. P.; France, R. M.; Zhu, K.; van de Lagemaat, J.; Luther, J. M.; Beard, M. C. Observation of a hot-phonon bottleneck in lead-iodide perovskites. *Nat Photon* **2016**, *10*, 53-59.
- (244) Young, K. F.; Frederikse, H. P. R. Compilation of the Static Dielectric Constant of Inorganic Solids. *Journal of Physical and Chemical Reference Data* **1973**, *2*, 313-410.
- (245) Rodina, A. V.; Golovatenko, A. A.; Shornikova, E. V.; Yakovlev, D. R.; Efros, A. L. Effect of Dangling Bond Spins on the Dark Exciton Recombination and Spin Polarization in CdSe Colloidal Nanostructures. *Journal of Electronic Materials* **2018**, *47*, 4338-4344.
- (246) Mann, C.; Hertel, T. 13 nm Exciton Size in (6,5) Single-Wall Carbon Nanotubes. *J. Phys. Chem. Lett.* **2016**, 2276-2280.
- (247) Luer, L.; Hoseinkhani, S.; Polli, D.; Crochet, J.; Hertel, T.; Lanzani, G. Size and mobility of excitons in (6, 5) carbon nanotubes. *Nat Phys* **2009**, *5*, 54-58.
- (248) Pankove, J. Temperature dependence of emission efficiency and lasing threshold in laser diodes. *Ieee J Quantum Elect* **1968**, *4*, 119-122.
- (249) Ettenberg, M.; Nuese, C. J.; Kressel, H. The temperature dependence of threshold current for double - heterojunction lasers. *J. Appl. Phys.* **1979**, *50*, 2949-2950.
- (250) Schnabel, R. F.; Zimmermann, R.; Bimberg, D.; Nickel, H.; Losch, R.; Schlapp, W. Influence of Exciton Localization on Recombination Line-Shapes - Inxgal-Xas/Gaas

Quantum-Wells as a Model. *Phys. Rev. B* **1992**, *46*, 9873-9876.

(251) Leosson, K.; Jensen, J. R.; Langbein, W.; Hvam, J. M. Exciton localization and interface roughness in growth-interrupted GaAs/AlAs quantum wells. *Phys. Rev. B* **2000**, *61*, 10322-10329.

(252) Hill, H. M.; Rigosi, A. F.; Roquelet, C.; Chernikov, A.; Berkelbach, T. C.; Reichman, D. R.; Hybertsen, M. S.; Brus, L. E.; Heinz, T. F. Observation of Excitonic Rydberg States in Monolayer MoS₂ and WS₂ by Photoluminescence Excitation Spectroscopy. *Nano Lett.* **2015**, *15*, 2992-2997.

(253) Sacra, A.; Norris, D. J.; Murray, C. B.; Bawendi, M. G. Stark spectroscopy of CdSe nanocrystallites: The significance of transition linewidths. *J. Chem. Phys.* **1995**, *103*, 5236.

(254) Dielectric constant. <http://macro.lsu.edu/howto/solvents/Dielectric Constant .htm>

(255) Pedetti, S.; Nadal, B.; Lhuillier, E.; Mahler, B.; Bouet, C.; Abecassis, B.; Xu, X. Z.; Dubertret, B. Optimized Synthesis of CdTe Nanoplatelets and Photoresponse of CdTe Nanoplatelets Films. *Chem. Mat.* **2013**, *25*, 2455-2462.

(256) Lewis, N. S.; Nocera, D. G. Powering the planet: Chemical challenges in solar energy utilization. *Proc. Natl. Acad. Sci.* **2006**, *103*, 15729-15735.

(257) Han, Z.; Qiu, F.; Eisenberg, R.; Holland, P. L.; Krauss, T. D. Robust Photogeneration of H₂ in Water Using Semiconductor Nanocrystals and a Nickel Catalyst. *Science* **2012**, *338*, 1321-1324.

(258) Chai, Z.; Zeng, T.-T.; Li, Q.; Lu, L.-Q.; Xiao, W.-J.; Xu, D. Efficient Visible Light-Driven Splitting of Alcohols into Hydrogen and Corresponding Carbonyl Compounds over a Ni-Modified CdS Photocatalyst. *J. Am. Chem. Soc.* **2016**, *138*, 10128-10131.

(259) Kalisman, P.; Nakibli, Y.; Amirav, L. Perfect Photon-to-Hydrogen Conversion Efficiency. *Nano Lett.* **2016**, *16*, 1771-1781.

(260) Berr, M.; Vaneski, A.; Susha, A. S.; Rodriguez-Fernandez, J.; Doblinger, M.; Jackel, F.;

Rogach, A. L.; Feldmann, J. Colloidal CdS Nanorods Decorated with Subnanometer Sized Pt Clusters for Photocatalytic Hydrogen Generation. *Appl. Phys. Lett.* **2010**, *97*, 093108-3.

(261) Berr, M. J.; Wagner, P.; Fischbach, S.; Vaneski, A.; Schneider, J.; Susha, A. S.; Rogach, A. L.; Jackel, F.; Feldmann, J. Hole scavenger redox potentials determine quantum efficiency and stability of Pt-decorated CdS nanorods for photocatalytic hydrogen generation. *Appl. Phys. Lett.* **2012**, *100*, 223903.

(262) Berr, M. J.; Schweinberger, F. F.; Döblinger, M.; Sanwald, K. E.; Wolff, C.; Breimeier, J.; Crampton, A. S.; Ridge, C. J.; Tschurl, M.; Heiz, U.; Jäckel, F.; Feldmann, J. Size-Selected Subnanometer Cluster Catalysts on Semiconductor Nanocrystal Films for Atomic Scale Insight into Photocatalysis. *Nano Lett.* **2012**, *12*, 5903-5906.

(263) Khon, E.; Lambright, K.; Khnayer, R. S.; Moroz, P.; Perera, D.; Butaeva, E.; Lambright, S.; Castellano, F. N.; Zamkov, M. Improving the Catalytic Activity of Semiconductor Nanocrystals through Selective Domain Etching. *Nano Lett.* **2013**, *13*, 2016-2023.

(264) Tongying, P.; Plashnitsa, V. V.; Petchsang, N.; Vietmeyer, F.; Ferraudi, G. J.; Krylova, G.; Kuno, M. Photocatalytic Hydrogen Generation Efficiencies in One-Dimensional CdSe Heterostructures. *J. Phys. Chem. Lett.* **2012**, 3234-3240.

(265) Bang, J. U.; Lee, S. J.; Jang, J. S.; Choi, W.; Song, H. Geometric Effect of Single or Double Metal-Tipped CdSe Nanorods on Photocatalytic H₂ Generation. *J. Phys. Chem. Lett.* **2012**, *3*, 3781-3785.

(266) Elmalem, E.; Saunders, A. E.; Costi, R.; Salant, A.; Banin, U. Growth of Photocatalytic CdSe–Pt Nanorods and Nanonets. *Adv. Mater.* **2008**, *20*, 4312-4317.

(267) Li, Z.; Peng, X. Size/Shape-Controlled Synthesis of Colloidal CdSe Quantum Disks: Ligand and Temperature Effects. *J. Am. Chem. Soc.* **2011**, *133*, 6578-6586.

(268) Nasilowski, M.; Mahler, B.; Lhuillier, E.; Ithurria, S.; Dubertret, B. Two-Dimensional

Colloidal Nanocrystals. *Chem. Rev.* **2016**, *116*, 10934-10982.

(269) Wu, K.; Du, Y.; Tang, H.; Chen, Z.; Lian, T. Efficient Extraction of Trapped Holes from Colloidal CdS Nanorods. *J. Am. Chem. Soc.* **2015**, *137*, 10224-10230.

(270) Riedinger, A.; Ott, F. D.; Mule, A.; Mazzotti, S.; Knusel, P. N.; Kress, S. J. P.; Prins, F.; Erwin, S. C.; Norris, D. J. An intrinsic growth instability in isotropic materials leads to quasi-two-dimensional nanoplatelets. *Nat Mater* **2017**, *16*, 743-748.

(271) Okuhata, T.; Tamai, N. Face-Dependent Electron Transfer in CdSe Nanoplatelet–Methyl Viologen Complexes. *J. Phys. Chem. C* **2016**, *120*, 17052-17059.

(272) Nakibli, Y.; Mazal, Y.; Dubi, Y.; Wächtler, M.; Amirav, L. Size Matters: Cocatalyst Size Effect on Charge Transfer and Photocatalytic Activity. *Nano Lett.* **2018**, *18*, 357-364.

(273) Nakibli, Y.; Kalisman, P.; Amirav, L. Less Is More: The Case of Metal Cocatalysts. *J. Phys. Chem. Lett.* **2015**, *6*, 2265-2268.

(274) Matsumoto, H.; Sakata, T.; Mori, H.; Yoneyama, H. Preparation of monodisperse CdS nanocrystals by size selective photocorrosion. *J. Phys. Chem.* **1996**, *100*, 13781-13785.

(275) Simon, T.; Carlson, M. T.; Stolarczyk, J. K.; Feldmann, J. Electron Transfer Rate vs Recombination Losses in Photocatalytic H₂ Generation on Pt-Decorated CdS Nanorods. *ACS Energy Letters* **2016**, *1*, 1137-1142.

(276) Garg, P.; Kumar, S.; Choudhuri, I.; Mahata, A.; Pathak, B. Hexagonal Planar CdS Monolayer Sheet for Visible Light Photocatalysis. *J. Phys. Chem. C* **2016**, *120*, 7052-7060.

(277) Bao, N.; Shen, L.; Takata, T.; Domen, K. Self-Templated Synthesis of Nanoporous CdS Nanostructures for Highly Efficient Photocatalytic Hydrogen Production under Visible Light. *Chem. Mat.* **2008**, *20*, 110-117.

(278) Reynolds, G. A.; Drexhage, K. H. New coumarin dyes with rigidized structure for flashlamp-pumped dye lasers. *Opt. Commun.* **1975**, *13*, 222-225.

(279) Saunders, A. E.; Ghezelbash, A.; Sood, P.; Korgel, B. A. Synthesis of High Aspect Ratio

Quantum-Size CdS Nanorods and Their Surface-Dependent Photoluminescence. *Langmuir* **2008**, *24*, 9043-9049.

(280) Zhu, H.; Yang, Y.; Hyeon-Deuk, K.; Califano, M.; Song, N.; Wang, Y.; Zhang, W.; Prezhdo, O. V.; Lian, T. Auger-Assisted Electron Transfer from Photoexcited Semiconductor Quantum Dots. *Nano Lett.* **2013**, *14*, 1263-1269.

(281) Li, X.-B.; Li, Z.-J.; Gao, Y.-J.; Meng, Q.-Y.; Yu, S.; Weiss, R. G.; Tung, C.-H.; Wu, L.-Z. Mechanistic Insights into the Interface-Directed Transformation of Thiols into Disulfides and Molecular Hydrogen by Visible-Light Irradiation of Quantum Dots. *Angew. Chem. Int. Ed.* **2014**, *53*, 2085-2089.

(282) Jensen, S. C.; Bettis Homan, S.; Weiss, E. A. Photocatalytic Conversion of Nitrobenzene to Aniline through Sequential Proton-Coupled One-Electron Transfers from a Cadmium Sulfide Quantum Dot. *J. Am. Chem. Soc.* **2016**, *138*, 1591-1600.

(283) Zhao, L.-M.; Meng, Q.-Y.; Fan, X.-B.; Ye, C.; Li, X.-B.; Chen, B.; Ramamurthy, V.; Tung, C.-H.; Wu, L.-Z. Photocatalysis with Quantum Dots and Visible Light: Selective and Efficient Oxidation of Alcohols to Carbonyl Compounds through a Radical Relay Process in Water. *Angew. Chem. Int. Ed.* **2017**, *56*, 3020-3024.

(284) Utterback, J. K.; Grennell, A. N.; Wilker, M. B.; Pearce, O. M.; Eaves, J. D.; Dukovic, G. Observation of trapped-hole diffusion on the surfaces of CdS nanorods. *Nat Chem* **2016**, *8*, 1061-1066.

(285) Grennell, A. N.; Utterback, J. K.; Pearce, O. M.; Wilker, M. B.; Dukovic, G. Relationships between Exciton Dissociation and Slow Recombination within ZnSe/CdS and CdSe/CdS Dot-in-Rod Heterostructures. *Nano Lett.* **2017**, *17*, 3764-3774.

(286) Cline, R. P.; Utterback, J. K.; Strong, S. E.; Dukovic, G.; Eaves, J. D. On the Nature of Trapped-Hole States in CdS Nanocrystals and the Mechanism of Their Diffusion. *J. Phys. Chem. Lett.* **2018**, *9*, 3532-3537.

- (287) Utterback, J. K.; Hamby, H.; Pearce, O. M.; Eaves, J. D.; Dukovic, G. Trapped-Hole Diffusion in Photoexcited CdSe Nanorods. *J. Phys. Chem. C* **2018**, *122*, 16974-16982.
- (288) Morris-Cohen, A. J.; Frederick, M. T.; Cass, L. C.; Weiss, E. A. Simultaneous Determination of the Adsorption Constant and the Photoinduced Electron Transfer Rate for a Cds Quantum Dot–Viologen Complex. *J. Am. Chem. Soc.* **2011**, *133*, 10146-10154.
- (289) Wu, K.; Liang, G.; Shang, Q.; Ren, Y.; Kong, D.; Lian, T. Ultrafast Interfacial Electron and Hole Transfer from CsPbBr₃ Perovskite Quantum Dots. *J. Am. Chem. Soc.* **2015**, *137*, 12792-12795.
- (290) Stranks, S. D.; Snaith, H. J. Metal-halide perovskites for photovoltaic and light-emitting devices. *Nat. Nanotechnol.* **2015**, *10*, 391-402.
- (291) Sutherland, B. R.; Sargent, E. H. Perovskite photonic sources. *Nat Photon* **2016**, *10*, 295-302.
- (292) Zhao, Y.; Zhu, K. Organic-inorganic hybrid lead halide perovskites for optoelectronic and electronic applications. *Chem. Soc. Rev.* **2016**, *45*, 655-689.
- (293) Manser, J. S.; Christians, J. A.; Kamat, P. V. Intriguing Optoelectronic Properties of Metal Halide Perovskites. *Chem. Rev.* **2016**, *116*, 12956-13008.
- (294) Tan, Z. K.; Moghaddam, R. S.; Lai, M. L.; Docampo, P.; Higler, R.; Deschler, F.; Price, M.; Sadhanala, A.; Pazos, L. M.; Credginton, D.; Hanusch, F.; Bein, T.; Snaith, H. J.; Friend, R. H. Bright light-emitting diodes based on organometal halide perovskite. *Nat. Nanotechnol.* **2014**, *9*, 687-692.
- (295) Cho, H. C.; Jeong, S. H.; Park, M. H.; Kim, Y. H.; Wolf, C.; Lee, C. L.; Heo, J. H.; Sadhanala, A.; Myoung, N.; Yoo, S.; Im, S. H.; Friend, R. H.; Lee, T. W. Overcoming the electroluminescence efficiency limitations of perovskite light-emitting diodes. *Science* **2015**, *350*, 1222-1225.
- (296) Song, J. Z.; Li, J. H.; Li, X. M.; Xu, L. M.; Dong, Y. H.; Zeng, H. B. Quantum Dot

Light-Emitting Diodes Based on Inorganic Perovskite Cesium Lead Halides (CsPbX₃). *Adv. Mater.* **2015**, *27*, 7162-7167.

(297) Wang, J. P.; Wang, N. N.; Jin, Y. Z.; Si, J. J.; Tan, Z. K.; Du, H.; Cheng, L.; Dai, X. L.; Bai, S.; He, H. P.; Ye, Z. Z.; Lai, M. L.; Friend, R. H.; Huang, W. Interfacial Control Toward Efficient and Low-Voltage Perovskite Light-Emitting Diodes. *Adv. Mater.* **2015**, *27*, 2311-2316.

(298) Wang, N.; Cheng, L.; Ge, R.; Zhang, S.; Miao, Y.; Zou, W.; Yi, C.; Sun, Y.; Cao, Y.; Yang, R.; Wei, Y.; Guo, Q.; Ke, Y.; Yu, M.; Jin, Y.; Liu, Y.; Ding, Q.; Di, D.; Yang, L.; Xing, G.; Tian, H.; Jin, C.; Gao, F.; Friend, R. H.; Wang, J.; Huang, W. Perovskite light-emitting diodes based on solution-processed self-organized multiple quantum wells. *Nat Photon* **2016**, *10*, 699-704.

(299) Zhang, X. Y.; Lin, H.; Huang, H.; Reckmeier, C.; Zhang, Y.; Choy, W. C. H.; Rogach, A. L. Enhancing the Brightness of Cesium Lead Halide Perovskite Nanocrystal Based Green Light-Emitting Devices through the Interface Engineering with Perfluorinated Ionomer. *Nano Lett.* **2016**, *16*, 1415-1420.

(300) Lee, J.-W.; Choi, Y. J.; Yang, J.-M.; Ham, S.; Jeon, S. K.; Lee, J. Y.; Song, Y.-H.; Ji, E. K.; Yoon, D.-H.; Seo, S.; Shin, H.; Han, G. S.; Jung, H. S.; Kim, D.; Park, N.-G. In-Situ Formed Type I Nanocrystalline Perovskite Film for Highly Efficient Light-Emitting Diode. *ACS Nano* **2017**, *11*, 3311-3319.

(301) Xiao, Z.; Kerner, R. A.; Zhao, L.; Tran, N. L.; Lee, K. M.; Koh, T.-W.; Scholes, G. D.; Rand, B. P. Efficient perovskite light-emitting diodes featuring nanometre-sized crystallites. *Nat Photon* **2017**, *11*, 108-115.

(302) Zhang, L.; Yang, X.; Jiang, Q.; Wang, P.; Yin, Z.; Zhang, X.; Tan, H.; Yang, Y.; Wei, M.; Sutherland, B. R.; Sargent, E. H.; You, J. Ultra-bright and highly efficient inorganic based perovskite light-emitting diodes. *Nat. Commun.* **2017**, *8*, 15640.

(303) Xing, G. C.; Mathews, N.; Lim, S. S.; Yantara, N.; Liu, X. F.; Sabba, D.; Gratzel, M.;

Mhaisalkar, S.; Sum, T. C. Low-temperature solution-processed wavelength-tunable perovskites for lasing. *Nat. Mater.* **2014**, *13*, 476-480.

(304) Stranks, S. D.; Wood, S. M.; Wojciechowski, K.; Deschler, F.; Saliba, M.; Khandelwal, H.; Patel, J. B.; Elston, S. J.; Herz, L. M.; Johnston, M. B.; Schenning, A. P. H. J.; Debije, M. G.; Riede, M. K.; Morris, S. M.; Snaith, H. J. Enhanced Amplified Spontaneous Emission in Perovskites Using a Flexible Cholesteric Liquid Crystal Reflector. *Nano Lett.* **2015**, *15*, 4935-4941.

(305) Wang, Y.; Li, X.; Song, J.; Xiao, L.; Zeng, H.; Sun, H. All-Inorganic Colloidal Perovskite Quantum Dots: A New Class of Lasing Materials with Favorable Characteristics. *Adv. Mater.* **2015**, *27*, 7101-7108.

(306) Yakunin, S.; Protesescu, L.; Krieg, F.; Bodnarchuk, M. I.; Nedelcu, G.; Humer, M.; De Luca, G.; Fiebig, M.; Heiss, W.; Kovalenko, M. V. Low-threshold amplified spontaneous emission and lasing from colloidal nanocrystals of caesium lead halide perovskites. *Nat. Commun.* **2015**, *6*, 8056.

(307) Fu, Y.; Zhu, H.; Stoumpos, C. C.; Ding, Q.; Wang, J.; Kanatzidis, M. G.; Zhu, X.; Jin, S. Broad Wavelength Tunable Robust Lasing from Single-Crystal Nanowires of Cesium Lead Halide Perovskites (CsPbX_3 , $X = \text{Cl, Br, I}$). *ACS Nano* **2016**, *10*, 7963-7972.

(308) Xu, Y.; Chen, Q.; Zhang, C.; Wang, R.; Wu, H.; Zhang, X.; Xing, G.; Yu, W. W.; Wang, X.; Zhang, Y.; Xiao, M. Two-Photon-Pumped Perovskite Semiconductor Nanocrystal Lasers. *J. Am. Chem. Soc.* **2016**, *138*, 3761-3768.

(309) Zheng, F.; Tan, L. Z.; Liu, S.; Rappe, A. M. Rashba Spin–Orbit Coupling Enhanced Carrier Lifetime in $\text{CH}_3\text{NH}_3\text{PbI}_3$. *Nano Lett.* **2015**, *15*, 7794-7800.

(310) Hutter, E. M.; Gelvez-Rueda, M. C.; Osherov, A.; Bulovic, V.; Grozema, F. C.; Stranks, S. D.; Savenije, T. J. Direct-indirect character of the bandgap in methylammonium lead iodide perovskite. *Nat Mater* **2016**, *16*, 115-120.

- (311) Tang, B.; Dong, H.; Sun, L.; Zheng, W.; Wang, Q.; Sun, F.; Jiang, X.; Pan, A.; Zhang, L. Single-Mode Lasers Based on Cesium Lead Halide Perovskite Submicron Spheres. *ACS Nano* **2017**, *11*, 10681-10688.
- (312) Deschler, F.; Price, M.; Pathak, S.; Klintberg, L. E.; Jarausch, D.-D.; Higler, R.; Hüttner, S.; Leijtens, T.; Stranks, S. D.; Snaith, H. J.; Atatüre, M.; Phillips, R. T.; Friend, R. H. High Photoluminescence Efficiency and Optically Pumped Lasing in Solution-Processed Mixed Halide Perovskite Semiconductors. *J. Phys. Chem. Lett.* **2014**, *5*, 1421-1426.
- (313) Zhu, H.; Fu, Y.; Meng, F.; Wu, X.; Gong, Z.; Ding, Q.; Gustafsson, M. V.; Trinh, M. T.; Jin, S.; Zhu, X. Y. Lead halide perovskite nanowire lasers with low lasing thresholds and high quality factors. *Nat. Mater.* **2015**, *14*, 636.
- (314) Fu, Y.; Zhu, H.; Schrader, A. W.; Liang, D.; Ding, Q.; Joshi, P.; Hwang, L.; Zhu, X. Y.; Jin, S. Nanowire Lasers of Formamidinium Lead Halide Perovskites and Their Stabilized Alloys with Improved Stability. *Nano Lett.* **2016**, *16*, 1000-1008.
- (315) Zhang, N.; Wang, K.; Wei, H.; Gu, Z.; Sun, W.; Li, J.; Xiao, S.; Song, Q. Postsynthetic and Selective Control of Lead Halide Perovskite Microlasers. *J. Phys. Chem. Lett.* **2016**, 3886-3891.
- (316) Liu, P.; He, X.; Ren, J.; Liao, Q.; Yao, J.; Fu, H. Organic-Inorganic Hybrid Perovskite Nanowire Laser Arrays. *ACS Nano* **2017**, *11*, 5766-5773.
- (317) Green, M. A.; Emery, K.; Hishikawa, Y.; Warta, W. Solar cell efficiency tables (version 37). *Progress in Photovoltaics: Research and Applications* **2011**, *19*, 84-92.
- (318) Correa-Baena, J.-P.; Saliba, M.; Buonassisi, T.; Grätzel, M.; Abate, A.; Tress, W.; Hagfeldt, A. Promises and challenges of perovskite solar cells. *Science* **2017**, *358*, 739-744.
- (319) Park, N.-G. Organometal Perovskite Light Absorbers Toward a 20% Efficiency Low-Cost Solid-State Mesoscopic Solar Cell. *J. Phys. Chem. Lett.* **2013**, *4*, 2423-2429.
- (320) Yang, W. S.; Noh, J. H.; Jeon, N. J.; Kim, Y. C.; Ryu, S.; Seo, J.; Seok, S. I. High-

performance photovoltaic perovskite layers fabricated through intramolecular exchange. *Science* **2015**, *348*, 1234-1237.

(321) Anaraki, E. H.; Kermanpur, A.; Steier, L.; Domanski, K.; Matsui, T.; Tress, W.; Saliba, M.; Abate, A.; Gratzel, M.; Hagfeldt, A.; Correa-Baena, J. P. Highly efficient and stable planar perovskite solar cells by solution-processed tin oxide. *Energy & Environ. Sci.* **2016**, *9*, 3128-3134.

(322) Bi, D. Q.; Tress, W.; Dar, M. I.; Gao, P.; Luo, J. S.; Renevier, C.; Schenk, K.; Abate, A.; Giordano, F.; Baena, J. P. C.; Decoppet, J. D.; Zakeeruddin, S. M.; Nazeeruddin, M. K.; Gratzel, M.; Hagfeldt, A. Efficient luminescent solar cells based on tailored mixed-cation perovskites. *Sci Adv* **2016**, *2*, 1501170.

(323) Momblona, C.; Gil-Escrig, L.; Bandiello, E.; Hutter, E. M.; Sessolo, M.; Lederer, K.; Blochwitz-Nimoth, J.; Bolink, H. J. Efficient vacuum deposited p-i-n and n-i-p perovskite solar cells employing doped charge transport layers. *Energy & Environ. Sci.* **2016**, *9*, 3456-3463.

(324) Saliba, M.; Matsui, T.; Domanski, K.; Seo, J. Y.; Ummadisingu, A.; Zakeeruddin, S. M.; Correa-Baena, J. P.; Tress, W. R.; Abate, A.; Hagfeldt, A.; Gratzel, M. Incorporation of rubidium cations into perovskite solar cells improves photovoltaic performance. *Science* **2016**, *354*, 206-209.

(325) Arora, N.; Dar, M. I.; Hinderhofer, A.; Pellet, N.; Schreiber, F.; Zakeeruddin, S. M.; Grätzel, M. Perovskite solar cells with CuSCN hole extraction layers yield stabilized efficiencies greater than 20%. *Science* **2017**, *358*, 768-771.

(326) Shin, S. S.; Yeom, E. J.; Yang, W. S.; Hur, S.; Kim, M. G.; Im, J.; Seo, J.; Noh, J. H.; Seok, S. I. Colloidally prepared La-doped BaSnO₃ electrodes for efficient, photostable perovskite solar cells. *Science* **2017**, *356*, 167-171.

(327) Stolterfoht, M.; Wolff, C. M.; Amir, Y.; Paulke, A.; Perdigon-Toro, L.; Caprioglio, P.; Neher, D. Approaching the fill factor Shockley-Queisser limit in stable, dopant-free triple

cation perovskite solar cells. *Energy & Environ. Sci.* **2017**, *10*, 1530-1539.

(328) Tan, H. R.; Jain, A.; Voznyy, O.; Lan, X. Z.; de Arquer, F. P. G.; Fan, J. Z.; Quintero-Bermudez, R.; Yuan, M. J.; Zhang, B.; Zhao, Y. C.; Fan, F. J.; Li, P. C.; Quan, L. N.; Zhao, Y. B.; Lu, Z. H.; Yang, Z. Y.; Hoogland, S.; Sargent, E. H. Efficient and stable solution-processed planar perovskite solar cells via contact passivation. *Science* **2017**, *355*, 722-726.

(329) Yang, W. S.; Park, B. W.; Jung, E. H.; Jeon, N. J.; Kim, Y. C.; Lee, D. U.; Shin, S. S.; Seo, J.; Kim, E. K.; Noh, J. H.; Seok, S. I. Iodide management in formamidinium-lead-halide-based perovskite layers for efficient solar cells. *Science* **2017**, *356*, 1376-1379.

(330) Sun, S.; Yuan, D.; Xu, Y.; Wang, A.; Deng, Z. Ligand-Mediated Synthesis of Shape-Controlled Cesium Lead Halide Perovskite Nanocrystals via Reprecipitation Process at Room Temperature. *ACS Nano* **2016**, *10*, 3648-3657.

(331) Shamsi, J.; Dang, Z.; Bianchini, P.; Canale, C.; Stasio, F. D.; Brescia, R.; Prato, M.; Manna, L. Colloidal Synthesis of Quantum Confined Single Crystal CsPbBr₃ Nanosheets with Lateral Size Control up to the Micrometer Range. *J. Am. Chem. Soc.* **2016**, *138*, 7240-7243.

(332) Weidman, M. C.; Seitz, M.; Stranks, S. D.; Tisdale, W. A. Highly Tunable Colloidal Perovskite Nanoplatelets through Variable Cation, Metal, and Halide Composition. *ACS Nano* **2016**, *10*, 7830-7839.

(333) Weidman, M. C.; Goodman, A. J.; Tisdale, W. A. Colloidal Halide Perovskite Nanoplatelets: An Exciting New Class of Semiconductor Nanomaterials. *Chem. Mat.* **2017**, *29*, 5019-5030.

(334) Protesescu, L.; Yakunin, S.; Bodnarchuk, M. I.; Krieg, F.; Caputo, R.; Hendon, C. H.; Yang, R. X.; Walsh, A.; Kovalenko, M. V. Nanocrystals of Cesium Lead Halide Perovskites (CsPbX₃, X = Cl, Br, and I): Novel Optoelectronic Materials Showing Bright Emission with Wide Color Gamut. *Nano Lett.* **2015**, *15*, 3692-3696.

(335) Makarov, N. S.; Guo, S.; Isaienko, O.; Liu, W.; Robel, I.; Klimov, V. I. Spectral and

Dynamical Properties of Single Excitons, Biexcitons, and Trions in Cesium–Lead-Halide Perovskite Quantum Dots. *Nano Lett.* **2016**, *16*, 2349-2362.

(336) De Roo, J.; Ibáñez, M.; Geiregat, P.; Nedelcu, G.; Walravens, W.; Maes, J.; Martins, J. C.; Van Driessche, I.; Kovalenko, M. V.; Hens, Z. Highly Dynamic Ligand Binding and Light Absorption Coefficient of Cesium Lead Bromide Perovskite Nanocrystals. *ACS Nano* **2016**, *10*, 2071-2081.

(337) Zhang, Q.; Chu, L.; Zhou, F.; Ji, W.; Eda, G. Excitonic Properties of Chemically Synthesized 2D Organic–Inorganic Hybrid Perovskite Nanosheets. *Adv. Mater.* **2018**, *30*, 1704055.

(338) Zhao, X.; Kitagawa, T. Solvent effects of 1,4-benzoquinone and its anion radicals probed by resonance Raman and absorption spectra and their correlation with redox potentials. *Journal of Raman Spectroscopy* **1998**, *29*, 773-780.

(339) Klimov, V.; Hunsche, S.; Kurz, H. Biexciton effects in femtosecond nonlinear transmission of semiconductor quantum dots. *Phys. Rev. B* **1994**, *50*, 8110-8113.

(340) Hu, Y. Z.; Koch, S. W.; Lindberg, M.; Peyghambarian, N.; Pollock, E. L.; Abraham, F. F. Biexcitons in semiconductor quantum dots. *Phys. Rev. Lett.* **1990**, *64*, 1805-1807.

(341) Hintermayr, V. A.; Polavarapu, L.; Urban, A. S.; Feldmann, J. Accelerated Carrier Relaxation through Reduced Coulomb Screening in Two-Dimensional Halide Perovskite Nanoplatelets. *ACS Nano* **2018**, *12*, 10151-10158.

(342) Klimov, V.; Bolivar, P. H.; Kurz, H. Ultrafast carrier dynamics in semiconductor quantum dots. *Phys. Rev. B* **1996**, *53*, 1463-1467.

(343) Klimov, V. I.; Schwarz, C. J.; McBranch, D. W.; Leatherdale, C. A.; Bawendi, M. G. Ultrafast dynamics of inter- and intraband transitions in semiconductor nanocrystals: Implications for quantum-dot lasers. *Phys. Rev. B* **1999**, *60*, R2177-R2180.

(344) Song, N. H.; Zhu, H. M.; Jin, S. Y.; Lian, T. Q. Hole Transfer from Single Quantum

Dots. *ACS Nano* **2011**, *5*, 8750-8759.

(345) Song, N. H.; Zhu, H. M.; Jin, S. Y.; Zhan, W.; Lian, T. Q. Poisson-Distributed Electron-Transfer Dynamics from Single Quantum Dots to C60 Molecules. *ACS Nano* **2011**, *5*, 613-621.

(346) Wu, K. F.; Song, N. H.; Liu, Z.; Zhu, H. M.; Rodriguez-Cordoba, W.; Lian, T. Q. Interfacial Charge Separation and Recombination in InP and Quasi-Type II InP/CdS Core/Shell Quantum Dot-Molecular Acceptor Complexes. *J Phys Chem A* **2013**, *117*, 7561-7570.

(347) Congreve, D. N.; Weidman, M. C.; Seitz, M.; Paritmongkol, W.; Dahod, N. S.; Tisdale, W. A. Tunable Light-Emitting Diodes Utilizing Quantum-Confined Layered Perovskite Emitters. *ACS Photonics* **2017**, *4*, 476-481.

(348) Tsai, H.; Nie, W.; Blancon, J.-C.; Stoumpos, C. C.; Asadpour, R.; Harutyunyan, B.; Neukirch, A. J.; Verduzco, R.; Crochet, J. J.; Tretiak, S.; Pedesseau, L.; Even, J.; Alam, M. A.; Gupta, G.; Lou, J.; Ajayan, P. M.; Bedzyk, M. J.; Kanatzidis, M. G.; Mohite, A. D. High-efficiency two-dimensional Ruddlesden–Popper perovskite solar cells. *Nature* **2016**, *536*, 312.

(349) Bouet, C.; Mahler, B.; Nadal, B.; Abecassis, B.; Tessier, M. D.; Ithurria, S.; Xu, X. Z.; Dubertret, B. Two-Dimensional Growth of CdSe Nanocrystals, from Nanoplatelets to Nanosheets. *Chem. Mat.* **2013**, *25*, 639-645.

(350) Naskar, S.; Lübke, F.; Hamid, S.; Freytag, A.; Wolf, A.; Koch, J.; Ivanova, I.; Pfnür, H.; Dorfs, D.; Bahnemann, D. W.; Bigall, N. C. Synthesis of Ternary and Quaternary Au and Pt Decorated CdSe/CdS Heteronanosheet with Controllable Morphology. *Adv. Funct. Mater.* **2017**, *27*, 1604685.

(351) Xie, G.; Zhang, K.; Guo, B.; Liu, Q.; Fang, L.; Gong, J. R. Graphene-Based Materials for Hydrogen Generation from Light-Driven Water Splitting. *Adv. Mater.* **2013**, *25*, 3820-3839.

(352) Zhang, J.; Yu, J.; Jaroniec, M.; Gong, J. R. Noble Metal-Free Reduced Graphene Oxide-ZnxCd_{1-x}S Nanocomposite with Enhanced Solar Photocatalytic H₂-Production Performance. *Nano Lett.* **2012**, *12*, 4584-4589.

(353) Li, Q.; Guo, B.; Yu, J.; Ran, J.; Zhang, B.; Yan, H.; Gong, J. R. Highly Efficient Visible-Light-Driven Photocatalytic Hydrogen Production of CdS-Cluster-Decorated Graphene Nanosheets. *J. Am. Chem. Soc.* **2011**, *133*, 10878-10884.